SAINT-PETERSBURG UNIVERSITY

Bashmachnikov Igor Lvovich

SUBSURFACE MESOSCALE EDDIES AND THEIR MANIFESTATIONS AT THE SEA SURFACE

Scientific specialty 1.6.17. Oceanology

DISSERTATION
submitted for the degree of
the doctor of geographical sciences

Translation from Russian

Saint Petersburg

2024

TABLE OF CONTENTS

INTRODUCTION

The relevance of the research topic and the degree of its elaboration

Ocean eddies can be defined as coherent rotating highly nonlinear dynamic structures that exist at least during one revolution of a particle around the axis and transport both energy and mass. As a rule, eddies have a rounded shape, which minimizes the surface area for a fixed volume of its core. This minimizes the area of contact of an eddy with the environment and reduces the intensity of its dissipation.

Contribution of eddies to the large-scale ocean dynamics is very high. Eddies close the mass balance of the large-scale ocean circulation, disturbed under the influence of external forcing. Thus, eddy transport balances the mass flux forced by Ekman pumping in large-scale ocean circulation gyres, in the Antarctic Circumpolar Current, or the Beaufort Sea Gyre (Marshall and Speer, 2012; Koshlyakov and Tarakanov, 2011; Meneghello et al., 2017, 2018). Regionally, eddy transport links together different parts of the Meridional Overturning Circulation (MOC) by forming the Guiana Current which connects the North and South Atlantic, executing mass transport from the Indian Ocean to the Atlantic through the Agulhas leakage (Tomczak and Godfrey, 2003; Lumpkin and Speer, 2007; Buckley and Marshall, 2016; Malysheva et al., 2020) or being involved in the formation of deep water MOC return transport in the northwest Atlantic (Lozier, 2010; Bower et al., 2019). Eddies play a critical role in stabilizing the boundaries of the areas of deep convection (Visbeck et al., 1996; Kovalevsky et al., 2020), regulate the gradients of thermohaline characteristics in frontal zones, and, consequently, the intensity of the associated geostrophic currents (Maddison et al., 2015).

Eddies play a crucial role in the exchange of energy and enstrophy between different ocean scales and make a path down to the final dissipation of the kinetic ocean energy into heat. Accounting for the effect of negative viscosity arising from an interaction of mesoscale eddies with mean currents in the ocean models results in a noticeable increase in the velocity of the western boundary currents (Luo and Lo, 2000; Zhmur et al., 2023).

Danabasoglu et al. (1994) showed that replacing the standard parameterization of subgrid-scale processes using coefficients of horizontal turbulent diffusion with the isopycnal transport of the gradients thermohaline pulsation (simulation transport with mesoscale eddies) significantly modlfies the results of hydrodynamic modeling, bringing them closer to observations. In particular, with such parameterization, the model more accurately reproduces the intensity of the thermocline, temperature of deep waters, the MOC intensity, heat fluxes across the Antarctic Circumpolar Current, and the areas of deep convection. Bringing together a number of studies, mesoscale ocean eddies represent one of the critically important element of the large-scale ocean dynamics.

The kinetic energy of coherent mesoscale eddies is on average 2 orders of magnitude higher than the kinetic energy of large-scale circulation (Wyrtki et al., 1976; Wunsch, 2002; Wunsch and Ferrary, 2004; Cushman-Roisin and Beckers, 2011). Mesoscale eddies of unusually high intensity are mentioned in Ancient Greek literature (Charybdis in Homer's poem). Some intense eddies were further drown on medieval maps and served as the basis of legends (Mahlström in Mercator's cartographic atlas of the 16th century). However, a scientific studies of the role of eddies in ocean dynamics began only in the middle of the 20th century. These studies were based of full-scale *in situ* experiments of the second half of the 20th century, when relatively small areas of the ocean

were covered with ship observations with unprecedented spatio-temporal resolution, while simultaneously a large number of moorings were deployed. The most famous of these experiments are Polygon 1967 (the Indian Ocean, USSR), Polygon 1970 and Mesopolygon 1985 (the eastern subtropical Atlantic, USSR), MODE 1973 (the western subtropical Atlantic, USA), POLYMODE 1977-1979 (in the same area, USSR and USA), MEGAPOLYGON 1987 (the western part of the Pacific, USSR). Numerous eddies were further found in the Arctic Ocean (AO), although the presence of the continuous ice cover resulted in a lower level of eddy kinetic energy of the Arctic compared to other areas of the World Ocean (Belyakov and Volkov, 1980; Timmermans et al., 2008; Kondrick and al., 2016; Wang et al., 2020; Meneghello et al., 2021). The results of the above-mentioned *in situ* experiments made it possible describing the main characteristics of large mesoscale eddies and planetary waves in the ocean, and to discover a number of features of their dynamics (see, for example, Kort and Neumann, 1974; Foux, 1977; Grachev et al., 1982; Kort, 1988; Koshlyakov, Panteleev, 1988; Koshlyakov, Yaremchuk, 1988; Egorikhin et al., 1987; Belkin and Kostyanoy, 1992; Koshlyakov, 2020; Filyushkin and Kozhelupova, 2020; Zhmur et al., 2020). In particular, observations made it possible to identify the "dense packing" of eddies, or the lows of energy transfer across the ocean scales (Kamenkovich et al., 1987; Kort, 1988; Robinson, 1983; Maximenko et al., 2001; Neumann and Morozov, 2020). These observations also permitted laying the theoretical foundations of oceanic eddy dynamics (Nezlin, 1986; Kamenkovich et al., 1987; Monin and Zhikharev, 1990; Zyryanov, 1995; Zhmur, 2010; Cushman-Roisin and Beckers, 2011; Sokolovskiy and Verron, 2014; Zhmur et al., 2020, etc.).

The advent in satellite observations, especially in the satellite altimetry at the end of the twentieth century, opened a new era for massive study of mesoscale phenomena in the ocean, including planetary waves and eddies (Belonenko et al., 2004; Chelton et al., 2007, 2011). The results confirmed many characteristics of mesoscale eddies previously obtained on the basis of regional *in situ* observations. The recent massive analysis of satellite radar images (SAR) makes it possible to approach a massively study not only mesoscale, but also submesoscale ocean processes including submesoscale eddies (Atajanova et al., 2017; Kostianoy et al., 2018; Kozlov and Atadzhanova, 2021).

To study mesoscale eddies using satellite data, the vast majority of researchers use AVISO satellite altimetry maps, which are formed by interpolating along-track data from different satellites onto a regular grid. The distance between the adjacent tracks can reach 100 km, therefore, to identify eddies, the number of altimeters simultaneously operating in orbit is of fundamental importance. Modern AVISO data are provided with a spatial resolution of $0.25^o \times 0.25^o$ which is at the limit for detection mesoscale eddies, whose dynamic radii are typically within the range of 10-100 km (Johannessen et al., 1983, 1987; Sandven et al., 1991; Bondevik, 2011; Richards and Straneo, 2015; Yu et al., 2017; Wang et al., 2020). The first global assessments of mesoscale eddies (Chelton et al., 2011) were limited to the joint observation zone of the TOPEX/Poseidon and ERS series satellites (to 66° latitude), and did not cover the Arctic Ocean and a significant part of the Southern Ocean. Further comparison of satellite data with sea level observations from tide gauges in the Nordic Seas showed that, despite the absence of TOPEX/Poseidon satellite data, the AVISO altimetry error in this region does not exceed the error in tropical latitudes (Fu and Cazenave, 2001; Volkov and Pujol, 2012). This is due to the convergence of satellite tracks in the subpolar and polar regions, which partially compensates a decrease in the number of simultaneously operating altimeters in these areas.

Using AVISO satellite altimetry, statistics of the characteristics of mesoscale eddies (radii, peak sea level anomalies, nonlinearity indicator, eddy propagation velocity, etc.) were obtained. In particular, it was shown that the vast majority of mesoscale elliptical structures observed at the ocean surface (90% or more) have a nonlinearity indicator (the ratio of the azimuthal rotation velocity v_θ to the eddy propagation velocity V_m) $v_\theta/V_m > 1$, which characterizes these features as highly nonlinear waves or eddies (Chelton et al., 2011). Moreover, outside the tropics, approximately 50% of such structures had $v_\theta/V_m > 5$, which suggests the capture and transfer of mass by the core and is one of the main indicators of an eddy. In this regard, most mesoscale structures in the ocean, characterized by closed streamlines and which were previously interpreted as Rossby waves, start being interpreted as eddies. Most eddies form a fairly pronounced sea level anomaly (>5 cm for 60% of all recorded eddies and >10 cm for 25% of all recorded eddies), which can be identified in AVISO satellite altimetry. The average eddy radii increase from subpolar latitudes to the equator, although not as quickly as the Rossby deformation radius (*Rd),* and the sea level anomalies, on the contrary, decrease towards the equator. Tracking surface eddies with the satellite altimetry showed that about 60% of mesoscale eddies existed for more than 1-1.5 months, 30% – for more than 3-4 months, and only 10-20% of the most intense eddies existed for more than a year (Chelton et al., 2011). Further overall improvements in the number and accuracy of altimetry observations, the algorithms of signal corrections, an improved geoid model (Raj et al., 2018, 2020; Taburet et al., 2019), and advances in automatic eddy detection techniques for AVISO altimetry data have provided with a corrected spatial statistics of the properties of mesoscale eddies in tropical and temperate regions (Capet et al., 2014): almost 40% more eddies were identified and their average radius decreased, which, in particular, affected the estimates of eddy propagation velocities, the azimuthal velocity of eddies increased, increasing estimates of their kinetic energy by 80%. Similar statistics were obtained for high latitude regions (see, for example, Bashmachnikov et al., 2020; Kubryakov et al., 2021).

Recent studies on the joint analysis of *in situ* observations, radar data and satellite altimetry have shown that AVISO satellite altimetry data, despite their generally good quality, somewhat "smear" eddy cores. This means that real eddies, on average, should have smaller radii, larger sea level anomalies and larger nonlinearity index than those obtained from AVISO data (Raj et al., 2016; Yu et al., 2017; Bashmachnikov et al., 2020).

Uisng *in situ* data, in besides various surface eddies, there were identified numerous subsurface eddies, which cores may be observed at considerable depths (Kostyanoy and Belkin, 1989; Richardson et al., 1991; Lozier, 2010). As an example, most of the eddies recorded in the Arctic Ocean have subsurface cores (Belyakov and Volkov, 1980; Meneghello et al., 2021). It has been shown that subsurface eddies observed near the sea surface can not only be directly generated at depth, but also be the result of subduction of surface eddies along deepening isopycnals (Thomas, 2008; Barcello-Llull et al., 2017). The dynamics of subsurface eddies has a number of features, but difficulties in observing subsurface eddies limit our ability of study using ocean observations. Currently, the dynamics of subsurface eddies is studied mainly with numerical models or theoretically (Carton, 2001; Zhmur, 2010; Sokolovskiy and Verron, 2014; Chouksey et al., 2023).

This thesis is devoted to investigation of "life cycles" of subsurface eddies based on observations, as well as on analyzing manifestations of the subsurface eddies at the sea surface. In the latter task the focus is in investigating the possibility for identifying and tracking the signal of subsurface eddies on the sea surface using satellite data. In addition to observations, data from

numerical quasigeostrophic and primitive equation hydrodynamic models, as well as theoretical estimates, were used for investigating some features of the dynamics of subsurface eddies. The "life cycle" of an eddy in the modern literature is understood as evolution of eddy properties from its generation to a final decay.

The study areas are the subtropical northeast Atlantic and the Lofoten Basin of the Norwegian Sea. Eddies life cycles studied includes investigation of the mechanisms of eddy generation, peculiarities of evolution and dissipation of eddy cores. Although this study is based on the data from two areas of the North Atlantic, it covers the dynamics of subsurface eddies with near-surface and deep cores, as well as different latitudinal ranges. The conclusions of this work are of a general nature and can be applied for describing time evolution of properties of subsurface eddies in any area of the World Ocean.

The main goal and tasks of the study

The goal of this study is to evaluate changes in the characteristics of subsurface eddies at consequent stages of their life cycles and to identify singularities of their manifestation at the sea surface.

To achieve this goal, the following **tasks were solved**:

1. Development of algorithms for identifying subsurface eddies, determining their characteristics and trajectories using *in situ* data, including ship-based vertical casts and data from RAFOS and ARGO floats.
2. Identification of the pathways and life cycles of subsurface eddies of The Mediterranean Water (meddies) in the Atlantic Ocean, including typical mechanisms of generation, evolution and dissipation of these eddies.
3. Investigation of the mechanisms of dissipation and regeneration of subsurface eddies in the ocean, as well as the mechanisms of maintaining resistance of subsurface eddies to external perturbations using the quasi-permanent Lofoten vortex of the Norwegian Sea as the case study.
4. Analysis of the singularities of manifestation of subsurface eddies at the sea surface in satellite altimetry and the sea surface temperature data (SST), identification of the mechanisms for the formation of these sea surface anomalies by subsurface eddies and of the possibility for identifying subsurface eddies using satellite data.
5. Development of a theory for a manifestation of subsurface eddies at the sea surface and assessment of a possibility for identifying the main aspects of their life cycles using satellite data.

The objects of the study are the subsurface eddies of Mediterranean water (meddies) in the subtropical Atlantic, as well as subpolar eddies of the Nordic Seas, including the quasi-permanent Lofoten vortex of the Norwegian Sea.

The subject of the study is an assessment of changes in the characteristics of subsurface eddies throughout their life cycles, identification of the main mechanisms responsible for the identified variability, and assessment of a possibility for identifying and tracking subsurface eddies with satellite data.

Scientific novelty

For the first time, a comprehensive statistical analysis of the variations of meddy characteristics as a function of distance from the areas of their generation (a proxy for meddy age) has been performed; a division into groups of northern and southern meddies has been carried out; Previously unknown or insufficiently studied features of the life cycles of each group of meddies have been identified, such as, for example, the role of mergers in meddy dynamics, the role of jet streams and topography in meddy dissipation.

Using the Lofoten Vortex as an example, the dissipation and regeneration of subsurface anticyclones were analyzed in detail. Differences in the mechanisms of regeneration of the available potential and kinetic energy of the anticyclone during differentiated winter convection and when merging with another anticyclone have been identified. Additional conditions necessary for an eddy merger has been suggested. It has been shown that the generation and separation of filaments from the eddy boundary is a mechanism for maintaining the stability of the eddy core during the development of a dynamic instability. It has been shown that even small topographical features (within 10% of the average sea depth) can radically change the degree of eddy stability.

For the first time, the statistics of variability in the manifestations of subsurface eddies with a deep core at the sea surface has been systematized using meddies as an example, a mechanism for formation of these signals has been proposed, theoretical estimates of the intensity of meddy manifestations at the sea surface have been obtained, and theoretical estimates have been compared with observations.

For the first time, a method for identifying subsurface anticyclones on satellite data has been proposed by combining altimetry and SST data; Mechanisms for the formation of a negative SST anomaly over subsurface anticyclones have been proposed; A new scheme of ageostrophic circulation in subsurface anticyclones is proposed that supports the SST anomaly above the eddy and the relative core vorticity.

Theoretical and practical significance of the work

Research in recent years has confirmed earlier assumptions about the important role of mesoscale eddies in the dynamics of large-scale oceanic processes, and also made it possible to identify new features of the dynamics of eddies in the ocean. Progress has been made possible by the increase in the volume and quality of satellite observations of the ocean, as well as the emergence of eddy-resolving hydrodynamic models of ocean dynamics. This made it possible to study mesoscale eddies not only under idealized conditions of physical and quasi-geostrophic numerical models, but also under conditions as close as possible to real ones. In this regard, the number of works on the characteristics and dynamics of surface eddies has sharply increased. However, the dynamics of subsurface eddies still remains predominantly the prerogative of idealized model studies with extremely limited natural material.

A comprehensive study of the life cycle of subsurface eddies based on full-scale and validated high-resolution model data, carried out in this work, allowed us to obtain new results about the features of their life cycles and to identify previously unknown aspects of the mechanisms of their regeneration and dissipation.

The theoretical relationships derived in the work and their validation on natural material made it possible to connect the characteristics of the cores of subsurface eddies with their signals on the sea surface. The fundamental possibility of identifying signals from subsurface eddies on

the sea surface is demonstrated. Similar to the new opportunities of investigation of surface eddies with emergence of the satellite data at the end of the 20th century, these results open new opportunities for studying dynamics of subsurface eddies and may significantly improve regional estimates of the contribution of subsurface eddies to dynamics of intermediate ocean waters.

As the resolution of modern ocean models increases to eddy-resolving ones, new data on the dynamics of eddies in the ocean is needed to validate and improve the numerical models. More accurate representation of the dynamics of mesoscale processes affects the efficiency for modelling large-scale ocean dynamics, and, ultimately, assessments of the role of the ocean in modern climate changes. The results of this work also serve to better representation of vertical exchange of heat, salt and nutrients within eddies, which is important for the estimates of the ocean-atmosphere heat exchange and assessing biological productivity of ocean waters.

An assessment of the credibility of the results

The reliability of the results obtained is determined by a comprehensive analysis of large amounts of modern datasets, which include in-situ, satellite and numerical model results, by objective and detailed comparison of the datasets, as well as by consistency of the results of the research between various types of subsurface eddies with different core depths and in different geographical zones.

Based on the results of the thesis, 24 papers were published in peer-reviewed scientific journals included in the Scopus, Web of Science (WoS) and/or Russian Science Citation Index (RSCI) databases, including 18 articles in Q1 journals. All these journals are included in the list of the Higher Attestation Commission of Russian Federation. Over the past 10 years, 11 articles have been published on the topic of the dissertation with leading participation of the author, including 10 papers in Q1 or Q2 level journals.

Chapters in books on the topic of the dissertation:

1. White, M., I. ***Bashmachnikov,*** J. Aristegui and A. Martins, 2007. Chapter 4. Physical Processes and Seamount Productivity. In: "Seamounts: Ecology, Conservation and Management" (eds. Pitcher, T. J., Morato, T., Hart, P. J. B., Clark, M. R., Haggan, N. and Santos, R. S.). Fish and Aquatic Resources Series, Blackwell, Oxford, UK, ISBN: 9781405133432, 65-84 (*Scopus)*

Publications in Scopus and Web of Science with leading participation of the author:

2. **Bashmachnikov,** I., C. Mohn, J. L. Pelegri, A. Martins, F. Machin, F. Jose, White M. Interaction of Mediterranean water eddies with Sedlo and Seine seamounts, Subtropical Northeast Atlantic //Deep Sea Research Part II: Topical Studies in Oceanography. – 2009a. - T. 56. – No. 25. – S. 2593-2605. doi: 10.1016/j.dsr2.2008.12.036 **(Q1)**
3. **Bashmachnikov,** I., F. Machin, A. Mendonca, A. Martins. In-situ and remote sensing signature of meddies east of the Mid-Atlantic ridge // Journal of Geophysical Research: Oceans. – 2009b. – T. 114. – No. C5 (C05018). - WITH. 1-19. doi: 10.1029/2008JC005032 ***(Q1)***
4. **Bashmachnikov,** I., X. Carton. Surface signature of Mediterranean water eddies in the North-East Atlantic: effect of the upper ocean stratification //Ocean Science. – 2012. – T. 8. – No. 6. – pp. 931-943. doi: 10.5194/os-8-931-2012 ***(Q1)***

5. **Bashmachnikov,** I., C. Loureiro, A. Martins. Topographically induced circulation patterns and mixing over Condor seamount //Deep Sea Research Part II: Topical Studies in Oceanography. – 2013a. – T. 98. – P. 38-51. doi: 10.1016/j.dsr2.2013.09.014 ***(Q1)***

6. **Bashmachnikov,** I., D. Boutov, J. Dias. Manifestation of two meddies in altimetry and sea-surface temperature //Ocean Science. – 2013b. – T. 9. – No. 2. – pp. 249-259. doi: 10.5194/os-9-249-2013 ***(Q1)***

7. **Bashmachnikov,** I., X. Carton, T. Belonenko. Characteristics of surface signatures of Mediterranean water eddies //Journal of Geophysical Research: Oceans. – 2014. – T. 119. – No. 10. – pp. 7245-7266. doi:10.1002/2014JC010244 ***(Q1)***

8. **Bashmachnikov,** I., F. Neves, A. Nascimento, J. Medeiros, I. Ambar, J. Dias, X. Carton. Temperature-salinity distribution in the Northeast Atlantic from ship and Argo vertical casts //Ocean Science. – 2015a. – T. 11. – No. 2. – pp. 215-236. doi: 10.5194/os-11-215-2015 ***(Q1)***

9. **Bashmachnikov,** I., A. Nascimento, F. Neves, T. Menezes, N. V. Koldunov. Distribution of Intermediate Water Masses in the Subtropical Northeast Atlantic //Ocean Science. – 2015b. – T. 11. – No. 5. – pp. 803-827. doi: 10.5194/os-11-803-2015. ***(Q1)***

10. **Bashmachnikov,** I., F. Neves, T. Calheiros and X. Carton. Properties and pathways of Mediterranean water eddies in the Atlantic //Progress in Oceanography. – 2015 c. – T. 137. – P. 149-172. doi: 10.1016/j.pocean.2015.06.001 ***(Q1)***

11. **Bashmachnikov** I.L., Belonenko T.V., Kuibin P.A. Application of the theory of columnar Q-vortices with helical structure for the Lofoten vortex in the Norwegian Sea // Bulletin of St. Petersburg University. Geosciences. – 2017. – No. 3. – pp. 221-236. doi : 10.21638/11701/ spbu 07.2017.301 (*WoS / Scopus / RSCI)*

12. **Bashmachnikov,** I., MA Sokolovskiy, TV Belonenko, DL Volkov, PE Isachsen, Carton X. On the vertical structure and stability of the Lofoten Vortex in the Norwegian Sea //Deep Sea Research Part I: Oceanographic Research Papers. – 2017. – T. 128. – P. 1-27. doi 10.1016/j.dsr.2017.08.001 ***(Q1)***

13. **Bashmachnikov,** I., Belonenko, TV, Kuibin, PA, Volkov, D., Foux, VR Patterns of vertical velocity of the Lofoten Vortex (the Norwegian Sea) //Ocean Dynamics. – 2018. – T. 68. – S. 1711-1725. doi: 10.1007/s10236-018-1213-1 (*Q2)*

14. **Bashmachnikov** IL, Kozlov IE, Petrenko LA, Glok, N., Wekerle C. Eddies in the North Greenland Sea and Fram Strait from Satellite Altimetry, SAR and High-Resolution Model Data // Journal of Geophysical Research: Oceans. – 2020. – T. 125. – No. 7 (e2019JC015832). - WITH. 1-26. doi: 10.1029/2019JC015832 ***(Q1)***

15. Santieva E.K., **Bashmachnikov** I.L., Sokolovsky M.A. On the stability of the Lofoten Vortex in the Norwegian Sea // Oceanology. – 2021. – T. 61. – No. 3. – pp. 353-365. doi: 10.31857/S0030157421030138 (*WoS / Scopus / RSCI)*

16. Ienna F., **Bashmachnikov** IL, Dias J. Meddies and their Sea Surface Expressions: Observations and Theory // Journal of Physical Oceanography. – 2022. – T. 52. – no. 11. – S. 2643-2656. doi: 10.1175/JPO-D-22-0081.1 ***(Q1)***

17. **Bashmachnikov** IL, Raj. R.P., Golubkin P., Kozlov I.E. Heat transport by mesoscale eddies in the Norwegian and Greenland Sea //Journal of Geophysical Research: Oceans. – 2023. – T. 128. – No. 2 (e2022JC018987). - WITH. 1-19. doi:10.1029/2022JC018987 ***(Q1)***

Publications in Scopus and Web of Science with the participation of the author:

18. Mohn, C., White, M., **Bashmachnikov,** I., Jose, F., Pelegri JL Dynamics at an elongated, intermediate depth seamount in the North Atlantic (Sedlo Seamount, 40°20'N, 26°40'W) //Deep Sea Research Part II: Topical Studies in Oceanography. – 2009. – T. 56. – No. 25. – S. 2582-2592. doi: 10.1016/j.dsr2.2008.12.037. ***(Q1)***
19. Barbosa Aguiar, A.C., A. Peliz, F. Neves, I. **Bashmachnikov,** X. Carton. Mediterranean outflow transports and entrainment estimates from observations and high resolution modeling //Progress in oceanography. – 2015. – T. 131. – P. 33-45. doi: 10.1016/j.pocean.2014.11.008. ***(Q1)***
20. Ciani, D., Carton, X., **Bashmachnikov,** I., Chapron, B. and Perrot, X. Influence of deep eddies on the ocean surface //Discontinuity, Nonlinearity and Complexity. – 2015. – T. 4. – No. 3. – S. 281–311. doi: 10.5890/DNC.2015.09.006. (*WoS/Scopus)*
21. Ciani, D., X. Carton, A. C. Barbosa Aguiar, A. Peliz, **Bashmachnikov** I., F. Ienna, B. Chapron, Santoleri R. Surface signature of Mediterranean water eddies in a long-term high-resolution simulation //Deep Sea Research Part I: Oceanographic Research Papers. – 2017. – T. 130. – S. 12-29. doi: 10.1016/j.dsr.2017.10.001 ***(Q1)***
22. Belonenko, T.V., **Bashmachnikov,** I.L., Koldunov, A.V., Kuibin, P.A. On the vertical velocity component in the mesoscale Lofoten Vortex of the Norwegian Sea // Proceedings of the Russian Academy of Sciences. Physics of the Atmosphere and Ocean. – 2017. – T. 53. – No. 6. – S. 728–737. doi: 10.7868/ S 0003351517060071 (*WoS / Scopus / RSCI)*
23. Raj R.P., I. Halo, S. Chatterjee, T. Belonenko, M. Bakhoday, **Bashmachnikov** I., A. Fedorov, Xie J. Interaction between mesoscale eddies and the gyre circulation in the Lofoten Basin //Journal of Geophysical Research: Oceans. – 2020. – T. 125. – no. 7 (e2020JC016102). - WITH. 1-13. doi:10.1029/2020JC016102 ***(Q1)***
24. Wang Q., Koldunov N.V., Danilov S., Sidorenko D., Werkerle C., Scholz P., **Bashmachnikov** I., Jung T. 2020. Eddy Kinetic Energy in the Arctic Ocean from a Global Simulation with a 1-km Arctic //Geophysical Research Letters. – 2020. – T. 47. – no. 14. – P. e2020GL088550. doi: 10.1029/2020GL088550 ***(Q1)***

Based on the results of the thesis research, 53 scientific conferences presentations were made, 7 at all-Russian and 46 at international conferences:

1. **Bashmachnikov** I.L., Golubkin P.A., Kozlov I.E. 2022. Heat transfer by mesoscale eddies in the Nordic Seas, abstracts of the All-Russian scientific conference "Russian Seas: Challenges of Russian Science", September 26 -30, 2022, Sevastopol, Russia, pp. 63-65, http://conf.mhi-ras.ru/archive/2022/morya_rossii-2022_tezisy.pdf
2. Kozlov I., **Bashmachnikov,** IL, 2022. Meso- and submesoscale eddies in the Arctic marginal ice zone and their influence on sea ice from satellite and high-resolution model data. Committee on Space Research (COSPAR) Scientific Meeting, 16-24.06.2022, Athens, Greece
3. Pryakhin, S., **Bashmachnikov,** I., Kozlov, I., and Wekerle, C., 2022. An effect of mesoscale and submesoscale eddies on sea ice processes in the Marginal Ice Zone, EGU22-13088, 23–27 May 2022, Vienna, Austria, https://doi.org/10.5194/egusphere-egu22-13088
4. Pryakhin WITH. S., **Bashmachnikov** AND. L., Kozlov AND. E., Petrenko L. A., Wekerle S., 2021. The role of mesoscale eddies in ice processes in the marginal zone in the Greenland Sea, Materials of reports " Seas of Russia: Year of Science and Technology in the Russian Federation - UN Decade of Ocean Sciences", September 20 -24, 2021, Sevastopol, Russia, pp. 165-167, http://conf.mhi-ras.ru/news/2021/9 /tezisy_dokladov_2021/

5. Novikova Y.S., **Bashmachnikov** I.L., 2021. Eddies of the Lofoten Basin according to satellite altimetry data, images in the radar and visible ranges, Report materials " Seas of Russia: Year of Science and Technology in the Russian Federation - UN Decade of Ocean Sciences", September 20 -24, 2021, Sevastopol, Russia, pp. 291-292, http://conf.mhi-ras.ru/news/2021/9 /tezisy_dokladov_2021/

6. **Bashmachnikov** I.L., Kozlov I.E., Petrenko L.A., Glock N.A., Weckerle K. 2020. Eddies in the Fram Strait according to data from satellite altimeters, radars and high-resolution models, Abstracts of the All-Russian Scientific Conference " Seas of Russia: studies of coastal and shelf zones." 21-25.09.2020, Sevastopol, Russia, 57-58.

7. **Bashmachnikov** I. L., Belonenko T. V., Kuibin P. A. 2019. Relationship between horizontal and vertical circulation in the subsurface Lofoten Eddy, Materials of the reports "Russian Seas: fundamental and applied research", September 23 -28, 2019, Sevastopol, Russia

8. Santieva E. K., M. A. Sokolovskiy, I. L. **Bashmachnikov,** 2019. Stability of an eddy in a bottom depression: implications for the quasi-stationary Lofoten Vortex in the Norwegian Sea. First International Conference on Ocean Fronts and Eddies. 27-31 October 2019, Zhoushan, China

9. Ienna, F., I. **Bashmachnikov,** J. Dias, A. Peliz, 2018, Deep Coherent eddies and their Sea Surface Expressions, AGU Ocean Sciences meeting, 11-16 February 2018, Oregon, USA.

10. **Bashmachnikov** IL, Sokolovskiy MA, Belonenko TV, Carton X., 2017. On stability of the Lofoten Vortex in the Norwegian Sea, "Vortices and coherent structures: from ocean to microfluids", August 28 - 31, 2017, Vladivostok, Russia

11. **Bashmachnikov** IL 2017. Intrithermoclinic eddies in subtropical Atlantic, "Vortices and coherent structures: from ocean to microfluids", August 28 - 31, 2017, Vladivostok, Russia, invited report

12. Ienna, F., I. **Bashmachnikov,** J. Dias, A. Peliz, 2017. Deep Coherent eddies (Meddies) and Their Sea Surface (EGU2017-1628) EGU General Assembly, 23 – 28 April 2017, Vienna, Austria.

13. Ciani, D., X. Carton, A. C. Barbosa Aguiar, A. Peliz, I. **Bashmachnikov,** F. Ienna & B. Chapron, 2017. Detection of subsurface-intensified eddies from observations of the sea-surface: a case study for Mediterranean Water Eddies in a long-term high-resolution simulation (EGU2017-6609) EGU General Assembly, 23 – 28 April 2017, Vienna, Austria.

14. **Bashmachnikov,** I., 2017., Oceanographic research in the Arctic and Nordic seas, Second Workshop on St. Petersburg University and Nansen Center for cooperation in Arctic research, April 26, 2017, St. Petersburg

15. **Bashmachnikov** I.L., Sokolovsky M.A., Belonenko T.V. 2017. Variability of the dynamic characteristics of the Lofoten Vortex in the MIT hydrodynamic model, 02/15/2017, final session of the St. Petersburg section of the Federal State Budgetary Institution "GOIN", St. Petersburg

16. **Bashmachnikov,** IL, Volkov, DL, Yurova, A.Yu., Bobylev LP, 2016. Interannual variability of oceanic heat fluxes in the Atlantic Sector of the Arctic Ocean, UArctic Congress, 12-16 of September, 2016, St. Petersburg, Russia.

17. Belonenko T., **Bashmachnikov** I., Koldunov A., Kuibin P., 2016. On modeling of the Lofoten Vortex structure in the Norwegian Sea, EUROMECH Colloquium [581]. Dynamics of Concentrated Vortices, May 30 – June 1, 2016, Novosibirsk, Russia

18. Ienna, F., **Bashmachnikov,** I., Dias, J., Peliz, A., 2016. Deep Coherent eddies and Their Sea-Surface Expressions, Liege Colloquium 2016 “Submesoscale Processes: Mechanisms, Implications and new Frontiers”, 22-26 of May 2016, Liege, Belgium

19. **Bashmachnikov** I.L., 2016. Manifestation of intrathermoclinic eddies on the ocean surface, 02/12/2016, final session of the St. Petersburg section of the Federal State Budgetary Institution "GOIN", St. Petersburg.
20. Ciani D., Carton, X., Verron, J., and **Bashmachnikov,** I., 2015. The merger of subsurface iIsolated eddies: an application to oceanic lens-like anticyclones, AGU Fall Meeting, 14-18 December, 2015, San Francisco, USA.
21. Ciani, D., Carton, X., **Bashmachnikov,** I. and Chapron, B., 2015. Influence of deep eddies on the ocean surface (EGU2015-5775) EGU General Assembly, 12 – 17 April 2015, Vienna, Austria.
22. Ciani, D., Carton, X., Chapron, B. and **Bashmachnikov,** I., 2014. Surface signature of subsurface-intensified vortices, AGU Fall Meeting, 15-19 December, San Francisco, USA, Poster.
23. Neves, F., **Bashmachnikov,** I., Nascimento, A., Medeiros, J., Dias, J., Ambar, I. and Carton, X., 2014. Detailed temperature-salinity distribution in the Northeast Atlantic from ship and ARGO vertical casts (EGU2014-4156), EGU General Assembly, 24 – 27 April, Vienna, Austria.
24. **Bashmachnikov,** I., Medeiros, J., Neves, F. and Carton, X., 2014. Properties of the Mediterranean water eddies (meddies) in the Northeast Atlantic as a function of distance from the Iberian Peninsular, (EGU2014-7674), EGU General Assembly, 24 – 27 April, Vienna, Austria.
25. Nascimento, A., **Bashmachnikov,** I. and Neves, F., 2014. The Mediterranean Water content in the Northeast Atlantic (EGU2014-12651), EGU General Assembly, 24 – 27 April, Vienna, Austria.
26. Calheiros T. and **Bashmachnikov** I., 2014. Circulation patterns in the deep Subtropical Northeast Atlantic with ARGO data (EGU2014-12651), EGU General Assembly, 24 – 27 April, Vienna, Austria.
27. **Bashmachnikov,** I., Medeiros, J., Neves, F., 2014. Census of the Mediterranean water eddies (meddies) in the Northeast Atlantic, Encontro de Oceanografia, 21 -22 March, Nazare, Portugal.
28. Neves, F., **Bashmachnikov,** I., Nascimento, A., Medeiros, J., Dias, J., Ambar, I. and Carton, X., 2014. A new climatology for the Northeast Atlantic region, Encontro de Oceanografia, 21 -22 March, Nazare, Portugal.
29. Nascimento, A., **Bashmachnikov,** I. and Neves, F., 2014. Intermediate water masses in the Northeast Atlantic, Encontro de Oceanografia, 21 -22 March, Nazare, Portugal.
30. Calheiros T. and **Bashmachnikov** I., 2014. Intermediate depth Northern Atlantic circulation derived from drifting buoys, Encontro de Oceanografia, 21 -22 March, Nazare, Portugal.
31. **Bashmachnikov** I. and Carton, X. 2012. On detection of Mediterranean water eddies with remote sensing data, MIA12, 16 - 20 of December 2012, FCUL, Lisbon, Portugal.
32. **Bashmachnikov** I.L., Carton, H. 2012. Surface "trace" of eddies of The Mediterranean Water in the Atlantic, 10th Open Conference "Modern problems of remote sensing of the Earth from space", November 12 - 16, Space Research Institute of the Russian Academy of Sciences, Moscow. (http://smiswww.iki.rssi.ru/d33_conf/default.aspx?page=26).
33. Santos, M., Moita, MT :, **Bashmachnikov,** I., Menezes, G. M. Carmo, V., Loureiro, C. M., Mendonca, A., Silva, A. F., and Martins, A., 2013. Phytoplankton biomass and community structure and related oceanographic conditions at Condor Seamount (SW Faial Island, Azores), Symposium of Marine Sciences, 17-18 June 2013, Lisbon, Portugal.

34. Medeiros, J. and **Bashmachnikov,** I., 2012. Thermohaline and dynamic properties of Mediterranean Water eddies, MIA12, 16 - 20 December 2012, FCUL, Lisbon, Portugal.
35. Nascimento, A., G. Dupuits, J.-H. Richardson and I. Bashmachnikov, 2012. Mediterranean water content in the Northeast Atlantic, MIA12, 16 - 20 December 2012, FCUL, Lisbon, Portugal.
36. **Bashmachnikov,** I., D. Boutov, J. Dias, A. Aguiar, and J. H. Monteiro, 2012. Surface signature of a meddy while interacting with the Azores current. EGU General Assembly, Ocean Science, Ocean Remote Sensing Session (XY362; EGU2012- 6152), 24 – 27 April, Vienna, Austria.
37. Martins, A., A. Mendonça, A. F. Carvalho, M. Figueiredo, C. Loureiro, I. **Bashmachnikov,** S. Sequeira, S. Gomes, A. Medeiros, and A. F. Silva, 2011. Oceanographic *in situ* and satellite data collection on CONDOR bank (Azores, NE Atlantic): comparison with NAO indices. Earth Observation for Ocean-Atmosphere Interactions Science, 29 November – 2 December 2011, European Space Agency, ESRIN, Via Galileo Galilei, Frascati, 00044 Italy.
38. **Bashmachnikov,** I. 2010. Theoretical and practical aspects of tracking meddies with altimetry, Fourth Coastal Altimetry Workshop, 14-15 October, Porto, Portugal.
39. **Bashmachnikov** I., Belonenko TV, Koldunov AV, 2010. Non-stationary cycles of primary productivity and underlying physical mechanisms in the Subtropical North-East Atlantic. Seminar in Oceanography Institute (Instituto de Oceanografia de FCUL) of the University of Lisbon, 04/07/2010, Lisbon, Portugal.
40. **Bashmachnikov** I., 2010, Theoretical principles of manifestation of deep-water eddies at the ocean surface, Seminar of analysis of differential equations, Center of mathematics and Fundamental Applications of the University of Lisbon, 03/10/2010, Lisbon, Portugal.
41. **Bashmachnikov,** I., A. Martins, A. Mendonca, and M. Santos, 2010. Circulation patterns and biochemical response over Condor seamount. 1as Jornadas de Engenharia Hidrografica, 21 - 22 Junho, Lisbon, Portugal.
42. **Bashmachnikov,** I., A. Mendonca, A. Martins, and I. Ambar 2009. Surface signatures of Mediterranean Water eddies. 4th ESF MedCLIVAR Workshop "Feedbacks of the Mediterranean Dynamics in the Global Climate System", 28-30 September, Sesimbra, Portugal.
43. **Bashmachnikov,** I., A. Mendonca, and A. Martins, 2009. Tracking of Mediterranean Water eddies with remote sensing data. EGU General Assembly, Ocean Science, Ocean Remote Sensing Session (EGU2009-11118), 19 – 24 April, Vienna, Austria.
44. Pereira, C., I. **Bashmachnikov,** C. Leote, C. Palma, A. Martins, M. P. Abreu, and P. Aguiar, 2009. Variation of microplanktonic communities composition with depth in an area under a meddy influence. International Census of Marine Microbes, 454 Spring Meeting, April 6-9th, The Marine Biological Laboratory in Woods Hole, Massachusetts, USA.
45. **Bashmachnikov** I., and Cordeiro A., 2008. Seasonal and intra-annual variability of water dynamics on large and meso-scales in the Azores region. Open Workshop “Exploring Circulation and Productivity Patterns in the Azores Region” (ECPP), 26-27 June 2008, Horta, Azores, Portugal.
46. **Bashmachnikov,** I.; F. Machin, A. Martins, and A. Mendonca, 2008. A. Remote sensing signature of three Meddies east of the Mid-Atlantic ridge, EGU General Assembly, Ocean Science, Ocean Remote Sensing Session (XY0638; EGU2008-A-07700; OS6-1WE5P-0638), 13 – 18 April, Vienna, Austria. (http://meetings.copernicus.org/egu2008/download/meeting_group_programme_OS.pdf)

47. Martins, A. A. Mendonça, I. **Bashmachnikov,** S. Sequeira, M. Figueiredo, 2008. Can Ocean Color satellite imagery identify Meddies in the Ocean? SPIE Europe Remote Sensing of the Ocean, Sea Ice, and Large Water Regions (http://spie.org/remote-sensing-europe.xml).
48. **Bashmachnikov,** I., A. Martins & A. Mendonça, 2006. Observation of 3 Meddies from in-situ and altimetry data in the Azores region, SPIE Europe Remote Sensing, Conference 6360-02: Session 1: Remote Sensing of the Ocean, Sea Ice, and Large Water Regions, Stockholm, Sweden, 11 - 14 September.
49. White, M., Mohn, C., **Bashmachnikov,** I., and Jose, F.P. 2005. Seamount dynamics at an elongated, multi-peaked, seamount in the NE Atlantic. ASLO Summer Meeting, 19-24 June 2005, Santiago de Compostela, Spain.
50. Machin, F., Pelegri, J. L., Emelianov, M., White, M., and **Bashmachnikov,** I. 2005. Inverse modeling the circulation over Sedlo seamount (Eastern North Atlantic). ASLO Summer Meeting, 19-24 June 2005, Santiago de Compostela, Spain.
51. **Bashmachnikov, I.,** V. Lafon and A. Martins, 2004. SST stationary anomalies in the Azores region. *Remote Sensing of Ocean and Sea Ice, 5569,* 148-155.
52. Lafon, V., A. Martins, I. **Bashmachnikov,** F. Jose, M. Melo-Rodriguez, M. Figueiredo, A. Mendonca and L. Macedo, 2004. SST variability in the Azores region using AVHRR imagery: regional to local scale study. *Remote Sensing of Ocean and Sea Ice,* 5569: 130-139.
53. Lafon, V., A. Martins, I. **Bashmachnikov,** M. Melo-Rodriguez and M. Figueiredo, 2003. Sea surface temperature spatio-temporal variability in the Azores using a new technique to remove invalid pixels. *Remote Sensing of Ocean and Sea Ice,* 5233: 89-97.

General publication activity of the author

In total, the author has currently published 77 Scopus/WoS papers (Scopus h-index = 20, WoS h-index = 18), including 58 papers during the past 10 years, and 22 papers in RSCI (RSCI h-index = 19).

Guidance of graduate students and doctoral students

2021-2024, Diana A. Yakovleva “The influence of oceanic circulation on the formation of the thermohaline structure of subpolar regions and the development of deep convection”, PhD candidate, St. Petersburg State University (in progress).
2018-2022, Mikhail M. Latonin “The influence of atmospheric and oceanic circulation on the long-term variability of the characteristics of the surface layer of the atmosphere in the Arctic region”, PhD degree, St. Petersburg State University (defended 06/08/2022).
2015-2018, Federico Ienna “Identification and tracking of lenses of The Mediterranean Water (meddy) in the North Atlantic from satellite data”, PhD degree, University of Lisbon. (protected 07/06/2021)
2017-2018, Polina V. Lobanova “Validation and analysis of error sources of satellite models of primary production in waters with different oceanological conditions using the example of the North-Eastern Atlantic and the Sea of Japan”, PhD degree, St. Petersburg State University (protected 06.13.2018).
2012-2015, Dr. Filipe Neves “Calculation of Mediterranean water transport in the subtropical North Atlantic using an inverse problem solution”, University of Lisbon, Portugal, doctoral research grant within the MEDTRANS project (supervisor).

2008-2011, Ana Mendonça “The influence of bottom heterogeneities on primary productivity in the subtropical North Atlantic”, PhD degree, University of Azores, Portugal (protected 10/13/2011, co-supervisor)

Author's personal contribution

The author's personal contribution consists of setting the tasks, choosing and development of the processing methods, writing the scripts, performing computations and visualization of the results, and writing the texts of scientific papers. The thesis uses materials only from those papers the text of which was written personally by the author and in which the author made a major contribution to the research.

The structure of the thesis

The thesis consists of an Introduction and 8 Chapters, contains 332 pages and including 127 pictures and 14 tables in the main text and appendices, as well as a bibliography of 569 references on national and foreign scientific works.

Chapter **1** provides a classification of eddies, including the type of eddies investigated in this study. The main aspects of eddy dynamics which are used in further work are described. A brief characterization of the subsurface eddies in the focus of this study, the subtropical Atlantic eddies (meddies) and the Nordic Seas eddy (the Lofoten Vortex) are given. A brief overview on the approaches for studying of subsurface eddy manifestation at the ocean surface is given.

Chapter **2** describes the data and the methods analysis used in this work. The methods for identifying eddies from *in situ* data, satellite data, and hydrodynamic model data are described. A comparative description of eddies identified from various types of data is given. The limitations of different types of data in identifying characteristics of eddies are discussed.

Chapter **3** first describes statistics of the 3D characteristics of surface mesoscale eddies in the Norwegian and Greenland Seas from combined satellite and *in situ* observations. The features of spatial distribution of the main characteristics of eddies (number per unit area, radius, vertical dimensions, core temperature anomalies, core rotation velocity and eddy propagation velocity) over the water area are described. It is shown that the eddies of the Norwegian and Greenland seas differ in almost all of their properties listed above. Based on *in situ* data, it was shown for the first time with *in situ* data that the merger of eddies is one of the characteristic features of their evolution in the vicinity of the region of their intensive generation. Estimates of heat fluxes with eddies generated by the eastern branch of the Norwegian Current are presented. It has been shown that eddies extract about 1/3 of the heat advected by the current into the region and can effectively smooth out the water temperature anomalies coming from the south.

Chapter **4** describes a refined pattern of the Mediterranean Water distribution in the Atlantic, for the first time objectively derived from climatological data and providing the 3D distribution of the percentage of Mediterranean Water (MW) content using the method of the Optimal Multiparameter Analysis. The pathways of the preferential propagation of the upper and lower MW cores were identified. A refined pattern of the mean currents at intermediate depths was obtained. It was shown that the currents contribute to the spread of the MW only within the first hundreds of kilometers from the Iberian Peninsula, which indicates the important role of

meddies in the propagation of the MW in the Atlantic. Statistical data on the variability of meddy characteristics with distance from their generation regions has been obtained. The main pathways of meddy propagation have been refined. It has been shown that the characteristics of meddies formed in the northern part of the continental slope of the Iberian Peninsula differ significantly from those in its southern part. This difference persists far to the west from the areas of meddy generation. This made it possible to divide the meddies into two groups: the northern and southern meddies. The life cycles of the northern and southern meddies are described, the role of meddy merger in their life cycles and a number of peculiarities of meddy destruction are revealed.

Chapter **5,** using the quasi-permanent Lofoten Vortex as an example, describes the mechanisms of eddy dissipation and merger. It is shown that the dissipation of eddies in the ocean can differ significantly from the results of quasigeostrophic (QG) models often used to assess the degree of eddy stability. The role of strong external deformations of the velocity field at the boundary of anticyclones in increasing their stability is shown. This is due to the "dumping" of the energy of instabilities through generation and separation of filaments from the eddy core. It is shown that the anomalously high stability of the Lofoten Vortex is associated with a small depression in the bottom topography, which, in combination with the mean circulation pattern formed by the Norwegian Current, leads to a multiple increase in the stability of the vortex. The role of the screen of potential vorticity at the periphery of the eddy and the presence of the velocity field of the third eddy in the merger of two anticyclones are studied.

In Chapter **6,** for the first time, a systematization of *in situ* studies of the dynamic manifestations of meddies at the sea surface was carried out through a joint analysis of characteristics of the identified meddies and the sea level anomalies which they form in AVISO satellite altimetry data. It is shown that despite the deep core (500-1200 m depth), meddies often form a pronounced signal at the sea surface, which is comparable in its intensity to the signals of surface anticyclones in the study region and which can be continuously monitored for several months. Theoretical estimates are obtained that relate the signal intensity to the characteristics of meddy cores for a contour eddy and a Rayleigh eddy. The theory is shown to well describe the observed changes in the intensity of the sea surface meddy signals for meddy cores with different characteristics, as well as the seasonal and latitudinal variability in the intensity of the observed meddy signals. A noted western intensification of meddy signals on the sea surface is not described by the theory. It is hypothesized that this intensification is associated with the interaction of meddies with the mean surface currents intensifying to the west.

Chapter **7** describes the features and mechanisms of formation of SST anomalies over subsurface anticyclones. It is shown that, in contrast to surface anticyclones, subsurface anticyclones are characterized by negative SST anomalies. Two mechanisms for formation of these anomalies have been identified, both being preconditioned by the rise of isopycnals above the core of a subsurface anticyclone. A mechanism for ageostrophic circulation in the core of a subsurface anticyclone that supports the rise of isopycnals above the core is proposed, and an expression for calculating the vertical velocity in the central part of the core of a Rayleigh eddy is derived.

Chapter **8** (Conclusion) briefly summarizes the conducted research. The emphasis is made on the integrity of the study performed and on the mutual complementarity of its individual parts.

Acknowledgments

The author sincerely thanks his colleagues and co-authors for their collaboration and support. A special gratitude is to my teacher, Honorary Professor Viktor Robertovich Foux (St. Petersburg State University), under whose supervision my scientific formation took place and who had a huge influence on the further scientific development of the author, to Professor Xavier Carton (University of Brest, France) for the invaluable experience of collaboration and help in the development theory of the manifestation of subsurface eddies on the ocean surface, to Professor Tatyana Vasilievna Belonenko (St. Petersburg State University) for all-out support and a series of joint studies on ageostrophic circulation in eddies, to Professor Mikhail Abramovich Sokolovsky (Institute of Water Problems of the Russian Academy of Sciences, Moscow) for a series of joint studies on the stability of the Lofoten Vortex and the materials of the quasi-geostrophic model of eddy contour dynamics which he developed, to Professor Denis Leonidovich Volkov (NOAA Atlantic Oceanographic and Meteorological Laboratory, USA) for providing the MIT model data and joint research on the dynamics of the Lofoten Vortex.

I would also like to express my deep gratitude to my family, who invariably supported the author throughout his scientific career, including the year which were difficult for national science, and with the support of which this work was also written.

The research resulting from this work has received financial support from a number of projects led by the author:

- 2016-2018, “Synoptic eddies in the ocean: their role in the transfer of thermohaline characteristics and the formation of areas of increased biological productivity,” 16-05-00452, RFBR, Russia.
- 2012-2015, MEDTRANS - “Mechanisms of Mediterranean water transport and dispersion in the subtropical North-East Atlantic” - PTDC/MAR/117265/2010, Portuguese Foundation for Basic Research (FCT), Portugal.
- 2007-2008, LAMAR - “LArge-scale and Mesoscale dynamics of the Azores Region form the remote-sensing and in-situ data and their effect on biological productivity” - M2.1.2/F/008/2007, Azores Regional Foundation for Basic Research (DRCT), Portugal.

Main scientific results

1. An overview of the dynamic processes associated with seamounts and their impact on bioproductivity is provided. It has been shown that variability in background forcing can temporarily disrupt the “idealized” response of the seamounts to external forcing in the form of the Taylor cone, as well as the characteristic cells of ageostrophic circulation (Bashmachnikov et al. 2007, p. 65, the degree of author’s participation in obtaining this result is 75%).
2. It was shown that when interacting with the Sedlo seamount, a meddy lost about 25% of the salt of its core, while when interacting with the Sein seamount, another meddy continued to move after several rotations around the mountain without any significant change in its characteristics (Bashmachnikov et al. 2009a, p. 2593, the degree of author participation in obtaining this result is 100%).
3. A methodology has been proposed that allows continuous monitoring of meddy signals on the sea surface over a period from several months to 2 years. It has been shown that the

meddy signal on the sea surface is quite stable, but can temporary disappear during the periods of meddy interaction with other intense dynamic structures (Azores Current, surface eddies) or near seamounts (Bashmachnikov et al. 2009b, p. 1, the degree of author's participation in obtaining this result is 100%).

4. Theoretical estimates of the intensity of the meddy signal at the sea surface are presented. It is shown that this intensity is directly proportional to the radius of the meddy core and the Coriolis parameter and inversely proportional to the depth of the meddy core and the buoyancy frequency of the upper layer of the ocean (Bashmachnikov and Carton, 2012, p. 931, the degree of author participation in obtaining this result is 75 %).
5. During 1.5 years of *in situ* observations of the dynamics at the top of the Condor seamount south of the central group of the Azores Islands, at least half of this period a subsurface anticyclone was observed, captured by the top of the mountain. The eddy was highly asymmetrical, shifted to the southern slope of the mountain and stretched over the gentle slopes of the mountain. The anticyclone was stable only during a constant direction of the impinging mean flow in the vicinity of the seamount. If the impinging flow periodically changed its direction, the anticyclonic eddy was absent or was significantly weakened (Bashmachnikov et al. 2013a, p. 38, the degree of author's participation in obtaining this result is 100%).
6. Field observations with a Doppler current meter showed that the dynamic signal generated above the moving meddy was more intense than the dynamic signal of the Azores Current. It was shown that, in contrast to the warm signal in sea surface temperature for surface anticyclones, the meddy surface signal was dominated by a negative SST anomaly. However, this anomaly was weak, often unstable and statistically significant only when observations lasted one month or longer (Bashmachnikov et al. 2013b, p. 249, the degree of author participation in obtaining this result is 90%).
7. New results have been obtained on the manifestation of meddies (and other eddies with deep cores) at the sea surface. It has been shown that meddies with a dynamic radius of 30 km and more will always be visible in AVISO altimetry data, whereas for a radius of 20 km only the most intense meddies with relatively shallow cores will be visible at the sea surface. Meddies with a radius of 10 km generally cannot be detected at the sea surface using AVISO data. Seasonal variability in the intensity of the meddy signal at the sea surface has been detected. For northern meddies it forms 2-3 cm, and for southern meddies – 5-10 cm. It is shown that an effective dispersion through generation of lee Rossby waves is only characteristics for the surface signals of meddies which propagate with the β-drift velocity of long baroclinic Rossby waves (Bashmachnikov et al. 2014, p. 7545, the degree of author participation in obtaining this result is 90%).
8. A new regional climatology of temperature and salinity MEDTRANS was derived using a new modification of the Barnes optimal interpolation method, where a gridding window changes its shape to account for the tendency of ocean water to spread along isobaths in the presence of significant bottom slopes. MEDTRANS, for example, more accurately describes the circulation of the Gulf of Cadiz and the division of the Mediterranean Water into two veins at the Gorringe and Galicia banks (Bashmachnikov et al. 2015a, p. 215, the degree of author's participation in obtaining this result is 90%).
9. A quantitative estimate of the content of intermediate water masses in the northeastern subtropical Atlantic has been obtained. It is shown that the Mediterranean Water spreads

along the Iberian Peninsula in three major veins having their cores at different depths. It is shown that the separation of the Mediterranean Water from the topographically trapped Mediterranean Undercurrent in the areas where the JBAR effect exceeds the topographic β-effect (Bashmachnikov et al. 2015b, p. 803, the degree of author's participation in obtaining this result is 80%).

10. Using *in situ* observation data, 241 meddies and 236 segments of meddy trajectories were identified for further analysis. It is shown that meddies generated to the south of the Extremadura Promontory (southern meddies) compared to meddies generated to the north (northern meddies) have smaller radii, higher Rossby numbers and higher stability. Meddies are shown to move along four main routes. At a distance of less than 600 km from the coast, the meddy cores regularly merge. As a rule, a meddy is destroyed within 1 to 2 years, although some meddies can exist for more than 3 years (Bashmachnikov et al. 2015c, p. 149, the degree of author's participation in obtaining this result is 100%).
11. Ageostrophic dynamic patterns in the ocean mesoscale eddies are investigated using the theory of columnar eddies with a helical structure. Expressions for the horizontal and vertical velocity components are derived for Q -distribution of the radial profile of the azimuthal current velocity in an eddy (Bashmachnikov et al., 2017, p. 1, the degree of author's participation in obtaining this result is 70%).
12. The decay rate of the Lofoten vortex in the presence of a background flow in a quasi-geostrophic three-layer contour dynamics model reaches 50-90% of the initial core volume within 4-5 months, while for a realistic conditions of the Lofoten Basin in the primitive equation hydrodynamic model the Lofoten Vortex loses only 10-30% of its volume over the same period. Introduction of the southwestward gradual deepening of the bottom topography of the basin in the quasigeostrophic model strongly reduces the decay rate brining it closer to the results of the primitive equation model (Bashmachnikov et al. 2017, p. 1, the degree of author's participation in obtaining this result is 70%).
13. Vertical velocities in and above the core of the anticyclonic Lofoten Vortex are directed upward along the vortex axis and downward at its periphery. These vertical velocities support the anticyclonic vortex rotation against the core dissipation. Under the eddy core, vertical velocities are directed downward everywhere and gradually converge towards the eddy axis with depth (Bashmachnikov et al. 2018, p. 1, the degree of author's participation in obtaining this result is 100%).
14. AVISO satellite altimetry data overestimate eddy radii by 1.5-2 times and underestimate the maximum azimuthal velocities of eddies by 1.5-2 times. Nevertheless, AVISO data make it possible to reliably estimate spatial variability of various characteristics of surface eddies and the direction of eddy propagation. The eddies detected in AVISO and SAR images form two complementary data sets (Bashmachnikov et al. 2020, p. 1, 21, 22, the degree of author's participation in obtaining this result is 90%).
15. It is shown that the lifetime of an eddy significantly depends on its position in the basin, the nature of the bottom topography and the speed of the oncoming flow. When the centers of concentric isobaths shift southwest, which more accurately simulates the topography of the Lofoten Basin, even in the absence of regeneration, the Lofoten Vortex can exist in the basin for at least 2 years. (Santieva, Bashmachnikov and Sokolovsky, 2021, p. 362, the degree of author's participation in obtaining this result is 75%).

16. Mean upper ocean currents can strongly intensify the surface dynamic manifestations of subsurface eddies. The westward intensification of the current velocities in the subtropical Atlantic explains the westerly intensification of the sea surface signals over the Mediterranean water eddies (meddies) (Ienna, Bashmachnikov and Dias, 2022, p. 2643, the degree of author participation in obtaining this result is 75%).
17. It is shown that mesoscale eddies have a significant impact on the redistribution of heat, extracting and dispersing around 60 TW in the Lofoten Basin, which forms over 30% of the heat, advected into the region by the Norwegian Atlantic Slope Current. Variations in the eddy heat flux can effectively damp the temperature anomalies coming into the Norwegian Sea from the south: an increase in the peak temperature of the eddy cores by 1°C leads to an increase in the eddy heat flux by 50 TW (Bashmachnikov et al. 2023, pp. 1, 14, the degree of author's participation in obtaining this result is 100%).
18. Observations showed an increase in anticyclonic circulation when moving upslope of a seamount to its summit, a possible change from anticyclonic to cyclonic circulation as one moves further up to the sea surface, and high mesoscale variability in the area of the summit. More intense dynamics create additional conditions for an accelerated dissipation of subsurface eddies during their interaction with the seamount summit (Bashmachnikov et al. 2023, pp. 2582, 2589, the degree of author’s participation in obtaining this result is 50%).
19. It is shown that the transport of the Mediterranean Undercurrent in the Gulf of Cadiz, at a distance of 250 km from the Strait of Gibraltar, is 5 times higher compared to the transport of the Mediterranean Water coming from the Strait. In the Mediterranean Water entrain mainly the surface and intermediate North Atlantic Central Water from the central and southern parts of the Gulf of Cadiz (Barbosa Aguiar et al., 2015, p. 33, the degree of author's participation in obtaining this result is 30%).
20. Expressions are obtained for a surface expression of a subsurface point vortex, the characteristics of which corresponds to the characteristics of a meddy with S- or R-screen. It has been shown that such meddies has weak sea surface signals, which grow with an acceleration of rotation of their cores. It has been shown that the surface manifestations of such eddies tend to grow somewhat with time (Ciani et al., 2015, p. 1, 33, the degree of author’s participation in obtaining this result is 40%).
21. The computations with a regional high-resolution hydrodynamic model, it is confirmed that meddies produce a stable signal at the sea surface, the intensity of which is proportional to potential vorticity of the meddy core. The main conclusions of Bashmachnikov et al. (2015c) derived from *in situ* data are confirmed by these computations (Ciani et al., 2017, p. 12, 24, the degree of author’s participation in obtaining this result is 40%).
22. The expression for estimating the vertical velocity in the Rayleigh eddy are derived using Kuibin-Okulov theory; the estimates of the maximum axial vertical velocity in the Lofoten Vortex are presented (Belonenko et al., 2017, p. 732, 734, the author’s participation in obtaining this result is 90%).
23. The dominating eddy propagation pattern of a counterclockwise circling around the Lofoten Basin has been revealed. The transfer of the energy from the mean current to the Lofoten Vortex was noted in the vicinity of the Vortex (Raj et al., 2020, p. 1, the degree of author's participation in obtaining this result is 25%).

24. The distribution of eddy kinetic energy, which is a measure of eddy activity, over the Arctic was obtained from the high-resolution FESOM model data. A significant increase in the eddy kinetic energy is derived along the topographically captured Norwegian, East Greenland and Arctic Slope Currents, as well as in the western part of the Barents Sea. This is associated with the transition of the available potential energy of the mean flow to the kinetic energy of eddies (Wang et al., 2020, p. 1, the degree of author's participation in obtaining this result is 20%).

Key points of the defense

1. Two groups of meddies have been identified, northern and southern meddies, which acquire their different properties during their generation. Southern meddies, compared to northern ones, are more compact, have higher salinity and temperature, higher core rotation and are more stable. It is shown that at distances less than 600 km from the Iberian Peninsula, meddy merger dominates over meddy destruction, while at greater distances meddy destruction dominates. It has been shown that meddies lose some of their mass and kinetic energy when crossing the Azores Current.
2. Using the example of the Lofoten Vortex, it is shown that mergers, in contrast to differential convection, lead to a significant increase in the integral kinetic energy of the vortex. The presence of a screen of potential vorticity at the periphery of eddies during summer impede mergers, and the overwhelming number of mergers of anticyclones with the Lofoten Vortex occurs during the winter-spring period, when the screen is destroyed by winter convection. The presence of a third eddy may facilitate the merger.
3. Using the Lofoten Vortex as an example, it is shown that the stability of an anticyclone can significantly depend on small topographic features. The high stability of the Lofoten Vortex is associated with the presence of a small depression at the bottom of the Lofoten Basin combined with the mean background cyclonic circulation in the Basin.
4. Using meddies as an example, it is shown that the signal at the sea surface of a subsurface eddy with a deep core is formed due to generation of an independent anticyclone by the conservation of potential vorticity by the flow impinging over the meddy core. The derived theoretical dependencies made it possible to explain the latitudinal and seasonal variability in the intensity of sea surface meddy signals by the variability in the ratio of the buoyancy frequency of the upper ocean layer to the Coriolis parameter. In addition to the factors allotted in the theory, the intensity of the surface meddy signal depends on the mean current velocity in the upper ocean.
5. In contrast to surface anticyclones, signals of subsurface anticyclonic eddies manifest themselves as cold anomalies of the sea surface temperature (SST). The ageostrophic circulation scheme is proposed to maintain cold SST anomalies over an anticyclone with a near-surface core. The strengthening of the negative SST anomaly occurs due to the capture and penetration of cold waters into the central part of the surface signal of the subsurface eddy while “wrapping” the warm waters around this cold center.

CHAPTER 1. GENERAL FACTS ABOUT COHERENT MESOSCALE EDDIES IN THE OCEAN

1.1 CLASSIFICATION OF OCEAN EDDIES BY SPATIAL SCALES

Eddies in the ocean are observed in a very wide range of spatio-temporal scales, from millimeters with a lifetime from a fraction of a second to seconds (in the lower limit these eddies are characterized by the Kolmogorov scale) to the first hundreds of kilometers with a lifetime from several weeks to several years (for example, Gulf Stream rings).

Based on dimension theory, the following eddy scales can be distinguished (Monin and Ozmidov, 1981), separating different types of vortices with different dynamics:

$L_k = \sqrt[4]{\frac{\upsilon^3}{\varepsilon}}$ (millimeters) – Kolmogorov scale, for which the forces of molecular viscosity play the most important role in dynamics of these eddies; υ – the molecular viscosity, ε – the rate of dissipation of turbulent kinetic energy.

$L_N = c_1 \varepsilon^{1/2} N^{-3/2}$ (tens of meters) – the scale at which buoyancy forces begin to influence the eddy dynamics; $N = \sqrt{-\frac{g}{\rho_0}\frac{\partial \rho}{\partial z}}$ – the buoyancy frequency, g – the gravitational acceleration, ρ and ρ_0 – the water density and its average value, $c_1 \sim 1$ is a constant.

$L_f = c_2 \varepsilon^{1/2} f^{-3/2}$ (hundreds of meters - kilometers) – the scale at which the Coriolis force begins to have a significant impact on the eddy dynamics, f – the Coriolis parameter, $c_2 \sim 1$ is a constant.

$L_\beta = c_3 \varepsilon^{1/5} f \beta^{-3/5}$ (tens and first hundreds of kilometers) – the scale at which the variability of the Coriolis force with latitude begins to influence individual aspects of the eddy dynamics, β – the rate of linear change of the Coriolis parameter with latitude ($f = f_0 + \beta y$), $c_3 \sim 1$ is a constant.

Between scales L_f and L_β submesoscale and mesoscale eddies are distinguished, the boundary between which is the baroclinic Rossby deformation radius $Rd = N H_L / f$, where H_L is the sea depth. For both types of eddies, the Coriolis force is one of the main acting forces, but for submesoscale eddies (with radius $R < Rd$) inertial acceleration is comparable to the Coriolis acceleration, and for mesoscale eddies (with radius $R > Rd$) inertial acceleration can be neglected and the eddy dynamics is well described through the geostrophic balance, as the first approximation.

The limiting size of the largest eddies is called the Rhines scale $L_R = \sqrt{v_\theta / 2\beta}$, where v_θ is the maximum azimuthal velocity in the eddy core. For a typical eddy, $v_\theta \sim$ 20-50 cm s^{-1} L_R is the first hundreds of kilometers. When this scale is reached in the equation of relative vorticity, the linear β-term begins to dominate over the inertial terms (Nezlin and Snezhkin, 1990; Belonenko and Sandaluk, 2018). This leads to the "transformation" of the eddy into a Rossby wave (Rhines, 1957; Danilov and Gurarle, 2002). However, some authors dispute the significance of this scale as the upper eddy limit (Sukoriansky et al., 2006).

The main characteristics of eddies of different scales are given in Table 1.1.

Table 1.1. Classification of eddies by scale and their dynamics (based on Monin and Ozmidov, 1981; Kamenkovich et al., 1987). A description of the scales that define the transitions between of different types of eddies is given in the text.

Characteristic radii of eddies	$R \sim L_K$ (centimeters)	$L_K << R << L_N$ (meters)	$L_N << R << L_f$ (10 kilometers)	$L_f < R < L_\beta$	
				$L_f < R < Rd$ (100 meters - kilometers)	$Rd < R < L_\beta$ (10 - 100 kilometers)
Reynolds eddy number $Re = \frac{v_\theta R}{\upsilon}$	$Re \sim 1$	$Re >> 1$			
Richardson eddy number $Ri = N^2 \Big/ \left(\partial v_\theta / \partial z\right)^2$	$Ri << 1$		$Ri \sim 1$	$Ri >> 1$	
Rossby eddy number $Ro = \frac{v_\theta}{f R}$	$Ro >> 1$			$Ro \sim 1$	$Ro << 1$
Characteristic	the movement in the eddies is laminar, energy is transferred into heat (the forces of molecular viscosity dominate), the vortices are 3-dimensional and spherical in shape	the movement is turbulent (breakdown into smaller eddies is regular), inertial forces dominate, the influence of stratification is insignificant, eddies are 3-dimensional and spherical in shape	the movement is turbulent, inertial forces dominate, but the influence of stratification is already significant; as a result eddies are vertically compressed	quasi-geostrophic balance, but the inertial forces are still large, the eddies look like “pancakes”, and the kinetic energy is concentrated in horizontal motion, eddy proper propagation velocity is insignificant	the balance of forces is close to geostrophic, the eddies look like “pancakes”, and the kinetic energy is concentrated in horizontal motion, eddy proper propagation velocity can be large and comparable to the velocity of mean currents
Russian classification	small-scale eddies			mesoscale eddies	synoptic eddies
Western classification	small-scale eddies			submesoscale eddies	mesoscale eddies

The thesis discusses the dynamics of mesoscale (synoptic) eddies. In the methodological chapter 2, some attention will also be given to submesoscale eddies.

1.2 SOME ASPECTS OF DYNAMICS OF MESOSCALE OCEAN EDDIES

According to AVISO satellite altimetry data, the characteristic dynamic radii of eddies in the subtropical and subpolar Atlantic are 50–75 km, decreasing slightly to the north (Chelton et al., 2011). Comparison of AVISO altimetry data with observations shows that the eddy radii obtained from AVISO altimetry are overestimated 1.5-2 times, on average (Raj et al., 2016, Yu et al., 2017; Bashmachnikov et al., 2020), which brings the values of the eddy radii closer to the 1st baroclinic Rossby radius of deformation. Eddies are characterized by relatively high azimuthal velocities compared to mean currents. Typical azimuthal velocities in mesoscale eddies derived by Chelton et al. (2011) using AVISO data, are underestimated 1.5-2 times (Yu et al., 2017; Bashmachnikov et al., 2020) and correspond to the real azimuthal eddy velocities of 15-40 cm s^{-1}. These rotation velocities are characteristic for eddies observed *in situ* (see, for example, Pingree and LeCann, 1992; Paillet et al., 2002; Yu et al., 2017). Due to high azimuthal velocities (v_θ) and relatively small rotation radii, the inertial term can account up to 20% of geostrophic terms in mesoscale eddy dynamics (Carton, 2001). This is confirmed by the typical values of Rossby numbers for mesoscale eddies, which are usually in the range of 0.1-0.3. Therefore, in the equation of an axisymmetric eddy in polar coordinates, besides geostrophic terms, sometimes inertial term is also included (Carton, 2001):

$$\frac{v_\theta^2}{r} + fv_\theta = \frac{1}{\rho_0}\frac{\partial P}{\partial r} \tag{1.1}$$

Here $\frac{\partial P}{\partial r}$ is the pressure gradient in the radial direction, r is the distance from the center of the vortex, f is the Coriolis parameter, ρ_0 is the average density of water. In this equation, f is usually assumed to be constant, because the influence of β-effect on the kinematics of eddy cores is negligible compared to the inertial terms: $v_\theta / \beta R^2 >> 1$ (Zhmur, 2010; Chelton et al., 2011). However, the β-effect plays the principal role in generating the proper velocity of propagation of eddies.

Ageostrophic effects in eddies increase with decreasing eddy size and are characterized by the so-called helicity, which is defined as the ratio of divergence in the eddy core (characterized by the radial velocity v_r) to the relative vorticity of the core (characterized by v_θ). Spiral streamlines are clearly visible in radar and ocean color satellite images in submesoscale eddies, but are weakly expressed in large mesoscale eddies.

The anomaly of potential vorticity of eddy core determines the degree of isolation of the core from to the surrounding ocean and is estimated as:

$$\Pi = \frac{1}{g}\left[N^2(\omega + f) - N_0^2 f \right], \tag{1.2}$$

where N and N_0 are the buoyancy frequencies of the eddy core and the surrounding ocean, respectively, ω is the relative vorticity of the eddy core, g is the acceleration of gravity. The core of the anticyclone has a negative anomaly of Π, and the core of the cyclone has a positive anomaly. For large ocean eddies, the magnitude Π is primarily determined by the buoyancy frequency

anomaly. The eddy core is usually limited vertically (and sometimes horizontally) by *П* anomalies of the opposite sign. When *П*-anomaly at the eddy periphery has the of the opposite sign to that in the eddy core is sometimes it is called the “screen”.

The vertical scale of an eddy is often determined by a change in the sign of *П*-anomaly above and below the eddy core. However, the vertical scale can also be estimated with other characteristics of the vortex which then may differ from the one above. Using equation (1.1), the ratio of the vertical dynamic scale of an eddy to the horizontal one can be approximately estimated as (Hassanzadeh et al., 2012) : $\frac{h}{R} \sim \frac{f}{N'}\sqrt{Ro}$, where $N' = \left|N - N_0\right|$ is the absolute value of the buoyancy frequency anomaly of the eddy core relative to the background. Considering the smallness of $\frac{f}{N'} \sim 0.1$ and of $Ro \sim 0.1$ in mesoscale eddies, the vertical scale of such eddies will be 1-2 orders of magnitude smaller than the horizontal one (see also Zhmur, 2010). This suggests that dynamic signal of an eddy with the 30 km radius can reach the ocean bottom even in the deep ocean. Indeed, observations in the ocean show that, despite the limited vertical scale of thermohaline anomalies of eddy cores of hundreds of meters, the rotation signal of large eddies can often extend over a significantly larger part of the water column, often covering the full range from the sea surface to ocean bottom (see, for example, Pingree and LeCann, 1993 a, b; Paillet et al., 2002; Soiland and Rossby, 2013; Such a significant (several times) difference in the vertical scales of vortices, determined by anomalies of various characteristics, is often ignored by researchers.

The ratio of the kinetic to available potential energy of the vortex, as well as the relative contribution of rotation in the formation of the anomaly of the potential vorticity of the eddy core compared to the anomaly of the buoyancy frequency, are determined by Burger number:

$$Bu = N'^2 h^2 \Big/ R^2 f^2 \sim \left(\frac{Rd}{R}\right)^2 \sim \frac{E_k}{E_p}, \qquad (1.3)$$

where $E_k = \rho_0 \iiint \frac{v_\theta^2 + v_r^2}{2}$ is the eddy kinetic energy; $E_p = \rho_0 \iiint \frac{g'}{2}(z_\rho - z_{\rho 0})$ is the eddy available potential energy, z_ρ and $z_{\rho 0}$ is the depth of a selected isopycnal ρ in the eddy core and in the surrounding ocean, respectively, $g' = g\frac{\rho - \rho_0}{\rho_0}$ is the reduced acceleration of gravity; $Rd = \frac{N'h}{f}$.

As can be seen from formula (1.3), Burger number decreases with a decreasing eddy horizontal scale (*R)*. In the mean currents the potential energy is 2 orders of magnitude higher than the kinetic energy, while for most of the mesoscale eddies these values differ by less than an order of magnitude at high latitudes and are comparable in the tropics. For submesoscale eddies, kinetic energy begins to clearly dominate over the available potential energy (Kamenkovich et al., 1987). A high level of kinetic energy leads to an increase of a relative role of the inertial forces and a decrease of the stability of the eddy to external forcing: if mesoscale eddies exist for weeks, months and even years (Chelton et al., 2011), then submesoscale eddies exist for hours and days (Eldevik and Dysthe, 2002; Kostianoy et al., 2018).

Altimetry data, as well as a number of regional observations of eddies with the sea surface drifters, indicate that, on average, the number and intensity of mesoscale cyclones and anticyclones

are at the same level (Barbosa Aguiar et al., 2011; Chelton et al., 2011). At the same time, there are significant differences in the dynamics of cyclones and anticyclones. In particular, writing equation (1.1) in terms of the scales of the variables and taking into account the hydrostatic equation, results in a quadratic expression with respect to the Rossby number (Olsen, 1991):

$$Ro^2 + Ro + Bu = 0 \qquad (1.4)$$

In accordance with the sign of the eddy azimuthal velocity, in equation (1.4) $Ro > 0$ for cyclones and $Ro < 0$ for anticyclones. The resulting curve in the *Ro-Bu* parameter space is a parabola with the respect to the Rossby number with a vertex in the region $Ro < 0$ and $Bu < 0$. This means that, according to equation (1.4), mesoscale anticyclones have the upper limits in growth of their *Ro* and *Bu* (i.e., the maximum possible values of v_θ and *h* of the core at a fixed radius and a peak anomaly of stratification of the eddy core), which indicate a quasi-geostrophic balance of forces in the core. Cyclones do not have such theoretical limitations, and their intensification is limited only by friction or the rate of their dynamic instability. This, in particular, explains the fact that, according to observations, cyclonic eddies in the ocean are destroyed faster than the anticyclonic ones (Chouksey et al., 2023). This is despite the fact that quasi-geostrophic modeling predicts the same rates of destruction of both anticyclones and cyclones, provided that their dynamic characteristics are equal (in absolute value) (Carton et al., 2014). In particular, with the initially comparable number of cyclones and anticyclones of Mediterranean water eddies, after 3 months of evolution the percentage of cyclones decreases from 30% to 10% of the total number of eddies of this type (Barbosa Aguiar et al., 2013). As a result, only anticyclonic Mediterranean water eddies (meddies) are observed at large distances from the coast (Richardson et al., 2000). Similar tendencies were obtained for eddies generated at the lee side the Canary Islands (Sangra et al., 2009). Another probable reason for the dominance of anticyclones may be a faster extension of cyclones into filaments in the external shear of the mean currents which is due to their lower vertical extent (Zhmur, 2010).

Eddy generation. The mechanisms of eddy generation are very diverse. The highest concentration of eddy energy is observed along the trajectories of the main ocean currents (see, for example, Fratantoni, 2001). This suggests that dynamic instability of the mean currents is the main mechanism for the generation of mesoscale eddies (Cushman-Roisin and Beckers, 2011; Thomas et al., 2016). One of the main conditions for development of barotropic and baroclinic instability is a change in the sign of the potential vorticity gradient across the current (Cushman-Roisin and Beckers, 2011), which regularly occurs in the ocean. The baroclinic instability develops the most effectively when the sizes of the instabilities is comparable to the 1st baroclinic Rossby deformation radius (Cushman-Roisin and Beckers, 2011), which determines the characteristic horizontal scale of the generated eddies. Eddies are also often generated on topographically trapped currents at abrupt changes of a continental slope or a coastline (see, for example, D'Asaro et al., 1988; Zyryanov, 1995; Pichevin and Nof, 1997; Zatsepin et al., 2011; Kubriakov et al., 2023), due to a velocity shear in the friction layer at the continental slope (Zatsepin et al., 1998; Gula et al., 2015; Elkin and Zatsepin, 2013; Zhurbas et al., 2019), when the mean current meet an island or a seamount (see, for example, Piedeleu et al., 2009), as a result of an increase of a nonlinearity of Rossby waves (Nezlin, 1986), as a result of destruction of larger eddies (Menesguen et al., 2012), due to a heterogeneity of the wind field, especially in the coastal zone or along the ice edge (Hakkinen, 1986; Manucharyan and Thompson, 2017). Zhmur (2010) also

showed that a region of relative vorticity along a mean flow with a certain horizontal velocity shear can be contracted into a compact classical eddy, which after some time is again expands by the flow into a filament and disappears. This way even relatively weak shear flows can form intense eddies. The most vulnerable to deformation by a shear flow are eddies of small vertical extent. Drawing an analogy, we can, in particular, assume that with close interaction of two vortices, a eddy of greater extent will "survive", while the other eddy will stretch into a filament around it. A similar process was observed when studying the merger of anticyclones with the Lofoten Vortex (see Chapter 5).

The merger of eddies of the same sign is a fundamental property of evolution of two-dimensional turbulence observed in numerical experiments. Ultimately, the result of the evolution of a system of eddies in an isolated region is a small number of large eddies (see, for example, McWilliams, 1985; Shchepetkin, 1995; Carton, 2001). Observations in the ocean provide a very limited number of the observed eddy mergers, including subsurface eddy mergers (see, for example, Schultz-Tokos et al., 1994; Filyushkin et al., 2002; Kohl, 2007; Volkov et al., 2015; Carton et al., 2017). After each such transformation, the eddy undergoes geostrophic adjustment to a new equilibrium state, during which part of the available potential energy transforms into kinetic energy. In this case, most of this energy is dissipated into space in the form of gravitational waves (McWilliams, 1988, 2016; Cushman-Roisin and Beckers, 2011), and some goes into filaments and small-scale eddies (Ciani et al., 2016; Oulhen et al., 2022; Reinaud and Carton, 2023).

One of the features of large eddies is an emergence of the proper **propagation velocity.** Under the influence of the planetary β-effect, the mesoscale eddies propagate westwards at a velocity $V_m \sim -\beta R^2$ (Nof, 1981; Cushman - Roisin, 1990; van Leeuwen, 2007; Cushman - Roisin and Beckers, 2011). For large eddies, their propagation velocity is a few centimeters per second, which is sufficient for the eddies to overcome a weak background current. For smaller submesoscale eddies, this effect is too small and such eddies are simply advected by the mean currents (Dewar and Meng, 1995). These eddy propagation velocities are at least an order of magnitude lower than the azimuthal rotation velocities in the eddy core, which indicates that the streamlines in the eddies are closed.

For mesoscale vortices, the radius of which is close to the first baroclinic Rossby radius of deformation (*Rd)*, the eddy propagation velocities correspond to those of long baroclinic Rossby waves. These and other signs of dynamic similarity of these two types of oceanic dynamic phenomena makes some researchers to equate mesoscale eddies with nonlinear solitons (Nezlin, 1986). While nonlinear solitons and eddies actually have a number of similar properties and can be considered dynamically similar, we note that the mechanisms of motion of linear Rossby waves and eddies are different. If in Rossby waves we are talking about the movement of a form, for which meridional translations of water parcels are sufficient, which leads to their rotation, which is transmitted to neighboring liquid columns, creating an appearance of translational movement to the west (Pedlosky, 2013), in eddies the mechanisms are associated with formation β-gyres in their core with a subsequent acceleration of the propagation by the volumes of fluid "pushed apart" by a moving eddy (Cushman-Roisin, 1990). The equivalence in the quasi-geostrophic approximation of topographic or baroclinic β-effects to the planetary one leads to similar mechanisms of eddy propagation when they interact with bottom slopes or with a homogeneous background flow. In particular, the baroclinic β-effect intensifies with the strengthening of the background current, which leads to a proportional increase in the intrinsic mesoscale eddy velocity. For easterly

currents, the baroclinic β-effect combines with the planetary β-effect, and the westerly velocity of the eddy can exceed the effect of eddy advection (Morel and McWilliams, 1995). In particular, this explains the westward movement of the Mediterranean water eddies (meddies) in the subtropical Atlantic against the mean easterly water advection in the region.

An interaction of an eddy with a jet (i.e., the transverse dimensions of which are comparable to the dimensions of the eddy) follows a different scenario. On the zonal flow an anticyclonic eddy forms an anticyclonic meander upstream and a cyclonic meander downstream. The latter, gradually intensifying, can push the eddy across the jet axis. The current can be crossed only by the eddies, the core of which have a potential vorticity anomaly noticeably exceeding that of the jet (Vandermeirsch et al., 2003 a, b).

The mechanisms of eddy decay are also diverse. These include turbulent diffusion (Martin et al., 2001; Meunier et al., 2015), horizontal intrusions (Hebert et al., 1990), dynamic instability of the eddy boundary (Sokolovskiy 1988; Sokolovskiy, 1997 a, b; Zatsepin and Kostyanoy, 1992; Sokolovskiy and Verron, 2000; Benilov, 2000, 2003, 2004, 2005b; Filyushkin et al., 2002; Baey and Carton, 2002; Makarov et al., 2012; Menesguen et al., 2012; Bashmachnikov et al., 2017), which may arise also as a result of interaction with other eddies (Dritschel et al., 1996; Carton et al., 2002; Bersanelli et al., 2016; Carton et al., 2016; Sokolovsky and Filyushkin, 2018) or with uneven bottom topography (Dykhno et al., 1991; Shapiro et al., 1992; Shapiro et al., 1996a; Van Geffen and Davies, 2000; Herbette et al., 2003; Adduce and Cenedese, 2004; Filyushkin et al., 2011; Sokolovskiy et al., 2013; Bashmachnikov et al., 2015c; Zyryanov and Egorova, 2019).

1.3 AZIMUTHAL VELOCITY PROFILES IN VORTICES. RAYLEIGH PROFILE

Detailed studies of the internal structure of eddies have shown that surface and subsurface eddies have the same structure of horizontal and vertical distributions of thermohaline and dynamic characteristics in their cores (see, for example, Olsen, 1991; Pingree and LeCann, 1992, 1993a; Shapiro et al., 1996 b). There are a number of more or less successful approximations of the radial profile of an axisymmetric or elliptical mesoscale eddy (Wu et al., 2007; Zhmur, 2010). The most popular models of axisymmetric eddies used in oceanology are the Rankine vortex (Acheson, 1990), Scully (1975), Q-eddy or Batchelor vortex (Batchelor, 1964) and Rayleigh vortex (Carton et al., 1989; Carton, 1992). The latest model is considered better represent the real structure of ocean eddies. For example, the Rayleigh model very closely reproduces the radial change in the characteristics of the Lofoten Vortex (Fig. 1.6) (see, for example, Belonenko et al., 2017; Bashmachnikov et al., 2017; Bashmachnikov et al., 2018) or of a meddy (see, for example, Pingree and Le Cann, 1993a; Paillet et al., 2002). Many theoretical and methodological aspects of the study of eddy dynamics in subsequent chapters will be based on the Rayleigh radial profile, the properties of which are described in detail below.

The Rayleigh azimuthal velocity profile (Fig. 1.6-1.7) is expressed as (Carton et al., 1989; Carton, 1992):

$$v_\theta(r) = \Omega\, r\, e^{-r^2 / 2R_{vm}^2} \qquad (1.5)$$

where r is the radial distance from the center of the vortex, R_{vm} is the radius at which the azimuthal velocity v_θ reaches its maximum ($v_{\theta m}$).

The amplitude factor can be expressed using R_{vm} and $v_{\theta m}$ as:

$$\Omega = \frac{\sqrt{e}\, v_{\theta m}}{R_{vm}}. \qquad (1.6)$$

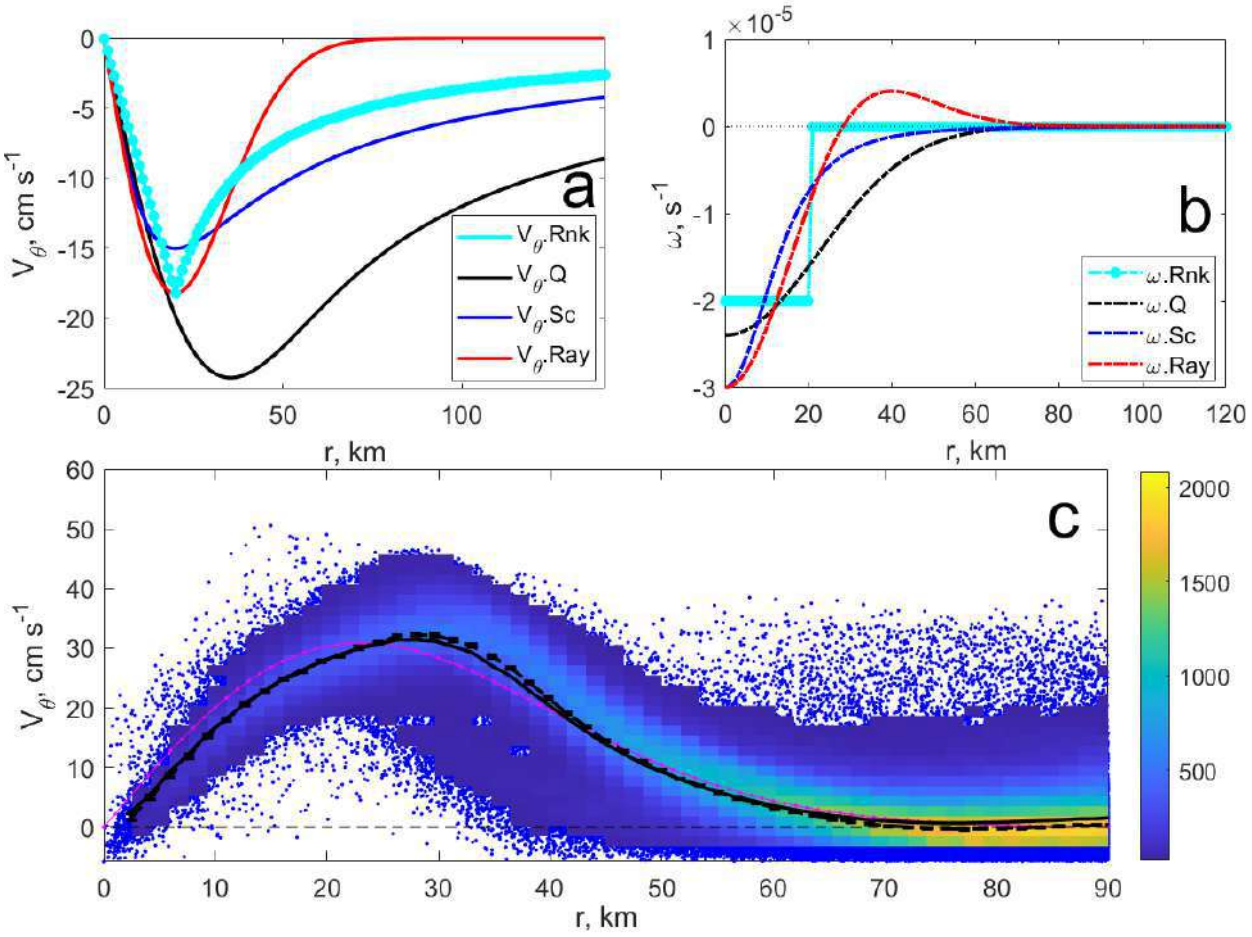

Fig. 1.1. Radial variability of (a) azimuthal velocity and (b) relative vorticity in an eddy with a dynamic radius R_{vm}= 20 km *according to the Rankine (Rnk), Scully eddy (Sc), Q-eddy (Q), Rayleigh (Ray) eddy models. (c) Azimuthal velocities (cm s^{-1}) as a function of distance from the center of the Lofoten Vortex (km) from 1993 to 2015 in the MIT model. The color scale shows the number of observations in the grid cells; black line – average velocity profile, magenta line – approximation by the Rayleigh profile with dynamic radius R_{vm}*= 20 km; *the thin black dashed line marks 0 cm s^{-1}.*

In the geostrophic approximation, such distribution will be generated by the Gaussian profile of pressure with the maximum pressure anomaly in the center of the vortex:

$$P(r) = P_{\max}\, e^{-r^2/2R_{vm}^2}, \qquad (1.7)$$

where $P_{\max} = \sqrt{e}\,\rho_0 f\, v_{\theta m} R_{vm}$ is the hydrostatic pressure in the center of the anticyclone. The numerous simultaneously acting forces should lead to dominance in the ocean of the Gaussian (normal) profile of variability of the scalar anomalies inside an eddy (Eq. 1.7), which, for a quasi-

geostrophic eddy, results in the Rayleigh velocity profile (Eq. 1.5). This explains the good agreement between the Rayleigh profile and observations. Anomalies of the scalar characteristics of the eddy core reduce to the background values at distances of 2-3 R_{vm} from the eddy center o (Fig. 1.6-1.7). Here the limit of the thermohaline core of an eddy can be put.

The relative vorticity for the Rayleigh eddy (ω) is expressed as:

$$\omega(r) = \left(2 - \frac{r^2}{R_{vm^2}}\right)\frac{v_\theta(r)}{r} = \Omega\left(2 - \frac{r^2}{R_{vm^2}}\right) e^{-r^2/2R_{vm}^2}. \qquad (1.8)$$

ω reaches its maximum value in the center of the eddy, equal to:

$$\omega_0 = \omega(0) = 2\sqrt{e}\,\frac{v_{\theta m}}{R_{vm}} \qquad (1.9)$$

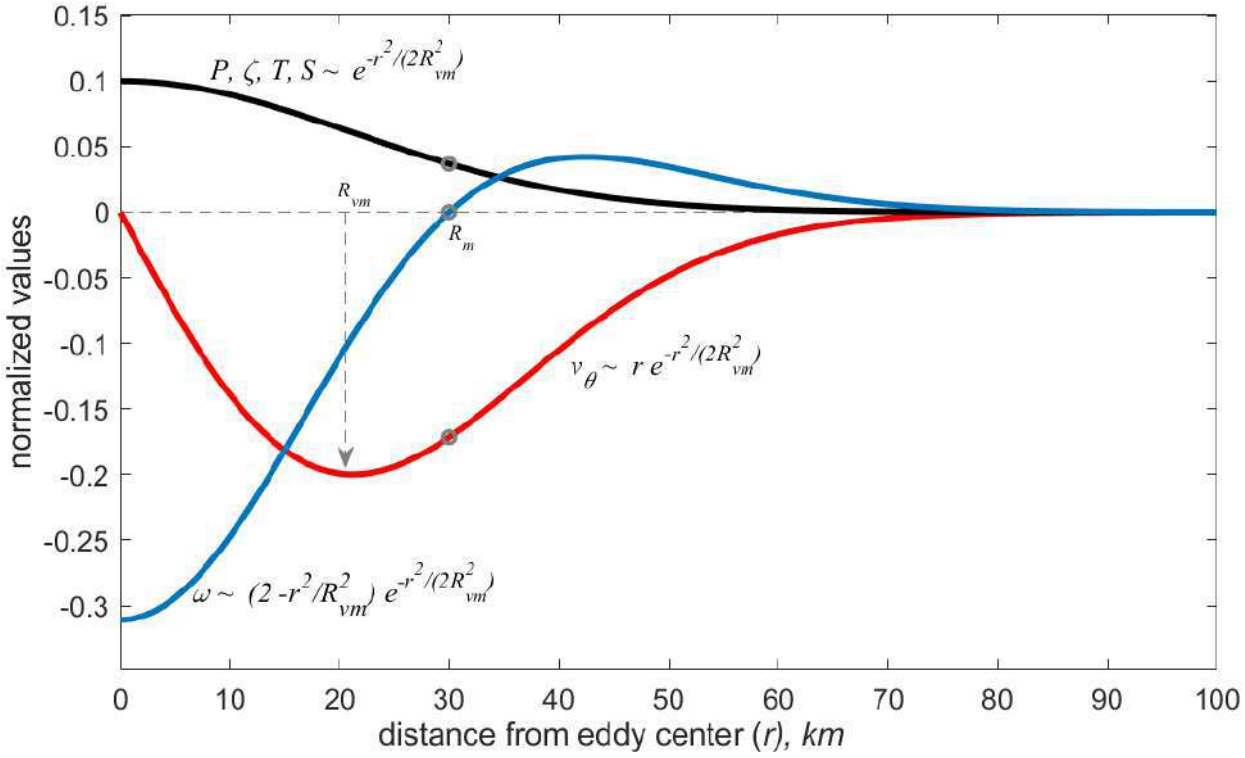

Fig. 1.2. Radial distributions of eddy characteristics with the Rayleigh velocity profile and a dynamic radius R_m = 30 km (R_{vm} = 21 km). P – the water pressure, ζ – the sea level, T – the water temperature, S – the water salinity, v_θ – the azimuthal current velocity, ω – the relative vorticity. The y-axis for different variables are not in scale for a better comparability of the plots.

For the Rayleigh profile, the radius where the relative vorticity crosses zero (R_m) is approximately 1.4 times greater than the radius where the azimuthal velocity reaches its maximum (R_{vm}):

$$R_m = \sqrt{2}\, R_{vm}\,. \qquad (1.10)$$

Here and below, unless specifically stated, the dynamic radius of an eddy is taken as R_m.

Observations show that the potential vorticity anomaly of an anticyclonic eddies often changes sign with distance from the center of the eddy core, both vertically (R-type eddy) and horizontally (S-type) (Morel and McWilliams, 1997). From the types of azimuthal velocity distributions listed above (Fig. 1.6), only the Rayleigh profile allows S-type vortices. The region of the opposite sign of the potential vorticity at the periphery of an eddy is called the "screen".

To conclude this section, we note that this study is devoted exclusively to the monopole-type vortices. Dipole eddy structures such as hetons (Sokolovskiy and Verron, 2014), mushroom-shaped flows or modons (Ginsburg and Fedorov, 1984; Afanasyev and Voropaev, 1989; Afanasyev et al., 1989; Fedorov et al., 1992; Carton, 2001; Ginzburg et al.., 2017), in which nuclei with relative vorticity of different signs coexist, separated vertically or horizontally and mutually compensating each other, are not considered in this study.

1.4 THE ROLE OF MESOSCALE EDDIES IN LATERAL HEAT TRANSPORT

The role of eddies in heat transport varies significantly between ocean regions. Wunsch (1999), using *in situ* observations, showed that the eddy heat flux is negligible compared to the advective heat transport almost everywhere in the ocean. The exceptions are the northern regions of the Western Boundary Currents, where both transports are comparable. In the Atlantic, this is a result of large temperature gradients between the subtropical and subpolar water across the current and the intense eddy formation in the Gulf Stream after its separation from the continental slope. It was also shown that in the region of the Antarctic Circumpolar Current (ACC), heat transport by eddies, being locally small, integrally (along the entire length of the ACC) plays a significant role in the mass balance across the current (Koshlyakov and Tarakanov, 2011; Marshall and Speer, 2012). The use of satellite data confirmed these conclusions: heat transport by eddies does not exceed 10-15% compared to heat advection by the mean currents, slightly increasing towards the tropics (Volkov et al., 2008; Dong et al., 2014; Groeskamp et al., 2020). Nevertheless, the contribution of eddies to the temporal variability of the horizontal heat transport is estimated already to form 30%, when averaged over the World Ocean, being higher in the tropical regions and in the Southern Ocean (Volkov et al., 2008). Eddy heat transport decreases with depth, as expected (Groeskamp et al., 2020). This is a natural consequence of decreasing temperature gradients in deep ocean layers.

The relative smallness of the eddy heat transport compared to that of the mean currents is explained primarily by the predominantly zonal propagation of eddies, while the water temperature gradients are predominantly meridional. Where zonal temperature gradients are large, eddies can play a significant role in the regional heat transport. Examples include upwelling zones or the Gulf Stream front in its northern section.

In further chapters of the thesis, there will be examined two areas where eddies can play an important role in the horizontal heat transport: area of spreading of the Mediterranean Water in the subtropical northeast Atlantic and the area of spreading of the Atlantic Water in the subpolar Norwegian and Greenland Seas (Fig. 1.1).

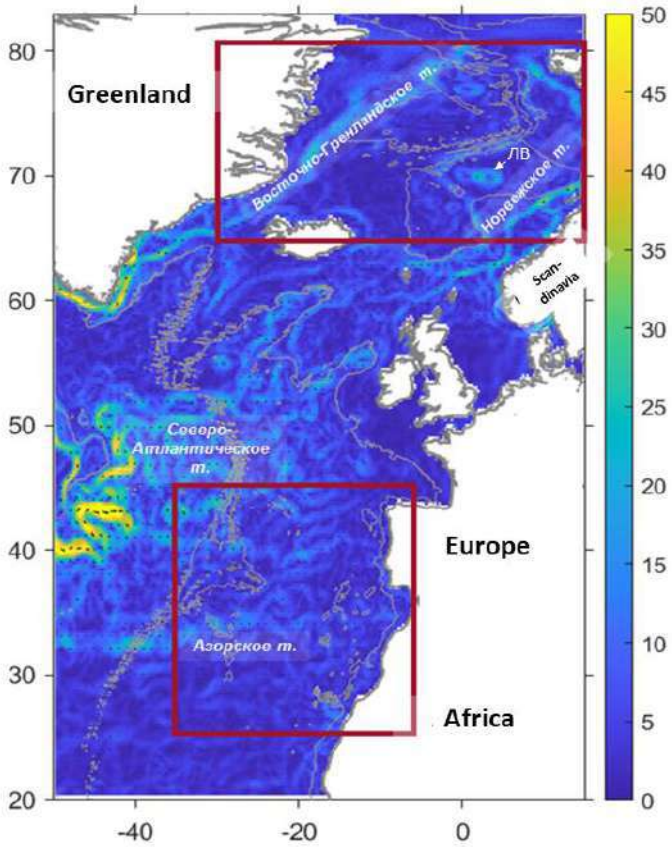

Fig. 1.3 The study regions (burgundy rectangles) overlayed on the map of the background current velocity module (cm s $^{-1}$, color) obtained from AVISO satellite altimetry. The gray contours show the 2500 m isobath and the coastline. LV is the Lofoten Vortex.

In the subtropical northeast Atlantic, the intrathermocline Mediterranean water eddies (meddies) were investigated. There are several advantages in studying this particular type of eddies. First, meddies can be relatively easily identified in the *in situ* data with high positive anomalies of salinity and temperature in the intermediate layers of the Atlantic. Thus, they cannot be confused with any other type of eddies (Fig. 1.2). Second, the region where meddies are formed is localized in a relatively small area of the continental slope of the Iberian Peninsula in the eastern part of the ocean. From here meddies spread west and southwest (Fig. 1.3). This allows, as a first approximation, to estimate the age of meddies from their distance from the peninsula. The outflow of the Mediterranean Water in the eastern part of the ocean favorably distinguishes meddies from similar eddies of the Red Sea Water (reddies) or the Persian Gulf Water (peddies), which originate and dissipate in a relatively small area of the western Indian Ocean (Ciani et al., 2016). Third, despite the deep meddy cores (500-1200 m), meddies from a strong dynamic signal that often reaches the sea surface (Stammer et al., 1991; Oliveira et al., 2004; Bashmachnikov et al., 2009a). Observations have shown that the intensity of this signal is comparable to the intensity of the strongest sea surface eddies in this relatively dynamically quiet ocean region (Bashmachnikov et al., 2012). These considerations, as well as a fairly large number of *in situ* experiments aimed at investigation of meddy dynamics, provide a unique material for studying the life cycle of these subsurface eddies, as well as investigating their manifestations at the sea surface.

In the Nordic Seas, the most intense eddy formation is observed in the Lofoten Basin. In the central, almost flat, part of the basin there exists a quasi-permanent Lofoten Vortex which has a subsurface core. This eddy changes its location so little that it stands out as a pronounced compact

anticyclonic formation on the mean current climatology of the Basin. The Lofoten Vortex does not directly contact either with the steep slopes of the Lofoten Basin or the topographically trapped currents directed along these slopes, which makes it possible to study various aspects of the dynamics of mesoscale eddies in, so to speak, idealized conditions (Fig. 1.1). The ability to observe the same eddy over a very long time makes the Lofoten Vortex a "natural laboratory" for studying mesoscale eddies in the ocean. Like meddies, the Lofoten Vortex has a subsurface core, although the upper boundary of the core lies very close to the sea surface. At the same time, the anomalies formed by the Lofoten Vortex in the sea surface level and temperature are in many ways similar to those above meddies. A detailed study of the vertical structure, dissipation processes in the Lofoten Vortex, as well as its merger with other eddies, makes it possible to better explain some features of the meddy dynamics. Therefore, both objects of this research are complementary.
In addition to the above advantages of analyzing dynamics of meddies and eddies in the Norwegian Sea, a significant influence of both types of eddies on the transport of thermohaline characteristics in the areas of their existence is assumed (Maze et al., 1997; Kohl, 2007; Zou et al., 2023).

1.5 SUBSURFACE MEDITERRANEAN WATER EDDIES, MEDDIES, IN THE SUBTROPICAL ATLANTIC (A BRIEF SUMMARY)

The first published references to field observations of Mediterranean water eddies in the Atlantic emerged almost simultaneously in the brief notes by Swallow (1969) and Piip (1969). In the first case, the observations were performed in the Gulf of Cadiz near the Strait of Gibraltar, and in the second one – somewhat further south, between the Canary and Madeira Islands. In 1978, McDowell and Rossby (1978) observed a Mediterranean eddy more than 5000 km from the Strait of Gibraltar in the vicinity of the Bahamas. The authors coined the term "meddies" to refer to subsurface eddies in the Atlantic, the core of which is filled with the Mediterranean Water. Soon Armi and Stommel (1983) discovered another meddy near the Mid-Atlantic Ridge (MAR) at the latitude of the Canary Islands. This showed that meddies can cross the Atlantic, i.e. that the lifetime of these eddies can be a few years. Subsequent cruises in the Canary Basin confirmed a regular occurrence of meddies in the observations (see, for example, reviews by Armi and Zenk, 1984; Belkin et al., 1986; Kostianoy and Belkin, 1989; Shapiro et al., 1996b; Shapiro and Meshanov, 1996; Richardson et al., 2000; Demidov et al., 2012; Bashmachnikov et al., 2015c; Filyushkin and Kozhelupova, 2020). It turned out that in the eastern part of the subtropical Atlantic, near the Iberian Peninsula, meddies are so numerous (Fig. 1.3) that almost any expedition perfoming *in situ* surveys in the area came across such a subsurface eddy, and often more than one (see, for example, Richardson and Tychensky, 1998). Unique, and currently the only data on the long-term evolution of the characteristics of the same meddy were obtained by Armi and Zenk (1984), who tracked one meddy during two years with RAFOS neutral buoyancy floats, conducting detailed oceanographic surveys of the meddy approximately every six months. During this experiment, it was possible to confirm the ability of the meddy to exist for a long time, and also to describe the processes of a gradual degradation of thermohaline and dynamic anomalies in its core (Armi et al., 1989; Hebert et al., 1990). In addition to individual *in situ* studies (Ivanov et al. 1990; Paillet et al., 1999; Pingree, 1995; Paillet et al., 2002; Carton et al., 2002) and their generalizations (Shapiro et al., 1996 b; Richardson et al.., 2000; Demidov et al., 2012; Bashmachnikov et al., 2015c; Filyushkin and Kozhelupova, 2020), meddies were studied in series of special experiments making a joint analysis of data from RAFOS float and in-situ surveys. Among them it is worth in particular

mentioning the AMUSE project, the goal of which was to identify areas and mechanisms of meddy generation at the Iberian Peninsula (Bower et al., 1997), and the SEMAPHORE project, where it was possible to track meddy trajectories at distances of more than 1000 km from the Iberian Peninsula over the time intervals from six months up to 1.5 years (Richardson and Tychensky, 1998; Tychensky and Carton, 1998). These and other studies have expanded our knowledge about the areas of meddy generation and the directions of their propagation. However, with a few exceptions (see Armi et al., 1989), the meddies life cycles remained unknown.

An analysis of the typical variability of meddy properties with age, in relation to the place of their generation and their propagation routes, was first carried out studies by the author and are presented below in Chapter 4. The obtained description remains the most comprehensive to the date. The study of the characteristics of meddy cores was further supplemented by a study of their manifestations at the sea surface. Analysis and synthesis of the scattered information from other studies and the author's own materials made it possible to identify physical mechanisms behind and to develop a theory of manifestation of subsurface eddies at the sea surface, as well as validate it using meddies as an example (see Chapters 6 and 7).

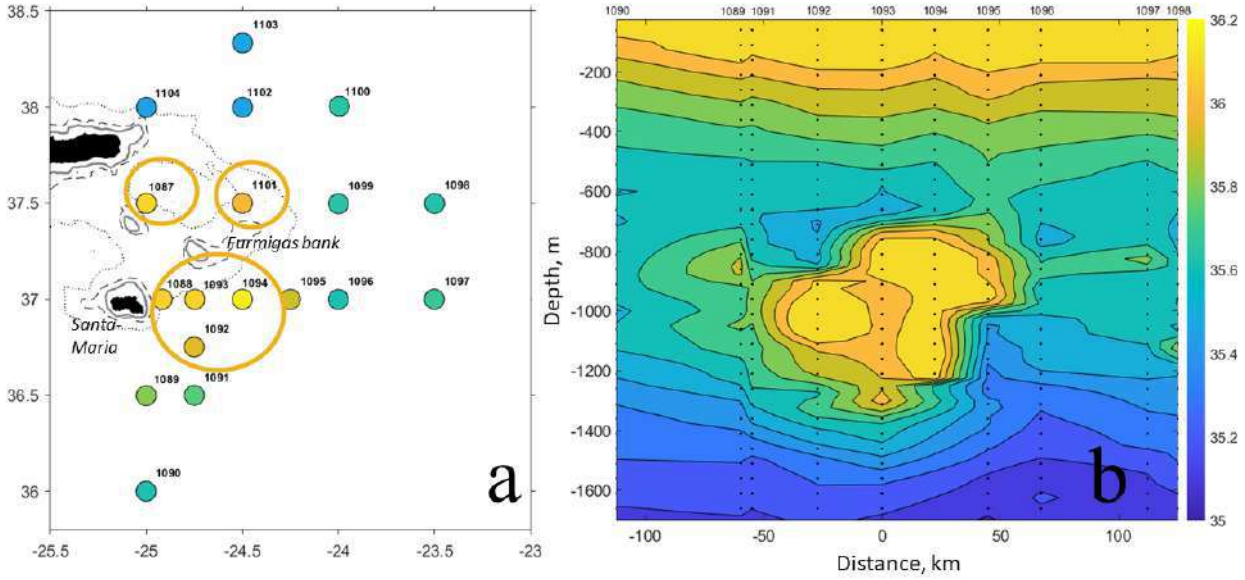

Fig. 1.4. An example of a meddy observed from vertical casts east of Santa Maria island (the Azores) in October 2008 (a) Positions of the vertical casts (circles). The color shows the water salinity averaged between 700 and 1100 m. Isobaths of 500 m (solid line), 1000 m (dashed line) and 2000 m (dotted line) are overlayed. The large yellow circle indicates the position of the main meddy core. The salinity maxima north of the seamount are presumably a result of a disintegration of the meddy core at steep topography. (b) Vertical section through the meddy. The color is the water salinity; the vertical dotted lines are the positions of vertical casts. The presence of salinity maxima separated from the main core indicates that the meddy core began to destroy during its interaction with the topography.

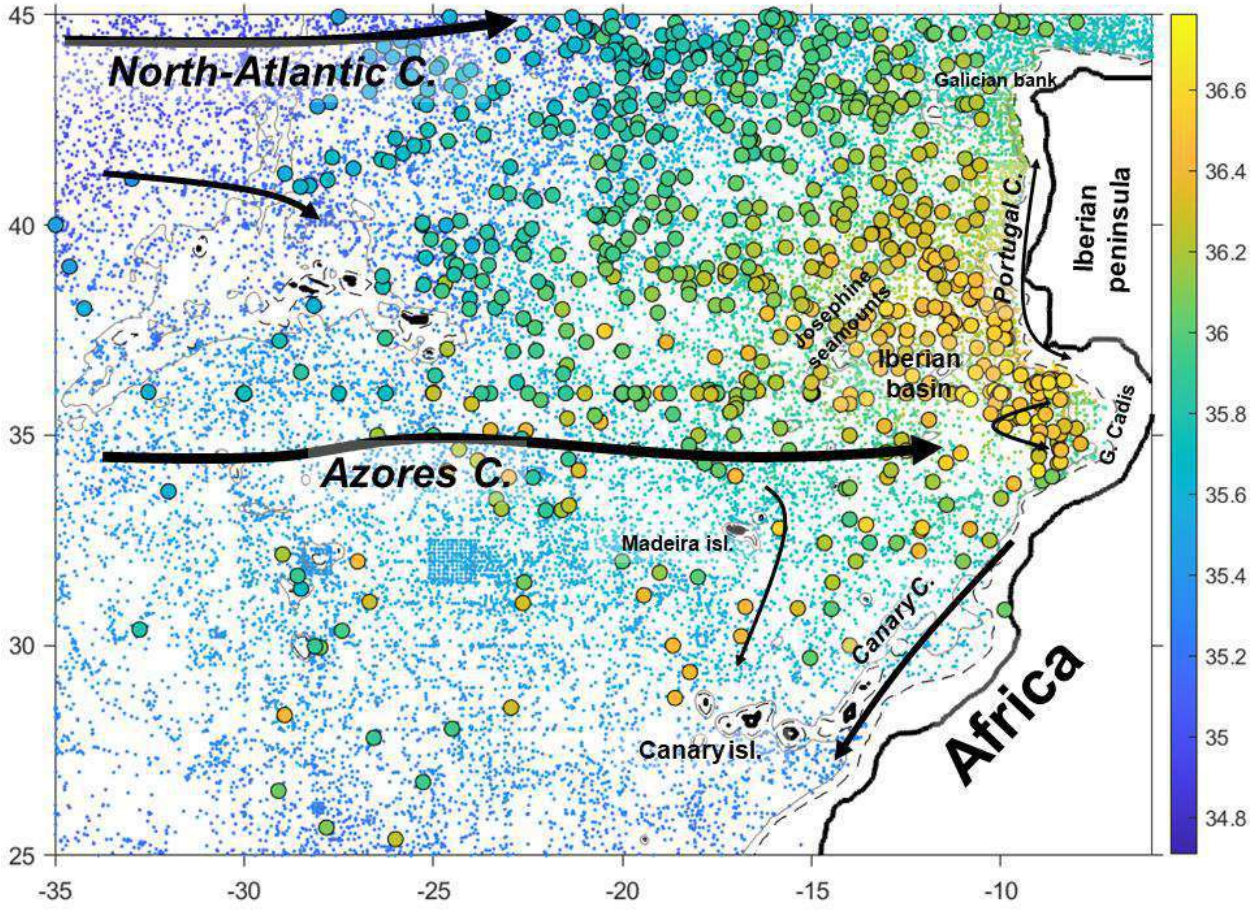

Fig. 1.5. Water salinity at 1200 m in the subtropical Atlantic from the individual vertical casts (1950-2012). Anomalous profiles identified as meddies are indicated with black circles, inside which the maximum salinity values of the identified meddy cores are shown (see Chapter 4 for details). Black arrows schematically indicate the surface currents.

1.6 THE SUBSURFACE LOFOTEN VORTEX IN THE NORWEGIAN SEA (A BRIEF SUMMARY)

The Lofoten Basin of the Norwegian Sea (68-72°N and 2°W-10°E) is a round trough-shaped depression with a maximum depth of about 3250 m (Fig. 1.6). From the northwest, the basin is bounded by the Mohn ridge (with a characteristic depth of about 2000 m), from the south and southwest – by the Jan Mayen fraction zone and uplift (about 2000 m deep) and the Voring Plateau, and from the east by the Scandinavian Peninsula. The maximum depth of the basin is slightly shifted to the southwest from the geometric center of the basin.

The water masses of the Norwegian Sea can be divided into two main types: the upper layer is occupied by warm and saline Atlantic water mass, below which there are cold and desalinated waters of Greenlandic origin (Blindheim and Rey, 2004; Nilsen and Falck, 2006; Rossby et al., 2009). The Lofoten Basin is characterized by an anomalously large for the region thickness of the upper warm water layer, reaching 800-1000 m (see, for example, Boyer et al., 2005) and making it the main heat reservoir of the Nordic Seas (Bjork et al., 2001).

The dynamics of the Lofoten Basin are determined by the dynamics of the Norwegian Atlantic Current (NwAC), which is the main source of warm and salty Atlantic Water in the Nordic Seas. The eastern branch of the Norwegian Current (Fig. 1.6), the Norwegian Atlantic Slope Current (NwASC), is a jet stream topographically trapped by the continental slope of the

Scandinavian Peninsula and having the average velocity of 20-30 cm s^{-1} (Blindheim and Rey, 2004, Koszalka et al., 2011, Lumpkin and Johnson, 2013). Western branch of the Norwegian Current, the Norwegian Atlantic Front Current (NwAFC), extends along the Jan Mayen Fracture Zone, Mohn and Knipovich ridges. It is confined to the subarctic frontal zone and has an average velocity of 10-15 cm s^{-1} (Orvik, 2004; Blindheim and Rey, 2004; Gascard and Mork, 2008; Koszalka et al., 2011; Lumpkin and Johnson, 2013). Along the inner slopes of the Lofoten Basin, a cyclonic circulation that intensifies towards the bottom was discovered, identified first from data of a hydrodynamic model (Nost and Isachsen, 2003; Gascard and Mork, 2008), and then confirmed with trajectories of Argo floats (Poulain et al., 1996; Jakobsen et al., 2003; Orvik, 2004). The velocity of the cyclonic circulation in the upper ocean is 5-10 cm s^{-1}. The circulation is supported by a strong downward deflection of the isopycnals in the Lofoten Basin: the difference in depth between the isopycnals in the central part of the Lofoten Basin and along its boundaries reaches 300 m (Ivanov and Korablev, 1995a, b; Pereskokov, 1999; Orvik, 2004; Rossby et al., 2009, Belonenko et al., 2014). Volkov et al. (2013) also found dipole and quadrupole wave structures (1st and 2nd azimuthal modes of topographic Rossby waves) that rotate counterclockwise around the Lofoten Basin, which further complicates the regional circulation patterns.

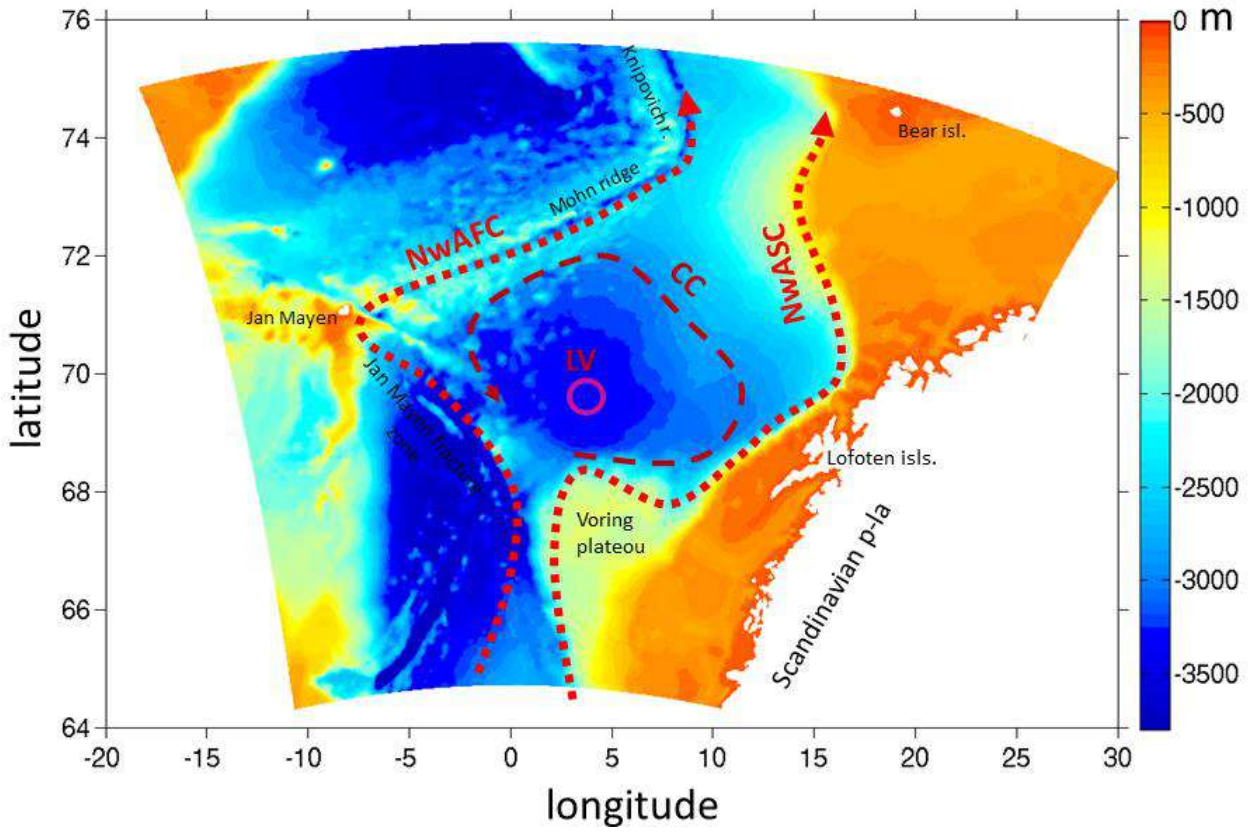

Fig. 1.6. Bottom topography of the Lofoten Basin (m). Red arrows schematically show the main currents: the Norwegian Atlantic Slope Current (NwASC), the Norwegian Atlantic Front Current (NwAFC) and the cyclonic gyre (CG). The pink circle shows the quasi-permanent location of the Lofoten Vortex (LV). The boundaries of this shown region are the isolines of the MIT model grid (see Chapter 5 for details).

A strong instability of the NwAC forms the source for intense mesoscale eddy dynamics of the Lofoten Basin (Koszalka et al., 2011; Volkov et al., 2015), which has been analyzed using

in situ data in a number of studies (see, for example, Blindheim and Rey, 2004; Gascard and Mork, 2008; Lumpkin and Johnson, 2013; Yu et al., 2017; Bosse et al., 2019; Sandalyuk et al., 2020).

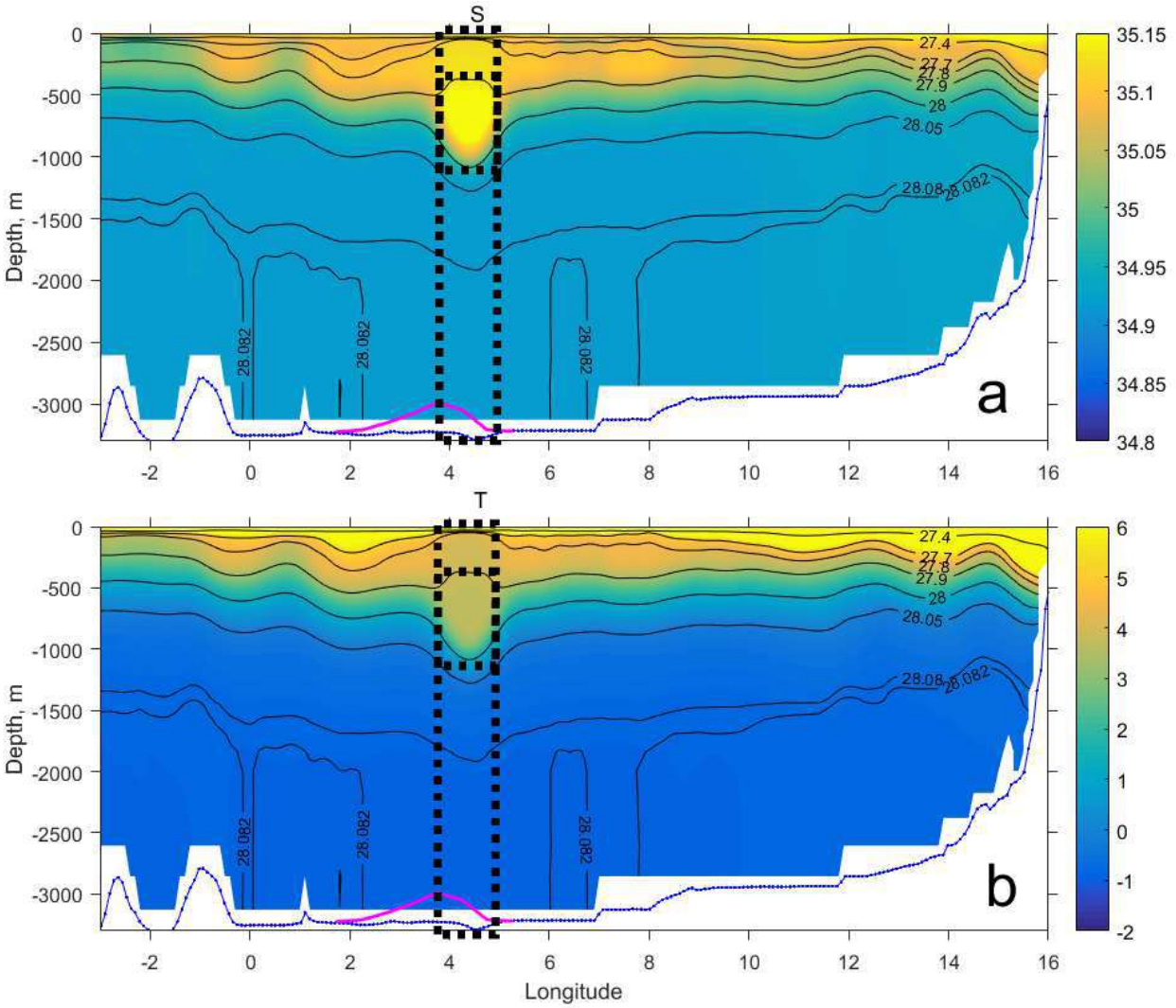

Fig. 1.7. Sections of (a) salinity and (b) water temperature (°C) through the center of the Lofoten Vortex (69.7°N) on 08.24.2005 from the MIT model. Black contours are potential density isolines reduced to 500 m. The LV core and the mean boundaries of three selected layers used in a quasi-geostrophic modeling of stability of the LV (see Chapter 5) are marked with dotted rectangles. The blue line is the bottom topography along the section, the height of the pink line above 3250 m characterizes a relative number of fixations of the center of the LV in the MIT model along the section over 15 years of model calculations (from Bashmachnikov et al., 2017).

Russian oceanographic surveys in the 1970s-1980s discovered a quasi-permanent eddy in the Lofoten Basin (Ivanov and Korablev 1995 a, b), called the Lofoten Vortex (LV, Fig. 1.6). The constant presence of the LV in the basin, the center of which is observed in a limited area of 69-70° N and 2-5° E, was later confirmed with analysis of float trajectories and satellite altimetry data (Soiland et al., 2008; Koszalka et al., 2011; Bashmachnikov et al., 2017). In temperature and salinity, the LV manifests itself as an isolated positive anomaly with a diameter of 60-80 km situated between 200 and 2000 m (Fig. 1.7, see also Alekseev et al., 1991; Romantsev, 1991; Pereskokov, 1999; Belonenko et al., 2018). The dynamic signal of the LV can be traced from the sea surface to the bottom of the basin (Rai et al., 2015). Constantly observed in the central part of

the Lofoten Basin, remote from sharp slopes of topography and main currents (Fig. 1.6), the LW is a “natural laboratory” for studying dynamics of mesoscale eddies in the ocean.

Based on the results of 15 oceanographic surveys of 1985-1991, seasonal variability of the thermohaline anomaly of the LV core was derived (Ivanov and Korablev, 1995a), which is also well reproduced by eddy-resolving hydrodynamic models (Kohl, 2007; Rai et al., 2015). In particular, it was shown that deep convection during the cold season can penetrate into the subsurface core of the LV. During these periods, the depth of the upper mixed layer above the LV significantly exceeded that in the surrounding areas of the Lofoten Basin. This mechanism of differential mixing has been proposed as an explanation for the quasi-permanent presence of the LV in the basin (Ivanov and Korablev, 1995a). Subsequent studies showed that frequent merging of anticyclones with the LV may be an alternative mechanism for its regeneration (Kohl, 2007; Volkov et al., 2015).

1.7 MANIFESTATIONS OF SUBSURFACE EDDIES AT THE SEA SURFACE

The potential vorticity conservation equation is used as the main diagnostic equation for studying dynamics of different nonlinear processes in the ocean, including the eddy dynamics. In the quasi-geostrophic approximation on f -plane in a continuously stratified ocean, the conservation of quasi-geostrophic potential vorticity (q) is (Pedlosky, 2013):

$$\frac{dq}{dt} = 0\,, \tag{1.11}$$

where $\frac{d\ldots}{dt} = \frac{\partial\ldots}{\partial t} + u\frac{\partial\ldots}{\partial x} + v\frac{\partial\ldots}{\partial y}$ and

$$q = \left(\frac{\partial^2\psi}{\partial x^2} + \frac{\partial^2\psi}{\partial y^2}\right) + \frac{\partial}{\partial z}\left(\frac{f_0^2}{N^2}\frac{\partial\psi}{\partial z}\right). \tag{1.12}$$

The stream function ψ in expression (1.12) is derived from the relations $u = -\frac{\partial\psi}{\partial y}$, $v = \frac{\partial\psi}{\partial x}$ and represents the unknown.

In their study, Lapeyre and Klein (2006) investigated splitting equations (1.11)- (1.12) into the stream function inside the fluid column (ψ_{int}), determined by the potential vorticity distribution inside the fluid, and the quasi-geostrophic stream function, determined by the water density distribution at the sea surface (ψ_s):

$$\psi = \psi_{int} + \psi_s. \tag{1.13}$$

Here:

$$\left(\frac{\partial^2\psi_{\text{int}}}{\partial x^2} + \frac{\partial^2\psi_{\text{int}}}{\partial y^2}\right) + \frac{\partial}{\partial z}\left(\frac{f_0^2}{N_0^2}\frac{\partial\psi_{\text{int}}}{\partial z}\right) = q \text{ at } \left.\frac{\partial\psi_{\text{int}}}{\partial z}\right|_{z=0} = 0\,, \tag{1.14}$$

$$\left(\frac{\partial^2\psi_s}{\partial x^2}+\frac{\partial^2\psi_s}{\partial y^2}\right)+\frac{\partial}{\partial z}\left(\frac{f_0^2}{N_0^2}\frac{\partial\psi_s}{\partial z}\right)=0 \text{ at } \frac{\rho_0 f_0}{g}\frac{\partial\psi_s}{\partial z}\bigg|_{z=0}=\rho\big|_{z=0}. \quad (1.15)$$

In equation (1.14), the initial distribution of potential vorticity q in the fluid column is predefined. At the sea surface, the boundary condition of equation (1.15) is used, $\frac{\rho_0 f_0}{g}\frac{\partial\psi}{\partial z}\bigg|_{z=0}=\rho\big|_{z=0}$, where the density field at the sea surface $\rho\big|_{z=0}$ is determined by the heat and freshwater balance at the sea surface. At the bottom, the following boundary condition is assumed: $\frac{\partial\psi}{\partial z}\bigg|_{z=H}=0$.

A numerical study of this system of equations showed that the density distribution at the sea surface affects the dynamics of the upper layer of the ocean, and this influence decreases exponentially with depth and can be traced for density heterogeneities of mesoscale down to 500 - 1000 m. The penetration depth depends on the upper ocean stratification and horizontal size of the sea surface inhomogeneity. In turn, anomalies of potential vorticity inside the fluid can manifest themselves in the nonlinear dynamics of the sea surface. Heterogeneities of q within the ocean can contribute up to 30% to the variability of dynamic characteristics at the sea surface (Lapeyre and Klein, 2006). The latter result is particularly important for this study because it allows relating the potential vorticity anomaly in the fluid to the sea surface dynamics recorded from satellites.

The manifestation of subsurface eddies at the sea surface will be determined by the stratification of the upper ocean. According to the Taylor-Proudman theorem, on a rotating Earth, a body moving in a barotropic ocean generates a barotropic signal, the characteristics of which are constant throughout the water column, from the sea surface to the bottom. For quasi-geostrophic movements, this immediately follows from a joint use of the equations of motion and hydrostatics. If the background flow does not significantly deform the geometric characteristics of an eddy with an independent velocity structure, then above the subsurface anticyclone we should observed an analogue of the Taylor vortex, similar to a formation of this pattern over seamounts during their interaction with the impinging flow (Proudman, 1916; Taylor, 1917; Huppert, 1975). If stratification is present, the rotation decreases in with distance from the eddy core or the top of the seamount. The rotation area narrows upwards and weakens, forming a Taylor cone (White et al., 2007). The vertical scale of the influence of subsurface structure on dynamics of the fluid column can be estimated as (Owens and Hogg, 1980):

$$H=\frac{f}{N}R, \quad (1.16)$$

where R is the horizontal scale of the eddy. For the subtropics, where the ratio $f/N \sim 0.01$, we get that an eddy with a radius of 10 km, moving relative to the upper ocean, will influence the 100 m layer of water above it, i.e. only eddies with a very shallow core can appear on the sea surface. A large mesoscale eddy with a radius of 100 km will affect already the 1000-meter water column, and the influence of intrathermocline eddies of this size can already be detected on the sea surface. At subpolar latitudes, where the f/N ratio is several times higher, the manifestation of subsurface eddies at the sea surface increases accordingly.

Although it is intuitively clear that the larger the radius and the shallower the depth of the core, the more intense the signal of the subsurface eddy on the sea surface should be, formula (1.16) does not allow us estimating the intensity of this signal and, therefore, an ability to detect it using satellite observations. In this sense, it is interesting to analyze the few *in situ* observations of the structure of current velocity over deep-core eddies in highly stratified tropical and subtropical regions of the ocean, such as meddies. Typical vertical profiles of azimuthal current velocities observed over a meddy core show a gradual decrease in rotation velocity above its core towards the sea surface. However, despite a significant depth of meddy cores (500-1200 m) and a fairly strong stratification, observations suggest a rather slow decrease in the rotation velocity towards the sea surface: from 15 cm s^{-1} in the core of the northern meddy Ulla to 10-15 cm s^{-1} at the surface seas (Paillet et al., 2002), from 20-30 cm s^{-1} in the core of a small meddy Pinball to 10-20 cm s^{-1} at the sea surface (Pingree, 1995), from 20-30 cm s^{-1} in the core of a meddy Bobby to 10-25 cm s^{-1} (Pingree and LeCann, 1993 b), from 20 cm s^{-1} in the Smeddy meddy core – to 10 cm s^{-1} at the sea surface (Pingree and LeCann, 1993a). For typical rotation velocities at the sea surface of 10-20 cm s^{-1} and a typical meddy radius of the order of 30 km, the sea level anomalies formed by the meddy are of the order of 10 cm, which corresponds to along-track altimetry observations over meddies (Oliveira et al., 2000). This makes it possible to identify the surface manifestations of these eddies in interpolated AVISO altimetry data (Bashmachnikov et al., 2009). On average, combining observations *in situ* and AVISO, it was shown that the relative vorticity of meddy signals at the sea surface was about 30% of that in the meddy cores (Bashmachnikov et al., 2014). The theory of influence of subsurface eddies on the sea surface is developed in the subsequent chapters of this work (Chapters 6 and 7).

Chapter 2. Identifying mesoscale and submesoscale eddies using *in situ* and remote sensing data

2.1 INTRODUCTION TO CHAPTER 2

In this chapter there are described *in situ*, satellite and high-resolution hydrodynamic modeling data used in further study, algorithms for identifying eddies in different datasets, and a comparative assessment of the information about eddies obtained using different types of data.

With *in situ* data identification of eddies and evaluation of their characteristics ideally requires polygon surveys. Polygon series of vertical sates also makes it possible to obtain a geostrophic estimate of the current velocity in eddies, which is sometimes supplemented with direct measurements. A detailed survey of a mesoscale eddy takes several days, up to a week. With an average propagation velocity of a mesoscale eddy of the first cm s^{-1}, one can assume a relative invariance of the position and properties of an eddy. In the case when eddies are unambiguously identified with thermohaline anomalies of their core relative to the background, it is also possible to identify an eddy using single cast. Another way to identifying eddies with *in situ* data is recording of cyclonic/anticyclonic rotation with freely moving floats. However, without additional *in situ* soundings, such observations often do not allow estimating the size, vertical extent, and other important characteristics of eddy cores.

The vast majority of satellite observations of eddies in the ocean are carried out using satellite altimetry data (sounding of the ocean surface in the microwave range at a frequency of 13 GHz and higher). In altimetry data, automatic algorithms for identifying eddies using the sea level anomalies have been developed. They allowed obtaining statistics of eddy characteristics in most areas of the World Ocean (see, for example, Chelton et al., 2011). The number of eddy surveys using satellite synthetic aperture radars (SAR, usually at frequencies of 1-10 GHz) is increasing. In both of the above-mentioned frequency ranges, the earth's atmosphere is transparent to electromagnetic waves, which makes it possible to use these ranges equally effectively both for cloudless subtropical regions and for polar regions covered with clouds most of the year.

Although both altimetry and SAR data are derived using radar instruments, the principles of obtaining ocean information and the spatial resolution of the resulting data differ significantly. Satellite altimeters measure the distance from the satellite to the sea surface along the satellite track only. The satellite receives a reflected signal from an area with a diameter of 2-10 km, which determines the along-track resolution, usually taken equal to 7 km. After applying numerous corrections, the final dataset represents the sea level height relative to the geoid. To cover a certain area, several satellite traks are required with a distance between tracks ranging from tens to a few hundred kilometers. Interpolation of along-track data in space and time makes it possible to obtain two-dimensional images of the sea surface height with a relatively low spatial resolution, 0.25x0.25 degrees, in the often used AVISO altimetry database (https://www.aviso.altimetry.fr/en/home.html). SAR images record the intensity of the reflected signal in two parallel bands along the satellite trajectory. The most effective reflection of the ocean comes from small-scale irregularities of the sea surface – capillary waves (ripples). The use of the synthetic aperture method makes it possible to achieve high spatial resolution (about 10-100 m) not only across, but also along the satellite track. The algorithms for automatic identification of

eddies in SAR images are still under development, and eddy structures in these data are the most often identified visually. Despite the difficulties of identification, sufficiently large regional datasets of a massive eddy detection in SAR images have already been accumulated and these results can be compared with the satellite altimetry data.

The widespread use of images in the infrared (IR) and visible ranges (ocean color, OC) for analyzing eddy dynamics is limited by the cloud cover, impenetrable in these frequency ranges, as well as by the signal distortion by thin high clouds and aerosols, which often cannot be fully eliminated. In addition, identification of eddies in IR or OC images is carried out by analyzing the spatial structure of the anomalies of the recorded characteristics, which implies the presence in the vicinity of an eddy fairly pronounced background gradients of the ocean surface temperature or chlorophyll-a.

In addition to satellite observations, progress in the hydrodynamic modeling and advances in computer recources presently allow the use of high-resolution numerical ocean climate models where mesoscale eddies are resolved. In this study the results of an eddy-resolving hydrodynamic Massachusetts Institute of Technology Global Climate Model (MIT GCM, USA) with a spatial resolution of 4x4 km (Marshall et al., 1997) and the Alfred Wegener Institute Finit Element System Ocean Model (FESOM, Germany) with a resolution of 1x1 km (Wang et al., 2014) were used.

The subsequent sections of this chapter describe in detail the different datasets used and the methods for identification of eddy structures in the datasets, as well as compare the eddies characteristics obtained by different methods.

2.2 CLIMATOLOGY OF WATER PROPERTIES IN THE SUBTROPICAL ATLANTIC FROM *IN SITU* OBSERVATIONS

In vertical *in situ* profiles eddies are usually identified as anomalies of thermohaline characteristics, and sometimes also nutrients, turbidity, etc., localized in a certain depth range, or as localized areas of rotating current velocity. The Mediterranean water eddies (meddies) in the Atlantic, further analysed in Chapter 4, are recognized particularly well by positive thermohaline anomalies of their cores. In the absence of background observations, eddy-related anomalies are determined relative to climatological temperature and salinity.

This section describes the *in situ* data, which were used to identify meddies, as well as the algorithms for construction of climatology of the thermohaline water propeties and of the mean mid-depth currents of the Northeast Atlantic.

2.2.1 IN SITU DATA

In the subtropical Atlantic as the main source of *in situ* data was the World Ocean Database (WOD) of the National Oceanographic Data Center (NODC, http://www.nodc.noaa.gov/). This dataset includes data from CTD (Conductivity-Temperature-Depth) probes with high vertical resolution (1 m or less), data from profiling ARGO floats (PFL - Profiling Float) with intermediate vertical resolution (1-10 m), as well as data from bathometers and probes (OSD - Ocean Station Data) with low vertical resolution (more than 10 m). All vertical profiles of the WOD dataset undergo automatic quality control procedures with the assignment of quality marks, both to observations at individual levels and to entire profiles. Over 54 000 *in situ* temperature and salinity

profiles of the WOD dataset since 1950, which have also passed a number of additional quality assessments, were used for meddy detection (Table 2.1).

For the Nordic Seas, vertical structure and temperature/salinity anomalies of mesoscale eddies were estimated using the EN4 Hadley Center database (https://www.metoffice.gov.uk/hadobs/en4/). The basis of the EN4 array forms the WOD dataset, enhanced with additional data, mainly in subpolar and polar latitudes, from Global Temperature and Salinity Profile Program (GTSPP), the Arctic Synoptic Basin-wide Oceanography (ASBO) and others. An additional technical convenience of using the EN4 array is the reduction of data to a selected set of depth levels. The EN4 data is subject to a more accurate procedure for data filtering of anomalous profiles and identifying duplicate stations than the WOD data (Good et al., 2013). However, this can also lead to the removal of actual temperature and salinity anomalies, which is especially critical for identifying the the Mediterranean Water lenses in the subtropical Atlantic.

Bathymetric data, in particular used to obtain the shape the averaging window when constructing a climatology of temperature and salinity, were derived from the ETOPO2 dataset (http://www.ngdc.noaa.gov/mgg/fliers/01mgg04.html).

Table 2.1. Statistics in situ profiles by the type of probes used, with high vertical resolution (CTD), medium vertical resolution (PFL) and low vertical resolution (OSD). Data from high- and medium-resolution profiles were reduced to 25-m vertical resolution. The percentages in the table show the percentage of WOD array profiles that passed all additional filtering procedures for both temperature and salinity.

Data type	Initial number of profiles	>50% quality values on vertical profile	>90% quality values on vertical profile
CTD	9,973	99%	96%
PFL	21,634	96%	95%
OSD	22 822	96%	91%
Total	54 429	97%	93%

Besides using the original WOD array data quality marks, additional quality control consisted of several steps. The first step was to screen out instrument malfunctions or calibration errors by assessing anomalies in temperature and salinity profiles relative to WOA climatology (Wold Ocean Atlas, https://www.ncei.noaa.gov/products/world-ocean-atlas). A profile was considered poor if the entire profile deviated from the climatological one by more than 5 standard deviations. The average standard deviations for the study area of 0.07 for salinity and 0.35ºC for temperature were used as a criterion. If critical deviations from the WOA climatology profile were observed only for a part of the profile, then the profile was considered “dubious” and the reliability of the data were checked with expert analysis. The decision was made based on the number of manifestations of the same type of “dubious” structures in the study area. In the upper 100 m layer and in the layer of propagation of the the Mediterranean Water (700-1500 m), this filter was not used, since in these layers the dispersion of thermohaline characteristics is higher than at other depth levels, and actual deviations from the climatology can significantly exceed the criterion used. The next step was to remove the density inversions. In the section of the profile where a density inversion higher than 0.02 kg m^{-3} was observed in the depth range of less than 200 m, an attempt was made to automatically correct the inversion by artificially “mixing” the anomalies.

The salinity profile was attempted to be smooth first, since salinity is generally more susceptible to observational errors, and then, if necessary, the temperature profile as well. If the automatic correction resulted in an increase in the local standard deviations of the adjusted temperature or salinity profiles compared to their original profiles, then these corrections were canceled. After passing these filtering procedures, sections of the profiles that were found to be unreliable but whose vertical thickness did not exceed 200 m were filled with interpolated values: linear interpolation for low-resolution OSD data and piecewise-cubic Hermite polynomial interpolation for higher-resolution CTD and PFL data. After these corrections, all high-resolution profiles were reduced to a standard vertical resolution of 25 m. In more than 90% of temperature and salinity profiles, at least 90% of all data-points passed all quality tests and did not require additional correction (Table 2.1).

In Fig. 2.1(ac) for selected horizons shows the coverage of the area with filtered observational data. In the upper 1900 m layer the data are distributed fairly evenly (Fig. 2.1ab). Below 2000 m, the lack of ARGO (PFL) data results in less dense observational coverage of the area. Areas of regular sounding of the area along standard sections are clearly visible (Fig. 2.1c). Peaks in the vertical profiles of the amount of data (Fig. 2.1d) – observations at standard oceanographic horizons with bottles (OSD): WOCE A03 (at 36ºN), WOCE AR21 (at 20ºW), WOCE A16 (at 25ºW).).

The density of the spatial distribution of CTD (and to a lesser extent OSD) profiles tends to decrease from the Iberian Peninsula to the Mid-Atlantic Ridge. ARGO profiles (PFL), in contrast, cover the study area fairly evenly, but are virtually absent in the areas with sea depths less than 1000 m. In time, OSD data were most widespread in 1970-1995. (with the maximum number of soundings between 1985 and 1990), CTD data - in 1985-2000. (with the maximum number of soundings between 1990 and 1995), and PFL data - after 2000. (with the maximum number of soundings after 2005). The data was fairly evenly distributed across the seasons. Climatology maps were constructed under the assumption that there were no strong interannual fluctuations in water characteristics below the upper 100th layer during the analysis period (since 1950).

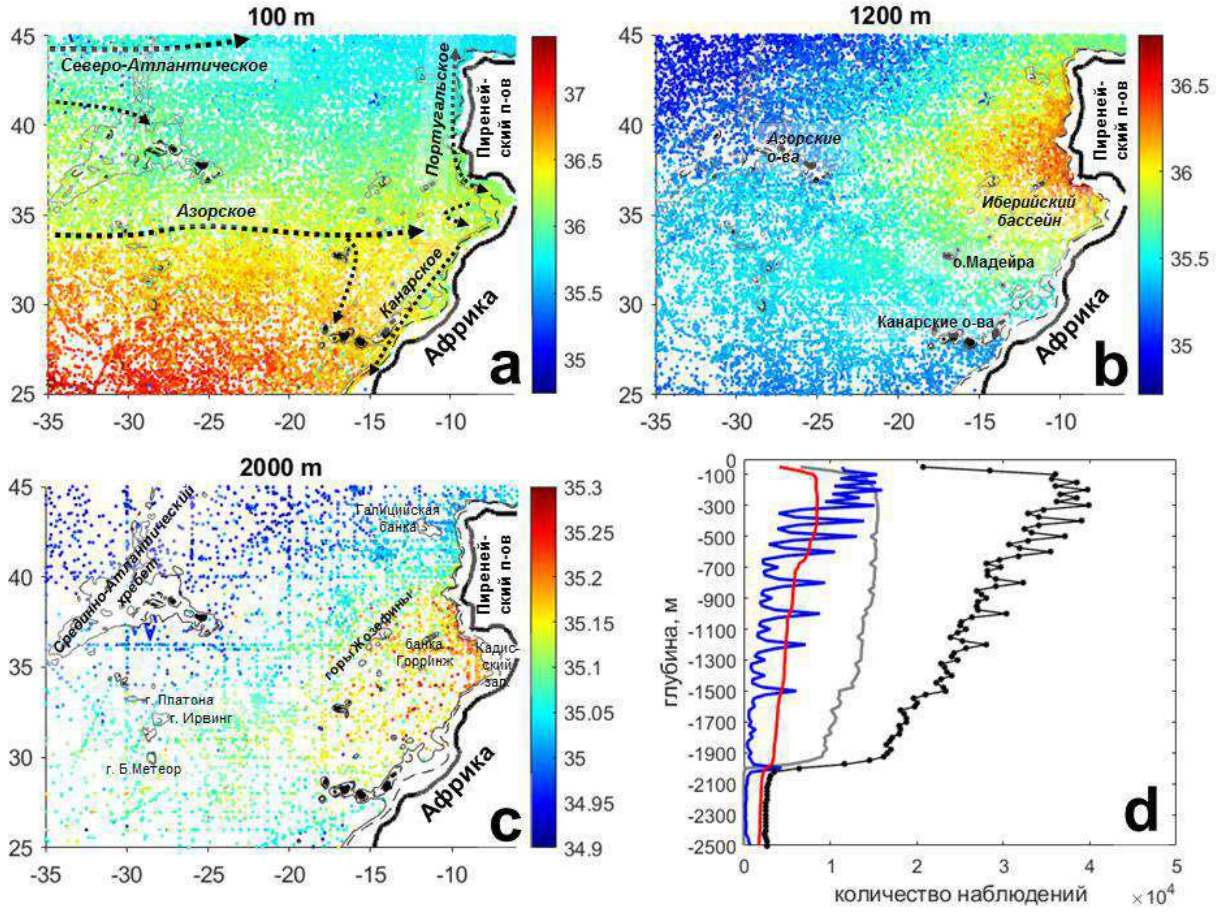

Fig. 2.1. Spatial distribution of temperature and salinity observations (1950-2013) at: (a) 100 m, (b) 1200 m, (c) 2000 m, which passed all quality checks. The color indicates water salinity. The black arrows in the panel (a) schematically show the main surface currents. (d) Number of temperature and salinity values, which passed the quality control procedures: the black line with markers shows the total number of data at different depth levels, the gray line shows PFL data only, the red line shows CTD data only, and the blue line shows OSD data only (from Bashmachnikov et al., 2015a,b).

2.2.2 Construction of MEDTRANS climatology using the modified Barnes optimal interpolation analysis

This section describes a new method for generating a climatology of the subtropical Atlantic (called MEDTRANS climatology), against which eddies of the Mediterranean Water were subsequently identified from data *in situ* observations.

At the time of development of the method and construction of the climatology, there were several databases of global and regional climatologies, including the study area. The most popular World Ocean Atlas 2009 (WOA09) with a window size for generating values on a regular grid of 444 km and a final grid resolution of 1ºx1º. The current edition of the World Ocean Atlas 2018 (WOA18) has a window size of 214-321 km and a grid resolution of 0.25ºx0.25º, however, the technique used in WOA18 for generating climatological distributions with a window of more than 200 km radius leads to an excessive smoothing of frontal zones (Bashmachnikov et al., 2015a). This is especially significant near the continental slope of the Iberian Peninsula, where the Mediterranean Undercurrent (MUC) has a width of 20-80 km and is characterized by very high

temperature and salinity gradients across the flow. It is poorly represented in WOA18. In the MEDTRANS objective analysis technique below, the topographically captured Mediterranean Undercurrent is represented significantly better, which, in particular, results from reducing the local window radius near the Iberian Peninsula to 70 km. In addition, the method of deformation of the smoothing window at the steep bottom slopes and the isopycnic mapping method are used. Both innovations make it possible to reduce the degree of smoothing of frontal zones compared to WOA, and also to avoid an appearance of artificial temperature and salinity anomalies in the vicinity of frontal zones, which is typical for isobaric mapping (Lozier et al., 1994).

Several alternative climatologies are freely available for the study area: AMA (Roemmich and Gilson, 2009), MIMOC (Schmidtko et al., 2013) and DIVA (Trupin et al., 2010). The AMA climatology is based solely on ARGO float data. This dataset does not allow mapping of the Mediterranean Undercurrent (where there are virtually no ARGO floats) and is not suitable for our analysis. DIVA climatology produces rather noisy data, which makes it difficult to identify anomalies against its background. The closest to the MEDTRANS climatology is MIMOC, which is based on isopycnic mapping. However, this climatology has coarse spatial resolution of 0.5ºx0.5º and contains significant errors in temperature and salinity distribution below 1500 m (see Bashmachnikov et al., 2015a).

In this study the neutral density surfaces γ_n are used as isopycnal surfaces (McDougall, 1987; Jackett and McDougall, 1997). This is a generalization of the concept of isopycnic surfaces of potential density σ_n (n = 0, 1, 2, etc., corresponding to a reference level of 0 m, 1000 m, 2000 m, etc.): at the reference level the surfaces σ_n and γ_n are parallel to each other, but they may diverge as the isopycnals move away from this level. Along the neutral buoyancy surface γ_n, the change in density due to salinity compression (β) is exactly compensated by thermal expansion (α): $\alpha \nabla_n \theta - \beta \nabla_n S = 0$, which makes precludes development of the gravitational instability when a fluid parcel propagates along γ_n (McDougall, 1987).

To map the values of the observed temperature and salinity profiles onto a regular grid, the Barnes optimal interpolation method was used on γ_n-surfaces, taking into account the peculiarities of hydrodynamics of the along-slope currents (Bashmachnikov et al., 2015a). The regional MEDTRANS climatology is available at https://www.mare-centre.pt/en/research/data-library/medtrans-data .

Climate mapping of temperature and salinity in the subtropical Northeast Atlantic (25-45ºN and 6-35ºW) was carried out to assess more accurately the distribution of the Mediterranean Water (MW) in the Atlantic, as well as to evaluate the characteristics of geostrophic currents at intermediate depths. The upper layers in the region are dominated by two zonal currents: the southern branch of the North Atlantic Current (SNAC), which crosses the Mid-Atlantic Ridge (MAR) at 45-48º N (Bower et al., 2002), and the Azores Current (AzC), which crosses the MAR at 34-35º N (Klein and Siedler, 1989; Jia, 2000). A jet AzC is about 60 km wide and separates the region of warmer and saltier tropical waters from the region of subtropical waters; the dynamic and thermohaline front of the AzC can be traced down to 1000-1500 m (Kase and Siedler, 1982; Volkov and Fu, 2010). SNAC separates subtropical waters from subpolar waters. The SNAC frontal zone can be traced to about 1000 m. In addition to the jet streams, in the upper 200-300-m layer of the subtropical Atlantic, Pollard and Pu (1985) note the predominance of distributed transport directed to the east and southeast. This transport was later found to be divided into several

relatively weak jet streams directed southeastwards (Paillet and Mercier, 1997). The number and the locations of the streams change over time. Near the Iberian Peninsula and the coast of northwestern Africa, the mean circulation is represented by the Portuguese Current (PC) and the Canary Current (CC), which are circulation systems consisting of branches of the open ocean and the most known coastal upwelling branches (Martins et al., 2002; Perez et al., 2001; Pelegri et al., 2005, Nolasco et al., 2013). Under the coastal branch of the Canary Current, there is a deep current captured by the continental slope of Africa, which transports north the Antarctic Intermediate Water (AAIW) as far as to the Gulf of Cadiz (Louarn and Morin, 2011). Beneath the upwelling branch of the Portuguese Current is the northward-directed Mediterranean Undercurrent (MUC), which is divided into the upper and lower veins (Ambar, 1983; Ambar et al., 2008).

Repeated occurrence of Mediterranean water eddies (meddies), which form pronounced anomalies of temperature (up to 4ºC) and salinity (up to 1) in the intermediate waters of the study area (Richardson et al., 2000), can significantly distort local climatological fields. At this stage, it was necessary to remove the strongest anomalies associated with meddies. After a profile inside a meddy was detected, all the nearby profiles within a 50 km distance and within the 30-day time interval from the date of the recorded meddy-profile were excluded. This was done in order to remove possible influence of the meddy skirt on the climatology. Eddy identification was carried out relative to WOA climatology using the Richardson criterion (Richardson et al., 1991), where a meddy is identified with the salinity anomaly of at least 0.2 in a layer at least 200 m thick, located in the depth range of 500-1500 m. In a further study (Chapter 4), this criterion was refined. The Mediterranean Undercurrent produces a strong local temperature and salinity anomaly which can be taken as that of a meddy in the highly smoothed WOA climatology. To avoid a false removal this climatological structure, the continental slope region of the Iberian Peninsula with the depths of 2500 m or less was excluded from the filtering procedure. As a result of the filtering, about 4% of all available profiles were discarded in the study area.

Next, the spatial distributions of temperature and salinity at various depth levels were formed. Persistent positive temperature and salinity anomalies (relative to WOA climate profiles) were identified. These were particularly noticeable below the 1500 m level in the OSD-type profiles performed along standard transects with XCTD instruments from merchant ships. This feature was not observed in the CTD and PFL data and was presumably caused by the drawbacks in the algorithms of depth estimation in the XCTD observations (Levitus et al., 2008). To exclude this effect, temperature and salinity deviations in OSD profiles from WOA in the depth interval between 1500 and 2000 m were summed in each 100x100 km cell. Given a normal distribution of data deviations from the climatology, one would expect the sum of the deviations to be close to zero, and at least within the range $\pm n\ 1.96\ std/\sqrt{n}$, where n is the number of data and *std* is the average standard deviation of temperature and salinity from the climatology. With a typical n = 30, those OSD soundings for which the sum of deviations from WOA exceeded 1 in salinity and 4ºC in temperature were excluded. The PFL profiles (ARGO floats) with signs of degradation of salinity sensors over time were also excluded, i.e. when the PFL salinity began to steadily decrease with time and showed a difference in the final part of the float trajectory by more than 5 climatic standard deviations either from the WOA climatology or from the average of the neighboring PFL profiles performed during the same time period.

The profiles remaining after all filtration were vertically interpolated to local levels of the surfaces of neutral buoyancy γ_n. In this study, 53 neutral buoyancy surfaces were used: γ_n = 25.50, 25.60, 25.80, 26.00, 26.20, 26.40, 26.60, 26.70, 26.80, 26.90, 26.95, 27.00, 27.05, 27.10, 27.15,

27.20, 27.25, 27.30, 27.35, 27.40, 27.45, 27.50, 27.52, 27.54, 27.56, 27.58, 27.60, 27.62, 27.64, 27.66, 27.68, 27.70, 27.72, 27.74, 27.76, 27.78, 27.80, 7.82, 27.84, 27.86, 27.88, 27.90, 27.92, 27.94, 27.96, 27.97, 27.98, 27.99, 28.00, 28.01, 28.02, 28.03, 28.04 (kg m^{-3}). These γ_n values were chosen to ensure their sufficiently uniform distribution with depth, so that the average vertical distances between the surfaces were no more than 50 m in the upper 1500 m layer and no more than 100 m at bigger depths. In the upper 100 m active layer, isopycnal surfaces were replaced with the isobaric ones (Gouretski and Kolterman, 2004). For surfaces γ_n, an additional filter is used: the estimated depth of the surface of neutral buoyancy can change for the casts located within the a distance of several dozens of kilometers from each other, by no more than 50-400 m (the value changes with the distance between the stations). Sharp changes in depth of γ_n can occur in frontal zones, in the presence of eddies, and also due to instrumental errors. Azimuthal velocities and their gradients in eddies are usually greater than the velocities and their gradients in the mean currents, and therefore, even at the same length scales, eddies usually bend isopycnal surfaces more strongly than the mean currents. This difference was used to create the filter: observations in which the pressure gradient along the isopycnals exceeded a specified critical value were eliminated. In geostrophic approximation, this limits the change in horizontal velocity vertically ($\Delta_z V$): $\frac{\Delta_z V}{\Delta z} = \frac{N^2}{f}\frac{\partial \gamma}{\partial l}$, where N is the buoyancy frequency, f is the Coriolis parameter and l is the direction along the γ_n surface. Taking $N^2 = 5\times10^{-5}$ s^{-1} and limiting the variations $\Delta_z V$ to a maximum value of 5 cm s^{-1} at Δz = 100 m, those data for which the values $\frac{\partial \gamma}{\partial l}$ exceeded 200 m per 200 km were filtered. For comparison, the vertical gradients of current velocity observed in AzC are less than 3 cm s^{-1} per 100 m (Comas-Rodriguez et al., 2011). These critical values $\frac{\partial \gamma}{\partial l}$ made it possible to filter deviations from climatology far from the Iberian Peninsula. In the Gulf of Cadiz, approximately 100 km from the Strait of Gibraltar, the vertical velocity gradient of the Mediterranean Undercurrent reaches 30 cm s^{-1} per 100 m (Baringer and Price, 1997), however, with the regional grid resolution of about 30 km used here, the gradients are smoothed out to 12 cm s^{-1} per 100 m. To take into account such features, the criterion $\frac{\partial \gamma}{\partial l}$ was weakened towards the region of the Iberian Peninsula and in the Gulf of Cadiz, where the critical values $\frac{\partial \gamma}{\partial l}$ corresponded to the vertical variability $\Delta_z V$ of no more than 15 cm s^{-1} per 100 m.

After all the filtering procedures above, the data were used in the Barnes optimal interpolation. The CTD and PFL profiles, in general, have a higher vertical resolution and accuracy than the OSD profiles, therefore, in the optimal interpolation procedure, the data from the OSD profiles was included with a weight of 1, and the CTD and PFL data with a weight of 2. The characteristic maps were built on a grid of AVISO satellite altimetry. This allows a direct comparison or a combination of the dynamic depths, obtained with in-situ data, with the sea surface topography from the satellite observations.

Barnes's optimal interpolation method (Barnes, 1964) consists in the following. At the regular grid point *ij* the Barnes interpolated value (F_{ij}) is the weighted sum of the temperature or salinity C_s observations at points *s*, located within a given radius. In the original version of the algorithm, the weights are the Gaussian functions of the distance r_{ijs} between grid node *ij* and the grid point *s* (Fig. 2.2a):

$$W_{ijs} = e^{-r_{ijs}^2 / R^2}, \tag{2.1}$$

where R is the spatial scale of the e -folding decrease in the weighting function, within which the values of temperature or salinity have a decisive influence on the final grid-point value.
The first iteration of data interpolation onto a regular grid is done using the expression:

$$F_{ij}^0 = \sum_{s:|s-ij|<R} W_{ijs} C_s \Big/ \sum_s W_{ijs}. \tag{2.2}$$

The response function of the first iteration has the form $D_0 = e^{-\left(\pi R/\lambda\right)^2}$, where the wavelength λ is the independent variable. Then the gridded results of F_{ij}^0 is interpolated to the location points of the original *in situ* data (F_{ijs}^0) and they are refined in the next iteration using the function:

$$F_{ij}^k = F_{ij}^{k-1} + \sum_{s:|s-ij|<R} W_{ijs}\left(C_s - F_{ijs}^{k-1}\right) \Big/ \sum_s W_{ijs}. \tag{2.3}$$

Each subsequent iteration increases the sharpness of the frontal zones by reducing the gap between the already taken into account (low-frequency) and the previously ignored (high-frequency) harmonics according to the law: $D_k = D_0 \sum_{n=1}^{k} (1 - D_0)^{n-1}$ (Barnes, 1964). In order to save computer time, it is usually recommended to do 3 such iterations.

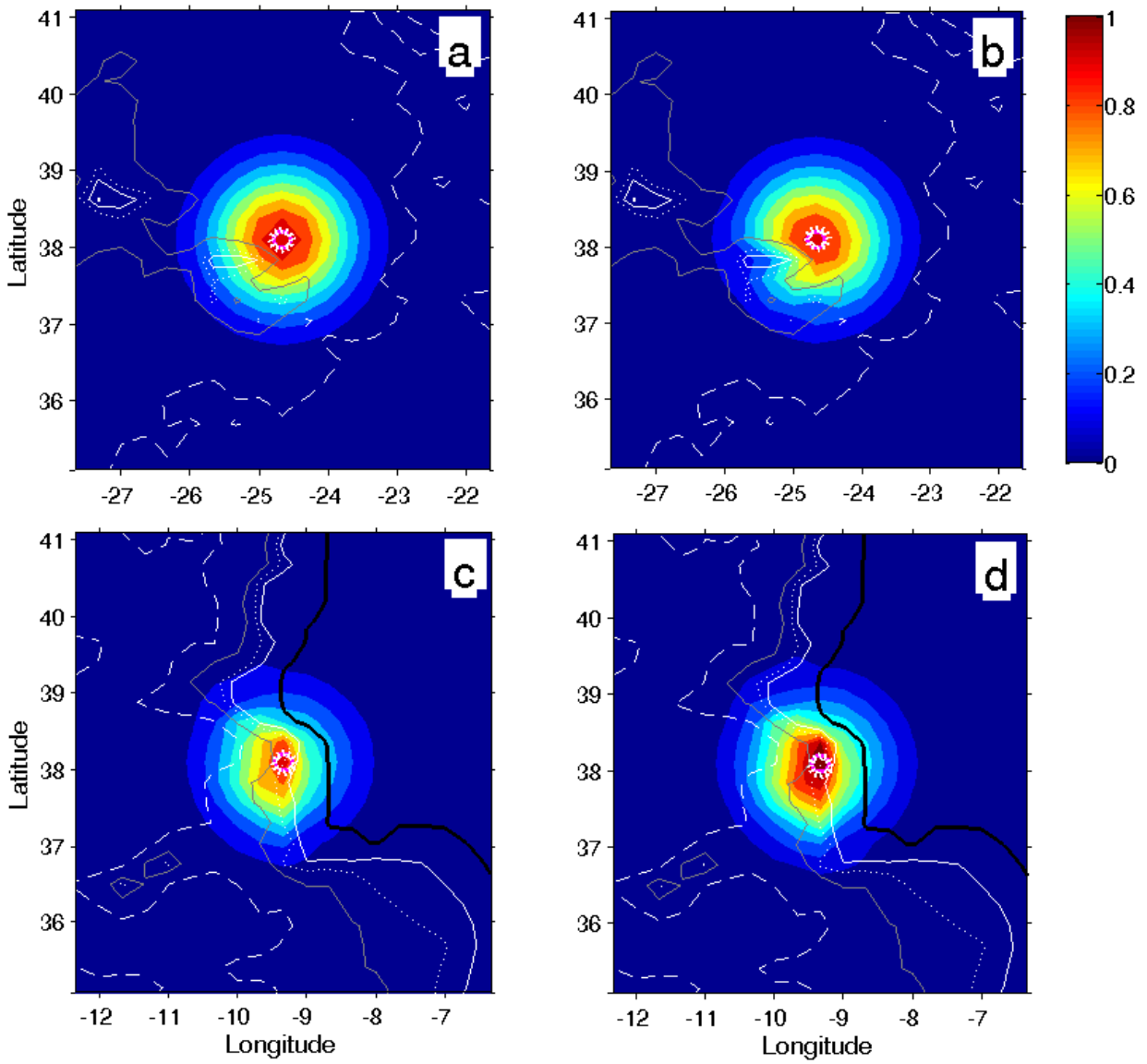

Fig. 2.2. Weighting function (W) for a 100 m level near the southern tip of the Iberian Peninsula: (a) no influence of the bottom topography on the weight function, (b) at the same point, but with the influence of the bottom topography down to a depth of 1500 m and (c, d) with a strong influence of the topography of the continental slope. The lower panels show the shape of the weighting function: (c) the correction factor w is not applied and (d) the correction factor w is applied. The color shows the distribution of weights depending on the distance to the grid node (the node is marked with a circle). The solid black line is 0 m isobath, gray lines are 500 m, 1000 m, 2000 m and 3000 (from Bashmachnikov et al., 2015a).

The weighting function of the algorithm was modified in accordance with the extension of frontal zones (for the quasi-geostrophic flows) observed along isobaths, or along zonal lines. The predominant extension depends on the local ratio of planetary and topographic β-effects, as it follows from the expression (Pedlosky, 2013):

$$V\beta/f - \vec{V}\cdot\vec{\nabla}H/H = 0. \qquad (2.4)$$

Here, the β-plane approximation is used ($f = f_0 + \beta y$), ∇H is the bottom slope, H is the average sea depth, $\vec{V}$ is the horizontal velocity vector and V is its meridional component. If the topographic β-effect dominates over the planetary effect, following Schmidtko et al. (2013), a circular Gaussian weighting function (W_{ijs}) is stretched along the isobaths. At the continental slope or the slopes of the MAR, the topographic β-effect is several orders of magnitude higher than the planetary β-effect, thus the influence of the latter on the direction of the flow is neglected. When the rotor of the wind field is taken into account, the right-hand side of equation (2.4) diverges from zero (Kantha and Clayson, 2000). The vorticity of the wind field forms the Sverdrup circulation, which in the eastern parts of the ocean has a meridional component comparable to the zonal one, i.e. is not negligible compared to the planetary β-effect (Pedlosky, 1998). This is confirmed by the structure of currents in the subtropical zone of the Northeast Atlantic (Paillet and Mercier, 1997). Therefore, for the study region, the shape of the weighting function was determined only by bathymetry, without taking into account the planetary β-effect.

The methodological novelty of the method lies in the algorithm automatic selection of the degree to which the topographic β-effect distorts the initially circular distribution of isolines of the weight function W_{ijs} from equation (2.4).
The resulting weight function is defined as:

$$W_{ijs} = \left[w_{ij}\, c_{ij}\, A_{h,ijs} + \left(1 - c_{ij}\right) \right] e^{-\left(r_{ijs}^2 \,/\, R^2 \right)} \quad (2.5)$$

Depth dependence of the function $A_{h,ijs}$ is as in the paper by Schmidtko et al. (2013):

$$A_{h,ijs} = \max\left(0.5, \left| 1 - 0.5 \left| \log \frac{H_{ij}}{H_s} \right| \right| \right). \quad (2.6)$$

The value of the function $A_{h,ijs}$ depends on the ratio of the sea depths between the full-scale profile point (H_s) and the grid node (H_{ij}). The ETOPO2 bathymetry used for calculations was smoothed by a moving average with a window width equal to half R.

The parameter $c_{ij} = \delta_{ij} \left(\nabla H_{ij} \,/\, H_{ij} \right) \Big/ \left(\beta \,/\, f \right)$ in expression (2.5) characterizes the relative role of the topographic β-effect referred to the planetary one. Possible variations of this parameter are limited to the range from 0 (no influence of bathymetry) to 1 (the maximum influence of bathymetry). The proposed modification of the method also takes into account the effect of baroclinicity, i.e. weakening of the effect of the bottom slope on circulation with distance from the bottom. This is achieved by using in the expression for c the parameter $\delta_{ij} = \max\left(0, \quad 1 + \frac{h_{ij} - H_{ij}}{H_m} \right)$, which is a function of the difference between the interpolation depth level h_{ij} and the local sea depth H_{ij} . The distance from the bottom at which the influence of the

topography on ocean circulation becomes insignificant was estimated as $H_m \sim L\frac{f}{N}$ (Ownes and Hogg, 1980). With a ratio of $\frac{N}{f} \sim$ 80-90, derived from the WOA for the upper 2000 m layer, and for a spatial scale of $L \sim$ 200 km, the typical width of the mean ocean currents, H_m = 2200-2500m. The latter value was used in the computations (Fig. 2.2bd).

The parameter w_{ij} in expression (2.5) accounts for a compensation of a possible decrease in the area of the region of non-zero W_{ijs}, which could occur above steep bottom slopes. Without this correction, the average value of W_{ijs} in the smoothing window on sufficiently steep slopes can decrease by 30% which increases the noise level in the resulting climatology. To avoid this effect, $w \le 1$ is introduced, which is the ratio of the average weight inside the window (expression 2.5) for a local estimate of c_{ij} to the average weight in the window with $c_{ij} = 0$. The use w_{ij} has virtually no effect on the shape and size of the smoothing window (Fig. 2.2c,d).

To calculate the weight function in expression (2.5), it is necessary to specify the radius R of the window with non-zero weights W_{ijs}. Minimization of smoothing of the mean field occurs when minimizing R. On the other hand, in order to reduce residual noise due to a temporal heterogeneity of the original array, climatological characteristics should be obtained by averaging a sufficient amount of observations. At least 30 observations are considered acceptable for estimating the first moments of data series (Emery and Thomson, 1997). Also, R must be large enough so that residual eddy wakes are filtered out by the optimal interpolation procedure.

In the upper 1900 m layer, the criterion of having at least 30 points within the radius R leads to an increase of R from 30-60 km near the Iberian Peninsula to 60-110 km in the western and southern parts of the study area, on average, being about 50 km for the whole region (Fig. 2.3). Below 1900 m, due to the strong decrease in the number of profiles (Figs. 2.1d and 2.3c), the window radius R has to be increased from 60-150 km near the Iberian Peninsula to 150-300 km in the western and southern parts of the area. The region-average R for 2000 m depth is 100 km, and for 2400 m depth – 170 km.

Meso- and sub-mesoscale anomalies in water temperature and salinity are among the main sources of noise in the climatologies. The influence of eddies is partially eliminated by the filtering methods mentioned above, but some residual noise still remains. To reduce this noise, the radius of the averaging window was chosen to be larger than the radius of a typical eddy. To estimate the minimum values of R that filter out residual eddy noise, correlation radii were calculated for each temperature or salinity profile around which there were at least 10 neighboring observations within a 200 km radius and a 30-day period (Fig. 2.4). Correlation radii were calculated in three ways: as the zero-crossing point of a cosine approximating the autocorrelation function, as the integral of the normalized autocorrelation function from the origin to the first zero-intersection of the function, and as the integral of the square of the normalized autocorrelation function over its entire domain of definition (Stammer, 1997). The resulting correlation radii were considered to be the characteristic radii of the eddies.

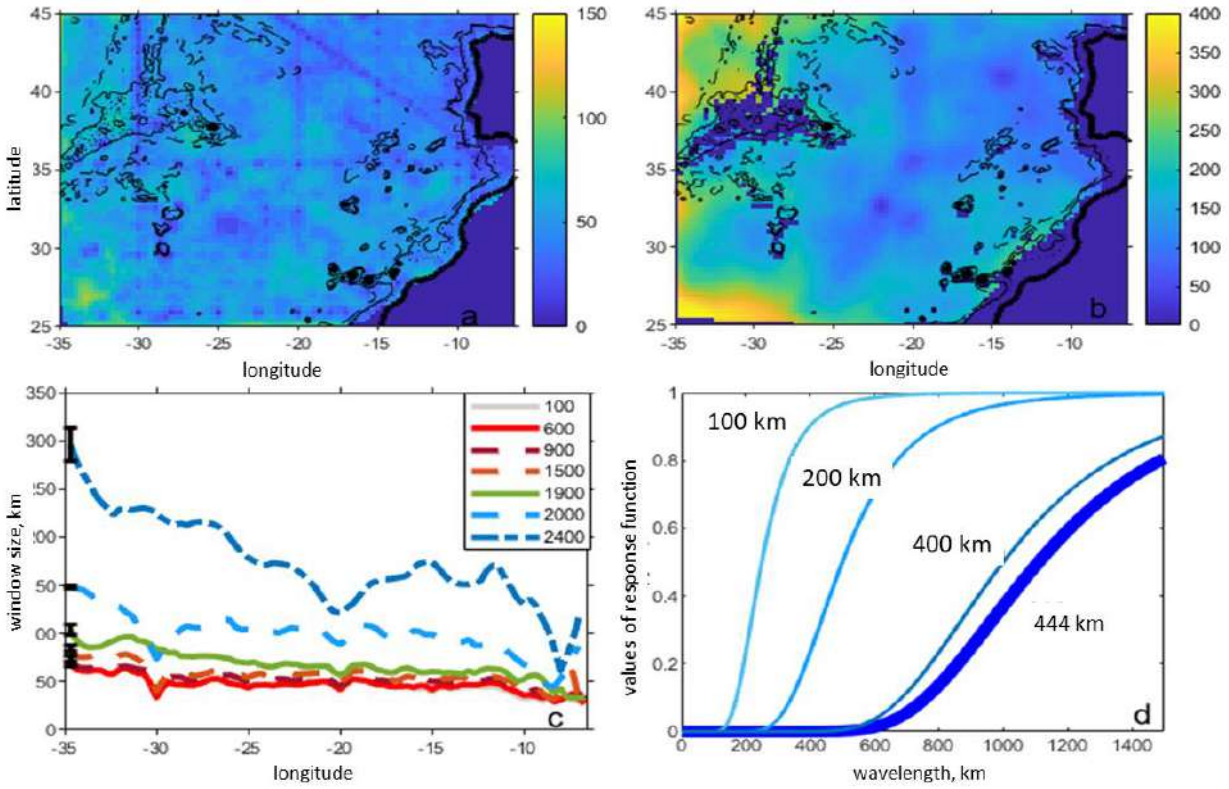

Fig. 2.3. Radius (km) of a window containing at least 30 data points: (a) at 100 m and (b) at 2500 m. (c) Variation of the average window radius (R) as a function of distance from the Iberian Peninsula and the depth level. (d) Barnes response function at different averaging radii after the 3rd iteration (from Bashmachnikov et al., 2015a).

The histogram (Fig. 2.4) shows that the correlation radii vary in the range from 10 to 100 km and that there exist two modes: 10-20 km and approximately 30 km. The latter mode is close to the Rossby deformation radius in the study region (Emery et al., 1984). The correlation radii practically do not change throughout the region and do not depend on the latitude of observations or proximity to an area with large bottom slopes. In satellite altimetry data, the characteristic sizes of eddies in the study area are estimated at 40-80 km (Le Traon et al., 1990) and 60-100 km (Stammer, 1997; Jacobs et al., 2001; Chelton et al., 2011). In in-situ data, the radii of large eddies are 40-100 km in the AzC region (Gould, 1985; Pollard and Pu, 1985; Pingree and Sinha, 1998; Alves and Verdiere, 1999; Alves et al., 2002; Pingree, 2002; Mourino et al., 2003) and are 10-60 km in the northern part of the study area (Arhan and de Verdiere, 1985; Mercier and de Verdiere, 1985; Shoosmith et al., 2005), as well as in the upwelling region off the coast of the Iberian Peninsula (Pingree and Le Cann, 1992; Oliveira et al., 2004). The *R* was chosen to at least exceeded the characteristic eddy radius of 30 km. *R* =60-70 km provided an acceptable compromise between the need for the maximum spatial resolution and the maximum reduction in mesoscale noise.

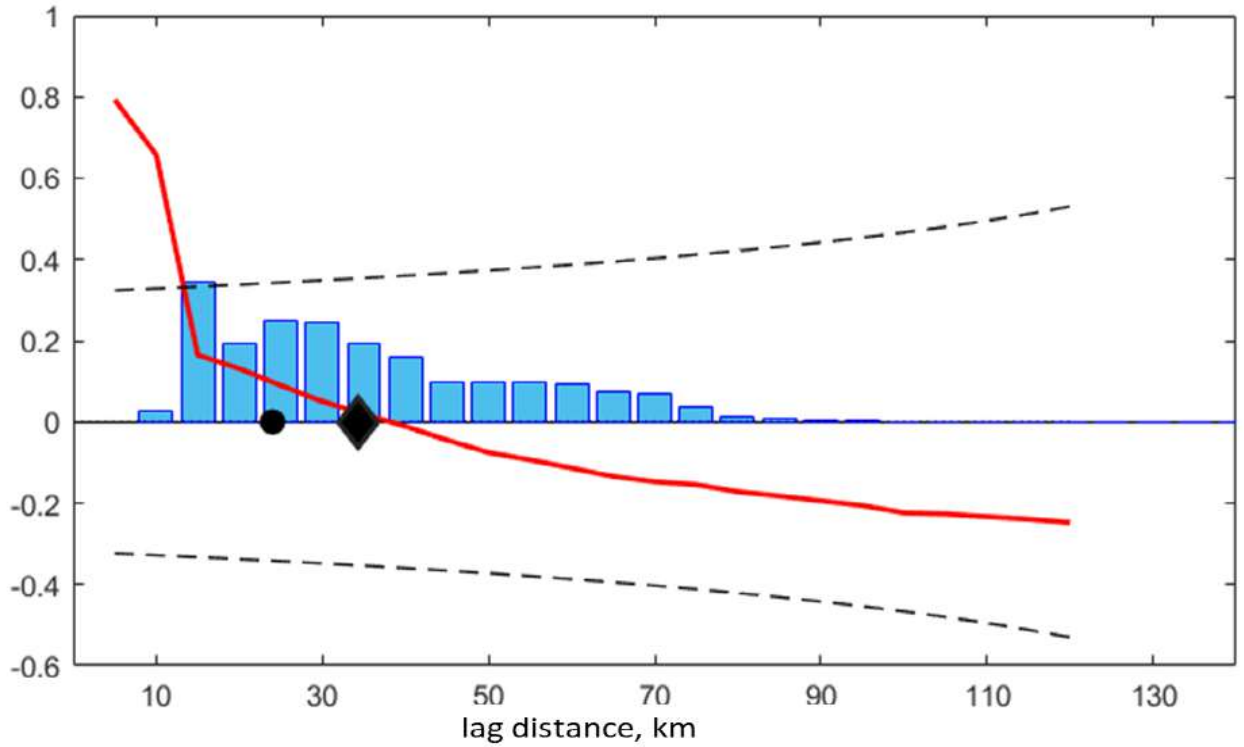

Fig. 2.4 The average correlation function over the study area (red curve) and average normalized histogram of correlation radii in the region (bars). The dotted lines indicate the significance level of the autocorrelation function. The black diamond indicates the average correlation radius from the histogram data, and the black circle shows the correlation radius estimated from the area average autocorrelation function (from Bashmachnikov et al., 2015a).

Thus, in the upper 1900 m layer in the eastern part of the study area, *R* was limited from below by the eddy size, and in the rest of the area by the data density (Figs. 2.3 and 2.4). Below 2000 m, *R* was doubled, taking into account the decrease in the amount of data. To obtain the highest possible resolution and since the density of observations decreases with distance from the Iberian Peninsula, a spatially varying *R* was used. With γ_n less than and equal to 27.96 kg m^{-3} (in the upper 1900 m layer), *R* gradually changed from 70 km near the Iberian Peninsula to 200 km in the open ocean (Fig. 2.5a). These values increased by a factor of 1.5 for γ_n ranging from 27.97 to 27.98 kg m $^{-3}$ (1900-2000 m) and doubled for higher γ_n (below 2000 m) (Fig. 2.5b).
The neutral buoyancy surfaces were tested for artificial mixing compaction effects that nay occur during spatial averaging during optimal interpolation (Schmidtko et al., 2013). However, these errors turned out to be so small that there was no need to correct the temperature and salinity values to restore the reference density at the isopycnal.

At the last stage of mapping, at each grid node, vertical profiles of temperature and salinity were interpolated vertically from isopycnic surfaces to fixed observation levels at the 25-m intervals using the piecewise cubic interpolation with Hermite polynomials. The selected range of γ_n values provided the complete coverage of the study area down to 2300 m with the grid of climatological data, which is sufficient for further detection of meddy anomalies.

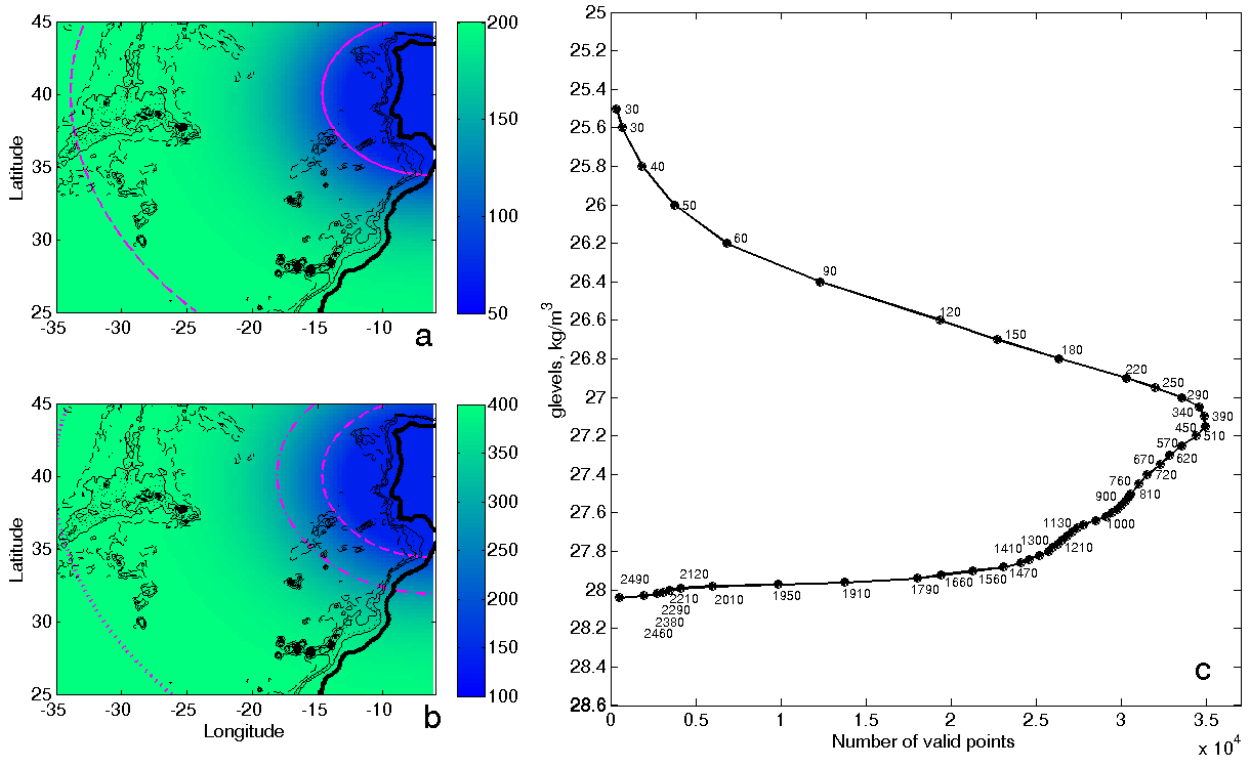

Fig. 2.5. Spatial variability of R: (a) in the upper 1900 m layer; (b) deeper than 2000 m. R contours added =100 km (magenta solid line), R =200 km (magenta dashed line), R =300 km (magenta dash-dotted line) and R =400 km (magenta dotted line). (c) The total number of salinity data points at different neutral buoyancy surfaces. The numbers to the right of the black circles show the average depth of the neutral buoyancy surfaces in the study area (not all points are labeled) (from Bashmachnikov et al., 2015a).

2.2.3 Peculiarities of the climatological distribution of water temperature, salinity and geostrophic currents in the eastern subtropical Atlantic

Figure 2.6 shows zonal and meridional sections of temperature and salinity obtained using the method above. Surfaces of neutral buoyancy are quite frequently distributed in vertical, and there are no intersections between the neighboring surfaces. Meridional temperature sections record a rapid rise of isopycnals at approximately 35ºN (the AzC), which, on the western section (Fig. 2.6a) can be traced to a depth of 1700 m (see also Bower et al., 2002), and in the east (Fig. 2.6b) – down to 1000 m. Further north, in the upper 500 m layer, a gradual rise of isopycnals is observed.

The tongue of the Mediterranean Water extends from the Iberian Peninsula to the Mid-Atlantic Ridge (Fig. 2.6d). The vertical influence of the Mediterranean Water can be traced to at least 2000 m (Reid, 1978; Harvey, 1982; Daniault et al., 1994). A plume of water with low temperatures on the eastern slope of the Mid-Atlantic Ridge, deeper than 1500 m, corresponds to the Labrador Sea Water (LSW), penetrating south along the MAR (Bower et al., 2002). In the southern part of the region, at 31ºN (Fig. 2.6c), between 1000 and 1500 m, only the lower fraction of the Mediterranean Water is distinguished in the eastern part of the section. The less saline and colder Antarctic Intermediate Water (AAIW) is observed at the same depths, but south of 26-27ºN (Louarn and Morin, 2011).

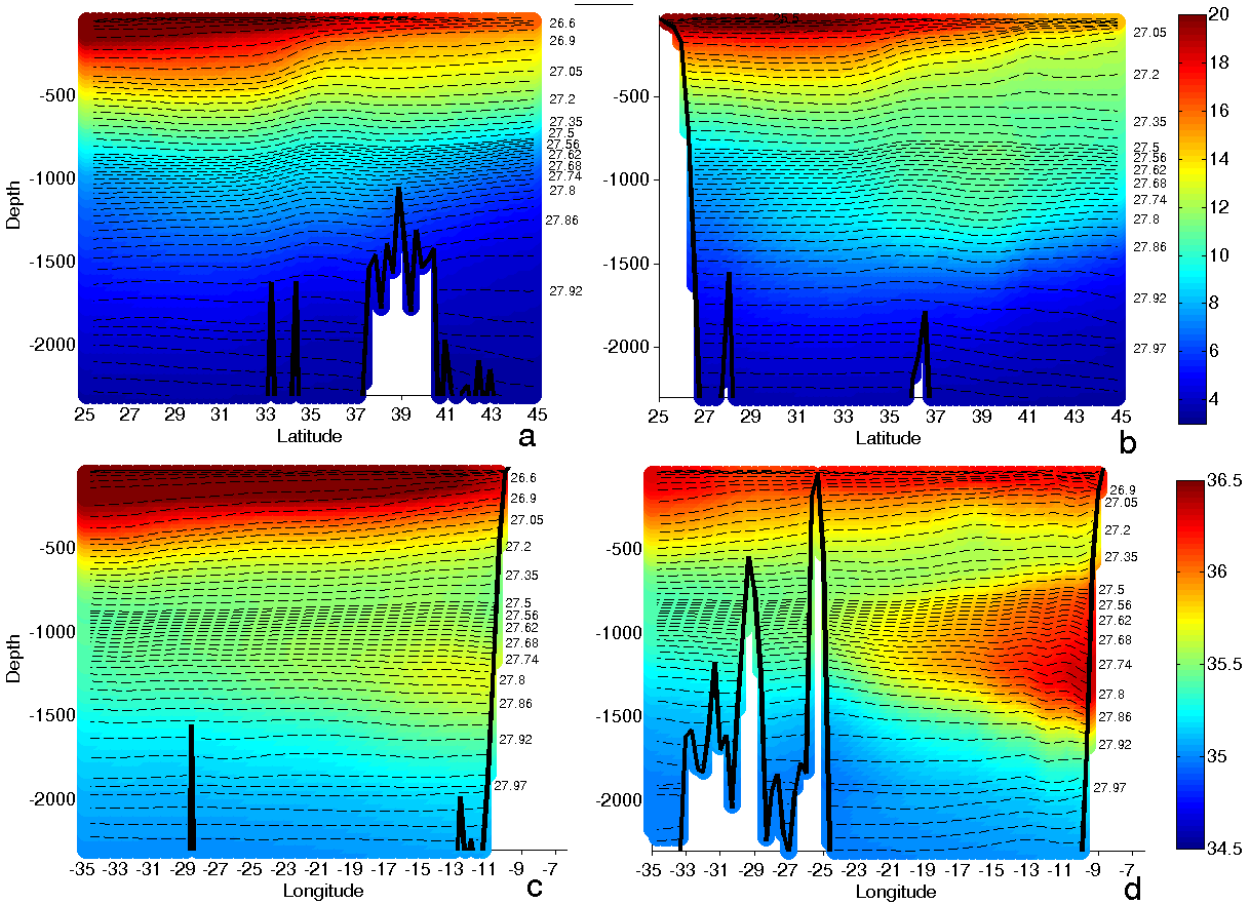

Fig. 2.6. Meridional temperature sections along (a) 30^0 W. and (b) 15^0 W; and zonal salinity sections along (c) 31^0 N. latitude. and (d) 38^0 N. The dotted isolines show the positions of the neutral buoyancy surfaces (only some of the 53 surfaces used are shown). Thick black contours mark the bottom topography (Bashmachnikov et al., 2015a).

At the Iberian Peninsula, the MEDTRANS climatology contains more details of the known features of distribution of the Mediterranean Water than WOA or MIMOC. This is due to a better account for the dynamics of topographically trapped currents. In particular, MEDTRANS reproduces in more detail the spatial features of the upper and lower cores of the Mediterranean Undercurrent. Geostrophic currents, computed from the zero level at 1900 m, compare well at the sea surface with the geostrophic circulation from AVISO altimetry (Fig. 2.7a, b). This includes: the AzC and the general decay of its average velocity from the MAR to the Gulf of Cadiz, intensification surface currents in the northern and southern parts of the Gulf of Cadiz, as well as structure of the currents south of the Canary Islands. The MEDTRANS climatology slightly overestimates the width of the AzC (Fig. 2.7a, b), but no more than other climatologies in this region, including WOA and MIMOC (see more details Bashmachnikov et al., 2015a). The Azores Current is well traced along its entire length, at least down to the 700 m (Fig. 2.7c), but is extremely weakly expressed in its eastern part at 1000 m (Fig. 2.7d), which is consistent with observations.

Similar to the average climatology, a seasonal MEDTRANS climatology was obtained for the warm (May-October) and cold (November-April) seasons. A rise in isotherms between 15 and 25ºW was revealed, which manifests itself only in the cold season. This feature is missing in WOA seasonal climatologies, but is described by Kase and Siedler (1982). MEDTRANS also reproduces a seasonal increase in temperature gradients across the Portuguese and Canary upwellings during the warm season, described by Navarro-Perez and Barton (2001) and Fraile-Nuez et al. (2010). At

the intermediate depth levels, which are of particular interest for further detection of meddies, seasonality was practically absent.

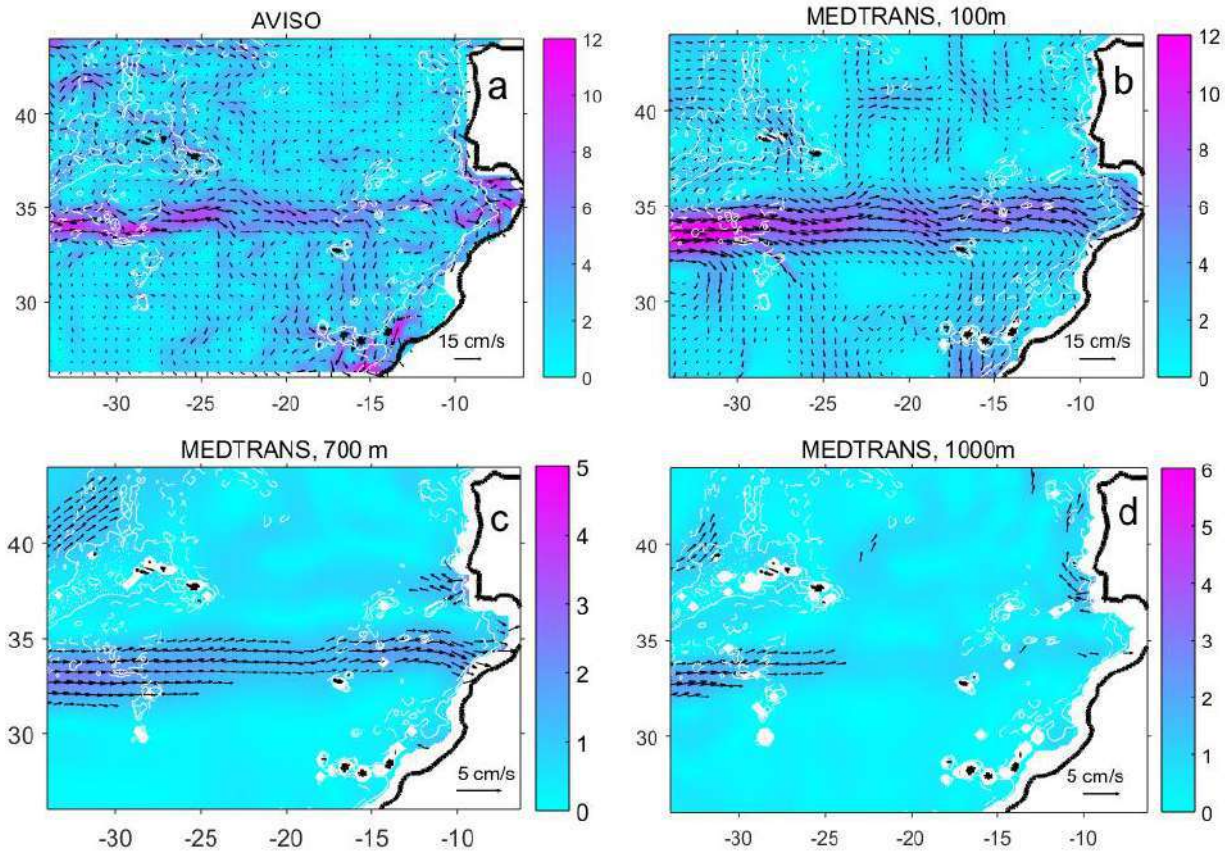

Fig. 2.7. (a) Mean geostrophic currents at the sea surface in multi-annual mean in AVISO satellite altimetry Mean geostrophic currents in MEDTRANS climatology (b) at 100 m, (c) at 700 m and (d) at 1000 m, referenced to 1900 m depth level. The color shows the current velocity (cm $s^{-1)}$, the arrows indicate the current direction for the current velocity exceeding 2 cm s^{-1}.

In summary, the MEDTRANS climatology provides improved climatic distributions compared to other widely used climatologies (WOA, etc.) due to the following innovations: 1) pre-filtering of the Mediterranean water eddies (meddies), which can provide a significant distortions of local temperature and salinity values; 2) a topographically shaped window of the weighting function for transferring scattered *in situ* data to a regular grid, which allows a better representation of the characteristics of the observed topographically trapped currents (such as the Mediterranean Undercurrent – MUC); 3) interpolation of *in situ* data along the neutral buoyancy surfaces, where gradients of thermohaline characteristics are reduced, which leads to less smoothing of *in situ* water properties during the interpolation process.

2.3 IDENTIFICATION OF EDDIES IN OBSERVATIONS AND HYDRODYNAMIC MODEL DATA

2.3.1 IDENTIFICATION OF THE SUBSURFACE MEDITERRANEAN WATER EDDIES (MEDDIES) USING *IN SITU* DATA

Mediterranean water eddies (meddies) were detected with salinity and temperature anomalies in the vertical casts of the World Ocean Database (WOD, section 2.2.1) since 1950, referenced to MEDTRANS climatology (see sections 2.2.2-2.2.3). Since the meddy cores are located in the depth range of 700-1500 m, only the profiles with a maximum sounding depth of 1500 m or more were used. Of the total number of more than 50 000 profiles that passed the data quality assessment procedures (see section 2.2.1), this limitation was by met about 26 000 profiles. The selected profiles were smoothed by moving averaging with a window of 100 m in order to reduce the influence of small-scale noise.

According to a slightly modified criterion by Richardson et al. (1991), the presence of a meddy in a vertical profile was recorded if, in the depth range of 500-1500 m, the salinity anomalies exceeded 0.2 (relative to the MEDTRANS climatology) within a layer of at least 200m thick. Relaxation of the criterion (Richardson et al. (1991) recorded salinity anomalies greater than 0.4) was possible due to a more advanced climatology used as the reference. If this criterion was met for the entire profile, not just for the range 500-1500 m, this profile was not further considered. Anomalies of this type can record a meander of a frontal zone or be associated with errors in calibration of the measuring equipment. Poor identification of the Mediterranean Undercurrent (MUC) near the continental slope of the Iberian Peninsula even in MEDTRANS climatology, as well as meandering of the MUC may lead to false allocations of meddies in this area. Therefore, to avoid errors, vertical profiles taken within 50 km of the 500-m isobath delineating the Iberian Peninsula were not used for the analysis. In this regard, the statistics obtained may not include some meddies at an early stage of their formation.

When a profile passing through a meddy was detected, all neighboring profiles within a radius of 150 km were searched for a time period of ±15 days from the date of execution of this profile. These spatial and time intervals were selected based on a typical meddy propagation velocity of 2 cm s^{-1} and assuming a meddy radius not exceeding 50 km (Richardson et al., 2000). A detailed analysis of the characteristics of the meddies was carried out only for meddies identified with at least 3 vertical casts, both in the core and on the periphery or outside the meddy. Next, the obtained anomalies of the thermohaline characteristics of each isolated meddies were visually checked for the presence of a lens-shaped salinity anomaly. To be included in the dataset of the meddies selected for detailed analysis, the depth-mean salinity in the 500-1500 m layer had to decrease monotonically with the distance from the profile with its maximum value. Some examples of selected meddies are presented in Figure 2.8. Visual analysis showed that in 15 cases, within a 150 km window there were two meddies simultaneously detected. 13 (90%) of them were located within 600 km of the Iberian Peninsula. These meddies were analyzed separately. Based on the results of the study, out of more than 775 profiles through different meddies, 241 meddies were selected for the detailed analysis in Chapter 4.

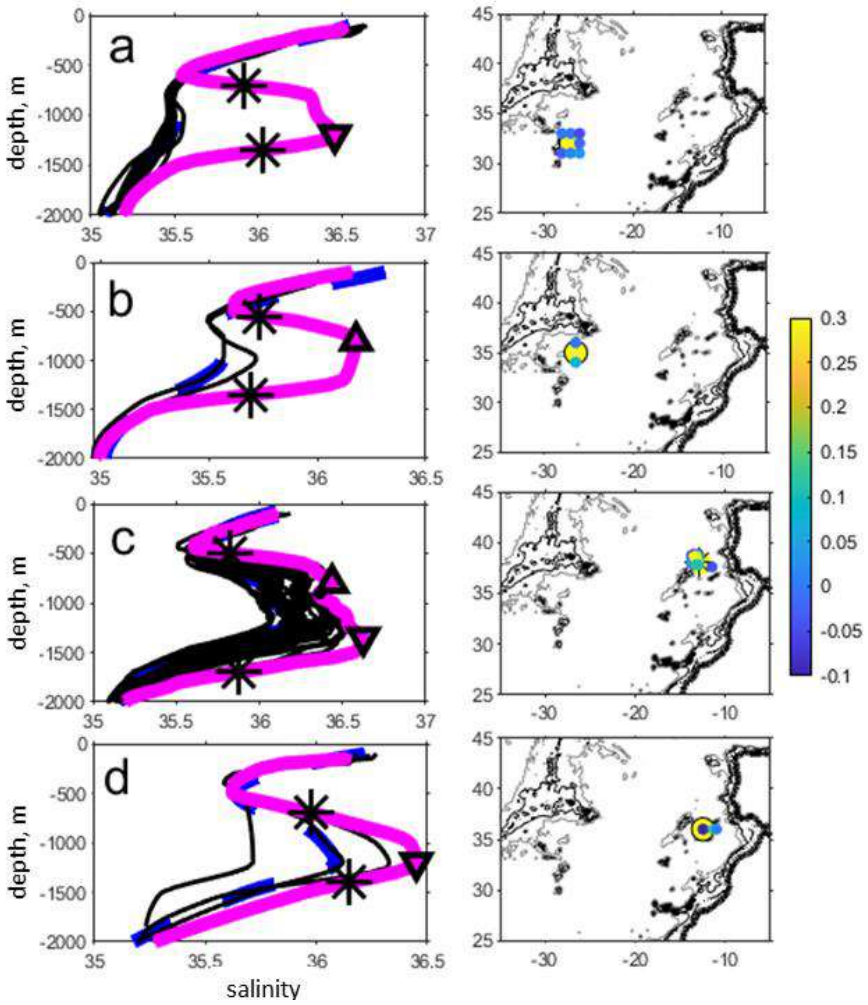

Fig. 2.8. Examples of vertical salinity profiles (left panels) and spatial distributions of sounding stations (right panels) for 4 meddies (a-d). In the left panels, the profile through the central region of the meddy core is shown with pink lines, other profiles – with black lines, and the climatology – with blue lines. Triangles show the centers of the meddy core (upper and lower, if 2 cores were identified) pointed by the algorithm; asterisks show the upper and lower boundaries of the meddy cores. On the right panels, the color of the points represent the salinity anomaly averaged in the 500-1500 m layer relative to climatology (from Bashmachnikov et al., 2015c).

For the selected meddies, the following characteristics were estimated: the maximum salinity in the core (S_m), the maximum temperature in the core (T_m), the buoyancy frequency in the core (N_m), the vertical extent (thickness) of the core (H) and the meddy radius (R_{vm}) using the following algorithms. First, a profile was found in the central part of the meddy core, i.e. profile with maximum salinity in the layer 500-1500 m. From this profile we determined S_m, T_m , N_m and H. H was defined as the distance between the levels with maximum vertical salinity gradients above the (upper) core and below the (lower) meddy core (Figs. 2.8 and 2.9a,c).

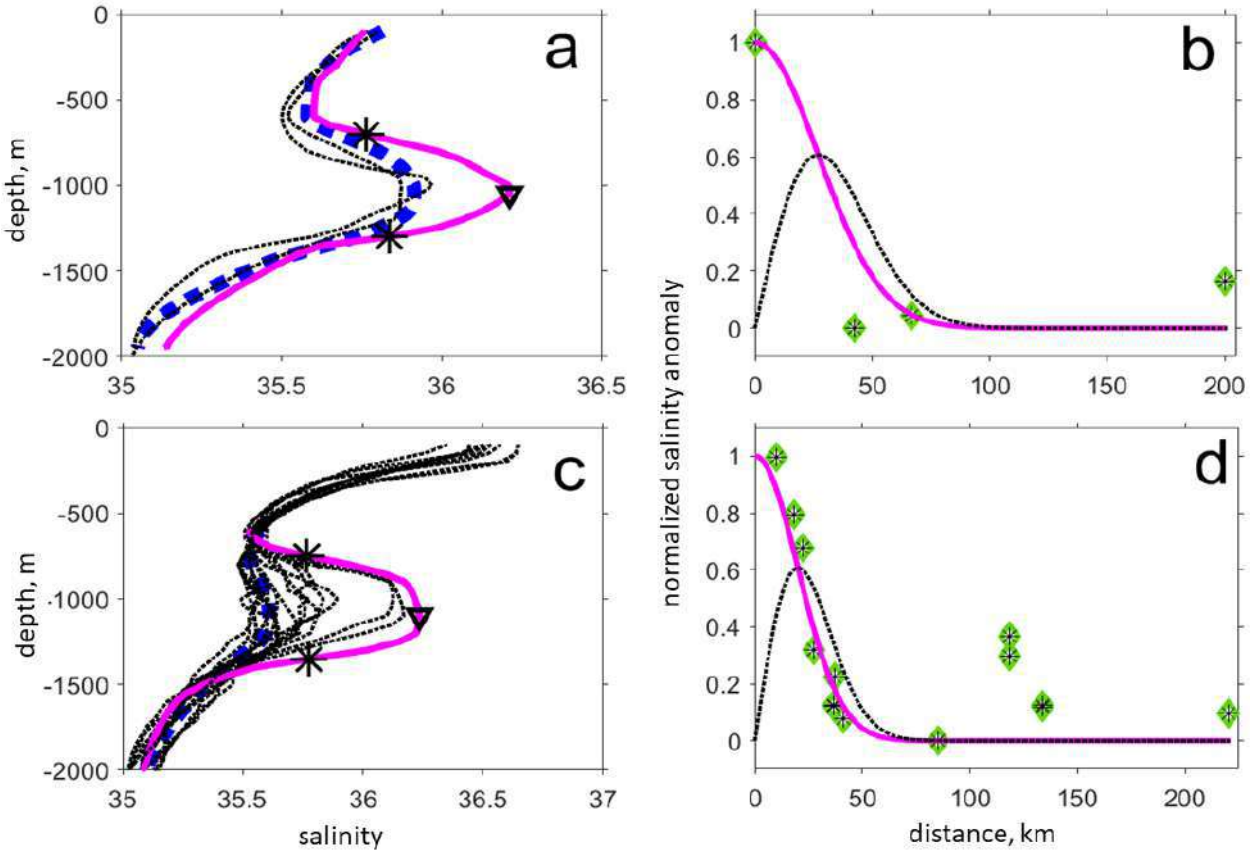

Fig. 2.9. Examples of estimating the meddy radius. In panels (a) and (c), the vertical casts through the central part of meddies are shown as pink lines, and other soundings are shown as black dotted lines, climatology is shown as thick blue dotted lines. In panels (b) and (d), diamonds with asterisks indicate normalized salinity anomalies relative to climatology, averaged over the depth range of ±100 m from the maximum salinity in the meddy core (see profiles on the left), the pink line is the Gaussian approximation of the data (expression 2.7), the black dotted line is the derivative from the Gaussian curve (the Rayleigh profile), the maximum of which fixes the dynamic radius of the meddy (R_{vm}). In panel (d), the second maximum of the salinity anomaly at a distance of 110 km from the center of the meddy is probably the result of the splitting of the meddy core (adopted from Bashmachnikov et al., 2015c).

To estimate the meddy radius, the salinity (and its anomaly) was averaged in each profile in a depth range of ±100 m from the level of the highest salinity value – the center of the meddy core. The geographic position of the "true meddy center" was estimated as the average of the positions of all soundings, taken with weights proportional to the corresponding salinity anomalies at the depth of the meddy core. The radial profile of salinity in the meddy was reconstructed from the values of the average salinity anomaly in the layer as a function of the distance from the "meddy center" (δS) regardless of their azimuthal position relative to this center (Fig. 2.9b, d). The normalized radial distribution δS was approximated by a Gaussian, which corresponds to a Rayleigh-type radial velocity profile (see section 1.3):

$$\frac{\delta S(r)}{\delta S_m} = \exp\left(-\frac{r^2}{2R_{vm}^2}\right) \quad , \qquad (2.7)$$

where r is the known distance between the profile with salinity anomaly δS and the "meddy center", where the maximum salinity anomaly δS_m was observed, R_{vm} is the unknown radius of the meddy. The data were approximated by function (2.7) using the bi-square method, one of the variations of the least squares method with reduced sensitivity to the presence of outliers. If there were only three or four profiles in the vicinity of the "meddy center", a zero salinity anomaly, a background, was added at a distance of 200 km from the "meddy center." This increased the stability of the approximation. R_{vm} obtained this way corresponds to the distance where the azimuthal velocity reaches its maximum (see Carton et al., 1989; Pingree and Le Cann, 1993a, Paillet et al., 2002).

For identifying meddy trajectories, there were used trajectories of ARGO buoys (from the WOD and Coriolis datasets, http://www.coriolis.eu.org/Data-Services-Products/View-Download/Access-to-Argo-floats-by-WMO-number), and trajectories of isopycnal RAFOS floats in the depth range of 700-1500 m (WOCE dataset, http://www.ewoce.org/data/index.html).

The time interval between fixing the consequent positions of ARGO profiling floats is typically 10-15 days. This does not allow tracking rotation of the floats inside mesoscale eddies, since the typical turnover period of trapped particles in a mesoscale eddy ranges from 3 to 7 days. Therefore, to identify sections of trajectories inside the meddies, data of the vertical ARGO soundings were used. These meddies had already been identified as part of the procedure for analyzing data of individual *in situ* profiles described above. For a higher degree of confidence, together with the previously described salinity anomaly criterion, two additional criteria were used: the presence at depths of 500-1500 m of a temperature anomaly exceeding 0.5°C relative to the climatology, and the presence of a negative buoyancy frequency anomaly in the meddy core identified using thermohaline anomalies. For the analysis, only the parts of the trajectories were all the above criteria showed the presence of meddies for at least 2 months were selected. A total of 149 such sections were identified in ARGO trajectories, with some ARGO floats being captured by the same meddy for a year or more. Meddy-captured ARGO floats rotate around the center of the meddy, but their successive locations, recorded every 10-15 days, are randomly positioned at azimuth around meddy centers. To reduce this scatter in the meddy trajectory, the resulting ARGO trajectories of meddies were smoothed by a moving average with a window of 30 days. Spectral analysis showed that after such filtration, the periodicity in the series of distances between successive positions of the ARGO floats disappeared, which indicates the effectiveness of the filtration.

RAFOS floats record only water pressure and often water temperature at the density level of their drift. However, the temporal resolution of recording RAFOS positions ranges from one to two observations per day, which makes it possible to see rotation of their trajectories, when they are trapped by eddies. Meddies were identified in the sections of RAFOS trajectories if they showed the anticyclonic rotation (at least 2 full rotations of a float) and if their water temperature anomaly exceeded 0.5°C relative to the climatology. A total of 87 meddy trajectories were identified from RAFOS data, of which 29 have previously been described in the literature (Richardson et al, 1989; Bower et al., 1997; Serra and Ambar, 2002; Richardson et al, 2000; L'Hegaret et al., 2014). The center of the meddy was defined as the geometric center of the trajectory over one full revolution of the float. To reduce random noise, successive positions of the centers were smoothed by a 7-day moving average.

2.3.2 IDENTIFICATION OF EDDIES AT THE SEA SURFACE FROM AVISO SATELLITE ALTIMETRY

To identify mesoscale eddies at the sea surface, sea level data from AVISO (Archiving, Validation and Interpretation of Satellite Oceanographic data, http://www.aviso.oceanobs.com/) satellite altimetry were used. This data (Stammer and Cazenave, 2017) combines observations from the TOPEX/ Poseidon – Jason1/2 satellites (TOPEX/ Poseidon series) with a period of complete coverage of the Earth's surface of about 10 days, and ERS1/2 – Envisat – SARAL/ AltiKa – Sentinel-3B (ERS series) with a coverage period of about 30 days, as well as with a number of other satellites: GFO with a coverage period of 17 days, ICESat with a coverage period of 91 days, HY-2A with a coverage period of 168 days, CryoSat-2 with a coverage period of 365 days. The longer is the period during which the satellite covers the entire Earth's surface with its tracks, the smaller is the distance between the neighboring tracks (from more than 300 km at the equator for the TOPEX/ Poseidon series to 80 km for ERS series satellites, and to 8 km for CryoSat-2), and the smaller is the maximum latitude of the coverage area (up to 66^o latitude for TOPEX/ Poseidon series satellites, up to 81 ^{o} latitude for ERS series satellites and 88 ^{o} latitude for CryoSat-2). Although the Topex/ Poseidon and Jason altimeter coverage reaches only 66° N, measurements in this southern part of the Nordic Seas are used only for a correction of the long-wavelength errors in the satellite orbits and assessment of the measurement errors of different satellite missions (Le Traon and Ogor, 1998). This ensures homogeneity of the data used throughout the Nordic Seas, which is discussed below.

Related to the above, in the subtropical and subpolar latitude regions studied in this work, the AVISO data uses a different set of satellite mission types. In the eastern subtropical Atlantic (Chapters 4 and 6-7), the data primarily combined TOPEX/ Poseidon and ERS satellite observations. In the subpolar regions of the Norwegian and Greenland Seas (Chapters 5 and 7), the main contribution to AVISO maps comes from the ERS satellite mission, with the addition of a limited amount of ICESat and CryoSat data. However, the convergence and change in the inclination of the satellite tracks at high latitudes partially compensates for the presence of a smaller number of satellites, providing minimally acceptable conditions for detecting mesoscale eddies. Thus, at 30° N, the distances between the ERS/ Envisat satellite tracks are about 100 km in longitude and 110 km in latitude, while at 70° N these distances are already about 60 and 110 km, and at 79° N – about 20 and 30 km, respectively.

AVISO altimetry data is provided to users on a grid with a spatial resolution of 0.25x0.25° and with a time resolution of 1 day. This spatial and temporal resolution is a consequence of the spatio-temporal interpolation of the data from multiple tracks performed at different time. Interpolation in AVISO takes into account these data with different weights, which decrease with increasing distance from the track to the grid point and with the time interval between the date of the map and the time of the along-track sea level recording (Le Traon and Ogor, 1998; Lazaro, 2008).

A continuous series of AVISO observations are available since 1993 (except for several months in 1994 north of 66^o N, when for there was a gap in the data from ERS satellites). Before 2000 data came from 2 satellite systems (TOPEX/ Poseidon and ERS series), after 2000 and to the present – from 3-4 satellite systems. In this latter period, the number of the satellite tracks is thought to be sufficient to reliably identify mesoscale structures, while before 2000, mesoscale structures may be periodically sifted between tracks (Tournadre, 1990).

The accuracy of the along-track data depends on the quality of corrections for changes in the speed of the signal through the atmosphere and ionosphere, for various types of non-geostrophic sea level variability processes, and for the accuracy of geoid determination. For modern satellites, starting with TOPEX/ Poseidon and ERS2, the declared mean along-track accuracy of sea level variability is about 2 cm with a spatial resolution of 6-7 km (Chavanne and Klein, 2010). The accuracy of the final interpolated AVISO data depends on the proximity of the satellite tracks to the point of interest. Taking into account the interpolation of data from different non-simultaneous tracks, the formal sea level error in AVISO altimetry ranges from 2 to 4 cm (Fu and Cazenave, 2001; Rosmorduc and Hernandez, 2003; Muller et al., 2019).

Despite the fact that the subpolar and polar regions are less densely covered with satellite altimetry missions, a good agreement between current velocities from surface drifters and of the satellite altimetry was obtained for the Nordic Seas already for the AVISO version from 2010 (AVISO10) (Volkov and Pujol, 2012). The difference between the observed and calculated from altimetry data in the average current velocity in the region, as a rule, did not exceed 5 cm s^{-1}. At the same time, the average pulsation velocities, estimated as the root of the eddy kinetic energy (EKE), were underestimated by AVISO10 altimetry by 10-15 cm s^{-1} (Volkov and Pujol, 2012). This, in particular, was due to errors in the amplitudes of short-period spherical harmonics in the geoid decomposition used, as well as to a decrease in the quantity and quality of altimetry data in the western Greenland Sea with the regular presence of the sea ice (Muller et al., 2017, 2019).

These errors were partially corrected in the subsequent version of AVISO14, which used an improved geoid model and more reliable atmospheric/oceanic corrections. In particular, tests showed (Capet et al., 2014; Raj and Halo, 2016) that, using the same algorithms, AVISO14 allows, on average, to detect more eddies than the version of AVISO10 used to create the eddy dataset in Chelton et al. (2011). The quality of AVISO14 altimetry measurements was verified against data of the coastal and the open ocean sea-bottom tide gauges (Volkov and Pujol, 2012), as well as against the trajectories of eddies identified with the sea surface drifters (Capet et al., 2014; Raj and Halo, 2016). It was found that, after filtering the high-frequency component, the AVISO14 data differed from the direct observations by 2–3 cm, which is within the declared accuracy of AVISO observations and is sufficient to detect 5–15 cm anomalies associated with the passage of mesoscale eddies (Raj et al., 2015). The positions of the eddy centers identified in drifter data and AVISO14 satellite altimetry also corresponded well to each other. AVISO14 altimetry data showed a more than two-fold increase in the EKE in the Lofoten Basin compared to the surrounding areas of the Norwegian and Greenland Seas (Raj et al., 2016). This is consistent with the change in the quantity and kinetic energy of mesoscale eddies, identified in the trajectories of surface and subsurface drifters (Rossby et al., 2009b; Koszalka et al., 2011).

In this study AVISO18 dataset is used (http://marine.copernicus.eu/), where several algorithms were improved, from a mutual calibration of satellites and atmospheric corrections to the use of an improved geoid model and more accurate elimination of tides. This provides more homogeneous data quality for various regions of the World Ocean (Taburet et al., 2019). This is especially important for the Nordic Seas, where the previous versions of AVISO showed significant shortcomings at the Greenland shelf and surrounding areas (Koldunov et al., 2020). However, additional analysis showed an expected degradation of the quality of AVISO18 data along the northeast Greenland shelf due to the regular presence of the sea ice (Figure 2.10a), which is particularly evident in the sea level gradient map (Figure 2.10b). At the same time, AVISO18 reproduces quite well the characteristic transverse scales of the main currents: 70-100 km for the

East Greenland Current, 20-40 km for the West Spitsbergen Current and both branches of the Norwegian Current (Koszalka et al., 2011; Havik et al., 2017; Bosse and Fer, 2019). To avoid errors associated with deterioration in the quality of altimetry observations near land, in further analysis all data located less than 20 km from the coast were filtered out. Figure 2.10(a,b) shows a mask applied to the AVISO data in the Nordic Seas.

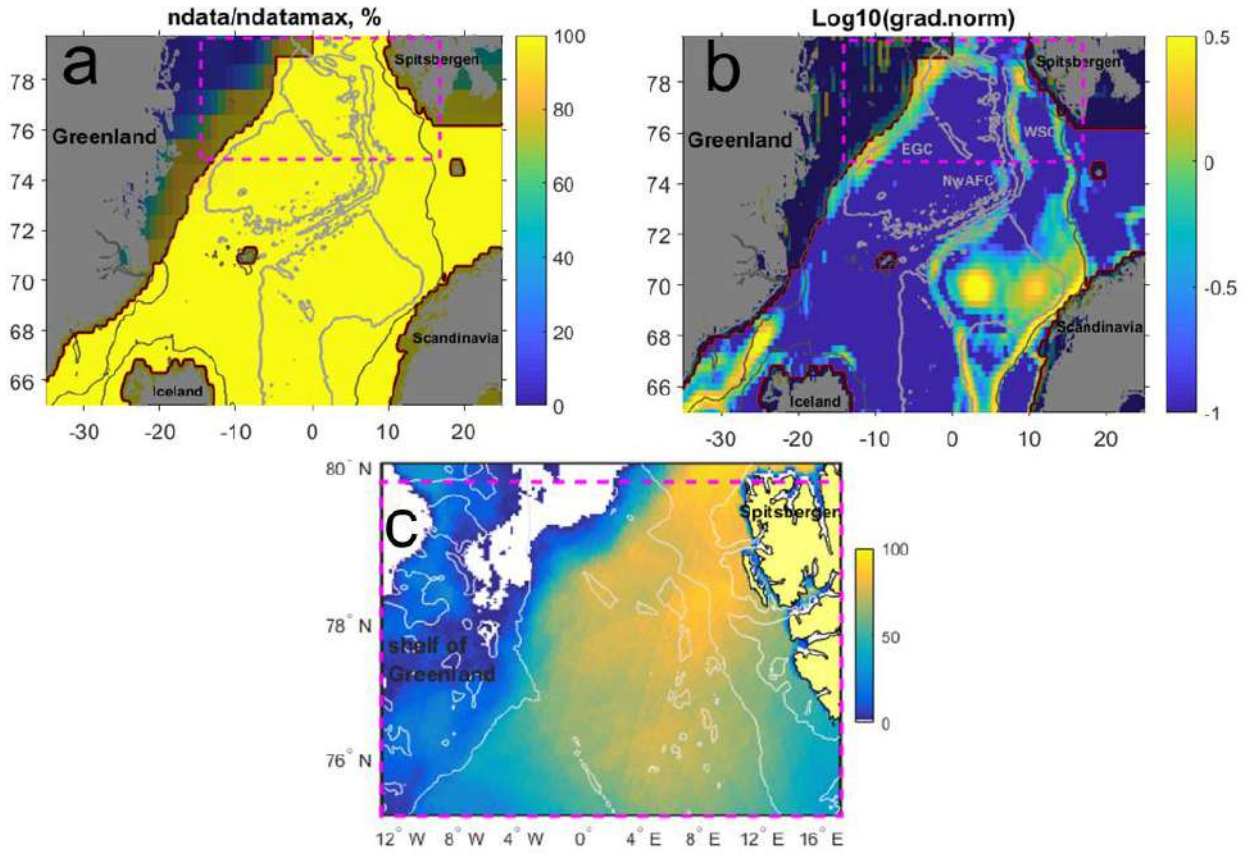

Fig. 2.10. (a) Spatial coverage of the Nordic Seas with AVISO18 altimetry data (in % from the maximum available days of observations for the study period). (b) The decimal logarithm of the normalized mean sea level gradients. Areas, where the data are unreliable, are artificially darkened. The purple boxes represent areas where AVISO data were compared with SAR data. NwAFC is the Norwegian Atlantic Front Current, NwASC is the Norwegian Atlantic Slope Current, WSC is the West Spitsbergen Current, EGC is the East Greenland Current. (c) Spatial coverage of the study area with SAR data during July-September 2007 in the northern Greenland Sea. The color scale indicates the total number of processed SAR images (the analysis was performed in the absence of packed ice), white areas indicate regions where there was no SAR data suitable for the analysis.

Chelton et al. (2011) showed that the AVISO10 gridded dataset, within the latitude band 66° S-66° N, can reliably detect eddies with a spatial scale of at least 0.4°, which in the subtropics corresponds to eddies with radii of 35-40 km. This is consistent with the results of Tournadre (1990), who showed that at a resolution of 30 km, one can reliably identify mesoscale eddies with a radius of 30-50 km or more. A comparison of the trajectories of near-surface drifters with sea level anomalies using AVISO14 satellite altimetry data showed that altimetry makes it possible to identify mesoscale eddies quite well, including in the Nordic Seas (Volkov and Pujol, 2012; Raj and Halo 2016). Raj et al. (2016) found that 15 km is the minimum dynamic eddy radius detected

by AVISO14 altimetry in the Lofoten Basin (68–73° N), which at these latitudes is equivalent to the 0.4° longitude criterion proposed by Chelton et al. (2011) for the subtropics.

A number of detailed *in situ* studies have been carried out for the quasi-permanent mesoscale Lofoten Vortex in the center of the Lofoten Basin of the Norwegian Sea (Kohl, 2007; Soiland and Rossby, 2013; Volkov et al., 2015; Soiland et al., 2016; Yu et al., 2017; Fer et al., 2018; Bashmachnikov et al., 2017, 2018; Bosse et al., 2019), which allows us to get a preliminary idea on the accuracy of eddy observations in satellite altimetry at these subpolar areas. It was shown that AVISO14 altimetry, in particular, correctly depicts the position of the eddy. The displacement of the eddy center in altimetry data relative to its simultaneous positions derived from glider observations was, on average, 7 km, varying from 0 to 20 km. This is within the spatial resolution of the AVISO dataset. Also, from satellite and *in situ* data, very close values of the Vortex propagation velocity were obtained (Yu et al., 2017). However, AVISO altimetry somewhat overestimated the dynamic radius of the eddy: 30 km versus 20-30 km obtained from direct observations (Yu et al., 2017; Fer et al., 2018; Bashmachnikov et al., 2017; Bosse et al., 2019). Here and below, the dynamic radius of the eddy is defined as the average distance from the eddy center to the point where the relative vorticity of the eddy core passes through zero. Azimuthal velocities in the Lofoten eddy obtained from AVISO14 data were 25-30% weaker compared to those obtained from quasi-simultaneous *in situ* observations *in situ* (70-80 cm s^{-1}) (Raj et al., 2016; Yu et al., 2017).

To interpret the results, in addition to interpolated AVISO altimetry data, along-track data obtained from the RADS (Radar Altimeter Database System, http://rads.tudelft.nl/rads), were also used. This dataset was used as an auxiliary one, since experimental attempts to study submesoscale processes using along-track altimetry (Chavanne and Klein, 2010) faced the problem of a limited number of quasi-simultaneous intersections of altimetry tracks, especially in polar and subpolar regions.

Using sea level (ζ) gradients and geostrophic relationships, the surface current velocity and relative vorticity ($\omega = \frac{g}{f}\nabla^2\zeta$) were determined. At the same time, white noise, which is enhanced when calculating gradients or second derivatives of sea level, was smoothed as in Arbic et al. (2012). The accuracy of calculating the maximum relative vorticity in an eddy passing from one altimetry track to another was assessed by constructing an artificial eddy with a characteristic radius of 50 km and a drop of ζ by 5 cm along the radial distance. The SLA at each grid point was then distorted by normally distributed random noise with a standard deviation varying from 1 to 1.5 cm and back to 1 cm along 5 consecutive fields of ζ. This method simulated weekly sounding of an eddy, propagating at a velocity of 3 cm s^{-1} from one Topex-Poseidon ground track to another. The resulting error of ω was 2 10^{-6} $s^{-1,}$ which is an order of magnitude less than the characteristic relative vorticity of mesoscale eddies.

Traditional estimates of eddy kinetic energy (EKE) were obtained at each AVISO satellite altimetry grid point using the Hilbert-Huang transform applied to the current velocity components. In this technique, the temporal variability of a variable is decomposed into "modes of its natural temporal variability" by removing the non-stationary ("long-period") component from the time series (Huang et al., 1999). The non-stationary component is estimated as the average between two curves, one of which passes through all the maxima, and the other through all the minima of the oscillating time series. The resulting curve is interpolated to all points of the original time series

and then is removed from the data. The procedure described above is repeated until all local extrema identified in a number of observations are separated by a single zero intersection. The time series obtained at the end of such a series of filterings is taken as the first “natural mode”, containing the highest frequency band, and is removed from the original time series. The whole procedure is then repeated to obtain the next "natural mode" of a lower frequency band. The use of the technique made it possible to identify 10 “natural modes” in the current velocity components. Four modes with characteristic temporal variability scales of less than 3 months were combined into the pulsation component.

Several algorithms have been developed to automatically identify eddies in satellite altimetry data: the Okubo-Weiss algorithm (Isern-Fontanet et al., 2006), the "winding angle" algorithm (Chaigneau et al., 2008), hybrid algorithm (Halo, 2012; Raj et al., 2016) and kinematic algorithm (Nencioli et al., 2010). In this study, the detection of eddy centers was performed using the kinematic algorithm by Nencioli et al. (2010). The distributions of current velocities and relative vorticity are used in this analysis. At the first stage, eddies are identified as regions where the velocity vectors demonstrate a rotational motion appears. In this case, three conditions must be simultaneously met: 1) the components of the current velocity vectors on opposite sides of the tested eddy center must have opposite directions and monotonically increase from the center outwards; 2) the velocity at the eddy center must have a local minimum; 3) the nature of rotation (cyclonic or anticyclonic) should remain the same in each 90-degree sector relative to the center of the supposed eddy. The last criterion allows filtering out meanders and saddle points in the velocity field. The algorithm can be adopted to datasets with different resolutions, but requires the presence of a sufficient number of points inside the eddy core. Due to the rather coarse resolution, AVISO altimetry data were previously interpolated using the cubic spline method onto an 8x8 km grid. When the algorithm parameters are correctly configured, the method by Nencioli et al. (2010) makes it possible to identify quite well the centers of even rather weak or small eddies, and gives a small number of false identifications.

Determination of eddy sizes by the last closed loop stream function method used by Nencioli et al. (2010), significantly underestimates the radii of eddies in AVISO altimetry, which is associated with inaccuracies in solving the inverse problem of converting the velocity field into the field of streamlines due to insufficient resolution of the original data. In this regard, another method was developed for determining the eddy radius (Bashmachnikov et al., 2017). The dynamic radius of the eddy (R_m) was determined by the contour of zero anomaly of the relative vorticity anomaly region, which surrounds the identified eddy center. For this, relative vorticity profiles were computed along 36 radial rays with an increment of 10º (Fig. 2.11). The eddy boundary along each profile was determined as the minimum of the following three distances: 1) the distance to the first zero-crossing of the relative vorticity profile (Fig. 2.11a), 2) the distance to the first point at which the increase in relative vorticity with the distance from the center of an anticyclone is replaced with its decrease (opposite for a cyclone), 3) the distance at which the rate of change of the relative vorticity significantly slows down (i.e. falls below 25% of its peak value along the profile). The last two criteria are used to correctly estimate the radius of the eddy in a situation where the eddy is in contact with another region of vorticity of the same sign (Fig. 2.11b), but of a different origin (another eddy, meander or gradient flow).

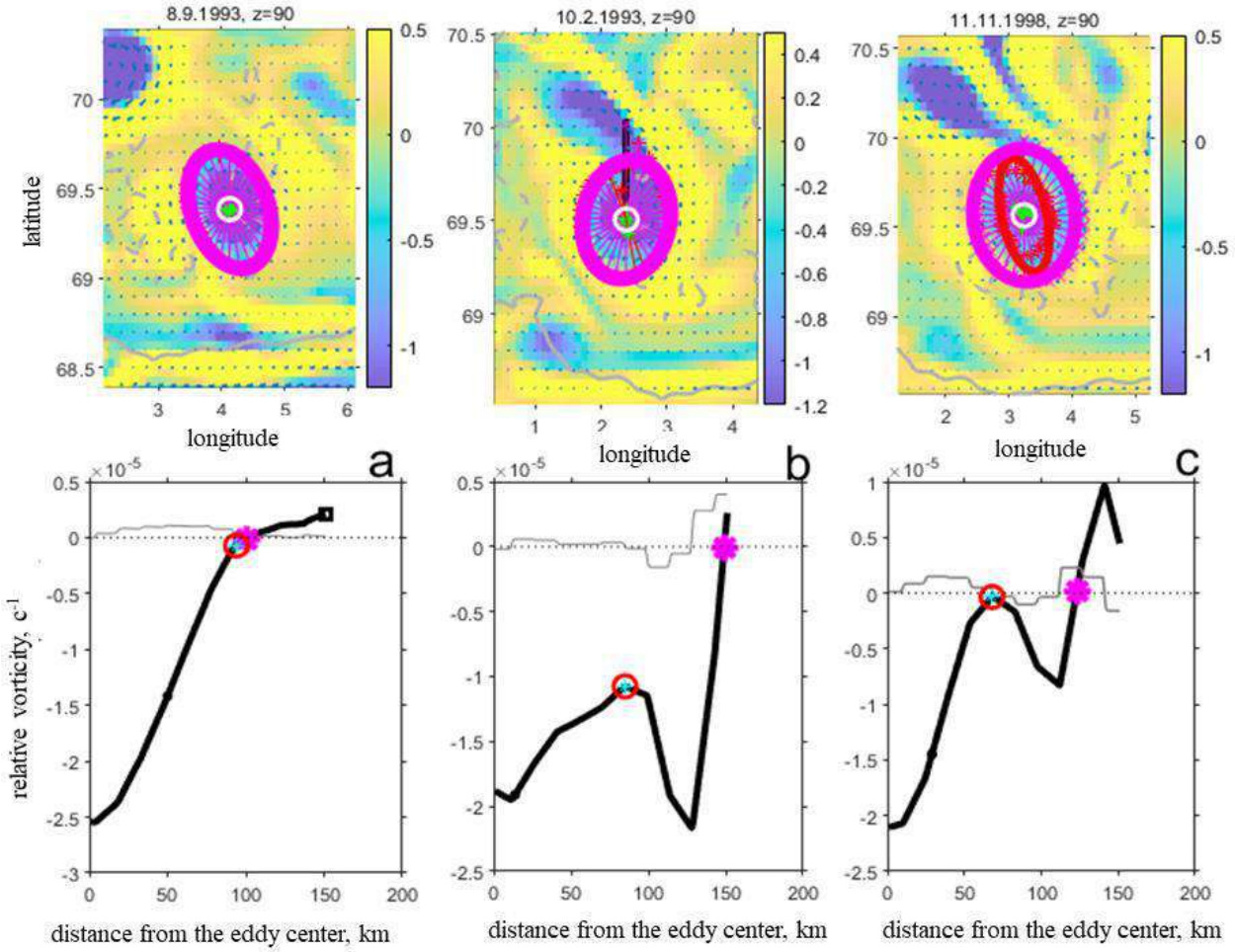

Fig. 2.11. The upper panels show distributions of relative vorticity (10^5 s^{-1}) near the center of an anticyclonic eddy. Red and pink rays connect the center of the eddy with the point of its boundary, determined by the algorithm. The lower graphs are the change in relative vorticity (s^{-1}) along the ray directed to the north. In graphs (c), red circles mark the boundary of the eddy at the first maximum of relative vorticity, pink circles mark the point where the relative vorticity passes through zero. The dotted circles are approximations of the eddy boundary by ellipses. Identification of the eddy boundary for the cases of: (a) isolated eddy (the most typical situation); (b) the process of a partial merger of an eddy with a neighboring anticyclone; (c) the process of complete merger of an eddy with another anticyclone with the latter being transformed into a peripheral ring of anomalous vorticity; at subsequent time steps this ring is absorbed by the core of the main eddy (according to Bashmachnikov et al., 2017).

A special case stands out when the eddy is surrounded by two nested rings of a higher and lower values relative vorticity (Fig. 2.11c). Such cases are usually observed in high-resolution model data immediately after a complete or a partial eddy merger. In this case, the outer ring, determined by the first criterion, is taken as the radius of the eddy. After identifying the eddy boundary, the position of the eddy center is further specified as the average of coordinates of all points of the detected boundary, and the radius of the eddy is then re-estimated as the average distance from the new center to the selected eddy boundary along all directions. In addition to the above approximation by a circle, it is also possible to approximate the eddy by an ellipse, for which the values of the maximum and minimum semi-axes of the eddy are estimated using the least squares method (Fig. 2.11). This method determines the boundaries of the eddy with greater

accuracy than using the algorithms by Isern-Fontanet et al. (2006) or Chaigneau et al. (2008), especially in complex cases where the eddy is in close contact with another synoptic structure characterized by a relative vorticity anomaly of the same sign.

With the exception of the above-mentioned special cases, most eddies represent isolated circular structures, and therefore the long-term average distributions of the main statistics of the eddies obtained in this study do not show a large difference from the results of other studies in the Lofoten Basin, derived using the method by Chaigneau et al. (2008) or the hybrid algorithm by Halo (2012), Raj et al. (2016), Raj and Halo (2016) and Raj et al. (2020). This confirms the objective nature of the results obtained below.

When calculating eddy trajectories, each successive position of the center of the monitored eddy is determined as the extremum of relative vorticity of the corresponding sign within one radius from the position of the center of this eddy at the previous step. This works well for mesoscale eddies with observation time step of 1-3 days. If the time step is about a week (the basic time interval between AVISO altimetry maps), then it is also considered a possibility when the eddy center covers a distance exceeding its radius during this week. Three consecutive iterations are made, for each of which the minimum (anticyclone) or maximum (cyclone) of the relative vorticity is searched within a radius around the center of the eddy is sought. Each new iteration starts from a newly defined position of the minimum (maximum), which becomes the new center of the search window. This "crawling window" method allows fixing the center of the eddy, even if it is located at a distance of two radii from the eddy center at the previous step, which is possible at high velocities of the eddy propagation (up to 10-15 cm s^{-1}). At the same time, this method avoids the unwanted jumps to the eddy center to those of the neighboring eddies, which may otherwise occur if the latter have a more pronounced relative vorticity anomaly. The reliability of this algorithm was additionally checked by visual inspection.

Following restrictions on the minimum spatial scales of the mesoscale structures which could be derived from AVISO altimetry (Chelton et al., 2011; Raj et al., 2016), all eddies with the dynamic radii R_m< 20 km were removed, as unreliable. Very weak eddies with a maximum azimuthal velocity in the AVISO altimetry of $V_m \leq 4$ cm s^{-1} were also filtered out. For a Rayleigh eddy with R_m = 20 km, $\zeta = \frac{1}{g}\sqrt{2ef}\, R_m V_m$, and this criterion corresponds to the maximum sea level anomaly at the center of the eddy ζ= 2 cm. The latter is at the level of random noise in AVISO altimetry data (for more details, see Bashmachnikov and Carton, 2012). Detection of eddies and defining their characteristics in the hydrodynamics models, the FESOM (Section 2.3.6) and MIT GCM (Section 2.3.7), were obtained using the same algorithms as for the satellite altimetry. Provided higher vertical resolution of the models, here eddies with radii $R_m \leq$1-4 km were filtered out.

2.3.3 Assessment of three-dimensional characteristics of eddies identified in AVISO satellite altimetry data

After determining the two-dimensional characteristics of eddies at the sea surface using AVISO satellite altimetry data, the vertical structure of the eddies was determined. For this purpose, vertical *in situ* casts of temperature and/or salinity from the EN4 Hadley Center dataset (https://www.metoffice.gov.uk/hadobs/en4/) were used. The vertical structure was determined only for eddies with at least one profile in the eddy core (at a distance of 0 - 0.75 R_m from the eddy center) and at least one profile at the background (at a distance R_m - 2 R_m from eddy center). The

areas where nearby eddies were identified were previously excluded from the background. If several profiles were detected in an eddy core or in the region around the eddy, they were all averaged. In further analysis, anomalies of temperature, salinity, and buoyancy frequency in the eddy core were used as the difference between the average profile in the eddy core and that outside the eddy.

The upper and lower boundaries of the eddy core were determined based on the following considerations (see Bashmachnikov et al., 2017). The eddies in the study area are formed mainly as a result of dynamic instability of the Norwegian and West Spitsbergen Currents, and to a lesser extent – of the East Greenland Current (Trodahl and Isachsen, 2018). Meandering currents form anticyclones with warmer and saltier cores on the cold side of the front and cyclones with colder and fresher cores on its warm side. Below the cores of anticyclones, isotherms (and isopycnals) are curved downwards, and in cyclones – upwards, i.e. the sign of the anomalies of thermohaline characteristics below eddies coincides with the sign of the corresponding anomaly of its core. In a subsurface eddy, isotherms and isohalines above the core of the anticyclones are curved upward, i.e. at some level above the core of a subsurface anticyclone, the positive thermohaline anomaly of the core can change to negative relative to the background, even if the core is warmer than the background. Thus, the lower boundary of the eddy core is fixed at a level where the anomaly of density, or at least water temperature, decreases to 25% of its maximum value in the core, while maintaining its sign. For subsurface cyclones/anticyclones, the upper boundary of core is fixed at the first level, where the corresponding thermohaline anomalies change their sign. The core of the eddy was considered to be superficial if the upper boundary was not detected or was located no more than 100 m from the sea surface (the depth of the upper mixed layer in the Nordic Seas during the warm season).

2.3.4 IDENTIFICATION OF EDDIES AT THE SEA SURFACE BASED ON SATELLITE SAR IMAGES

To identify not only mesoscale, but also submesoscale eddies, SAR images from ENVISAT (Advanced SAR - ASAR) satellite data of the European Space Agency archive were used for July-September 2007, as well as SAR images from Sentinel-1A satellite (Sentinel Data Hub, https://scihub.copernicus.eu/) for April-May 2015 and May-August 2016. Both dataset cover some areas of the Nordic Seas. The SAR images were obtained in the C-band wide-angle mode. For ENVISAT data, the average spatial resolution was 150 m, and for Sentinel-1A – 20-40 m, which made it possible to identify not only mesoscale, but also submesoscale eddies (the Rossby deformation radius in the region is 5-10 km). Daily ice concentration maps from AMSR-E data were used to eliminate the ice-covered areas (Spreen et al., 2008).

The warm period of 2007 was chosen due to a relatively small sea ice extent of during this, which allowed the identification of eddies over most of the study region. In total, in July-September 2007, 258 ASAR images were processed in the northern Greenland Sea and 1609 eddies were identified. Data coverage was relatively uniform in the central part of the study area, at each point of which an average of 80-100 SAR images were analyzed (Fig. 2.10c). In the Lofoten Basin, the analysis was carried out using Sentinel-1A data only for periods of interactions of the Lofoten Vortex with other eddies, previously identified using AVISO satellite altimetry data. Four episodes were identified, for which 40 SAR images were analyzed and a total of 1569 eddies were identified. A larger number of identified eddies is associated with a better quality of the Sentinel SAR images.

Identification of eddy structures on SAR images was carried out visually by I.E. Kozlov's group and by Yu.S. Novikova, using the European Space Agency's SNAP software (http://step.esa.int/main/toolboxes/snap/) and the method described in Kozlov et al. (2015, 2019). On satellite SAR images, eddies are identified as oval or spiral structures. Brightness contrasts in eddies are associated with modulation of small-scale sea surface roughness by currents, accumulations of surface films or the presence of broken ice in convergence zones (Johannessen et al., 2005; Lavrova et al., 2011; Kozlov et al., 2012, 2019; Kudryavtsev et al., 2014; Kostianoy et al., 2018). Most often, SAR images highlight eddies of relatively small spatial scales, comparable or smaller than the first baroclinic Rossby deformation radius (Dokken and Wahl, 1996; Johannessen et al., 1996; Karimova, 2012; Atajanova et al., 2017).

The wind regime has a significant impact on ability to identify eddies in SAR images (Karimova and Gade, 2016). In light and moderate winds (Fig. 2.12c), the most typical mechanism for the manifestation of eddies in SAR images is associated with the presence of slicks which is due to the accumulation of surface films (Espedal et al., 1998; Karimova, 2012; Kozlov et al., 2012; Munk et al., 2000; Zhurbas et al., 2019). In moderate winds, eddies are also detected by the presence of spiral bands with a higher brightness in the enhanced backscatter which is due to the collapse of short wind waves in areas of convergence of currents in the eddies (Johannessen et al., 2005; Kudryavtsev et al., 2014). The eddies are not visible on SAR images for very weak winds (less than 2 m s^{-1} – there are no ripples yet) and for fairly strong winds (more than 10-12 m s^{-1} – intense wave mixing masks linear convergent structures). Spatially varying oceanic and atmospheric conditions complicate the identification of large mesoscale eddy structures (Zhurbas et al., 2019; Kozlov et al., 2019; Bashmachnikov et al., 2020).

For each eddy visually identified on the SAR image, the major and minor eddy axes, the eddy center and the direction of rotation were identified (Fig. 2.12c-d). The average value of two quasi-perpendicular segments through the eddy center, ending at the spiral line, which is the most distant from the eddy center, were taken as the average diameter of the eddy. Due to the fact that the significant convergences of eddy currents are expected in the zone of high velocity gradients of the azimuthal currents adjacent to the region of high current velocities, the eddy boundaries identified on SAR images largely correspond to the dynamic radius of eddies determined from AVISO altimetry data. Visual examination of spiral isolines, interpreted as streamlines, identifies areas with pronounced positive or negative vorticity associated with the core of the eddy structure.

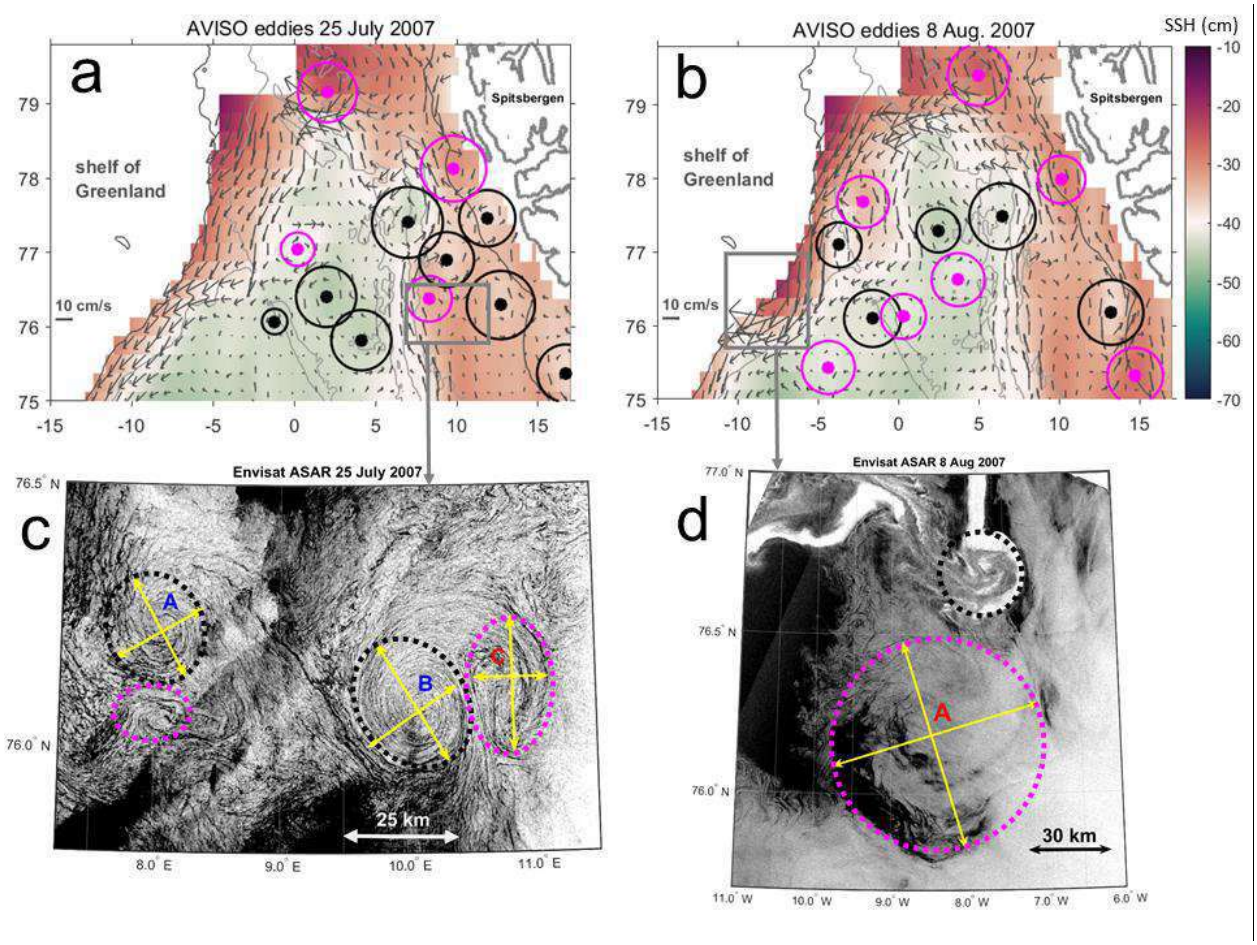

Fig. 2.12. Examples of eddies identified in AVISO data (a) for the last week of July 2007 and (b) for the first week of August 2007. Eddies detected from SAR data on: (c) July 25, 2007 (d) and August 8 2007. In (a, b), pink dots and circles show the centers and radii of anticyclonic eddies, black dots and circles - cyclonic eddies. The color scale shows the sea level (cm), gray vectors are currents in altimetry data (cm s^{-1}). Gray contours indicate the coastline, 500 m and 2000 m isobaths. Gray squares in (a, b) mark the areas shown on the SAR images (panels (c) and (d)). The yellow lines in (c) and (d) mark the directions along which the diameters of eddies A-C were estimated (from Bashmachnikov et al., 2020).

Despite the fact that the visual method for detecting eddy structures may contain some inaccuracies associated, in particular, with the expert determination of the eddy boundaries, and that this method is very labor-intensive, at the moment it is the only effective method for mass assessment of the characteristics of submesoscale eddies. The use of this technique has recently made it possible to evaluate the characteristics of eddies in different seas of the subpolar North Atlantic and Arctic Ocean (AO) for some limited periods of time (Zimin et al., 2016; 2018; Atadzhanova et al., 2017; Mensa et al., 2018; Kozlov et al., 2019).

2.3.5 IDENTIFICATION OF EDDIES AT THE SEA SURFACE USING SATELLITE DATA OF THE SEA SURFACE TEMPERATURE AND OCEAN COLOR (CHLOROPHYLL)

Mesoscale and submesoscale eddies can also be identified in the sea surface temperature (SST) or chlorophyll fields (Thomas et al., 2008; Zatsepin et al., 2011; Zimin, 2016; Mensa, 2018; Zatsepin et al., 2019: Kubryakov et al. 2023; Morozov and Kozlov, 2023). Using such images,

mesoscale and submesoscale eddies were studied both in the marginal seas of the Russian Federation and in other areas of the ocean (see, for example, Fernandes, 2009; Karimova, 2012; 2014; Karimova and Gade, 2016; Ginzburg et al., 2017; Kostianoy et al., 2018; Bashmachnikov et al., 2018), including the Arctic Ocean (Rodionov et al., 2014; Kozlov et al., 2015; Romanenkov et al., 2016; Atadzhanova, et. al., 2017; Kozlov et al., 2019; Bosse et al., 2019; Novikova, Bashmachnikov, 2021). In almost all studies, eddies were identified visually, while the eddy automatic detection algorithms in SST are is still experimental (see, for example, Fernandes, 2009; Dong et al., 2011). Isolation of eddies in SST requires the presence of horizontal temperature gradients and becomes significantly more difficult *in situ*ations with weak winds and high insolation. Under these conditions, the sea surface warms up fairly uniformly, which masks SST gradients associated with dynamic structures, but enhances the influence of spatial variability of atmospheric forcing on SST (Gentemann et al., 2003; Zhurbas et al., 2019). A significant disadvantage of working in these frequency bands is the limitation of the eddy observation due to the presence of cloud cover. In the Atlantic, the average percentage of water area covered by cloud cover increases from 40% in the subtropics to 60-80% in the subpolar regions.

In area of the Lofoten Vortex (subpolar region), an experimental identification of eddies was carried out using three data sets: altimetry, SAR imagery and chlorophyll-a. Processing of the original data was carried out by Yu.S. Novikova. Chlorophyll data was downloaded from the website of Ocean Colour - Climate Change Initiative (OC-CCI) version 3.1 (www.oceancolour.org), which are combined data from the European Space Agency's MERIS, NASA's MODIS- Aqua and SeaWiFS, and NOAA's VIIRS data. The data has a spatial resolution of 1x1 km and are available since 1997. The peculiarity of these data is that the initial data on ocean radiation spectra for the visible range is used, and the data for any of the sensors are then processed using a single processing algorithm, including the atmospheric corrections, masks for cloudiness and expression for estimation of chlorophyll-a values (Sathyendranath et al, 2019).

2.3.6 BASIC INFORMATION ABOUT AN EDDY-RESOLVING NUMERICAL OCEAN MODEL FESOM

In this study, the results of the hydrodynamic ocean model FESOM-1.4 (Wang et al., 2014) were used. The model is built on a triangular unstructured grid, which allows a rather arbitrary refinement of the coordinate grid in the areas the dynamics of which requires a higher resolution. The global model configuration used here was configured to increase the regional resolution in the northern Greenland Sea and Fram Strait to 1x1 km (Wekerle et al., 2017). Since the first baroclinic Rossby deformation radius in the study area is 6-10 km, the model is eddy-resolving. Bathymetry for the model was taken from RTopo-2 data with a grid resolution of 0.5 minutes (Schaffer et al., 2016). Vertically, 47 z-levels were used with a vertical layer thickness of 10 m in the upper 100 m layer and a gradual increase in the layer thickness with depth. Reanalysis COREv.2 (Large and Yeager, 2009) was used as the atmospheric forcing. Previous long runs of a coarser resolution version of FESOM were used to initialize as the boundary conditions for the nested regional model.

Comparison of epy modeling results with observations from series of long-term moorings in the Fram Strait showed that the high-resolution model well reproduces the mean currents, temperature and salinity fields, including the structure and intensity of the East Greenland Current (Wekerle et al., 2017). The main Atlantic water recirculation pathways in the model in the northern Greenland Sea are in good agreement with the observations (see, for example, von Appen et al., 2016). The model also reproduces well the observed dynamics of eddies in the region and the

seasonal cycle of the eddy kinetic energy. Comparison with FESOM model of a coarser resolution (4x4 km) showed that FESOM-1.4 more accurately reproduces the characteristics of the mean currents, EKE distributions and the structure of water masses (Wekerle et al., 2017).

The eddies in the FESOM model were identified using the same algorithm as in AVISO satellite altimetry. The two-dimensional characteristics of the eddies were also assessed in a similar manner (see Section 2.3.2).

2.3.7 Basic information about an eddy-resolving numerical ocean model MIT

The data from the regional ocean model of the Arctic Ocean of Massachusetts Institute of Technology (Massachusetts Institute of Technology Global Climate Model – MIT GCM), provided by Vokov D.L. (Volkov et al., 2015), were used to analyze the dynamics of the Lofoten Vortex. The model was configured on the structured Arakawa C-grid and hade a 4x4 km horizontal resolution in the Nordic Seas. With the value of the first baroclinic Rossby deformation radius in the Norwegian Sea of 7-8 km (Nurser and Bacon, 2014) this model can be considered an eddy-permitting one. The model has 50 vertical layers with an average layer thickness from 10 m in the upper ocean to 456 m at a depth of more than 1000 m. The high-resolution Arctic Ocean model is nested in the global model of the Estimating project the Circulation and Climate of the Ocean 2 - ECCO2 (Marshall et al., 1997; http://ecco2.jpl.nasa.gov) of a coarser resolution, used to form the initial model conditions and the liquid boundary conditions south of Iceland. The ECCO2 model is one of the modern oceanic reanalysis, which uses a physically based and time-evolving synthesis of the majority of available *in situ* World Ocean data for assimilation, including sea ice (Menemenlis et al., 2005). Quality control of the model results against observations is carried out for several parameters, including temperature and salinity, characteristics of the atmospheric boundary layer; background values of the vertical turbulent diffusion; values of critical Richardson number used for the K-profile vertical mixing parameterization scheme; friction coefficients at the ocean-atmosphere, ice-ocean and atmosphere-ice interfaces; ice-ocean-snow albedo; bottom friction and vertical viscosity (Large et al., 1994). The optimized ECCO2 solution in the next model step is obtained by integrating the model equations forward in time using these control parameters calibrated at the current step. The model uses GEBCO (General Bathymetric Charts of the Oceans) bottom relief (Smith and Sandwell, 1997). As the external forcing the atmospheric 25-year Re-Analysis of the Japan Meteorological Agency (JRA25-JMA) is used. The nested model reached a quasi-stationary regime within the first 3 years of calculations (1993-1995), which are not used for the analysis. A detailed description of the MIT GCM configuration used is given in the works by Losch et al. (2010), Nguyen et al. (2011) and Volkov et al. (2015).

Eddies in the MIT GCM model were identified using the same algorithm as in AVISO satellite altimetry. The two-dimensional characteristics of the eddies were assessed in a similar manner (see Section 2.3.2).

2.4 Comparison of the results of eddy identification and derivation of eddy characteristics using various types of satellite and model data in the Nordic Seas

In this part of the work, using the Norwegian and Greenland Seas as examples, the characteristics of detected eddies reproduced from three types of satellite data, AVISO satellite

altimetry, radar satellite imagery (SAR) and ocean color, are jointly analyzed. The results of the high-resolution numerical hydrodynamic model FESOM-1.4 are also used for comparison.

2.4.1 Results of eddy identification in SAR, AVISO satellite altimetry and FESOM hydrodynamic model data in the northern Greenland Sea

The spatial distribution of eddy kinetic energy (EKE) shows a consistent increase along the paths of the main currents (Fig. 2.13). Within the annual cycle, the spatial distribution of the pulsation component practically did not change when using together from 2 to 4 high-frequency components of the Hilbert- Huang transform. The highest EKE was observed along the West Spitsbergen Current at 78-79° N, previously identified as an area of intense eddy formation in the region (Hattermann et al., 2016; Trodahl and Isachsen, 2018). Along the East Greenland Current, the highest EKE was observed at 76-78° N. This is the Nordbukta area, which is usually ice-free in winter, even during periods of high ice concentration in the areas around (Comiso et al., 2001; Germe et al., 2011).

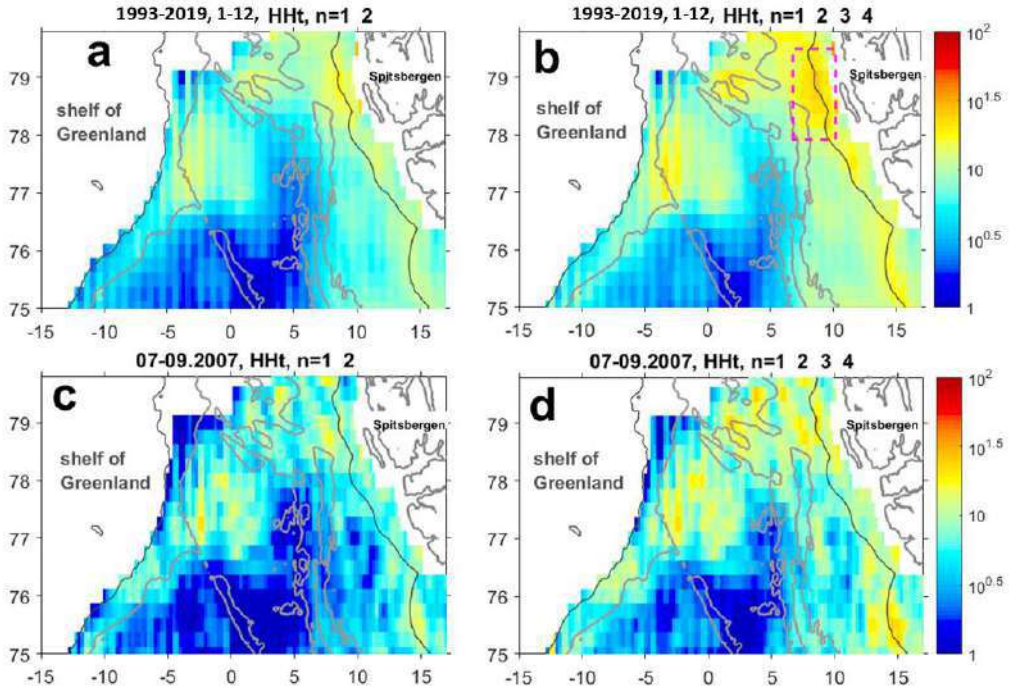

Fig. 2.13. Average values of the decimal logarithm of the eddy kinetic energy (EKE, cm ^{2} s$^{-2)}$ in the northern part of the Greenland Sea from AVISO altimetry data: (a, b) for the entire AVISO dataset analyzed (1993-2019), (c, d) for July-September 2007 – the period of comparison of altimetry with SAR data. (a) and (c) are the sum of the first two components of the Hilbert- Huang transform with a characteristic time scale of variability less than 1 month, (b) and (d) are the sum of the first four components of the Hilbert- Huang transform with a characteristic time scale of variability less than 3 months. The magenta dotted line in (b) shows the area where the most intense eddy formation in the region is assumed (Hattermann et al., 2016; Trodahl and Isachsen, 2018). The isobaths of 500 m and 2000 m are shown with gray lines of different brightness (from Bashmachnikov et al., 2020).

In the northern Greenland Sea, from AVISO data, on average, about 10 eddies per week were recorded (Fig. 2.14a). The total number of eddies detected in altimetry data during the period

of visual identification of eddies in SAR data (July-September 2007) were 125 (Fig. 2.14c). This is not enough to obtain reliable spatial statistics, but the histograms of properties of these eddies in summer of 2007 did not show significant differences from the histograms for the entire period of altimetry observations. This relative stability in the number and characteristics of eddies in AVISO data suggests the possibility of comparing the statistics of AVISO data for the entire period with SAR data obtained over a relatively short period of time. Eddy propagation vectors were obtained for approximately 50% of the identified eddies, i.e. for approximately 6000 AVISO eddies.

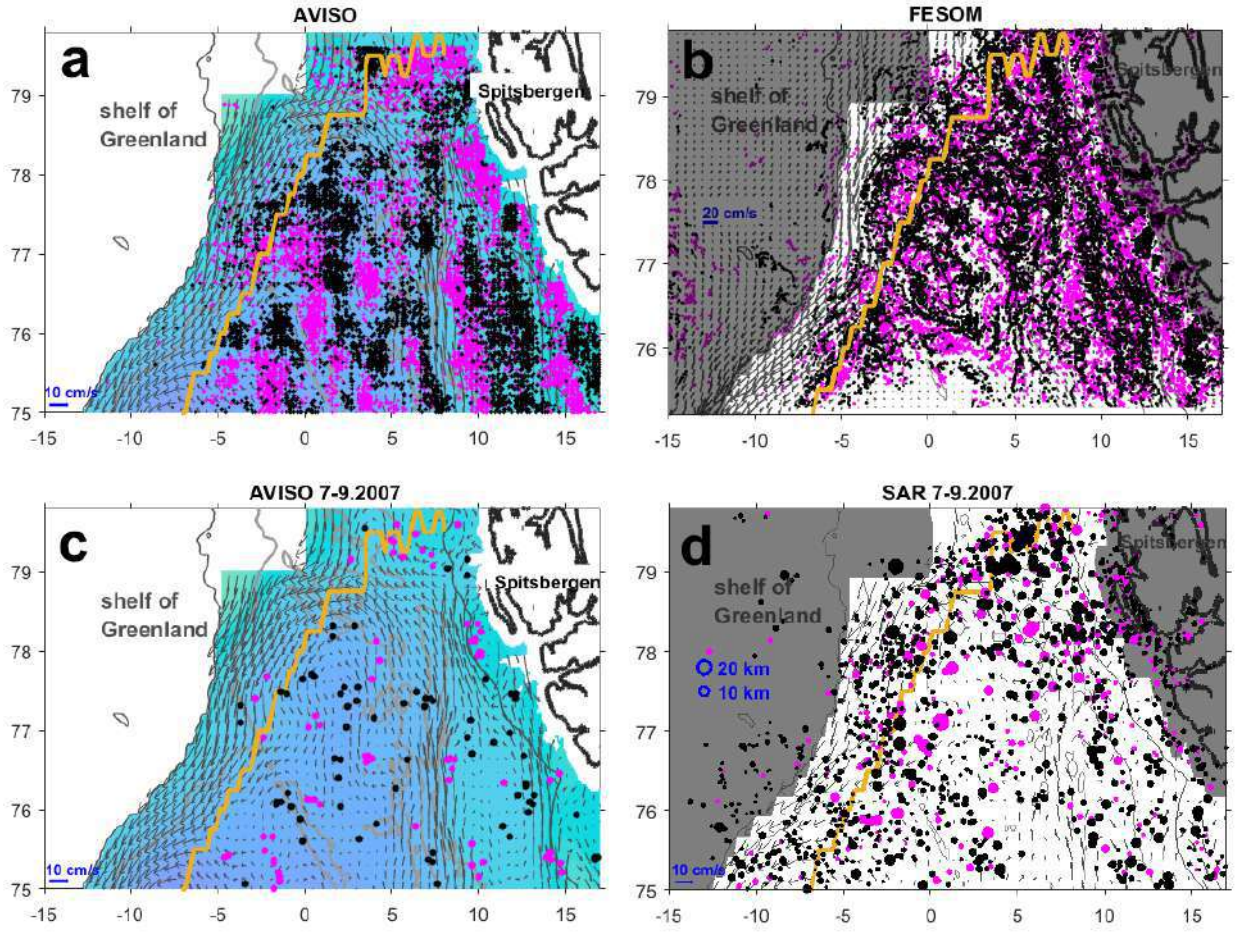

Fig. 2.14. Eddy centers identified in: (a) AVISO altimetry data since January 1993, (b) in FESOM model data for 2007, (c) in AVISO altimetry data between July and September 2007, and (d) in SAR data between July and September 2007. Pink dots mark the centers of anticyclones, black dots mark the centers of cyclones. For better visibility, the dots in (c) are larger than those in (a). The color scale in (a) and (c) is the average sea level for the period (blue color – low values, greenish color – high values). In (d), the size of the dots reflects the eddy radius. Gray shading marks the AVISO mask - this area is not used for further analysis. Gray arrows are the average currents for the corresponding time periods in AVISO data (panels a,b,c) or FESOM (panel d). The dark yellow line defines the climate-mean winter sea ice limit (based on PIOMAS data, https://pscfiles.apl.uw.edu/zhang/PIOMAS/); gray lines – isobaths of 500 m and 2000 m (from Bashmachnikov et al., 2020).

In FESOM model 25,300 eddies were detected for the entire 2007 (Fig. 2.14b), 487 eddies per week. Eddy propagation vectors were estimated for 65% of the eddies, i.e. for more than 16,000 eddies.

In 258 SAR images analyzed, between July and September 2007, 1609 eddy structures were identified (Fig. 2.14d), i.e. 536 eddies per week. This is approximately 50 times more than in AVISO. In July 2007, 56% of all SAR eddies were recorded, in August – 28%, in September – 16% (see also Atadzhanova, et al. al., 2017; Kozlov et al., 2019).

In the altimetry data, eddies practically were not identified on the East Greenland Current (Fig. 2.14a, c), which is due to the almost constant presence of ice and the rather poor quality of AVISO data in this region. In SAR images and FESOM data, the density of eddies in the East Greenland Current was comparable to the rest of the Greenland Sea; the number of eddies decreased only in the vicinity of the Greenland shelf (Fig. 2.14b,d). A fairly dense concentration of SAR eddies was observed on the Spitsbergen shelf (water depth 100-200 m or less), where small eddies with an average radius of 2 km dominated (Fig. 2.14d). These eddies cannot be detected in altimetry data. For further comparison, in the SAR and FESOM data, all eddies in the regions, which were masked in AVISO data, were removed (see gray mask in Fig. 2.14b,d).

In AVISO, the number of identified cyclones and anticyclones, both for the entire observation period and for July-September 2007, was approximately the same (Fig. 2.14a, c). This is consistent with the results of altimetry measurements in different areas of the World Ocean (Chelton et al., 2011; Raj et al., 2016, 2020). Identification of mesoscale eddies from the trajectories of surface floats in the subtropical Northeast Atlantic showed similar results with a certain predominance of cyclones - 60% of all eddies identified (Barbosa Aguiar et al., 2011). Approximately the same result was obtained from the analysis of FESOM model (recall that the technique used for identifying eddies was identical to their identification in AVISO altimetry). However, analysis of SAR images shows that the data are clearly dominated by cyclones – about 80% of all detected eddies (Kozlov and Atadzhanova, 2022), which is consistent with similar results for the East Greenland Current (Bondevik, 2011), the Barents and Kara seas (Atadzhanova et al., 2017).

The spatial distribution of eddy characteristics obtained from the AVISO altimetry data, the FESOM model and SAR data is analyzed on a regular 50x50 km grid (Fig. 2.15). All data types show an increase in the number of eddies along the main currents in the region. Moreover, in SAR data, the maximum number of eddies is located closer to the coast than in AVISO altimetry (Fig. 2.15a, c). In FESOM, the regions of increased number of eddies combine the above-mentioned regions of both AVISO and SAR (Fig. 2.15b).

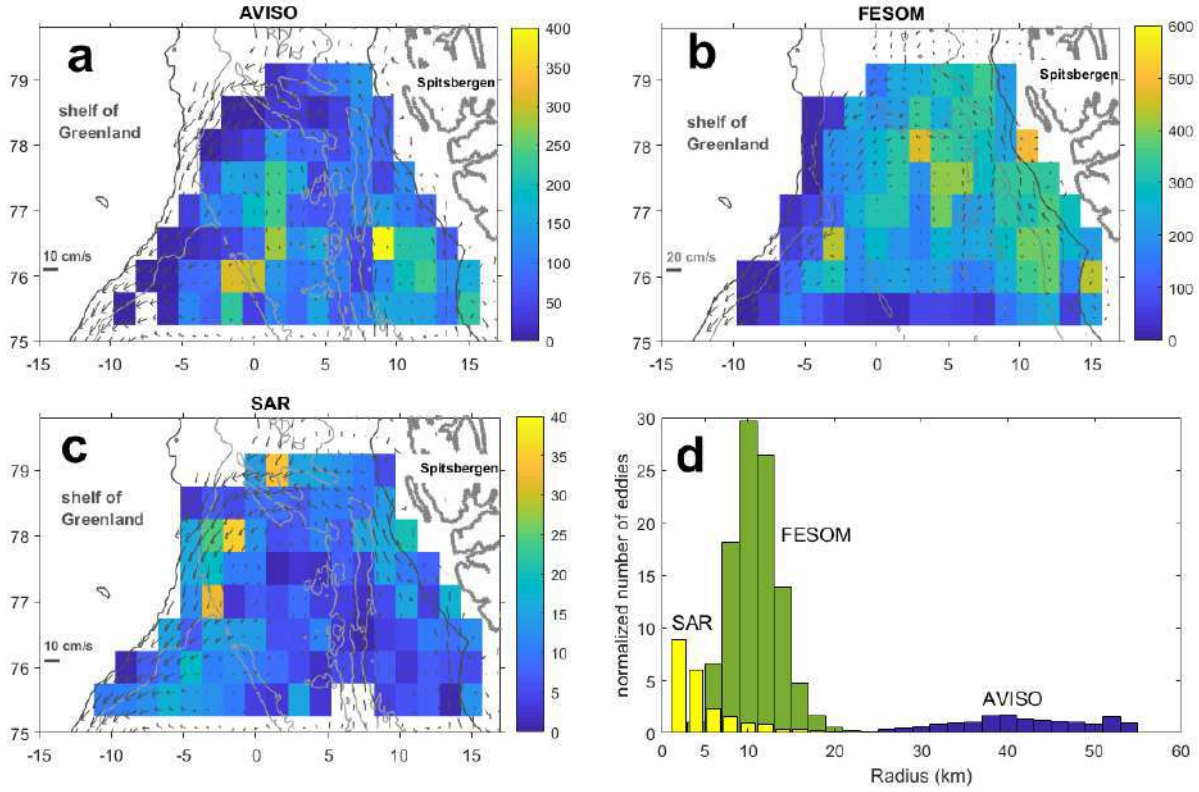

Fig. 2.15. Spatial distribution of the number of detected eddies: (a) in AVISO altimetry data for 1993-2019, (b) in FESOM model data for 01-12.2007 and (c) in SAR data for 07-09.2007. Gray arrows are the mean AVISO currents (a, c) or the mean FESOM currents (b) for the corresponding periods of observations. (d) Histograms of eddy radii from AVISO (blue), FESOM (green), and SAR data (SAR, yellow). The number of eddies was normalized to the total number of the processed images (daily in SAR and FESOM data, weekly in AVISO data) (from Bashmachnikov et al., 2020).

AVISO, SAR and FESOM data have similar trends of the northwards increase of the eddy radii (Fig. 2.16ac). The greatest differences are observed along the core of the East Greenland Current, where the AVISO and FESOM results show that the eddies are larger than average, and the SAR eddies, on the contrary, are smaller than average (Fig. 2.16a-d). The correlation between the spatial distribution in AVISO and SAR images were low: below 0.1 for the entire study area and 0.3 for its eastern part (east of 2° W).

The most significant differences between the three data sets were observed in the histograms of eddy radii, largely related to the different spatial resolution of the datasets (Fig. 2.16 d). In the AVISO data, the mean and mode of the dynamic eddy radii is about 40 km, and the dynamic radii cover the range of 20-55 km, within the spatial resolution of the data. In SAR data, the average radius of the eddy is about 4 km, on the order of the average summer value of the Rossby radius of deformation (Nurser and Bacon, 2014), while the mode is about 1-2 km. Therefore, 80% of SAR eddies belong to the submesoscale. Larger eddies are more often met in water areas with a bigger depth (Fig. 2.16c), where the average radii are4-5 km and the maximum reach 32 km. FESOM resolution does not allow identifying 1-2 km eddies. The mode of FESOM eddy radii is at 10 km, which is an intermediate value between the AVISO and SAR results.

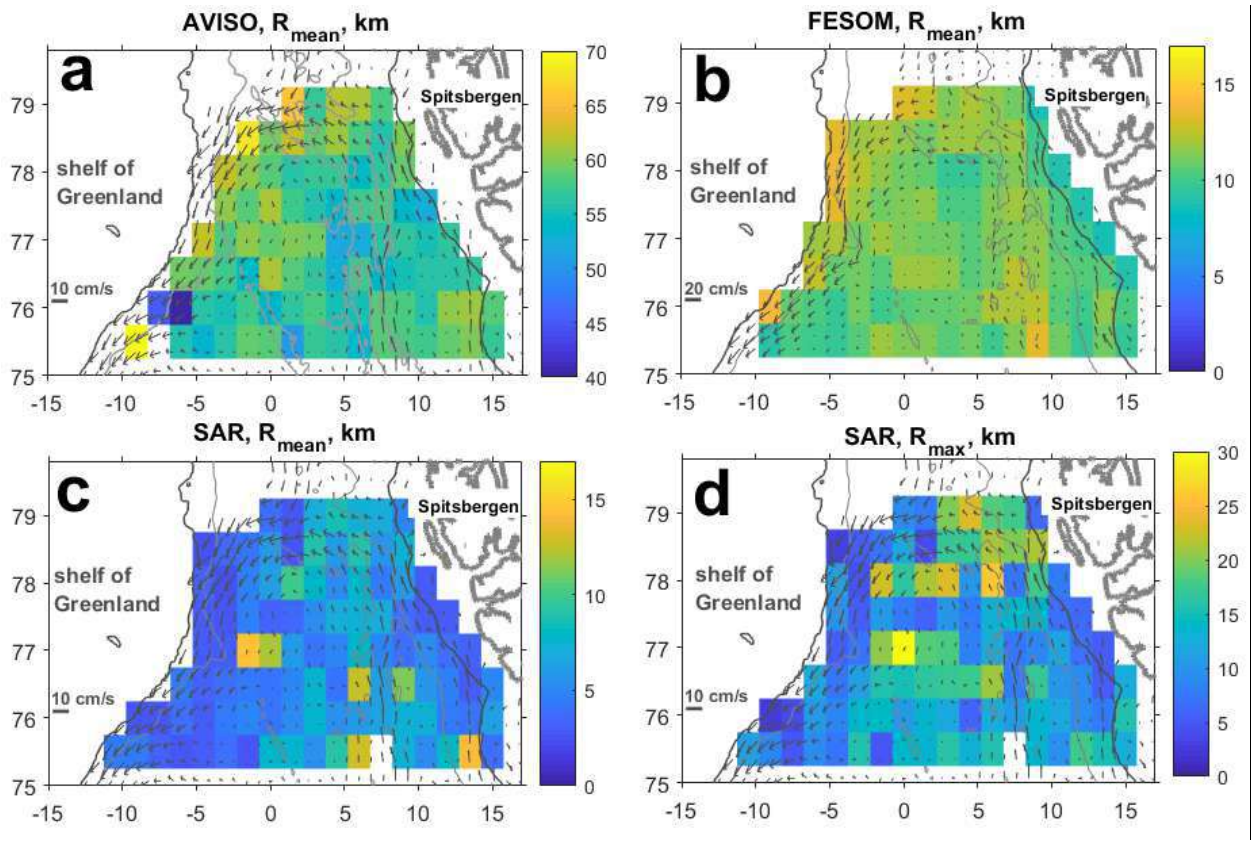

Fig. 2.16. Spatial distribution of eddy radii (km): (a) average dynamic radii in AVISO data (1993-2019); (b) average dynamic radii in FESOM (2007); (c) average radii in SAR data (07-09.2007); (d) same as (c), but for the maximum value of the eddy radius in the grid cell (note the difference in the color scales). Gray arrows—average current values over the observation period (a, c, d—AVISO; b—FESOM). Gray lines mark the 500 m and 2000 m isobaths (from Bashmachnikov et al., 2020).

In AVISO and FESOM data, the peak of relative vorticity the, in its absolute value (Fig. 2.17a, b), and the maximum azimuthal velocity of the eddy cores (not shown) are located along the main currents. Since these regions also have an increased level of the EKE in AVISO (Fig. 2.15), mesoscale eddies are the main contributor to the EKE (see also Fratantoni, 2001). These areas were previously identified as the areas of an increased EKE and areas of the most intense formation of eddies in the study region, obtained from the ROMS (Regional Ocean Modeling System) model with a spatial resolution of 0.8x0.8 km (Trodahl and Isachsen, 2018).

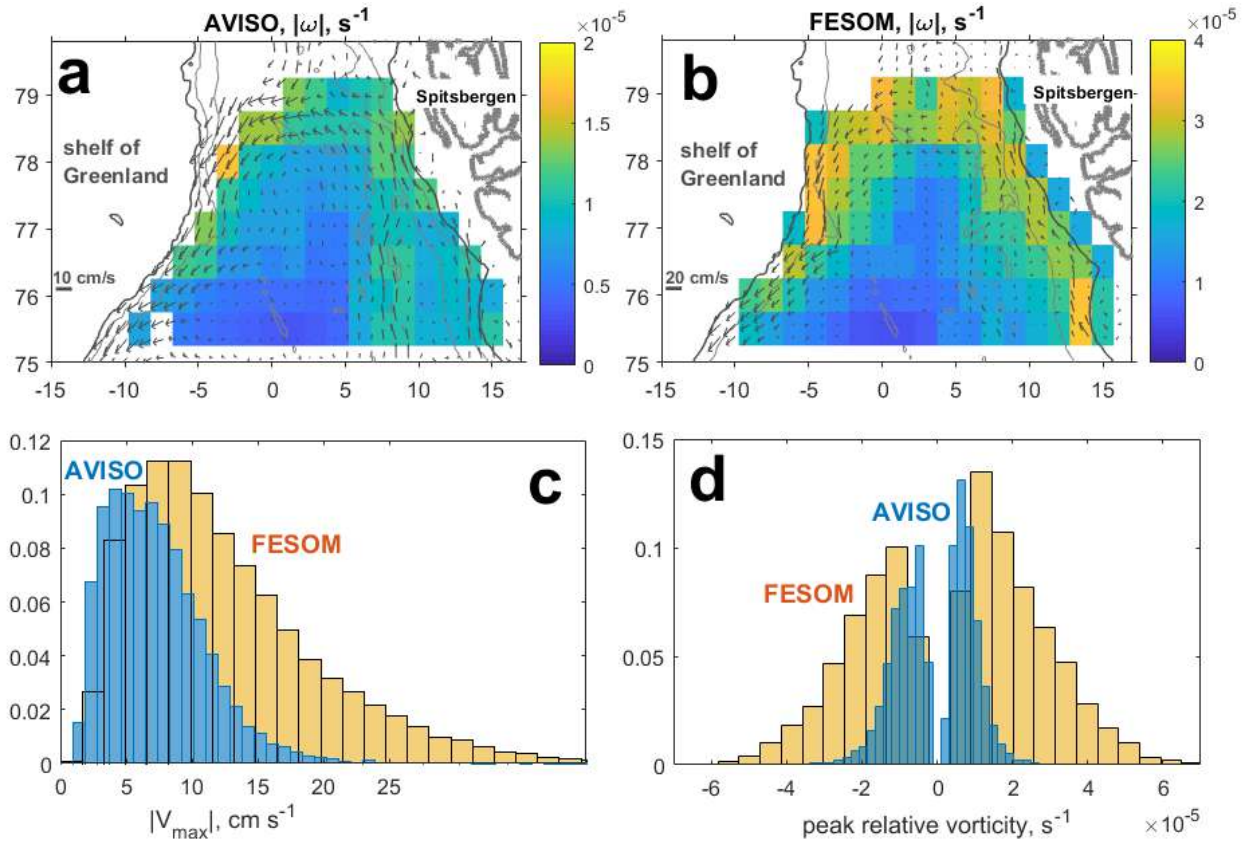

Fig. 2.17. Spatial distributions of the absolute value of the maximum relative eddy vorticity (s^{-1}), in: (a) AVISO altimetry and (b) FESOM data. Note the difference in the color scales: the maximum value in (b) is 2 times higher than in (a). Gray lines mark the 500 m and 2000 m isobaths. Normalized histograms of (c) the maximum azimuthal eddy velocity (cm s^{-1}) and (d) peak relative vorticity (s^{-1}) in eddy cores from AVISO (blue) and FESOM (yellow) data. (from Bashmachnikov et al., 2020).

The average Rossby number (*Ro)* of eddies, estimated as the ratio of the peak relative vorticity of the eddy core to the Coriolis parameter, in the AVISO data does not exceed 0.07, while in the FESOM data its value is twice as large and reaches 0.14 (Fig. 2.17c,d). The latter is closer to the characteristic value of *Ro* ~ 0.2 for mesoscale eddies (Carton, 2001). Comparison with FESOM results shows that AVISO also underestimates the peak azimuthal velocity by about a factor of 2. This is due to the spatial smoothing of the sea level anomalies in AVISO during the data processing and interpolation of the along-track data onto a regular grid. Similar results were obtained for the Lofoten Basin somewhat further south (Yu et al., 2017; Bashmachnikov et al., 2018). In both the AVISO and FESOM data, the mean intensities of anticyclones and cyclones are close to each other (Figure 2.17d).

The results of this section show that eddies detected in AVISO, SAR and FESOM altimetry data show similar spatial structure, despite the fact that different data predominantly characterize eddies of different spatial scales: from large mesoscale in AVISO to predominantly small submesoscale in SAR. In general, there is an increase in the number and in the intensity of the eddies along the main currents, which is consistent with previous studies (Trodahl and Isachsen, 2018). There is also an increase in the kinetic energy of eddies to the north, towards the Fram Strait, where the highest azimuthal eddy velocities in the region were observed (Nilsen et al., 2006; von Appen et al., 2015, Hattermann et al., 2016; Kolas and Fer, 2018).

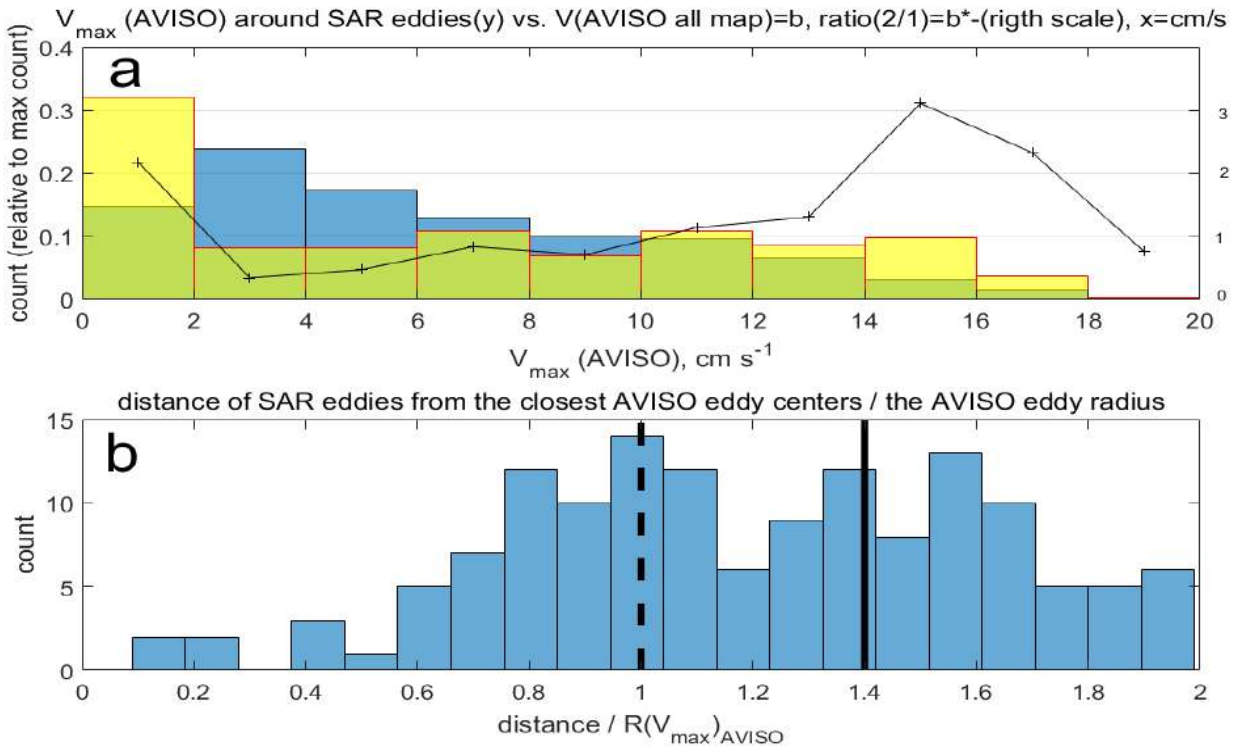

Fig. 2.18. (a) Statistics of AVISO current velocities in the vicinity of the eddies identified on the SAR image on July 25, 2007. The blue color shows the normalized histogram of AVISO current velocities (cm s^{-1}) throughout the entire study area; yellow – the normalized histograms of the maximum velocity of the background current (cm s^{-1}) near the eddies detected on SAR images (at a distance of ≤25 km). The black line characterizes the ratio of the second parameter to the first (right Y axis). Histograms are normalized by the total number of grid points used, so that the sum of all columns is 1. (b) Histogram of the number of SAR eddies as a function of distance from the center of the nearest mesoscale AVISO eddy. The X-axis is normalized by the radii of the corresponding AVISO eddies. Vertical lines mark the radius of maximum azimuthal velocity (dashed black line) and the dynamic radius (solid black line) of AVISO eddies (from Bashmachnikov et al., 2020).

Small mesoscale and submesoscale eddies detected in SAR imagery are often the result of instability of larger (mesoscale) eddies, while mean flows tend to generate primarily mesoscale structures ranging in size from 1 to 3 times the first baroclinic Rossby deformation radius (Cushman-Roisin and Beckers, 2011), i.e. about 5–15 km for the study area. In the vicinity of the eddies with $R_m \leq 15$ km observed in SAR, the maximum background current velocity was estimated at four AVISO grid nodes around the center of the eddies. The ratio of the histogram of AVISO current velocities throughout the study area to the histogram of the maximum AVISO current velocities in the vicinity of SAR eddies (Fig. 2.18a) shows that the majority of submesoscale SAR eddies are concentrated either in areas of very weak currents (below 2 cm $s^{-1)}$, or in areas of fairly strong currents (12-18 cm $s^{-1,}$ which is close to the maximum speed of the mean currents in the region). The increase in the number of submesoscale SAR eddies in the areas of the mean currents suggests that they can be generated both as a result of a rapid disintegration of the generated mesoscale eddies, or directly by the mean current, for example, when it interacts with topographic irregularities (see, for example, Zatsepin et al., 2011).

A histogram of the distances of SAR eddy centers from the center of the nearest mesoscale AVISO eddy, where the distances from the center are normalized by the radius of the mesoscale eddy (Fig. 2.18b), shows that the maximum number of the submesoscale eddies is found at the periphery of the mesoscale eddies, i.e. where the azimuthal velocity of the mesoscale eddy and its lateral shear are close to maximum. This indicates the probable generation of submesoscale eddies observed in SAR images by the mesoscale eddies identified in AVISO data.

2.4.2 Eddy identification based on SAR and along-track satellite altimetry in the northern part of the Greenland Sea

This section presents a comparison of eddies characteristics detected on a single AVISO altimetry map (12 eddies) and on SAR images observed during July 22-28 of 2007. The choice of the time period was determined by the complete coverage of the study area with high-quality SAR images, which made it possible to identify a total of 410 eddies during this week (Fig. 2.19). The overlap of several eddies observed here and there is a consequence of the fact that in two successive SAR images (taken with an interval of 1–2 days), the same eddy could be re-identified or broken up into several eddies. Since the lifetime of submesoscale eddies is usually short (1-3 days), it is assumed that in the vast majority of cases different eddies are observed.

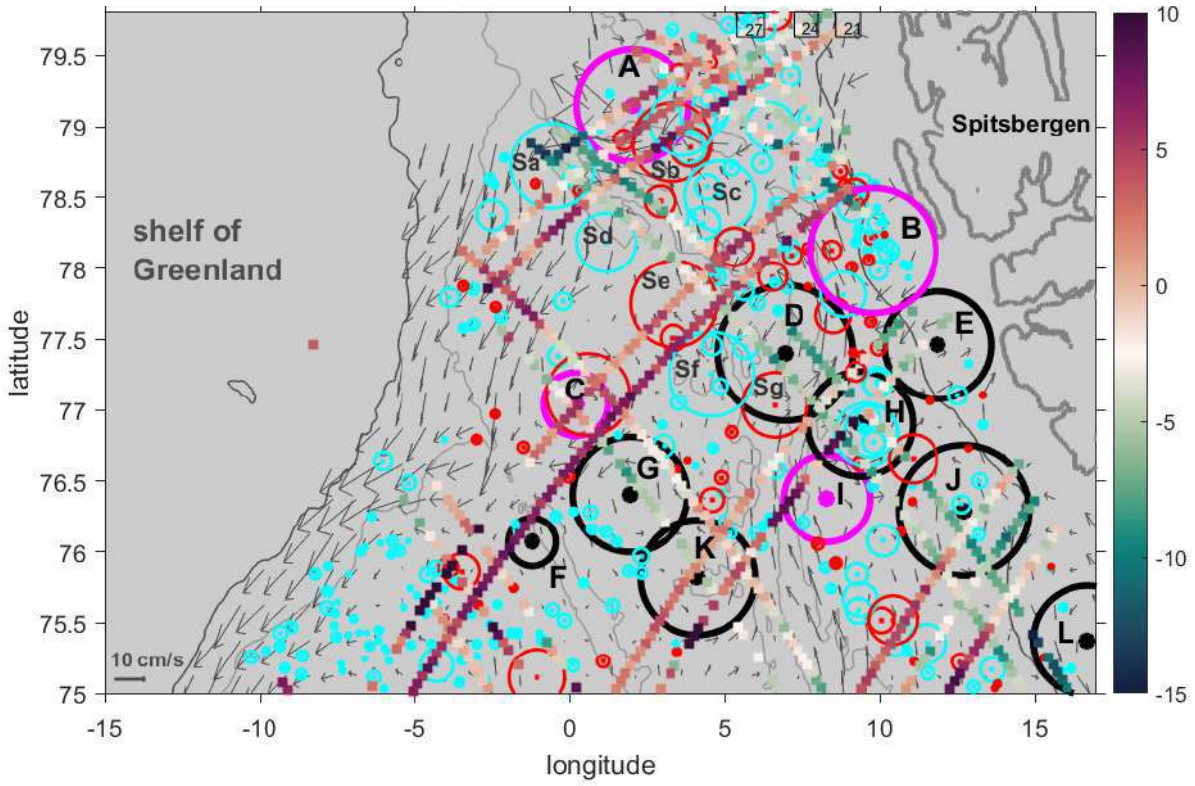

Fig. 2.19. Eddies identified in AVISO altimetry data (pink circles - anticyclones, black - cyclones) and in SAR data (red circles - anticyclones, blue - cyclones) during 22-28.07.2007. The dots mark the centers of the eddies; the size of the circles characterizes the eddy radii. Colored lines show all RADS altimetry tracks crossing the region from July 22 to July 28 of 2007, color is the sea level height (cm). Gray contours – isobaths of 500 and 2000 m (from Bashmachnikov et al., 2020).

On the AVISO map from July 22-28 of 2007, 12 eddies were identified. Along-track data indicate that each of the detected eddies is intersected by at least one track, with the exception of eddy **B** (Fig. 2.19). The closed current pattern, resulting in eddy **B** is a result of interpolation from other tracks performed outside the analyzed period, and eddy **B** itself is an artifact of AVISO processing procedures. This eddy was excluded from further analysis.

For the one-week period used, the distance between adjacent tracks ranges from 25 km to more than 100 km (Fig. 2.19). Using a one-month window, which is an average interval for track-data collection for the AVISO maps, tracks cover the entire area almost evenly, and the distances between adjacent tracks are between 15 and 30 km. However, when spatio-temporally interpolating data onto an AVISO map, the data from tracks, more distant in time, are "smeared out" due to time variability of the sea level. Thus, the vast majority of eddies on the AVISO maps are located in the locations of a set of tracks collected over a week-long period, between which there are large gaps in observations, where the eddies, as a rule, are not identified.

The radii of the 10 largest mesoscale eddies in SAR images (denoted by the letters Sa - Sg in Fig. 2.19) are on average 1.5 times smaller than the radii of 12 eddies identified in AVISO altimetry: the average radius of mesoscale SAR eddies is 30 km, and the average radius of eddies in AVISO is 42 km. The similar ratio was obtained by Yu et al. (2017) when comparing the Lofoten Vortex as represented in AVISO altimetry with direct *in situ* observations.

The next few paragraphs are devoted to the analysis of a link between the eddies identified in AVISO maps and along-track data, with those identified in SAR data. In only two cases, eddies identified in AVISO could be identified as eddies of approximately the same size in SAR images: anticyclone **C** (centered at 77° N 0.4° E, which is 32 km in SAR and 26 km in AVISO) and cyclone **N** (76.9° N, 9.5° E, which is 20-25 km in SAR and 40 km in AVISO). Both eddies are located at the intersections of altimetry tracks made during the week for the study period (Fig. 2.19), which makes their identification more reliable. It is also possible that the anticyclonic eddy **A** in AVISO with R_m = 45 km corresponds to the neighboring anticyclonic SAR eddy **Sb** with R_m = 30 km, and the cyclone **D** with R_m = 50 km could be identified in the SAR image as the cyclone **Sf** with R_m = 33 km (Fig. 2.19). The displacement of the centers of these eddies in altimetry could be the result of the intersection of different parts of the moving eddy by the altimetry tracks at different time.

The cyclonic eddy **E** (78.1° N, 10° E) is crossed by two altimetry tracks, but it is not seen in SAR. Instead, several cyclonic and anticyclonic SAR eddies with radii an order of magnitude smaller are observed on the periphery of eddy **E**, which can be interpreted as a result of the interaction of eddy **E** with topography, the West Spitsbergen Current and neighboring eddies.

Several small SAR eddies were detected inside the cyclonic eddy **J** (76.3° N, 13° E), intersected by several AVISO tracks. However, the eddy is weak, with an extremely low peak relative vorticity of 2×10^{-6} s^{-1}. It is likely that such weak but large AVISO eddies are the result of an artificial merger of several smaller eddies of the same sign by smoothing of along-track information on AVISO maps during the interpolation and noise suppression procedures (Le Traon et al., 1998; Ducet et al., 2000).

Some the eddies identified in the SAR images are large enough to be detected in AVISO data, but "sifted" between the altimetry tracks (**Sc, Sd** and **Sg)** (Fig. 2.19). Other SAR eddies (**Se** and **Sa)** are intersected by altimetry tracks, which reveal the corresponding sea level anomalies, but are not identified as eddies on AVISO maps. This may be due to their short lifetime or a high propagation velocity. Thus, with the highest recorded velocities of eddy propagation detected in the region of 5-10 cm s^{-1} (see also Raj et al., 2016), in 3-7 days an eddy with a radius of 30-km

will cover distance of one eddy radii. Then, the structure of the current velocities will be smeared on the non-simultaneous altimetry tracks, and in the interpolated AVISO maps the rotating core may lose its insularity. Indeed, the AVISO map highlights weak relative vorticity anomalies of the corresponding sign shown in the areas where these eddies are located, however, they are not pronounced enough for their automatic identification by the algorithm.

Thus, the reliability of eddy detection based on data from non-simultaneous altimetry tracks also depends on the eddy propagation velocity and on its dynamic stability. A similar effect in AVISO altimetry may artificially underestimate the number of eddies along strong mean currents, and could be responsible for the reduction in the number of eddies in the East Greenland in AVISO dataset, which was not observed in SAR or FESOM data (Figs. 2.14-2.15).

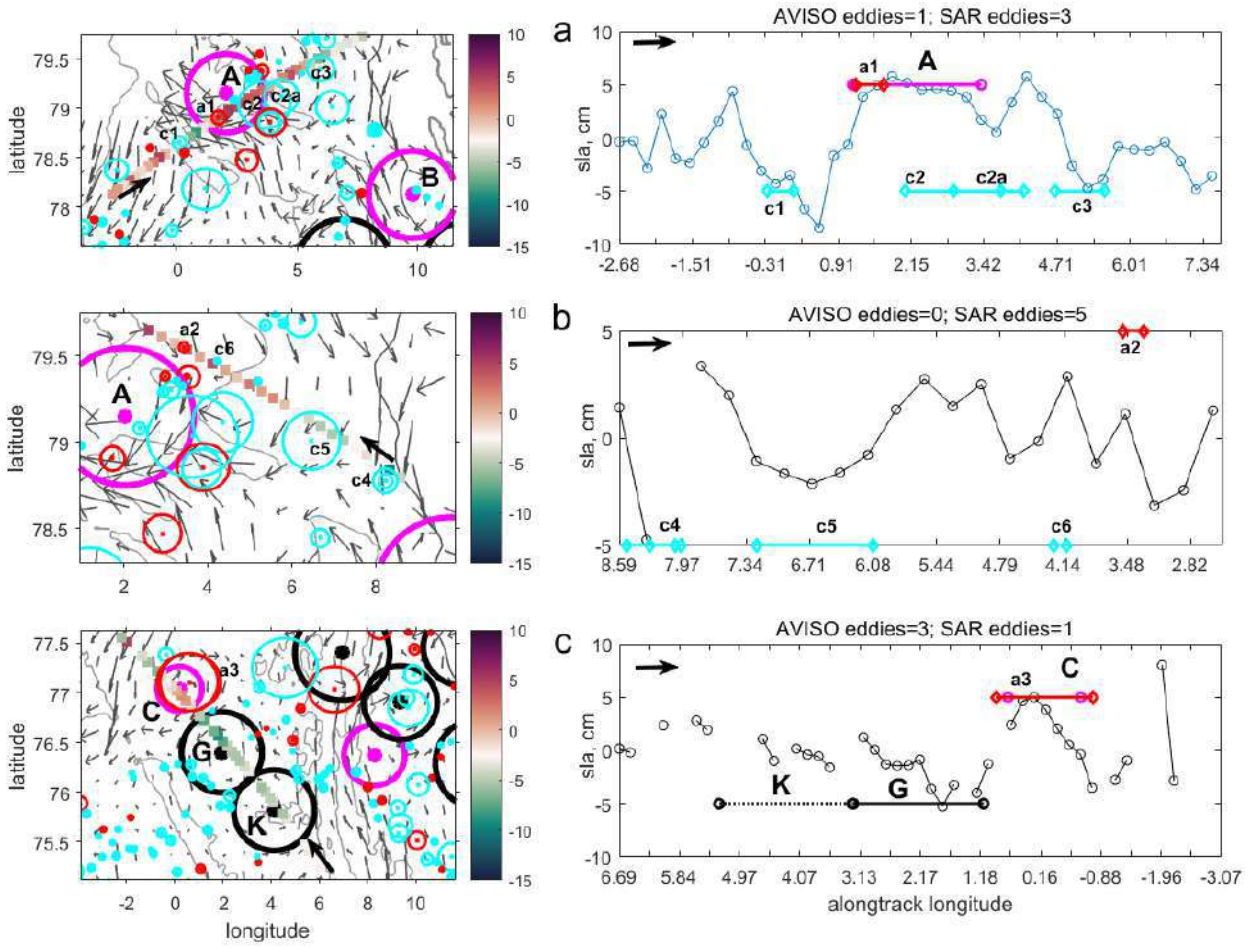

Fig. 2.20. On the left there are extracts from Fig. 2.19, on which only one of the altimeter tracks is indicated, on the right there are the corresponding along-track sea level anomalies (cm) with the trend removed. a – track No. n1p0220c60 from 07.24.2007 and SAR image eddies detected on 07.23–25.2007; b – track No. n1p0225c60 from 07.24.2007 and SAR image eddies detected on 07.23-25.2007; c – track No. n1p0255c60 from 07.25.2007 and SAR image eddies detected on 07.25-26.2007. Black arrows mark the direction of the along-track progress. In the right panels, the segments mark the boundaries of the eddies identified in AVISO (pink - anticyclones, black - cyclones) and in SAR (red - anticyclones, blue - cyclones), which are intersected by the tracks. A smaller number of SAR eddies presented in the figures compared to Fig. 2.19 is the result of a reduction of the time interval used in this figure by half (from Bashmachnikov et al., 2020).

A joint analysis of along-track sea level anomalies over eddies in altimetry data and SAR images intersected by the same track (Fig. 2.20) made it possible to formulate two basic conditions for detecting an eddy in the AVISO grided products in the study region: 1) the dynamic radius of an eddy must be at least 20-30 km, and 2) the sea level anomaly in the center of the eddy should exceed 5-10 cm. Also, an increase in the eddy lifetime and a decrease in the eddy propagation velocity contribute to the appearance of the eddy on AVISO maps. Condition 1) is in good agreement with the statistical analysis of the modeling data by Tournadre (1990): the probability of detecting an eddy with a radius of more than 50-60 km is 80-90%, an eddy with a radius of 25-30 km is 50-70%, and an eddy with a radius of less than 20 km is 0-5%.

2.4.3 Eddy identification based on SAR and ocean color data in the Lofoten Basin of the Norwegian Sea

Additional information about the ability to identify eddies in different frequency bands was obtained by comparing AVISO altimetry, SAR imagery and ocean color data in the central part of the Lofoten Basin, over an area of approximately 300 × 300 km, which included the quasi-permanent Lofoten Vortex (Fig. 2.21a). Here we used SAR data from the Sentinel-1A satellite in the C-band with a spatial resolution of 20×40 m and ultra-wide mode (sweep width of 400 km). Three episodes were selected for the analysis during 2015-2016 of 3-4 weeks each. The criteria were: 1) an observed interaction of the Lofoten eddy with another mesoscale eddy (derived from AVISO data) and 2) the cloud cover was dispersed enough to see the ocean surface in ocean color. A total 10 weeks were analyzed, during which 1560 eddies were identified on SAR images. These data were compared with the ocean color (chlorophyll) data from OS–CCI version 3.1 at a spatial resolution of 1 × 1 km (see section 2.3.5). Over 10 weeks of observations, 35 ocean color fields with relatively large cloud-free areas were analyzed and a total of 1631 eddies were identified (Fig. 2.21b). Eddyes in chlorophyll were identified visually based on the presence of spiral structures, which is similar to their identification in SAR data.

The histograms of the eddy radii in SAR and ocean color data differed due to the lower resolution of the latter dataset (Fig. 2.21c). The difference is similar to that between the histograms of the SAR image and FESOM model data of the previous section (Fig. 2.15d): a clear shift in the radii of SAR eddies towards smaller scales is visible. If the SAR data has radii in the range from 1 to 32 km and the mode of 1-2 km, then the chlorophyll data has them in the range from the first km to 50 km and the mode of 3-4 km. The number of eddies increased with their decreasing size. Thus, the data in the Lofoten Basin confirm the data in the north Greenland Sea (section 2.4.2), and show that SAR data do not allow large-scale eddies to be identified en masse. Since the satellite altimetry does not detect small-scale eddies, SAR data should be considered as a complement to AVISO altimetry data in eddy detection, rather than as an alternative.

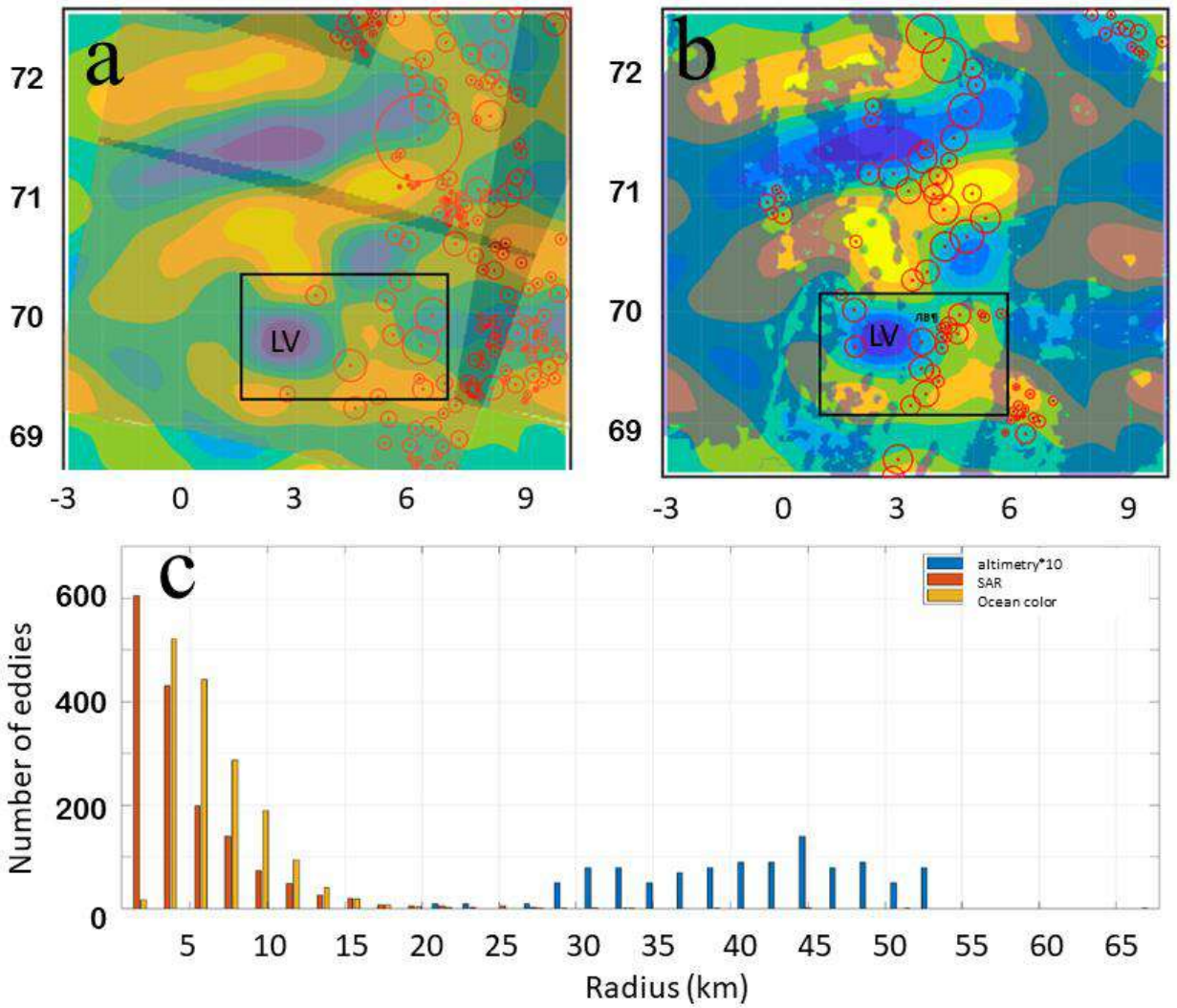

Fig. 2.21. Composite map of selected eddies for April 9-16 of 2015: (a) in SAR data (shadows show the coverage areas of the SAR images used: darker shadows indicate the areas of an overlap of 2 or more images) and (b) in chlorophyll-a data (shadows show the cloud cover where data is missing). The color is the relative vorticity from AVISO altimetry data. The black square shows the area of possible influence of the Lofoten Vortex (LV). (c) Histogram of eddy radii based on satellite altimetry data (blue), SAR images (red), and the ocean colour data (yellow). For better visualization in the histogram, the number of eddies in the satellite altimetry data is multiplied by 10 (from Novikova and Bashmachnikov).

2.4.4 Eddy propagation velocities identified in AVISO satellite altimetry and in FESOM hydrodynamic model in the Greenland Sea

The eddy translation velocities were estimated using the following algorithm. For each eddy, at the next time step, a search was carried out for an eddy of the same sign at a distance equal to two dynamic radii of the analyzed eddy. If such an eddy was detected, the eddy translation velocity vector was estimated. If several eddies met these criteria, then the one closest to the original eddy was selected, or, if the distances to several eddies were almost identical (within the AVISO grid step), the eddy located along the vector of the mean current was selected. The final map of the average eddy displacement velocities was obtained by averaging all eddy displacement

vectors in 50 x 50 km grid cells. Cells with less than five recorded eddy displacements were excluded from further analysis.

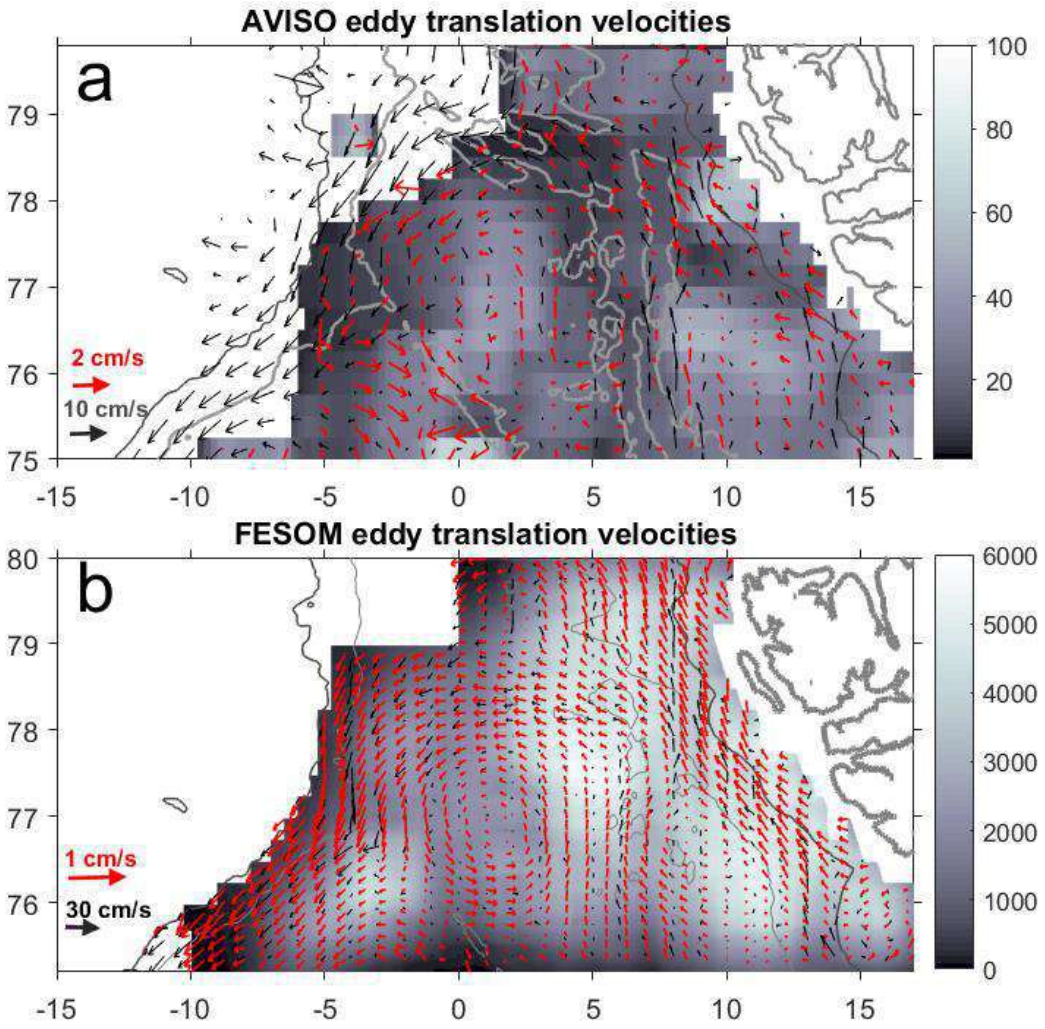

Fig. 2.22. Red vectors show the time-average vectors of eddy displacement velocities (cm s^{-1}), smoothed by a 50 x 50 km window: (a) in AVISO altimetry data for 1993-2019, (b) in FESOM model data for 2007. The color scale shows the number of eddy pairs used to calculate average velocities. Background current velocities (cm s^{-1}) averaged over the same period are shown as black vectors. Notice the difference in scales between vectors of different color (bottom left). 500 and 2000 m isobaths are shown.

The patterns of eddy propagation in AVISO altimetry data (1993-2019) and the FESOM hydrodynamic model (2007) show very similar results (Fig. 2.22a, b). The eddies move predominantly along topographic features, along the topographically trapped currents, cyclonically circulating arond the northern Greenland Sea (Fig. 2.22a,b). This is in good agreement with the known mechanisms of eddy propagation under the influence of the topographic β-effect (the role of which increases towards the poles relative to the planetary β-effect) and advection of eddies by mean currents (Fu, 2009; Koszalka et al., 2011). The average velocity of eddy propagation is 1-2 cm $s^{-1,}$ which is typical for mesoscale eddies in the ocean (Koszalka et al., 2011; Bashmachnikov et al., 2015; Raj et al., 2016).

Two zones of convergence of eddy trajectories are distinguished (Fig. 2.22a): in the western part of the Fram Strait (eddies come from the north and east) and in the area 75-76° N.

latitude. 3-0° W. (eddies come from the west and east). The first zone is also identified as a local maximum in the number of eddies in SAR data (Fig. 2.15). The second zone is located in the region of increased (although not the maximum) number of SAR eddies (primarily small eddies) and is the zone of the maximum number of mesoscale eddies in AVISO data (Fig. 2.15). The concentration of eddies mimics the concentration of ARGO floats in the cyclonic circulation gyre of the Greenland Sea (Fedorov and Bashmachnikov, 2020) and is likely associated with large-scale convergence of mean currents in this area. The abundance of small SAR eddies in this area (Fig. 2.19) is likely the result of the destruction of large eddies.

The higher resolution FESOM data (Fig. 2.22b) provide more detailed information about the nature of these convergence zones. The northern zone of eddy convergence is located in the area of contact of the West Spitsbergen and East Greenland currents, in the convergence zone between the cyclonic circulation south of the Fram Strait in the Boreas Basin (centered at 77° N and 2° E) and the gyre over the Molly Hole in the Fram Strait (centered at 79° N and 2° E). The southern convergence zone represents the contract area of the large cyclonic gyre of the Norwegian-Greenland region (centered at 75° N and 3° W) with the already mentioned gyre in the Boreas Basin (centered at 77° N and 2° E).

2.5 DISCUSSION OF THE RESULTS OF CHAPTER 2

The results of a comparative analysis of AVISO with SAR data showed that the blurring of the satellite altimetry signal on AVISO maps leads to an artificial increase in the radii of AVISO eddies, on average, by 1.5-2 times. This is consistent with previous estimates for the Lofoten Vortex in the Norwegian Sea, based on comparisons of AVISO results and *in situ* observations (Yu et al., 2017). However, in those rare cases when an eddy is detected in the area where altimetry tracks intersect, it is possible to accurately fix the radius of the eddy in AVISO (eddy **C** in Fig. 2.19). It is also desirable to have a neighboring track passing through the periphery of the eddy. It should, however, be remembered that dynamic radii R_m, used here, characterizes the transition of the relative vorticity of the eddy core across zero. At a distance R_m from the center of the eddy, the Rayleigh eddy velocities are about 80% of their maximum value in the core and, in fact, the transition of the thermohaline and dynamic characteristics from the eddy skirt to the background is usually observed at distances of 1.5-2 R_m from the eddy center. In this sense, the radii obtained in AVISO data are close to the radii of thermohaline anomalies in an eddy. This should be taken into account when using AVISO data to analyze volume and thermohaline transport by eddies.

Comparisons with FESOM data also showed that AVISO data underestimate the azimuthal velocities in the eddies by approximately 2 times, for the reasons above. This is consistent with the 30-50% underestimate of azimuthal velocities of the Lofoten Basin eddies, obtained by comparing satellite altimetry data with *in situ* observations (Raj et al., 2016, Yu et al., 2017).

A comparison of different data sources also showed that AVISO satellite altimetry allows one to reliably detect eddies with dynamic AVISO radii of $R_m \geq$ 40-50 km (which corresponds to real dynamic eddy radii of 20-25 km). Eddies with dynamic radii of 20–40 km (corresponding to real dynamic radii of 10–20 km) can be detected sporadically when their centers are sufficiently close to the altimetry tracks. This is slightly larger than the minimum eddy radii of 15-20 km detected in AVISO, which are given in the literature for areas of lower latitudes (Tournadre, 1990; Chelton et al., 2011; Raj et al., 2016). This difference is probably due to the absence of the data from TOPEX/ Poseidon satellites series in the Nordic Seas. Eddies with dynamic radii of 15-20

km (real radii 7-10 km) can only be identified using along-track altimetry data (see Chavanne and Klein, 2010), while smoothing, denoising and data interpolation eliminate these structures in AVISO maps, except for the cases of very intense eddy (the sea level anomaly exceeds 5-10 cm) and when an altimetry track passes through its core (for example, eddy **C** in Fig. 2.19). At the same time, a large number of fairly large eddies detected in SAR (such as **Sa, Sc, Sd, Se** in Fig. 2.19-2.20) are sifted through the AVISO grid, sometimes, however, leaving a weak signal in the relative vorticity field due to the influence their peripheries on remote altimetry tracks.

Besides the near the shore regions and the areas of high ice concentration, one can expect an artificial reduction in the number of eddies in the AVISO data also in the areas of the higher velocities of the background currents. Here eddy identification in AVISO data is difficult due to a high translation velocities of eddy displacements, as it was derived when comparing AVISO and FESOM model results (Fig. 2.16a,b).

Nevertheless, despite all the limitations, comparison with the results of statistical analysis of hydrodynamic modelling or SAR data, show that AVISO altimetry correctly reflects the main features of distribution of time-averaged eddy characteristics, as well as the eddy propagation patterns. Due to its accessibility and the availability of automatic identification algorithms, AVISO altimetry remains a useful tool for analyzing the mesoscale eddy dynamics. The results also indicate the critical importance of the number of satellites for correctly estimating the geometric properties of eddies in AVISO altimetry data. It is believed that three altimetry missions with a coverage period of the globe from 10 to 30 days and a distance between the adjacent tracks at the equator from 100 to 300 km are sufficient to reliably identify mesoscale structures in the combined AVISO data.

It was shown that the SAR data do not duplicate, but complement the information on eddies obtained from AVISO altimetry data, as each sensor detects eddies of different spatial scales. For SAR data, small eddies (with a radius of less than 5 km) are mostly detected, but detection of large eddies on SAR is hampered. Thus, although the largest eddies detected in the SAR images had dynamic radii of 20-25 km, their number was much less than in the results of the FESOM model. Also, the Lofoten eddy was quite rarely identified in the SAR data (Fig. 2.21), although AVISO and modeling data indicate its almost constant presence in the central part of the Lofoten Basin. The limitations on identifying large eddies in SAR, first, are due to the fact that with a large eddy size (diameter of 40-100 km), the intensity of the reflected SAR signal can strongly vary in different parts of the eddy due to change in the local reflection conditions, such as variability of the wind, of concentration of surface films, etc. Second, the smaller the eddy, the stronger are the ageostrophic effects, which determine the divergence (convergence) of currents in the core. The latter ensure eddy identification on SAR images as spiral lines. Thus, altimetry and SAR images make it possible to study two practically non-overlapping areas of eddy scales in the ocean.

The number of submesoscale eddies near mesoscale eddies (not always visible in SAR, but detected in AVISO) increased to the periphery of mesoscale eddies (at a distance of 1-1.5 radii of the maximum azimuthal velocity of mesoscale eddies). This conforms the suggestion of generation of submesoscale eddies along the boundaries of mesoscale eddies as a result of the decay of the latter (Nof et al., 1993). In the Lofoten basin, in addition to the predominant concentration of submesoscale eddies at the boundary of the Lofoten Vortex, a certain increase in the number of submesoscale eddies was detected after mergers of the Lofoten Vortex with other anticyclones. This corresponds conforms the intensive generation of submesoscale structures during eddy merger derived from modelling data (Ciani et al., 2016; Oulhen et al., 2022).

The clear predominance of cyclones (80%) in SAR, compared to modeling data (in FESOM results there was only a slight predominance of cyclones - 60%) and to AVISO data (approximately 50% of cyclones were observed in various water areas), is due to several reasons (see also discussion in Zhurbas et al., 2019; Kozlov et al., 2019; Bashmachnikov et al., 2020). It has been show a preferential generation of cyclonic submesoscale eddies by barotropic and baroclinic instability (Munk et al., 2000; McWilliams, 2016), as well as more efficient generation of submesoscale cyclones at the boundary of large anticyclonic eddies compared to the generation of anticyclones at the boundary of large cyclonic eddies (Nof, 1993; McWilliams, 2016). Moreover, unlike mesoscale eddies (Sangra et al., 2009; Carton et al., 2014), submesoscale anticyclones are more dynamically unstable and dissipate more easily than cyclones (Munk et al., 2000; Kostyanoy et al., 2018). Thus, in the submesoscale Karman paths behind the topographic features, a violation of the initial symmetry is observed in favor of the dominance of submesoscale cyclones at some distance from the generation area. At the same time, for mesoscale eddies generated behind the islands the result was exactly the opposite. In addition to physical reasons, the dominance of submesoscale cyclones is an artifact of their greater visibility in SAR images (Zhurbas et al., 2019). This is due to a stronger accumulation of surface films in cyclones, while anticyclones disperse the films away from their centers. Another reason is an intense formation of spiral streamlines in cyclones due to their higher rotation velocity and the greater radial gradients of relative vorticity, while in anticyclones spirals may not have time to form during a relatively short lifetime of the submesoscale structure.

Visual detection of eddies in the chlorophyll field is based on the same principles of identifying emerging spiral-shaped convergent and divergent zones of eddy currents as in SAR images. In this sense, ocean color images possess all the drawbacks of SAR in identifying eddies, associated with the formation of these ageostrophic features, tending to identify predominantly submesoscale eddies and predominantly cyclones.

2.6 Conclusions of Chapter 2

1. AVISO altimetry data, due to limited spatial resolution and non-simultaneous receipt of information from different tracks, significantly underestimate the number of eddies, especially of the short-lived or rapidly moving ones. The latter results in an artificial decrease in eddy number in the zone of strong ocean currents. AVISO data overestimate the eddy radii by 1.5-2 times and also underestimate the maximum azimuthal velocities of the eddies by 1.5-2 times. Eddy-resolving models suggest that in mesoscale eddies (2 or more Rossby deformation radii in FESOM) contain the largest fraction of the EKE. Therefore, AVISO data allows reliably estimate spatial variability of the surface characteristics of eddies, their trajectories and seasonal variability even in the subpolar regions of the Greenland and Norwegian Seas, where there is less source data available.
2. The eddies detected in AVISO and in the SAR images form two complementary data sets. Altimetry allows one to identify only large mesoscale eddies with typical radii of 30-50 km, while SAR mainly small eddies with typical radii of 1-5 km can be identified. In AVISO altimetry, both cyclones and anticyclones are equally well manifested, while in SAR the identification of anticyclones is more difficult due to the peculiarities of their dynamics. Ocean color (chlorophyll-a) data, in general, makes it possible to cover a slightly

larger range of eddy scales than SAR imagery, but have the same fundamental disadvantages for identifying eddies as SAR data.

3. The concentration of submesoscale eddies in SAR data increased from practically zero values in the centers of large-scale AVISO eddies to maximum values at the boundary of the eddy cores (regions of high values of the azimuthal eddy velocity and of horizontal velocity shear), which clearly indicates the regular generation of submesoscale eddies as a consequence of dynamic instability of mesoscale eddies and/or their interaction with the environment.
4. A comparison of the eddy propagation patterns in AVISO altimetry and the FESOM model data showed the reliability of the satellite altimetry results. The eddies of the Norwegian and Greenland Seas move along topographic features, circling counterclockwise around the basins, in the direction of their transport by the mean currents, but with significantly lower propagation velocities (1-2 cm s^{-1}).

CHAPTER 3. LIFE CYCLE OF EDDIES OF THE NORWEGIAN AND GREENLAND SEAS AND THEIR ROLE IN HEAT REDISTRIBUTION IN THE REGION

3.1 INTRODUCTION TO CHAPTER 3

Oceanic heat enters the Arctic mainly through the Nordic Seas. The heat is advected by two main branches of the Norwegian Atlantic Current (NwAC): the eastern branch, or the Norwegian Atlantic Slope Current (NwASC), and the western branch, or the Norwegian Atlantic Front Current (NwAFC) (Fig. 3.1).

The NwAC transport through the Svinoy section at 64-65ºN is approximately 8–9 Sv (Dickson et al., 2008). About 2±1 Sv goes east, into the Barents Sea (Rudels, 2015; Smerdsrud et al., 2013; Bashmachnikov et al., 2018), and 6–11 Sv enters the Arctic Basin with the West Spitsbergen Current (WSC) (Schauer et al., 2004; Schauer et al., 2008; Beszczynska-Moller et al., 2012; Rudels, 2015). Discrepancies in the estimates of various authors are associated with different methods for taking into account for the recirculations in the Fram Strait, as well as with the variability of transport over the different periods of time averaging. The recorded interannual variability at the Svinoy transect reaches 1-2 Sv (Skagseth et al., 2008), and for the WSC it is 5 Sv (Beszczynska-Moller et al., 2012; Rudels, 2015). Within this variability, the data obtained indicate an approximate balance of water transport across the northern and southern boundaries of the Norwegian Sea.

The Atlantic Water at the Svinoy section is characterized by a salinity over 34.88 and a temperature over 2ºC. If we take into account the Atlantic Water only, then out of approximately 8 Sv entering through the Svinoy section with the NwAC, 1.5 Sv leaves to the Barents Sea (Rudels, 2015), and 3 Sv enters the Fram Strait with the WSC (Beszczynska-Moller et al., 2012; Kolas and Fer, 2018). The imbalance results from a decrease in the total volume of the Atlantic Water as it moves north. This occurs as a result of water cooling, partly due to mixing with the waters of the Greenland Sea and to heat release to the atmosphere (Smersrud et al., 2022), and partly due to the heat release by generating eddies (Bashmachnikov et al., 2023). The average temperature of the Atlantic water decreases from 5ºC at the Svinoy section (Mork and Skagseth, 2010) to 3-4ºC at the entrance to the Barents Sea (Skagseth et al., 2008; Bashmachnikov et al., 2018) and to 2-4ºC in the Fram Strait (Kolas and Fer, 2018). Heat advection by the NwAC through the Svinoy section has increased over recent decades from approximately 300 TW in the early 1990s to 400 TW in the late 2010s, when using a reference temperature T_b = 0 ºC (Hansen et al., 2008; Bacon et al., 2015, Vesman et al., 2023). The intensity of heat advection with the Atlantic Water alone is estimated at 150 TW (T_b =0°C) (Skagseth et al., 2008). The average annual advection of the oceanic heat into the Barents Sea over the past decades is estimated at 30-90 TW (T_b = 0º C) and has been increasing since the 1990s (Skagseth et al., 2008; Smerdsrud et al., 2010, 2013; Skagseth et al., 2011; Walkzowski, 2014; Bashmachnikov et al., 2018; Kalavichchi and Bashmachnikov, 2019; Vesman et al., 2023). During the same period, heat advection of the WSC in the Fram Strait fluctuated between 50 ± 20 TW, showing no significant tendency to increase (Schauer et al., 2008; Fahrbach, 2006; Schauer and Beszczynska-Möller, 2009; Rudels, 2015; Vesman et al., 2023). According to the estimates above, on average, 50-75% of the heat entering the Nordic Seas with the Norwegian Current does not reach Nansen Basin of the Arctic Ocean (AO).

In this chapter, the leading role of mesoscale eddies in reducing the amount of heat advected by the Norwegian Current into the Arctic Basin will be shown. Previously, the important regional role of mesoscale eddies in heat redistribution within a sea basin was shown for other ocean areas (Spall and Chapman, 1998; Dutkiewicz et al., 2001).

3.2 ADVECTION OF OCEANIC HEAT ACROSS THE NORDIC SEAS

Following Vesman et al. (2023), and the oceanic heat advection was estimated referred to the seawater freezing temperature (T_b = −1.8°C). Estimates of the heat transports by the current advection (Vesman et al., 2023) and with eddies were carried out through the same sections and using the same data sets, which makes them comparable (Fig. 3.1). The western boundary of the meridional sections follows the Jan Mayen Fracture Zone, the Knipovich and Mohn ridges, while the eastern boundary follows the Scandinavian shelf, the western edge of the Barents Sea Opening and the western shelf of Spitsbergen. To estimate advection, we use the ARMOR3D dataset, where the surface currents represent AVISO altimetry currents. The eddy parameters are estimated using AVISO dataset and *in situ* vertical casts from EN4 dataset.

Heat advection with the Atlantic Water through the Svinoy section is 320 TW (250 TW), through the Jan Mayen section it is 200 TW (150 TW), through the Sorkapp section it is 62 TW (43 TW), through the Fram section it is 61 TW (38 TW) (Fig. 3.1). The values in parentheses correspond to similar calculations from other studies, which T_b = 0°C is used (Schauer et al., 2008; Schauer and Beszczynska-Möller, 2009; Smedsrud et al. 2013; Rudels et al., 2015).

Results from Vesman et al. (2023) showed that of the total advective heat flux with the Norwegian Current across the Svinoy section, about 75% is lost within the Lofoten Basin, mainly in its northern part, and only 25% continues its way further north. Calculation of the heat balance of the upper 500 m of the Lofoten Basin showed that of the heat coming from the NwAC, 19% is released into the atmosphere, 2% is lost to the mixing with the cold Greenland Sea Water across the polar front at the Mona Ridge, 21% of the heat goes with the North Cape Current into the Barents Sea, 38% enters the deeper layers of the basin due to vertical mixing, and 20% accumulates in the Lofoten Basin, which has led to an increase in the water temperature in the upper 500-meter layer of the Basin in recent decades (Mork et al., 2019; Vesman et al., 2023). This turns the Lofoten Basin into the largest reservoir of warm water in the Norwegian and Greenland Seas (Bjork et al., 2001), despite the rather high average annual heat release to the atmosphere (about 90 W m^{-2}). Due to an intense vertical mixing, in the Lofoten Basin warm waters are observed to 700-1000 m, while the characteristic thickness of the Atlantic Water layer in the Norwegian Current is around 500 m (Rossby et al., 2009). A total estimate of the heat accumulation within the Lofoten Basin suggests that the average ocean heat convergence in the upper 500 m of the basin within the study period (1993–2017) exceeded 100–150 TW. This suggests heat losses from the NwAC branches in the Lofoten Basin.

In this section the following hypothesis is examined: the heat is extracted from the branches of the NwAC and redistributed throughout the Lofoten Basin primarily by mesoscale eddies. In fact, the region of the highest heat loss from the NwAC (Vesman et al., 2023) is also the region of the most intense eddy generation along the steep continental slope of Scandinavian Peninsula (Kohl, 2007; Koszalka et al., 2011; Chafik et al. 2015; Isachsen, 2015; Raj et al., 2020). Another important eddy-forming region is the eastern part of the Fram Strait (Boyd and D'Asaro, 1994; Nilsen et al., 2006; von Appen et al., 2015; Hofmann et al. 2021). For both branches of the NwAC, as well as for the WSC, the criteria of both, barotropic and baroclinic dynamic instability are met, and these branches are considered the main sources of eddy formation in the region (Koszalka et al., 2011; Isachsen, 2015; Ghaffari et al., 2018; Trodahl and Isachsen, 2018). With this mechanism of eddy formation, the expected vertical extent of eddy temperature anomalies should approximately correspond to the thickness of the Atlantic Water layer. In the region of the most intense eddy formation of the NwASC it is about 500 m.

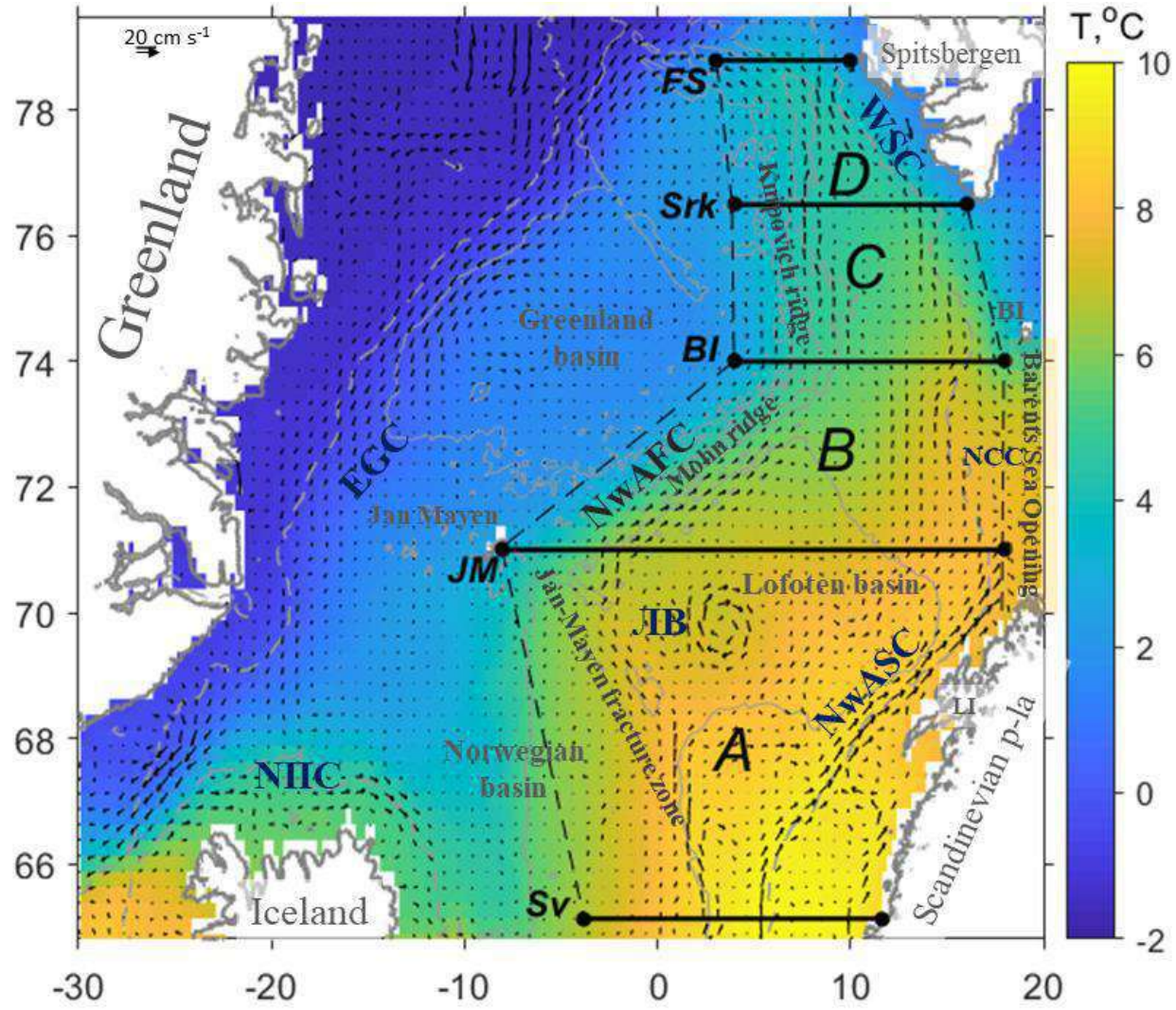

Fig. 3.1. Sea surface currents (vectors) in AVISO altimetry data (average over 1993-2018) and SST (color) from the all-weather MUR satellite data (average over 2002-2018). NwASC is the Norwegian Atlantic Slope Current, NwAFC is the Norwegian Atlantic Front, WSC is the West Spitsbergen Current, EGC is the East Greenland Current, NIIC is the North Icelandic Irminger Current, NCC is the North Cape Current, o.M is Bear Island. Sections: Sv – Svinoy, JM – Jan Mayen, BI – Bear Islands, Srk – Cape Sorkapp, FS – Fram Strait (from Bashmachnikov et al., 2023).

However, modeling of Lagrangian particle trajectories shows that mesoscale eddies are not the only factor in heat redistribution in the basin (Fedorov et al., 2021). Submesoscale structures (eddies and filaments), episodic jets crossing the basin, and Ekman transport may also be important.

3.3 CHARACTERISTICS OF EDDIES IN THE NORDIC SEAS IN SATELLITE ALTIMETRY DATA

Eddies in the Norwegian and Greenland Seas were identified using AVISO18 satellite altimetry data (see methods in Section 2.3.3). From 1993 to 2018, more than 900 000 mesoscale eddies were identified in the study area. The total number of eddies in the Norwegian Sea significantly exceeds that in the Greenland Sea (Fig. 3.2a). The number of cyclones in the Greenland Sea exceeds the number of anticyclones, while in the Norwegian Sea this ratio is close to unity.

To estimate the eddy heat fluxes, information about the eddy vertical structure is required, which can be obtained from *in situ* vertical casts. The number of eddies with a detected vertical

structure per grid cell, on average, were over 20 values. The number of observations makes it possible to obtain fairly reliable statistics of eddy characteristics in the Norwegian Sea, but over the most of the Greenland Sea the same estimates must be treated with caution due to insufficient number of available casts (Fig. 3.2b).

Eddies in the central Greenland Sea, outside the EGC, generally have smaller radii than those in the Norwegian Sea (Fig. 3.2c), while eddy radii in the EGC are comparable to or larger than those in the NwAFC. Since AVISO altimetry data overestimate the eddy radii in these northern regions by an average of 1.5 (Bashmachnikov et al., 2020), the mode of eddy radii in the Greenland Sea is about 25-30 km, and in the Norwegian Sea it is 30-35 km. The growth of eddy radii is limited from above by the Rhines scale $\sqrt{V_m/2\beta}$= 70-100 km, where $V_m$is the maximum azimuthal velocity in the eddy core, and β is the rate of linear change of the Coriolis parameter with latitude (Danilov and Gurarle, 2002).

The relative vorticity of the most of the recorded eddies is quite weak: the ratio of the peak relative vorticity of the eddies to the Coriolis parameter (Rossby number, *Ro)* usually does not exceed 0.15 (Fig. 3.2d). The exception is the Lofoten Vortex with *Ro* greater than 0.6 (see also Yu et al., 2017). Eddies of the Greenland Sea and southwestern Norwegian Sea have significantly lower peak relative vorticity compared to the eastern Norwegian Sea (Figure 3.2d). A decrease in the eddy kinetic energy in the Greenland Sea compared to the Norwegian Sea was previously noted using data of surface drifter (Koszalka et al., 2011), but the extremely small number of the drifters present in the Greenland Sea did not provide unequivocal confidence in such a trend. The highest intensity of the absolute values of eddy peak relative vorticity is observed along the eastern branch of the Norwegian Current and, above all, in the eastern and central parts of the Lofoten Basin, where also the maximum number of eddies is observed (Fig. 3.2a, d). Such variability in the energy of eddies (or of pulsations) is objective, because confirmed by altimetry data using alternative methods of eddy identification (Raj and Halo, 2016; Raj et al., 2016; Raj et al., 2020), by an analysis of the trajectories of surface floats (Rossby et al. al., 2009; Koszalka et al., 2011) and by hydrodynamic modeling data (Kohl, 2007; Isachsen, 2015; Volkov et al., 2015; Bashmachnikov et al., 2017; Raj et al., 2020). The results indicate that the eastern Lofoten Basin is the region of the most active eddy generation, as previously identified by analyzing the extent of baroclinic and barotropic instability from high-resolution models (Trodahl and Isachsen, 2018). Further north, both the number and intensity of eddies decrease. This is consistent with the decrease in the EKE north of the Lofoten Basin inferred from observations of surface drifters (Koszalka et al., 2011), as well as the northward decrease in the rate of baroclinic and barotropic instability of the Norwegian Atlantic Current (Trodahl and Isachsen, 2018).

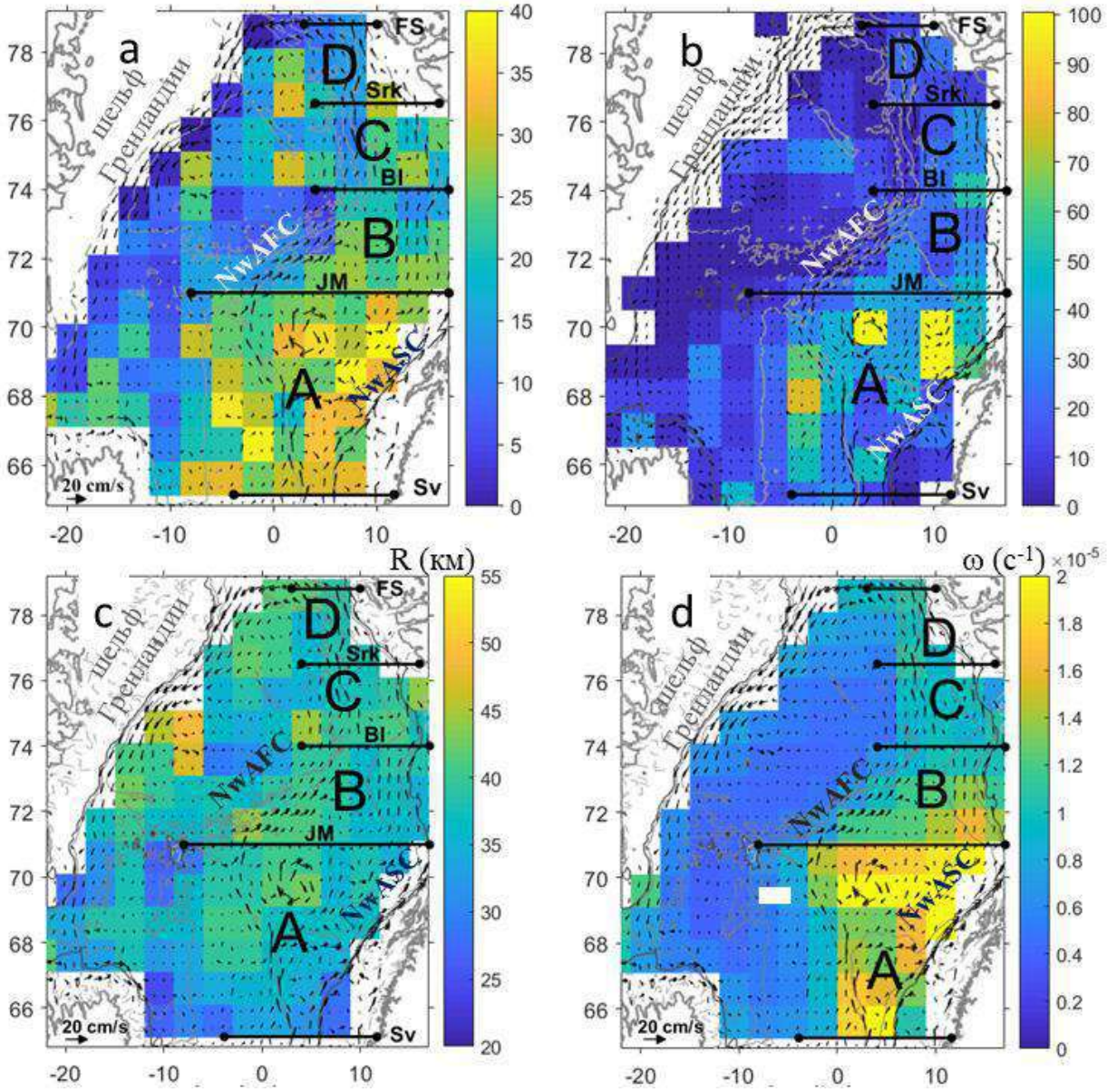

Fig. 3.2. The total number of mesoscale eddies in the Norwegian and Greenland Seas on a regular grid of 100×100 km: (a) identified from AVISO altimetry data for 1 month; (b) the total number of eddies (1993-2018) for which it was possible to identify their vertical structure in EN4 data; (c) dynamic eddy radii (km); (d) absolute value of eddy peak relative vorticity (s^{-1}). Black vectors are the mean geostrophic currents derived from AVISO altimetry; black zonal lines are the sections, where the meridional heat fluxes were estimated (from Bashmachnikov et al., 2023).

The fastest growing dynamic instability mode of the NwAC in the Lofoten Basin has a wavelength of 15 km, which decreases in the WSC to 7-10 km (Trodahl and Isachsen, 2018). It can be expected that the characteristic radii of the generated eddies should be on the order of half this wavelength, i.e. to be close to the first baroclinic Rossby deformation radius (R_d), which varies from 7-10 km in the south to 5-8 km in the north of the Nordic Seas (Nurser and Bacon, 2014). However, the characteristic eddy radius recorded in altimetry (Fig. 3.2c) is approximately 2.5-3.5 times greater than R_d. This contradiction can be explained by a regular merger of eddies, which was often noted in the studies of the Lofoten Basin (Kohl, 2007; Volkov et al., 2015; Raj et al., 2016; Bashmachnikov et al., 2017). The regular eddy merger is indicated by a gradual decrease in the number of eddies, with an increase in the eddy radii, observed between the area of the frequent eddy generation in the east of the Lofoten Basin and down the eddy propagation path in the

northwestern part of the basin (Fig. 3.2a, c). The maximum radii of the eddies were observed at a distance of 300-400 km from the generation region (Fig. 3.2c).

A similar phenomenon was noted in the subtropical North Atlantic (Bashmachnikov et al., 2015c; see also Chapter 4), where there was observed an increase in the dynamic radii of meddies by 10-15 km for every 100 km. The dynamic radii reached maximum values at a distance of 400-600 km from generation region. The growth in eddy size due to mergers is additionally indicated by an increase in regions B and C (Fig. 3.3) of the peak of the second mode of the histogram (at $R_m \sim 50$ km) relative to the peak of the first mode of the histogram (at $R_m \sim 40$ km) relative to regions A and D of intense vortex generation (Trodahl and Isachsen, 2018). A significant part of the eddies in regions B and C presumably has a non-local origin, as it is indicated by the directions of preferential eddy propagation paths (Fig. 3.4).

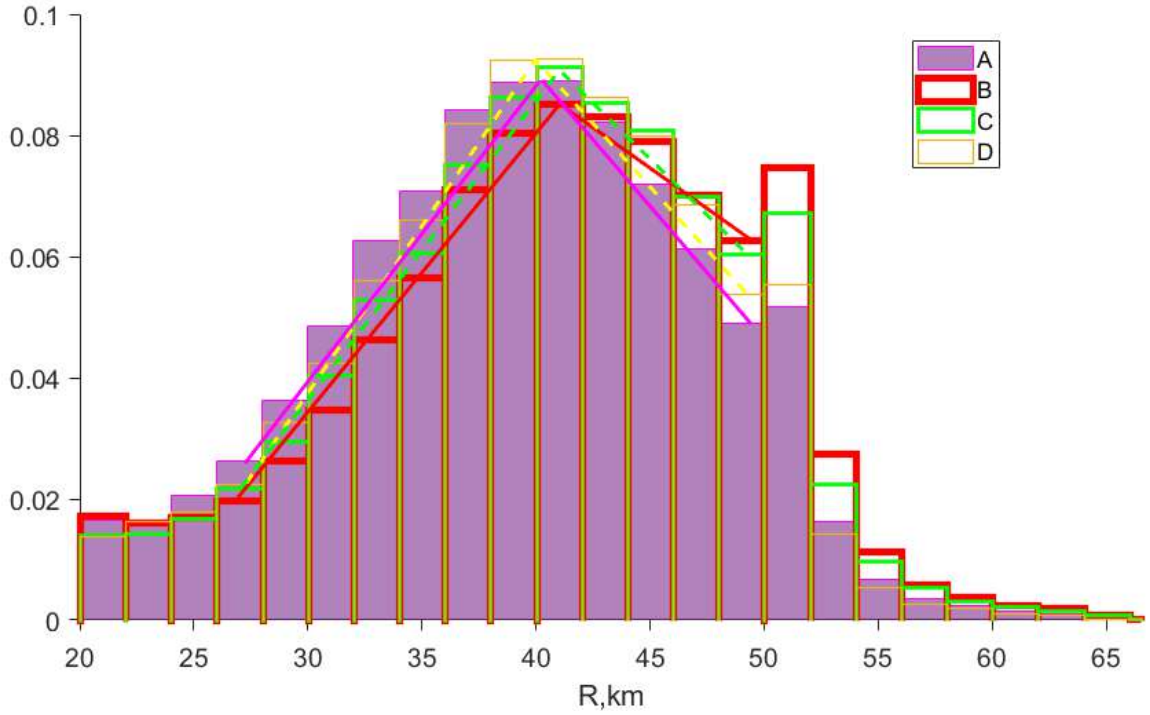

Fig. 3.3 Normalized histogram of dynamic radii (R_m) of eddies in the regions A-D.

Bypassing the entire region counterclockwise (see also Kohl, 2007; Isachsen, 2015; Volkov et al., 2015; Raj and Halo, 2016; Bashmachnikov et al., 2017; Raj et al., 2020), the mean direction of eddy propagation has a significant the western component in the eastern part of the study region, and the southern component in its western part. An average speed of eddy propagation is 2-3 cm s^{-1} (Fig. 3.4a, b). Two particularly pronounced paths of eddy propagation to the west start from the Lofoten Islands and from the northwestern part of Spitsbergen, known areas of intense eddy generation in the Nordic Seas (Isachsen, 2015; Trodahl and Isachsen, 2018; 2019, Boyd and D'Asaro, 1994; Nilsen et al., 2014; von Appen et al., 2016; Kolas and Fer, 2018; Hofmann et al., 2021). The eddy translation vectors show that eddies enter the Norwegian and Greenland Seas from neighboring areas: from the south (together with the NwAC), from the east (from the Barents Sea) and from the north (together with the EGC through the Fram Strait) (see also Johannessen et al., 1983, 1987; Sandven et al., 2011; Bondevik, 2011; von Appen et al., 2018; Kubryakov et al., 2021; Kozlov and Atadhzanova, 2022).

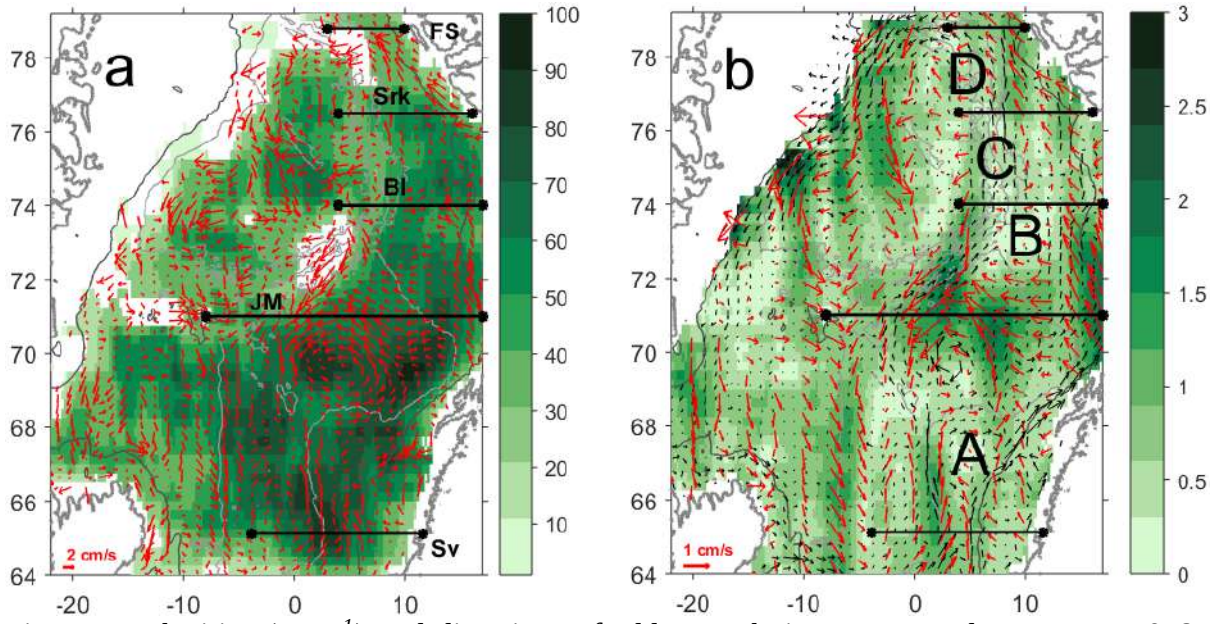

Fig. 3.4. Velocities (cm s^{-1}) and directions of eddy translations, averaged over 1993-2018. (a) Vectors of eddy translations on a 25 km × 25 km grid (red arrows); shown only in the grid cells with at least five recorded eddy displacements. The color shows the number of the registered eddy translations. (b) Vectors of eddy translations (red arrows, different scale from (a)) on a 275 km × 275 km grid. The color shows the modulus of the eddy translation velocity (cm s^{-1}). Black arrows (not to scale) in the background are the mean surface currents from AVISO data.

The mesoscale eddy translations in the study area occurs, as a rule, downstream, while in the subtropical region (Fig. 1.3), the intrinsic mesoscale eddy velocity was often sufficiently high to allow eddies moving against relatively weak regional currents (Morel and McWilliams, 1997; Bashmachnikov et al., 2015c). This has several explanations. First, the eddy translations in the deep subtropical North Atlantic is caused by the planetary β-effect and, to a lesser extent, by the baroclinic β-effect against the eastward background gradient flow. There the topographic β-effect manifests itself only locally, in areas of the underwater ridges. The complex topography of the Nordic Seas implies an important role for the topographic β-effect. In addition, the role of the planetary β-effect decreases with increasing latitude. At the same time, the recorded eddy translations velocities of 1-3 cm s^{-1} are much inferior compared to those of the mean background currents with the average velocities of 5-30 cm s^{-1}. Therefore, here we observed rather the own propagation of eddies under the influence of the topographic β-effect.

3.4 EDDY HEAT TRANSPORT IN THE NORDIC SEAS

To estimate eddy heat fluxes, estimates of the vertical extent and temperature of the eddy cores were done using *in situ* vertical profiles (see the methodology in Section 2.3.3). The number of such assessments in the Greenland Sea has been relatively small (Fig. 3.2b), so the estimates below of the eddy heat fluxes over most of the Greenland Sea must be regarded with caution. Nevertheless, the analysis below allows identifying persistent differences in eddy characteristics in the Greenland and Norwegian Seas.

The majority of eddies in the region (>75%) had with surface or near-surface cores. The typical vertical thickness of eddies in the Greenland Sea is 100-400 m versus about 500 m in the Norwegian Sea (Fig. 3.5a). The maximum eddy thickness of about 800 m is achieved in the Lofoten Basin (the Lofoten Vortex). In the Norwegian Sea, eddy cores usually have clear positive temperature (and salinity) anomalies. In the Greenland Sea these anomalies are close to zero; negative temperature anomalies are often observed (Fig. 3.5b).

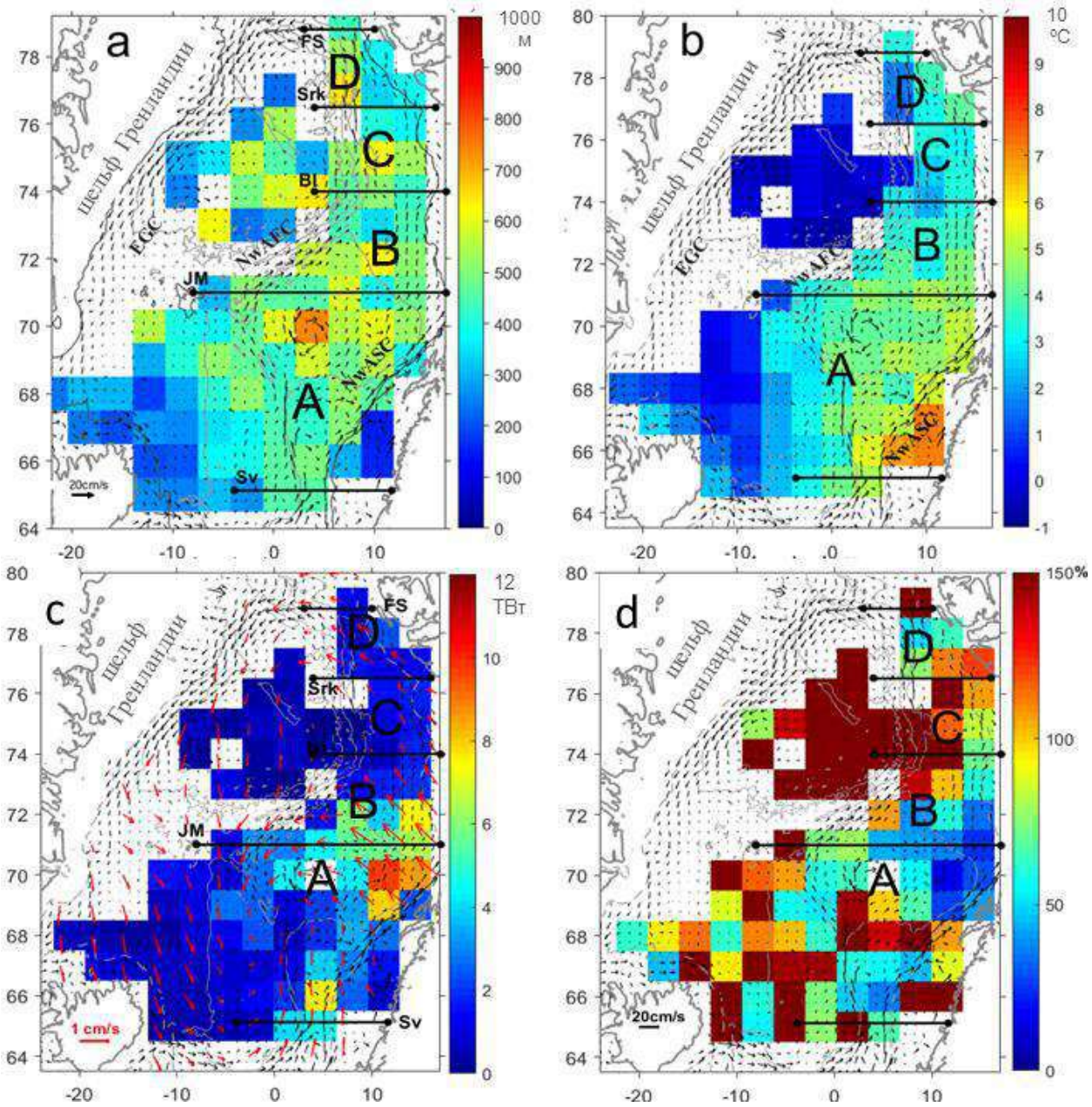

Fig. 3.5. Spatial distribution of 3-dimensional characteristics of eddies: (a) vertical extent of eddy cores (m); (b) average temperature in eddy cores (° C); (c) magnitude (TW, color) and direction (red arrows) of eddy heat transport; (d) relative error of the eddy heat transport (%). The computations were carried out only for the grid cells with at least five estimates available. The vectors of the eddy heat transport are smoothed by a moving mean with a window of 500×500 km. Black arrows are mean geostrophic currents at the sea surface (from Bashmachnikov et al., 2023).

Following Abernathey and Haller (2018), eddy heat transport was estimated as the amount of heat passing through the diameter of an average eddy per unit time multiplied by the average number of eddies per cell:

$$. \vec{Q} = nC_p \rho \vec{V}_e \int_{Z_{low}}^{Z_{up}} T_{int}(z)\, dz \approx 1.7 nC_p \rho \vec{V}_e R \int_{Z_{low}}^{Z_{up}} (T_0(z) - T_b) dz \qquad (3.1)$$

Here C_p =4200 J °C^{-1} kg^{-1} is the specific heat capacity of ocean water, ρ = 1030 kg m^{-3} is the average water density, temperature is integrated from the lower (Z_{low}) to the upper (Z_{up}) boundary

of the eddy core (see section 2.3.3), T_b = -1.8 °C is the reference temperature, *R* is the eddy radius, $\vec{V}_e$ is the vector of the average eddy propagation velocity in a grid cell, *n* is the number of eddies detected in a grid cell per unit of time (a week in AVISO data).

The integral temperature in the eddy core $T_{int}(z)$ for a fixed level *z* was determined using the Rayleigh eddy profile (see Section 1.3):

$$T_{\text{int}}(z) = 2\int_0^R (T(r,z) - T_b)dr = R\left(\sqrt{2\pi}\ erf\left(1/\sqrt{2}\right)T_0(z) - 2T_b\right) \approx 1.7R\,(T_0(z) - 1.17T_b), \quad (3.2)$$

where $T(r,z) = T_0(z)e^{-r^2/2R^2}$ is the water temperature in the eddy core at depth *z*, $T_0(z)$ is its peak value, and *r* is the distance from the eddy axis.

To calculate the total eddy heat transport in a cell, all variables in the expressions (3.1)-(3.2) were initially averaged over the cell area. This reduces random noise which arise from possible errors in determining the eddy parameters, and also makes it possible to use the total recorded number of eddies *n*, and not just a subset for which the vertical structure was identified.

The integral eddy heat transport to the west from the topographically trapped NwASC (from the Svinoy section to the Fram section) was estimated at approximately 60 TW (Table 3.1). 80–90% of this transport is generated along the Scandinavian continental slope, mainly in the northern Lofoten Basin (Figure 3.5c). This heat transport is comparable to the heat transport entering the Barents Sea with the North Cape Current (Smerdsrud et al., 2010; Bashmachnikov et al., 2018; Vesman et al., 2023), and accounts for up to 20% of the heat transport into the Norwegian Sea with the Norwegian Current across the Svinoy section (320 TW), and 30% of the total advective heat transport passing across the Jan Mayen section in the northernmost part of the Lofoten Basin. Taking into account only the heat transport by the NwASC, this eddy heat flux accounts for 35% of the advective heat flux with the NwASC across the Svinoy section (175 TW), 50% across the Jan Mayen section (125 TW) and 100 % – across the Sorkapp section (about 50 TW). The eddy heat transport from the eastern branch of the Norwegian Current (NwASC) completely explaines the difference of 50 TW between the average NwASC advective heat fluxes across the Svinoy and Jan Mayen sections (region A in Fig. 3.5c), which indicates the importance of taking into account the mesoscale eddy heat transport. Further north, between the Jan Mayen and Sorkupp sections, the heat loss by the NwASC is 75 TW (regions B and C in Fig. 3.5c). This is approximately the amount of heat that goes into the Barents Sea with the North Cape Current (Skagseth, 2008; Bashmachnikov et al., 2018). Approximately 10 TW returns with eddies from the Barents Sea back into regions B and C, and the same amount of heat eddies carry out of the regions B and C to the west (Fig. 3.5c).

The total heat fluxes with mesoscale eddies from the west from the NwAFC, i.e. into the Norwegian and Greenland Basins constitute, on average, about 25% of that extracted by eddies from the NwASC (Table 3.1). It follows that most of the eddy heat flux from the NwASC remains between the two branches of the Norwegian Current and, in particular, accumulates in the Lofoten Basin.

The eddy heat transport from the NwASC to the interior regions of regions A and B is of the same order as the total ocean-to-atmosphere heat loss in these regions, including the heat loss to the atmosphere from the NwASC itself, amounting to 5 TW (Tables 3.1 and 3.2, see also Richards and Straneo, 2015). The imbalance in the upper 500-m layer of the Lofoten Basin arises as e result of the eddy heat transport from the NwAFC further west, as well as from the vertical turbulent exchange with eh lower layers, which is significant in the Lofoten Basin (Fedorov et al., 2021).

In region C, the eddy heat transport from the NwASC may contain relatively large errors due to small number of observations in the area (Fig. 3.2b). Mesoscale eddies redistribute over this

region at least 44% of its total heat loss to the atmosphere. To the north, in region D, eddies can also be an important source of the heat loss by the West Spitsbergen Current (von Appen et al., 2015, Hattermann et al., 2016; Bashmachnikov et al., 2020). However, due to the small number of available *in situ* eddy profiles, estimations of this transport are not reliable.

Table 3.1. Westwards eddy heat fluxes (TW) across the meridional boundaries (Q_e) of the regions A-C: from the NwAFC out of the region (denoted with subscript F) and from the NwASC into the region (denoted with subscript S). dQ_{eW} is the zonal divergence of eddy heat fluxes.

	Q_{eF} from the NwAFC, + is out of the region	Q_{eS} from the NwASC, + is into the region	$dQ_{eW} = Q_{eS} - Q_{eF}$	Q_{eF}/Q_{eS} (%)
region C	1.3*	6.2*	4.9*	20%
region B	2.5	15.3	12.8	15-20%
region A	15.0	51.7	36.7	30-40%

* Heat fluxes are inaccurate due to too few eddies used for estimation.

Table 3.2. Eddy heat fluxes (TW) in the regions A-D: Q_{eN} is the meridional eddy heat flux across zonal sections (Fig. 3.1), dQ_{eN} is the divergence of Q_{eN} in A-D regions, Q_{eS} is the zonal eddy heat flux from the NwASC across the eastern boundary (from Table 3.1), $dQ_e = dQ_{eN} + dQ_{eW}$ is the overall divergence of the eddy heat fluxes, and Q_{atm} is the ocean-to-atmosphere heat transport.

area	dQ_{eN} = Q_{eN} (north) - Q_{eN} (south)	$\lvert Q_{eN}/Q_{eS} \rvert$	$dQ_e = dQ_{eN} + dQ_{eW}$	Q_{atm}	dQ_e/Q_{atm}, %
Section Fr	No data				
area D	No data	-	-	11	-
Section Srk	Q_{eN} = 2.4* TW				
area C	1.2	0.2*	6.4*	16	44%
Section BI	Q_{eN} = 3.6* TW				
area B	10.9	0.9	26.2	27	96%
Section JM	Q_{eN} = 14.5 TW				
area A	-6.9	0.2	44.8	55	82%
Section Sv	Q_{eN} = 7.6 TW				

* Heat fluxes are inaccurate due to too few eddies used for estimation.

3.5 SEASONAL AND INTERANNUAL VARIABILITY OF EDDY CHARACTERISTICS IN AVISO ALTIMETRY AND FESOM MODEL DATA ALONG THE WEST SPITSBERGEN CURRENT

Seasonal variability (Fig. 3.6a) indicates a simultaneous increase in the intensity of the West Spitsbergen Current and the maximum azimuthal speed of the AVISO eddies in the cold season with a maximum in November-March and a minimum in June-September (correlation coefficient 0.6 is significant, at a significance level of 95%). The winter increase in the number of eddies and CEF corresponds to a seasonal increase in baroclinic and barotropic instability (Trodahl and Isachsen, 2018, Wekerle et al. 2017, 2020) with an increase in the speed of the West Spitsbergen Current (von Appen et al., 2016). The seasonal variability of the maximum azimuthal eddy velocity lags by approximately 1 month. This may be due to a time delay in filling the area with more intense eddies after their generation on the West Spitsbergen Current (Hattermann et al., 2016). Seasonal variability of eddy radii follows the variability of azimuthal velocity with a lag of 1-2 months. The increase in the radii of eddies at the end of winter corresponds to a decrease in their number, which may be associated with the dominance of eddy merger. The decrease in eddy radii in summer corresponds to an increase in the number of eddies, which is an evidence of the dominance of eddy breakdown.

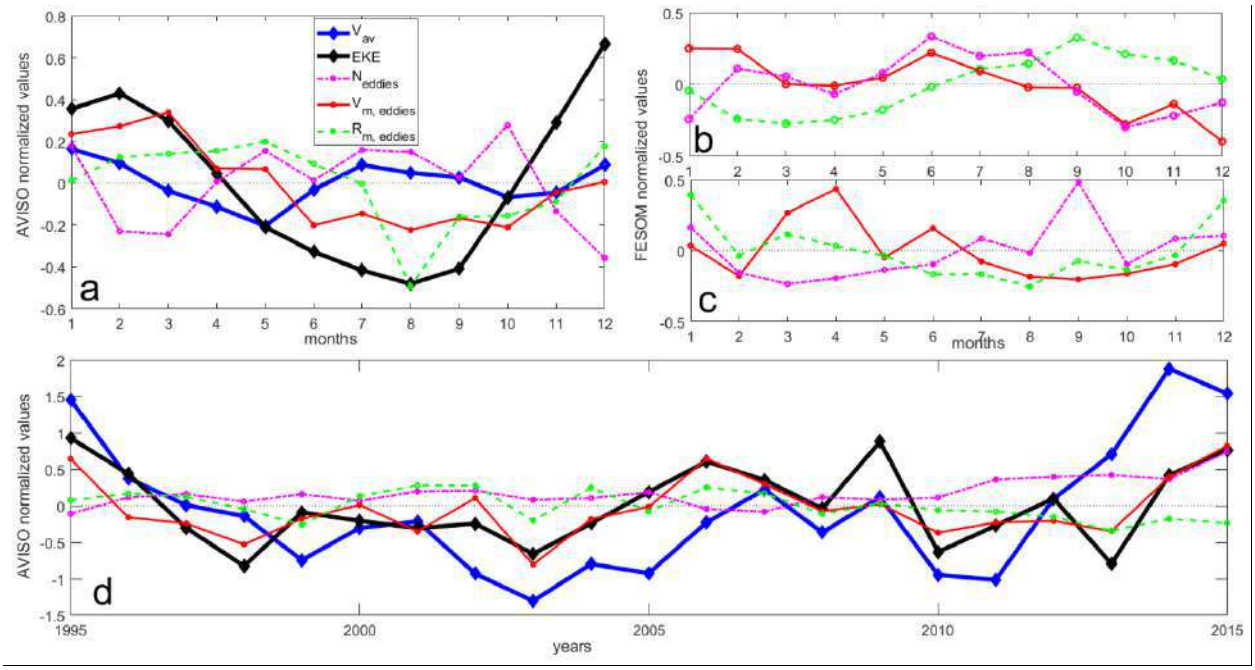

Fig. 3.6. Normalized values of the intensity of the mean currents, EKE, quantity and other characteristics of eddies in the West Spitsbergen Current, averaged over the rectangle area in Fig. 2.14(b). (a) Seasonal variations in AVISO; FESOM seasonal variations (b) for all eddies, with eddies of R=5-15 km are clearly dominating, and (c) only for large eddies with R> 20 km. (d) Interannual fluctuations of dynamic characteristics in AVISO data: V_{av} is the average velocity of the mean jet currents (after filtering pulsations and only for the areas with current velocity over 5 cm s^{-1}); EKE is the eddy kinetic energy, N_{eddies} is the number of eddies, $V_{m.eddies}$ is the peak azimuthal velocity in eddies, $R_{m.eddies}$ is the dynamic eddy radius (from Bashmachnikov et al., 2023).

The results of the high-resolution FESOM model allow us to separately analyze the evolution of characteristics of eddies with a dynamic radii R ~ 5-15 km (Fig. 3.6b, see also Fig. 2.15-2.16), and a subset of only large mesoscale eddies with R > 20 km (115 eddies, Fig. 3.6c). The nature of the seasonal evolution of large eddies is similar to that in the results of AVISO altimetry (Fig. 3.6a, c). A comparison of Figures 3.6(b) and 3.6(c) shows that the number (and radii) of large and small eddies vary almost out of phase. It can be assumed that the intense large eddies are actively generated in winter and spring. In summer the eddy dynamics is dominated by the eddy merger. During this period, there is a decrease in the number of large eddies, an increase in their average radius, and a decrease in their rotation velocity (Fig. 3.6b). With age, eddies become dynamically unstable, and in late summer and autumn the decay of eddies into smaller ones predominates. This forms a pronounced peak in the number of relatively small eddies (Fig. 3.6c) with a continuing decrease in the number of large eddies (Fig. 3.6b).

The interannual variability of the mean velocity of the West Spitsbergen Current, obtained from AVISO altimetry results (Fig. 3.6d), correlates with the intensity of the EKE (the correlation coefficient is 0.56), as well as with the maximum azimuthal velocity of mesoscale eddies V_m (the correlation coefficient is 0.82). This indicates that the kinetic energy of mesoscale eddies forms the main part of the recorded EKE and is related to the intensity of the mean current. Previous model studies indicate that an increase in the average velocity of the West Spitsbergen Current favors the development of its baroclinic instability (Ghaffari et al., 2018; Trodahl and Isachsen, 2018).

Since 2010, the number of eddies (but not their maximum azimuthal velocity) has tended to increase over time, and the radii of eddies have tended to decrease (the correlation coefficient is -0.55). The intensification (Fig. 3.6d) occurs simultaneously with an increase in the winter North Atlantic Oscillation index (Yashayaev and Seidov, 2015; Selyuzhenok et al., 2020), which was also noted in a number of hydrodynamic model studies (Walczowski, 2014; Chatterjee et al.,

2018). However, this interannual trend may also be an artifact of the increase in the number of altimetry satellites at high latitudes after 2010. This potentially allows more eddies to be identified in AVISO altimetry data and their radii to be determined with higher accuracy.

Assessing the interannual variability of heat fluxes with eddies using satellite and *in situ* data is still difficult due to the insufficient amount of data on the vertical structure of eddies per year. Altimetry data show that in regions A-D the annual mean number of simultaneously observed eddies does not vary much from year to year, usually being within 15% of the climate average. The mean eddy radius (estimated from altimetry data) also remains virtually unchanged over time. This suggests that the NwASC variability of 2 Sv (Skagseth et al., 2008), i.e. about 40% of its mean value, is not affected by eddy generation. With the remaining parameters of the eddies being constant (vertical extent, propagation velocity, mean core temperature), i.e. if the variability of the eddy heat transport from the NwASC would depend exclusively from fluctuations in the number of eddies, the typical interannual variability eddy heat transport from the NwASC would be within 10 TW. This does not make a significant contribution to interannual variability of the heat loss by the NwASC while crossing the Nordic Seas.

A change in the temperature of the NwASC waters entering the region, on the contrary, significantly changes the amount of heat extracted by eddies. It can be expected that the change in the mean temperature in eddy cores will be close to the change in the mean temperature of the NwASC waters. Then an increase in water temperature of the NwASC by 1^{o} C will lead to an increase in heat extraction by eddies by 50 TW, i.e. the eddy heat transport from the NwASC will almost double. These variations are comparable to the typical amplitude of the interannual variability in heat advection of the NwASC of 40 TW (Skagseth et al., 2008). Thus, eddies can effectively damp the temperature changes translated north by the Norwegian Atlantic Current. As a consequence, the amplitude of time variation of the heat advection should decrease significantly between the Svinoy to Fram sections. This is consistent with observations (Vesman et al., 2023). In particular, it is the eddy damper that may be responsible for the rapid drop in correlations of interannual variability of heat advection between the Svinoy section and more northern sections, which lowers down to insignificant values at the sections west of Spitsbergen.

3.6 DISCUSSION OF THE RESULTS OF CHAPTER 3

The time mean eddy properties and associated eddy heat transport in the Norwegian and Greenland Seas over 1993-2018 is evaluated, as well as its impact on heat advection to the Arctic.

The statistics of 2-dimensional characteristics of surface eddies in the Norwegian and Greenland Seas obtained above is currently the most complete. The average characteristics of eddies at the sea surface and the patterns of their propagation obtained from altimetry closely correspond to the results previously derived in some areas of the study region from surface drifters or from hydrodynamic models (Koszalka et al., 2011; Kohl, 2007; Isachsen, 2015; Volkov et al. al., 2015; Raj et al., 2020).

The study shows that mesoscale eddies in the Greenland Sea are much less numerous and less intense compared to the Norwegian Sea. These statistical differences are consistent with observations, numerical models, and theoretical studies showing that eddy generation in the region is mainly confined to the NwASC and WSC, while eddy generation along the EGC is much less efficient (Koszalka et al., 2011; von Appen et al., 2015; Isachsen et al. 2015; Hattermann et al., 2016; Ghaffari et al., 2018; Trodahl and Isachsen, 2018). In addition, observations show that eddies generated in the EGC remain near the western boundary and do not fill the central areas of the basin, while eddies generated in the NwAC and WSC attain a westerly velocity component (under the influence of the planetary β-effect), allowing them to fill the central Lofoten basin and cross the Fram Strait (Fig. 3.4, see also Hofmann et al., 2021).

The first large-scale joint analysis of the 3-dimensional characteristics of eddies in the Norwegian and Greenland Seas was also carried out using satellite and *in situ* observations. In the

central Greenland Sea, eddies are not only less numerous, but also have smaller radii, intensity and vertical thickness compared to the Norwegian Sea (Figs. 3.2 and 3.5). Very weak or negative temperature anomalies of the eddies cores in the Greenland Sea, as well as the dominant southern direction of their movement, suggest a predominantly local origin of the observed eddies, and their relatively weak generation at the NwAFC. Noteworthy is a certain dominance of cyclones in the Greenland Sea, in contrast to the Norwegian Sea. This is probably a consequence of the weakening role of the dynamic instability of the EGC in the generation of eddies, compared to the mechanisms of eddy generation due to interaction of the EGC with topography, emergence of gradients of the intensity of Ekman transport near the edge ice, formation of local convective "chimneys", among others.

In the Lofoten Basin, the radii of eddies increase along the main paths of their propagation to the west and northwest of the Lofoten Islands. This indicates that the eddies generated at the NwASC merge, increasing in size. Mergers also dominate at the end of the winter period in another active region of eddy generation – at the West Spitsbergen Current. Individual episodes of eddy mergers were previously observed in model and satellite data for the quasi-permanent Lofoten Vortex (Khol, 2007; Raj et al., 2015; Volkov et al., 2015; Bashmachnikov et al., 2017; Trodahl et al., 2020). It is also typical for meddies in the subtropical Atlantic (Bashmachnikov et al., 2015c).

It was shown that the generation of eddies at the NwASC significantly reduces the intensity of the advective heat transport across the Norwegian Sea and its further translation into the Arctic Basin. Thus, from the Svinoy to Sorkapp sections, about 60 TW is extracted by eddies from the NwASC, which forms approximately 1/3 of the amount of heat entering with the NwASC across the Svinoi section. This heat loss with eddies is comparable to the advective oceanic heat transport into the Barents Sea (70–100 TW, Smerdsrud et al., 2010; Bashmachnikov et al., 2018), as well as to the amount of heat that continues further north across Sorkapp section. The objective nature of the assessment of the heat loss with eddies is evidenced by the fact that the obtained values close the balance in oceanic heat transport with the NwASC between the Svinoy and Sörkap sections (see also Smedsrud et al., 2022; Vesman et al., 2023). Due to small temperature anomalies of eddy cores, the heat flux with eddies from the NwAFC to the Greenland Sea is much weaker and forms, on average, 20-25% of that from the NwASC (Table 3.1).

Despite the rather large values, the eddy heat flux from the NwASC into the Lofoten Basin is insufficient to fully compensate for the heat loss of the 500-m upper layer in the Basin, which is mainly is composed from the heat release to the atmosphere and mixing with the underlying ocean layers (Vesman et al., 2023). To close the heat balance of the upper 500-m layer of the Lofoten Basin, this flux must be at least doubled. Eddies coming from the south through the Svinoy section, generated at the NwAFC and entering the Lofoten Basin (Belonenko et al., 2020), transitional dynamic structures such as jets, filaments, submesoscale eddies (Zhmur et al., 2023) may also be unimportant components of the heat balance. Analysis of SAR images and the results of the very high-resolution FESOM numerical model indicate that eddies with radii of 2-5 km are most common in this area (Kozlov et al., 2020; Bashmachnikov et al., 2020; Kozlov and Atadzhanova, 2022). A single submesoscale eddy does not live long, usually a day, and no more than 5-7 days (Eldevik and Dysthe, 2002). During its lifetime, such an eddy is translated only over a few kilometers and, given its relatively small size, transports two to three orders of magnitude less heat than a single mesoscale eddy. However, the cumulative effect of a very large number of such eddies (see Sections 2.4.1, 2.4.3) can be significant.

The data available on the three-dimensional structure of eddies is not enough to assess the interannual variability of the 3-dimensional characteristics of the eddy cores and the associated change in heat fluxes. The observed relatively small interannual variability in the number of generated eddies can explain no more than 25% of the recorded interannual variability in the NwASC heat advection. Therefore, it can be assumed that changes in the NwASC transport have little effect on the intensity of mesoscale eddy generation and the associated variability in the heat fluxes. On the other hand, temperature fluctuations of the NwASC water entering the Norwegian Sea from the south result in a comparable magnitude of variability in eddy heat transport, which

is a likely cause of the previously reported significant damping of temperature anomalies downstream of the NwASC (Vesman et al., 2023).

3.7 CONCLUSIONS OF CHAPTER 3

1. Three-dimensional properties of mesoscale eddies in the Norwegian and Greenland Seas, as it follows from altimetry data and *in situ* observations, show that eddies in the Norwegian Sea generally have significantly bigger volume, rotation velocity, and core temperature anomalies compared to eddies in the Greenland Sea. The likely reason for this difference is the significant role of eddy generation mechanisms in the Greenland Sea, different from the dynamic instability of the mean currents dominating in the Norwegian Sea.
2. The most intense eddies are concentrated along the main currents and are most intensively generated in the area of the continental slope west of the Lofoten Islands and west of Spitsbergen. The large-scale pattern of eddy translations shows that the eddies move counterclockwise around the entire Norwegian-Greenland region, as well as in the Lofoten Basin. This is the result of the influence of the topographic β-effect on eddy dynamics with the weakening of the planetary β-effect at high latitudes.
3. An increase in the eddy radius along their trajectories of their propagation from the Lofoten Islands to the northwestern part of the Lofoten Basin at a distance of 300-400 km is revealed. This is interpreted as the result of regular eddy mergers.
4. The seasonal winter increase in the number of high-intensity eddies in the Fram Strait occurs during a period of increased dynamic instability of the main currents. After this, a period of active eddy merger is observed, when, with an increase in the average eddy radius, the number of eddies and their rotation velocity gradually decrease. Further aging of the eddies during summer, together with a decrease of the intensity of their generation, leads to an increase in the number of small eddies, which indicates the dominance of the process of a breakdown of large eddies.
5. Mesoscale eddies have been shown to have a significant impact on heat flux redistribution in the Lofoten Basin, extracting and dispersing over the Basin approximately 1/3 (60 TW) of the heat flux of the NwASC to the Arctic. Nevertheless, the heat inflow with mesoscale eddies from the NwASC was not enough to close the heat balance of the upper 500-m layer of the Lofoten Basin. This indicates a presence of other mechanisms of heat translation into the Basin (as mesoscale eddies from other sources, submesoscale eddies, filaments, etc.).
6. The interannual variability of the heat transport as a result of the observed interannual variability in the number of generated eddies (15% of the mean value) is 10 TW. An increase in temperature of the eddy cores by 1°C leads to an increase in the eddy heat flux by 50 TW. Thus, the variability of the eddy heat transport is associated with variability in the temperature of incoming waters. The variability of the eddy heat transport can effectively dampen the water temperature anomalies entering the Norwegian Sea from the south.

CHAPTER 4. LIFE CYCLE OF SUBSURFACE INTRATHERMOCLINE EDDIES IN THE SUBTROPICAL NORTH ATLANTIC: MEDITERRANEAN WATER EDDIES (MEDDIES) AND THE MEDITERRANEAN WATER

4.1 INTRODUCTION TO CHAPTER 4

The Mediterranean Water (MW) is one of the major water masses at the mid-depth (500–1500 m) of the North Atlantic, which extends from the continental slope of the Iberian Peninsula and northeastern Africa to the Mid-Atlantic Ridge. In relatively small concentrations the MW is also observed in the western subtropical Atlantic. The MW is formed when salty and warm surface waters of the Mediterranean Sea enter the Atlantic through the Strait of Gibraltar with the sill depth of 60 m. The waters rapidly submerge to the level of its neutral buoyancy (800-1200 m) within the first 100 km west of the strait. When submerged, the water from the Mediterranean Sea is significantly modified, increasing its volume several times due to mixing with the North Atlantic Central and Deep Water (Barbosa Aguiar et al., 2015). As a result, the MW is formed. Strong positive anomalies of temperature and salinity, nutrient anomalies and an enhanced content of suspended matter makes the MW easily identifiable among the subpolar mid-depth water masses of the Atlantic.

The MW significantly influences the thermohaline and chemical characteristics, as well as the stratification of the ocean water column from at least 500 to 2000 m (Mauritzen et al., 2001). Numerical experiments with the open and closed Strait of Gibraltar showed that in the absence of the MW in the Atlantic, the Azores Current significantly weakens or disappears, and the main paths of the North Atlantic Current change (Jia et al., 2007). This suggests an important role of the MW in water dynamics of the North Atlantic.

The mechanisms of MW propagation in the Atlantic fit into two competing hypotheses: advective transport and eddy transport (Bower et al., 1997; Maze et al., 1997; Iorga and Lozier, 1999a,b; Sparrow et al., 2002; Lozier and Stewart, 2008; Filyushkin et al., 2017b). Observations of both advective transport and eddy transport at intermediate depths are not yet sufficiently abundant to separate the relative effect of each of these mechanisms in the MW spreading.

The highest concentrations of the MW are found in the waters of the Mediterranean Undercurrent (MUC), spreading along the continental slope of the Iberian Peninsula, and in the Mediterranean water eddies (meddies), which are generated due to dynamic instability of the MUC. meddies carry the MUC waters to the west and southwest. In the subtropical northeast Atlantic, meddies are quite common and, due to their fairly high stability, can be found thousands of kilometers from the place of their generation (Kostyanoy and Shapiro, 1986; Belkin and Kostyanoy, 1992; Richardson et al., 1989; Richardson and Tychensky, 1998; Iorga and Lozier, 1999b; Siedler et al., 2005; Filyushkin and Kozhelupova, 2020). One meddy was recorded on the opposite side of the Atlantic, near the Bahamas (McDowell and Rossby, 1978).

Meddies are anticyclonic rotating lenses with an anomalously warm and saline core, having characteristic radii of 10 to 50 km and azimuthal velocities up to 50 cm s^{-1}. They may have one or two cores (located one above the other). The center of the upper core is usually in the depth range of 700-900 m, and of the lower – at 1000-1200 m (Richardson et al., 2000). Meddies retain the characteristics of the MW of the region of their formation for a long time, and can form salinity anomalies up to 1 and temperature anomalies up to 4°C (Fig. 1.4-1.5). The meddy core is usually

well mixed and has abnormally low potential vorticity. One meddy carries about 10^9 -10^{11} tons of salt (Shapiro et al., 1996b; L'Hegaret et al., 2014), gradually releasing salt and heat into the environment. However, a sudden collapse of the meddy core can also occur, causing an immediate release of heat and salt. Richardson et al. (1989), Arhan et al. (1994) and Bower et al. (1997), using independent data and analysis methods, estimated that 15 to 20 meddies should be annually formed off the Iberian Peninsula. At this generation rate, meddies would account for at least 50% of the total westwards transport of the MW. However, these values may be underestimated, because the authors did not consider all currently known areas of meddy formation (Shapiro and Meschanov, 1996; Serra and Ambar, 2002; Filyushkin et al., 2009). In a further study with a high-resolution hydrodynamic model, an average annual meddy generation rate of 26 meddies was reported (Barbosa Aguiar et al., 2013). Some authors suggest even 30 to 50 meddies generated per year (Filyushkin et al., 2009). Having analyzed a number of hydrological sections in the Iberian Basin, Maze et al. (1997) found no evidence of sustained advection west of 12°W, concluding that 100% of the westward MW transport is formed by meddies. Following the trajectories of RAFOS floats, Sparrow et al. (2002) found that MW advection plays an important role north of 36° N, while transport south of this latitude is dominated by meddies. Barbero et al. (2010) did not find stable advective transport of the MW in the area of detailed *in situ* observations during repeated surveys in the area of 39-45°N and 16-21°W. Thus, the estimates of the contribution of meddies to the formation of the MW tongue in the Atlantic vary greatly. Due to a lack of information on the number of meddies generated annually, this issue remains unresolved.

4.2 DISTRIBUTION OF THE MEDITERRANEAN WATER IN THE SUBTROPICAL NORTHEAST ATLANTIC

In this section the spatial distribution of the main types of water masses in the subtropical northeast Atlantic (25-45°N, 5-35 °W) are presented (Fig. 4.1). The main attention is paid to the distribution of the Mediterranean Water. Quantitative assessment was performed using the Optimum Multiparameter Analysis (OMP) (see section 4.6.1 for details). This study extends the previous qualitative studies on the distribution of the water masses in the region (van Aken, 2000a,b, 2001), quantitative OMP analysis of the content of various water types of the main pycnocline in the North Atlantic (Poole and Tomczak, 1999), as well as OMP analysis of water types along individual synoptic sections in different parts of the study area (Hinrichsen and Tomczak, 1993; Perez et al., 1998, 2001; Cabecadas et al., 2002; Alvarez et al., 2004; Barbero et al., 2010; Lourn and Morin, 2011; Pastor et al., 2012). The results below give is first full quantitative description of the climatological distributions of intermediate water types based on OMP analysis, described in detail in Bashmachnikov et al. (2015b).

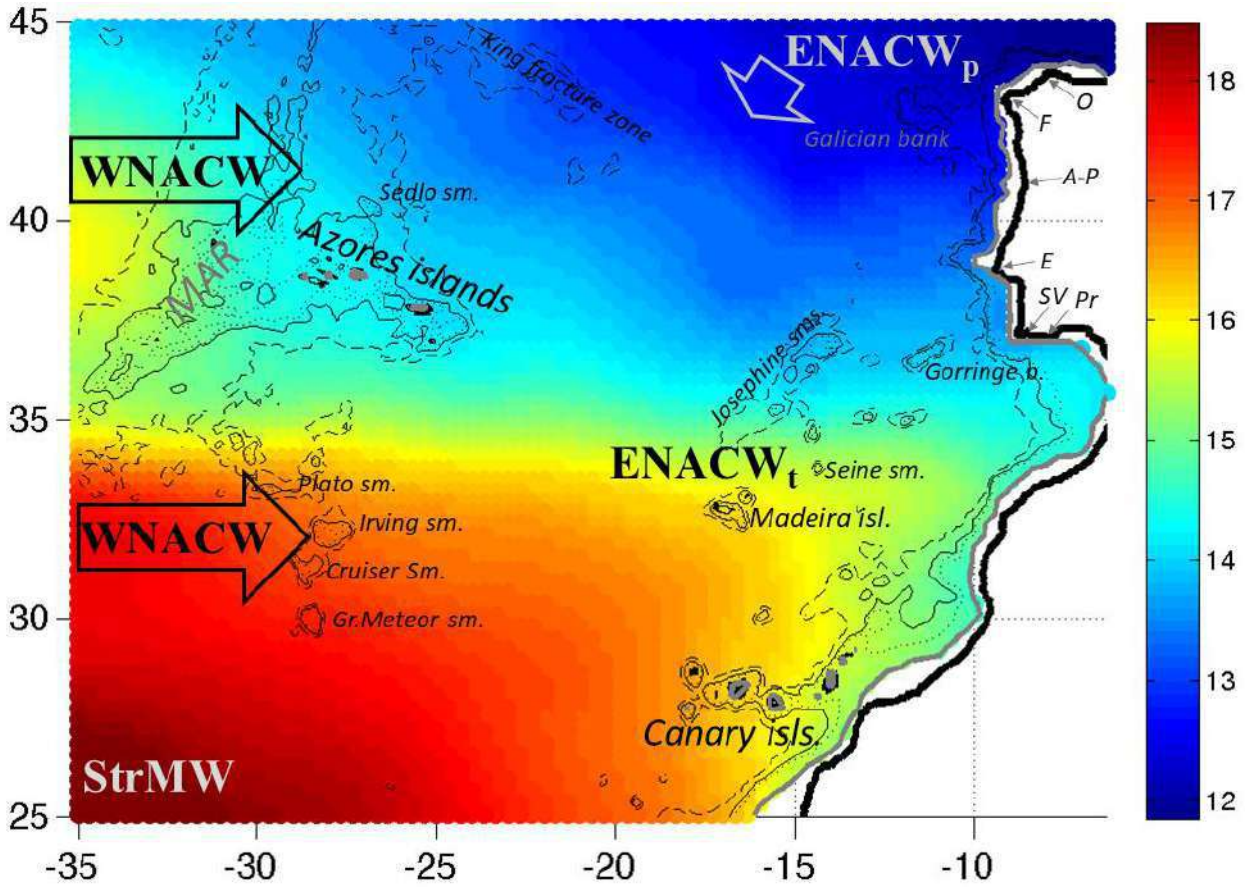

Fig. 4.1. Water temperature at 200 m in the study area (MEDTRANS climatology). The main water types of the main pycnocline are indicated: StrMW is the Subtropical Mode Water, WNACW is the Western North Atlantic Central Water (all modifications), ENACW$_p$ is the lower ("polar") Eastern North Atlantic Central Water, ENACW$_t$ is the upper ("tropical") Eastern North Atlantic Central Water. Arrows indicate the predominant direction of water propagation. O – Cape Ortegal, F – Cape Finisterre, A-P – Aveiro and Porto canyons, E – Extremadura Promontory, SV – Cape Saint Vincent, Pr – Portimao Canyon. The gray dotted line shows the 3000 m isobath, the gray solid line shows the 2000 m isobath.

Thermohaline characteristics of deep waters are formed at the ocean surface. These waters become water masses when they lose connection with the upper mixed layer of the ocean. The water masses change their thermohaline and other characteristics very slowly, mainly as a result of mixing with surrounding waters with other characteristics. Homogeneous in their characteristics, the cores of water masses form local minima of potential vorticity.

The main mechanisms of water submerging from the sea surface are Ekman pumping and convection. The first mechanism (ventilated thermocline) dominates in the tropics and subtropics, where the rotor of tangential wind stress is negative (Pedlosky, 1998). The most favorable conditions for water subduction are in frontal zones, where the isopycnals outcrop at the sea surface a relatively big angle. In the Northeast Atlantic, such zones are confined to various branches of the North Atlantic Current and the Azores Current, where various modifications of the North Atlantic Central Water (NACW), which compose the main pycnocline, are formed (Tomczak and Godfrey, 2003; Cianca et al., 2009). In the subpolar regions of the North Atlantic, intensive convection develops during the winter-spring seasons, which reaches big depths and forms deep water masses (van Aken, 2000a).

4.2.1 WATER MASSES OF THE SUBTROPICAL NORTHEAST ATLANTIC

A list of the main water masses of the subtropical Northeast Atlantic is given in Table 4.1 (according to Tsuchiya et al., 1992; Perez et al., 1998, 2001; Poole and Tomczak, 1999; van Aken, 2000 a, b, 2001; Cabecadas et al., 2002; Alvarez et al., 2004; Barbero et al., 2010; Lourn and Morin, 2011).

Table 4.1. Main water masses of the Northeast Atlantic.

StrMW	Subtropical Mode Water
NACW	North Atlantic Central Water
H	North Atlantic Central Water, the maximum inflection point at TS diagram of the NACW
mAAIW	modified Antarctic Intermediate Water
AAIW	Antarctic Intermediate Water
SAIW	Subarctic Intermediate Water
MW	Mediterranean Water
L.S.W.	Labrador Sea Water
NADW	North Atlantic Deep Water

The main thermocline of the North Atlantic is formed by the North Atlantic Central Water (NACW). The NACW consists of various modifications that form in different areas of the North Atlantic (Fig. 4.1). To the west of the Mid-Atlantic Ridge, a western modification of the NACW – the Western NACW (WNACW) is formed, which is transported into the study area by a system of surface currents (McCartney, 1982; Pollard and Pu, 1985; Harvey and Arhan, 1988; Pollard et al. 1996; Paillet and Arhan 1996b). The Eastern NACW (ENACW) is formed in the Eastern Atlantic. It occupies the same depth range as the WNACW, but its salinity is, on average, 0.1 higher (van Aken, 2001). The lower fraction of the ENACW, also called the polar fraction ($ENACW_p$), is formed in winter in the southwestern area of the Bay of Biscay (40-50°N, 20°W). The upper fraction of the ENACW, also called tropical ($ENACW_t$), is formed in the recirculation system of the Azores Current near the Iberian Peninsula (Perez et al., 1993; Pollard et al. 1996) and near the Madeira Island (Siedler et al., 1987; Pingree et al., 1999; New et al., 2001). In the study area, most of the upper fraction of the NACW (200-400 m) is represented by the upper fraction of the WNACW, while the $ENACW_t$ is observed only in a limited area near the Iberian Peninsula (Pollard and Pu, 1985; Paillet and Arhan, 1996a,b). The lower part of the main pycnocline is dominated by the $ENACW_p$ (Perez et al., 1993; Pallet and Arhan, 1996a,b; van Aken, 2001). Due to the limited number of water masses that can be jointly analyzes in the OMP system (see section 4.6.1), in further analysis WNACW and ENACW were combined into NACW, where the upper fraction of NACW was formedby the upper fraction of WNACW, and the lower fraction NACW – by $ENACW_p$. On TS diagrams, the NACW lines connecting its lower and upper fractions are somewhat curved and are well approximated by two segments of a broken line. To take this feature into account, in the section of maximum curvature TS of the WNACW and ENACW curve (in the study area this happens at 500 m depth), an intermediate NACW fraction (H) was defined (Perez et al., 1998; Alvarez et al., 2004; Barbero et al., 2010). In the southwestern part of the study area, the influence of the Subtropical Mode Water (StrMW), with a higher temperature and

salinity, and a low oxygen content (Kremeur et al., 2009), was taken into account. The StrMW forms in the tropics, south of the Gulf Stream (Maze and Marshall, 2011).

The mid-depth water masses are described in detail in the next section.

The deep water masses include the Labrador Water (LSW), cold, of low salinity and with high oxygen content, which penetrates into the study area from the northwest. The LSW crosses the Mid-Atlantic Ridge (MAR) along the Charlie-Gibbs Fracture Zone (Talley and McCartney, 1982; Straneo et al., 2003) and further spreads south along the eastern slope of the Mid-Atlantic Ridge at depths of 1200-2500 m (Harvey and Arhan, 1988; Paillet et al., 1998; Bower et al., 2002a). The LSW is separated from the deep fractions of the MW by a weak thermohaline front (Paillet et al., 1998). Below and southeast of the LSW, in the depth range of 1000-4000 m, the waters are dominated by the North Atlantic Deep Water (NADW). The upper fraction of the NADW ($NADW_u$) is the overflow Greenland Sea water that passes the sill of the Faroe-Shetland Strait. Its lower fraction (LDW, 2500-3000 m and deeper) overflows the sill of the Denmark Strait (Harvey and Arhan, 1988; Schmitz, 1996; Hansen and Osterhus, 2000; Brix and Gerdes, 2003). The deepest layers are dominated by the Antarctic Bottom Water (Antarctic Bottom Water, AABW) (van Aken, 2000a; Orsi et al., 2001), which do not affect the mid-depths and are not considered in further analysis.

4.2.2 MEDITERRANEAN WATERS IN THE SUBTROPICAL NORTHEAST ATLANTIC

The mid-depths layer (700-1500 m) of the study area is occupied by the Mediterranean Water (MW), Subarctic Intermediate Water (SAIW) and Antarctic Intermediate Water (AAIW) (Table 4.1, Fig. 4.2).

The SAIW (relatively cold, of a lower salinity and with high oxygen content) is formed west of the MAR along the northern branch of the North Atlantic Current (50-54°N). Part of the SAIW (with a temperature of 9-10°C) propagates along the MAR southwards and eastwards, reaching the southernmost limit at 40-45°N and in the easternmost limit at 10-25°W. Along its way, the SAIW gradually mixes with the NACW and LSW, and its core deepens to 700-1000 m (McCartney and Talley, 1982; Harvey and Arhan, 1988; Tsuchiya, 1989; Arhan, 1990; Arhan et al., 1994).

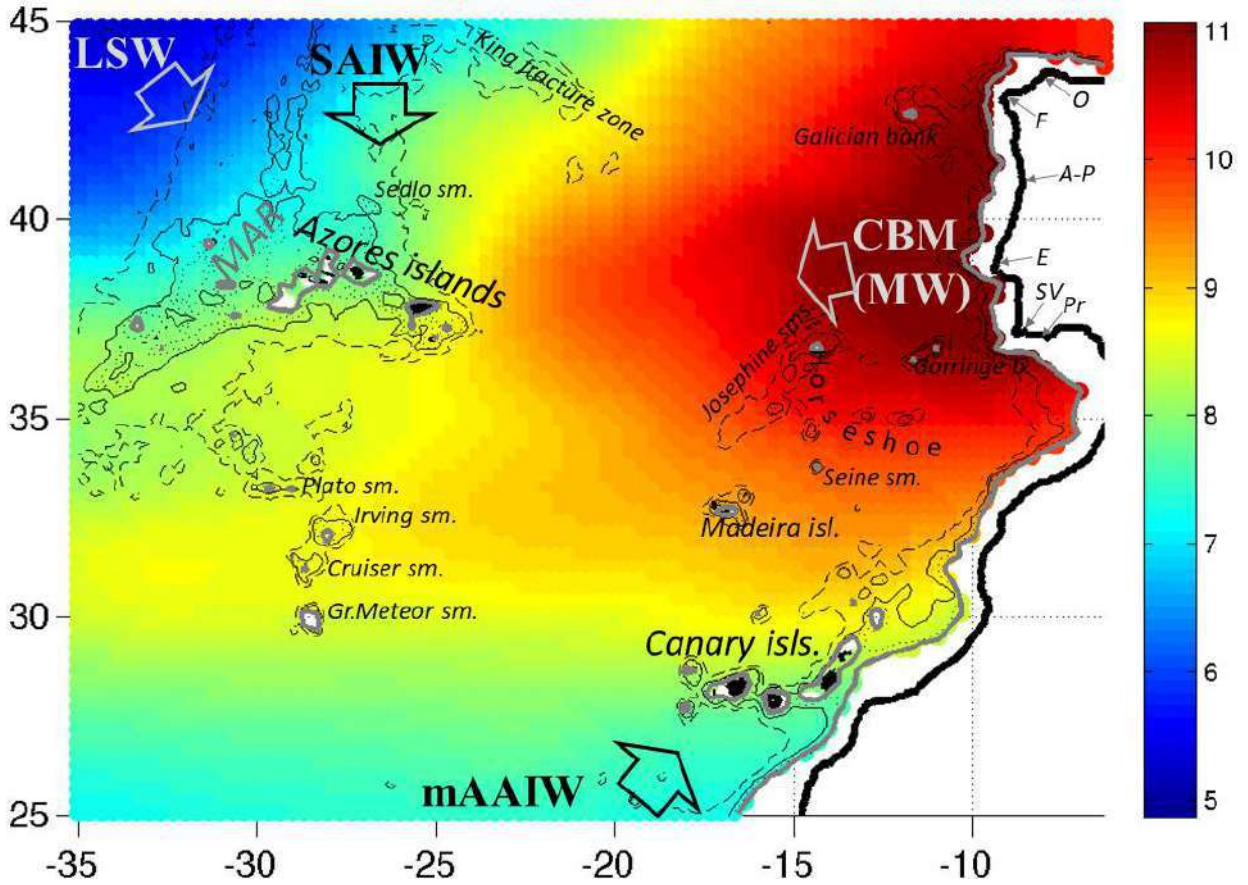

Fig. 4.2. The main mid-depth water masses overlaid on the water temperature at 1000 m depth (MEDTRANS climatology). mAAIW is the modified Antarctic Intermediate Water, SAIW is the Subarctic Intermediate Water, MW is the Mediterranean Water, LSW is the Labrador Sea Water mass. O – Cape Ortegal, F – Cape Finisterre, A-P – Aveiro - Porto canyons, E – Extremadura Rise, SV – Cape Saint Vincent, Pr – Portimao Canyon. The gray dotted line shows the 3000 m isobath, the gray solid line shows the 2000 m isobath.

The AAIW forms along the Antarctic Polar Front, including the Scotia Sea in the Atlantic sector of the Southern Ocean (Schmitz, 1996; Tomczak and Godfrey, 2003). In the North Atlantic the AAIW is characterized by minima of salinity and oxygen, a maximum of silicon and a high nutrients content at depths of 700-900 m (Tsuchiya et al., 1992; Schmitz, 1996). The AAIW is observed up to approximately 25ºN, but along the African coast the traces of the modified AAIW (mAAIW or AA) can be traced to 30-32ºN latitude (Perez et al., 1998, 2001; Alvarez et al., 2004)), and even reach the Gulf of Cadiz (Machin et al., 2006; Machin and Pelegri, 2009; Lourn and Morin, 2011; Pastor et al., 2012). Here the mAAIW is found above the MW, at depths of 500-800 m, identified as a silicon maximum and weak minima of salinity and oxygen (Tsuchiya et al., 1992; Arhan et al., 1994). Another branch of the mAAIW extends along the continental margin of America and, further, with the North Atlantic Current. Its weak influence may be traced in the northwest of the study region (Tsuchiya, 1989).

The MW is formed by the outflow of saline and warm waters of the Mediterranean Sea from Strait of Gibraltar and their further mixing with the NACW and the upper layers of $NADW_u$ (upper North Atlantic Deep Water) during their rapid descend in the eastern part of the Gulf of Cadiz. Due to this mixing the transport of the Mediterranean Undercurrent (MUC), which carries the MW, increases three to five times (Price et al., 1993; Baringer and Price, 1997; Baringer and

Price, 1999; van Aken, 2000b; Barbosa Aguiar et al., 2015). Downstream, the entrainment of surrounding waters in the MUC continues, but at a significantly smaller rate (Barbosa Aguiar et al., 2015). Despite this mixing, the MW retains high positive anomalies of temperature and salinity, and low oxygen and nutrient content, typical for the sea surface waters of the western Mediterranean Sea (Fig. 4.2).

The subsurface topographically trapped MUC skirts the Iberian Peninsula from the west. The MUC is divided into the upper core (upper MW fractions) at depths of 800-1000 m and the lower core (lower MW fractions) at depths of 1000-1200 m (Harvey and Arhan, 1988; Iorga and Lozier, 1999a; van Aken, 2000b). Figure 4.3 shows the depth and intensity of the near-slope salinity maximum, characterizing the lower MUC core, and the temperature maximum, characterizing the upper MUC core, derived from MEDTRANS climatology (see section 2.2). The fictitiously low salinity values of the MUC core along the southern edge of the Iberian Peninsula (7-8.5ºW) are a result of a very small width of the MUC in this area - only 20-50 km (Baringer and Price, 1997), while using the 70 km window in MEDTRANS climatology results in an artificial mixing with the surrounding waters. The upper core of the MUC gradually deepens, while the lower one becomes sallower. Thus, these two cores, separated by topographical features in the southern slope of the Iberian Peninsula, are gradually merging together. An interesting feature is the abrupt changes in the depth of the lower core of the MUC. Being stable over a fairly large section, there are jumps in the MUC depth collocated with some topographic features (Fig. 4.3a,b). Thus, with a gradual tendency to increase due to mixing with the NADW, the MUC depth sharply decreases by about 100 m near Cape Saint Vincent (37ºN, the exact place depends on the season), then makes a similar jump in the area of the Aveiro Canyon (40.5-41ºN) and near Cape Finisterre (43ºN). The identified changes in the depth of the lower core of the MUC are consistent with previous estimates of variations in the depth of the maximum salinity of the Mediterranean Water (Daniault et al., 1994; Bower et al., 2002b; Bashmachnikov et al., 2015a). It will be shown further that these topographic features are also areas of active meddy formation.

The seasonality of the MUC is weak. During the warm season, the MUC salinity increases by 0.02-0.04, and the density at the depth of the salinity maximum increases by 0.01 kg m^{-3} (Fig. 4.3b). This is explained by an increased summer salinity of the sea surface waters of the Mediterranean Sea (Sparnocchia et al., 1994) and of the subtropical Atlantic.

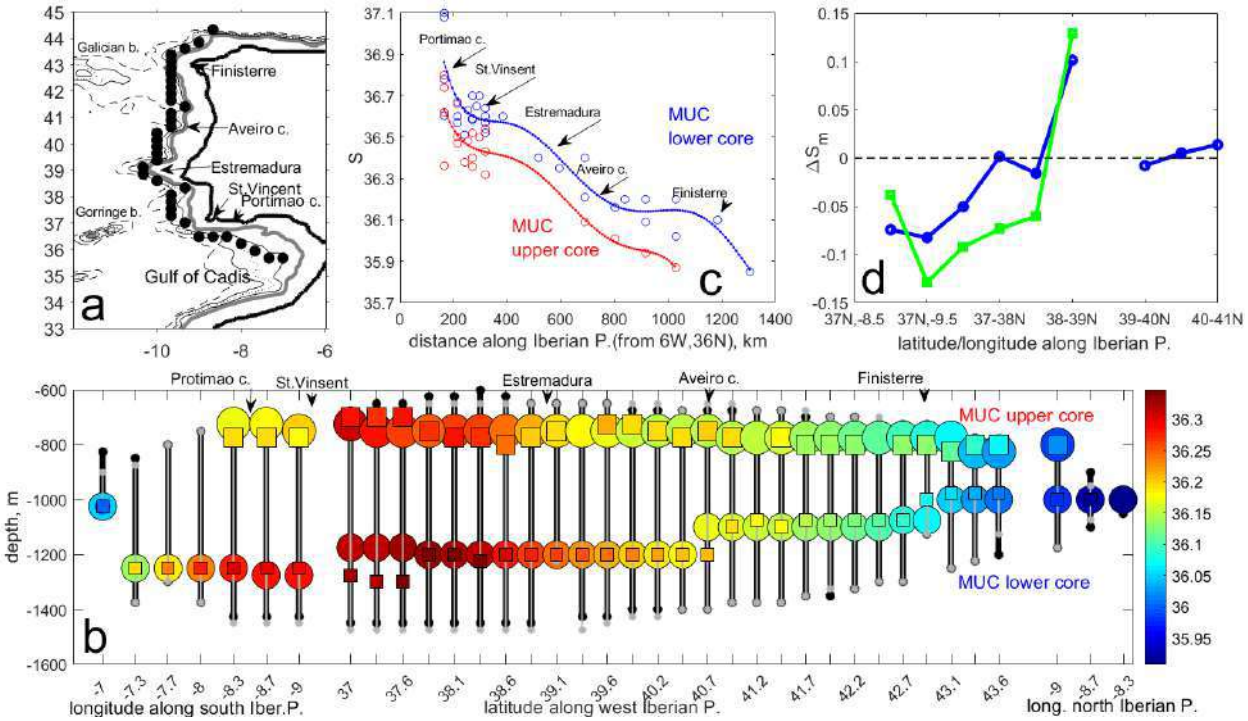

Fig. 4.3. (a) Trajectory of the lower MUC core along the MEDTRANS array (black dots) at the Iberian Peninsula. (b) Variation in depth and peak salinity (color) of the upper and lower core of the MUC along the Iberian Peninsula during winter (circles) and summer (squares). Vertical segments represent the limits of depths with salinity $S \geq 0.99\ S_{max}$, where S_{max} is the maximum salinity at a segment of the MUC (following Bashmachnikov et al., 2015a). (c) Variation of the maximum salinity of the upper (red line) and lower (blue line) cores of the MUC with distance from the Strait of Gibraltar; circles indicate salinity in meddy cores (derived from literature) observed within 300 km from the Iberian coast. (d) Salinity anomaly in meddy cores relative to the nearest point of the MUC (ΔS_m), along the continental slope of the Iberian Peninsula (see section 4.3.3.3); blue line – data from the analysis of this study, green line – according to literature (Ambar et al., 1976; Ambar and Howe, 1979a,b; Baringer and Price, 1997; Bower et al., 2002b; Daniault et al., 1994; Fiuza et al., 1998; Rhein and Hinrichsen, 1993).

The results of OMP analysis (see section 4.6.1) showed that the MW makes a significant input to the water structure the northeastern Atlantic between 600-1500 m (Fig. 4.4). The vertical thickness of the MW layer decreases westwards, from 900 m near the Iberian Peninsula to 100-200 m near the MAR (see also Tsuchiya et al., 1992; Arhan et al., 1994). Over much of the region, the MW mixes with the NACW above γ_n = 27.70-27.75 kg m^{-3} (approximately 1100-1200 m depth) and with the NADW/LSW below this γ_n. The SAIW "intrudes" in the MW between the neutral density surfaces γ_n = 27.65-27.80 kg m^{-3} (Fig. 4.4 a), i.e. these two types of waters actively mix east of the MAR. Water advection along the eastern slope of the MAR (Bower et al., 2002a) carries the SAIW as far south as the Azores Current (Fig. 4.4 b, c). East of the Azores, the SAIW enters a cyclonic deep water gyre (at 15-25°W and 34-39°N), which plays an important role in the eastwards penetration of the modified SAIW and its mixing with the MW (Bashmachnikov et al., 2015b). The at the southern limit of the MW, the front between the MW and the mAAIW is quite sharp (Fig. 4.4 d).

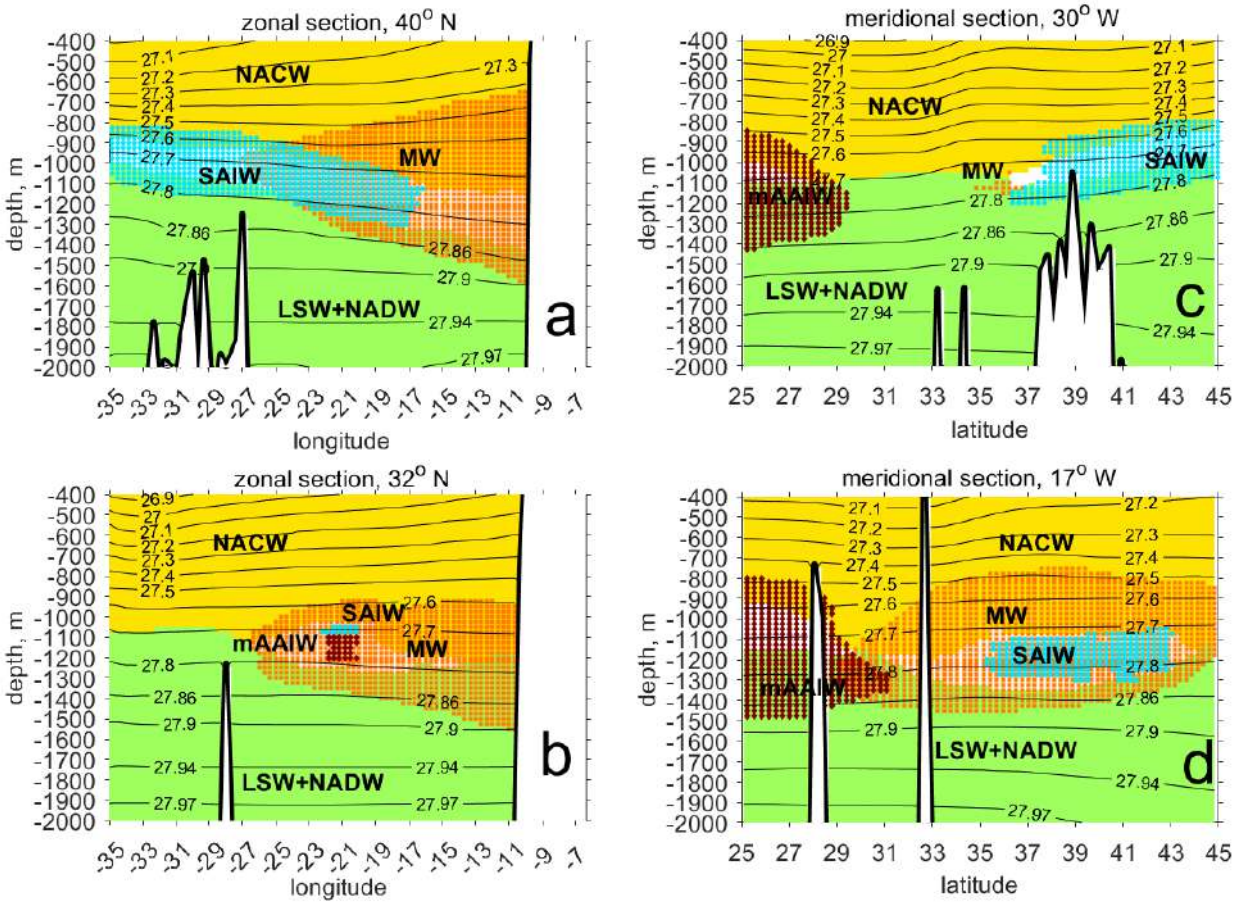

Fig. 4.4. Distribution of water masses, the contribution of which exceeds 25%, along zonal sections (see Fig. 4.5 c,d): (a) 40°N, (b) 32°N, and meridional sections (c) 30°W, (d) 17°W. Yellow color shows the area of significant concentrations of the NACW, green – of the LSW and NADW, orange – of the MW, blue – of the SAIW, brown – of the mAAIW. If the contribution of several water masses exceeds 25%, then there is an overlap of different colors. The presence of a water mass in the foreground does not mean its dominance.

The MW has the highest concentration of 50-65% near the Iberian Peninsula between 34 and 40°N, which decreases to west by about 2% for every 100 km and makes no more than 10% near the MAR (Fig. 4.5a).

The upper core of the MW is the most pronounced at f 1000-1100 m between 30 and 40°N. (Fig. 4.5c), and the lower core of the MW – at depths of 1250-1350 m between 28 and 30°N (Fig. 4.5d) (see also Harvey and Arhan, 1988). In addition to the fact that the cores are formed from different veins of the MUC, the anomalously weak stratification of the deep waters of the Gulf of Cadiz (Iorga and Lozier, 1999a) promotes a deeper regional penetration of the MW after being vertically mixed with the NADW. This results in an increase in the density of the lower core of the MW, which start exceeding the density of the lower vein of the MUC along the southern slope of the Iberian Peninsula.

The results indicate that the upper core of the MW extends mainly westwards, and the lower –the southwards and southwestwards (Fig. 4.5 c,d). As a consequence, the layer of maximum MW concentration deepens from the northwest (900-1000 m) to the southeast (1200-1300 m) (Fig. 44.5b), more than can be explained by the slope of the isopycnals (Fig. 4.4d). The region of increased depth gradients of the MW core (Fig. 4.5b) represents the boundary of the

areas of preferential distribution of the upper and lower MW cores, separated by the Azores Current.

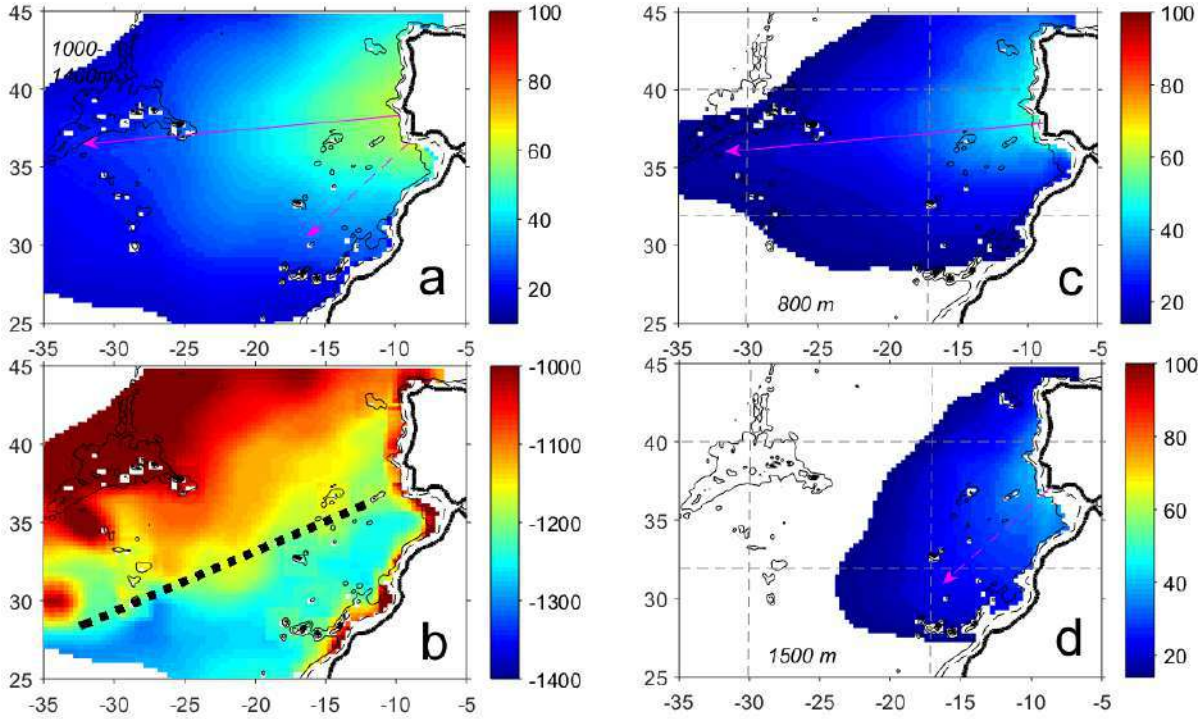

Fig. 4.5. Distribution of the MW. (a) The maximum percentage of the MW in the water column, pink lines show the main directions of propagation of the MW: solid line is the upper MW core, dotted line is the lower MW core. (b) Depth (m) at which the maximum percentage of the MW is reached; The black dotted line marks the area of highest depth gradients of the MW core, which characterizes the approximate boundary between the areas of dominance of the upper and lower MW cores. Isobaths of 500 and 2000 m are shown. Percentage of MW content at fixed depths levels: (c) 800 m and (d) 1500 m. Dotted gray lines indicate the locations of vertical sections in Figure 4.4.

4.2.3 ADVECTION OF THE MEDITERRANEAN WATER BY MEAN CURRENTS

Eulerian velocity fields at mid-depth levels were computed for a regular grid 1^o x 1^o using data from the ARGO floats (6560 months of trajectories at the data time step of 10-15 days) and RAFOS (6700 months of trajectories at a data time step of 6-24 hours). The methodology for assessing the characteristics of the mean currents using these data is outlined in Appendix 4.6.2.

To identify the possible role of advection in the propagation of the MW, ocean currents, estimated from the float trajectories, were extrapolated to the local level of the maximum MW concentration (Fig. 4.5b) using geostrophic relationships. The resulting vectors of average currents ($\vec{V}$) were decomposed into two components – parallel ($v_{//}$) and perpendicular ($v_{\perp}$) to the isolines of the MW concentration at a given point. In areas where the direction of $v_{\perp}$ is from large to smaller concentrations of the MW, advection can play an important role in the propagation of this water mass (pink vectors in Fig. 4.6a). The average current velocities at intermediate depths were quite small and amounted to a few cm s^{-1}. The errors in calculating the current velocity (v_{err}) were

comparable to the values of $v_{\perp}$ for approximately 50% of the computed values (see Appendix 4.6.2): areas $v_{\perp} > v_{err}$, shown in pale color (Fig. 4.6a).

Along the continental slope, currents, as a rule, are not detected due to the absence of floats. The MUC, which transports the MW north along the continental slope of the Iberian Peninsula, can be traced at some limited sections, as, for example, in the area of an active launch of RAFOS floats inside MUC during the AMUSE experiment. The subsurface flow that transports highly diluted mAAIW into the Gulf of Cadiz along the northwestern slope of Africa, described in the literature (Tomczak and Godfrey, 2003; Machin and Pelegri, 2009; Lourn and Morin, 2011; Carracedo et al., 2014), is detected in only one grid cell.

Weak westwards currents at about 1000 m is observed between 39 and 40°N. (previously noted by Daniault et al., 1994; Iorga and Lozier, 1999a; Carracedo et al., 2014) and at 45°N (previously noted by Bower et al., 2002 a, b). The area in the southern current region corresponds to the distribution paths of the highest concentration of the upper core of Mediterranean waters (Fig. 4.6 a, b). The possible role of advection in the propagation of the upper core of the MW north of 36°N. previously indicated Sparrow et al. (2002). However, the currents at these depths are weak and probably quite unstable (Barbero et al., 2010).

Deeper MW fractions (1500 m or more) extend from the Gulf of Cadiz to the southwest, parallel to the African coast (Figs. 4.5b, 4.6). This corresponds to the area of radial spreading of waters from the southwestern tip of the Iberian Peninsula, between 34 and 39°N, i.e. also correspond to the main directions of water advection by currents. Here the highest concentration of Mediterranean waters outside the MUC is observed (Fig. 4.6a).

However, at a distance of several hundreds of kilometers, the link between the direction of the deep water advective transport and the of the MW spreading is no longer traceable (Fig. 4.6b). Thus, at the depths of the MW maximum, the North Atlantic Current (along 43-45°N) and the Azores Current (at 35°N) have an opposite direction to that of the MW propagation. In a significant area of distribution of the MW, currents are directed along the isolines of the MW (Fig. 4.6a). Thus, advection can partly explain the nature of spreading of the MW at relatively short distances from the Iberian Peninsula. Following Maze et al. (1997), Iorga and Lozier, (1999a), Filyushkin et al. (2009) and other studies, it can be assumed that meddies, the characteristics of which are discussed below, may play an important role in the westward transport of the MW (section 4.3). In particular, the area of the highest concentration of the MW between Cape Saint-Vincent and the Extremadura Promontory (Fig. 4.2, 4.5c) is also an area of intensive meddy formation and their detachment from the continental margin (Daniault et al., 1994; Bower et al., 2002b, Richardson et al., 2000; Bashmachnikov et al., 2015c).

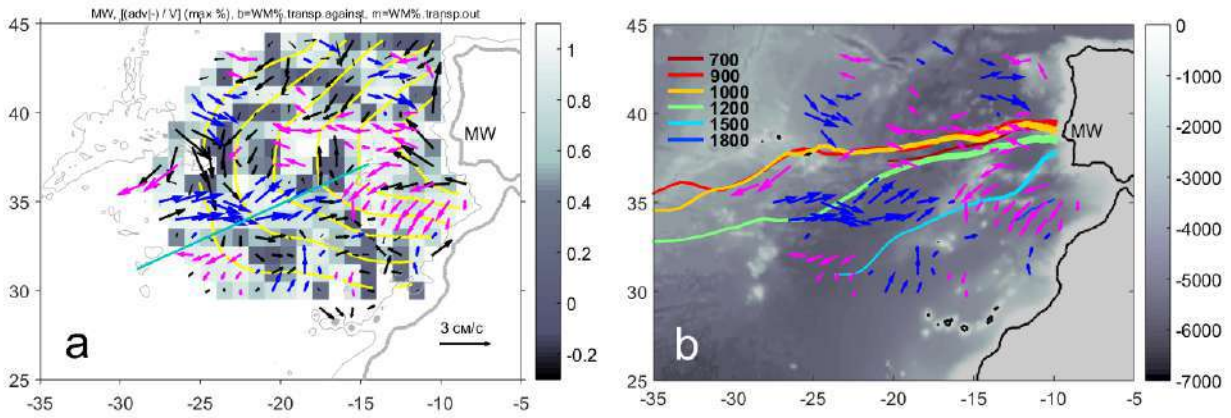

Fig. 4.6. (a) Transport of the MW with advection. The isolines of the MW concentration are shown in yellow. The solid green line shows the approximate boundary between the predominant distribution of the upper (about 800-1000 m) and the lower (about 1200-1500 m) MW cores. The arrows show currents at the level of the maximum MW concentration: pink - from the source of the MW (from a higher to lower MW concentration), blue - to the source of the MW (from a lower to a higher MW concentration), black – directed along the isolines of the MW concentration. The color shows the relationship $|v_\perp/V|$*: the lighter the color, the stronger the effect of advection on the MW transport. The solid gray contours show the 2000 m isobath and the coastline. (b) Main directions of the MW propagation at different depth levels. The mid-depth currents from (a) are overlaid. The water depth (m) is shown in color.*

To explain the reasons for separation of currents (and meddies) from the continental slope, which is mainly observed between Cape Saint Vincent and the Extremadura Promontory, the system quasi-geostrophic equations depth-integrated equations was reduced to (Pedlosky, 1998):

$$\frac{\beta v}{f} - \frac{\vec{V}\cdot\vec{\nabla}H}{H} = \frac{1}{f\,H^2}\,J(\Phi,H) \qquad (4.1)$$

where β is the change in the Coriolis parameter with latitude, H is the water depth, $\vec{\nabla}H$ is the sea depth gradient, $\vec{V}$ is the mean current velocity in the layer, v is the northern component of $\vec{V}$, $J(\Phi,H)=\frac{\partial\Phi}{\partial x}\frac{\partial H}{\partial y}-\frac{\partial\Phi}{\partial y}\frac{\partial H}{\partial x}$, $\Phi=\frac{1}{\rho_0}\int_{-H}^{-H_1}\left(\int_{-H}^{-z} g\rho\,dz'\right)dz$, H_1 is the upper boundary of the layer over which the integration is carried out. In equation (4.1), the first term characterizes the planetary β-effect, the second term is the topographic β-effect, and the expression on the right side is the Joint Effect of Baroclinicity and Bottom Relief (JEBAR). To estimate Φ, the water density was vertically integrated over the entire vertical thickness of the MUC, from 600 m to 1500 m (or to the bottom) (see section 4.2.2, as well as Ambar and Howe, 1979; Ambar et al., 2008; Baringer and Price, 1997; Bashmachnikov et al., 2015b). Friction at the sea bottom can be neglected, since even within the first 100 km from the Strait of Gibraltar, where V exceeds 50 cm s^{-1}, the MUC has the spatial scale L ~ 50 km and the coefficient of horizontal turbulent viscosity $K \sim 0.002\,L^{4/3}$ ~

3700 m ^{2} s^{-1}, the Ekman number is much smaller than unity: $E = \frac{K}{\bar{f}L^2} \sim 10^{-2}$ (see also Price et al., 1993).

Derived in the absence of external sources or sinks of relative vorticity, equation (4.1) imposes restrictions on the direction of geostrophic currents. When a current does not reach ocean bottom, only the planetary β-effect operates, and the geostrophic flow is strictly zonal ($v = 0$). The topographic β-effect requires the geostrophic flow to follow the isobaths ($\vec{V} \cdot \vec{\nabla} H = 0$). The relative role of the topographic β-effect compared to the planetary one can be assessed as:

$$R_\beta = \frac{|\nabla H| / H}{\beta / f}. \qquad (4.2)$$

Along the continental slope of the Iberian Peninsula, the topographic β-effect exceeds the planetary one, on average, by 2-3 orders of magnitude. However, there are two areas of minimum values R_β : between Cape Saint Vincent and the Extremadura Promontory, and northwest of Cape Ortegal (Fig. 4.7a). In these areas, the dominance of the topographic β-effect is weakened, which favors a stronger destabilization of the MUC by external factors.

JEBAR can deflect current from isobaths towards shallow or deep water. Particularly important here are the cases where JEBAR deflects the MUC towards bigger depths, because then this effect contributes to the separation of the current from the continental slope. Along the western edge of the Iberian Peninsula this happens if JEBAR< 0, and along its southern and northern edges– if JEBAR>0. The computed JEBAR distribution is quite spotty. Above a steep slope $\vec{\nabla}\Phi$ it is almost parallel to $\vec{\nabla} H$. In this case, both terms, $\frac{\partial \Phi}{\partial x}\frac{\partial H}{\partial y}$ and $\frac{\partial \Phi}{\partial y}\frac{\partial H}{\partial x}$, have the same sign and the difference between these relatively large quantities is sensitive even to small errors in the determination of each. In further estimates of JEBAR, of topographic and of planetary β-effects, the sliding median values were used, with the ±25 km window along the continental slope and limited depth range from 500 m to 2000 m. MEDTRANS climatology was used for the computations.

In certain areas of the continental slope, JEBAR can exceed not only the planetary, but also the topographic β-effect (Fig. 4.7b). This is a fairly large area around Extremadura Promontory, as well as some small areas at the continental slope south of Cape Saint Vincent, near Porto and Aveiro canyons, west and north of Cape Finisterre, and north of Cape Ortegal (Fig. 4.7a-c). For the base of the continental slope (depth 1500-2000 m), the value of the topographic β-effect exceeds JEBAR by several orders of magnitude, except for the area near the Extremadura Promontory, where JEBAR dominates the topographic β-effect also along the base of the continental slope (Fig. 4.7). This explains why the MW advective flow breaks away from the continental slope precisely in the area of the Extremadura Promontory (Fig. 4.6). The results indicate that JEBAR is the main mechanism for the detachment of part of the MUC flow from the continental margin. The identified areas of JEBAR dominance are also known as the areas of active formation and detachment of meddies from the continental margin (Richardson et al., 2000; Aiki and Yamagata, 2004; Bashmachnikov et al., 2015c).

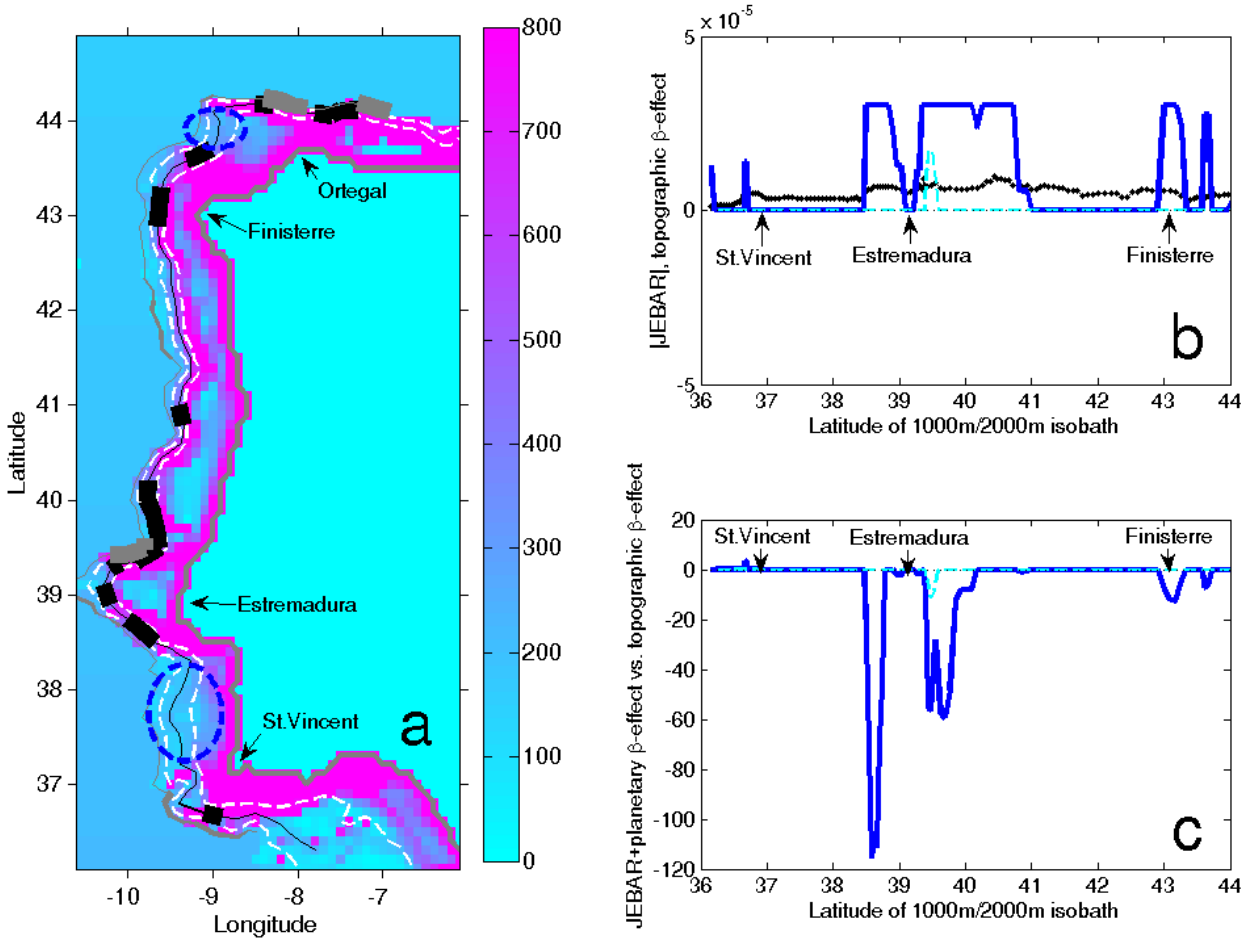

Fig. 4.7. Topographic β-effect, planetary β-effect and JEBAR along the continental slope of the Iberian Peninsula. (a) Color indicates spatial variability of R_β *(expression (4.2)). The areas of anomalously small* R_β *along the continental slope are highlighted with blue dotted ellipses. The relative role of JEBAR along the continental slope is marked with the thickness of the lines: the thicker the solid line is, the greater is the JEBAR compared to local topographic β-*effect; *the black line shows JEBAR along the 1000 m isobath, gray line – along the base of the continental slope (the 2000 m isobath). The white dotted lines additionally show isobaths of 500 m and 1500 m. (b) Topographic β - effect (black line) and |JEBAR| at the continental slope (blue line) and at its base (dashed light blue line) as a function of latitude along the 1000 m isobath. Only those JEBAR values that deflect the flow from the slope towards the sea have non-zero values. (c) Similar to (b), but for the ratio of the sum of JEBAR and the planetary β-effect to the topographic β-effect.*

4.3 CHARACTERISTICS AND DYNAMICS OF MEDITERRANEAN WATERS EDDIES AT DIFFERENT STAGES OF THEIR LIFE CYCLES

Mediterranean water eddies (meddies) in the North Atlantic are thought to have a significant contribution to the distribution of the Mediterranean Water, from 50 to 100%, according to different estimates (Richardson et al., 1989; Arhan et al., 1994; Bower et al., 1997; Maze et al., 1997; Filyushkin et al., 2009). The wide range of these estimates is partly due to an uncertainty in the number of meddies simultaneously present in the Atlantic, and partly due to an

insufficient knowledge of their statistical characteristics, life cycles and propagation pathways. Meddies are difficult to study because of significant depths of their cores and relatively small radii.

This section describes the results of analysis of the largest to date dataset of meddies from *in situ* observations. The fairly extensive material below makes it possible to describe the main statistical features of the distribution of meddy characteristics in the subtropical Atlantic, clarify their propagation paths and study the features of their life cycles from the moment of their generation. Meddies are known to be generated at the MUC along the entire length of the Iberian Peninsula and, as will be shown below, move offshore at a fairly constant average velocity. In this regard, the distance from the Iberian Peninsula characterizes the meddy age, which makes it possible to evaluate statistical features of characteristics of meddies of a certain age.

Meddies were identified using vertical casts, and their trajectories were determined using ARGO profiling floats and RAFOS neutral buoyancy floats (see sections 2.2.1, 2.3.1). Based on 26 062 vertical casts available, using the refined Richardson criterion (Richardson et al., 1991) with a critical salinity anomaly in the MW layer of 0.2 (section 2.3.1), the overall 775 meddies were identified (Fig. 4.8a). From this dataset, 241 meddies were selected for a detailed analysis (Fig. 4.8b). These meddies were samples with a sufficient amount of *in situ* casts to estimate their radii and other characteristics of their cores. About ¼ of these meddies were identified with 3-4 cast, and ¾ of the meddies – with more than 5 casts (Table 4.2). Based on the ARGO data set, 149 trajectories in meddies were identified, for each of which a float remained within the meddy core for at least 2 months. In the dataset of RAFOS neutral buoyancy floats, 87 such trajectories were identified. RAFOS were launched mainly along the southern and southwestern continental slope of the Iberian Peninsula (experiments AMUSE, MEDTOP, CANIGO, etc.), while ARGO floats were trapped by meddies mainly in the northern part of the region (where the maximum concentration of ARGO floats was detected), and both datasets complemented each other (Fig. 4.9).

Only 9 out of 241 meddies detected from *in situ* data were previously described in literature. In addition to the identified meddies, 41 meddies were studied (Fig. 4.8b), which did not enter this dataset due to lack of relevant observations available, but characteristics of which were described in detail in literature (Armi and Zenk, 1984; Armi et al., 1989; Kase et al., 1989; Zenk et al., 1992; Hinrichsen et al., 1993; Prater and Sanford, 1993; Pingree and Le Cann, 1993a,b; Schultz Tokos et al., 1994; Shapiro et al., 1996a; Pingree, 1995; Kase and Zenk, 1996; Bower et al., 1997; Richardson and Tychensky, 1998; Tychensky and Carton, 1998; Richardson and Wooding, 1999; Cherubin et al., 2000; Paillet et al., 2002; Carton et al., 2002).

Table 4.2. Number of temperature and salinity profiles in meddies, identified from in situ observations from 1950 to 2013, for which the characteristics of their cores were determined (241 meddies in total).

number of vertical casts performed in a meddy core	number of meddies
3-4	63
5-10	98
>11	80

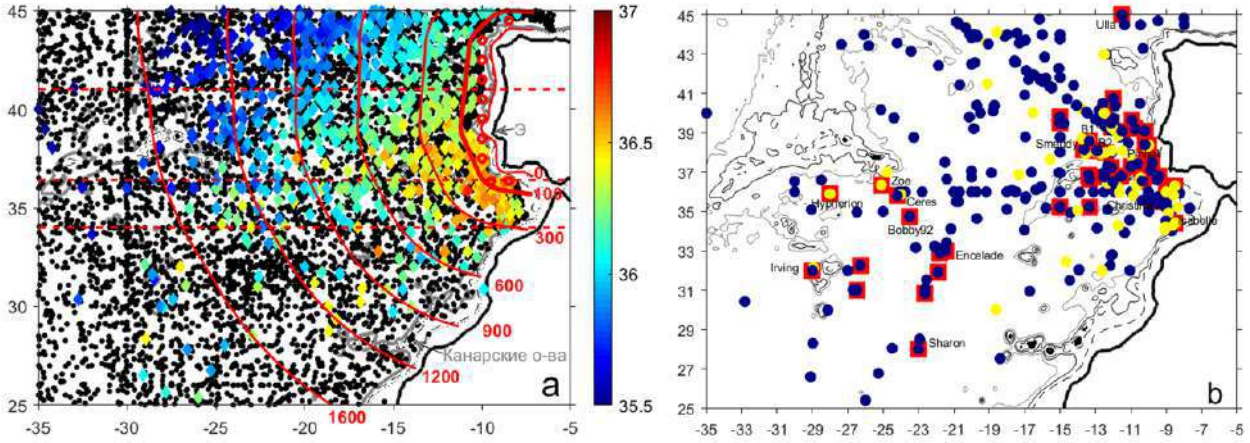

Fig. 4.8. (a) All vertical profiles (black dots) and all identified meddy (color dots, the color indicates maximum salinity of meddy cores) from 1950 to 2013. Red semicircles (distance to the continental slope of the Iberian Peninsula is given in red numbers) and zonal dotted lines indicate the boundaries of the areas used for providing statistics of meddy parameters in section 4.3.3); red circles indicate areas along the continental slope of the Iberian Peninsula (within the 100 km zone) in which estimates of meddy parameters along the MUC were performed. E- cape and underwater promontory of Extremadura. (b) meddies selected for detailed analysis and derived from in situ data in this study (circles: blue - with 1 core, yellow - with 2 cores) and described in literature (red squares, some meddies with known names are labeled).

South of the Iberian Peninsula, in the Gulf of Cadiz and the Iberian Basin, double-core meddies are frequently observed (Fig. 4.8b), while north of the Extremadura Promontory, single-core meddies are clearly dominating. This corresponds to the vertical structure of the MUC, which has two cores (lower and upper) on the southern slope of the Iberian Peninsula (Ambar and Howe, 1979a,b; Arhan et al., 1994; Baringer and Price, 1997), and the branches gradually merge together as the current progresses north (Fig. 4.3, Daniault et al., 1994; Fiuza et al., 1998).

Trajectories derived from the RAFOS and ARGO float data show that the meddies spread radially from the Iberian Peninsula west, southwest or northwest (Fig. 4.9). The directions of the meddy propagation often did not coincide with the directions of the mean background currents in the MW layer (Fig. 4.6). Meddy propagation velocities amounted to a few cm s^{-1} and were slightly higher near the Iberian Peninsula.

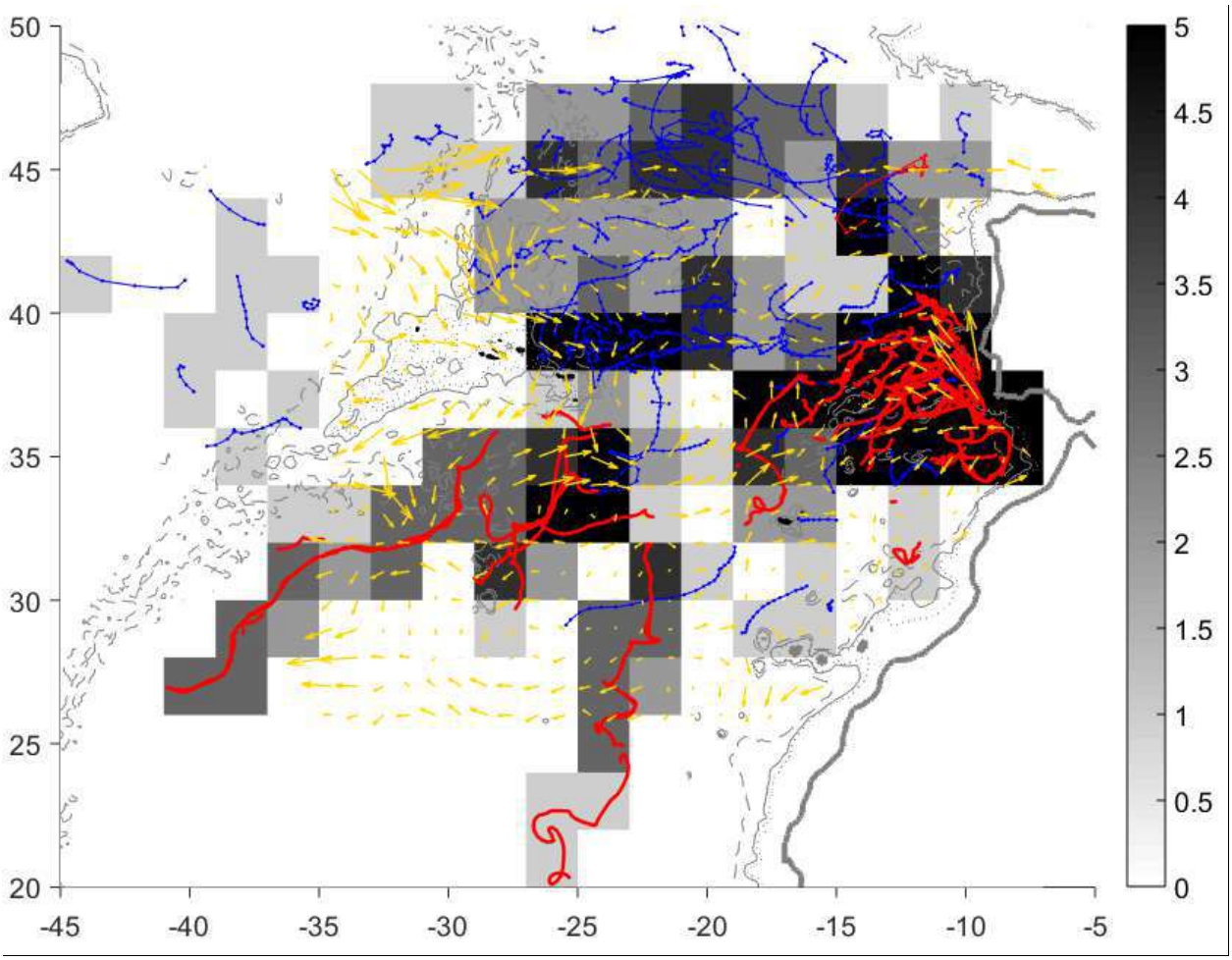

Fig. 4.9. Meddy trajectories as observed with ARGO (blue) and RAFOS (red) floats. The color shows the number of floats in 2°x2° squares. Meddy propagation along the trajectories is directed west, northwest or southwest. Yellow arrows show the directions of the main background currents at the depths of the highest concentration of the MW (1000–1300 m, Fig. 4.6a).

4.3.1 MEDDY GENERATION

Meddies form as a result of instability of the MUC. Three main mechanisms of meddy generation are proposed: baroclinic instability of the MUC (McWilliams, 1985; Cherubin et al., 2007), barotropic instability of the MUC and detachment of the shear bottom boundary layer of the MUC at capes or canyons (D'Asaro, 1988; Aiki and Yamagata, 2004). Estimates show that already at a distance of 100 km downstream from the Strait of Gibraltar (i.e. east of the Portimao Canyon), bottom friction at the continental slope can generate in the bottom layer of the MUC a relative vorticity of the order of 0.2-0.3 *f*, comparable to the peak vorticity in meddy cores (Prater, 1992). Aiki and Yamagata (2004) showed that a rapid change in the direction of the continental slope (a promontory or a canyon) is a necessary condition for the detachment of the meddy from the continental slope. Therefore, some meddies that separate from the coast at capes or canyons may form upstream in the MUC. One of the reasons for such separation is the simultaneous formation of a surface-intensified cyclone north of the same cape in the oppositely directed Portuguese Current. Intensifying as it interacts with the meddy to the south, the cyclone intrudes between the meddy and the continental slope and detaches the meddy from the slope (Richardson et al, 2000; Serra et al. 2002; Aiki and Yamagata, 2004; L'Hegaret et al., 2014). The same way

cyclones can form as part of a mushroom-like structure as a result of instability of the MUC in canyons (Serra et al., 2005). Another mechanism, described in literature, can be formation of a meddy in the topographically trapped flow when the latter is skirting an area of sharp bending of the slope line and is associated with the need to conserve angular momentum. The conservation of the angular momentum is possible only with a regular generation of anticyclonic eddies in the area of a sharp bending of the continental slop (Pichevin and Nof, 1997). At each such bend the current loses about 15% of its transport.

The relative efficiency of meddy generation by different section of the Iberian continental slope can be derived from the number of meddies detected over the period of observations in the immediate vicinity of the continental slope (Fig. 4.10), as well as from the trajectories of RAFOS floats launched in the MUC in series of experiments of the 1990s (Richardson et al., 2000). The largest number of meddies is found between the Portimao Canyon and the Extremadura Promontory. This area includes the main known areas of meddy formation (separation from the coast): Portimao Canyon (Serra and Ambar, 2002), Cape Saint Vincent (Prater and Sanford, 1993; Bower et al., 1997; Richardson et al, 2000), the Lisbon and Setubal canyons immediately south of Extremadura Promontory and the Nazare canyon further north (Richardson et al, 2000). The results show that in the area around Extremadura Promontory there are even more meddies detached from the continental margin than at Cape Saint Vincent, traditionally considered as the area of intense meddy generation. In literature, it is also discussed a possible formation of meddies at the Gorringe Bank, 200 km from the shelf edge of the Iberian Peninsula (Serra and Ambar, 2002). The data of this study suggest some increase in the number of meddies near the southern flank of the bank, but this may also be the result of stagnation and accumulation of meddies. In any case, the results do not allow to reliably assert the existence of a meddy generation region here.

To the north of the Extremadura Promontory, the number of meddies on the continental slope decreases by 3 times, i.e. it can be assumed that here the formation of meddies is much less efficient (see also Fig. 4.9). To the north of the Extremadura Promontory, 3 areas of meddy generation can be outlined: Aveiro/Porto canyons (40-41°N, see also Cherubin et al., 1997), the area northwest of Cape Finisterre (see also Paillet et al., 2002; Carton et al., 2013) and the area of the Galician Bank (Carton et al., 2013). In this latter case meddies may form at on one of the branches of the MUC, which skirts the bank from the west (Iorga and Lozier, 1999a,b), and which suggestion is supported by a significant increase in meddy abundance near the western end of the Bank (Fig. 4.11b). Meddy generation is also possible along the northern slope of the Iberian Peninsula (Carton et al., 2013).

In addition to anticyclones, cyclones of the Mediterranean Water are also generated by the MUC, but these eddies make a significantly smaller contribution to the dynamics of the Mediterranean Water in the Atlantic, because they are usually short-lived and of a much smaller in size (Ivanov et al., 1990; Chouksey et al., 2023).

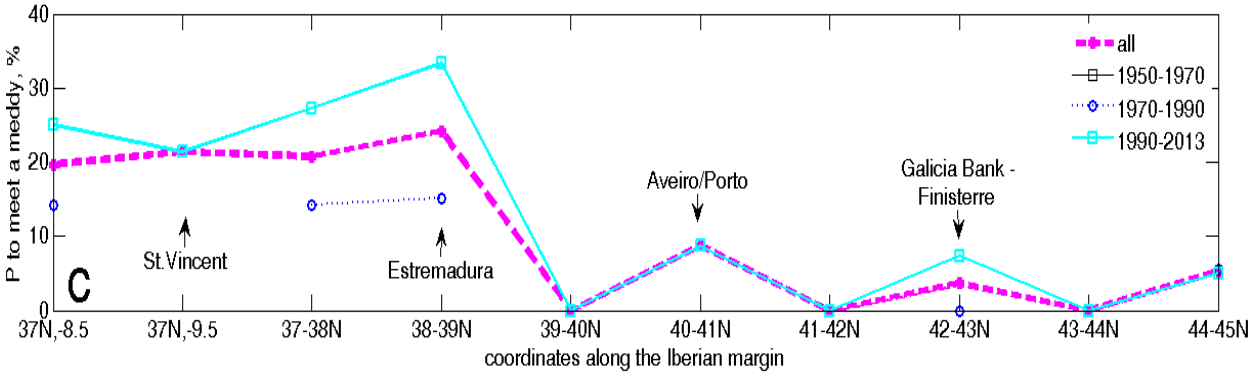

Fig. 4.10. Probability of finding a meddy within 100 km of the continental slope of the Iberian Peninsula (from south to north, see geographical names in Fig. 4.2). Different observation time intervals are given in different color.

4.3.2 MEDDY PATHWAYS

After detachment from the continental slope, the meddies spread mainly westwards. The trajectories of the RAFOS and ARGO floats in meddies (Fig. 4.9) were used for computation of the Eulerian velocity vectors of meddy translations (Fig. 4.11a). With the results of analysis of the vertical casts, the probabilities of meeting a meddy were mapped (Fig. 4.11b). The probability is estimated at 1°x1° grid as the ratio of the number of casts through meddy cores (of the overall 775 meddy observations) to the total number of casts in the same grid cell (see Bashmachnikov et al., 2015c). Summing these results, the following meddy pathways were identified, largely consistent with the previous studies (Shapiro and Meschanov, 1996; Richardson at al., 2000; Demidov et al., 2012; Menesguen et al., 2012): 1) the Northern path – from the Galicia Bank to the west (44-45°N), 2) the Central-Northern path – from the Extremadura Promontory to the west, skirting the Josephine seamounts from the north (39-40° N), 3) the Central-Southern path – from Cape Saint Vincent westwards, along the northern edge of the Azores Current (35-36°N), 4) the Southern path – from the Gulf of Cadiz and the Iberian Basin to the south or south-west, towards the Canary Islands (see Bashmachnikov et al., 2015c). In addition to the derived paths, the predominantly zonal character of meddy translations is confirmed by the fact that meddies, formed in different areas of the MUC with different thermohaline characteristics (Fig. 4.3c), conserve these meridional differences westwards of the areas of their generation (Fig. 4.17). However, there is a limited exchange between different meddies paths (Fig. 4.11, see also Cherubin et al., 1997; Demidov et al., 2012; Carton et al., 2013; Ciani et al., 2017).

Near the Iberian Peninsula, the Northern, Central-Northern and Southern paths can be linked to mean water advection at intermediate depths (Fig. 4.9). The formation of the Central-Southern paths is supported by the screening effect of the Azores Current, which does not allow weak meddies to cross the current southwards, while intense meddies, before crossing the current, usually drift for some time along its northern edge (Bashmachnikov et al., 2009a). The emergence of the Southern path is preconditioned by a noticeable weakening of the Azores Current as it approaches the Gulf of Cadiz (Fig. 2.8). In this area, moreover, a number of branches in the southwestern direction are separated from the Azores Current, which merge with the Canary Current (Iorga and Lozier, 1999b), which may facilitate the southward transport of meddies (Richardson et al., 2000; Sokolovskiy et al., 2013). Some meddies may bypass the Gulf of Cadiz counterclockwise, in conjunction with the dominant regional cyclonic circulation (Fig. 4.9, also

see Carton et al., 2002; L'Hegaret et al., 2014), but the rare detected cases of such trajectories do not allow determining to what extent this forms a characteristic regional meddy translation pattern.

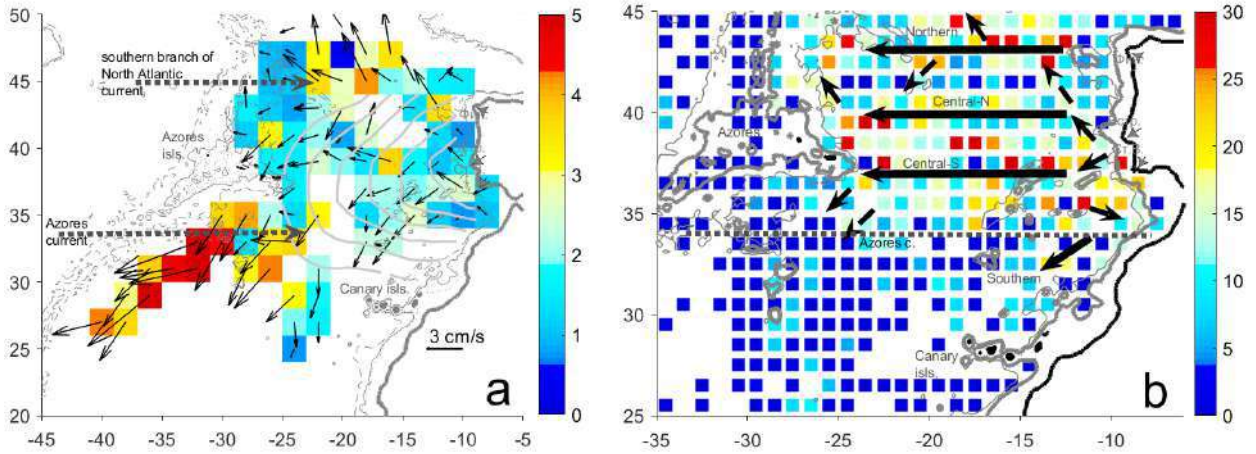

Fig. 4.11. (a) Average velocities and directions of meddy translations (black vectors) from to ARGO and RAFOS floats. The color shows the modulus of the velocity of meddy translations (cm s^{-1}) at the 2°x2° grid. The isolines of the MW concentration are shown in gray (see Fig. 4.6a). (b) Probability for meeting a meddy (%) from a random cast at 1°x1° grid (see methodology in Section 4.6.3). The arrows indicate the main expected routes for meddy translations, identified by a higher probability of detecting meddies.

The velocity of translation of a subsurface eddy along the isolines of the background potential vorticity, on the planetary β-plane is directed westwards and can be expressed as (Marshall, 1988; Cushman-Roisin et al., 1990; Morrow et al., 2004):

$$V_m \sim - \beta \, Rd^2 \, (1 + \Delta H / h_a) \qquad (4.3)$$

Here Rd is the Rossby deformation radius, taken as a measure of the horizontal size of the eddy, h_a is the thickness of the isopycnal layer in which the eddy core is located, ΔH is a maximum isopycnal uplift above the core of the anticyclonic eddy relative to their background level. The expression in the parentheses indicates that the velocity of eddy propagation is also a function of the intensity of the meddy (Nof, 1983, van Leeuwen, 2007).

The average velocities of meddy translation is 2-3 cm s^{-1}, and does not exceed 5 cm s^{-1} (Fig. 4.11a). These values correspond well to the results of previous studies, where the typical velocity of a meddy translation is estimated as 2-3 cm s^{-1}, with short-term accelerations up to 5-8 cm s^{-1} during periods of active interaction of a meddy with other dynamic structures (Schultz Tokos et al., 1994; Richardson et al., 2000; Carton et al., 2002). A slightly increased velocity of meddy translation along the eastern slope of the MAR is derived from a single trajectory of a very intense meddy (Hyperion). This anomaly cannot be considered representative, because according to expression (4.3), the velocity of movement of an anomalously intense meddy should be higher than that of an average meddy.

Meddies can either accelerate when interacting with the bottom topography (the topographic β-effect over the slopes of the Mid-Atlantic Ridge significantly exceeds the planetary one), or can slow down near topographic features, and also sharply change the velocity vector when interacting with other dynamic structures. Entrainment of surrounding fluid in meddy

rotation, as well as the distortion of the shape of the eddy core as a result of arising β-circulations inside, lead to the emergence of a southwards component in trajectories of the anticyclonic eddies (Cushman-Roisin et al., 1990). The latter effect is at least an order of magnitude smaller than the westward eddy displacement given by expression (4.3) (see, for example, Chelton et al., 2011). A southwards component of meddy propagation can also arise due to a decrease in the potential vorticity of meddy core during its dissipation through lateral intrusions or scattering of its energy with lee Rossby waves (Flierl, 1984; Colin de Verdiere, 1992). Therefore, a predominantly western or southwestern propagation of meddies is expected.

The intensity of β-circulations, generated by the baroclinic β-effect in the background flow, increases with an increasing intensity of the flow (Morel and McWilliams, 1997). This works for a barotropic (van Leeuwen, 2007), as well as for a baroclinic (Vandermeirsch et al., 2001) background flow. For easterly currents that dominate in the upper ocean of the study area down to 500-1000 m, this mechanism acts together with the planetary β-effect, and is so effective that a meddy can propagate against the direction of the dominant background flow, even in the absence of a deep westwards current (Morel and McWilliams, 1997). For a southward background flow, only the baroclinic β-effect operates and the resulting proper propagation of meddies is an order of magnitude less, which results in an advective transport of meddies south (Morel, 1995).

In a large-scale background flow with a horizontal shear, a mesoscale anticyclonic eddy migrates towards the axis of the flow in a region with a background relative vorticity opposite to that of the eddy core, and away from the flow axis – for the same sign of the background relative vorticity (Bell, 1990). Such dynamics contributes to the intersection of eastwards currents from north to south and southwards currents from east to west. Therefore, the southern branch of the North Atlantic Current (at about 45°N) should limit the northwards spreading of meddies, and the Azores Current should redirect the meddies south. However, the horizontal dimensions of the Azores Current are comparable to the meddy size, and the mechanism for crossing such a jet flow is somewhat different. As a meddy approaches the Azores Current from the north, an anticyclonic meander is formed somewhat upstream of the meddy, and a cyclonic meander is formed slightly downstream. The zonal jet, in a way, is locally divided into an anticyclone-cyclone pair. Intensifying, the cyclone pushes the meddy south. However, only a sufficiently intense meddy, the potential vorticity anomaly of which exceeds that of the Azores Current can cross the jet (Vandermeirsch et al., 2003a,b). In fact, not all meddies can cross the Azores Current, but some are “pushed back” by the jet and continue their westerly drift north of the axis of the current (Bashmachnikov et al., 2009a). This forms the previously mentioned Central-Southern path. After crossing the jet stream, a meddy may either remain trapped at the southern periphery of the jet or become detached from the jet and continue moving southwestwards. It all depends on the relative intensity of the cyclone and anticyclone, simultaneously formed by the meddy in the current. Analysis of meddy trajectories (Richardson and Tychensky, 1998; Tychensky and Carton, 1998; Bashmachnikov et al., 2009a; Ciani et al., 2017) indicates the rapid transport of a large intense meddy Hyperion across the Azores Current and the capture of a less intense meddy Encelade at the southern periphery of the Azores Current for at least 6 months (Fig. 4.9).

When a meddy interacts with a cyclone of the same intensity, the resulting dipole will also drift along the isolines of the effective β-effect, composed of the planetary, topographic and baroclinic β-effects (Velasco Fuentes and van Heijst, 1995). Large and powerful anticyclones and cyclones (including surface ones) affect a meddy as strong local anomalies of the background

potential vorticity and can sharply change the direction of meddy propagation at their peripheries (Schultz Tokos et al., 1994; Richardson et al., 2000; Carton et al., 2010).

Aside from relatively short-term interactions with other eddies, the movement of eddies along effective β-contours means that a meddy will propagate along the contours of the background potential vorticity (Marshall, 1988; Kostyanoy and Shapiro, 1989; Cushman-Roisin et al., 1990; Van Leeuwen, 2007). The Ertel integral potential vorticity in a water column, neglecting the relative vorticity of the background currents compared to *f*, can be estimated as:

$$\Pi_{\text{int}} = \frac{f}{Z}\int_{Z}^{0}\frac{N^2}{g}\,dz = \frac{f(y)}{Z(x,y)}\left[\frac{\left(\rho(Z(x,y)) - \rho_0(x,y)\right)}{\bar{\rho}}\right]. \qquad (4.4)$$

Here Z is the lower limit of the depth of the dynamic influence of meddies on the water column, $\rho(Z)$ and ρ_0 are the density of water at depth Z and at the sea surface, respectively. If the ocean depth exceeds Z, then $Z = const$ and there is no topographic β-effect. Otherwise, variations in Z usually play the leading role in the formation of the gradients of Π_{int}. The latter situation is often observed over steep slopes of the continental margin, the Mid-Atlantic Ridge and other underwater rises.

From theoretical results and observations, most meddies extend their dynamic influence to the sea surface (Bashmachnikov et al., 2014). The lower limit of the dynamic influence of a meddy can be roughly estimated as $Z = Z_c + H_m$, where Z_c is the depth of the meddy core, and the dynamic scale H_m is estimated as follows. The theoretical estimates suggest that the vertical scale of the *e*-fold attenuation of the dynamic influence of a meddy should be of the order of $\frac{R}{1.5}\frac{f}{N}$ (Bashmachnikov et al., 2014). The typical peak azimuthal velocity in a meddy core is 20 cm s^{-1} (Bashmachnikov et al., 2015c). It decreases to values of mean background current velocities at the mid-depths of the study region of 1 cm s^{-1}, at a scale 3 times larger than the *e*-folding attenuation scale. Then we get: $H_m = 2R\frac{f}{N}$ (Owens and Hogg, 1980; Bashmachnikov et al., 2014). With $\frac{N}{f}$ ~ 70-80 for the subtropics and for a meddy with a dynamic radius of 50 km, we obtain H_m of the order of 1300 m. Adding this value to the typical depth of meddy cores Z_c = 1100-1200 m, we find that a meddy will be influenced by the bottom topography for water depths of 2500 m or less. However, this is a lower estimate of Z, since a meddy can interact with the topography not directly, but through interaction with dynamic structures associated with the topography (such as Taylor cone), which “extends” its influence over several hundred meters upwards.

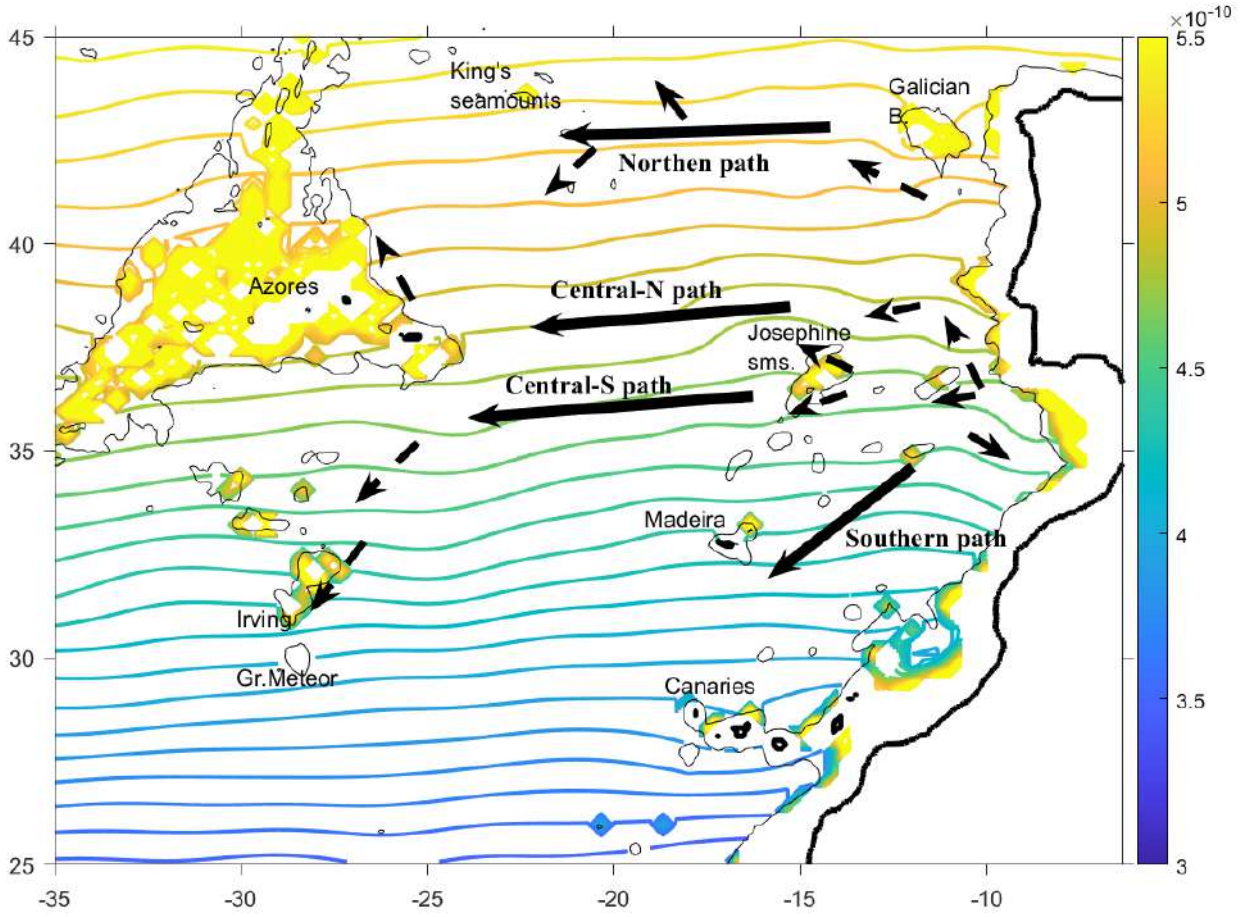

Fig. 4.12. Integrated background potential vorticity (Π_{int}) between 0 and 2500 m ($m^{-1}\ s^{-1}$, see expression 4.4). Black arrows indicate the pathways of the preferential meddy translations.

Taking Z = 2500 m and using MEDTRANS temperature and salinity climatology (Bashmachnikov et al., 2015a), Π_{int} can be estimated using formula (4.4). The predominantly zonal orientation of the isolines Π_{int} (Fig. 4.12), in the absence of influence of bottom topography, is due to the fact that the baroclinic β-effect is several times less than the planetary one. Nevertheless, the presence of the baroclinic β-effect leads to a slight inclination of the isolines of Π_{int} to the zonal direction. Thus, one can expect the presence of a southern component in meddy translation even in the absence of secondary effects, which deflect the anticyclones from zonal to the south. The Northern and Central meddy pathways in the deep ocean are directed along the isolines of Π_{int}. In areas of underwater rises, the meddy translations are determined by the bottom topography. For their Southern path, meddies move across the contours of Π_{int}. Apparently, advection of these meddies by the mid-depth currents is important in this region (Dewar and Meng, 1995; Morel, 1995). The figure does not take into account the influence of relative vorticity, which plays a fundamental role when crossing the Azores Current (Vandermeirsch et al., 2003a,b).

4.3.3 EVOLUTION OF MEDDY CHARACTERISTICS WITH AGE

Meddy cores, separated from the surrounding water by large gradients of potential vorticity, are fairly stable structures whose lifetime is often no more than a year (Hebert et al., 1990; Bashmachnikov et al., 2015c). Mechanisms for meddy decay are numerous. They include

double diffusion (Hua et al., 2013), loss of volume and momentum while interacting with the background flow (Mariotti et al., 1994), energy dissipation by internal waves at meddy boundaries and by Rossby waves (Flierl, 1984; Biescas et al., 2008; Early et al. 2011; Benilov et al., 2020), isopycnic lateral intrusions (Hebert et al., 1990), dynamic meddy instability, leading to deformation of the core and generation of filaments (Menesguen et al., 2012), splitting or complete destruction of meddy during their interaction with seamounts and other topographic irregularities (Richardson et al., 2000; Cenedese, 2002; Bashmachnikov et al., 2009a; Sokolovskiy et al., 2013).

The only long-term and detailed observations of a meddy were carried out for meddy Sharon, which was tracked over 2 years (Hebert et al., 1990). The results suggested that lateral isopycnal intrusions might be the most effective mechanism for a gradual destruction of the meddy core in the deep ocean. Interaction with a seamount often become a critical point of the existence of a meddy. Such interaction can be intense and lead to either complete collapse of the meddy core or the loss of a significant part of the core volume. It can be moderate and lead to core splitting with possible reunification of newly formed cores on the opposite side of the seamount. It can be weak and lead to rotation of the meddy around the seamount with a subsequent separation from the topography without a significant change in its characteristics (Shapiro et al., 1996a; Richardson et al., 2000; Cenedese, 2002; Herbette et al., 2003; Adduce and Cenedese, 2004; Bashmachnikov et al., 2009b; Sokolovskiy et al, 2013). The intensity of the interaction depends on the horizontal dimensions of the seamount compared to the meddy radius, the depth of the top of the seamount compared to the depth of the meddy core (van Geffen and Davies, 2000; Sokolovskiy et al, 2013), presence of a background current (Cenedese, 2002). Presumably, the intensity of the potential vorticity anomaly of the meddy core also strongly preconditions the results of the meddy collision (Bashmachnikov et al., 2015c). *In situ* observations and numerical modeling suggest that when interacting with a seamount, a meddy often loses 25 to 40% of its core volume (Shapiro et al., 1996a; Richardson et al., 2000; Wang et al., 2003; Bashmachnikov et al., 2009b).

4.3.3.1 Number of meddies as a function of distance from the Iberian Peninsula. Meddy lifetimes

Despite significant advances in our understanding of the average characteristics and dynamics of meddies in recent decades, only some parts of lifecycles of some meddies are covered with observations (Shapiro et al., 1996b; Richardson et al., 2000; Demidov et al., 2012; Filyushkin and Kozhelupova, 2020). This paper presents the most complete to the date and systematic study of meddies lifecycles, which is based on study of meddy characteristics with the distance from their generation regions. Such formulation of the problem turned out to be possible due to the limited area of meddy generation at the continental slope of the Iberian Peninsula and the unique characteristics of meddies in the subtropical Atlantic.

Figure 4.13 shows the probability of finding a meddy as a function of distance from the Iberian Peninsula (see boundaries of the areas in Figure 4.8(a) and the methodology in Appendix 4.6.3). The average probability of detecting a meddy in a random set of casts decreases from 10-15% at a distance less than 1200 km from the Iberian Peninsula to 1-2% or less at a distance of 1600 km or more (Fig. 4.13a). The average probability for the entire region is approximately 8%, slightly higher than the 5% estimate by Richardson et al. (1991). Some increase in the probability of detecting meddies at 100 km or more from the Iberian continental slope occurs north of Extremadura Promontory (Fig. 4.13a,b), where some meddies may accumulate, coming from more

southern regions (Fig. 4.11a). Another reason may lie in the methodology of meddy identification, where, in order to avoid errors, the MUC neighborhood was excluded from the analysis (see Section 2.3.1). A certain role may be played by a relatively small size of the newly formed meddies (Fig. 4.14), which makes it difficult to detect them, as well as the rapid movement of meddies away from the continental slope when interacting with its accompanying cyclone (Richardson et al., 2000; Serra et al. 2002; Aiki and Yamagata, 2004). Farther from the slope, meddies typically stagnate and accumulate in the Iberian Basin, being stopped by seamount chains or captured by the cyclonic circulation in the Gulf of Cadiz (Richardson et al., 2000; L'Hegaret et al., 2014). The very low probability of encountering a meddy over or to the west of the MAR means that the MAR represents a barrier to the zonal propagation of meddies. The probability of encountering a meddy also rapidly declines south of the Azores Current, which, as has been noted above, represents a partially permeable barrier for the meridional propagation of meddies (Fig. 4.13b).

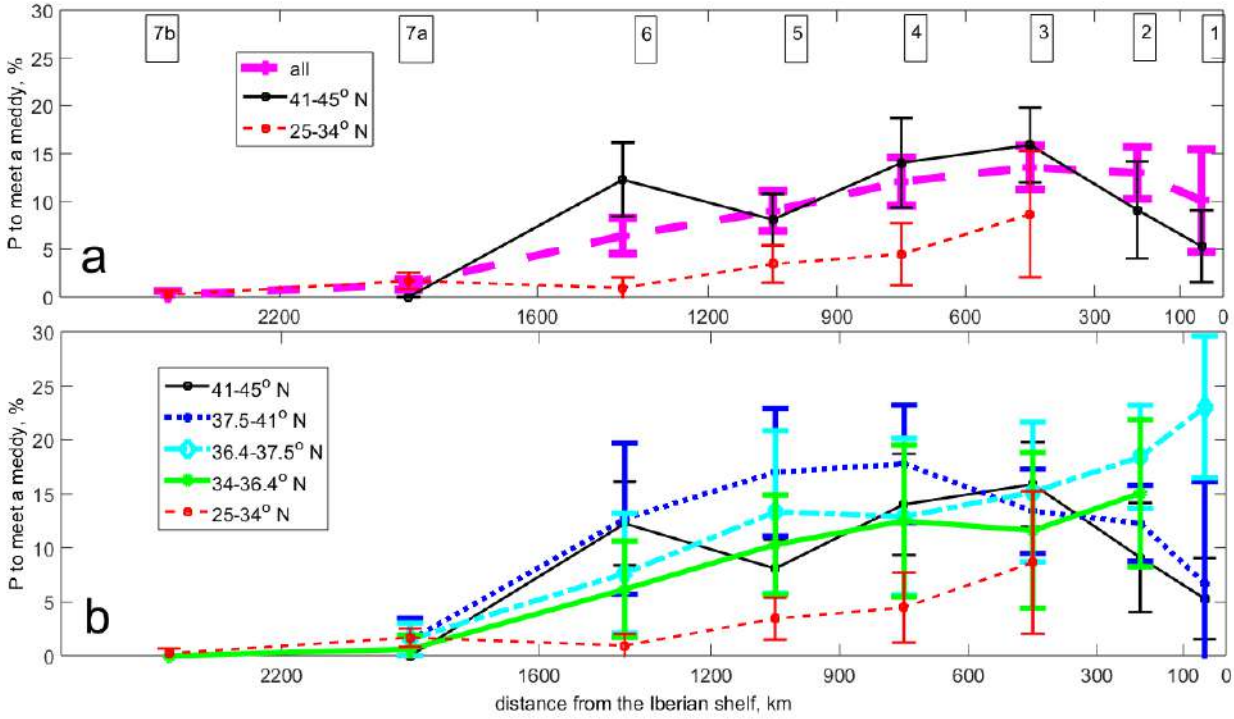

Fig. 4.13. Probability of finding a meddy in the subtropical northeast Atlantic as a function of distance to the Iberian Peninsula (X-axis, km). The numbers mark areas 1-7, the boundaries of which are shown in red semicircles in Fig. 4.8a. (a) Average over all latitudes (pink line), only in the northern part of the study region (black line), and the southern part of the study region (red line). Latitude ranges are given in the legend. (b) Same as (a), but with intermediate latitudinal zones added. The mean values are provided along the meddy pathways. Vertical segments characterize the error of the mean according to Student's t -test.

Based on the change in the probability of detecting a meddy with the distance from the Iberian Peninsula (Fig. 4.13) and the meddy translation velocities (Fig. 4.11), one can estimate the meddies lifetime. The probability of encountering a meddy decreases particularly rapidly between 900 and 1600 km from the Iberian Peninsula. This range can be taken as the distance at which most meddies are destroyed. With an average velocity of movement of 2.3 ± 0.5 cm s^{-1}, travelling 900 km would require, on average, 15 months (taking into account the error in determining the translation velocity – from 12 to 19 months), traveling 1200 km – 20 months (16-26 months), 1600

km – 26 months (22-34 months). Thus, the lifetime of a typical meddy is 1-2 years, and only a few meddies, that had travelled more than 1600 km from the Iberian Peninsula, existed over 2.5-3 years. Lifetime of a meddy recorded off the Bahamas by McDowell and Rossby (1978) then should be 5 years or more.

4.3.3.2 GEOMETRIC CHARACTERISTICS OF MEDDIES

The average dynamic radii of the meddies vary from 10 km to 70-100 km (Fig. 4.14a). Small meddy radii are observed near the Iberian Peninsula, primarily at its southern tip, as well as in the Iberian Basin and the Gulf of Cadiz. Along the continental slope of the Iberian Peninsula, meddy radii increase northwards (Fig. 4.14b) from approximately 10 km at the southern part of the peninsula (13 meddies observed) to 20 km between Cape Saint Vincent and Extremadura Promontory (55 meddies observed) and 30 km or more north of Extremadura Promontory (9 meddies observed). These data do not include meddies in direct contact with the MUC, which were filtered due to the difficulty of separating them from the MUC (see section 2.3.1). However, data from literature sources, which recorded meddies in direct contact with the MUC, among others (Zenk et al., 1992; Prater and Sanford, 1993; Pingree, 1995; Bower et al., 1997; Cherubin et al., 2000) show the same tendency (green line in Fig. 4.14b).

With the distance from the Iberian margin, within the first 600km, meddy radii *R* increase in all latitudinal zones (Fig. 4.14c,d). The consistent increase in meddy radii was associated with their frequent mergers, as indicated by changes in other meddy characteristics described below. Mergers are facilitated by the high concentration of meddies in the area (Fig. 4.14a), while numerous elevations of the bottom topography (banks and seamounts) limit westerly drift and promote the accumulation of meddies. Within the first 900 km from the Iberian Peninsula, northern meddies mostly have larger radii than the southern ones (Fig. 4.14a,d), mimicking the northward increase of *R* along the continental slope (Figure 4.14b).

At a distance of more than 900 km, the tendency to a decrease in *R* with the distance from the Iberian Peninsula indicates the predominance of the process of destruction and decay of meddy cores. The most rapid decrease in meddy radii is observed in the north of the region (Fig. 4.14 c,d). This is consistent with the rapid decrease in the potential vorticity anomaly of the meddy cores along the Northern meddy path (see Fig. 4.22d below) and indicates a more rapid destruction of meddies along this path. South of the Azores Current, meddy radii are smaller than along the Central path, suggesting a loss of part of meddy volume while crossing the Azores Current.

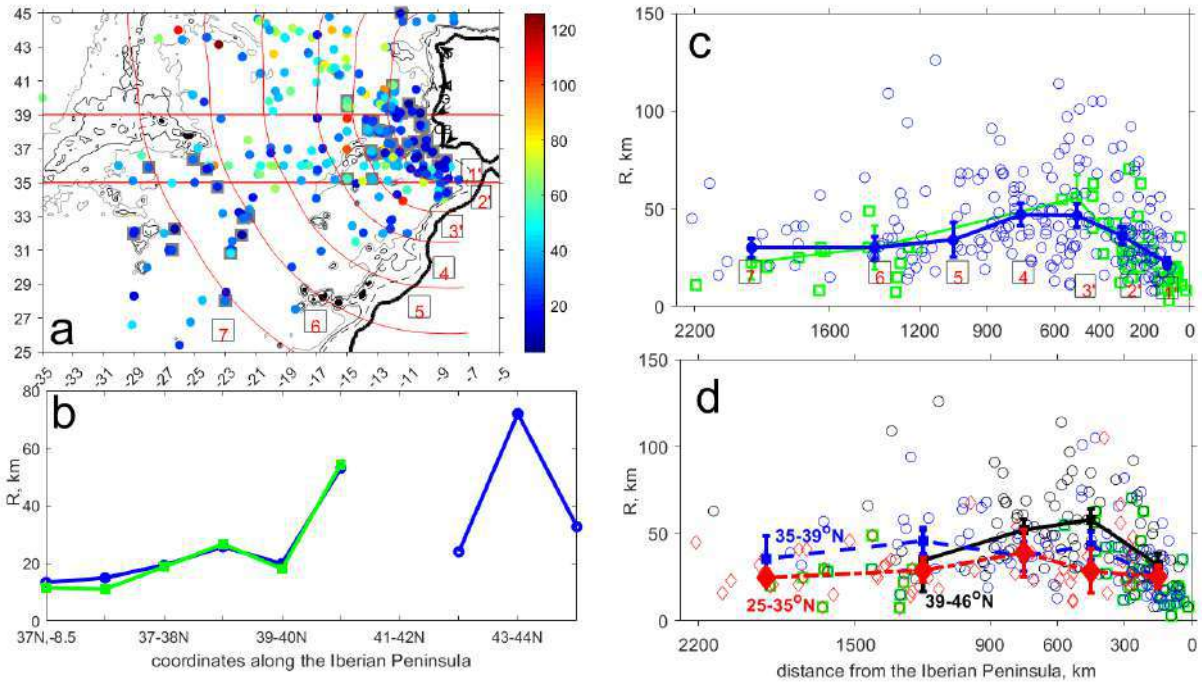

*Fig. 4.14. Meddy radii (R, km). **(a)** Spatial distribution of R. F = Cape Finisterre, A-P = Aveiro-Porto Canyons, E = Extremadura Promontory, NE = Cape Saint Vincent. Isobaths of 1000 m (gray dotted line), 2000 m (thick gray line) and 3000 m (thin gray line) are shown. **(b)** Variation of meddy radii along the Iberian Peninsula, within a 100 km distance to the continental margin: the blue line are results of this study, the green line – from literature. **(c)** R as a function of distance from the Iberian Peninsula: blue line and blue circles are data from this study, green line and green squares are data from literature. **(d)** radius R as a function of distance from the Iberian Peninsula in the three latitudinal bands marked in panel (a): 25-35°N (red), 35-39°N (blue), 39-45°N (black), according to literature (green). Vertical segments – errors of the mean; red numbers in squares – number of the area shown in panel (a) (from Bashmachnikov et al., 2015c).*

The vertical thickness of meddy cores (*h*) ranges from 300 to 1000 m, with an average of 600 m (Fig. 4.15a). The vertical thickness of meddy cores in the 100-kilometer zone from the coast (Fig. 4.15b) increases up to the Extremadura Promontory (and slightly north of it), and then begins to decrease, following changes in the vertical thickness of the MUC (Fig. 4.3b, Bashmachnikov et al., 2015c). This once again indicates the local origin of the meddies observed near the MUC. With distance from the coast, *h* decreases slightly, on average from 700-800 m near the Iberian Peninsula to 500 m at a distance of more than 2000 km from the coast (Fig. 4.15c). Consistent with the variability *of h* along the MUC, maximum values of *h* are observed along the Central path, between 37 and 41°N, and primarily in the Iberian Basin (Fig. 4.15 a,d). Along the Northern meddy path, the mean value of *h* decreases more rapidly over the first 900 km offshore than along other routes. This confirms the conclusions about the accelerated dissipation of northern meddies along the Northern Route.

h/R ratio shows that, on average, the horizontal dimensions of meddy cores are 2 orders of magnitude larger than the vertical ones (Fig. 4.16a,c). A tendency for *h/R* to decrease in a northerly direction is observed both along the Iberian Peninsula and away from it (Fig. 4.16 b,d). Overall, northern meddies are larger and flatter than in the southern ones. *h/R* decreases rapidly over the first 600 km from the Iberian Peninsula (Fig. 4.16c), which is typical for eddy mergers (Reinaud

and Dritschel, 2002; Bambrey et al., 2007). The further evolution of *h/R* proceeds differently for different latitudes, slowly decreasing along the Northern and Central paths under the influence of a gradual decay of meddy cores (see Hebert et al., 1990), but remaining at the same level, and even increasing slightly with the distance from the Iberian Peninsula south of the Azores Current (Fig. 4.16b,d). Probably, the latter is due to a continuous translation of only of the most intense meddies from the north (Fig. 4.9), while weak meddies cannot cross the Azores Current. This shifts the statistics towards the most intense meddies.

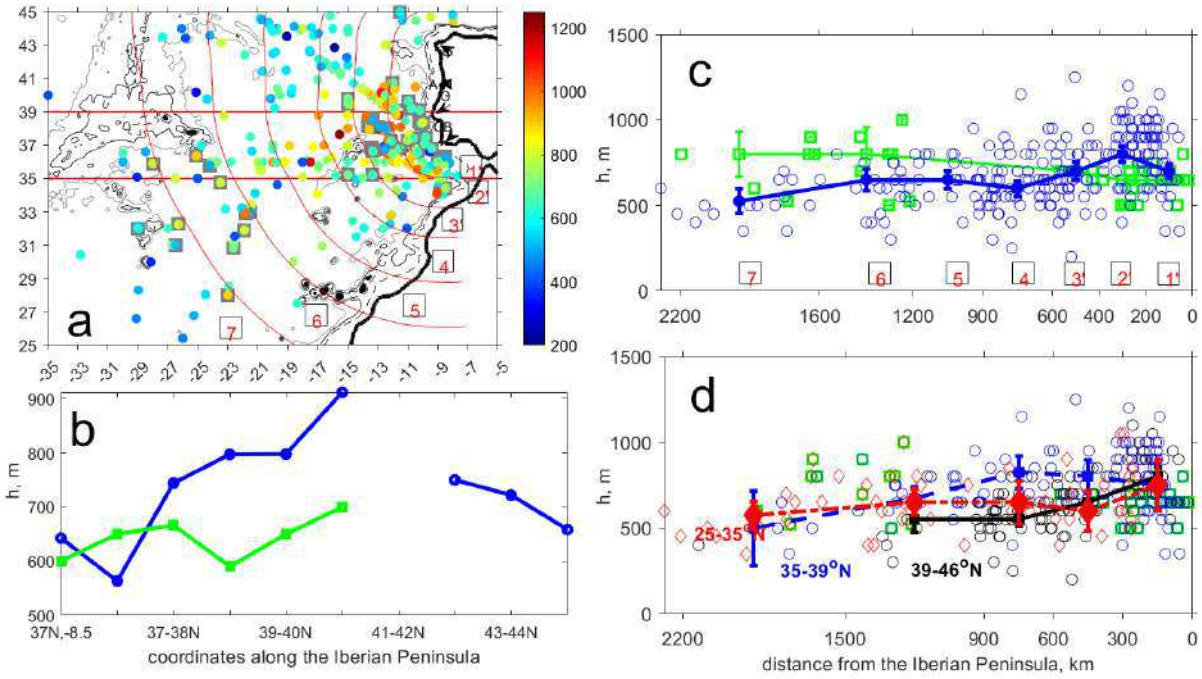

Fig. 4.15. Vertical thickness of meddy cores (h, m). ***(a)*** *Spatial distribution of h.* ***(b)*** *h along the Iberian Peninsula, within a 100-kilometer distance: blue line – data from this study, green – according to literature.* ***(c)*** *h as a function of distance from the Iberian Peninsula: blue line and blue circles are data from this study, green line and green squares – from literature.* ***(d)*** *h as a function of distance from the Iberian Peninsula in three latitudinal bands. See the detailed description in Fig. 4.14 (from Bashmachnikov et al., 2015c).*

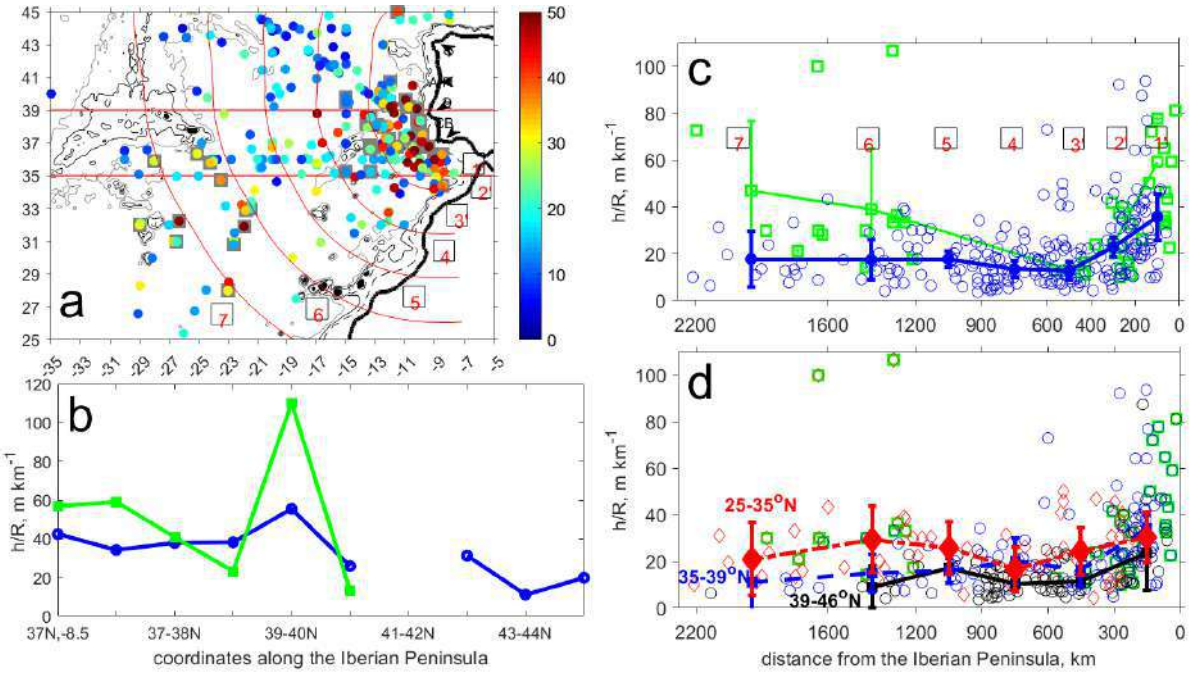

*Fig. 4.16. Ratio of vertical to horizontal scales in meddy cores (h/R, m km^{-1}). **(a)** Spatial distribution of h/R. **(b)** h/R along the coast of the Iberian Peninsula, within a 100-kilometer distance: blue line – data from this study, green – according to literature. **(c)** h/R as a function of distance from the Iberian Peninsula: blue line and blue circles are data from this study, green line and green squares - according to literature sources. **(d)** h/R as a function of distance from the Iberian Peninsula in three latitudinal bands. See the details in Fig. 4.14 (from Bashmachnikov et al., 2015c).*

With distance from the coast, the observed variability of *h/R* does not agree with the theoretical one (Hassanzadeh et al., 2012): $h/R = f\sqrt{Ro/(N_0^2 - N_m^2)}$, although the average theoretical values are of the same order of magnitude as the observed ones. Here *Ro* is the Rossby number of the eddy, N_m^2 is the buoyancy frequency in the eddy core, N_0^2 and is the buoyancy frequency of the background ocean. Thus, along the Central path, the buoyancy frequency anomalies in meddy cores relative to the background (N_o^2-N_m^2) decrease from 1.74 s^{-2} at 300-600 km to 0.88 10^{-6} s^{-2} at 1200-1600 km from coast, and *Ro* remains equal to 0.125; f = 8.5 10^{-5} s^{-1}. Accordingly, the theoretical *h/R* ratio increases with distance from the Iberian Peninsula from 0.023 (at 300-600 km) to 0.032 (at 1200-1600 km), while the observed ratio remains at 0.015-0.016. This discrepancy may be a consequence of both the inaccuracy in assessing the variability of parameters (especially *Ro)* and the features of dissipative processes in meddies (Benilov et al., 2020), which are not taken into account in the theoretical relationship.

4.3.3.3 SALINITY OF MEDDY CORES

The peak salinity in 241 meddies selected for detailed analysis (Fig. 4.17a, see also Fig. 4.8a for 775 meddies) shows a northward decrease along the Iberian Peninsula, matching well with the change in salinity of the MUC (Figs. 4.3c and 4.17c). Despite some scatter (Fig. 4.3c), as a rule, the salinity in the meddy cores is 0.1 lower than the average mean salinity at the nearest MUC location (Fig. 4.17b). This value is slightly greater than the local standard deviation of the salinity

of the MUC (±0.08) and is the result of the entrainment of less saline surrounding water into the meddy core during its formation (Prater, 1992). A feature stands out near the Aveiro and Porto Canyons, where the salinity of the meddy cores is clearly higher than that of the MUC (Fig. 4.17c). A similar, although not as strong, anomaly is also observed in the area of Cape Finisterre and the Galician Bank (Figs. 4.3d and 4.17c). This confirms the assumption that some of the meddies in these areas are not generated locally, but come from the south, from the Extremadura Promontory (see meddy pathways in Fig. 4.11a).

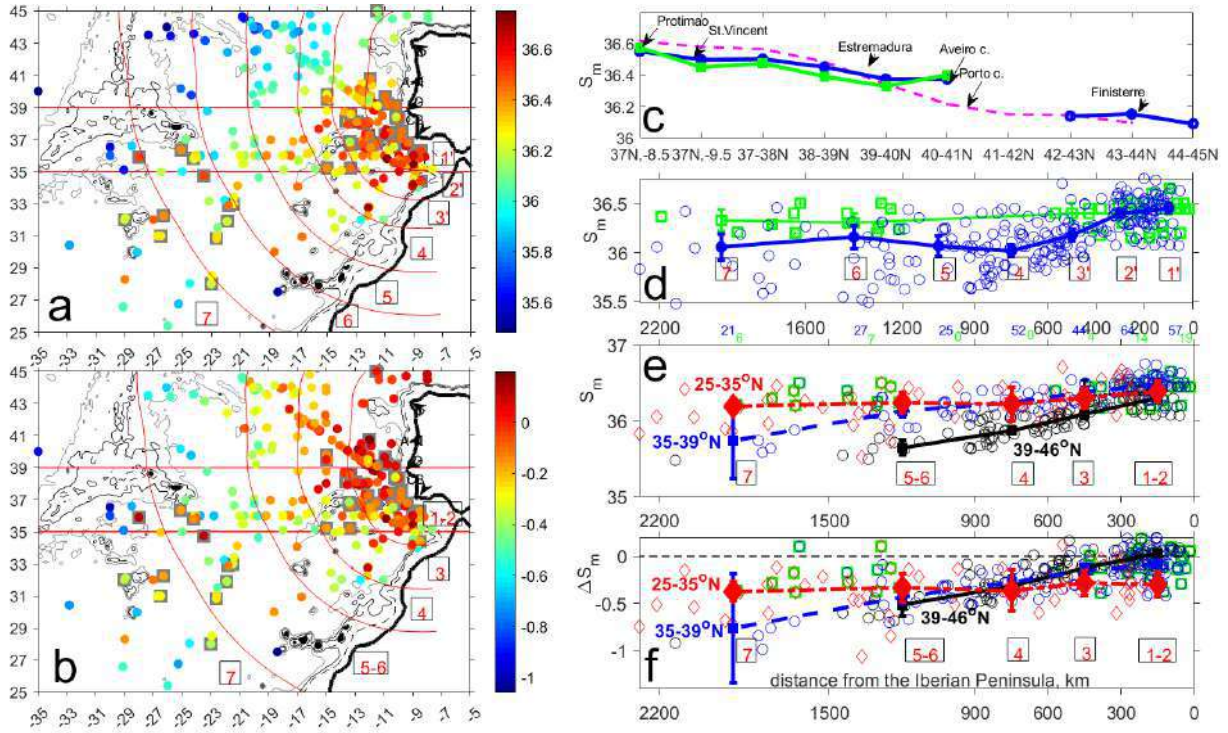

Fig. 4.17. Salinity in the meddy cores. ***(a)*** *Spatial distribution of meddy salinity maxima (S_m, color); circles represent meddies found in this study; gray squares are meddies according to literature.* ***(b)*** *The same as (a), but for the maximum salinity anomaly in the meddy cores relative to the nearest MUC point (ΔS_m).* ***(c)*** *Maximum salinity of the MUC (pink line) and S_m in meddy cores in a 100 km zone along the Iberian Peninsula: blue line is for data from this study, green line is for data from literature.* ***(d)*** *S_m as a function of distance from the Iberian Peninsula: blue line and blue circles are data from this study, green line and green squares – from literature.* ***(e)*** *S_m as a function of distance from the Iberian Peninsula in the three latitudinal bands marked in graph (a).* ***(f)*** *same as (e), but for salinity anomalies (ΔS_m). See the details in Fig. 4.14 (from Bashmachnikov et al., 2015c).*

Within the first 900 km from the Iberian Peninsula, salinity in meddy cores drops quite noticeably (Fig. 4.17d). Moreover, salinity (and its anomaly) decreases the most quickly along the Northern path, less quickly along the Central path, and remains almost unchanged south of the Azores Current (Fig. 4.17e,f). The first observation suggests an increased erosion of the cores of northern meddies. The second one confirms the assumption that only the strongest meddies cross the Azores Current. Such meddies can maintain a pronounced salinity anomaly of their cores for a longer time. At a distance of 1500 and 2200 km from the Iberian Peninsula, the accelerated decline in the core salinity along the Central path (Fig. 4.17e) indicates the beginning of the

accelerated meddy destruction, which, among other issues, is a consequence of meddies contacting with topographic rises of the Mid-Atlantic Ridge (Fig. 4.17a,b).

The meddies mergers within the first 600 km, revealed by the variability of eddy radii, is most clearly demonstrated with the change in the integral amount of salt in the meddy cores (S_v) as a function of distance from the Iberian Peninsula. With a Gaussian radial distribution of salt in Rayleigh eddies (see Section 1.3), the integral amount of salt in a meddy can be determined as (Bashmachnikov et al., 2014):

$$S_v = S_m \iint\limits_{|x|,|y|<\sqrt{2}R_m} e^{-x^2/(2R_m^2)-y^2/(2R_m^2)}dxdy \int\limits_{|z|<\sqrt{2}\,\delta h} e^{-z^2/(2\,\delta h^2)}dz = 0.5\,(2\pi)^{3/2}\,erf(1)^3 S_m\,h\,R_m^2 \sim$$

$$\sim 4.71\,S_m\,h\,R_m^2 \qquad (4.5)$$

Here $\delta h = h/2$ means half the thickness of the meddy core, and $erf(x) = \frac{2}{\pi}\int_0^x e^{-t^2}dt$ is the error function. The amount of salt in ϕ meddy core varies between 10^{10} - 10^{12} tons, averaging 1.4 10^{11} tons (Fig. 4.18a). This estimate is close to the estimate of 10^{10} -10^{11} tons by L'Hegaret et al. (2014), but exceeds estimate of 10^9 tons by Shapiro et al. (1996a,b). In the northern part of the region, S_v are higher than in the southern part. This reflects an increase in the meddy volumes (increase in R and h), which compensates for the decrease in S_m in meddy cores northwards in the study region (Fig. 4.18b). The westward increase in S_v north of the Azores Current within the first 600 km of the Iberian Peninsula (Fig. 4.18c,d) confirms that the meddy merger dominates over meddy breakup at these distances. In the literature, there are several documented observations of meddy mergers, all observed in this area (Schultz Tokos et al., 1994; Richardson et al., 2000; L'Hegaret et al., 2014). Further west, S_v decreases due to exchange of salt with the environment in meddy cores and splitting of meddies (Herbert et al., 1990). This goes especially fast in the north of the region (Figure 4.18d). A local increase in S_v south of the Azores Current (25-35°N) between 600 and 900 km presumably occurs due to the active movement of meddies along the southern edge of the Gorringe Bank and their further penetration to the south across the weaker stretches of the Azores Current (see Fig. 4.11, and also Armi et al., 1989, Richardson et al., 2000).

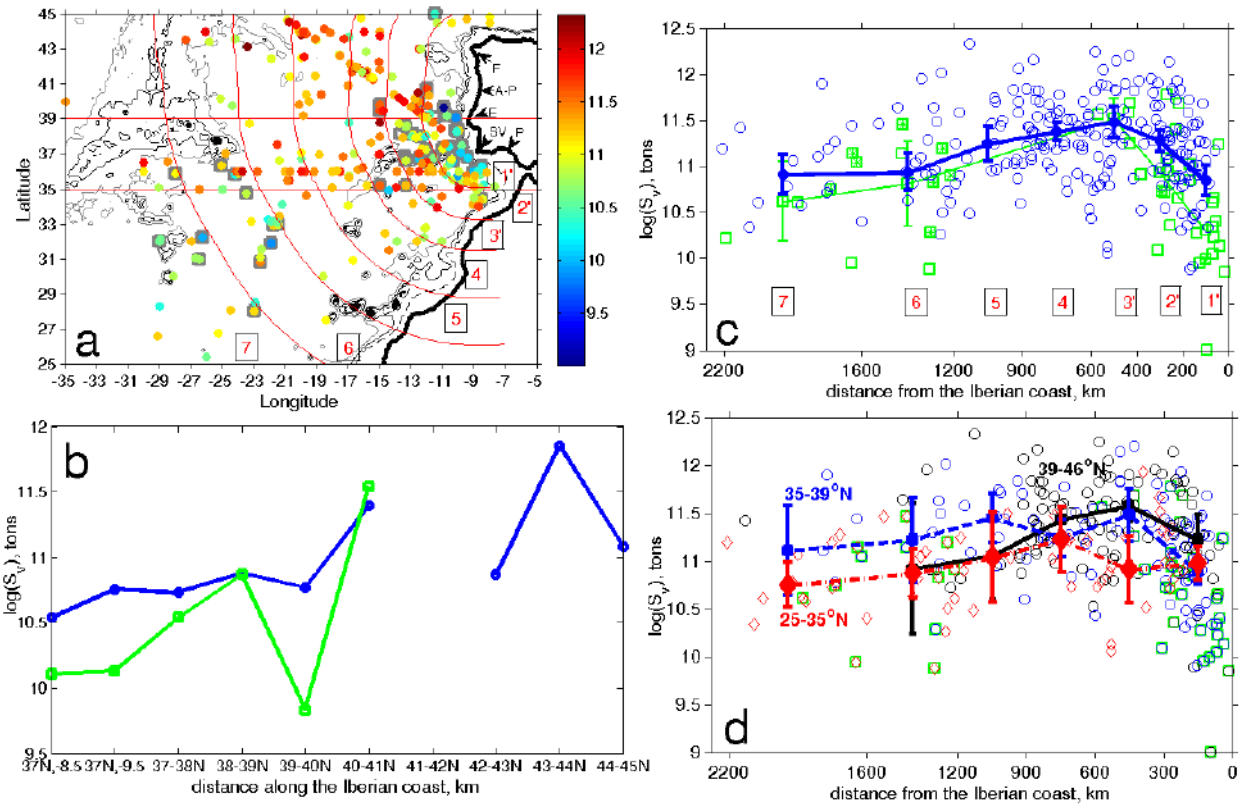

*Fig. 4.18. Logarithm of the amount of salt in meddy (S_v, tons). **(a)** Spatial distribution of S_v. **(b)** S_v along the Iberian Peninsula, within a 100-kilometer distance: blue line – data from this study, green – data from literature. **(c)** S_v as a function of distance from the Iberian Peninsula: blue line and blue circles are data from this study, green line and green squares – data from literature. **(d)** S_v as a function of distance from the Iberian Peninsula in three latitudinal bands. See the details in Fig. 4.14 (from Bashmachnikov et al., 2015c).*

4.3.3.4 DYNAMIC CHARACTERISTICS OF MEDDY CORES

The maximum azimuthal velocity in the meddy cores (v_θ) can be determined for the relatively small subset of meddies that were tracked using RAFOS floats (Fig. 4.9). Because RAFOS remain inside a meddy long enough, only if they are far within the meddy core, then the azimuthal velocity estimated from the floats will, in general, be less than v_θ. This determines v_θ to be somewhat underestimated compared to that described in literature (Fig. 4.19).

Having a fairly significant dispersion, v_θ averages 20 cm s^{-1}, reaching 30-40 cm s^{-1} in some meddies. Near the Iberian Peninsula, the most intensively rotating meddies are observed off Extremadura Promontory (Fig. 4.19a,b). Within the first 600 km from the coast, v_θ decreases twofold (Fig. 4.19c). This is consistent with the assumption of meddy merger, during which the radius increases and the h/R ratio decreases. As a consequence, azimuthal density gradients decrease and v_θ decreases. At a bigger distance from the coast, on the contrary, the azimuthal velocity has a slight tendency to increase away from the meddy generation region. This is consistent with a faster reduction in the horizontal meddy dimension compared to the vertical one when meddies are decaying by horizontal intrusions in the meddy skirts (see also Hebert et al., 1990). South of the Azores Current, the meddies are generally less intense than north of it (Figure 4.19d). Previously it was said that only the most intense meddies cross the Azores Current,

however, when crossing the current, meddies lose some of their mass and kinetic energy, as was, for example, observed for meddy Ceres (Richardson and Tychensky, 1997; Filyushkin et al., 2002; Bashmachnikov et al., 2014).

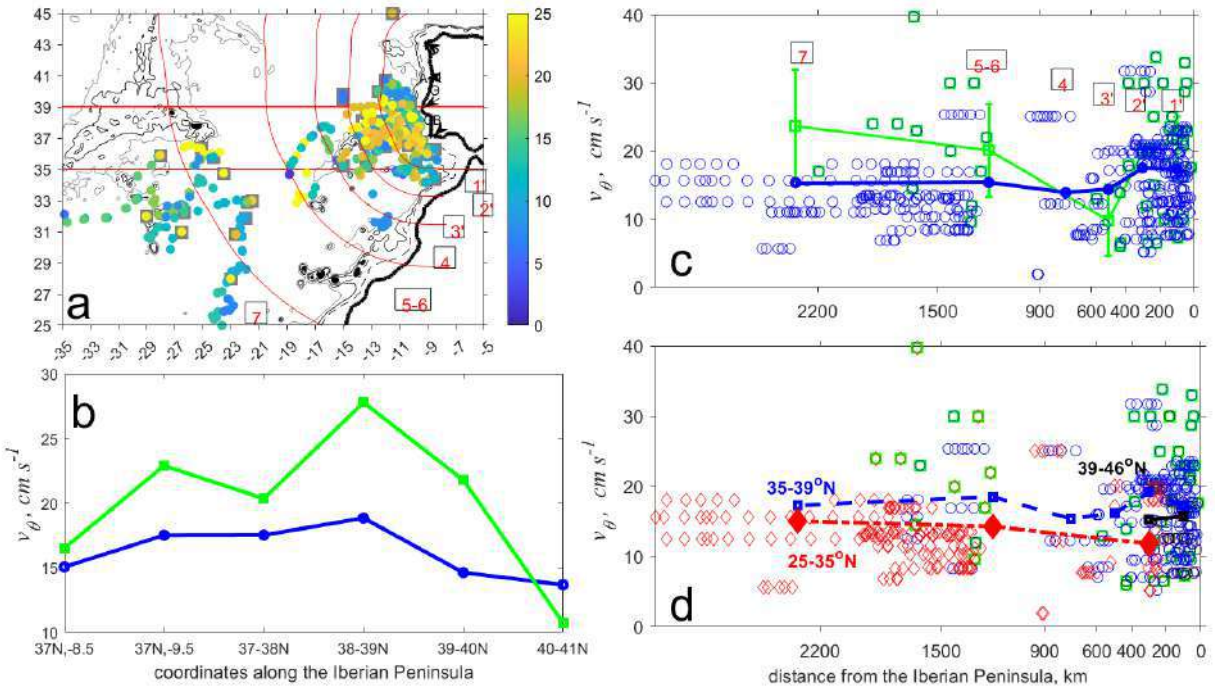

*Fig. 4.19. The maximum azimuthal velocity in meddy cores v_θ (cm s^{-1}). **(a)** Spatial distribution of v_θ. **(b)** v_θ along the Iberian Peninsula, within a 100-kilometer distance: blue line – data from this study, green – data from literature. **(c)** v_θ as a function of distance from the Iberian Peninsula: blue line and blue circles - data from this study, green line and green squares – data from literature. **(d)** v_θ as a function of distance from the Iberian Peninsula in three latitudinal bands. See details in Fig. 4.14 (by Bashmachnikov et al., 2015c).*

RAFOS float data allows determining the rotation period of the meddy core (τ) and estimating Rossby number:

$$Ro = \frac{2\pi}{f\tau}, \tag{4.6}$$

which is the ratio of the relative vorticity of the meddy core to the Coriolis parameter. *Ro* allows one to estimate the degree of eddy nonlinearity.

The results obtained (Fig. 4.20) were compared with literature estimates, where the Rossby number was computed as:

$$Ro = \frac{v_\theta}{fR}. \tag{4.7}$$

Ro calculated from observations and literature were of the same order of magnitude, on average, 0.14 with the maximum values close to 0.30 (Fig. 4.20 b,c). Small *Ro* values characterize

quasi-geostrophic long-lived eddies (Carton, 2001). In general, the large-scale variability of *Ro* was determined by its inverse proportionality to meddy radii and, to a lesser extent, by the variability of v_θ. In the meridional direction, Rossby numbers are minimal in the north of the Iberian Peninsula (Fig. 4.20b), due to the inverse dependence of *Ro* on *f* and *R* with an almost constant v_θ. With distance from the meddy generation region, the generally high values of *Ro* for newly formed meddies decreased rapidly with distance from the Iberian Peninsula, within the first 200-600 km (Fig. 4.20c). This behavior is in agreement with the dominant meddy merger at the initial stage of their evolution. With the subsequent slow dissipation starting from the periphery of meddy cores at greater distances, *Ro* began to grow slowly. This indicates an increase in the nonlinearity of the vortices and contributes to the growth of their dynamic instability with distance from the Iberian Peninsula.

Eddy Burger number:

$$Bu = \nabla^2\psi \Big/ \frac{f^2}{N_m^2}\frac{\partial^2\psi}{\partial z^2} \sim \left(\frac{N_m\, h}{f\, R}\right)^2 \qquad (4.8)$$

is the ratio of the relative vorticity to the degree of isopycnal deformation in the eddy core, i.e. ratio of kinetic to available potential energy of an eddy (Cushman-Roisin and Beckers, 2011).

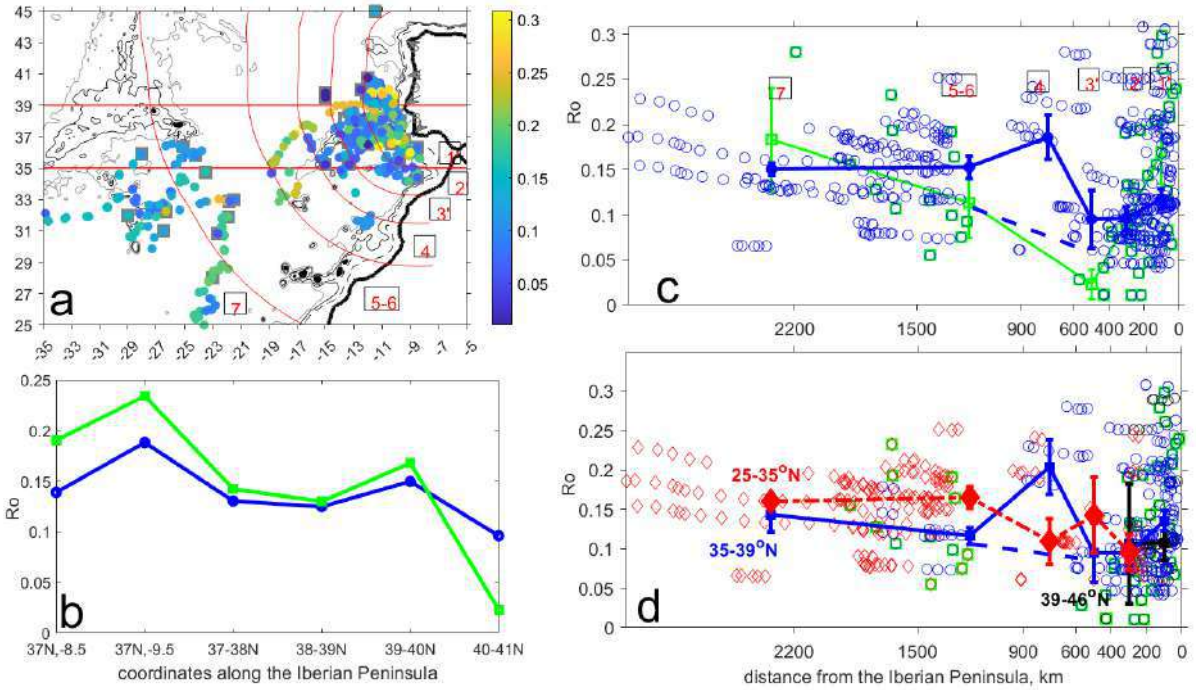

*Fig. 4.20. Rossby number of meddy cores Ro. **(a)** Spatial distribution of Ro. **(b)** Ro along the Iberian Peninsula, within a 100 km distance: blue line – data from this study, green – data from literature. **(c)** Ro as a function of distance from the Iberian Peninsula: blue line and blue circles are data from this study, green line and green squares – data from literature. **(d)** Ro as a function of distance from the Iberian Peninsula in three latitudinal bands. The outlier along the Central path at 600-900 km is associated with observations of only 2 meddies (see panel (a)). See Fig. 4.14 for more details (according to Bashmachnikov et al., 2015c).*

Expression (4.8) is equivalent to another definition used: $Bu' = \left(\frac{Rd}{R} \right)^2$, where $Rd = \frac{N_m h}{\pi f}$ is the first baroclinic Rossby radius of deformation for meddies, where N_m is the buoyancy frequency in the meddy cores.

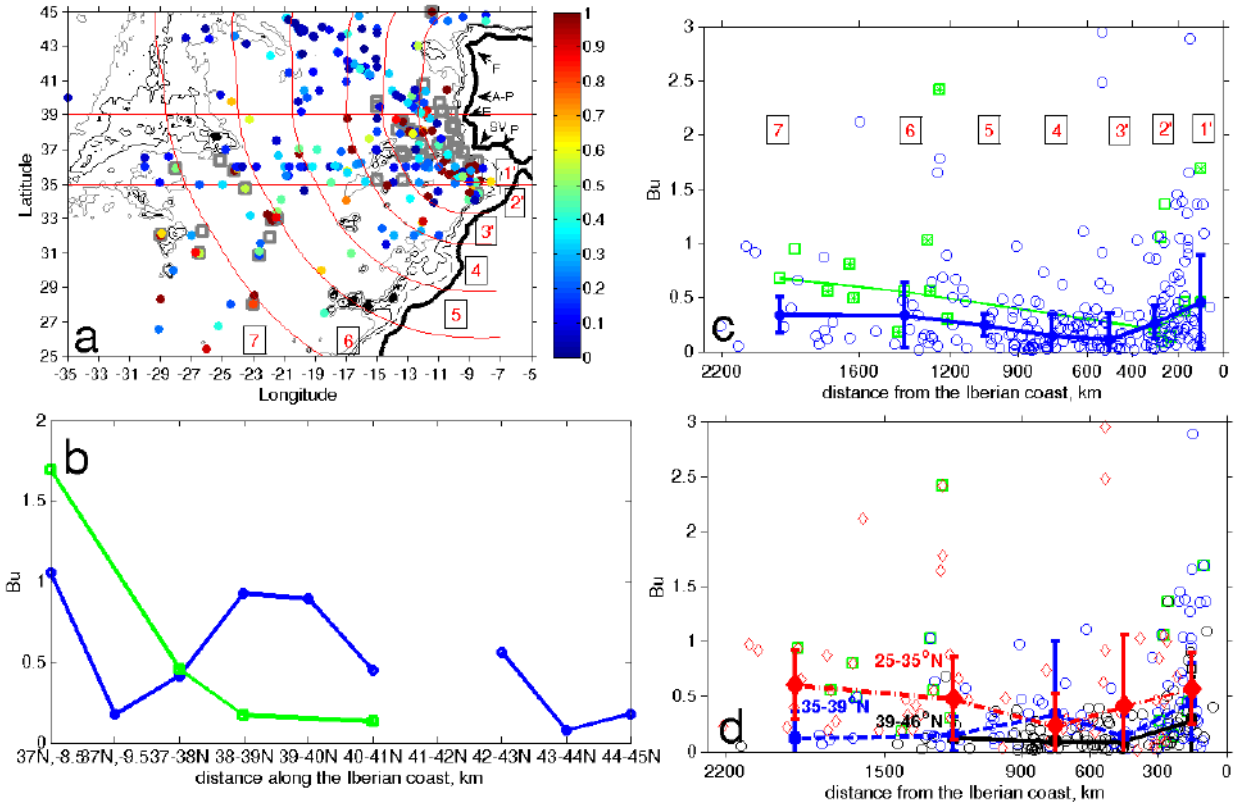

*Fig. 4.21. Burger number of meddy cores (Bu). **(a)** Spatial distribution of Bu. **(b)** Bu along the Iberian Peninsula, within a 100 km distance: blue line – data from this study, green – data from literature. **(c)** Bu as a function of distance from the Iberian Peninsula: blue line and blue circles are data from this study, green line and green squares – data from literature. **(d)** Bu as a function of distance from the Iberian Peninsula in three latitudinal bands. See Fig. 4.14 for more details (according to Bashmachnikov et al., 2015c).*

The average *Bu* for meddies across the region is 0.47 (Figure 4.21), indicating a greater relative role for potential energy and significant core stability. Following changes in *Rd*, *Bu* decreases northwards along the Iberian margin (Fig. 4.16b). The corresponding decrease in the relative role of kinetic energy in the formation of the potential vorticity anomaly corresponds to a decrease in the MUC velocity from 20 cm s^{-1} at Cape Saint Vincent (Ambar and Howe, 1979a,b; Bower et al., 2002) to 6-8 cm s^{-1} north of Extremadura Promontory (Daniault et al., 1994). With distance from the coast, within the first 600 km, a decrease in the *h/R* ratio (Fig. 4.16c) due to meddy merger leads to a decrease of *Bu* (Fig. 4.21c). Thus, mergers increase the dynamic stability of the meddy cores. Further to the west, *Bu* begins to grow slowly following an increase in *h/R*, and also due an increasing stratification anomaly of the meddy cores (Fig. 4.22). This trend is pronounced south of the Azores Current. It is confirmed by more than two years of observations of the evolution of meddy Sharon (Fig. 4.9), for which it was observed a more rapid decrease in

the horizontal dimensions of the core, compared to the vertical one, as well as a more rapid decrease in the eddy kinetic compared to the available potential energy (Hebert et al., 1990; see also Menesguen et al., 2012).

South of the Azores Current, where there those meddies that could cross this jet, *Bu* increases sharply. This can be interpreted as a result of the partial loss of meddy skirts (a decrease in *R*) on the shear flow, which has been repeatedly observed in numerical experiments (Maksimenko and Orlov, 1991; Menesguen et al., 2012; Sokolovskiy et al., 2013).

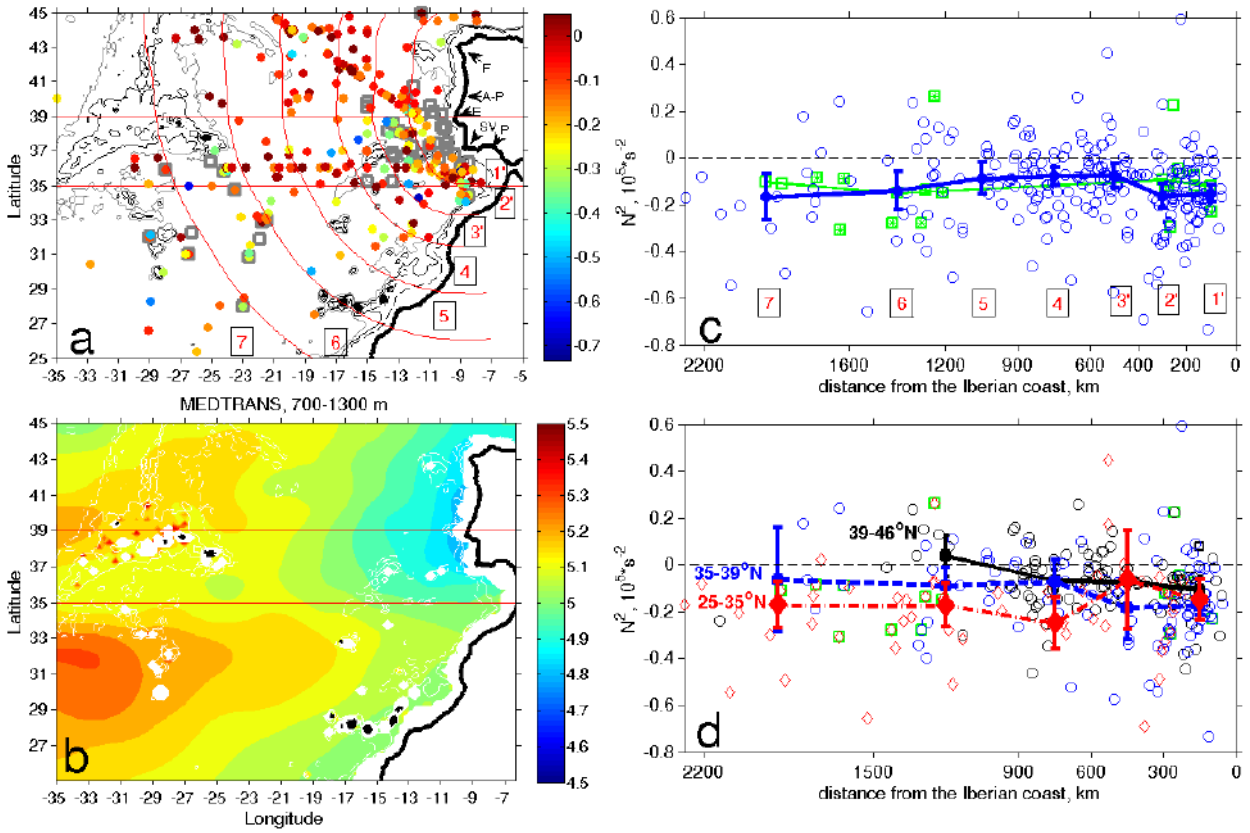

Fig. 4.22. *Anomaly of the buoyancy frequency in meddy cores relative to the nearest climatological values in the MW layer ($\Delta N^{2} = N_m^2 - N_0^2$, 10^5 s^{-2}). **(a)** Spatial distribution of ΔN^2 **(b)** climatological value of N_0^2 (10^5 s^{-2}) in the 700-1300 m layer, from MEDTRANS climatology. **(c)** ΔN^2 as a function of distance from the Iberian Peninsula: blue line and blue circles – data from this study, green line and green squares – data from literature. **(d)** ΔN^2 as a function of distance from the Iberian Peninsula in three latitudinal bands. See Fig. 4.14 for details (from Bashmachnikov et al., 2015c).*

The long-term survival of meddies as isolated structures is associated with their inherent strong anomalies of potential vorticity (*dP)* in their cores (Carton, 2001):

$$d\Pi = \frac{N_m^2}{g}(\omega + f) - \frac{N_0^2}{g} f \approx \frac{(N_m^2 - N_0^2) f}{g}, \qquad (4.9)$$

where N_m^2 characterizes stratification in a meddy core, N_0^2 characterizes stratification of the background at the level of the meddy core from MEDTRANS climatology (Bashmachnikov et al., 2015a). Meddy cores are initially characterized by an anomalously low N_m^2, which is associated with a weak stratification in the MUC. This anomaly is known to persist even at distances one-two

thousand kilometers from the Iberian Peninsula (Tychensky and Carton, 1998; Benilov et al., 2020). Observations show that the peak relative vorticity of meddies cores $|\omega|<<f$ (Fig. 4.20). Therefore, taking into account the weak variability *of* N_m^2, *dP* is determined mainly by the spatial variability *of* N_0^2 (Fig. 4.22 a, b).

To the north of the Azores Current, N_0 at the mid-depths is less than to the south (Fig. 4.22b). Indeed, Fig. 4.22(c,d) shows that, on average, south of the Azores Current, ΔN^2 remains almost constant (about -0.2), while along the Central path (35-39°N) ΔN^2 decreases at least two times at a distance of 600-900 km from the Iberian Peninsula (Fig. 4.22d). This is due to the westwards increase of N_0, which compensates for the decrease in N_m associated with the exchange between meddy cores and the environment. This results in meddies remaining stable, in spite of a growth of *Bu*, also south of the Azores Current. Along the Northern path (north of 39°N), having initially low values, ΔN^2 approaches zero already at a distance of about 1000 km from the Iberian Peninsula, despite some (significantly weaker than in the south) increase in N_0 to the west. Therefore, we can expect that most northern meddies decay much faster than the southern ones.

From dynamic considerations, one should expect a negative anomaly of potential vorticity in anticyclonic eddies, such as meddies. Meanwhile, Fig. 4.22(c,d) shows that 45 meddies (about 18%) have positive values of ΔN^2. This does not automatically mean a positive *dP* anomaly since the approximate expression (4.9), plotted in Figure 4.22, does not takes into account the contribution of the anticyclonic relative vorticity $N_m^2/g\,\omega$. Assuming a Rayleigh radial profile of the azimuthal velocity in meddies, the peak values of the relative vorticity (Bashmachnikov and Carton, 2012): $\omega = 2\sqrt{e}\,v_\theta / R_{vm}$. Here R_{vm} is the distance from the center of the meddy, where the azimuthal velocity reaches its peak value v_θ. Without data on v_θ for most of the meddies, its characteristic value v_θ= -20 cm s^{-1} is used (Fig. 4.19). For the full formula for *dP* in expression (4.9), only 8 meddy cores (3%) have positive adjusted *dP* values, within the calculated error in determination of *dP* of 5×10^2 m^{-1} s^{-1}. These cases can be met by meddies with exceptionally strong rotation or with a non-Rayleigh radial distribution of their azimuthal velocity. Thus, for two meddies described in the literature, Ulla and Encelade with $\Delta N^2 > 0$ (two green squares in Fig. 4.22c,d above the dashed line), observations indicate negative *dP* in their cores (Tychensky and Carton, 1998, Paillet et al., 2002).

4.3.3.5 INTERACTION OF MEDDIES WITH SEAMOUNTS

In situ observations suggest that interaction with the irregularities of bottom topography can be an effective mechanism for an eddy decay (including meddies) and can result in their complete destruction (Zhurbas et al., 1991; Shapiro et al., 1996a; Richardson and Tychensky, 1998; Bashmachnikov et al., 2009b; Cenedese, 2002; Filyushkin et al., 2011; Bashmachnikov and Carton, 2012; Sokolovskiy et al., 2013).

Bashmachnikov et al. (2009b) analyzed the results of the interaction of meddies with two seamounts: Sedlo (near the MAR, north of the Azores) and Sein (in the Iberian Basin, near the Iberian Peninsula) using repeated *in situ* surveys and data from moorings (Fig. 4.23). Meddies were tracked both using *in situ* observations and from their sea surface manifestations using satellite altimetry data (see Chapter 6).

Near Sedlo seamount, there was recorded a meddy with a radius of about 50 km, which had the core center at 900 m, the vertical core thickness of 400 m, and the maximum salinity

anomaly in the core of about 0.4. To estimate the amount of salt transported by the meddy, it was represented by an ellipsoid with a homogeneous core, where the salinity anomaly was constant and equal to 0.4, being 15% of the total meddy volume. Outside the core, the anomaly decreased linearly to zero at a distance of 200 m from the center of the core vertically and within a radius of 50 km horizontally. The total amount of salt in the meddy was estimated at 4 10^8 tons (the same order as for the 1-2 year old meddy in the study by Armi et al., 1989). The meddy interacted with the southeastern peak of the Sedlo seamount at a depth of 780 m. The meddy's path was assessed using *in situ* observations and its trace at the sea surface from AVISO satellite altimetry data. The results of the meddy interaction with the seamount were assessed from changes in the background salinity at the mid-depths at the southeastern peak of the Sedlo, using surveys from July 2003 (before the collision of the meddy with the seamount), November 2003 (during the collision) and July 2004 (after the collision) (Fig. 4.23b-4.25).

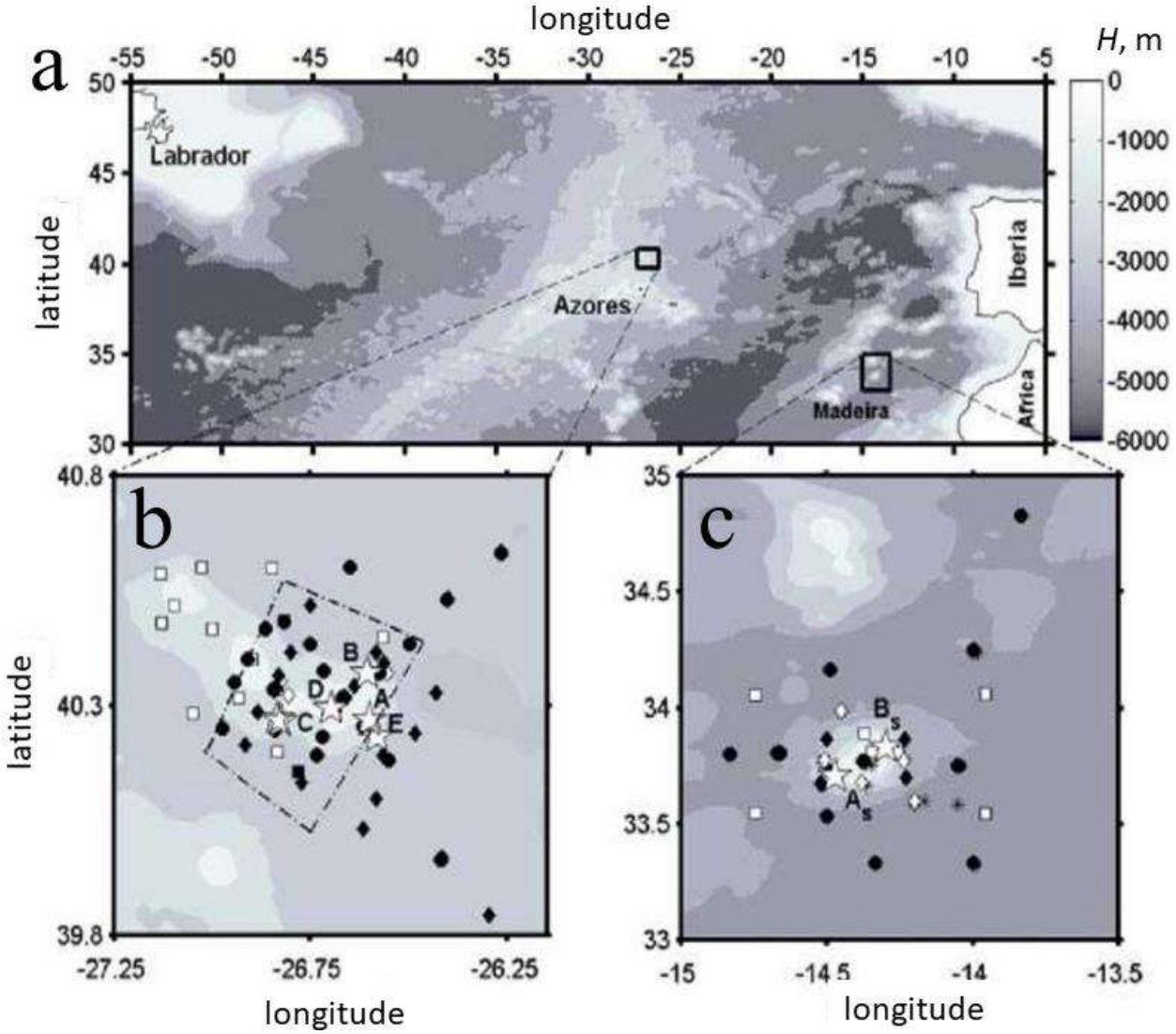

Fig. 4.23. In situ observations at the Sedlo and Sein seamounts: (a) study areas in the subtropical North Atlantic; stations of in situ observations in the vicinity of (b) Sedlo Seamount, (c) Sein Seamount. Color indicates bathymetry (m). The locations of the moorings are marked with stars and designated with letters (A, B, etc.). Symbols (squares, circles and diamonds of different colors) mark the locations of vertical casts of various in situ surveys of 2003-2005 (from Bashmachnikov et al., 2009b).

Observations indicate two contacts between the meddy and Sedlo seamount during the study period (Fig. 4.24). The first contact of the eddy with the seamount was registered from mid-May to the end of June 2003. During its closest approached to Sedlo, meddy was approximately 200 km from its southeastern summit (Fig. 4.24a). Salinity at mooring *C*, after some increase during the period of the maximum approach of the meddy to the seamount, latter decreased to its original values (Fig. 4.25). This suggests that the interaction of the meddy with the seamount did not result in any noticeable loss of salt from the eddy core. During the second collision with Sedlo in September-November 2003 (Fig. 4.24b), the meddy approached the Sedlo from the south, being pushed towards the seamount by a northerly background current. For some time meddy was registered above the southeastern peak of Sedlo, and then it moved southwestwards. During this period, a significant increase of salinity at all moorings was registered, which persisted even after the meddy left the seamount (Fig. 4.25).

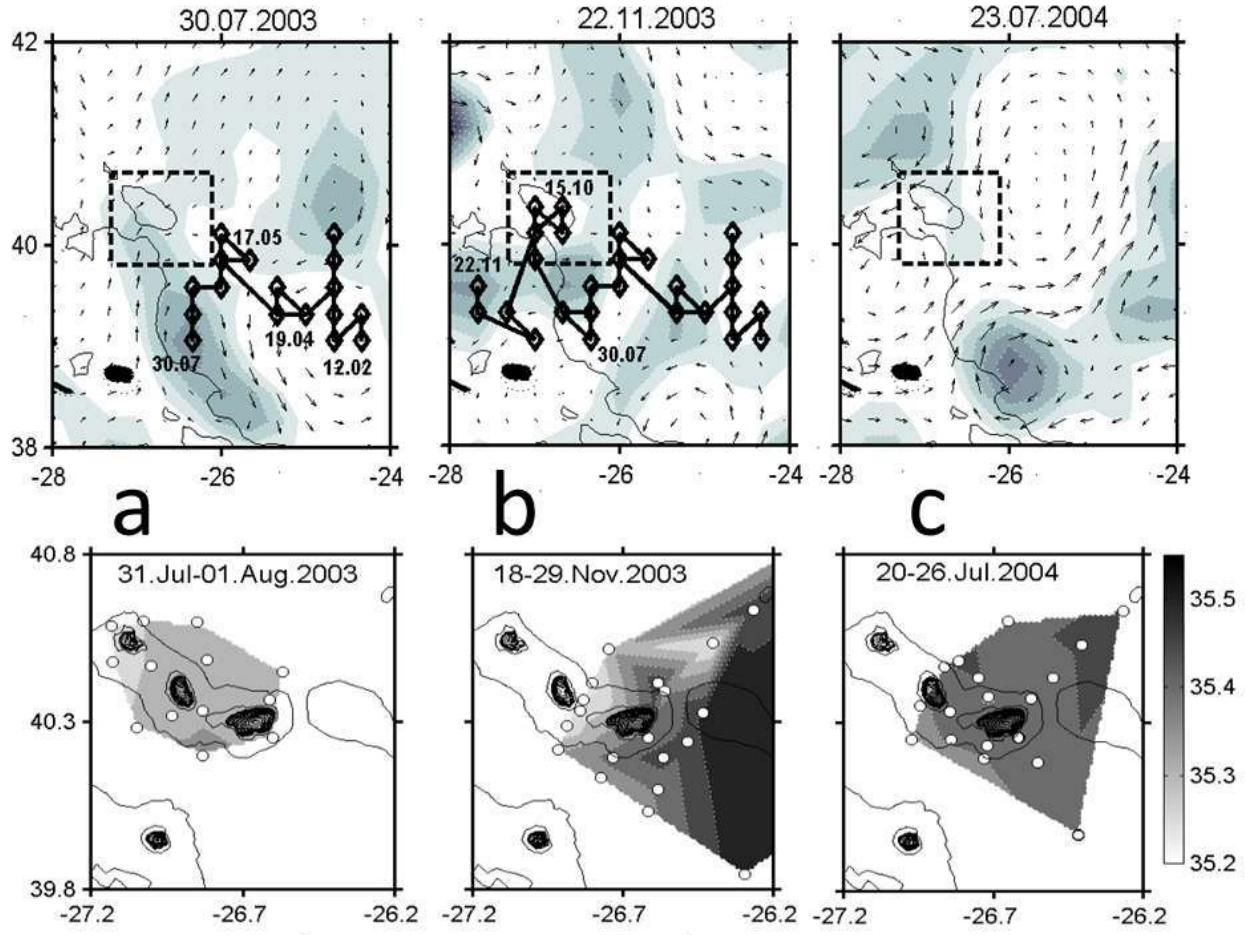

Fig. 4.24. The upper panels (a), (b) and (c) show relative vorticity and currents derived from AVISO datasets for the periods of in situ surveys. The latter are shown in the lower panels. Relative vorticity varies from -2 10^{-5} c^{-1} to 0; and dark color corresponds to negative vorticity values. The black line with diamonds marks the trajectory of the meddy at the sea surface; thin solid line – 2000 m isobath. Dashed rectangles indicate the area in situ surveys. The lower panels (a), (b) and (c) show the distribution of salinity at the 900 m according to vertical casts (in situ stations are shown with white dots).

In situ surveys immediately after this interaction recorded several relatively small anticyclonic eddies (with a radius of less than 10 km) with increased salinity in their cores (Fig. 4.24b), which disappeared with time. At the same time, the average salinity around the top of the seamount, at 800-1100 m depth, increased by approximately 0.2 units (Fig. 4.24c), and the dominant anticyclonic vorticity above the top was temporally replaced by a cyclonic one (Mohn et al., 2009). The increase in salinity in the vicinity of the peak of Sedlo is interpreted as a result of a partial decay of the meddy core during its interaction with the seamount (Bashmachnikov et al., 2009b).

The increase in salinity was recorded in a layer 300 m thick over an area of 75 km^2, which allows estimating the increase in salt content around the southeastern peak of Sedlo seamount as 1 10^8 tons. This forms 20-25% of the total salt content in the meddy before hitting the seamount. The analysis showed that the result obtained was weakly dependent on the choice of the volume of the inner homogeneous meddy core, but was sensitive to the assessment of the maximum salinity anomaly in the core. If the initial peak salinity anomaly in the meddy was in the range of 0.3-0.6 units, then a meddy mass loss varies between 15 and 30%. This volume loss during meddy interaction with the seamount is consistent with the data of numerical experiments by Wang and Dewar (2003), as well as with model data of Filyushkin et al. (2014).

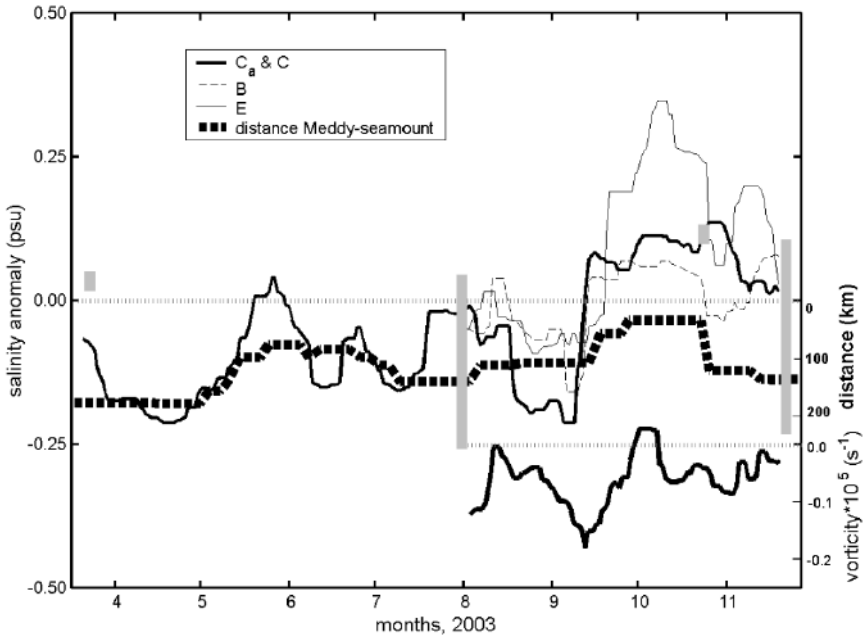

Fig. 4.25. Time series of salinity anomalies (smoothed by a 9-day median filter) over the Sedlo seamount from moorings C_a/C, B and E in the 800-900 m layer (Fig. 4.23b). The thick dotted line shows the distance (km, right scale) between the southeastern summit of Sedlo seamount and the center of the meddy (see Fig. 4.24). The meddy center was defined as the local minimum of the relative vorticity over the meddy, tracked with AVISO altimetry data. The thick black solid line in the lower right sector of the figure and the right vertical scale at the bottom correspond to the variability of the 9-day median relative vorticity (s^{-1}), estimated from the current meters in the triangle of the moorings A, B and C (Fig. 4.23b). The timings of the field surveys are plotted as gray vertical lines. The vertical extent of each line corresponds to the range of salinity anomalies near the seamount in the 800-900 m layer detected during the survey.

Sein seamount (the depth of the mountain top is 170 m with a surrounding ocean depth of about 2000 m) showed no indirect evidence of any significant loss of meddy mass after the collision, despite the close and rather prolonged contact. Analysis of observations suggested that the meddy made one or more revolutions around the seamount (Fig. 4.26). After the meddy had detached from the seamount, no traces of an increase in background salinity at mid-depth levels were recorded in the vicinity of the seamount. This was interpreted as a sign of preservation of the original mass of salt in the meddy.

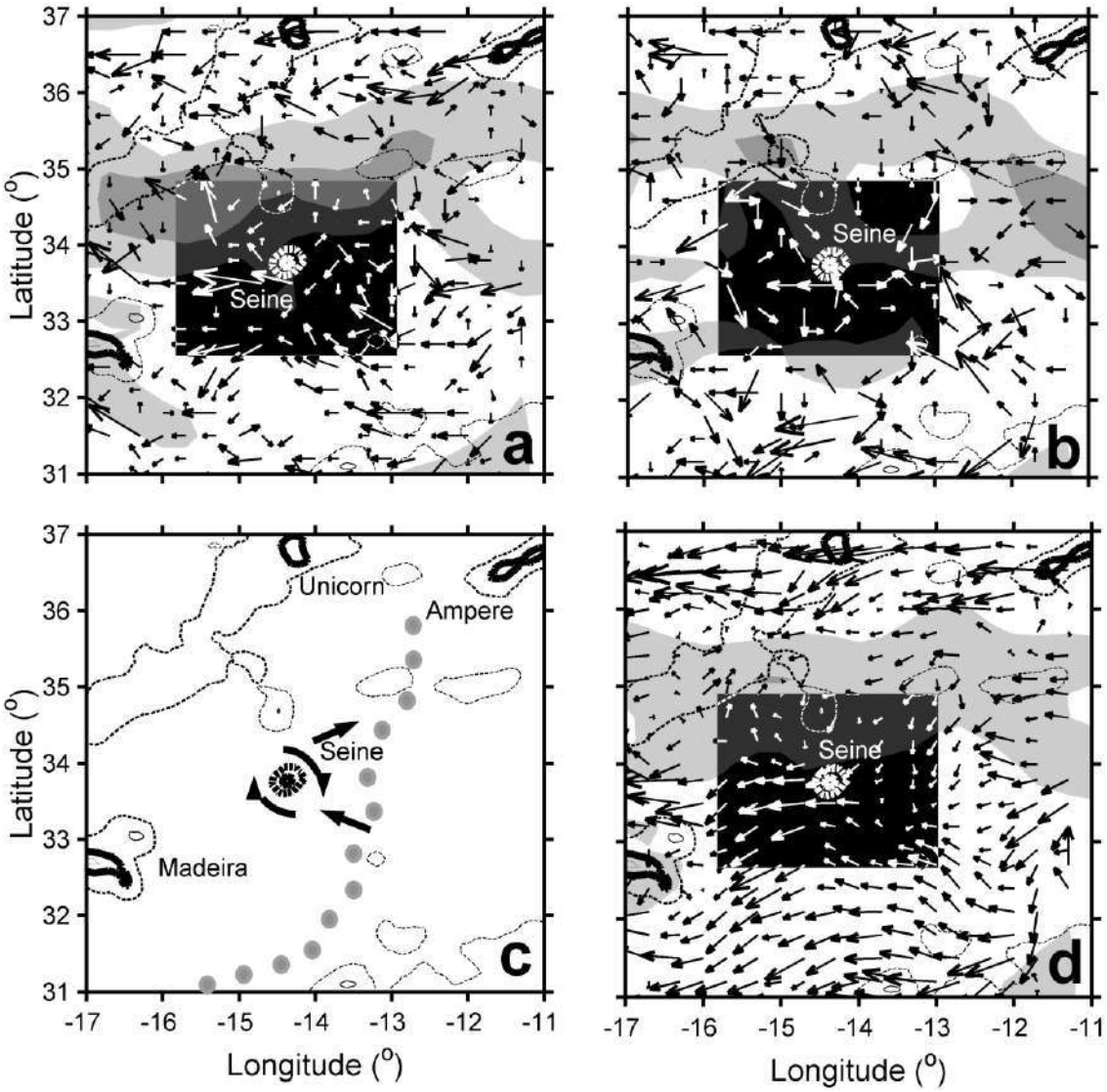

Fig. 4.26. Directions of translations of relative vorticity minima at the sea surface in the vicinity of Sein seamount from AVISO satellite altimetry (a) in April 2003-August 2004 (when a meddy was observed near the seamount) and (b) from January to December 2005. Black transparent rectangles show the areas of vector rotation of eddies around the seamount. (c) Schematic illustration of the meddy movement from March 2003 to July 2005 (gray arrows). (d) Directions of translations of relative vorticity minima at the sea surface for January 2003 - December 2005, smoothed by a 4th order Savitsky-Golay filter with a 5-point window.

Different meddy behavior at Sedlo and Seine seamounts may be due to several factors. At Sedlo seamount, meddy interacted with its summit located at the level of the meddy core, which

determined an active interaction of the meddy with the topography and with an enhanced circulation over the top of the seamount (Ciani et al., 2017). At Sein seamount, the meddy interacted with the slope of the mountain, which usually does not lead to significant mass effects from eddy cores (Wang and Dewar 2003; Filyushkin et al., 2011). The larger horizontal dimensions of Sedlo seamount also contributed to its more intense impact on the eddy core (Van Geffen and Davies, 2000; White et al., 2007). A more intense interaction was also facilitated by a more intense dynamics in the area of the top of the seamount, compared to its slope, associated both with the interaction of the seamount with the impinging flow, and with enhanced tidal motions and internal waves (White et al., 2007; Mohn et al., 2009; Bashmachnikov et al., 2013 a). And finally, Sedlo seamount is situated much further from the areas of meddy generation than Sein. Therefore, seamounts of this area are interacting with meddies of a greater age. Comparison of number of meddies crossing the seamount chains of the Iberian basin and the MAR indicate that old meddies are much more likely to disintegrate when interacting with underwater topography than young meddies (Richardson et al., 2000).

4.3.4 LIFECYCLES OF NORTHERN AND SOUTHERN MEDDIES

Meddies form as a result of instability of the Mediterranean Undercurrent (MUC) along the continental slope of the Iberian Peninsula (Prater and Sanford, 1993; Richardson et al, 2000; Serra and Ambar, 2002, etc.), most actively south of Extremadura Promontory (Fig. 4.2). This follows from approximately 3 times the occurrence of meddies in the immediate vicinity of the Iberian Peninsula between the Portimao Canyon and Extremadura Promontory, compared with the areas of the Porto-Aveiro Canyons (Cherubin et al., 1997), Cape Finisterre and the Galician Bank (Paillet et al., 2002; Carton et al., 2002; Demidov et al., 2012). This ratio is probably even higher because the meridional variations of meddy properties and the trajectories of some meddies indicate that many of the meddies recorded north from the Extremadura Promontory came here from the southern part of the Iberian Peninsula.

The meridional variability of meddy characteristics along the Iberian Peninsula quite closely follows the variability of the corresponding characteristics of the MUC from Cape Saint-Vincent to Cape Finisterre (number of cores, S_m, ΔN^2, H), which indicates a predominantly local origin of meddies, registered near the Peninsular. The meridional change in the salinity of meddy cores corresponds to that along the MUC and is, on average, 0.1 unit less than the salinity of the closest position of the MUC. This is a consequence of the capture of some amount of surrounding water by meddy core during their formation. The vertical extent of newly formed meddies reaches its maximum between 38°N and 41°N, and then decreases, which is also controlled by a corresponding change in the vertical extent of the MUC (Bashmachnikov et al., 2015a,c). Strong mixing of the MUC waters at the initial stage of its formation, when the flow of Mediterranean waters runs down the continental slope in the immediate vicinity of the Strait of Gibraltar (Baringer and Price, 1997), determines an anomalously weak stratification of meddy cores. Downstream, from Cape Saint Vincent to Cape Finisterre, the stratification of the MUC increases by a factor of 3-4 (Daniault et al., 1994) and approaches stratification for surrounding waters at intermediate depths. This reduces the potential vorticity anomaly of the meddies and decreases stability (Benilov et al., 2020) of meddies formed along the northern part of the Iberian Peninsula, compared to the southern part.

Numerical experiments show that, due to the stabilizing influence of the planetary or topographic β-effects, the characteristic radii of the resulting eddies should be slightly larger than the baroclinic Rossby radius of deformation (McWilliams, 1985; D'Asaro, 1988; Aiki and Yamagata, 2004; Cherubin et al., 2007; Cushman-Roisin and Beckers, 2011). Due to their intrathermocline nature, meddies should have radii of the order of the second Rossby radius of deformation (Rd_2), which decreases from 13 km in the south to 10 km in the north of the Iberian Peninsula (Chelton et al., 1998). In the southern part, this is in good agreement with the observed radii of newly formed meddies obtained from literature (Fig. 4.14). However, the pronounced tendency for meddy radii to increase along the Iberian Peninsula from 12 to 40 km (130% of the average value) contradicts both the theory and the observed decrease of the MUC cross-section to the north. Observations show that in the northern direction the h/R ratio decreases by half, from 0.04 at the southern tip of the Iberian Peninsula to 0.02 at the northern one, while according to the theoretical relationship (4.10) it should, on the contrary, increase (Hassanzadeh et al., 2012):

$$h/R = f\sqrt{Ro/(N_0^2 - N_m^2)}. \qquad (4.10)$$

In the northern direction, the stratification anomaly in the meddy cores (N_0^2 - N_m^2) decreases from 1.8 to 1.2 $\times 10^{-6}$ s^{-2} (by 40% of its average value), as well as Ro, from 0.15 to 0.10 (by 40%). With an increase in f from 8.7 to 10.1 $\times 10^{-5}$ s^{-1} (by 16%), the theoretical ratio of the vertical to horizontal dimensions of the meddies should have increased from 0.025 to 0.028 (by 10-15%). Presumably the observed trends in R and h/R are the result of the early meddy evolution. During the process of geostrophic adjustment, vertical flattening of eddies often occurs, accompanied by the energy loss via radiation of internal waves (McWilliams, 1988). An increase in kinetic energy in northern meddies during their formation means a sharp decrease in their potential energy compared to southern meddies, i.e. a stronger vertical flattening of the northern meddies, which was mentioned above in relation to their anomalously small values of h/R. This should lead to acceleration of their cores. In fact, south of Extremadura Promontory the peak azimuthal velocity in meddy cores v_θ ~15-20 cm s^{-1}, which is comparable to the current velocity in the MUC of slightly more than 20 cm s^{-1} (Ambar and Howe, 1979a,b; Bower et al., 2002a), while north of Extremadura Promontory meddy v_θ~15 cm s^{-1}, which significantly exceeds the local MUC velocity of 5-8 cm s^{-1} (Daniault et al., 1994).

From the regions of their generation, meddies spread mainly westwards (Fig. 4.12), retaining the features of their characteristics of the regions of their formation near the Iberian Peninsula. From the Gulf of Cadiz and the Iberian Basin, the most intense meddies also spread southwestwards, crossing the Azores Current along its entire length and losing part of its mass and energy during this crossing.

According to their characteristics associated with their generation and the initial stage of evolution, meddies can be divided into two groups: northern and southern. The southern meddies often have two cores, while this is rare for the northern meddies. The southern meddies, in comparison with the northern ones, are more compact (average radius of about 30 km versus 50km for the northern meddies), have greater vertical thickness (800 m versus 600 m for the northern meddies), greater salinity of the core (on average by 0.3 units, compared to the northern meddies), greater dynamic stability (about 3 times the buoyancy frequency anomaly in the core compared to the northern meddies) and a slightly higher rotation current velocity of their cores. The observed meridional variability *of Bu* shows that the buoyancy frequency anomaly plays a leading role in

the formation of the potential vorticity anomaly of the northern meddies, despite even some acceleration of their rotation during the flattening in course of their formation. For the southern meddies approximately the same contribution of rotation and buoyancy anomaly in *dP* is observed. which indicates that they captured part of the kinetic energy of the MUC. However, the ongoing merger of the southern meddies in the Iberian Basin leads to a decrease in their rotation velocity and an increase in the stability of those meddies that have passed through this process. The average lifespan of such meddies is from 1 to 2 years. The most probable reason for destruction of the southern meddies is their collision with seamounts and other topographic rises. The destruction of the northern meddies usually occurs over relatively deep regions of the oceanic basin, before they approach the MAR. It can be assumed that the destruction of the northern meddies occurs as a result of growth of instability inside their cores, which is especially intensified when meeting the southern branch of the North Atlantic Current (Fig. 2.7a). In fact, the number of northern meddies (north of 41°N) sharply decreases to almost zero already after passing 25°W (Fig. 4.8a), where a branch of the North Atlantic Current is registered, while the 2000 m isobath of the eastern slope of the MAR at these latitudes is positioned approximately at 30°W.

4.4 DISCUSSION OF THE RESULTS OF CHAPTER 4

This chapter provides a description of the relative concentration of the Mediterranean Water () in the subtropical North Atlantic based on the objective results of the Optimal Multiparameter Analysis (OMP). MW propagates in the depth range where other Atlantic water masses have a significantly lower temperature and salinity, which determines the relatively high accuracy and objectivity of identification of the MW. The dataset for the OMP analysis served the newly created MEDTRANS climatology with improved characteristics compared to other climatologies, especially in the region of the subsurface topographically trapped Mediterranean Undercurrent (MUC) (see section 2.2). As a result, it was possible, for the first time, to obtain objective variability of the MW concentrations in the entire subtropical northeastern Atlantic. Improved climatology also provided the basis for more objective identification of meddies in data of *in situ* observations, allowing the threshold salinity anomaly, used for identification of meddies, to be lowered compared to previous studies (Richardson et al., 1991, Richardson et al., 2000).

It has been shown that as one moves from the Strait of Gibraltar along the continental slope of the Iberian Peninsula, the lower branch of the MUC (at 1300 m) and the upper branch of the MUC (at 400-500 m) converge north of Extremadura Promontory of the Iberian Peninsula, forming a single vein centered at the depth of 800-1000 m. This occurs, first of all, due to a decrease in the depth of the lower branch of the MUC. The MUC depth changes abruptly in the vicinity of capes and canyons (Capes Saint Vincent and Finisterre, Porto-Aveiro Canyons), which are also areas of intensive meddy formation. The likely cause is a local weakening of the topographic β-effect compared to the Joint Effect of Baroclinicity and Bottom Relief (JEBAR), where the latter tends to deflect the MUC towards the open ocean (Fig. 4.7). It is likely that the described changes in the depth of the topographically trapped MUC are a consequence of formation of favorable conditions for the development of instability of the MUC, which also results in an intensive meddy generation.

Studies of eddy lifecycles in the ocean are usually hampered by the difficulty of their tracking and the uncertainty in knowledge of areas of their generation. In this sense, meddies form a specific dataset. The areas of their generation form the MUC are localized at the continental

slope of the Iberian Peninsula. Meddies themselves form a well-defined positive anomaly of temperature and salinity, easily detected from *in situ* observations and which cannot be confused with other eddies of the subtropical North Atlantic at these depths. Meddies spread over hundreds and thousands of kilometers from the places of their generation, making it possible to track evolution of their cores. Long lifetime of meddies (as a rule, mesoscale eddies in the ocean exist for no more than 1 month – Chelton et al., 2011), is associated with a high potential vorticity anomaly of their cores, a consequence of trapping of the highly mixed MUC waters, enhanced by the anticyclonic rotation of the meddy cores. This vertical mixing also decreases stability of cyclones formed at the MUC. Therefore, only meddy-anticyclones survive at distance from the MUC, called meddies.

The regular presence of a double core in southern meddies may likely be a consequence of better separation of the upper and lower branches of the MUC along the southern and southwestern slope of the Iberian Peninsula, as well as a consequence of frequent mergers of meddies whose cores are located at different levels (Belkin et al., 2020; Chouksey et al., 2023). The presence of two cores at the level of the upper and lower branches of the MUC in the areas of meddy formation (Prater, 1992) indicates the generation of meddies simultaneously by both branches of the MUC, though different branches are captured by different areas of the continental slope of the Iberian Peninsula and are somewhat separated in space.

The greater stability of the southern meddies is not only a consequence of stronger anomalies in the potential vorticity of their cores and the maintenance of these anomalies due to increased ocean stratification to the west and south along the main meddy paths, but also the result of their regular mergers. Small, rapidly rotating eddy, dominated by kinetic energy, disappears fairly quickly unless it merges with another eddy to form a more stable larger eddy with a lower peak relative vorticity. The theory of the quasi-geostrophic 2D turbulence states that the dissipative evolution of the chaotic turbulent field leads to a decrease in enstrophy (relative vorticity integrated over the volume of the meddy), eddy kinetic energy and eddy potential energy, but enstrophy decreases the quickest, eddy kinetic energy decreases somewhat slower, and eddy potential energy decreases at the slowest rate (Cushman-Roisin and Beckers, 2011). Indeed, statistical data analysis showed that with the distance from 100 to 600 km from the Iberian Peninsula, the radius of the southern meddies doubled, the vertical thickness of their cores increased by 15% (i.e., the h/R ratio decreased significantly), the maximum salinity of their cores almost did not change, and the integral amount of salt in meddies (S_v) increased by an order of magnitude. A twofold decrease in v_θ is also noted, which is also a typical consequence of eddy merger (Polvani et al., 1989). At the same time, there was a decrease of the *Ro* (degree of nonlinearity) and *Bu* (ratio of kinetic energy to available potential) of meddy cores. Thus, the kinetic energy of the merged eddies fell faster than the potential one, which is consistent with theory. Although the merger is a well-known property of the closed turbulent system, previously derived from theoretical and model results (Kamenkovich et al., 1987; Chuksey et al., 2023), for the significant role of mergers in meddy dynamics was revealed for the first time with *in situ* data. A few sporadic observations of meddy mergers in the Iberian Basin further supports these results (Schultz Tokos et al., 1994; Richardson et al., 2000; L'Hegaret et al., 2014).

For eddies to merge, the distance between their centers must be no more than 3 eddy radii (Polvani et al., 1989; Filyushkin et al., 2010). In the resulting dataset of over 200 meddies (Fig. 4.8 b), there were 15 cases when the centers of two meddies were located within 150 km apart. More than 90% of these cases occurred in the Iberian Basin. The frequent merger of the southern

meddies was facilitated by a relatively large number of meddies in the vicinity of their generation regions, as well as by the topography of the Iberian basin, bounded on the west and south by a chain of submarine rises – sometimes named the "Horseshoe" seamount system (Filyushkin et al., 2017). Large topographic slopes can trap meddies, causing their local accumulation as a result of their stagnation near complex topography, reducing the degree of freedom of their translations, and favoring the mergers (Richardson et al., 2000; Carton et al., 2017; Belonenko et al., 2021). Splitting of meddies by seamounts was also observed (Shapiro et al., 1996a; Sokolovskiy et al., 2013; Filyushkin et al., 2014), however, the results above (Fig. 4.14c, 4.18c) indicate that meddy merger dominate in the Iberian Basin.

Comparing the statistics of variations in meddy radii with the results of the analysis of the interaction of meddies with seamounts (section 4.3.3.5), we can assume that meddy interaction with rises in bottom topography leads to an effective destruction, mainly of weakened meddies that have existed for more than a year (Shapiro et al., 1996a; Richardson and Tychensky, 1998; Richardson et al., 2000; Wang et al., 2003; Bashmachnikov et al., 2009a; Benilov et al., 2020). The role of topography in the destruction of old, but not young, meddies is evidenced by the almost complete absence of meddies west of the MAR and over the Azores Plateau, while the number of meddies west and east of the "Horseshoe" seamount chain (Fig. 4.2) is practically the same (Fig. 4.8a, 4.13). In fact, numerous observations near the Iberian Peninsula indicate that, as a rule, encountering a seamount with a young meddy passes without any strong consequences for meddy cores (Richardson et al., 2000; Bashmachnikov et al., 2009a,b). With distance from their generation region, there is a gradual weakening of the kinetic and available potential energy anomalies in meddies. This, for example, was observed for meddy Sharon, monitored for 1.5 years at distances of 1300 - 1700 km from the southern tip of the Iberian Peninsula (Armi et al., 1989; Hebert et al., 1990; Menesguen et al., 2012). For old meddies, interaction with a seamount may often lead to a loss of a significant part of their volume, described in section 4.3.3.5 (Bashmachnikov et al., 2009b), or the complete collapse their cores described for meddies Encelade and Ceres during their interaction with the Irving and Cruiser seamounts south of the Azores Plateau (Richardson and Tychensky, 1998; Richardson et al., 2000). At the same time, the more intense meddy Hyperion, located in the same area, survived (albeit not without losses) a close interaction with the Plato seamount (Richardson and Tychensky, 1998; Bashmachnikov and Carton, 2012). Besides weakened stratification anomalies in their cores (Bashmachnikov et al., 2015c), destruction of old meddies is facilitated by an observed decrease in meddy thickness (Benilov et al., 2020). In addition to meddy age, other important factors also determine the intensity of meddy interaction with a seamount: geometric characteristics of the seamount and especially the relative depth of the seamount summit. Intense dynamics in the area of the summit (White et al., 2007; Mohn et al., 2009; Bashmachnikov et al., 2013 a) contributes to the destruction of a meddy, when its core is observed at practically the same depth.

The Azores Current forms a semi-permeable barrier for meddies, and the number of meddies south of the current is significantly less than to the north (Fig. 4.8a). This is due to the fact that not all meddies can cross this jet stream, but only those that are quite intense (Vandermeirsch et al., 2003a,b). When crossing the Azores Current, meddies lose part of their mass (1.5-3-fold decrease in R and S_v, and a decrease in v_θ) and some of their dynamic stability (increase in Ro and Bu when crossing the current), however, maintaining the integrity of the core (S_m in center of the core practically does not change on different sides of the current). This indicates

predominantly lateral destruction of meddies at strong velocity gradients of the Azores Current (Maksimenko and Orlov, 1991).

4.5 CONCLUSIONS OF CHAPTER 4

1. The percentage of the Mediterranean Water, at the depth of its maximum concentration, decreases by approximately 5-6 times from the continental slope of the Iberian Peninsula to the Mid-Atlantic Ridge (in the area of the Azores Islands), at a rate of 2% for every 100km.
2. The upper core of the Mediterranean Water (800-1000 m) spreads mainly to the west, and the lower core (1200-1500 m) – to the south-southwest.
3. The main directions of propagation of the Mediterranean Water near the Iberian Peninsula correspond to the directions of the main mid-depth currents, but advection does not explain the spreading of the Mediterranean salt tongue at distances of more than 500-600 km from the Peninsula. In these areas, the transport of the Mediterranean Water is carried out by the meddy.
4. Detachment of the topographically trapped Mediterranean Undercurrent (MUC) from the continental slope of the Iberian Peninsula occurs in areas, where the JEBAR effect significantly exceeds the topographic β-effect. These areas are also areas of intense meddy generation.
5. Changes in meddy characteristics with latitude are consistent with changes in the corresponding characteristics of the MUC along the Iberian Peninsula. Meddies keep the meridional differences in the characteristics of their core at distances of thousands of kilometers from the Peninsula. This allows dividing all meddies into 2 groups: the northern and southern meddies. Compared to the northern ones, the southern meddies have smaller radii and stratification of their cores, as well as greater vertical extent, core salinity, azimuthal velocity, relative vorticity, potential vorticity anomaly, and the ratio of kinetic energy to available potential energy. With the larger anomalies of potential vorticity, the southern meddies propagate over bigger distances from their generation sites compared to the northern ones.
6. Within the first 600 km from the Iberian Peninsula (in the Iberian Basin), the meddy dynamics is dominated by mergers, which leads to an increase in the average meddy radius and the integral amount of salt in their cores.
7. There have been identified three main pathways of meddy propagation: Northern (44-45°N), Central (composed from of Central-Southern at 35-36°N and Central-Northern at 39-40°N) and Southern (south of 34°N). It has been also noted the areas of frequent meddy crossing between the Central and Northern paths. The average lifetime of a meddy is 1-2 years, but individual meddies can exist up to 2-3 years.
8. It has been shown that when crossing the Azores Current, the meddies lose part of their volume.
9. The interaction of meddies with seamounts is different for young and old meddies: young meddies tend to turn round the slopes of seamount without significant consequences, whereas when an encounter of a seamount by an old meddy the most likely causes a significant loss of the core volume or its full collapse.

4.6 APPENDICES OF CHAPTER 4

4.6.1 APPENDIX: THE OPTIMAL MULTIPARAMETER ANALYSIS (OMP)

In the OMP analysis, the observed water characteristics (temperature, salinity, oxygen, etc.) at each data-point and at each level of observations are considered to be a result of mixing of a predefined set of water masses (types) with known characteristics, but in unknown proportions. The analysis seeks for a contribution of each of the water masses to the known result of their mixing (observations) by solving the following system of linear equations (Karstensen and Tomczak, http://omp.geomar.de):

$$\begin{aligned}
&x_1\theta_1 + x_2\theta_2 + x_3\theta_3 + x_4\theta_4 + x_5\theta_5 = \theta_{obs} + R_\theta \\
&x_1 S_1 + x_2 S_2 + x_3 S_3 + x_4 S_4 + x_5 S_5 = S_{obs} + R_S \\
&x_1\left[PO_4\right]_1 + x_2\left[PO_4\right]_2 + x_3\left[PO_4\right]_3 + x_4\left[PO_4\right]_4 + x_5\left[PO_4\right]_5 + \Delta P = \left[PO_4\right]_{obs} + R_{PO_4} \\
&x_1\left[NO_3\right]_1 + x_2\left[NO_3\right]_2 + x_3\left[NO_3\right]_3 + x_4\left[NO_3\right]_4 + x_5\left[NO_3\right]_5 + \Re_{N/P}\Delta P = \left[NO_3\right]_{obs} + R_{NO_3} \\
&x_1\left[O_2\right]_1 + x_2\left[O_2\right]_2 + x_3\left[O_2\right]_3 + x_4\left[O_2\right]_4 + x_5\left[O_2\right]_5 - \Re_{O/P}\Delta P = \left[O_2\right]_{obs} + R_{O_2} \\
&x_1\left[Si\right]_1 + x_2\left[Si\right]_2 + x_3\left[Si\right]_3 + x_4\left[Si\right]_4 + x_5\left[Si\right]_5 = \left[Si\right]_{obs} + R_{Si} \\
&x_1 + x_2 + x_3 + x_4 + x_5 = 1 + R_\Sigma
\end{aligned} \qquad (4.11)$$

The set of the equations above is written for the water mass characteristics used in this study: potential temperature (θ), salinity (S), oxygen ($O2$), nitrates (NO_3^-), phosphates (PO_4^{3-}), and silica ($Si(OH)_4$, hereafter referred to as Si). The left side of system (4.11) shows the known properties of selected water masses $\left(\theta_1,\theta_2,...,S_1,S_2,...,\left[Si\right]_1,\left[Si\right]_2,...,\left[Si\right]_5\right)$, and the right side shows the known observations of the water properties $\left(\theta_{obs},...,\left[Si\right]\right)_{obs}$. Square brackets indicate nutrient concentrations. The unknown parameters are the percentage contributions of various water masses $x_1,...,x_5$ to the formation of the observed parameter values. The residual terms $\left(R_\theta,...,R_{Si}\right)$ are associated with errors in the measured water properties, an insufficiently complete set of the water masses used in the analysis, or an insufficiently accurate determination of their properties. The relationship of the residuals is determined by the predetermined relative weight for each of the equations (last line in Table 4.3). Additional restrictions are imposed on x_n: the contributions of all water masses used in the analysis ($x_1,...,x_5$) must be non-negative and in sum equal 100%. Deviation from 100% constitutes the overall error of the analysis R_Σ.

The relative role (weight) of each of the equations of system (4.11) in the final result is determined from considerations of a reliability and representativeness of in-situ observations of the water property, used in the system of equations (4.11), as well as from the degree of spatio-temporal variability of this water property in the areas of generation of the analyzed water masses, compared with other water properties used. As a rule, when compared with observations of temperature and salinity, nutrient profiles are fewer in number, determinations of nutrient concentrations from *in situ* data are less reliable, they are less conservative, and their spatiotemporal variability is significantly higher. Therefore, following Tomczak and Large (1989), Alvarez et al. (2004), Barbero et al. (2010) and Louarn and Morin (2011), the equations for

temperature and salinity were given the highest weights, and those for nutrients – lowers weights. The least accurately determined silica had the lowest weights (Table 4.3).

The classical OMP analysis assumes that all water properties behave as passive tracers (see, for example, Klein and Tomczak, 1994; Gasparin et al., 2014). However, when applying OMP to spatial scales comparable to the size of ocean basins, it is also necessary to take into account the aging of the water mass, which is expressed in changes in the concentrations of nutrients not only due to water mixing, but also due to biochemical processes. To take them into account, an additional variable is introduced into the system of equations (4.11) – the unknown rate of change in the concentrations of nutrients as a result of the oxidation of the suspended organic matter (which in the open ocean is predominantly of phytoplankton origin) and is proportional to the rate of oxygen consumption for oxidation (Karstensen and Tomczak, 1997; Poole and Tomczak, 1999). Assumptions about the equal mineralization rates of all nutrients and the proportional rate of the dissolved oxygen loss during the oxidation process allow us to express the biochemical variability of the concentrations of nutrients in the system (4.11) through the variability of only one parameter – the rate of phosphate mineralization ΔP (Karstensen and Tomczak, 1997; Poole and Tomczak, 1999). The rate of nitrate mineralization (and oxygen consumption) is determined through the product of ΔP with the relative mass fraction of these nutrients in phytoplankton in the areas of the water mass formation – Redfield stoichiometric ratios ($\mathcal{R}$) (Redfield et al., 1963). For the analysis, the Redfield ratio O_2:NO_3:PO_4 =150:16:1 was used, which is a balance between estimates $\mathcal{R}$ for different parts of the study region and different depths (Anderson and Sarmiento, 1994; Dafner et al., 2003; Perez et al., 1998, 2001). *Si* was considered as a conservative tracer (van Aken, 2000a; Alvarez et al., 2004), which is due, first, to the low intensity of mineralization of silica compared to other nutrients, second, to the fact that assessments of mineralization of *Si* are complicated by the change of the rate of this process with depth, and third, due to strong regional variability in the ratio of silica to other nutrients content in phytoplankton. This makes it ineffective to uniformly take into account the rate of *Si* mineralization in water masses of various origins (van Aken, 2000a). The algorithm described above for taking into account the mineralization of a substance used in this study is known as Extended OMP analysis (Karstensen and Tomczak, 1997). A non-trivial value R_Σ requires the system to be overdetermined. In other words, the seven equations of system (4.11) allow simultaneous analysis of no more than five different water masses.

The characteristics of water masses were selected using literature sources at the boundaries of the study region, and not in the area of the water mass formation (Table 4.3). Thus, there is no need to take into account transformation of these characteristics on the way to the study region. In particular, MW characteristics were selected on the continental slope of the Iberian Peninsula, approximately 150 km west of the Strait of Gibraltar. This allows ignoring the initial stage of mixing of Mediterranean waters with the waters of the North Atlantic, which is not of interest for this study, and where the climatology is imprecise due to the very narrow MUC (see section 4.2.2). Properties of the water masses were ensured to contain all point of *in situ* observations inside the mixing triangles (Fig. 4.27ab). If necessary, the water masses properties were slightly adjusted.

A preliminary selection of 5 main water masses was carried out separately for 3 sub-layers, dividing the full depth layer analyzed (0-2000 m), and in each of the 5°× 5° squares. Figure 4.27(c-d) shows the depths of the boundaries between the top, middle and bottom layers. The initial selection was based on previous studies in the region (Tsuchiya et al., 1992; Perez et al., 1998, 2001; Poole and Tomczak, 1999; van Aken, 2000a,b, 2001; Cabeçadas et al., 2002; Alvarez et al.,

2004; Barbero et al., 2010; Lourn and Morin, 2011; Carracedo et al., 2014) and on analysis of scatter diagrams of different combinations of water properties (see examples in Fig. 4.27ab). Moreover, the same water masses were present in different layers and different 5°× 5° squares in such a way as to cover the area of their expected distribution with a study region. After the first trial runs of the OMP analysis, the distribution areas of water masses were adjusted to minimize the R_{Σ} error. The area of coverage of each of the water masses was expanded from the area of its maximum concentration until its concentration fell below insignificant values (<10%).

Table 4.3. The main water masses and their characteristics used in the OMP analysis: the Subtropical Mode Water (StrMW), the upper, middle and lower fractions of the North Atlantic Central Water ($NACW_{u,}$ H and $NACW_{l}$), the Mediterranean Water (MW), the modified Antarctic Intermediate Water (mAAIW), the Subarctic Intermediate Water (SAIW), the Labrador Sea Water (LSW), the upper North Atlantic Deep Water ($NADW_{u}$).

water mass\water characteristics	T (°C)	S	O_2 *(μmol/l)*	PO_4 *(μmol/l)*	NO_3 *(μmol/l)*	Si *(μmol/l)*
StrMW	19.0	36.70	100	0.16	2.0	2.0
$NACW_u$	18.0	36.45	250	0.15	2.0	2.0
H	12.2	35.60	230	0.70	12.0	4.5
$NACW_l$	8.8	35.15	195	1.20	20.0	12.0
MW	13.2	37.10	170	1.00	16.0	7.0
mAAIW	6.5	34.90	110	2.10	32.0	23.0
SAIW	5.6	34.70	280	1.00	15.0	6.0
LSW	3.4	34.89	295	1.10	17.0	12.0
$NADW_u$	2.5	34.94	250	1.30	20.0	35.0
weight of the water property	24	22	7	2	7	1

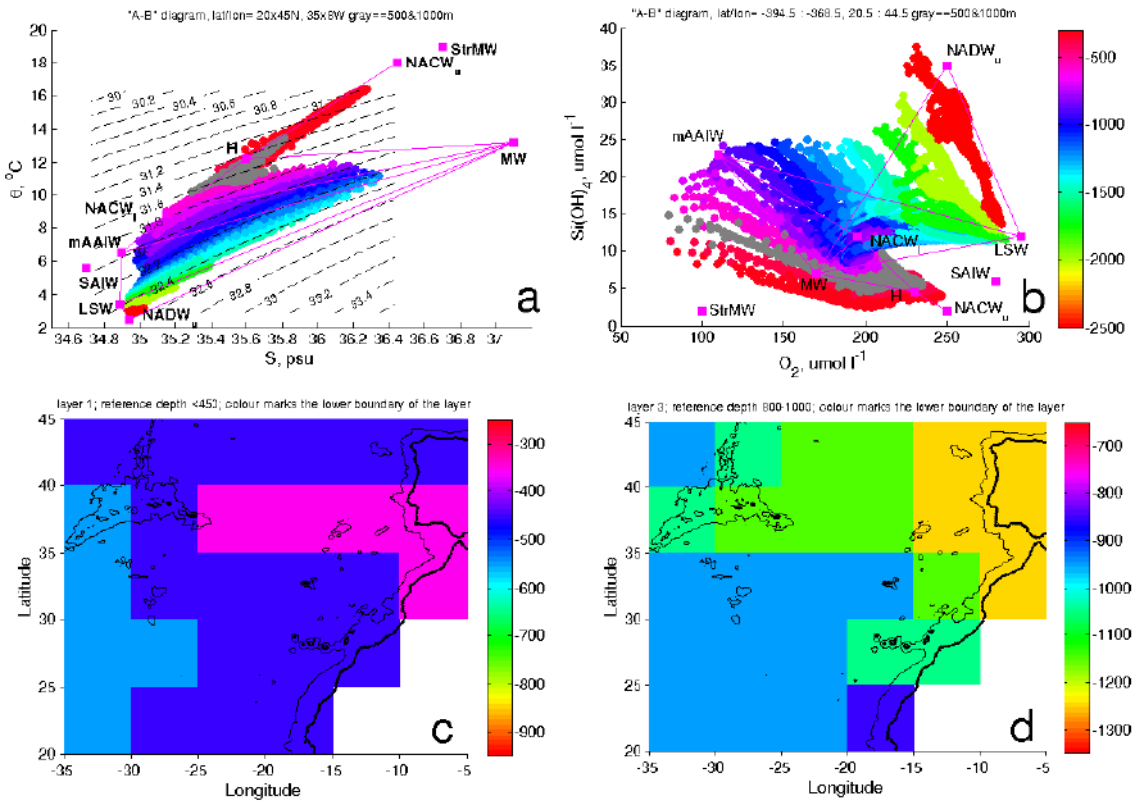

Fig. 4.27. Examples of (a) θ-S diagram and (b) Si-O_2 diagram used to determine the set of water masses in OMP analysis. Color scale – observation depth. The potential water density in figure (a) refers to 1000 m (σ_1). (c) Depth of the lower boundary of the upper layer (m); (d) depth of the lower boundary of the middle layer (m).

The main formal error of the OMP approximation was estimated by R_Σ should not exceed 10-15% (Karstensen and Tomczak, 1997). The obtained R_Σ were below 6% (Fig. 4.28), which indicates an adequate choice of the main water masses within the 5-degree areas and the vertical layers. The maximum errors occurred near the boundary between layers 1 and 2, where the number of different water masses with non-zero concentration may exceed the maximum permissible amount to be analyzed in the system of equations (4.11). Based on the derived R_Σ, 10% can be considered as the minimum significant concentration of a water mass.

Additionally, sensitivity of the OMP analysis to the variability of characteristics of water masses was performed. The characteristics of a water mass varied within the values defining this water mass in the study region by different authors (Karstensen and Tomczak, 1997; Perez et al., 1998, 2001; Poole and Tomczak, 1999; van Aken, 2000a,b, 2001; Cabeçadas et al., 2002; A lvarez et al., 2004; Barbero et al., 2010; Lourn and Morin, 2011; Carracedo et al., 2014): ±0.2°C for temperature, ±0.05 for salinity, ±20 µmol/L for oxygen, ±0.1 µmol/L for phosphates, ±1.5 µmol/L for nitrates and ±2.0 µmol/L for silicates. The sensitivity of MW to the changes in the characteristics of various water masses was the lowest and amounted to no more than 3%. However, the LSW and $NADW_u$ could in some cases exchange a significant proportion of their percentages, while the errors of the sum of percentages of both water masses were within the accuracy of the analysis (<10%). Therefore, for the final results only the sum of the percentages of the LSW and $NADW_u$, denoted as the NADW (the North Atlantic Deep Water), was considered.

For the same reason, the resulting concentrations of the StrMW, $NACW_u$, H and $NACW_l$ were combined into the NACW (the North Atlantic Central Water).

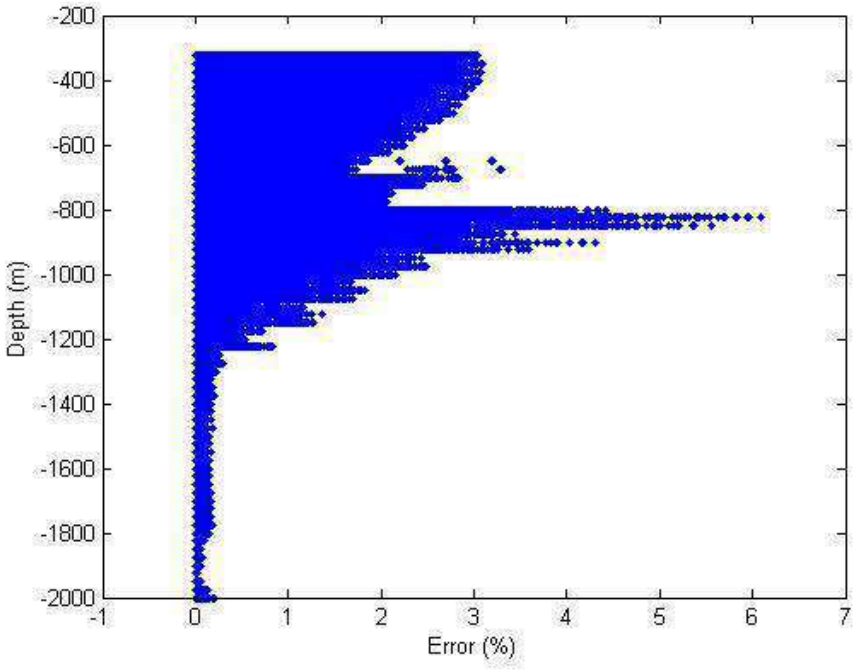

Fig. 4.28. Residuals (R_Σ) of the mass conservation equation in the OMP analysis.

The consistent change in the depth of the MW with changes in the depth of the neutral density surfaces and the observed propagation of the maximum concentrations of the MW, SAIW and mAAIW along the main currents, derived from the analysis of trajectories of floats at the mid-depth, serve independent confirmations of the reliability of the OMP results.

4.6.2 APPENDIX: ESTIMATES OF THE VELOCITIES OF THE MEAN MID-DEPTH CURRENTS FROM TRAJECTORIES OF RAFOS AND ARGO FLOATS

RAFOS dataset used (from WOCE Subsurface Float Data Assembly Center, http://wfdac.whoi.edu/) included data from 353 neutrally buoyant floats for 1982-2002, drifting in the depth range of 400-1700 m. Typical time intervals between determinations of the float coordinates ranged from 6 to 24 hours, and the total duration of the tracked trajectories was 6700 months. ARGO dataset used (from Coriolis operational data center, ftp://ftp.ifremer.fr) consisted of 242 floats from 1999-2013, drifting at fixed depths of the same range (400-1700 m). Typical intervals between observations of float positions were 10-15 days, and the total duration of tracked trajectories was 6560 months.

To track mean currents, parts of the float trajectories within the mesoscale eddies were first removed. This is necessary to avoid associated distortions, since it is known that mesoscale eddies often have velocities very different from those of the average flow and can even move against the current (Morel, 1995). In particular, Mediterranean water eddies (meddies), which are very intense eddies in the intermediate layers of the subtropical Northeast Atlantic, were filtered out. Because the characteristic periods of rotation of a meddy core range from 3 to 10 days; their rotation can be recorded using RAFOS data, but not ARGO. A RAFOS float was considered to be caught in

an eddy if it completed at least two full rotations within 20 days. Comparison with literature data shows that most of the intrathermocline eddies detected in this study have previously been identified as meddies (Richardson et al., 2000; Ambar et al., 2001; Bashmachnikov et al., 2015b). RAFOS floats only record temperature (not always) and pressure at the depth of the float. ARGO profiling floats also provide vertical profiles of temperature and salinity down to 2000 m depth. Similar to other *in situ* data, meddies in ARGO vertical profiles were identified as salinity anomalies of the order of 0.2 or more, observed in a layer at least 200 m thick and located in the depth range of 500-1500 m (Richardson et al., 1991; Bashmachnikov et al., 2015c). The anomalies were calculated relative to the previously obtained MEDTRANS climatology (see Section 2.2). Moreover, only those parts of the trajectories were considered to be within meddies, where the given criteria were met for at least 3 consecutive profiles, i.e. over at least 20 days.

Next, all trajectories of floats from a depth range of ±500 m around fixed reference level (1000 or 1500 m) were reduced to a given reference depth using geostrophic relationships:

$$\frac{\partial \vec{V}}{\partial z} = -\frac{g}{f\ \bar{\rho}}\left(\vec{k} \times \nabla \rho\right), \tag{4.12}$$

where $\vec{V}$ is the Lagrangian horizontal velocity of the float, g is the acceleration of gravity, f is the Coriolis parameter, ρ is the water density (from MEDTRANS climatology), $\bar{\rho}$ =1030 kg m $^{-3}$ is the characteristic value of water density. The average Eulerian velocities and the corresponding errors were then estimated in each of 1°×1° squares. The use of floats form a certain depth range instead of a fixed depth level allowed to significantly increase the number of analyzed floats, which increased the reliability of the analysis. To take into account the difference in the time intervals between fixing the consequent positions of RAFOS and ARGO floats, used for estimating the average Eulerian velocities, the Lagrangian velocities of both types of floats were multiplied by weight functions proportional to the corresponding time intervals (Lavender et al., 2005). When constructing the mean current velocity distributions, outliers were excluded using the Discrete method cosine transform - penalized least square method (Garcia, 2011). This filtering was not applied near steep bottom slopes, where rapid variability in the mean velocity of topographically trapped currents is expected.

Errors in average current velocities were estimated for each of the components as:

$$v_{err} = z_{95} SD / \sqrt{n}\,, \tag{4.13}$$

where n is the number of data, SD is the standard deviation (average of the meridional and zonal components of the current velocity) and z_{95} is the 95% confidence level of the Student t distribution. Figures 4.6 and 4.11(a) show average current velocities only in the grid cells where the obtained means exceeded v_{err}.

Baseline errors in the current velocity estimates from ARGO floats were mainly due to the float drift during their ascending and descending cycles and are, on average, within 4 cm s^{-1} (Rosell-Fieschi et al., 2015). Taking SD = 4 cm s$^{-1,}$ we can estimate the minimum number of velocity values required to determine the current velocity from ARGO data with a given accuracy. An error in the current velocity of 1 cm s $^{-1}$ or less requires at least 60 velocity observations in a

grid cell, 1.5 cm s^{-1} requires 30 observations and 2 cm s^{-1} requires 18 observations. At 1000 m, approximately 40% of the grid cells meet the first criterion, 60% – the second one and 80% – the third one. At a depth of 1500 m these values are 15%, 40% and 70%, respectively. Thus, the accuracy of the average current velocity using ARGO floats can be estimated at 1.5-2.0 cm s^{-1}. v_{err} was taken to be 2.0 cm s^{-1} for ARGO or, if RAFOS floats were also present, the maximum error for each dataset was fixed.

4.6.3 APPENDIX: CALCULATING THE MEDDY OCCURRENCES

The probability of detecting a meddy in Figure 4.11(b) was calculated as the ratio of the number of casts within a meddy to the total number of casts in a cell of 1°x1°. To avoid biases in the probability distribution resulting from multiple soundings of the same meddy, soundings made at approximately the same location and time counted to belong to the same meddy. This clustering was performed for meddy and for non-meddy profiles. The spatiotemporal clustering window was centered at a randomly selected cast and there were merged the data for a period of ±30 days and within a radius of ±50 km for the casts located within 300 km off the Iberian Peninsula, and within a radius of ±75 km – at a greater distance. The selected radii form $\sqrt{2}$ the typical dynamic radius of a meddy at different distances from the Iberian margin. To avoid the effect of continuous repeated probing of the same meddy with an AGRO profiling float trapped in a meddy core, the width of the windows was increased 3 times compared to the described above. With an average velocity of meddy translations of 2-5 cm s^{-1} (Richardson et al., 2000), this time is enough for the meddy to travel about 300 km – the size of the areas, in which averaging of the statistical properties of meddies with distance from the Iberian Peninsula was carried out (Fig. 4.8a). In this way, 775 independent observations of meddy cores were obtained, identified from at least one vertical cast (Fig. 4.8a).

Chapter 5. Mechanisms of destruction and regeneration of ocean eddies using the example of the quasi-permanent Lofoten Vortex in the Norwegian Sea

5.1 QUASI-PERMANENT EDDY OF THE LOFOTEN BASIN OF THE NORWEGIAN SEA

In this section the destruction and regeneration of the quasi-permanent Lofoten Vortex (LV) in the Lofoten Basin of the Norwegian Sea (Fig. 1.6) is examined, using the primitive equations Massachusetts Institute of Technology General Circulation Model (MIT GCM, Marshall et al., 1997), as well as analysis of numerical experiments of the quasi-geostrophic (QG) model by M.A. Sokolovsky (Sokolovskiy, 1997a,b; Bashmachnikov et al., 2017; Santieva et al., 2021).

5.1.1 CHARACTERISTICS OF THE LOFOTEN VORTEX USING IN SITU DATA, SATELLITE ALTIMETRY AND HYDRODYNAMIC MODELS

The dynamics of the Lofoten vortex were analyzed using data from a regional implementation of the MIT GCM with a spatial resolution of 4x4 km (Volkov et al., 2015), which makes it possible to study large mesoscale eddies with a radius of at least two Rossby deformation radii. These include the LV and large eddies of the Norwegian Current, which take part in regeneration of the LV. 15 years of model data (1998-2012) were analyzed. A detailed description of the model is given in section 2.3.7.

Detailed comparisons of the results of the MIT GCM configuration used here with data from satellite and field observations were made in a number of studies (see, for example, Kohl, 2007; Soiland and Rossby, 2013; Volkov et al., 2015; Bashmachnikov et al., 2017; Travkin and Belonenko, 2019). The MIT GCM results have shown to adequately reproduce the observed features of the large-scale and mesoscale dynamics of the Lofoten Basin, including the main thermohaline and dynamic characteristics of the LV and their variability over time, as well as the seasonal variation of the relative vorticity of the LV core (see also Volkov et al., 2015). Both *in situ* observations and the model results suggest the dynamic radius of the LV equal to $R \sim 30$ km $\sim 4\ Rd$ (Fig. 5.1a). In the vertical structure of the LV, in addition to the barotropic component, a noticeable baroclinic component presents. Subsurface intensification of the LV core (the maximum azimuthal velocity and relative vorticity and minimum dynamic radius) is observed in the layer between 50-200 m and 1000-1100 m (Fig. 5.1b,c). The strongest thermohaline anomalies of the LV were also recorded at these depths (Fig. 1.7). The dynamic signal of the vortex propagates to the bottom, although below 1200 m its relative vorticity weakens more than 5 times (Fig. 5.1bc). The radial/vertical velocities and density structure of the LV core in the model also well reproduce the results of the analysis of *in situ* vertical profiles of thermohaline characteristics (from CTD casts) and current velocity (from ADCP data) (Soiland and Rossby, 2013). However, in Bashmachnikov et al. (2017) it was shown that the MIT GCM slightly underestimates the azimuthal rotation velocity and peak relative vorticity of the LV core compared to detailed *in situ* observations obtained with gliders (Yu et al. 2017; Fer et al., 2018; Bosse et al., 2019).

The relative vorticity of the MIT GCM model show a rich eddy dynamics of the Lofoten Basin (Fig. 5.1a). In the northeastern part of the basin, anticyclonic eddies are regularly generated

in the Norwegian Current, especially often near the Lofoten Islands. These eddies then move west along the northern boundary of the basin (see section 3.3).

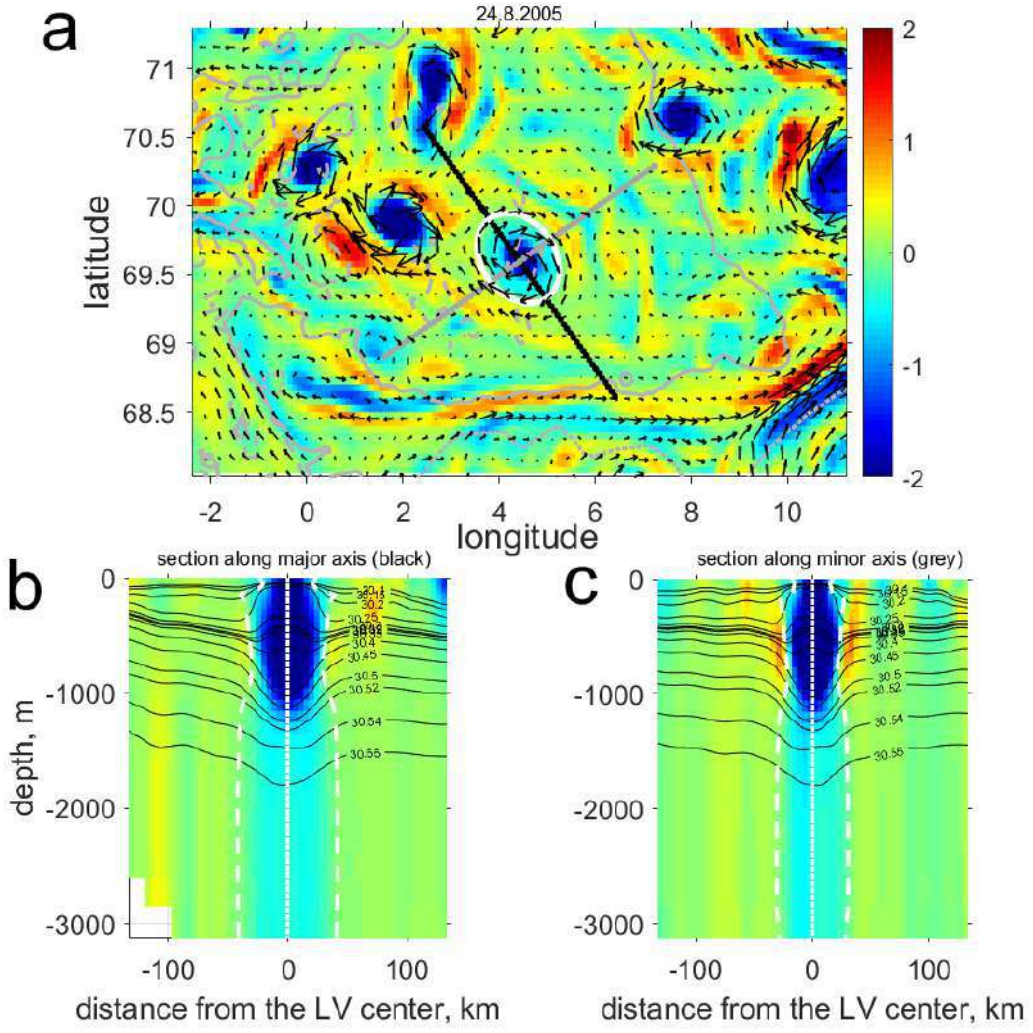

Fig. 5.1. Relative vorticity in the Lofoten Basin (colored, 10^{-5} s^{-1}) according to MIT GCM on 08.24.2005: (a) horizontal distribution of relative vorticity (color) and current (black vectors) at 100 m. The white ellipse marks the LV. Vertical sections along (b) the major axis of the LV core (black segment in (a)) and (c) the minor axis of the LV core (gray segment in (a)). In (b) and (c), black isolines mark isopycnals $\sigma_{0.5}$ (kg m^{-3}), the vertical white dotted line is the LV axis, and the dashed white lines are the LV limits, identified by zero values of the relative vorticity.

The stability of eddies is related to the intensity of the anomaly of the potential vorticity of their core. The anomaly of quasi-geostrophic potential vorticity for a layer n (Π_n) bounded by two isopycnals, in the case of neglecting the β-effect, is computed as:

$$\Pi_n(x,y,t) = \omega_n(x,y,t) + f\ \Delta h_n(x,y,t) / h_n\ . \qquad (5.1)$$

Here ω_n is the relative vorticity of the layer n, f is the Coriolis parameter, Δh_n is the distance between isopycnals (thickness of layer n) at a given point, h_n is the average thickness of layer n over the entire area selected.

Based on the distribution of potential vorticity, as well as other dynamic parameters, the vertical structure of the LV can be split into three layers (Fig. 5.1bc, 5.2a). Layer 2 contains the LV core, located between 200 m and 1000-1200 m depth, characterized by a negative anomaly of potential vorticity (Π_2), as well as extrema of relative vorticity and azimuthal velocity, reaching peak values at 400-800 m (Fig. 5.1, 5.2 A). The subsurface position of the LV core can also be traced with thermohaline anomalies (Fig. 1.7). For the upper layer (0-200 m), the potential vorticity (Π_1) is positive and in absolute value is almost an order of magnitude less than Π_2 . Layer 3, from 1000-1200 m to the ocean bottom, is characterized by a 3 times lower peak azimuthal velocity than in the LV core, an increase of R from 25 to 35 km and 5-6-fold decrease of relative vorticity. Pronounced positive anomalies of potential vorticity are observed directly below the core. The change in the signs of Π in the vicinity of the core indicates that the LV has properties of an S-vortex (Morel and McWillams, 1997). During some periods of time, positive anomalies of potential vorticity are also observed in layer 2 along the outer perimeter of the LV core – the so-called "screen" (Zhmur et al., 2021). During these periods, the LV can be considered as a combination of S- and R-vortices.

The seasonal evolution of the LV was assessed, using MIT GCM data, from the mutual variability of potential vorticity in the upper 2 layers, where the time variability was the most pronounced. Using K-means cluster analysis in (Π_1, Π_2) parameter space, 4 configurations (A, B C, D) of the vertical LV structure were identified (Fig. 5.2b,c). The critical distance in (Π_1, Π_2) parameter space, which determines the largest distance between the cluster center to its boundary, was taken equal to 0.3 s^{-1}. With this value, the areas with the maximum data density in (Π_1, Π_2) space were clearly separated (Fig. 5.2b). Although not all points were assigned to one of the clusters, this choice made it possible to better outline the difference in isopycnal configurations for the most typical LV states, not distorted by rare intermediate situations. In total, the identified clusters A-D covered 62% of the period of the analysis. Most of the remaining 38% of unclassified states tended to be close either to cluster D or to cluster A.

Isopycnal configurations for clusters A-D are shown in Figure 5.3. Isopycnals bounding the core of the LV from above (below) were selected using the depth of the change in the sign of the potential vorticity above (below) the LV core (see Bashmachnikov et al., 2017).

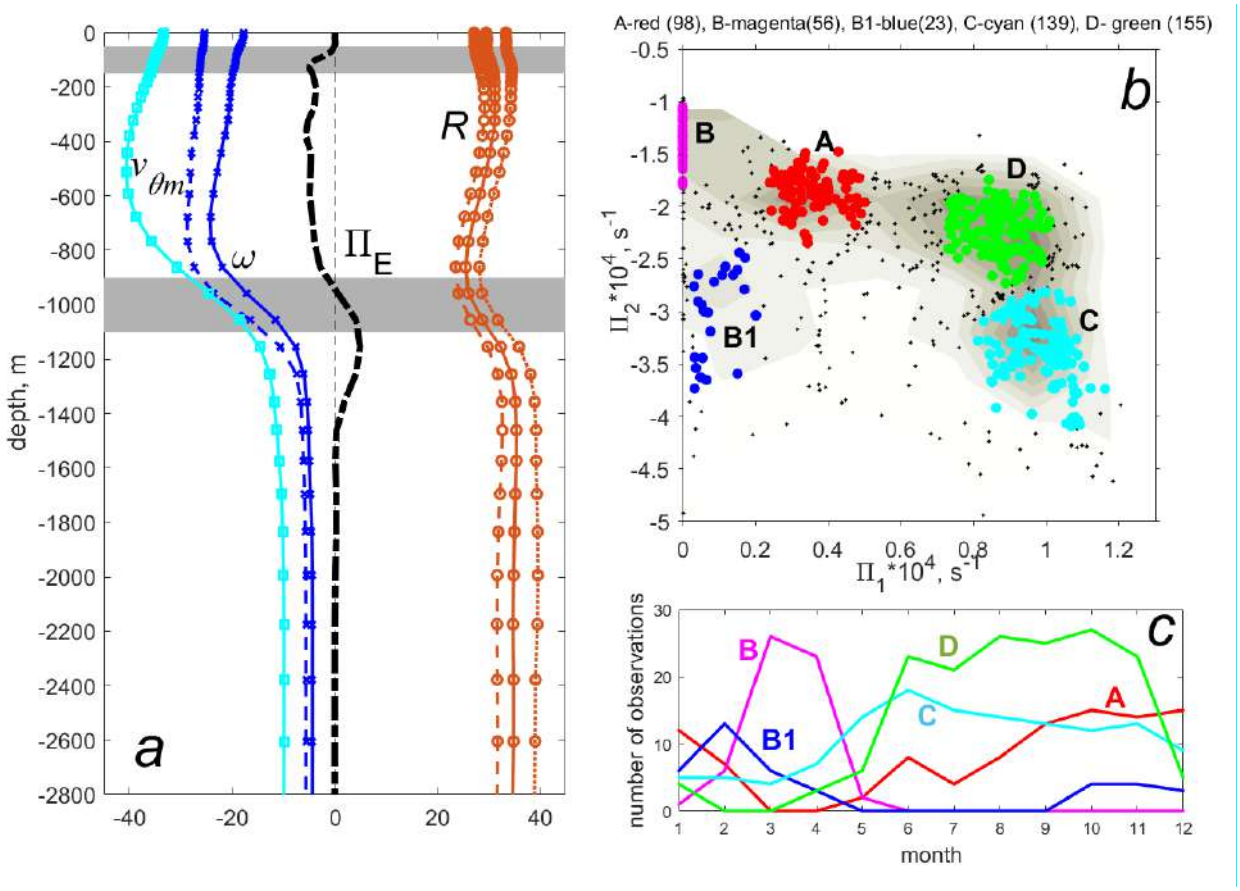

Fig. 5.2. (a) Vertical profiles of mean characteristics of the LV (1998-2012): $v_{\theta m}$ is the maximum azimuthal velocity in the LV core (cm s^{-1}); ω is the relative vorticity of the core (10^{-6} s^{-1}) defined in a circle with radius $R/2$ (maximum – blue dotted line and average – blue solid line); P_E is the peak Ertel potential vorticity in the vortex core (10^{-11} s^{-1}); R is the dynamic radius of the LV (km). (b) Clusters of states of the LV core (A-D) in the space of Π_1-Π_2 (10^4 s^{-1}). (c) Occurrence of clusters A-D by month (from Bashmachnikov et al., 2017).

Configuration A (Figures 5.2b and 5.3a) covered approximately 13% of the entire period of the analysis for 1998-2012, with a weekly time interval. It is characterized by small deviations of isopycnals above the LV core (η_1) from the average thickness of layer 1 (h_1). The frequency of occurrence of this configuration increased from summer to autumn, decreased in winter, and it was almost absent in spring (Fig. 5.2c).

Configuration B is formed during the cold period of the year, especially in early spring, due to more intense convection in the LV core compared to the surrounding ocean (Fig. 5.2b,c and 5.3b). In this case, the upper LV layer disappear (h_1 =0 and η_1 =0), and the thickness of layer 2 (h_2) becomes abnormally large. A similar configuration is B1 (Fig. 5.2b, not shown in Fig. 5.3), where the upper layer could be identified, but its isopycnic boundary it is located significantly deeper than the upper mixed layer of the Lofoten Basin in the vicinity of the LV. Configuration B1 was observed sporadically from late autumn to late winter, before the configuration B, and mark the periodic restratification of the upper layer before the active development of deep convection in the LV core (Fig. 5.2c). In total, configurations B and B1 covered about 13% of the analysis period.

Configuration C (Figs. 5.2b and 5.3c) is characterized by an anomalously big rise of isopycnals above the LV core (η_1), while the depth of h_2 return to its typical summer values. This configuration covered about 16% of the analysis period and could be observed in any season, most often during the spring-summer restratification of the upper ocean layer after active autumn-winter mixing (Fig. 5.2c).

Configuration D (Figs. 5.2b and 5.3d) represents an intermediate configuration between A and C. It is the most frequently observed isopycnal configuration, covering at least 20% of the entire analysis period and occurring throughout the entire warm period of the year (Fig. 5.2 c).

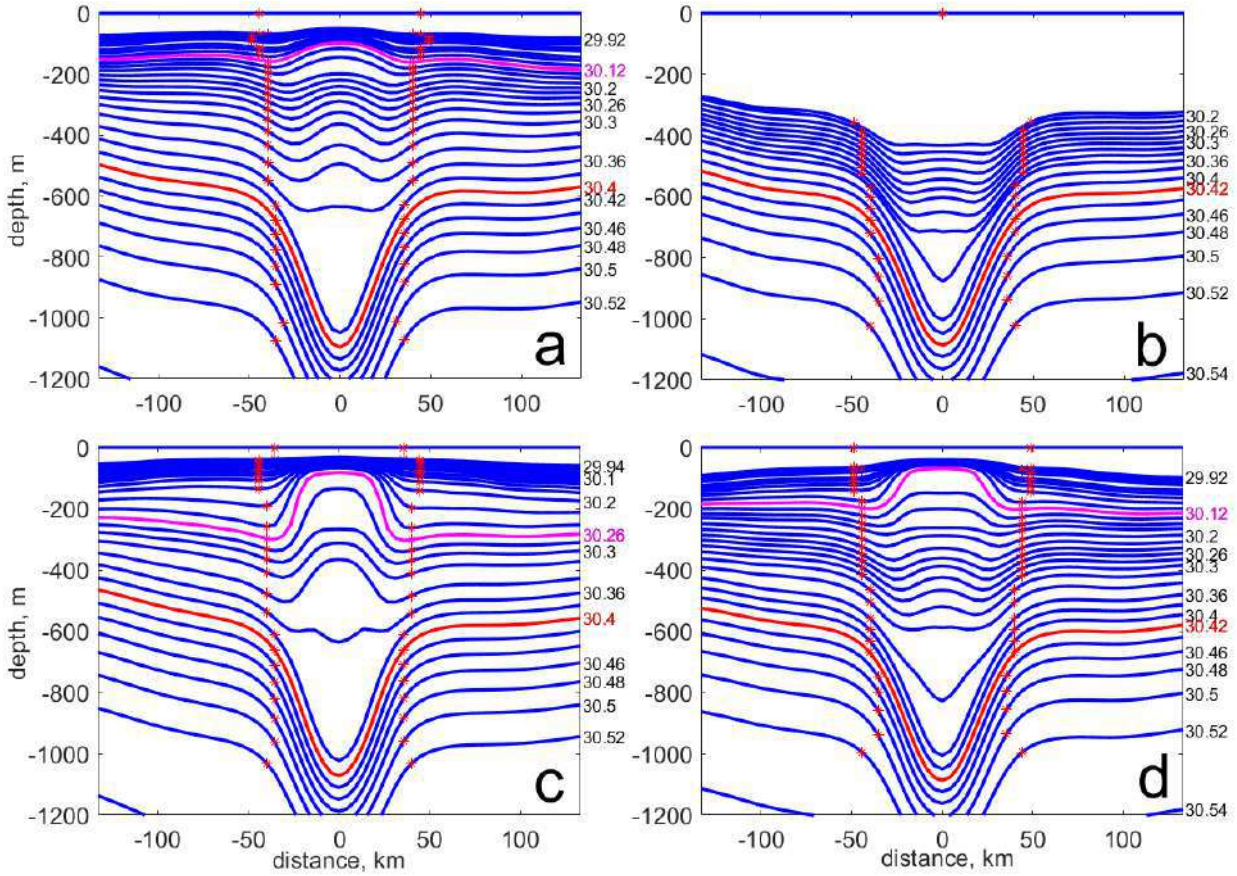

Fig. 5.3. Depths of isopycnals (blue lines) on a section through the LV for clusters AD (see Fig. 5.2 b,c) a (cluster A) – typical configuration of isopycnals in the region of the LV core for autumn - early winter, b (cluster B) – for the end winter - early spring, c (cluster C) – for the end of spring, d (cluster D) – for summer. The purple and red isopycnals mark the superior and inferior boundaries of the LV core, respectively; red dots mark the boundaries of the LV core at the level of the drawn isopycnals (from Bashmachnikov et al., 2017).

In-situ observations are too sporadic to make a classification of isopycnal configurations in LV similar to that from the MIT GCM data. Nevertheless, observations confirm the existence of at least two limiting states – the summer-autumn (clusters A, C, D) and winter (clusters B, B1) ones (Ivanov and Korablev, 1995a, b; Ray et al., 2015). In-situ sections across the LV also indicate that the 3-layer structure of the LV can be maintained throughout winter and spring (types B1, A or D in Fig. 5.3), and only in some years the 2-layer structure is formed (types B in Fig. 5.3). During such periods, the depth of the mixed layer in the central part of the Lofoten Basin (LV region) can reach 500-800 m (Alekseev, 1991; Nilsen and Falck, 2006; Fedorov et al., 2019), while

the typical depth of the mixed layer outside the central regions of the basin from summer to winter ranges from 50 m in summer to 200-400 m in winter (Nilsen and Falck, 2006; Rossby et al., 2009a).

5.1.2 Regeneration of the Lofoten Vortex

The Lofoten Vortex, like any coherent oceanic dynamic structure, gradually dissipates energy into the surrounding ocean. The constant presence of the LV in the Lofoten Basin is a consequence of the periodic energy supply from external sources. The first LV studies showed that the thermohaline LV anomaly intensifies in winter and spring, while the LV radius decreases and the maximum rotation velocity increases. A hypothesis of the regeneration of the LV potential vorticity anomaly by anomalously strong convective mixing in the LV core in winter was put forward (Ivanov and Korablev, 1995 a,b). Such enhanced mixing in the LV compared to the surrounding areas of the Lofoten Basin will be called the "differentiated convection." The presence of a regular differential convection leads to a regular emergence of configuration B and its replacement with configuration C at the end of spring. The sharp rise of the isopycnals in configuration C should contribute to an intensification of the anticyclonic rotation of the LV (Figs. 5.2c and 5.3c). Another hypothetical mechanism for the regeneration of LV is the mechanism of LV mergers with anticyclones (Kohl, 2007; Volkov et al., 2015). The vast majority of anticyclones are generated in an area of rapid growth of baroclinic instability of the Norwegian Current west of the Lofoten Islands, where the continental slope is very steep (Soiland et al., 2008; Koszalka et al., 2011; Isachsen, 2015; Bashmachnikov et al., 2023). Guided by the bowl-shaped shape of the Lofoten Basin, the anticyclones move west (Fig. 5.1) and some of them merge with the LV (Raj and Halo, 2016; Filyushkin et al., 2017b; Bashmachnikov et al., 2017, 2023). Large-scale features of the basin topography are the most important prerequisite for the accumulation of eddies and, ultimately, the existence of LV in the basin (Belonenko et al., 2021).

To study the mechanisms of variability of the LV energy with time, anomalies of potential and kinetic energy were integrated over the volume of the LV core (Fig. 5.4), i.e. inside an area limited by a radius of $1.6R$ (where R is the LV dynamic radius) and by the depth interval between the upper and lower boundaries of the LV core (Fig. 5.3). The integral kinetic energy was estimated as:

$$KE = 0.5\rho \iiint v_\theta^2 dx\, dy\, dz, \tag{5.2}$$

integral available barotropic potential energy as:

$$PE_s = 0.5\, g\, \rho_s \iint \zeta^2\, dx\, dy, \tag{5.3}$$

and the integral available baroclinic potential energy as (Oort et al., 1989):

$$PE_i = 0.5\, g \iiint \Delta\rho^2 \Big/ \left|\frac{\partial \overline{\rho}}{\partial z}\right| dx\, dy\, dz. \tag{5.4}$$

Here v_θ is the azimuthal velocity of the LV, g is the acceleration of gravity, ρ and ρ_s are the water density (the subscript s denotes the sea surface), ζ is the sea level anomaly above the LV, $\Delta\rho$ is the anomaly of water density in the LV relative to the background values near the LV, $\frac{\partial\overline{\rho}}{\partial z}$ is the vertical gradient of the background water density. Anomalies of the available potential energy in the LV core were computed relative to the background, which was represented by the average characteristics in the ring $[2R; 4R]$. As one would expect, the variability of the total energy of the LV was dominated by the PE_i, while the KE was almost an order of magnitude smaller, and the PE_s was 4 orders of magnitude smaller (Fig. 5.4).

In most cases, the merger of anticyclones with the LV observed in winter, which makes it difficult to separate the effects of mergers and convection (vertical black and gray bars in Fig. 5.4, respectively). The effect of mergers on the LV energy can be derived from the rare summer mergers in 2001, 2003, and 2009. After this, not only an increase in PE_i, but also a sharp increase in PE_s and KE (see also Wang et al., 2019). In winters when convection was observed, but no mergers were recorded (2000, 2004, 2005, 2010), an increase in the PE_i anomalies and some growth of the PE_s was observed, while the KE remained almost unchanged. This explains why Volkov et al. (2015), using relative vorticity as a measure of the LV intensity, found no clear influence of winter convection on the LV. Recently Trodahl et al. (2020) also suggested that it is mergers that enhance the LV rotation, while enhanced winter convection in the LV core leads to vertical homogenization of the core, which is disrupted when the cores of the surface anticyclone are vertically aligned with the subsurface LV. The winter vertical mixing in the LV leads to an increase of the potential vorticity anomaly of its core, which increases the stability of the vortex.

The results presented here show that both mechanisms, mergers with anticyclones and intense winter convection in the LV core, lead to a pronounced increase in the anomalies of the available potential energy of the LV, which adds to an increase in the LV stability through an increase in the related anomaly of Π. Outside of regeneration periods, there was a gradual decrease in both, the potential and kinetic energy of the LV at a rate of 2-3% per month (Fig. 5.4). This slows the energy loss and allowed the LV to exist without significant changes in its volume for many months (for example, from spring 2005 to early winter 2006), until the next moment of regeneration (see section 5.1.3 below). If linearly extrapolating this rate of the LV destruction in time, one can expect the complete disappearance of the LV in 2-4 years, if in the case of no external energy supply. This is a fairly long period of time, since most of mesoscale eddies live no more than a month (Chelton et al., 2011). Nevertheless, this is much less than the 10-year period of the complete destruction of the LV when its energy is dissipated exclusively by turbulent diffusion (Soiland and Rossby, 2013).

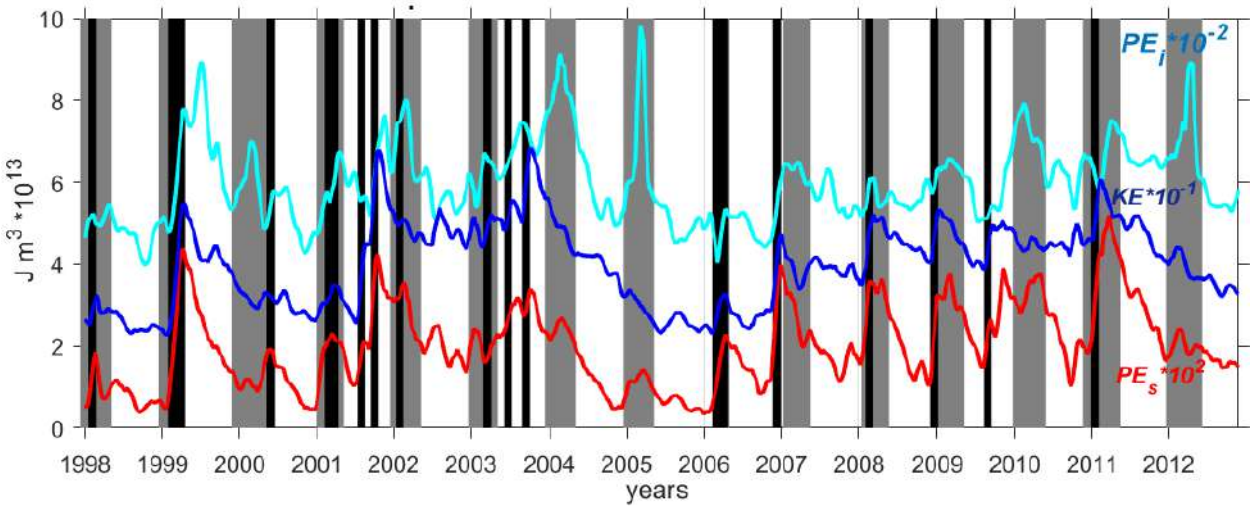

*Fig. 5.4. Time variability of the energy integrated over the volume of the LV core (*10^{13} J m^3): the available barotropic potential energy (PE$_s$ *10 $^{2)}$, the available baroclinic potential energy (PE$_i$ *10^{-2}) and the kinetic energy (KE*10^{-1}). Mergers of the LV with other anticyclones are marked with black vertical lines. The gray bars show the periods of the recorded deep (winter) in the LV core (cluster B, Fig. 5.3).*

The mechanism of the LV merger with surface anticyclones is given in detail below. Over the 15 years of the LV evolution analyzed (1998-2012) using the MIT GCM, 21 mergers were recorded (Fig. 5.4), with an average of 1-2 mergers per year. This is close to the number of mergers identified from satellite altimetry data of approximately 0.8 per year (Belonenko et al., 2020), especially considering the known shortcomings of eddy detection in altimetry data (see Section 2), which may not have allowed identifying all the merger episodes.

For a detailed study, we selected the time period from August 2002 to July 2003, during which the LV interacted 6 times with the same surface anticyclone (hereinafter referred to as AC), formed on the eastern branch of the Norwegian Current. The LV and AC had similar dynamic radii (about 30 km) and relative vorticity anomalies of their cores of approximately the same intensity (3-4 10 $^{-5}$ s $^{-1}$) during the entire period of the analysis (Fig. 5.5).

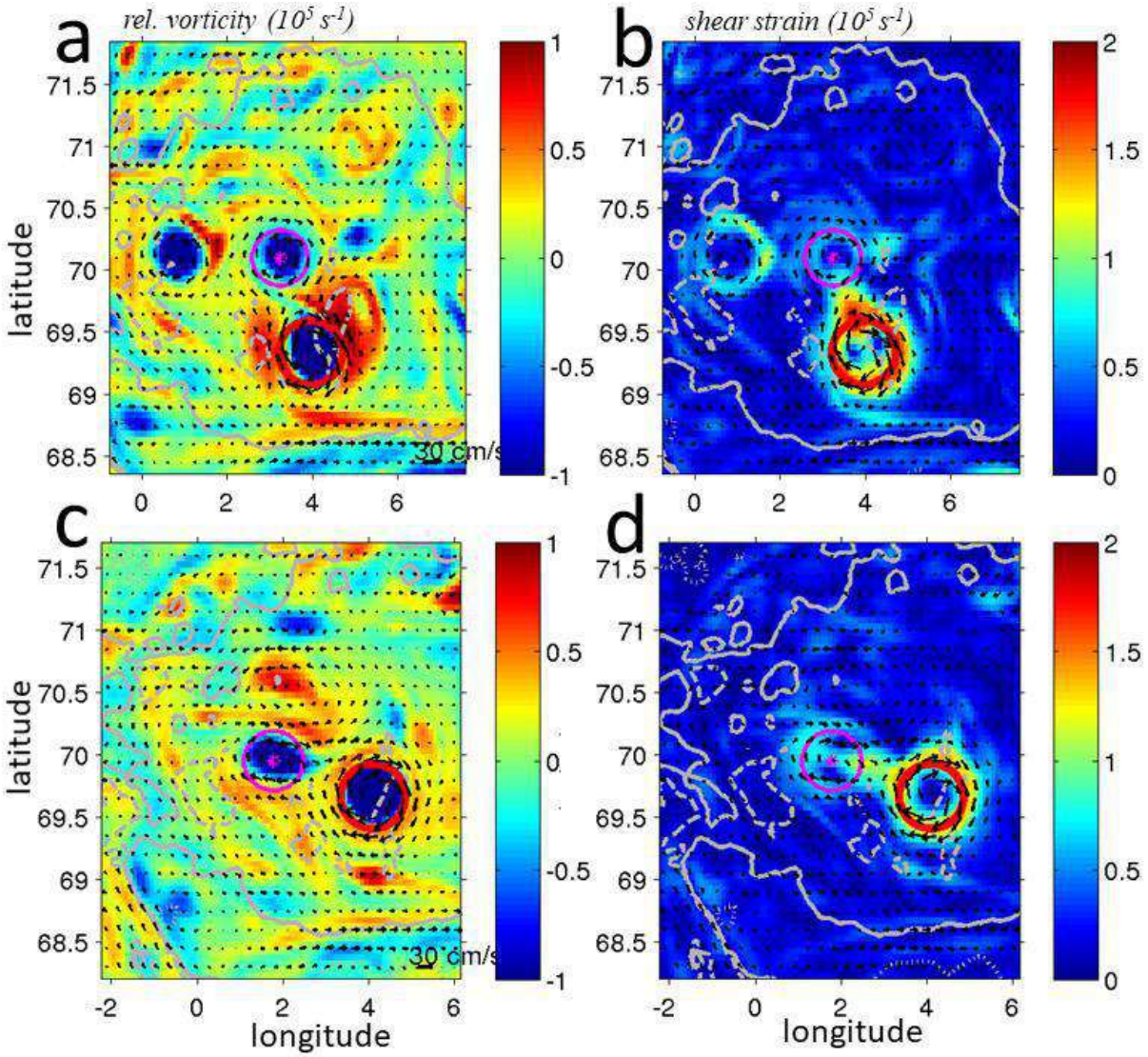

Fig. 5.5. Anticyclone AC (pink circle) and the LV (red circle) shown in the relative vorticity distribution at the sea surface (10^{-5} s^{-1}, panels a-c on the left) and in the field of shear and compression strain intensity (10^{-5} s^{-1}, panels b-d on the right); MIT GCM data. (a-b) – during the 1st approach (09.04.2002, model week 557) with subsequent repulsion; (c-d) – during the 6th approach (06.11.2003, model week 597), shortly before the merger. Black vectors – current velocity; gray contours – isobaths of 3000 m (solid line) and 3240 m (dashed line).

Over the course of almost a year of analysis, the structure of the velocity field in the AC has somewhat evolved, also under an influence of AC mergers with three other surface anticyclones and, probably, of winter convection (Fig. 5.6 a, b). The vertical structure of both the AC and LV is well described by the exponential function (Morel and McWilliams, 1997): $v_{\theta m}(z) \sim V_{deep} + V_0 \exp\left(\frac{(z-H)^2}{h_z^2}\right)$, where H is the depth of the center of the vortex core, h_z is the vertical scale of the exponential decrease in the azimuthal velocity from the center of the core, V_{deep} is the current velocity below the core (at depths of more than 1500 m) and V_0 is the amplitude. For the LV, the vertical scale h_z did not change throughout the entire analysis period and amounted to 650-750 m. For the AC, at the beginning of the analysis period, h_z = 350 m was significantly less than in the LV, and the maximum azimuthal velocity was significantly higher than in the LV. Immediately before the merger, the characteristics of the AC were much closer to those of the LV:

h_z increased 1.5 times (to 530 m) in the AC, and the peak azimuthal velocity decreased and became lower than that in the LV. At the depth of the core, the azimuthal velocity of each of the eddies was well approximated by a Gaussian profile: $v_\theta(r) \sim \exp\left(-\frac{r^2}{R^2}\right)$.

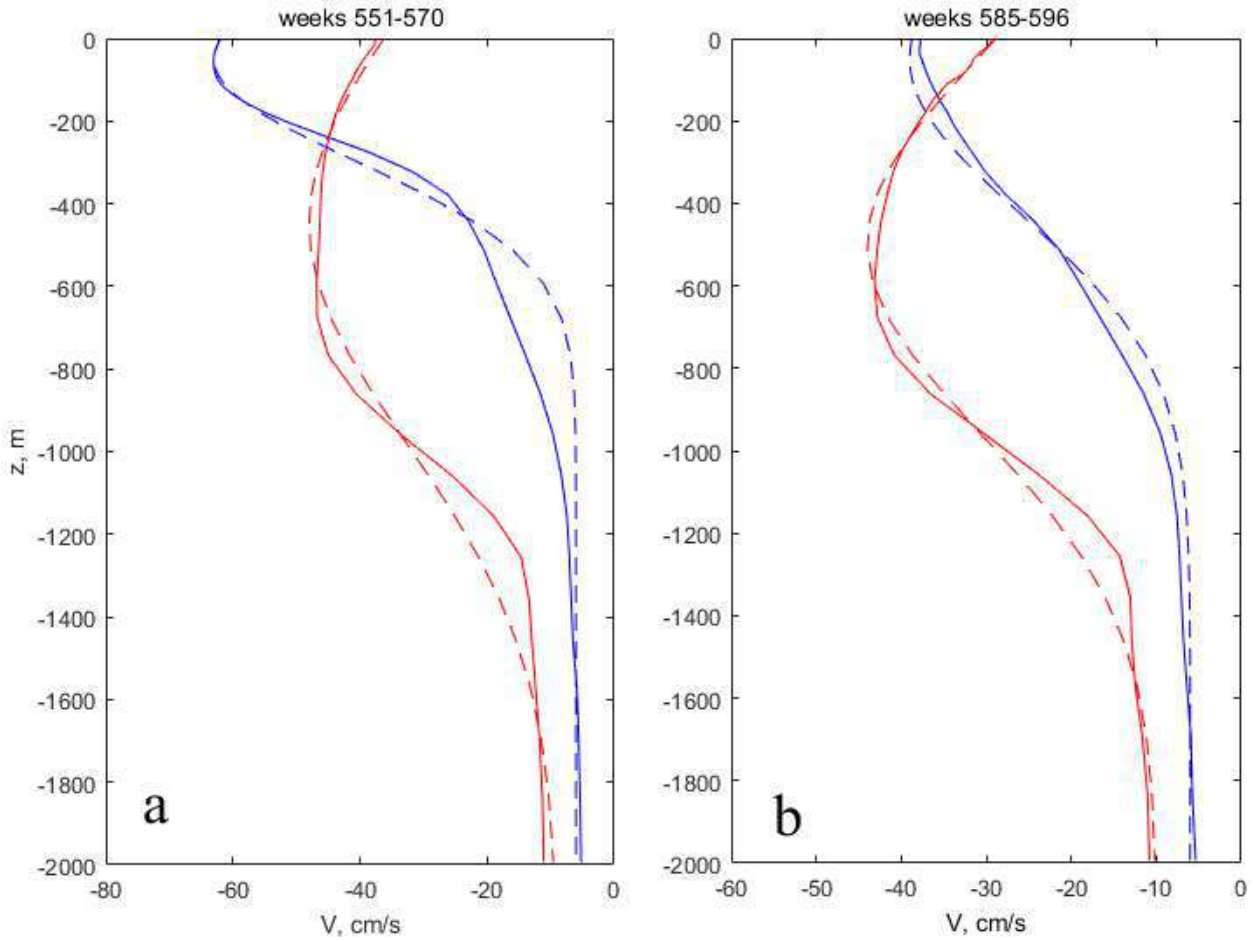

Fig. 5.6. Vertical structure of the azimuthal velocity v_θ at: (a) the initial period of analysis (08.21-04.12.2002 – weeks 555-570) and (b) immediately before the merger (19.03-04.06.2003 - weeks 585-596). AC (blue solid line) and LV (red solid line). Their vertical approximations with the exponential function (see text) are represented with dashed lines.

The potential vorticity anomaly was computed as $\Pi = \frac{N^2(x,y,z)}{g}(f+\omega) - \frac{N_0^2(z)}{g} f_0$, where N_0 is the buoyancy frequency profile for the entire period of the analysis, averaged over the Lofoten Basin outside eddy cores (i.e., estimated at the points where the absolute value of the relative vorticity ω did not exceed the selected threshold of 0.5 10^{-5} s^{-1}), and f_0 is the average Coriolis parameter for the Lofoten Basin. Anomalies of Π, negative in the cores of anticyclones and positive at their boundaries (the so-called screen), create a strong barrier that prevents water exchange between eddy core and the environment, and also makes it difficult for eddies to merge.

Previous studies on eddy mergers has shown that the interaction of two eddies of the same sign can lead to the following consequences: elastic repulsion of the eddy cores, partial eddy merger with a partial exchange of water between the merging eddies, or complete eddy merger with an absorption of a smaller vortex by a larger one, if the initial eddy volumes were different

(Polvani et al., 1989; Dritschel and Zabusky, 1996; Zhmur, 2010; Carton et al., 2016). Model results predict that the merger of unshielded eddies begins at a distance of 3-4 radii between their centers. The critical distance depends on the characteristics of the eddies, as well as on the presence or absence of an external deformation field of divergent or convergent mean currents (Carton et al., 2002; Maze et al., 2004). For two shielded eddies, models predict the possibility of merging at a smaller critical distance of 2.2-2.5 vortex radii, which means that the merging process is more difficult (Carton, 1992, Ciani et al., 2016).

During the period of their interaction, the AC approached the LV to a distance of slightly less than 3 dynamic radii 6 times, but a distance of 2 radii was never reached until the AC was stretched into a filament during its merger with the LV (Fig. 5.5-5.6). At the same time, it was noted that when the eddies approached at a distance of the order of 3 radii, the peripheral regions of their azimuthal rotation overlapped. In the area of their contact, a sharp increase in the tangential shear stresses of the current velocity was noted, with, as well as without the eddy screens (Fig. 5.5, 5.7c,f). This indicates a strong interaction of the dynamic fields of both eddies during these periods (see also Maze et al., 2004) and, therefore, the distance of 3 radii was chosen as the criterion for the beginning of eddy-eddy interaction. Of the 6 interactions, 5 followed the scenario of elastic repulsion and only the last one ended in merger with absorption of the AC by the stronger LV.

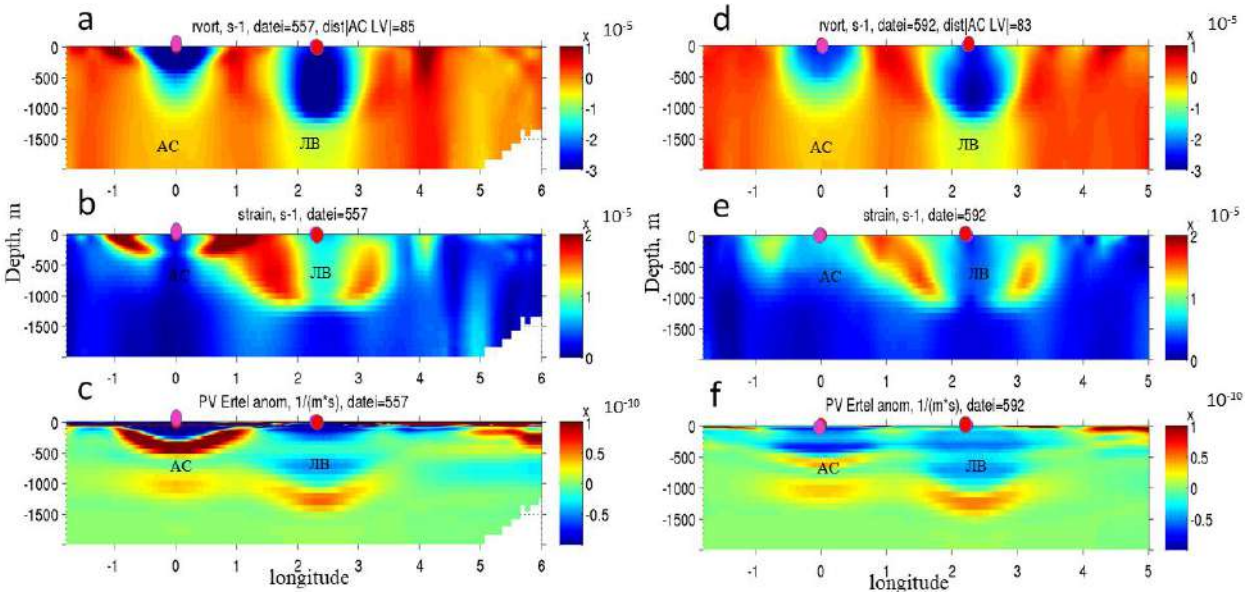

Fig. 5.7. Characteristics of the LV and AC on a vertical section connecting the centers of two eddies, during the first interaction of the AC with the LV (a-c: 08.28.2002 - week 556) and immediately before the merger of the AC with the LV (d-f: 05.07.2003, week 592); the merger occurred 06.25-07.02.2003 (weeks 599-600, see Fig. 5.10). From top to bottom: (a,d) relative vorticity (10^{-5} s^{-1}), (b,e) shear strain (10^{-5} s^{-11}) and (c,f) Ertel potential vorticity (10^{-10} m^{-1} s^{-1}). The center of the LV is marked with a red dot, and of the AC – with a purple dot.

The main dynamic characteristics of the LV and AC during the period of their interaction were integrated in the upper 500-meter layer, with the exception of the potential vorticity anomalies, for which the depth range of 100-500 m was taken (Fig. 5.2a, 5.7a, d). In the radial direction, integration was carried out over the central part of the core (i.e. for $r \le 0.5R$), along the inner periphery ($0.5R \le r \le R$) and along the outer periphery ($R \le r \le 1.5R$) of the eddies. The circulation and integral angular momentum of inertia of the AC ($\iiint v_\theta r^2 \, dr \, d\varphi \, d\theta$), which increased

slightly after the merger with other anticyclones between the 1st and 2nd interactions, then permanently decreased in the time, and the characteristics of the LV remained practically unchanged until its merger with the AC (Fig. 5.8a). Each interaction (from the 1st to the 6th) led to an increase in shear stresses in the area of contact of the eddies, especially at their periphery (Fig. 5.7b,e). All 6 interactions of the AC and LV can be divided into two subsets: 1-3 – AC with a screen, 4-6 – AC without a screen.

During the first three interactions between the AC and the LV (from August 2002 (week 555) to January 2003 (week 570)), the strong potential vorticity screen of the AC (Fig. 5.7c) prevented the merger with the LV (Carton, 1992). At the same time, mergers of the AC with other surface anticyclones were observed. During the interactions of the AC with the LV, the shear stresses in the area of contact of the eddies continued to increase throughout the entire interaction time (Fig. 5.8b). However, shear stresses were concentrated at the periphery, without penetrating into the vortex cores. Even before the start of active interaction (reaching a distance of 3 radii), the initially present tendency towards the convergence of two eddies slowed down and soon was replaced with divergence (Fig. 5.10). As a result, the time of the eddy contact was limited, joint rotation of the AC-LV system around their common center was not observed, the moment of inertia of the AC core was not converted into energy of the mutual rotation of the eddies, and, therefore, there was no change in the angular momentum of the AC core (Fig. 5.8a). In the shielded AC, the circular motion in the cores was quickly restored after the contact, and distortions of the axisymmetric shape did not penetrate into the eddy core.

From December 2002 (week 570) to March 2003 (week 582), a significant decrease in of the potential vorticity anomalies in the AC core was observed both, as well as in the skirts of the AC and LV (Fig. 5.7f). This is presumably due to a decrease in the anomalies of vertical distance between of isopycnals in the core and of their convergence at the periphery of the AC relative to the background, as a result of the deepening of the upper mixed layer from 20-50 m to 200-300 m in winter. The radius of the AC did not change, therefore, the relative vorticity of the core and angular momentum of inertia in the AC decreased as a result of a decrease in its rotation velocity (Fig. 5.8a). Immediately after the initial rapid decrease in the Π anomaly in the core region in winter (weeks 570-574), an increase in the eccentricity of the AC was observed (from the 575th week), which indicates the development of elliptical instability of the vortex. The slowdown in rotation of the AC in winter was apparently a consequence of the development of instability at its periphery (see a similar analysis for the LV in Section 5.1.3). An increase in eccentricity was not observed in the LV, the core of which is located below the level of winter convection at 2002-2003. Thus, winter convection led to a weakening of the negative Π anomaly of the AC core, a weakening of the Π screen at its periphery, which, altogether, led to an increased instability of the AC and formed the conditions for a complete shed of its Π screen.

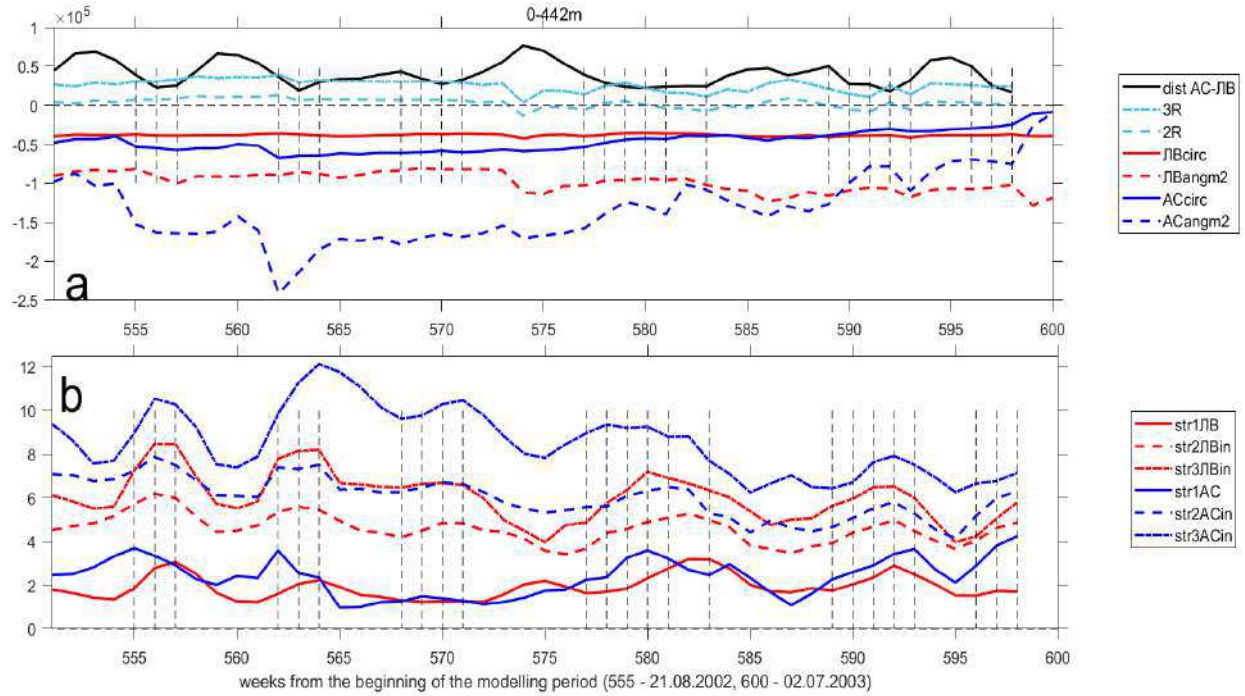

Fig. 5.8. Evolution of characteristics of the LM and of an anticyclonic vortex (AC), averaged in the upper 500m layer. The x-axis shows weeks (August 2002 - July 2003) from the start of the MIT GCM simulations. In panel (a): The black solid line is the distance between the centers of the AC and LV (not in scale: the minimum distance between the eddy centers is about 80 km), dotted vertical lines mark weeks when this distance was less than 3 radii of the LV. The critical distances between the centers of the LV and AC of 3 LV radii (blue dash-dotted line) and 2 LV radii (blue dashed line); circulation of the LV core ($m^2 s^{-1}$, red solid line) and the AC core ($m^2 s^{-1}$, blue solid line), the integral momentum of inertia of the LV core ($m^4 s^{-1}$, red dashed line) and of the AC core ($m^4 s^{-1}$, blue dashed line). Panel (b) shows the average shear stress ($5\ 10^5\ s^{-1}$) along the line connecting AC and LV (see Fig. 5.7): in the vortex cores (solid lines), in the internal regions of the eddy peripheries (dashed lines) and in the outer regions of the eddy peripheries (dash-dotted lines). The results are given for the LV (red lines) and for the AC (blue lines).

The final removal of the Π -screen in the AC occurred during its 4th interaction with the LV. The higher intensity of the interaction was promoted by the deformation velocity field formed by another anticyclone to the north of the AC-LV pair. The LV captured part of the positive Π-anomaly in the AC skirt and transported it northwestwards. This is suggested to be a reason for generation of a cyclone northwest of the AC, which contributed to the further eddy convergence and the acceleration of the release of the Π-screen by the AC (Fig. 5.9).

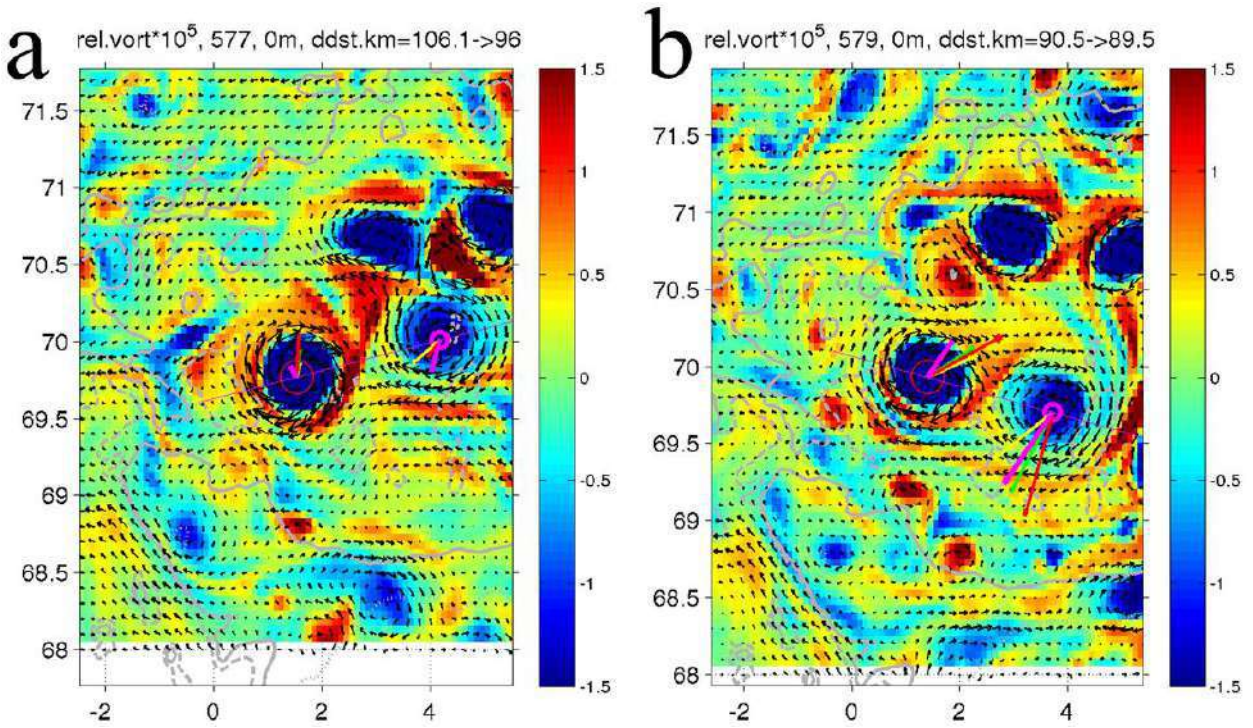

Fig. 5.9. Two successive images during the 4th interaction of the AC (red circle, eddy on the left) and LV (pink circle, eddy on the right) in the relative vorticity field (color, 10^{-5} s^{-1}): a) model week 577 and b) 579. Pink arrows indicate the directions of movement of the eddy centers, red arrows indicate the directions of the background current (external forcing), average outside the peripheries of each eddy.

From the 4th to 6th interactions, there was no potential vorticity screen around the AC (Fig. 5.7f). During these interactions, shear stresses peaked in the AC core not at the very beginning of the interaction (as for episodes 1–2), but in the middle or at the end of the interactions (Fig. 5.8b). Also, in contrast to the first 3 interactions, the velocity of the eddy approach decreased slower after reaching the critical distance, and the interaction period increased from 3-4 weeks to 5 weeks at 5th and 6th interactions (Fig. 5.10). Starting from the 4th interaction, when the AC was at the stage of transition from the shielded to the unshielded eddy, a joint rotation of the AC and LV around a common center began to be observed during interactions of the eddies (Fig. 5.9). The velocity of joint rotation such eddies around their common center was proportional to the circulation of the interacting eddies $\Omega \sim \Gamma$ (Meunier et al., 2005). The circulation of the LV remained practically unchanged, and the circulation and angular momentum of inertia of the AC decreased significantly with each interaction, which was the result of the transfer of the angular momentum of inertia of the AC to the joint rotation of the interacting eddies (Fig. 5.8a). During the interactions, the formation of filaments and submesoscale eddies was also observed, which was not typical for the first 3 interactions of eddies with screens. These structures also dissipated part of the angular momentum of the AC (Fig. 5.9).

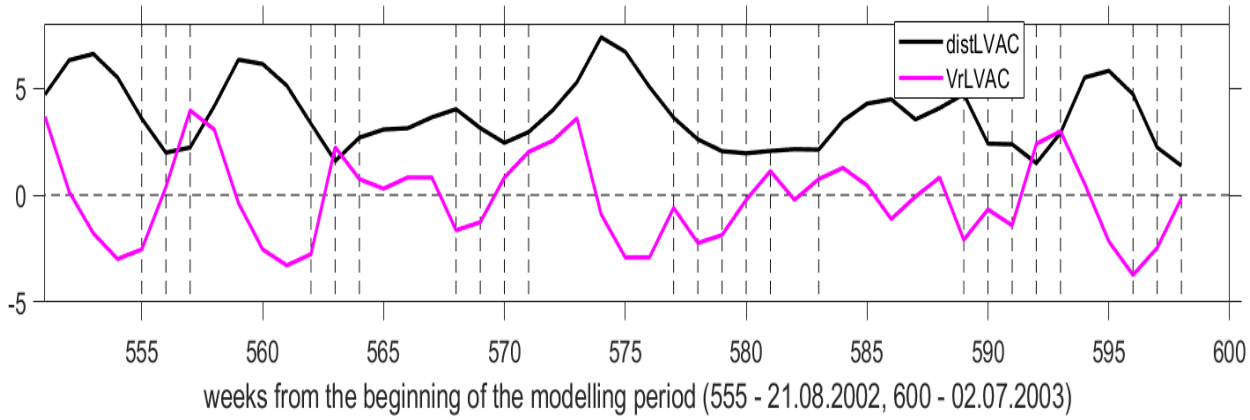

Fig. 5.10. Evolution of the velocity of the approach of the AC and LV along the line connecting their centers (cm s^{-1}, purple line, the negative values characterize the approach of the AC to the LV). The black solid line is the distance between the centers of the AC and LV (not to scale; the minimum distance is ~80 km), dashed vertical lines mark weeks when this distance was less than 3 radii of the LV. The x-axis shows the weeks from the beginning of the MIT GCM simulations (August 2002 to July 2003).

During the last (6th) interaction of eddies, immediately before their merger, the AC was significantly weakened (Fig. 5.7a). During the interaction, shear deformation penetrated deep into the AC core (Fig. 5.7e), changing the spatial structure of azimuthal velocities around the center of the eddy from initially almost circular to pronounced elliptical (Fig. 5.5 c, d). This means that there was a rapid increase in the amplitude of the elliptical azimuthal instability mode in the velocity field of mutual deformation of the interacting eddies (see Maze et al., 2004).

The weakening during winter of the summer potential vorticity screen is a characteristic feature of eddies in this region. This is due to the seasonal deepening of the upper mixed layer by an average of 200-400 m. Thus, in the upper 100-m layer above the LW, the potential vorticity anomaly in summer was 2.5 times bigger than in winter (see example in Fig. 5.11). This hinders the merger. Modeling of an interaction of the LV with the anticyclone in the QG model showed that in the absence of a screen, the anticyclone merged with the LV when the eddies approached at a distance of 3 LV radii, whereas in the presence of a screen, even a direct contact of the peripheries of the eddies, with the distance between their centers of 2 LV radii, did not lead to a merger (X. Carton, personal communication, see also Ciani et al., 2016).

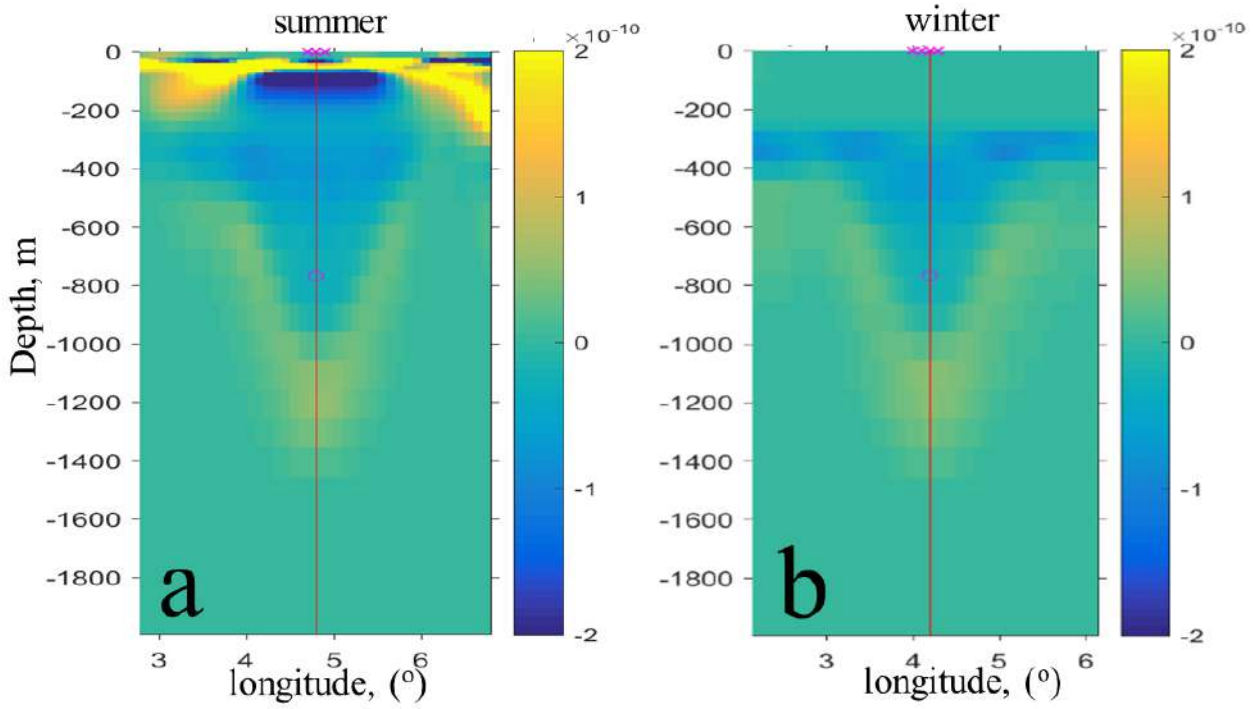

Fig. 5.11. Ertel potential vorticity ($m^{-1} s^{-1}$) at zonal sections through the LV center: a) in summer (example from 09.03.2008); b) in winter (example from 04.02.2008)

Despite the AC lost its *П*-screen already during the 4th interaction with the LV, it did not merge with the LV neither during the 4th, nor during the 5th interactions. This means that the presence of *a П*-screen was not the only obstacle for the merger. During the initial period of every interaction, the component of the approach velocity of the eddies along the line connecting their centers is negative (the AC approached the LV) and relatively high (Fig. 5.10). The approach velocity decreases and then becomes positive during the period of interaction of the eddies, i.e. interacting eddies of the same sign begin to repel each other. For the unshielded AC, this trend is somewhat less pronounced. The merger of the AC with LV occurred only when an intense cyclone to the northeast of the AC pushed it towards the LV (Fig. 5.5c). Due to this, the initial velocity of the AC approaching the LV was 1.5 times higher than during other interactions (Fig. 5.10). A similar effect of a cyclone promoting the merger of two anticyclones was observed in simplified quasi-geostrophic models of eddy-eddy interactions (Dritschel, 1995; Dritschel and Zabusky, 1996; Reinaud and Carton, 2023). However, the opposite effect was also observed, when a cyclone prevented the merger of two anticyclones (Rodriguez-Marroyo et al., 2011). The rsult of the merger strongly depends on the relative positions and parameters of the interacting eddies (Reinaud and Carton, 2023).

Thus, the final merger of anticyclones (AC and LV) was facilitated by at least two circumstances: the absence of a *П* -screen at the peripheries of both eddies and the presence of an external deformation field of neighboring eddies, which contribute to the convergence of the AC and LV, as well as to an increase in the time of their interaction. During the interactions, the momentum of inertia of the AC decreased, turning into the momentum of inertia of the mutual rotation of the AC and LV. At the same time, penetration of the shear stress deep into the AC core was observed, followed by elongation of the core, presumably as a consequence of the development of elliptical instability of the AC. All this contributed to a decrease in the isolation

of the AC and further extension of the AC into a filament, which then “coiled” around the LV core (see also Zhmur et al., 2023).

5.1.3 Stability of the Lofoten Vortex, dissipation mechanisms from the MIT model results

In this section, it is shown that the quasi-permanent existence of the LV is ensured not only by its periodic regeneration, but, above all, by the initial high dynamic stability of the LV. The abnormally high stability of the LV is associated with the topography of the Lofoten Basin. As was shown in the previous section, episodes of LV regeneration through its merger with other anticyclones or deep winter convection in the vortex core usually occur in the winter-spring season (Fig. 5.4). During many months, the LV exists without external energy supply. During these periods, the kinetic and available potential energy of the vortex gradually decreases with time, but this does not lead to any significant decrease in the volume of the vortex.

The LV stability was studied by setting up experiments with the quasi-geostrophic (QG) model of M.A. Sokolovsky, the results of which were compared with the results of the MIT GCM primitive equation model, as well as with observations. Dynamic instability has been investigated as the main mechanism of the eddy break up (Smeed, 1988b).

The QG theory suggests that for a uniformly rotating axisymmetric Rankine vortex with constant relative vorticity of its core, a stationary solution of the two-dimensional Euler equations in the barotropic ocean is robust to small-amplitude disturbances of the vortex periphery (Lamb, 1885). For a two-layer fluid, with different signs of potential vorticity anomaly of the vortex core in different layers, the Rankine vortex can become unstable (Pedlosky, 1985; Kozlov et al., 1986; Sokolovsky, 1988; Ripa, 1992; Mesquita and Prahalad, 1999; Sokolovskiy and Verron, 2000; Benilov, 2005 a, b; Reinaud and Carton, 2009; Sokolovskiy et al., 2009; Cohen et al., 2015). For a three-layer fluid, a sufficient instability condition is achieved when at least one of the stratification parameters γ_1 or γ_2 (proportional to the first and second Rossby radii of deformation, respectively) reaches a certain threshold value (Holmboe, 1968; Davey, 1977; Wright, 1980; Smeed, 1988a, 1988b; Sokolovskiy, 1991; Ikeda, 1993; Sokolovskiy, 1997a,b). For typical ocean conditions, when the density jump at the upper interface (between layers 1 and 2) is much larger than at the lower interface (between layers 2 and 3), instability develops by exciting long waves on an inclined upper isopycnal surface around the vortex core, and short waves on an inclined lower isopycnal surface around the vortex core (Smeed, 1988a,b; Sokolovskiy, 1997a,b).

Theoretical results predict that ocean eddies are largely unstable and should collapse rapidly (see, for example, Ikeda 1981; Flierl, 1988; Helfrich and Send, 1988; Carton and McWilliams 1989; Ripa 1992; Killworth et al., 1997; Benilov et al., 1998; Baey and Carton, 2002; Benilov, 2003; Katsman et al., 2003), while observations indicate that some oceanic eddies can exist for several years (see, for example, Lai and Richardson, 1977; Filyushkin and al., 2009: Bashmachnikov et al., 2015c). An attempt to resolve this contradiction was made by Dewar and Killworth (1995) and Benilov (2004), who showed that for Gaussian or any other type of eddies in a two-layer fluid, the presence of a projection of the vortex circulation into the lower layer, even a significantly weakened one, strongly decreases the development of instability in the vortex. Such vertical structure is often found in ocean anticyclones, including meddies and LV.

The three-layer linear analytical and nonlinear numerical QG models by M.A. Sokolovskiy (Sokolovskiy, 1997a,b) used below, suggest a fundamental possibility of an instability

development via a growth of the baroclinic Rossby waves trapped by the vortex, which is noted to be the most common reason for a rapid eddy destruction. In this regard, the QG model, despite obvious simplifications, should adequately describe the changes in the rate of LV destruction s a function of external conditions.

The parameters of the LV in layers of constant density ρ_j (j =1 – layer above the LV core, which is 250 m thick, j =2 – layer of the LV core, which is 405 m thick, j =3 – layer above the LV core, which is 2345 m thick) were specified according to their average values derived from in the MIT GCM (Table 5.1).

Table 5.1. Mean values of LV parameters in 3 vertical layers: R – the LV radius, $v_{\theta m}$ – peak azimuthal velocity, ω – relative vorticity, Π – potential vorticity, $\overline{\Pi}$ – normalized potential vorticity in the model (expression 5.5), $\sigma_{0.5}$ – average potential layer density relative 500 m.

Parameter	Layer 1	Layer 2	Layer 3
Depth of the lower boundary of the layer (z, m)	250	655	3000 (sea bottom)
Deviation of the isopycnal in the center of the LV from its average position, for the lower boundary of the layer (η, m)	135	-500	0 (sea bottom)
Layer thickness (h, m)	250	410	2345
R, km	30.5	30.0	32.0
$v_{\theta m}$, cm s $^{-1}$	-34	-37	-eleven
$\lvert v_{\theta m\,1,3}\rvert \le \lvert v_{\theta m\,2}\rvert$,%	97%	-	100%
ω, s^{-1}	-1.13 10 $^{-5}$	-1.32 10 $^{-5}$	-0.38 10 $^{-5}$
$\lvert\omega_{1,3}\rvert \le \lvert\omega_2\rvert$,%	97%	-	100%
Π, s^{-1}	0.66	-1.61	0.21
$\overline{\Pi}$ ±std	4.6±1.9	-13.2±5.6	1.4±0.1
$\sigma_{0.5}$, kg m^{-3}	30.11	30.29	30.54

The dynamic LV radius was set to 30 km, and the normalized anomalies of the potential vorticity of the LV in each of the 3 layers were taken $\bar{\Pi}_1 = 0.66\,c^{-1}$, $\bar{\Pi}_2 = -1.61\,c^{-1}$, $\bar{\Pi}_3 = 0.21\,c^{-1}$. The normalized potential vorticity was determined by the following expression:

$$\bar{\Pi}_n = \tilde{\omega}_n + \Delta\tilde{h}_n / \tilde{h}_n, \qquad (5.5)$$

where $\tilde{\omega} = \omega / \left(\frac{V}{R_{vm}} \right)$, $\Delta\tilde{h} = \Delta h / \left(Ro \cdot H_L \right)$, $\tilde{h} = h / H_L$, R_{vm} is the radius of the maximum azimuthal velocity of the vortex, *Ro* is the Rossby number of the vortex, H_L = 3000 m is the depth

of the basin. A detailed description of the model configuration used is given in Bashmachnikov et al. (2017).

In the first experiments, a flat bottom basin was considered. The areas of instability for various azimuthal modes in the parameter space $(\bar{\Pi}_1, \bar{\Pi}_3)$ form the areas to the right of the $(\bar{\Pi}_1, \bar{\Pi}_2)$ neutral curve of the corresponding mode shown in the figure (Fig. 5.12). For the main isopycnal configurations in the LV (Fig. 5.3), configurations A-D fall into the region of instability of the azimuthal modes 2, 3 and, partially, 4. During the periods when the deep winter convection penetrates into the LV core (configurations B and B1), only instability of the 2nd and, rarely, the 3rd azimuthal modes can develop (Fig. 5.12).

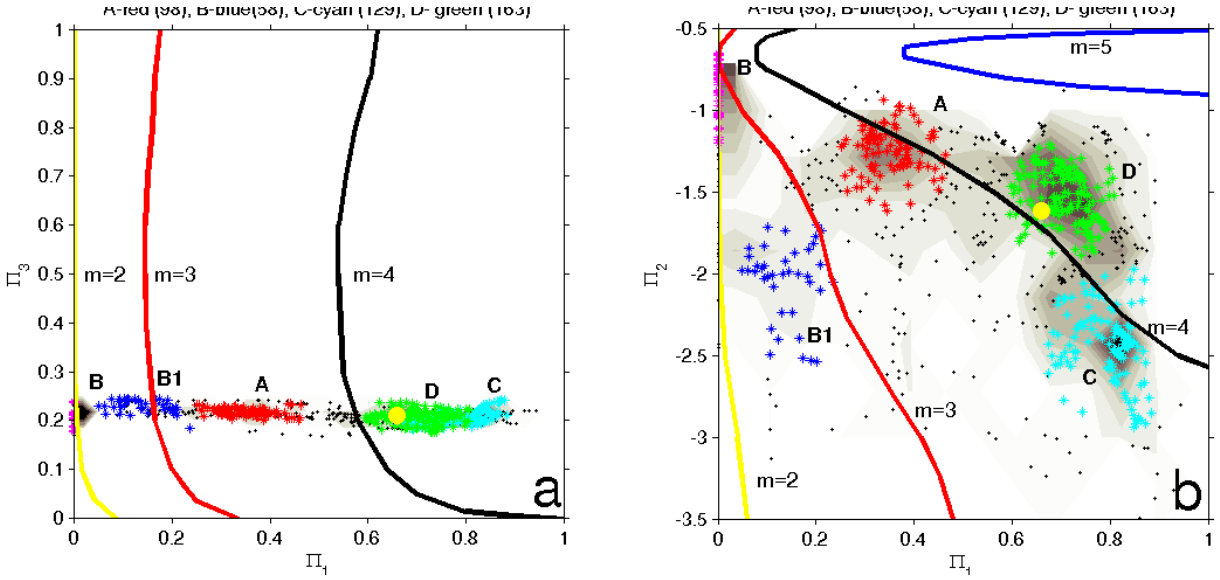

Fig. 5.12. Potential vorticity anomalies in the LV (MIT GCM) in the parameter space: (a) $(\overline{\Pi}_1, \overline{\Pi}_3)$ and (b) $(\overline{\Pi}_1, \overline{\Pi}_2)$. The subscripts, as before, indicate the layer numbers:1, 2 (the LV core) and 3. Anomalies of potential vorticity in the LV for the entire MIT GCM modelling period for weekly data are marked with black dots. Colored symbols indicate configurations of the vertical LV structure classified as the clusters A, B, B1, C and D (see Fig. 5.3). The yellow circle indicates the time-mean LV parameters for the entire period (1998-2012), used for analytical calculations with the 3-layer model. At the top are the lines of neutral stability of the LV in the analytical model for the azimuthal modes: m=2 (yellow), m=3 (red), m=4 (black) and m=5 (blue). The regions of the LV instability to disturbances with the azimuthal mode m are located to the right of the corresponding line (from Bashmachnikov et al., 2017).

Of all the theoretically possible modes, only the instability of the fastest growing mode actually develops. A numerical study of the rate of development of instability in a nonlinear QG model was carried out for small initial disturbances of the eddy boundary with the normalized amplitude of $\varepsilon_j = 0.02$ and for finite initial disturbances with $\varepsilon_j = 0.20$.

For small perturbations, the LV core persisted for at least 8 months. The most effective destruction of the core of the vortex occurred for m = 3, when the core of the vortex was destroyed within 5-6 months (Table 5.2). For the azimuthal mode m = 4, the instability developed faster, but affected only the periphery of the LV, while the volume of the LV core remained almost the same even 8 months latter. A tenfold increase in the amplitude to the level of finite initial disturbances

led to a significant acceleration of the development of instability (Table 5.2). For all three first azimuthal modes, the LV core lost more than 50% of its initial volume after 3-4 months. The destruction of the LV core went most quickly also for m= 3. A similar theoretical study of the instability of meddies in the subtropical Atlantic showed that for large eddies (R ~ 1-5 Rd , as in the LV), the most unstable was also the 3rd azimuthal mode (Carton et al., 2014).

Table 5.2. The rate of destruction of the LV, expressed in % of the remaining volume of the LV relative to its initial value in each layer (1, 2 and 3) after a 5-month period of calculations using the numerical QG model for small disturbances ($\varepsilon_j = 0.02$) and finite disturbances ($\varepsilon_j = 0.20$). The data are presented for the average LV characteristics over the entire period of the analysis (configuration D), as well as for the 2-layer winter period (configuration B). The results given in parentheses represent the 8-month period of computations, if the LV core survives until this time.

Intensity of initial disturbances		ε = 0.02 (small disturbances)			ε = 0.20 (finite disturbances)		
Azimuthal mode:		*m* =2	*m* =3	*m* =4	*m* =2	*m* =3	*m* =4
3-layer configuration for warm season (configuration D)							
Layer No. (*j*)	1	100% (37%)	15%	46%	31%	5%	36%
	2 (LV core)	100% (37%)	27%	89%	44%	20%	46%
	3	100% (17%)	16%	99%	0%	6%	15%
2-layer configuration for winter (configuration B)							
Layer No. (*j*)	2 (LV core)	100% (59%)	100% (45%)	100% (54%)	71%	51%	52%
	3	100% (36%)	100% (20%)	100% (165)	100%	26%	17%

In the MIT primitive equation model, the near-surface 200 m level was selected for the analysis because, according to the QG model results, the upper layer above the core was the most unstable (Table 5.2). This was also confirmed by MIT GCM results. For analysis, three rings were selected inside the area of the anticyclonic rotation of the LV: the boundary of the core $R_1 \pm dr$ ($R_1 = R$ is the LV dynamic radius), the inner periphery of the LV $R_2 \pm dr$ (where the relative vorticity has the opposite sign with respect to the LV core and reaches its local maximum), on the outer periphery of the LV $R_3 \pm dr$ (where the vortex rotation velocity decreases to 10% of its maximum value). dr was taken equal to half-distance of $R_2 - R_1$. Within each ring, the average potential vorticity ($\Pi = N^2(f + \omega)/g$) was computed and the obtained values were converted into deviations of the potential vorticity isolines from circular ones ($\varepsilon = \Pi' / \partial\tilde{\Pi}/\partial r$, where $\tilde{\Pi}$ means the average value of Π in the ring, and $\Pi' = \Pi - \tilde{\Pi}$). The resulting series of ε were decomposed into azimuthal modes using wavelet analysis in the periodic domain with Morlet mother wavelets (Torrence and Compo, 1998).

As in the QG model, according to the MIT GCM data, in the LV, the 2nd, 3rd, 4th and, at times, 5th azimuthal modes were detected (Fig. 5.13) with the respective median deformations of: 12%, 5%, 3% and 1% of R_1; 16%, 11%, 7% and 3% of R_2; and 25%, 20%, 16% and 8% of R_3. The strengthening and weakening of the identified azimuthal modes in time occurred in a consistent manner. Thus, the MIT GCM was dominated by elliptical azimuthal mode 2, and the perturbation energy decreased with an increasing mode number. With distance from the core, the relative intensity of the higher modes increased: at the outer periphery of the LV, the intensity of the 3rd mode reached 80% of the intensity of the 2nd mode, and the 4th mode – 65% of the 2nd mode. Azimuthal disturbances of the 2nd mode were clearly visible in the vertical velocity field and visually, although rather weakly, manifested themselves in the relative vorticity field at the periphery of the LV (Fig. 5.14).

The nonlinear QG model, where the 3rd disturbances mode dominated, indicates an increasing importance of the 2nd azimuthal mode with increasing intensity of the disturbances (Table 5.2). Considering the limitations of the QG model, the identified development of the 2nd azimuthal mode in the MIT GCM (Fig. 5.13), in general, does not contradict the results of the QG model.

The normalized intensity of disturbances ε in the MIT GCM is on the order of 0.10-0.20, which in the quasi-geostrophic model represent the disturbances of finite amplitude. The MIT GCM results show that, similar to the QG model, the total time of instability growth ranged from 3 to 7 months (Fig. 5.13). However, the development of instability in the MIT GCM did not lead to a significant change in the dynamic radius of the LV, in contrast to the QG model, where instability invariably led to the splitting of the LV core (for the most unstable mode 3, more than 50% of its initial LV volume dissipated in 4-5 months). Only in 2001 (weeks 420-460) and 2006 (weeks 680-740), the development of disturbances at the LV boundary led to a decrease in the LV dynamic radius by 5 km (15% of the original value), which is equivalent to a loss of approximately 30% of the original core volume. However, after 3-4 months, the original volume of the LV core was restored, also due to a merger with other eddies (Fig. 5.13).

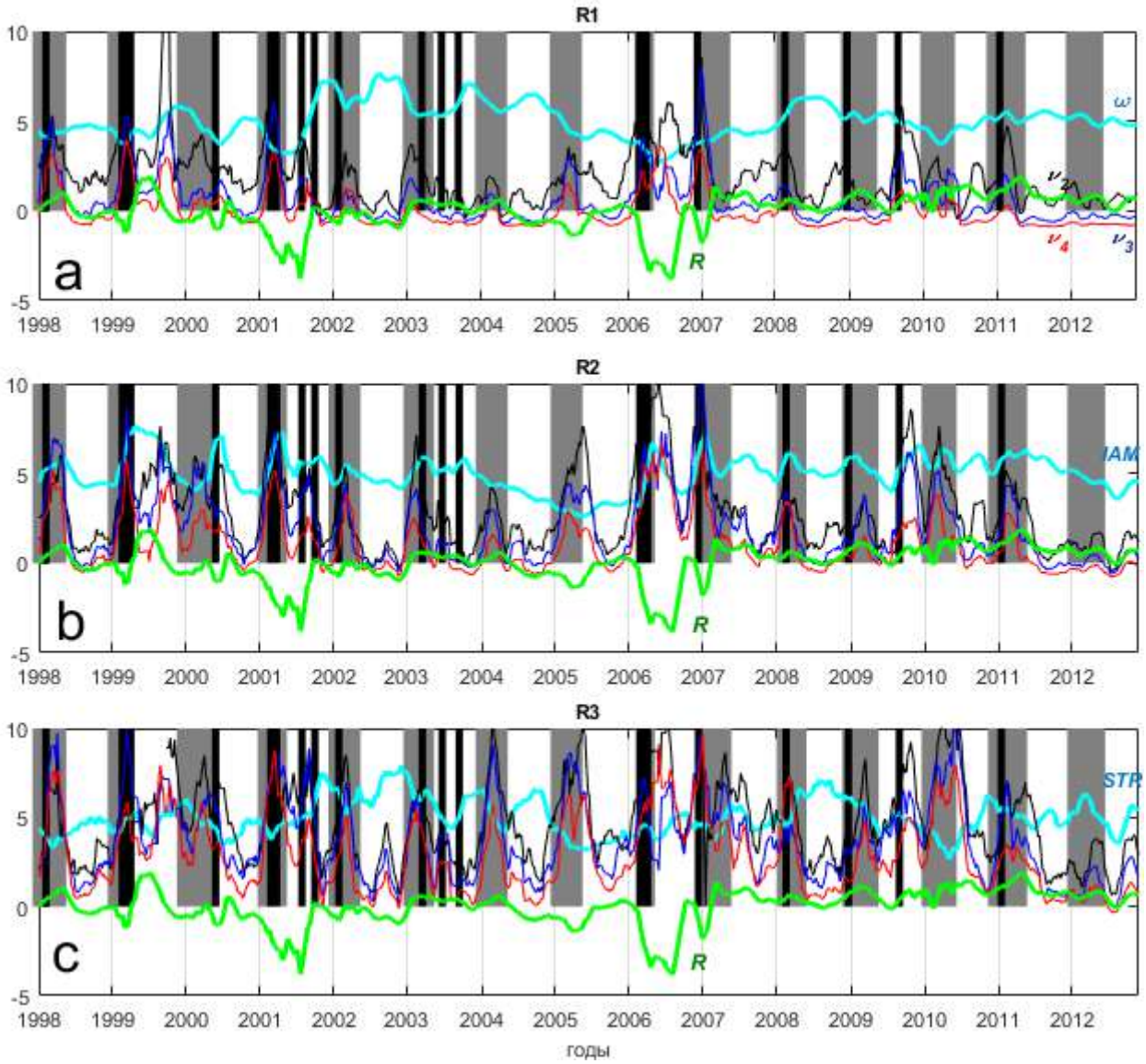

Fig. 5.13. Time variability of LV characteristics in the MIT GCM at a 200 m in rings $R_i \pm dr$ *: (a) in ring 1 (the outer boundary of the LV core with a mean radius* $R_1 = R$*), (b) in ring 2 (the inner periphery of the LV with a mean radius* $R_2 = 1.5R$*), and (c) in ring 3 (the outer periphery of the LV with a mean radius* $R_3 = 2R$*). All panels show:* R *- the dynamic radius of the LV (km, minus its mean value) and the normalized intensity of disturbances of the 3 most intense azimuthal modes: m=2 (black line), m=3 (blue line) and m=4 (red line). Normalization was carried out using the expression:* $v_i = \left(v_i - v_{4,av}\right)/v_{4,std}$*, where* v_{4av} *and* v_{4std} *are the average and the standard deviation of the 4th azimuthal mode, respectively. The blue lines show: (a) the mean relative vorticity of the LV core (|* ω*|*10^5 s^-1, averaged within 0.5* R*); (b) the mean angular momentum (IAM, averaged over* R*); (c) the shear stress (STR*10^5 s^-1, averaged in the ring* $R \le r \le 2R$*). Episodes of LV mergers with other anticyclones are marked with black vertical lines. Gray bars indicate periods when anomalously deep winter mixing in the LV core was recorded (following Bashmachnikov et al., 2017).*

The cross-correlation of the average relative vorticity of the LV core and the intensity of the azimuthal modes (-0.5) shows that, despite the lack of influence on the dynamic radius, the

development of instability led to a decrease in the rotation velocity of the core, the minimum of which is observed 1-2 weeks after the amplitude azimuthal disturbances reached their maximum (Fig. 5.13a). The average monthly rate of the decrease in the relative vorticity of the LV core was 2-3.5% (similar to the results of Kohl, 2007), i.e. over a 5-month period, in the absence of external energy supply, the relative vorticity of the core decreased only by 10-18%. In average annual values, the correlation coefficients of the average relative vorticity of the LV core and the intensity of azimuthal modes increase to -0.7÷-0.8. At the same time, the correlation of the average relative vorticity of the LV with the average annual number of mergers of the LV with other anticyclones is only 0.3. The integral angular momentum of inertia after the mergers increased (Fig. 5.13b), which indicates an increase in the rotation velocity at the periphery of the LV and is consistent with the increase in the kinetic energy of the LV after the mergers. Thus, it is the instability rate that determines the interannual variability of the rotation intensity of the LV core.

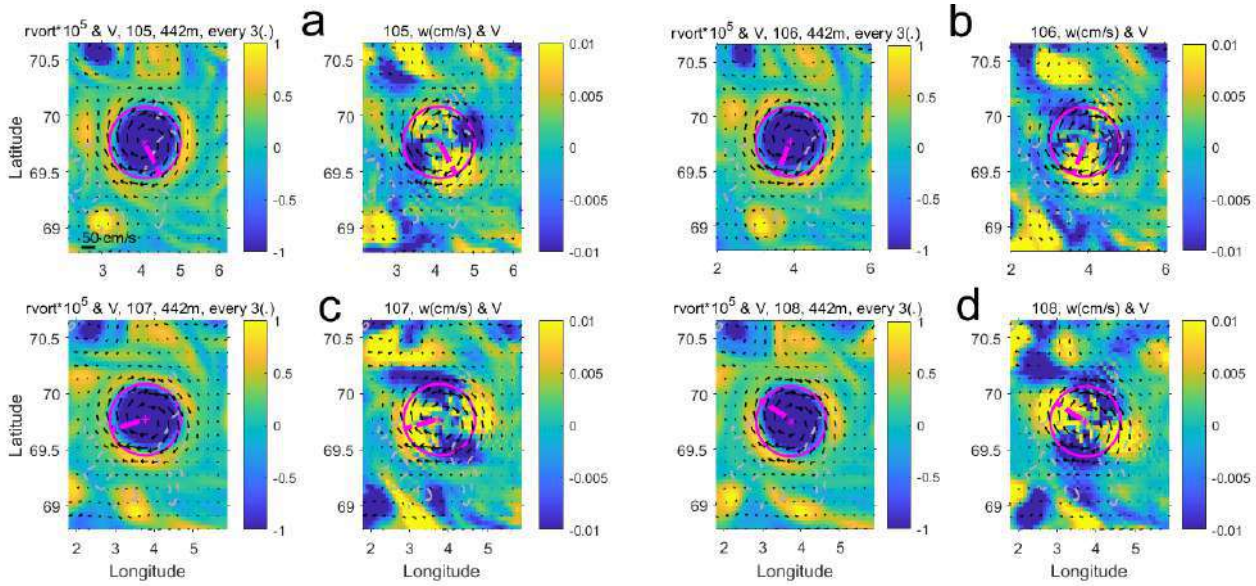

Fig. 5.14. Relative vorticity (10^{-5} s^{-1}, left panels) and vertical velocity (cm s^{-1}, right panels) in the MIT GCM at 450 m for four consecutive dates in January 1994, with a 3-day increment ((a)-(d)). The LV center is marked with a purple dot, its dynamic radius is marked with a circle. The magenta radial ray from the center of the LV allows one tracking the rotation velocity of the disturbance of the 2nd azimuthal mode (from Bashmachnikov et al., 2017).*

Instead of penetrating deep into the core, as the perturbations in the QG model, in the MIT GCM the instability was concentrated at the periphery of the LV. Here filaments and secondary submesoscale eddies were formed, which broke away from the LV, taking with them anomalies of the angular momentum and relative vorticity. The formation of the filaments was facilitated by an increase in the shear stresses in the LV. After that the intensity of the instabilities decreased (Fig. 5.13b). This allowed the LV core to maintain its volume, responding to dissipation by decreasing its rotation velocity. The circulation got redistributed between the core and the periphery of the vortex, restoring the radial profile of the Rayleigh velocity and weakening the general decrease in the angular momentum of the vortex after the separation of some parts of the vortex periphery. These processes inside the LV core could not be reproduced in the simplified QG model used above, where the LV core is represented by a homogeneous region of potential vorticity.

Kohl (2007), using theoretical results from Benilov (2005a), suggested that the LV should be stabilized by the large-scale bowl-shaped topography of the Lofoten Basin. However, theoretical calculations imply the stability of the LV only for a strongly overestimated values of the first baroclinic Rossby deformation radius. We also note that the LV is located near the center of the Lofoten Basin, where the bottom is almost flat, and the depth begins to decrease rapidly only at a distance of more than 4 dynamic radii from the LV center (Fig. 1.7, 5.15). Therefore, the large-scale concavity of the basin shape could not be the main reason for the stability of the LV.

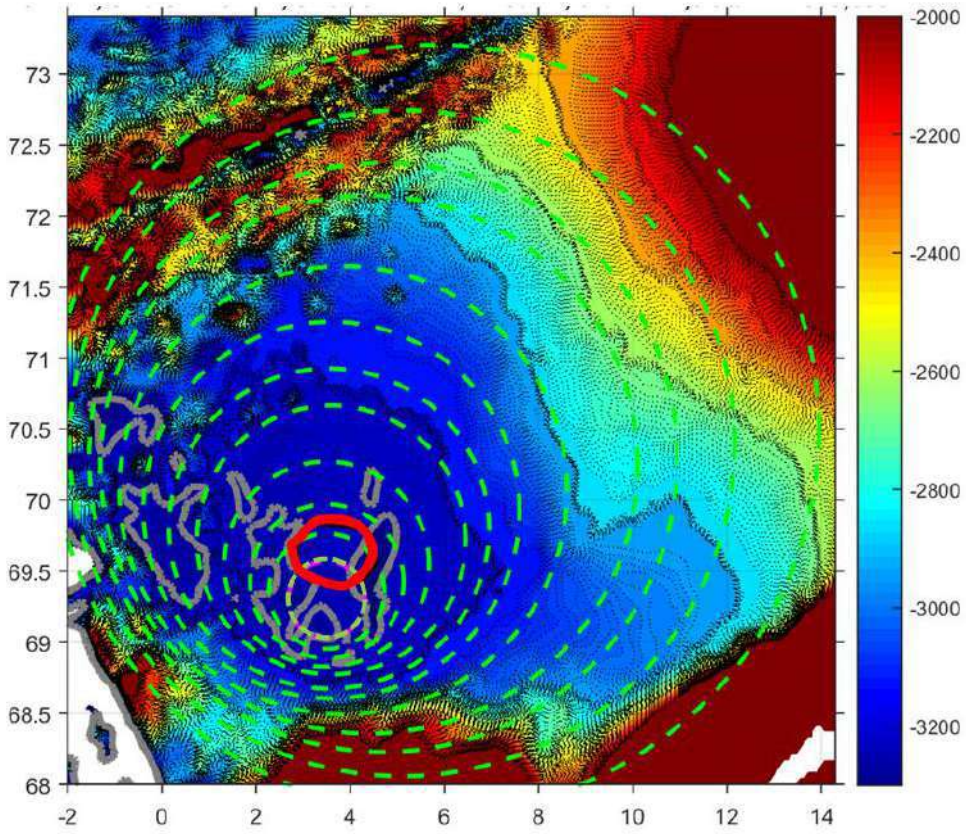

Fig. 5.15. Detailed topography of the Lofoten Basin (m) with the area, where the center of the LV was observed in the MIT GCM, highlighted with the thick red contour. The green dotted circles are examples of approximations of the 2000, 2300, 2600, 2800, 3000, 3100, 3150, 3200, 3225, 3230, 3235, 3240 m isobaths with nested cylinders of the QG model. One can see a slow deepening of the bottom in the central part of the basin to the southwest. For the QG model with 8 cylinders, only the 8 deepest isobaths were selected.

It is shown below that one of the important factors for the high stability of the LV was the combination of the velocity pattern of the mean flow and a small depression in the bottom topography of the Lofoten Basin. A detailed examination of the topography of the central part of the Lofoten Basin shows that, despite the almost flat bottom, there is a small depression situated southwestern from the geometric center of the Lofoten Basin (Fig. 5.15). To account for changes in basin topography in the QG model, the topography of the central part of the Lofoten Basin was approximated by several nested cylinders with different vertical extent. For the “smoothness” of the bottom profile, the distance between adjacent cylinders was chosen to be significantly less than the LV dynamic radius. Two configurations of bottom topography were considered: an approximation with 8 cylinders with a 5-m depth step between the inner cylinders of smaller radii

and 100-m depth step between outer cylinders (Fig. 5.15) (see Bashmachnikov et al., 2017), and an approximation by 10 cylinders with a fixed distance between adjacent cylinders and a fixed depth step of 25 m for the basic experiment (Fig. 5.16) (see Santieva et al., 2021). In both experiments, the same QG vortex model was used (Table 5.1). In both experiments, the southwestward deepening of the bottom of the basin significantly increased the stability of the LV.

In QG experiments with 10 cylinders, 3 background parameters were additionally varied (Fig. 5.16): the depth of the local depression in the central part of the basin (from 200 to 300 m), the velocity of the incident background flow (from 15 to 25 cm $s^{-1)}$ and the position of the depth minimum in the basin (in the geometric center of the basin or shifted to the southwest). Analysis of the results showed that the intensity of the vortex stretching and the vortex decay rate were approximately the same in all three layers of the model. Therefore, below the evolution of the middle layer (the core of the LV) is described in detail. Since the planetary β-effect was not taken into account, the vortex was simply advected by the background flow and simultaneously had its own propagation velocity along the isobaths. The streamlines of the background current crossed the isobaths (Fig. 5.16), and therefore the vortex moved in the changing field of the background potential vorticity, which generated disturbances at its boundary. In the presence of necessary conditions for the dynamic instability of the vortex, these disturbances grew, led to deformation of the vortex boundary and a decrease in its volume.

As before, the vortex in the QG model was approximated by a constant anomaly of potential vorticity in each of three layers, and the changes in the shape of the vortex boundary were recorded using the method of contour dynamics (Zabusky et al., 1979; Kozlov, 1983; Sokolovsky, 1991; Sokolovskiy, 1997; Sokolovskiy and Verron, 2014). The modeling time interval in all experiments corresponded to 2.5 years.

The area of the vortex core in layer 2 (S_{max}) at any model time t_i was estimated inside the largest contour, representing the LV and was expressed in % of the initial area of the LV core (S_{ini}), which was the same in all 3 layers:

$$S(t_i) = \frac{S_{\max}(t_i)}{S_{ini}} * 100\%. \quad (5.6)$$

The degree of elongation of the outer boundary of the LV during its evolution ($L_m(t_i)$) was estimated in % relative to the length of the boundary of a circular vortex with the same area ($L_{\mathrm{m.n}}(t_i) = 2\pi\sqrt{\frac{S(t_i)}{\pi}}$), i.e. of the figure of the same area and the shortest length of its boundary (for a circular vortex L = 0%):

$$L(t_i) = \left(\frac{L_m(t_i)}{L_{m.n}(t_i)} - 1\right) * 100\%, \quad (5.7)$$

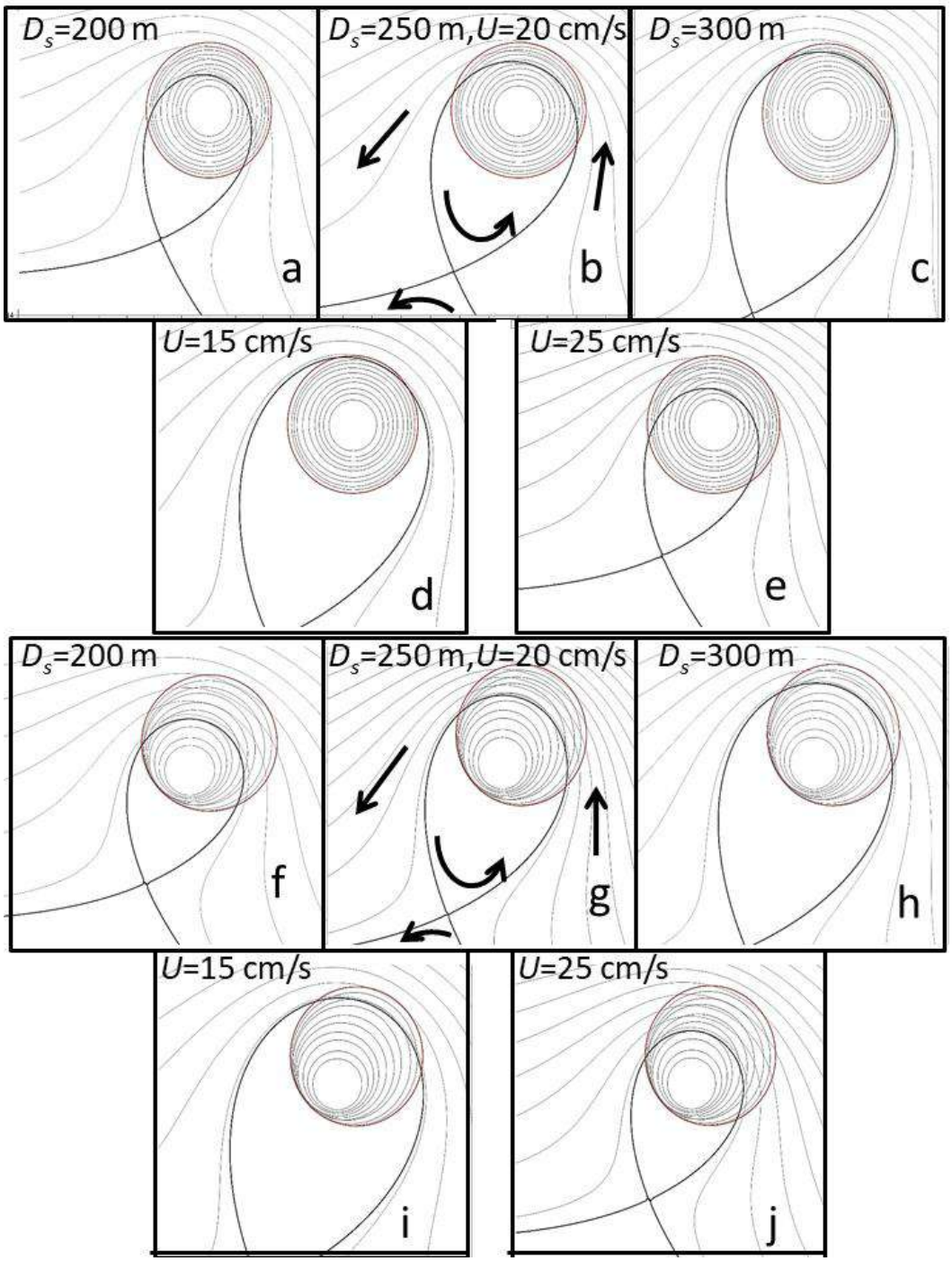

Fig. 5.16. Streamlines in layer 2 of the background flow in the Lofoten Basin in the absence of LV and approximation of the topography by 10 cylinders. The gray circles inside the brown circle represent the isobaths of the depression: (a) - (e) – concentric isobaths, (f) - (j) – the centers of the isobaths are shifted southwest. On top of the isobaths the streamlines of the mean current are plotted only outside the separatrix (the thick black line). The separatrix separates the inner region with closed streamlines (not shown for better visibility of the topography) from the outer region, where all streamlines cross the boundaries of the model region (gray open contours). The arrows in panels (b) and (g) indicate the direction of the mean flow. (a) and (f) the background flow velocity U =20 cm s^{-1} and local depression depth D_s = 200 m, (b) and (g) U =20 cm s^{-1} and D_s = 250 m (base experiment); (c) and (h) U =20 cm s^{-1} and D_s = 300 m; (d) and (i) U=15 cm s^{-1} and D_s = 250 m; (e) and (j) U =25 cm s^{-1} and D_s = 250 m (following Santieva et al., 2021).

In the basic experiment, which has the closest parameters to those in the Lofoten Basin, the depth of the central depression was 250 m, and the velocity of the impinging flow was 20 cm s^{-1}. With an axisymmetric configuration of isopycnals (Fig. 5.16b), the greatest stability of the vortex was observed at its initial position in the center of the basin, where the vortex core lost about 50% of its original area in 1.6 years, and the deformation rate of the boundary was the smallest. With the initial position of the vortex to the west or east of the center of the depression, its area decreased to less than 20% of the initial one after 1.1-1.4 years, and the vortex stretching rate increased significantly. This is explained by the fact that the gradients of the background potential vorticity decrease towards the center of the basin, which reduces the intensity of the initial disturbances generated at the vortex boundary.

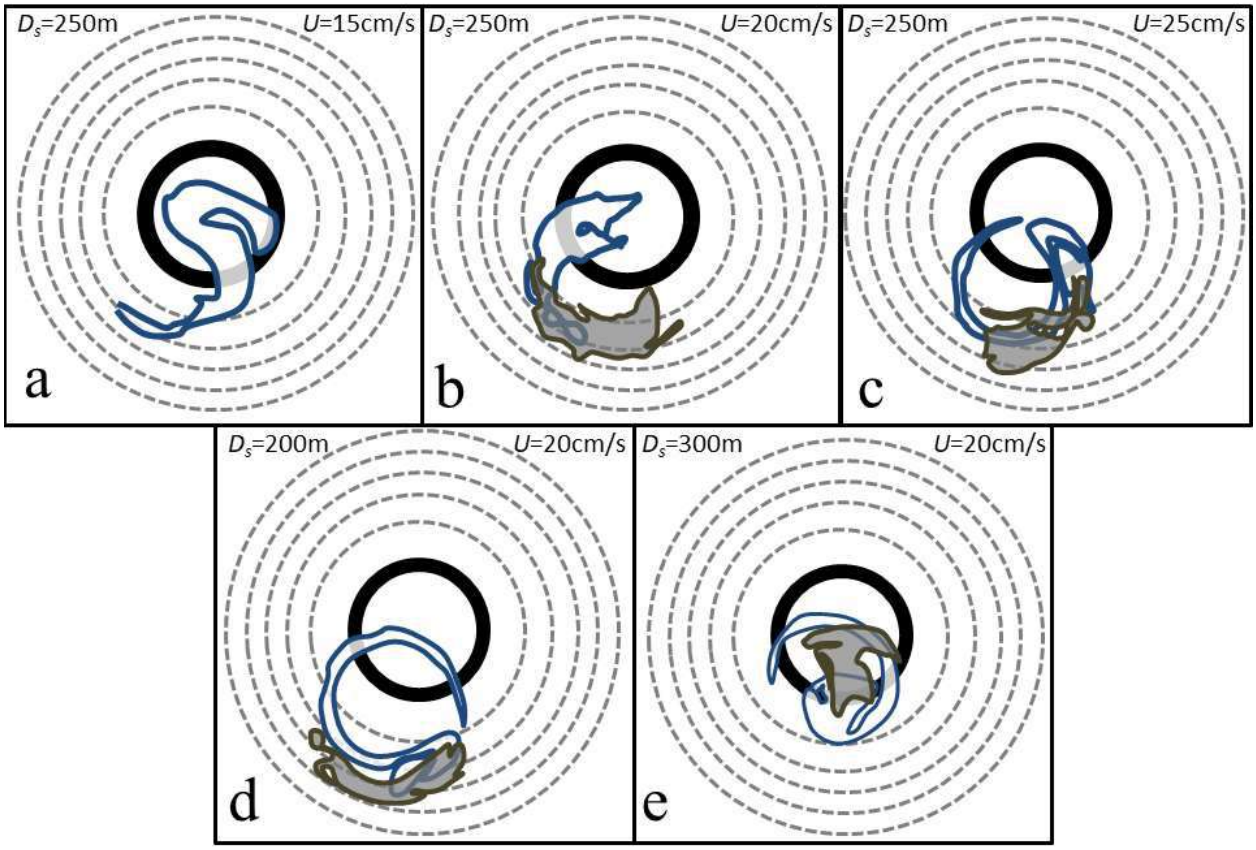

Fig. 5.17. Contour of the vortex in layer 2 for the concentric isobaths for some fixed moments of the vortex evolution (see caption to Fig. 5.16) for the experiments with the fixed D_s = 250 m and different background flow velocities: (a) U = 15 cm s^{-1}, (b) U= 20 cm s^{-1} and (c) U = 25 cm s^{-1}, as well as for the experiments with changing maximum depth of the depression in the basin: (d) D_s = 200 m, (e) D_s = 300 m. Circles (dotted lines) mark 5 deepest isobaths of the depression. The thick black circle is the boundary of the vortex at the initial moment; the white area bounded by the dark blue contour is the vortex at the moment when its area for the first time amounted to no more than 50% of the original value; the gray area, bounded by the greenish contour, is the vortex at the end of the model experiment or at the moment when its area was no more than 20% of the original one. The overall time of the model runs corresponds to 2.5 years of the vortex evolution (following Santieva et al., 2021).

An increase in the velocity of the background current, as well as an increase in the depth of the depression in the center of the basin, led to more intense stretching and destruction of the LV, and a decrease in these parameters, on the contrary, led to a slowdown in its stretching and decay (Fig. 5.17). This is due to an increase/decrease in the background potential vorticity gradients in the LV region.

However, the situation changed dramatically when the centers of the circular isobaths were shifted to the southwest, closer to the central region of the separatrix of the background flow streamlines (Fig. 5.18). In all experiments, the shape of the vortex was distorted significantly less than in experiments with a flat bottom, and by the end of 2.5 years of simulation, the loss of core volume in all experiments except one was less than 50%.

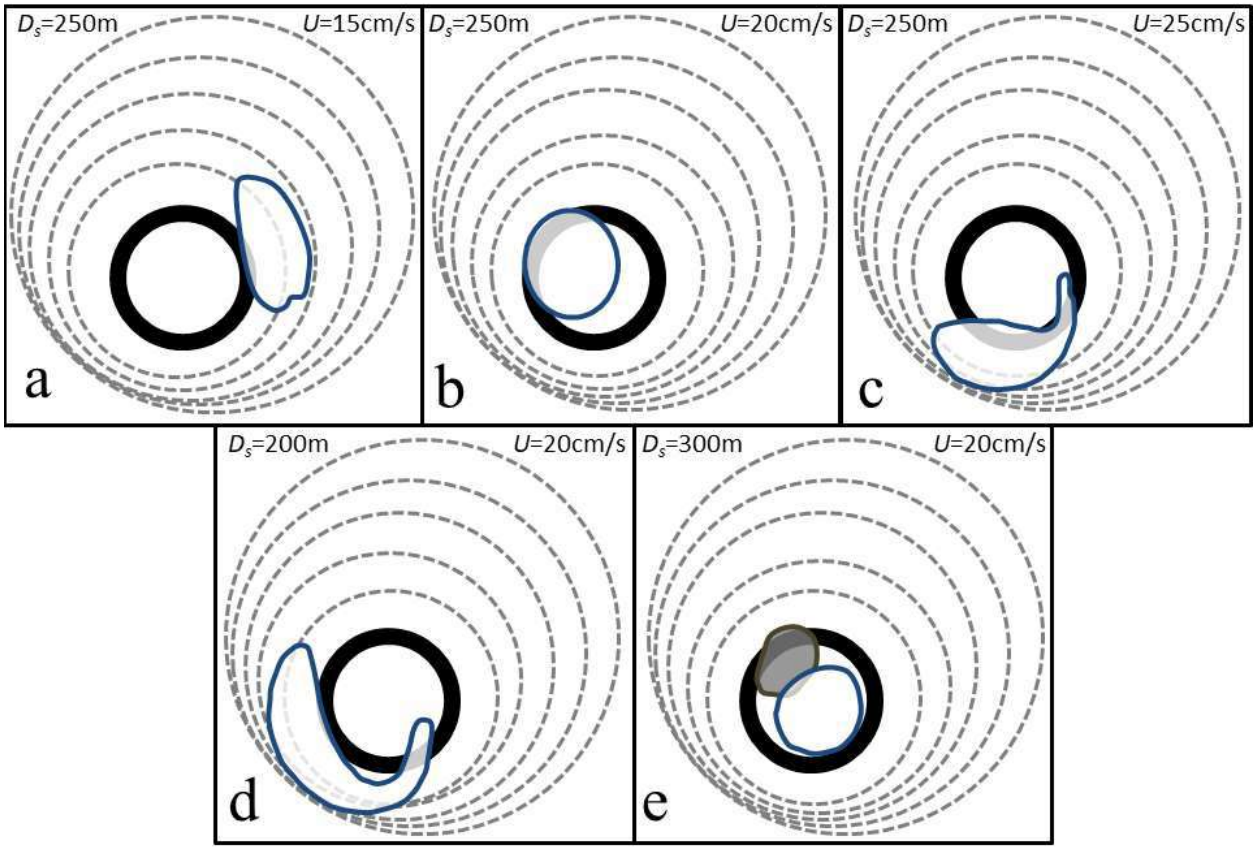

Fig. 5.18. Same as in fig. 5.17, but with displaced centers of the circular isobaths. In panels (a) - (d), the presence of only a white area limited by a black contour shows that even after 2.5 years of evolution, the area of the vortex was less than 50%, but more than 20% of the original one. In (e), the vortex decays faster, and at the end of the modelling period it is represented by a gray area, which is less than 20% of the original (according to Santieva et al., 2021).

The plotted variability of the vortex area and the degree of stretching of the vortex boundary shows that the variability of the current velocity is more important in changing the area of the vortex for concentric isobaths (the higher the velocity, the faster the vortex is destroyed), while changes in the depth of the depression have little effect on the destruction of the vortex (Fig. 5.19a). With concentric isobaths, by the end of the modelling period time the vortex area in the basic experiment was 40% (from 30 to 60% for different background flow speeds). Its shape was

highly deformed (Fig. 5.19b), which indicates a high probability of further rapid destruction of the vortex. With the centers of the circular isobaths shifted to the southwest, on the contrary, the highest effect had the change in the depression depth, while the change in the current velocity had little effect on the decay rate of the vortex (Fig. 5.19c). With a depression depth of 250 m, the vortex area after 2.5 years of modeling was about 60% of the initial one and had a rounded shape (Fig. 5.19d). At a depression depth of 200 m, the vortex area after 2.5 years was about 90% of the original one, and at 300 m – about 25% of the original one.

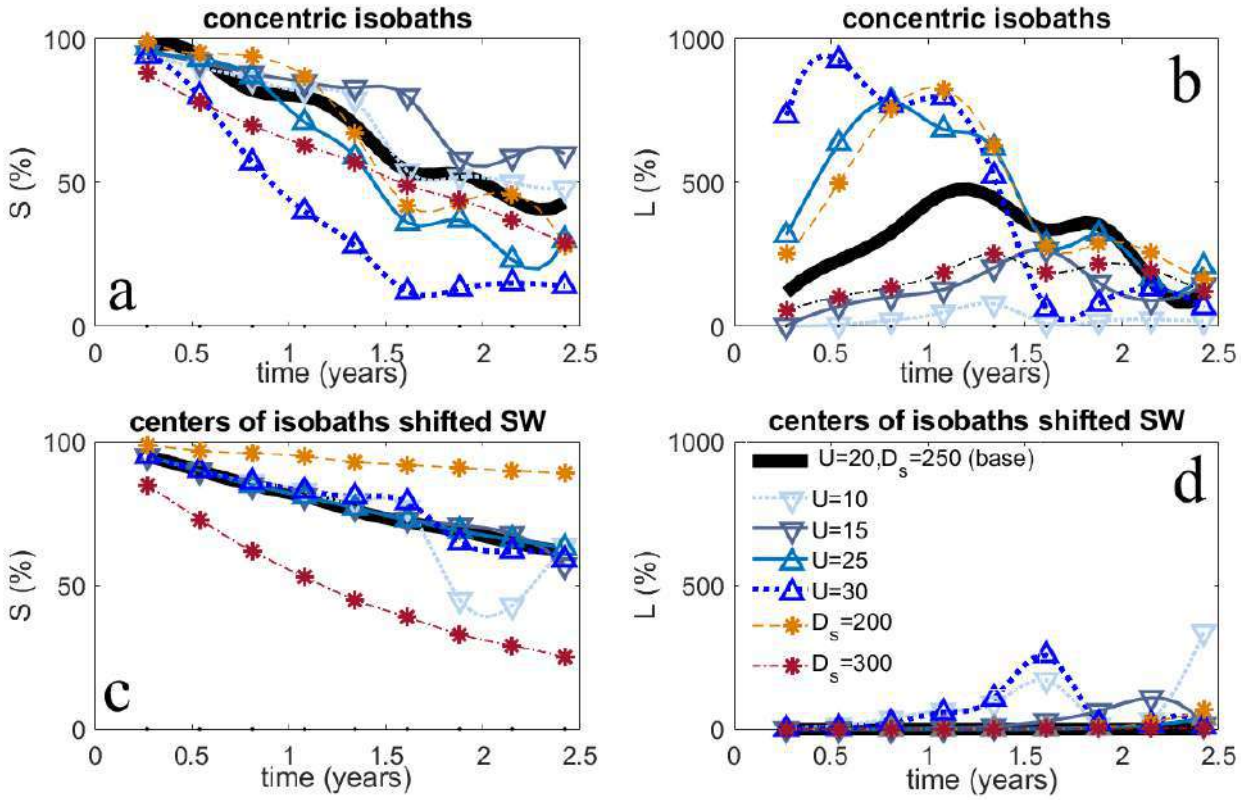

Fig. 5.19. Evolution of the area of the vortex core in layer 2, expressed in % of its initial value (a, c) and the relative increase in the length of the vortex boundary, expressed in % of the length of the boundary of a circle of the same area (b, d). Concentric isobaths – (a), (b), isobath centers displaced southeastwards – (c), (d). Lines in the plots: thick black line – U= 20 cm s^{-1} and D_s = 250 m (the basic experiment); light gray dotted line with triangles pointing down – D_s =250 m and U=10 cm s^{-1}, gray solid line with triangles pointing down – D_s =250 m and U=15 cm s^{-1}, blue solid line with triangles pointing up – D_s =250 m and U= 25 cm s^{-1}, blue dotted line with triangles pointing up – D_s =250 m and U=30 cm s^{-1}; light brown thin dashed line with asterisks – U=20 cm s^{-1} and D_s =200 m, red-brown thin dashed line with asterisks – U=20 cm s^{-1} and D_s = 300 m (following Santieva et al., 2021).

With concentric isobaths, the vortex area often decreased abruptly following the stage of a significant stretching of the vortex. This indicates that the vortex decay goes through its disintegration into several relatively large parts in these experiments. Such behavior is a result of an increase in the growth increments of low azimuthal modes, the accelerated growth of which has been previously noted during the development of LV instability in the flat-bottom experiments (Bashmachnikov et al., 2017). With the centers of the circular isobaths shifted southwestwards, the gradual decrease of the LV area is observed. This indicates the separation of a number of small

eddies from the original vortex (Fig. 5.19c). This is equivalent to generation of high azimuthal instability modes at the vortex boundary that do not penetrate into the core. The absence of strong elongation of the main vortex confirm this mechanism. With shifted isobaths, the only episode of the vortex break up was recorded for a low velocity of the background current of 10 cm s^{-1} (Fig. 5.19c). However, latter the LV area restored as a result of the merger of the formed eddies.

The variability of the vortex area in layer 1 (above the core) shows that, although sharp decreases in the vortex area occurred there somewhat later than in layer 2 (vortex core), in all experiments at the final vortex area in the 1st layer was smaller than in the 2nd. The rate of destruction of the vortex in layer 3 (under the core) was approximately the same as in layer 2.

5.2 DISCUSSION OF CHAPTER 5

The analysis of the stability of the LV was carried out both in the approximation of the nonlinear quasigeostrophic (QG) theory and for the system of primitive equations of the MIT model. It was found a good agreement between the characteristics and dynamics of the LV in MIT GCM and *in situ* data. As expected, the dynamic instability of the LV led to a much faster destruction of the vortex (from several months to 2-4 years) than turbulent diffusion (10 years in Soiland and Rossby, 2013). The possibility for development of dynamic instability results from fairly pronounced vertical or horizontal gradients of potential vorticity (Sokolovskiy, 1997b; Cushman-Roisin and Beckers, 2011), always present in the LV. The eddy Rossby number (*Ro* = 0.03-0.15) and Burger number (*Bu* = 0.05-0.10), derived from the MIT GCM for the LV, suggest the most effective development of baroclinic or mixed instability of the LV boundary (Ripa, 1992, Carton et al., 2014; Cohen et al., 2015). However, *in situ* observations indicate that the MIT GCM underestimates the LV Rossby number by several times (Yu et al., 2017), and in the real ocean the nonlinear effects should be stronger.

The intensity of the LV destruction due to dynamic instability depended significantly on the bottom topography. Previously (Chapter 4) it was shown that the main areas of meddy destruction are topographic rises, as well as the region of the Azores jet (Bashmachnikov et al., 2015 c). In such areas, a sharp increase in the amplitudes of the instability modes in eddy cores is expected, leading to a faster eddy decay rate (Filyushkin et al., 2002; Menesguen et al., 2012). This chapter shows that in the case of a small topographic depression, as observed in the center of the Lofoten Basin, can, on the contrary, stabilize an anticyclonic eddy. In the QG model, with the flat bottom approximation of the Lofoten Basin, the LV was completely destroyed over a 8-month period (slightly slower for the 2-layer winter configuration). The rate of destruction of the LV decreased sharply, if a small depression of only 200-300 m was formed in the central part of the basin, which is 3000 m deep (Fig. 5.15-5.16). If this depression is located in the geometric center of the basin, then, in the basic experiment (close to the conditions of the Lofoten Basin), the LV core decreased by 50% of the original volume in 1.5-2 years. If the depression was shifted to the southwest from the geometric center of the basin, closer to the central region of the separatrix loop of the impugning current (as it is observed in the Lofoten Basin), then the loss of 50% of the initial volume of the LV core would take more than 2.5 years. In both cases, the LV core existed as a coherent structure during the entire 2.5 years modelling period (up to the date of the end of the experiment). The of LV dissipation rate of this latter result of the QG model most closely matches the MIT GCM results with the real topography and background flow. In the MIT GCM, in the absence of LV regeneration processes (mergers or deep winter convection in the LV core), the LV

radius remained virtually unchanged for 5-8 months, although the rotation of the core gradually slowed down. The effect of a significant increase in the LV lifetime in the presence of minor depression of the bottom topography is associated with a decrease, with its corresponding configuration of the mean current, of the gradients of the background potential vorticity in the vicinity of the LV.

It was shown that in the MIT GCM, better reproducing the real ocean, as well as for a more simplified QG model, in the presence of a small depression in the bottom topography southwest of the geometric center of the basin, the LV decay was going through separation of filaments and small submesoscale eddies from the LV periphery. This resulted, first of all, in a decrease of the LV rotation velocity (approximately by 15% in 5 months), but had little effect on the LV radius. Thus, a higher stability in the presence of a bottom depression close to the center of the separatrix loop of the mean flow is explained by the fact that at reduced gradients of the background potential vorticity, the instability generated at an eddy boundary does not penetrate deep into the core, but is concentrated along the eddy boundary. This kind of dissipation, due to the formation and separation of filaments from the outer periphery of the LV, was observed in the MIT GCM. A similar effect of detachment of the vortex periphery in a shear flow was previously observed in modeling studies (see, for example, Maksimenko and Orlov, 1991; Mariotti et al., 1994). Such filamentation was found in observations along the periphery of a meddy (Menesguen et al. al., 2012). It was previously shown that, under certain conditions, nonlinear effects can stabilize linearly growing disturbances, even if sufficient conditions for the development of the dynamic instability of the vortex are met (Sutyrin, 2015). In numerical QG experiments, this was called nonlinear saturation of the growing perturbations of finite-amplitude elliptical eddy instabilities (Flierl, 1988; Ripa, 1992). Moreover, such a nonlinear evolution of disturbances can be observed in numerical experiments in the primitive equation MIT GCM, generated, for example, by the turbulent friction, which is not taken into account in the QG model (Boss et al., 1996).

The mechanism, limiting the development of instability to the periphery of the LV, according to the results of MIT GCM, consists in strong shear stress at the LV boundary, which usually arises when the LV interacts with numerous cyclones and anticyclones (Fig. 5.5). As a result, the disturbances quickly separate from the LV in the form of filaments, latter compacted into small submesoscale eddies (Fig. 5.9), instead of penetrating into the LV core. This indicates an influence of the turbulent dynamics of the surrounding waters on the development of dynamic instability in the LV. The nonlinear QG model correctly described only the initial stage of the development of LV instability.

The decrease in the relative vorticity of the LV core in the MIT GCM was accompanied by a redistribution of the rotation velocity from the core to its periphery, reducing the loss of angular momentum of inertia of the LV during its decay. This tendency to maintain the momentum of inertia during separation of a part of the LV periphery allowed the LV radius to remain unchanged for a long time, despite dissipation. Presumably, in the absence of external energy sources, such a process should lead to a sudden collapse of the vortex core, after it had maintained its size practically unchanged for a long time. Such a collapse apparently can be the reason for the destruction of old meddies (Chapter 4).

The LV maintains a quasi-permanent state due to its episodic regeneration as a result of mergers with other anticyclones and/or differentiated deep winter convection (Ivanov and Korablev, 1995a; Kohl, 2007; Ray et al., 2015). Volkov et al. (2015), using results from the MIT GCM, indicated that winter intensification could only explain 1/3 of the change in LV intensity,

with 2/3 explained by mergers. Probably, the role of convection was somewhat understated, because the LV intensity was estimated from the relative vorticity of its core, it has been shown above that differentiated convection usually does not lead to an increase in the kinetic energy and vorticity of the LV core, but always increases the available potential energy and the momentum of inertia of the vortex (see also Wang et al., 2019). At the same time, not every merger led to intensification of the LV or an increase in its volume. This is probably due to the often observed significant increase in disturbances in the cores of merging eddies, which leads to a more active dissipation of their mass and energy into the environment during a merger.

It was shown above that the interannual variability of the intensity of the LV relative vorticity is more correlated with the intensity of dissipative processes (-0.7 ÷ -0.8), rather than with the number of LV mergers with other anticyclones per year (+0.3). In other words, with a fairly uniform distribution of the LV regeneration episodes in time, the intensity of dissipation is subject to significant interannual variability. This may be due to interannual variability in the intensity of other dynamic structures in the basin interacting with the LV.

5.3 CONCLUSIONS OF CHAPTER 5

1. It is shown that the overall high stability of the LV is determined by a combination of the topography of the Lofoten Basin and the parameters of the impinging Norwegian Current. The maximum stability is achieved due to a small bottom depression, shifted to the southwest from the center of the Lofoten Basin, towards the central area of the separatrix loop of the branches of the Norwegian Current encircling the basin. This minimizes the gradients of the background potential vorticity in the area where the LV is located and reduces the amplitude of external disturbances that generate dynamically unstable first azimuthal modes at the periphery of the vortex.
2. Clustering of LV characteristics in the parameter space of potential vorticities of the LV core and the area above the core made it possible to identify the characteristic seasonal evolution of the LV core, including periods of the winter-spring mixing (cluster B), spring restratification (cluster C) and summer-autumn relaxation of isopycnals (clusters D and A). A higher stability of the LV was in winter, when the growth rate of the fastest growing azimuthal modes of the LV disturbances decreases.
3. Both, the merger of the LV with other anticyclones (AC) and winter convection are sources of restoration of the LV energy against dissipation. Both processes led to an increase in the available potential energy of the LV, but only mergers with anticyclones directly increased the kinetic energy of the LV.
4. The processes of LV regeneration, including mergers, was mostly observed during winter-spring period, when the deepening of the upper mixed layer forms a favorable background for a release by surface eddies of the positive anomaly of potential vorticity at their peripheries (“screen”). The second important precondition for a merger was the presence of a cyclone to the north of the AC-LV pair, “pushing” the AC towards the LV. Both effects led to an increase in the contact time of the anticyclones and contributed to their merger.
5. Using the example of an interaction of the LV with an AC, it was shown that in the presence of Π -screen, disturbances did not penetrate deep into the vortex cores, and the instability generated at the core boundary was “released” by separating filaments from the eddy peripheries. This was enabled by high shear stresses in the contact area of the anticyclones.

6. After the separation of the filaments, the change in the momentum of inertia of the LV was minimized due to a redistribution of the rotation velocity from the center to the periphery of the vortex. This allowed the LV to maintain its radius after separation of the filaments, but reduced the intensity of rotation of the LV core.

Chapter 6. Manifestation of subsurface intrathermocline eddies in the sea level anomalies

6.1 Introduction to Chapter 6

In this chapter the signal of subsurface eddies with a deep core on the sea surface is investigated. The limited meddy size allows obtaining a coherent picture of their propagation pathways and life cycles with *in situ* data mainly from indirect evidences (see Chapter 4). The ability to remotely track meddies using satellite data would provide an effective tool for assessing the characteristics of meddy life cycles and their dynamics, comparable to remote monitoring of the evolution of the sea surface eddies. Individual observations indicate that, despite the deep position of their cores (700-1200 m), meddies can form a fairly strong dynamic signal on the sea surface, which can be detected in satellite altimetry. This suggest that the task of tracking meddies on the sea surface is essentially possible.

In this chapter, the stability of the meddy signal on the sea surface is examined, as well as the relationship between the signal intensity with characteristics of meddy cores and of the background ocean, and the reasons for the episodic disappearance of the signal in satellite altimetry data, which creates difficulties for meddy tracking. The theoretical estimates of the signal intensity, obtained for a contour eddy and for a Rayleigh eddy, make it possible to evaluate the fundamental possibility of tracking vortices with different characteristics on the sea surface at the current level of accuracy of satellite data.

6.2 Observations of meddy signal in sea level anomalies

The possibility of observing meddies on the sea surface was first suggested by Kase and Zenk (1987), who found that, above meddies, surface floats tended to rotate anticyclonically. These, not very reliable due to a limited information, *in situ* observations were confirmed with the results of numerical hydrodynamic modeling (Kase et al., 1989). With the advent of satellite sea level observation, Stammer et al. (1991), using Geosat altimetry data (still of a rather low accuracy), were able to track several meddies in the Iberian Basin, with the strongest signal being observable for more than a year. However, it remained unclear whether the meddy signal recorded by a single *in situ* survey was actually being tracked, or whether the sea level anomaly was moving independently of this deep eddy. Later, Oliveira et al. (2000) found that four Iberian meddies discovered during 1994 with sections *in situ* and tracked over several weeks with RAFOS floats, were clearly visible on along-track data of the Topex/Poseidon (T/P) satellites as bell-shaped sea level rises with an amplitude of about 10 cm. The signal was clear even when the track crossed the meddy at 50 -60 km from the meddy center. At 90-100 km from the center (at the meddy boundary), the meddy surface signal was still faintly visible, but its amplitude was already at the level of the background noise. In one case, when a meddy moved along the T/P track, it was possible to follow an evolution of the meddy dynamic signal during a month. The coherent propagation of meddies and signals above them could also be traced in SST data for 1.5 months.

To detect sea surface meddy signals in the gridded AVISO altimetry data, 2 conditions must be met: (1) the sea level anomaly generated by a meddy must exceed the noise level of the altimetry data; (2) the radius of the surface signal must be large enough to be crossed by at least

one of the altimetry tracks used for constructing the AVISO map. Tournadre (1990) calculated the probability of detecting an eddy from AVISO altimetry data as a function of the distance to the nearest satellite track, the repeat period of the tracks, and the eddy diameter and propagation velocity. The results showed that the combined Geosat (ERS type - see Chapter 2) and T/P missions can, with 80% probability, detect 95% of eddies with a diameter of 130 km and 60% of eddies with a diameter of 60 km if their propagation velocity is below 10 cm s^{-1}. Given a typical meddy dynamic radii of 30 km (see Section 4.3.3.2) and assuming the same dynamic radii for the meddy surface signals, we can expect a diameter of the sea level anomalies of the meddy surface signals to be of the order of 120 km. According to Tournadre (1990), the probability for detecting such eddies in AVISO altimetry data is very high. In general, estimates of the AVISO group (http://www.aviso.oceanobs.com/en/altimetry/multi-satellites/index.html) indicate a confident detection of mesoscale ocean structures in the presence of at least three altimetry satellites in orbit with the orbital parameters of T/P and ERS type. Such situation persisted since 2000, however, even before 2000, the presence of even 2 satellites provides such an opportunity for large eddies (Tournadre, 1990) or eddies crossed by a satellite track.

As an example, the results of the voyage of the R/V Archipelago in August 2005, in which the author observed several meddies is given below (Fig. 6.1). The core of a large meddy (M131) had peak salinity anomalies of 0.4 and temperature anomalies of 2.0-2.5°C in the 700-1000 m layer (Fig. 6.2), which matches the Richardson criterion (Richardson et al., 1991; Basmachnikov et al., 2015c, see section 2.3.1). Anomalies of high salinity, extending from the meddy core downward and radially outward towards the slope of the bottom rise (Fig. 6.2a, b), were interpreted as the result of the interaction of the meddy with the Ekman bottom layer, which is characterized by the divergence at the bottom of an anticyclonic eddy (Pedlosky, 2013), and a further swirling of this anomaly around the meddy. Geostrophic currents estimated by solving the inverse problem (Wunsch, 1996) showed a pronounced anticyclonic rotation above and below the meddy core from the sea surface to the lowest level of observations (2000 m). This confirms that the anticyclone observed in the altimetry data, between stations 130 and 132 (Fig. 6.1), was a dynamic manifestation of a meddy. According to altimetry data, it can be assumed that the center of the meddy was 30-60 km west of station 131, and its dynamic radius was 60-80 km.

During the same cruise, two more similar structures were discovered, with smaller salinity and temperature anomalies at intermediate depths, at stations 106 and 111 (Basmachnikov et al., 2009a), which can be interpreted as small meddies (Fig. 6.1). Over the small meddy M106, the sea surface anticyclonic signal was not discernible. Meddy M111 also did not form an isolated eddy signal on the sea surface, but was located within an anticyclonic meander of the Azores Current, which presumably interacted with this meddy (Vandermeirsch et al., 2003a,b).

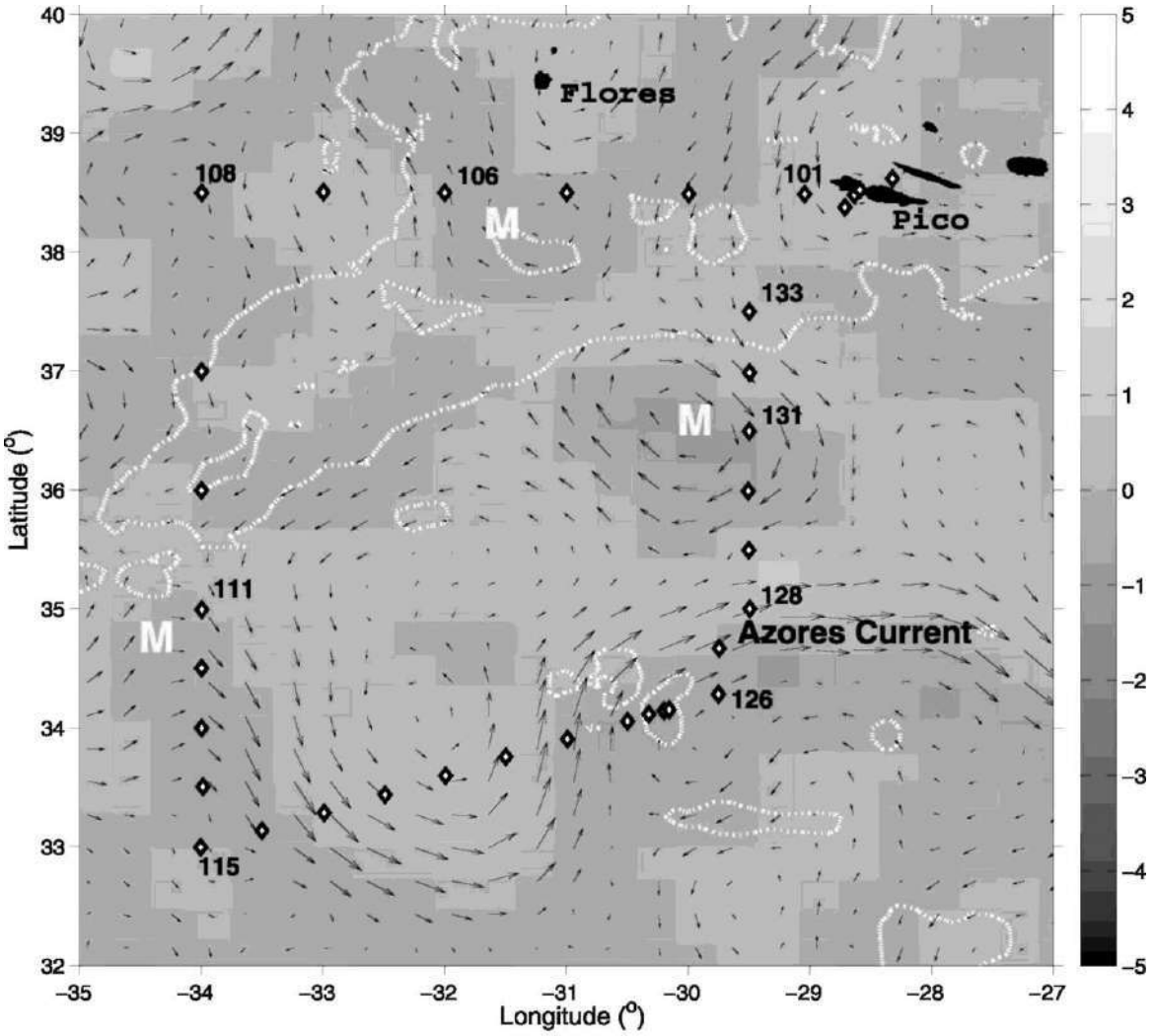

Fig. 6.1. Vertical casts during a cruise of the R/V Archipelago (diamonds) in August 2005. The color shows the relative vorticity (10^{-5} s^{-1}), arrows are the geostrophic currents on August 17, 2005, according to AVISO altimetry data. Meddy locations are marked with the letter "M", which are designated in the text by the station with the highest salinity anomaly: M131, M111 and M106. White dotted line is the 2000 m isobath (from Bashmachnikov et al., 2009a).

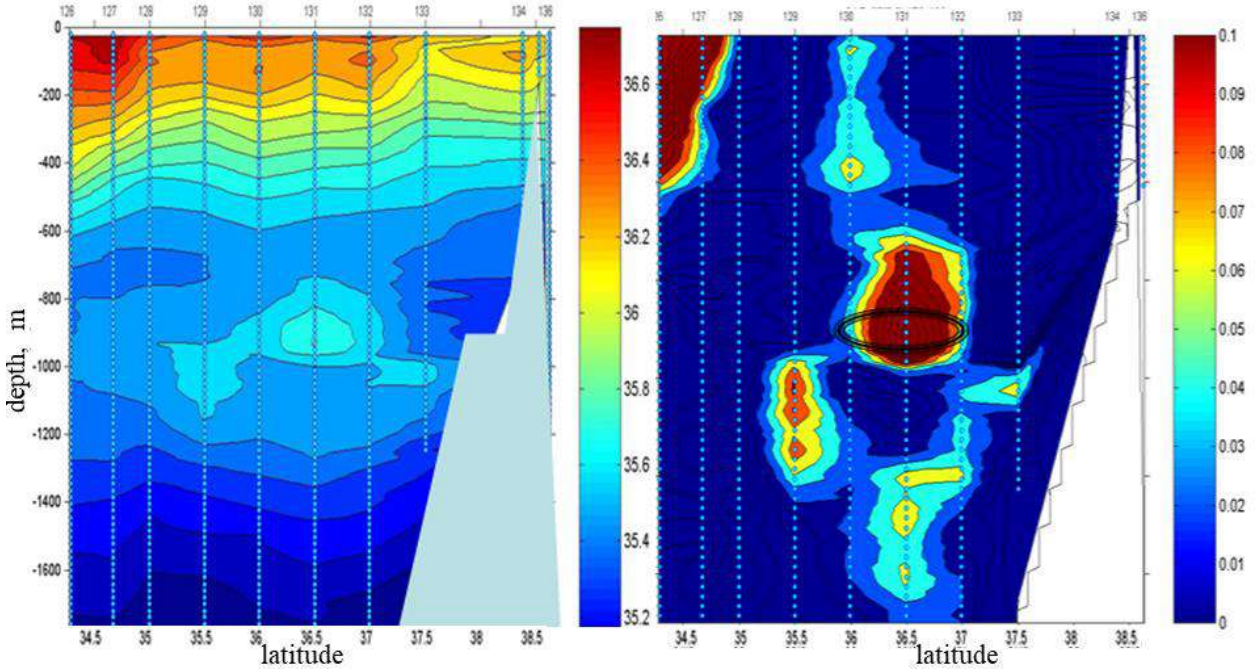

Fig. 6.2. (a) Salinity on the meridional section on August 17, 2005 (see the position of stations 126-133 in Fig. 6.1), (b) the corresponding salinity anomalies of Meddy M131 relative to the average salinity at each of the levels of the section; triple ellipse marks the meddy core with the maximum salinity from panel (a). The bottom topography north of M131 is schematically shown.

Another example is the Don Carlos meddy in the Iberian Basin, propagation of the dynamic signal of which to the sea surface was obtained using the ship 75 kHz ADCP data in August 2010.(Fig. 6.3a). The center of the meddy was located approximately 5 km south of the section (see Bashmachnikov et al., 2013b). The dynamic core of the meddies was located in the layer of the Mediterranean Water (800 m and below). Meddy had a dynamic radius of 10-15 km and the maximum azimuthal velocities of 30-40 cm s^{-1}, well corresponding to those of meddies in the Iberian basin (see section 4.4, also Pingree and Le Cann, 1993b; Schultz Tokos et al., 1994). Weak positive anomalies of salinity (0.2) and temperature (0.5°C) in the 800-1100 m layer, in comparison with the climatic mean, obtained from two vertical profiles of ARGO floats at the northern periphery of the eddy in mid-September 2010, serve as additional confirmation that this was a meddy (see Bashmachnikov et al., 2013b).

Surface currents obtained from AVISO data are in good agreement with *in situ* ADCP measurements at three sections performed during the cruise (Fig. 6.3a), and can be used to form a complete picture of the sea surface current field. AVISO data show that, during the observations, meddy Don Carlos was in contact with the Azores Current. The weaker signal from the Azores Current, compared to the meddy, was filtered out. To do this, the data from section 1 were used to make an empirical model of the profile of the Azores Current (Fig. 6.3c), which was then removed from the data of section 2 (Fig. 6.3b,d). Filtration did not change the general structure of the currents over the meddy, making it only more symmetrical relative to the meddy center. The dynamic influence of the meddy signal was observed up to the sea surface (Fig. 6.3d).

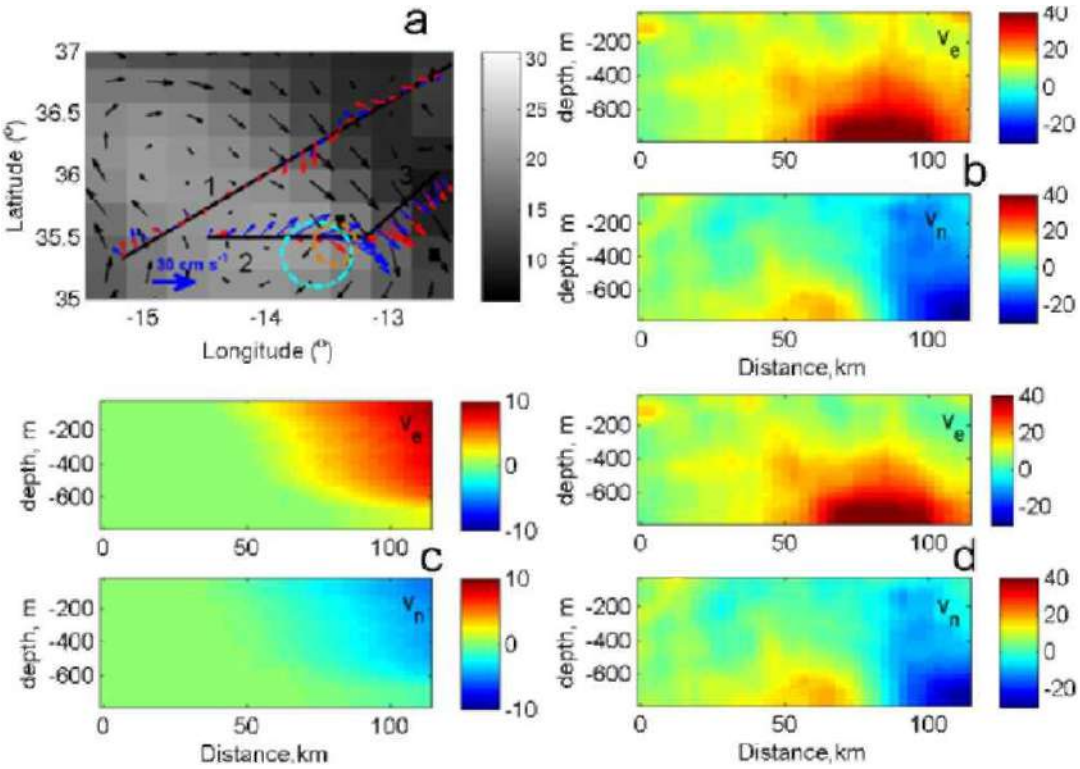

Fig. 6.3. (a) Sea level (cm, color) and surface currents (black arrows) from AVISO dataset on 24th of August 2010. Ship transects (black lines numbered 1, 2, 3) and currents according from ADCP on 27th of August 2010 at 100 m (red arrows) and at 700 m (blue arrows). The position of the meddy, derived from ADCP data is shown by the orange circle, and the position of its surface signal is shown by the blue circle. (b) Eastern (v_e) and northern (v_n) current velocity components (cm s^{-1}) from ship ADCP data on 27th of August 2010 along transect 2. (c) Estimated contribution of Azores Current at transect 2 (cm s^{-1}), modeled using data from section 1. (d) Current velocity at section 2 (cm s^{-1}) associated with meddy Don Carlos and obtained by subtracting (c) from (b) (from Bashmachnikov et al., 2013b).

The minimum current velocity in the center of the dynamic core of the eddy was interpreted as the point along the section 2, closest to the center of the meddy (Fig. 6.4a). In the upper 500-m layer, the axis of the quasi-axisymmetric structure of the dynamic signal was shifted approximately 18 km to the southwest relative to the meddy center at depths of 650-800 m (Fig. 6.4a, b). The dynamic radius of the meddy core (here determined by the maximum azimuthal velocity) was about 13 km, which is close to the second baroclinic Rossby deformation radius. The radius approximately doubled in the upper 500-m layer, reaching 25 km, which is close to the first baroclinic Rossby deformation radius. Due to the doubling of the radius, the surface signal completely covered the meddy, despite the displacement of its axis (Fig. 6.3d, 6.4a). Between the meddy and its surface signal there was a transition layer, where the velocity decreased approximately by half in the 200th layer: from 40-45 cm s^{-1} at 700 m to 20-25 cm s^{-1} at 500 m (Fig. 6.4a,b). In the subsurface structure itself, the velocity decreased by another 15 cm s^{-1} in the 500th layer, amounting to 5-10 cm s^{-1} on the sea surface. The sum of the above data allows us to conclude that the surface signal of the meddy is an independent eddy, which interacts with the meddy. Such connected eddies in different layers, the centers of which are separated by a distance of less than two eddy diameters, are usually involved in a joint rotation around the common center (Polvani, 1991). Due to the significantly lower intensity of the surface eddy, one can expect its circular

motion around the meddy, while the center of the meddy, due to its smaller radius, will always remain below the surface eddy during this rotation (Fig. 6.3a, 6.4a).

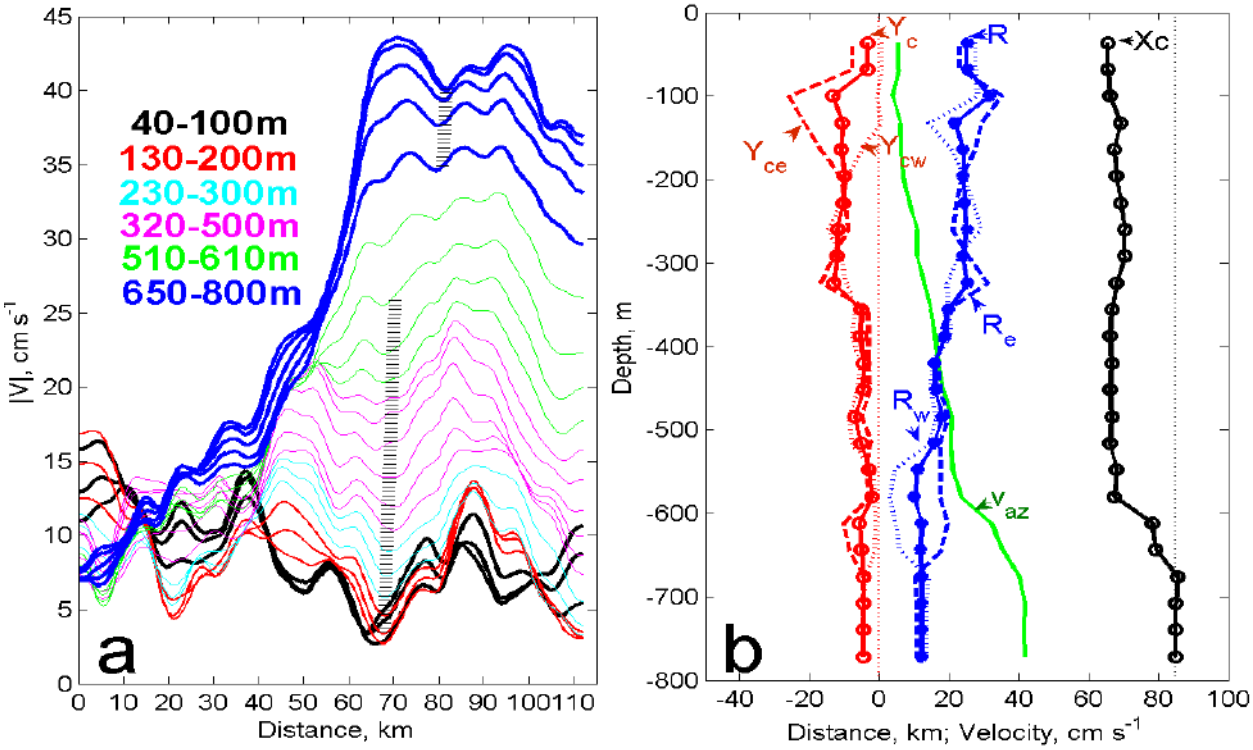

Fig. 6.4. (a) Current velocity (cm s^{-1}) along transect 2 from ADCP data. Different depth ranges are shown in different colors: black – levels 40-100 m, red – 130-200 m, blue – 230-300 m, pink – 320-500 m, green – 510-610 m, blue – 650-800 m. Almost vertical black dotted lines indicate the centers of meddy Don Carlos (the upper segment) and of its surface signal (the lower segment), identified by the local minimum of the current velocity modulus. (b) Vertical variability of the eddy characteristics: dynamic radius of the eddy (R, km, blue lines), maximum azimuthal current velocity ($v_{\theta m}$, cm s^{-1}, green line), distance from the center of the eddy to the western end of section 2 (X_C, km, black line), the distance from the center of the eddy to section 2 (Y_C, km, red lines, which is the average of two alternative estimates Y_{cw} and Y_{ce} for different approximations of the structure of the Azores Current). Straight vertical dotted lines mark the zero lines of the reference systems for R, $v_{\theta m}$, Y_C and X_C (from Bashmachnikov et al., 2013b).

Table 6.1 presents characteristics of various meddies described in literature together with the intensity of the linked anticyclonic signal on the sea surface, recorded using direct observations (floats and LADCP) and geostrophic estimates.

Table 6.1. ***Observations*** *of surface manifestations of meddy:* $v_{\theta m}$ and $v_{\theta 0}$ are the maximum azimuthal velocity in the meddy core and of the meddy surface signal, respectively; ω_m and ω_0 are the corresponding peak values of relative vorticity; *H is the depth of the center of meddy core,* R_{vm} *is the radius of maximum azimuthal velocity. The sea level anomaly (*ζ*) over the meddy is estimated using the quasi-geostrophic approximation as* $\zeta=(f*v_0 + v_0^2/R_0) * R_0/g$*, where* $R_0 = 2 R_{vm}$ *(see section 6.3.5). For eddies since 1993, the sea level anomaly is additionally determined using AVISO altimetry data (*ζ_{alt}*) as the mean difference between the sea level values averaged in the areas 0 - 20 km and 60 - 120 km around the meddy center.* Relative meddy vorticity (ω_m)*, obtained from observations or* calculated *from the Rayleigh model* $\omega_m = 2\sqrt{e}\, v_{\theta m} / R_{vm}$. Since the last ω_m *turned out to be, on average, 20% greater than its value according to the experimental distribution of* v_θ*, an appropriate correction was introduced into the results. This difference is apparently due to the deviations of the velocity profile in the cores from the Rayleigh model (see in particular Richardson et al., 1989; Armi et al., 1989).*

Meddy: name, position, time, minimum observation depth	*H*, m / R_{vm}, *km*	$v_{\theta m}$, cm s^{-1}	$v_{\theta 0}$, cm s^{-1}	$v_{\theta 0} / v_{\theta m}$ (%)	$\zeta(\zeta_{alt})$ cm	$\lvert\omega_m\rvert$ / f	$\lvert\omega_0\rvert$ / f	ω_0 / ω_m, %	*N/f*	reference, instruments*
the Iberian Basin (young meddies)										
Ulla, 04.1997, 45°N, 12°W, 0 m	1000 / 15	17	7	44%	2 (2)	0.36	0.07	21%	69	*Paillet et al., 2002, CTD, XBT, LADCP, RAFOS, DDB, SF*
Pinball (A3), 01.1994, 37-38° N, 10-12° W, 0 m	1100 (700-1200) / 18 (10-35)	25 (20-30)	15 (10-20)	60%	6 (0)	0.52	0.16	thirty %	81	*Pingree, 1995; Oliveira et al., 2000; RAFOS, SF, SLA, SST*
B2, 04-05.1991, 38°N, 13°W, 100 m	1300 / 25	31	18	58%	8	0.39	0.11	29%	81	*Schultz Tokos et al., 1994; CTD, RAFOS, SF*
Aska(Bl), 04-05.1991, 38° N, 13° W, 100 m	1000 / 18	27	15	55%	5	0.55	0.15	28%	81	*Schultz Tokos et al., 1994; CTD, RAFOS, SF*
Smeddy, 03.1992, 36° N, 9° W, 0 m	800 / 12	17	8	47%	2	0.55	0.13	24%	85	*Pingree and Le Cann, 1993a; CTD, XBT, PF, SST*
Model meddy	- / <50	10	7	70%						*Kase et al. (1989), numerical hydrodynamic model*
A	- / -	5	3	60 %						*Stammer et al., 1991, CTD, moorings, SLA*
B	- / -	7	2	29 %						*Stammer et al., 1991, CTD, moorings, SLA*

Continuation of Table 6.1.

Meddy: name, position, time, minimum observation depth	H, m / R_{vm}, *km*	$v_{\theta m}$, cm s^{-1}	$v_{\theta 0}$, cm s^{-1}	$v_{\theta 0}$ / $v_{\theta m}$ (%)	$\zeta(\zeta_{alt})$ cm	$\lvert\omega_m\rvert$ / f	$\lvert\omega_0\rvert$ / f	ω_0 / ω_m, %	*N/f*	reference, instruments*
D	- / -	12	4	33 %						*Stammer et al., 1991, CTD, buoy stations, SLA*
Aska (A)	- / 17	23	12	56 %	4	0.48	0.12	26%	81	*Schultz Tokos et al., 1994, probes (CTD), RAFOS, SF*
B1	- / 25	25	10	40 %	5	0.35	0.07	20%	81	*Schultz Tokos et al., 1994, probes (CTD), RAFOS, SF*
B2	- / thirty	31	18	58 %	10	0.36	0.10	thirty %	81	*Schultz Tokos et al., 1994, probes (CTD), RAFOS, SF*
A1	- / 18	23	23	100 %	8	0.45	0.22	50%	81	*Oliveira et al., 2000, RAFOS, SF, SLA, TPO*
A2	- / 37	20	17	83 %	12	0.19	0.08	42%	81	*Oliveira et al., 2000, RAFOS, SF, SLA, TPO*
the Azores region (old meddies)										
Ceres, 07-09.1993, 36° N, 24° W, 0m	1000 / 30	12	23	192%	13 (10)	0.15	0.14	96%	89	*Tychensky and Carton, 1998; CTD, XBT, SF, SLA*
Encelade, 10-11.1993, 33° N, 21° W, 0m	1000 / 35	14	8	57%	5 (8)	0.17	0.06	29%	95	*Tychensky and Carton, 1998; CTD, XBT, SF, SLA*
Hyperion, 07.1993, 35° N, 28° W, 0 m	900 / 35	20	13	65%	8 (12)	0.23	0.07	33%	89	*Tychensky and Carton, 1998; CTD, XBT, SF, SLA*
Bobby92, 03.92, 35°N, 23°W, 0 m	1100 / 22	thirty	15	58%	6	0.54	0.13	23%	91	*Pingree and Le Cann, 1993b; CTD, ADCP, SF*
A2 (Azores-Biscay rise)	<40	15	13	87 %	9	0.14	0.06	43%		*Le Cann et al., 2005; CTD, RAFOS, ARGO, SF*
Sharon84, 09.1984 32° N, 22° W, 100m	1000 / 23	25	9	36%	4	0.47	0.08	18%	91	*Schultz Tokos and Rossby, 1991; CTD*

Continuation of Table 6.1.

Meddy: name, position, time, minimum observation depth	H, m / R_{vm}, *km*	$v_{\theta m}$, cm s^{-1}	$v_{\theta 0}$, cm s^{-1}	$v_{\theta 0} / v_{\theta m}$ (%)	$\zeta(\zeta_{alt})$ cm	$\lvert\omega_m\rvert$ / f	$\lvert\omega_0\rvert$ / f	ω_0 / ω_m, %	*N/f*	reference, instruments*
Sharon85, 10.1985 27 ° N, 24°W, 100m	1100 / 17	18	3	17%	1	0.53	0.04	8%	116	*Schultz Tokos and Rossby, 1991; CTD*
AVERAGE		**19**	**12**	**62%**	**7**	**0.40**	**0.11**	**32%**	**85**	

**CTD – conductivity-temperature-depth probe; XBT – consumable expandable bathythermograph; (L)ADCP – (lowered) acoustic Doppler current meter;* SF – surface floats; *DDB – floats with a submerged sail; RAFOS, ARGO – subsurface floats*; SLA – sea level anomalies; *SST – sea surface temperature.*

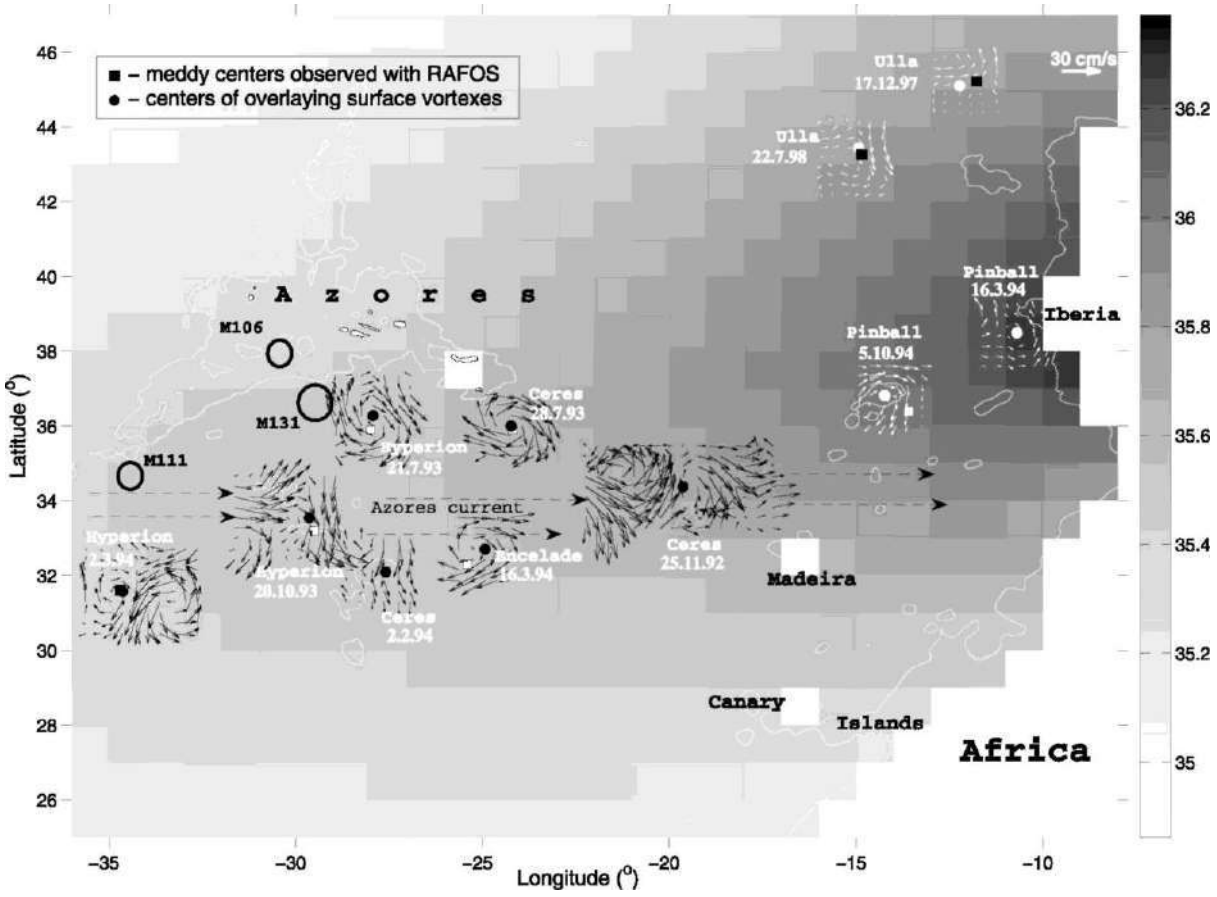

Fig. 6.5. Salinity at a depth of 1000 m (color, the Mediterranean Waters tongue is clearly visible) White squares are the positions of meddy centers on trajectories of RAFOS floats on the indicated dates (see also Tables 6.1 and 6.2). Black and white arrows are the geostrophic currents derived from altimetry data for the period of meddy observations; black/white circles are the centers of anticyclonic eddies on the surface closest to the meddy centers. The dashed horizontal lines show the average position of the Azores Current. Black circles are the positions of three meddies observed during the voyage of the R/V Archipelago (Fig. 6.1). White line is the 2000 m isobath (from Bashmachnikov et al., 2009a).

Observations indicate that all observed meddies transmit their dynamic signals to the sea surface, with the peak velocity of anticyclonic rotation on the sea surface averaging to 72% of that of the meddy core. The exception was meddy Ceres, over which the azimuthal velocity of the surface signal noticeably exceeded that of the core rotation at 800 m depth. The reason was the

merger of the surface manifestation of this meddy with the anticyclonic meander of the Azores Current, which significantly intensified the meddy signal on the sea surface (Richardson and Tychensky, 1998).

Figure 6.5 demonstrates the manifestations in AVISO altimetry of some of the meddies listed in Table 6.1, detected with *in situ* vertical casts at the initial position in their trajectories and further tracked with RAFOS neutral buoyancy floats, released in the meddy cores, over a long time (up to 1.5 years) (Tychensky and Carton, 1998). The same meddy sometimes gives a clear signal on the sea surface and sometimes this signal is practically absent. Below a detailed analysis of the surface manifestations of these meddies along their trajectories is given.

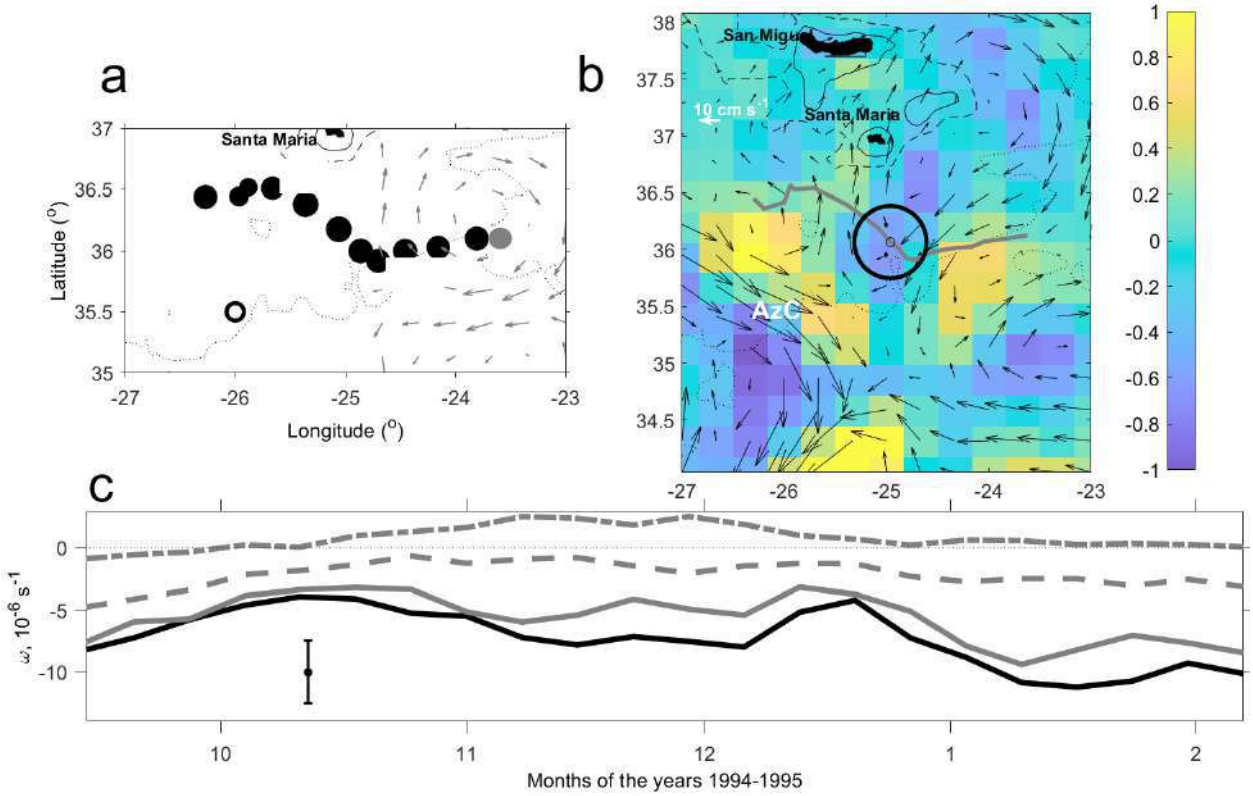

Fig. 6.6. Trajectory and time evolution of characteristics of meddy Zoe and its surface signal. ***(a)*** *Trajectory of Zoe derived from RAFOS floats (the propagation is to the west). Numbers (month and year) indicate the beginning of the corresponding months. The size of the black circles characterizes the radius (km) of rotation of the RAFOS floats. Arrows – surface currents from AVISO altimetry on the date of the first observation in September 1994 (gray circle). Isobaths of 1000 m (solid), 2000 m (dashed line), 4000 m (dashed line) are presented.* ***(b)*** *An example of the relative vorticity field (10 $^{-5}$ s^{-1}, color) and geostrophic currents (arrows) form AVISO data at 11.22.1994. The position of the meddy, marked with a black circle. The gray line shows the trajectory of the meddy from 09.13.1994 to 02.10.1995.* ***(c)*** *Evolution during the observation period of the peak relative vorticity (10^{-6} s^{-1}) of the meddy core from data of RAFOS floats (solid black line) and the relative vorticity of the surface signal over the meddy, average in the region r < 20 km (meddy center - solid gray line), r = 20-60 km (gray dashed line), r = 60-80 km (gray dash-dotted line), from AVISO data. The vertical segment shows the maximum error in the peak relative vorticity values in AVISO data (from Bashmachnikov and Carton, 2012).*

Meddy Zoe was observed for 5 months (09/1994-02/1995) by RAFOS floats south of the Azores (Richardson and Tychensky, 1998). At the very beginning of its trajectory, the characteristics of the meddy are determined by a series of shipboard vertical casts. The meddy surface signal was very clear in altimetry during the entire time of its tracking with RAFOS floats (Fig. 6.6a-c).

In January 1995, the signal increased sharply (Fig. 6.6c), with an increase in relative vorticity of the meddy core and accompanied by a rapid drift of the RAFOS float towards the center of the meddy (Fig. 6.6a), signs of strong changes within the core. The correlation of the average and peak relative vorticity of the surface signal (ω_0) with variations in the relative vorticity of the meddy core (ω_m) was 0.76, indicating a close link between changes in characteristics of the meddy core and the intensity of its surface signal. Presumably this variability is associated with the merger of Zoe with another meddy east of island Santa Maria. This can be derived from a merger of the surface signal of Zoe with another intense surface anticyclone, skirting the eastern tip of the Azores plateau and approaching Zoe from the northeast (Fig. 6.6b).

Meddy Hyperion (07.1993 - 12.1994) (Richardson and Tychensky, 1998; Richardson et al., 2000) was observed with RAFOS floats propagating from 36°N to 27°N (Fig. 6.7a). Meddy was clearly visible on the sea surface in July 1993 south of the Azores, at the time when it was discovered and studied in detail with vertical casts (Figure 6.5). The associated surface anticyclone moved together with the meddy and was continuously tracked until September-October 1993, when it merged with an anticyclonic meander of the Azores Current (Fig. 6.7b). In October 1993, the meddy began to move rapidly southward, having broken away from the meander. During 20 days, its average velocity was 5 cm s^{-1}, while the anticyclonic vorticity above, on the sea surface, weakened significantly and became difficult to distinguish against the background of the Azores Current (Fig. 6.5 and Fig. 6.7c). Already from the end of October, the signal strengthened again, making it possible to track the meddy south of the Azores front, but it became significantly less intense.

In October-November, the meddy passed over the Plato Seamount (vertical line in Fig. 6.7c). Here the RAFOS float temporarily stopped rotating and recorded a sudden drop in temperature. After rounding the plateau, it resumed its rotation, but with a significantly larger radius (Fig. 6.7a, see also Richardson et al., 2000). During the contact with the seamount, one can assume a partial destruction of the meddy core, which, however, was not accompanied by its complete break up. This is indicated not only by the behavior of the float, but also by the rapid restoration of the surface signal of the meddy (Fig. 6.7c). Since the surface signal passed to the west of Plato Seamount, and the RAFOS float passed to the east, it can be assumed that the meddy split and subsequently remerged behind the seamount. Such process has been observed in model studies (Cenedese, 2002).

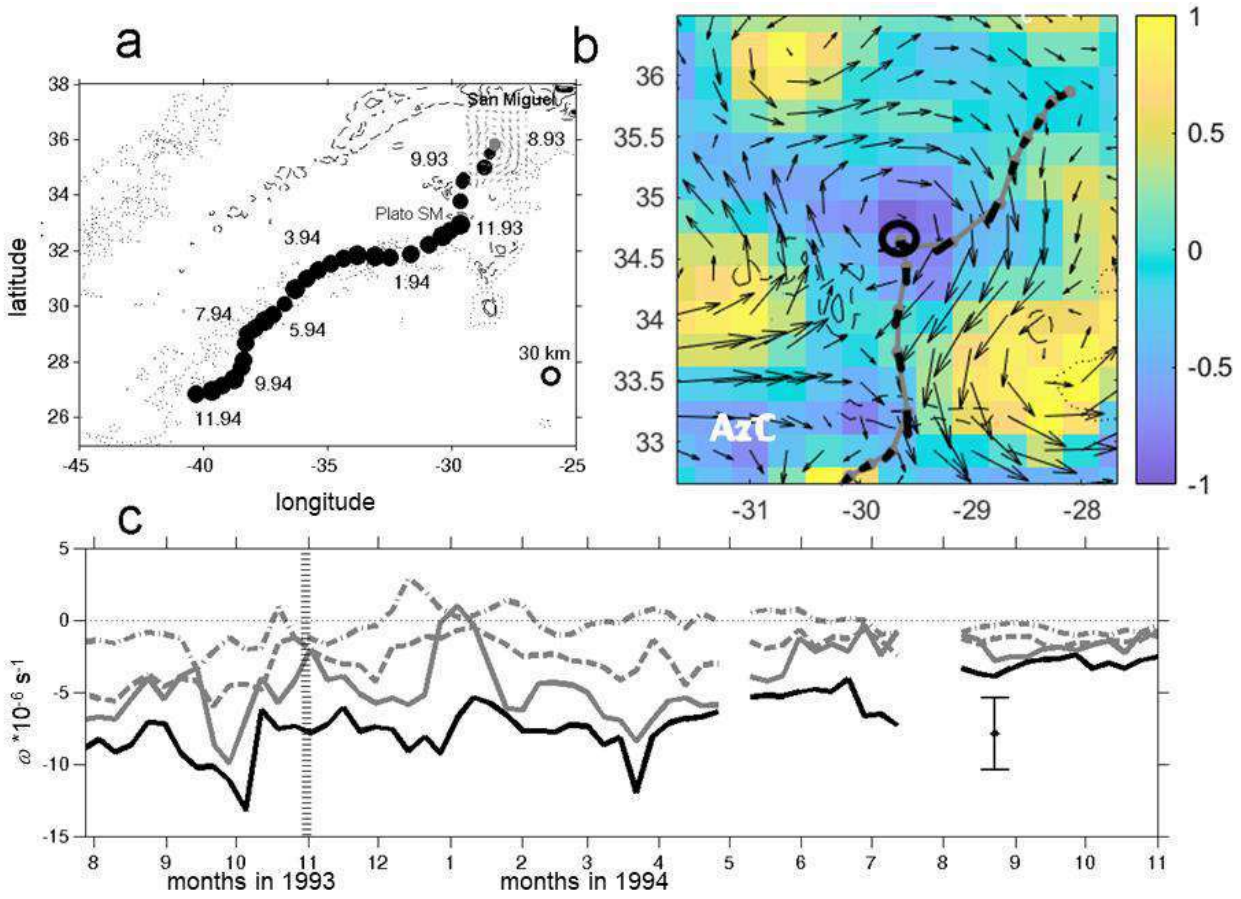

Fig. 6.7. ***(a)*** *Trajectory and change in time of the characteristics of meddy Hyperion (the direction of propagation is southwestwards);* ***(b)*** *AVISO geostrophic currents are given for September 22, 1993.* ***(c)*** *Peak relative vorticity of the meddy core and of its surface signal in satellite altimetry. The vertical dashed line in November 1993 marks the period of interaction with Plato seamount. See description in Fig. 6.6 for more details (from Bashmachnikov and Carton, 2012).*

The next disappearance of the surface signal over the meddy occurred 3 months later, when two strong surface cyclones which accompanied the meddy during its westwards propagation along the southern boundary of the Azores Current, converged over the meddy (Fig. 6.5).

Then the meddy signal, gradually weakening, was traced for 17 months with three short interruptions (Fig. 6.7c). The RAFOS floats surfaced in January 1995. However, the floats circled anticyclonically on the surface for another 3 weeks, continuing their overall westwards propagation along the meddy trajectory (Richardson and Tychensky, 1998). After the floats surfaced, it was possible to trace the anticyclonic structure, moving westward, for at least another 3 months with satellite altimetry (black line in Fig. 6.11, see methodology in section 6.7).

Meddy Ceres (08.1993 - 01.1994) was a meddy of fairly moderate intensity during the period of its observation (Richardson and Tychensky, 1998), but it was nevertheless clearly visible with the surface in altimetry data (Fig. 6.5). Since the release of RAFOS floats in the meddy core in July 1993, the surface signal of Ceres has been monitored for 4 months. Meddy moved west and then south (Fig. 6.11). Since mid-October 1993, the meddy interacted with the meander of the Azores Current, and then it was registered a rapid southwards translation of the meddy at a velocity of up to 10 cm s^{-1}. The anticyclonic meander moved separately from the meddy. From this point on, the surface signal of Ceres became intermittent (Fig. 6.5). his may be explained by the increased weakening of the meddy, which, three months after crossing the Azores Current, broke

up during its interaction with the Cruiser and Irving seamounts (Richardson et al., 2000). The characteristic weakening and loss of a part meddy volume, when crossing the Azores Current, was noted in Chapter 4.

Meddy Encelade (09.1993 - 05.1994) was a fairly intense eddy with an initially strong surface signal (Fig. 6.5). The high intensity of the anticyclonic signal over the meddy was associated with trapping of the Azores Current meander. After 2 weeks, the Azores Current shifted north, while the meddy began to move west (Fig. 6.11), along the southern boundary of the current, carrying the meander with it. A cyclone, formed to the southwest of meddy Encelade, also followed the meddy. Further fluctuations in the intensity of the meddy surface signal were linked with changes in the distance between the meddy and the center of the cyclone (as the centers approached each other, the anticyclonic signal over the meddy weakened). In May-June 1994, after its interaction with Cruiser Seamount, the meddy split into two meddies, each of which was tracked by one of the RAFOS floats trapped by the meddy (Richardson et al., 2000).

In addition to old meddies near the Azores Islands, two young meddies were tracked with floats in the vicinity of the Iberian Peninsula.

Meddy Pinball (01-09.1994) was discovered during its formation in the Lisbon Canyon, south of the Extremadura Promontory (Fig. 6.8a, see also Pingree, 1995, 2002). It was initially a fairly small meddy, and during the initial period of its stagnation (January-June 1994), no stable signal was observed on the sea surface above the meddy (Fig. 6.5 and Fig. 6.8b,c). The Pinball signal began to appear 30-40 days after the beginning of the observations, but then the meddy dived under a cyclone, formed to the northeast (Richardson et al., 2000), and its surface signal practically disappeared again (Fig. 6.8b). The formation of the cyclonic signal near the coast was likely due to the interaction of Pinball with the southerly sea surface upwelling current (Aiki and Yamagata, 2004). From April-May 1994, Pinball began to move away from the continental slope, leaving the cyclone to the east. The anticyclonic surface signal over the meddy became stable, but remained rather weak (Fig. 6.8c). The signal increased sharply after the Pinball merger from Meddy-18 in May-June 1994 (Fig. 6.8a,c) near the northern tip of the Josephine Seamounts. When Pinball collided with Meddy-18, two separate sea surface anticyclonic signals over the two meddies merge together on the sea surface. This was accompanied by an increase in the sea level anomaly over meddy Pinball (Fig. 6.19c), which indicates an increase in the meddy radius and confirms the fact of the merger. The next merger was recorded with Meddy-R in November-December 1994 (Fig. 6.5, see Pingree, 2002), but this happened when no RAFOS track of the meddy was available. The loss of the RAFOS float in late 1994 may have been due to the splitting of meddy Pinball at Lyon Seamount (Richardson et al., 2000).

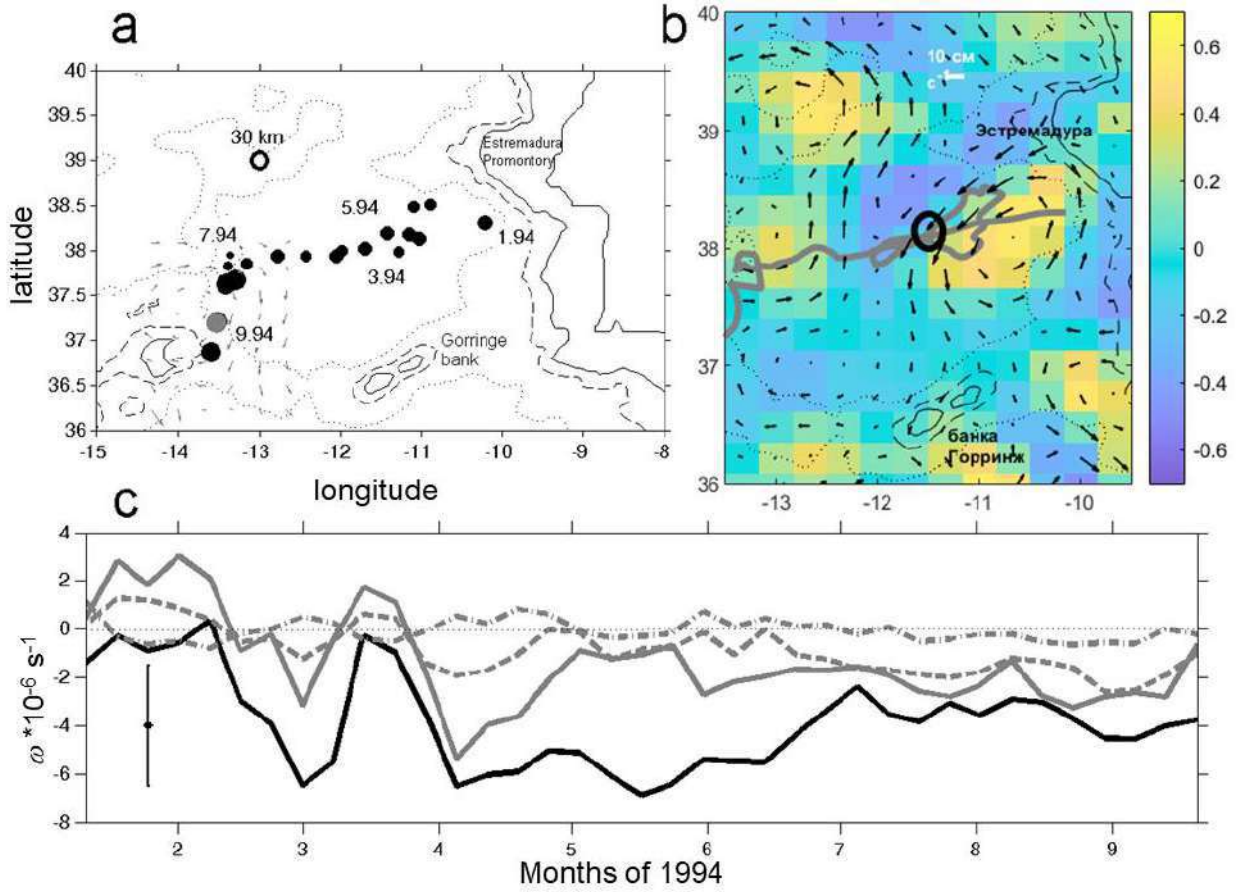

Fig. 6.8. ***(a)*** *Trajectory and change in time of the characteristics of meddy Pinball (the meddy propagation was to the west and then to the south);* ***(b)*** *AVISO geostrophic currents on 05.04.1994.* ***(c)*** *Peak relative vorticity of the meddy core and of its surface signal in satellite altimetry. See description in Fig. 6.6 for more details (from Bashmachnikov and Carton, 2012).*

The northernmost meddy, observed with RAFOS floats for more than a year, was a fairly intense northern meddy Ulla (04.1997 - 09.1998) (Paillet et al., 2002). This meddy was recorded at approximately 45°N, northwest of Cape Finisterre, and was tracked for 1.5 years (Figs. 6.5 and 6.11 – black dots). The surface floats, released over the meddy, confirmed that the meddy had an anticyclonic signal on the sea surface. Despite this, tracking of meddy Ulla in altimetry was difficult (Fig. 6.5). During the initial period of stagnation (Fig. 6.11), when the meddy made only a few rapid chaotic translations around its original position during a year, the meddy surface signal often disappeared, and its continuous tracking was possible over 3 to 4 months. From May to August 1998, when Ulla began to rapidly move southward, its surface signal became quite pronounced. In August 1998, the surface signal of Ulla merged with another anticyclonic signal that was moving from the west and may have belonged to another meddy. The merged surface signal then continued to move southwest. However, by this time, Ulla had already lost its RAFOS float and identification of the observed weak anticyclone as a meddy signal remains speculative.

All of the above-mentioned meddy surface signals, continuously monitored in 1993-1994 for many months, were detected from a single T/P satellite mission. Only when tracking meddy Ulla, the T/P data were supplemented with data from the ERS-1 satellite in AVISO altimetry. Continuous recording of a signal, albeit a rather weak one, over small meddy Ulla (Table 6.1) suggests the importance in an increase of the number of altimetry missions for eddy detection.

This also suggests that the statistical estimates by Tournadre (1990) above somewhat underestimate the probability of eddy tracking with AVISO altimetry data.

Table 6.2. Mean relative vorticity (normalized to f) on the sea surface from AVISO data at different distances from the meddy center (ω). ω_0 is the peak relative vorticity within 100 km from the meddy center.

Meddy (period of observations)	Zoe (09.94-02.95)	Hyperion (07.93-06.94)	Encelade (11.93-05.94)	Ceres (08.93-01.94)	Pinball (01-09.94)
ω/f at a distance of 20 km	-0.07 ±0.02	-0.06 ±0.03	-0.08 ±0.02	-0.05 ±0.06	-0.02 ±0.02
ω/f at a distance of 45 km	-0.03 ±0.01	-0.03 ±0.02	-0.06 ±0.01	-0.03 ±0.03	-0.01 ±0.01
ω/f at a distance of 75 km	0.01 ±0.01	-0.01 ±0.01	-0.02 ±0.01	-0.01 ±0.01	-0.00 ±0.01
Average background value of ω/f in 4°x4° square	-0.005 ±0.003	0.001 ±0.005	0.004 ±0.002	0.000 ±0.003	0.001 ±0.001
ω_0/ω_m, %	20 ±5%*	40 ±20%	35 ± 5%	45 ±45%	20 ± 35%**
$\omega_0 < 0$, $\omega_{0min} < 0$, % of observation time	100, 100%	93.94%	100, 100%	70, 100%	78, 100%
% of time when max. relative vorticity was observed over meddy (in 4°x4° square)	20%	35%	90%	40%	20%

* Due to the lack of information, the relative vorticity of the core was assumed constant and equal to -0.2 *f*.
** Includes the initial period of eddy stagnation, when the anticyclonic signal has not yet been formed.

Table 6.2 shows statistics of the characteristics of the surface meddy signals described above for the entire periods of their observations with RAFOS floats. The relative vorticities of the meddy surface signals (ω_0), derived from AVISO altimetry and averaged along the meddy trajectories, was comparable to those in the meddy cores (ω_m) and ranged from 20 to 50% (on average 30%) of ω_m, which is consistent with the ratio ω_0 / ω_m for single *in situ* observations for 17 different meddies (Table 6.1). The dynamic radii of the relative vorticity anomalies of the meddy surface signals in AVISO altimetry was approximately twice the dynamic radii of the meddy cores. However, this difference may partly be due to the "smearing" of the signal in the interpolated AVISO data (see Section 2.4).

Relative vorticity anomalies on the sea surface typically peaked near the centers of the observed meddies (i.e., at distances of no more than 20-50 km from the meddy center determined with RAFOS floats), exceeding by more than an order of magnitude the average background values around meddies. The magnitude of the relative vorticity of the surface signal decreased monotonically from peak values above the meddy center to almost zero at distances of 50-100 km from the center. Moreover, meddies were accompanied by anomalies of negative relative vorticity from 80 to 100% of the time of their tracking. The exceptions were meddy Pinball at the initial part of its trajectory (i.e., for some time after its formation) and meddy Ceres. The latter lost its surface signal when crossing the Azores Current and did not restore it until its collapse at the Irving Seamount (Richardson et al., 2000).

The peak relative vorticity of the surface signal of the analyzed meddies, probably underestimated in the AVISO data (see section 2.4), was on the order of -0.1 *f*.

The identified intensity and relative stability of signals over meddies, permits making an attempt to track meddies using satellite altimetry data for the periods when they were not tracked with *in situ* observations (see the methodology in Section 6.7). The sea surface signal of meddy M131, detected in a relatively dynamically calm area south of the Azores Current in August 2005 (Fig. 6.1 and Fig. 6.2), was continuously tracked back in time to October-December 2003 (Fig. 6.9). During this time, there was a 4-month stagnation of the meddy at Josephine Seamounts and the meddy signal was weak. Later, from February to December 2004, M131 was actively moving westward and its sea surface signal significantly intensified. The average propagation velocity was about 2cm s^{-1}, which is typical propagation of meddies (see section 4.3.2). In January 2005, when M131 skirted the southeastern tip of the Azores plateau, the meddy surface signal acquired an elliptical shape, but already in February it regained its rounded shape. The surface meddy signal passed along the southern edge of the Azores plateau, bending around it along an isobath of 2000 m. In June 2005, shortly before the meddy was recorded with *in situ* observations, the M131 captured part of the Azores Current meander, making its signal on the sea surface significantly stronger. This is confirmed by observations with the ship thermometer, which in August 2005 noted an increase in sea surface temperature relative to the surrounding ocean (by 0.3-0.6°C) at the periphery of the surface manifestation of M131 in altimetry. This indicates the capture by the meddy of the warmer water of the Azores Current. Later the meddy slowly moved southwestwards and in October 2005, after merging with another meander of the Azores Current, the meddy quickly moved south, crossing the current. At the moment of separating from the anticyclonic meander and crossing the Azores Current, the meddy temporarily lost its surface signal (see the analysis for meddies Hyperion and Ceres above) and tracking it further became problematic.

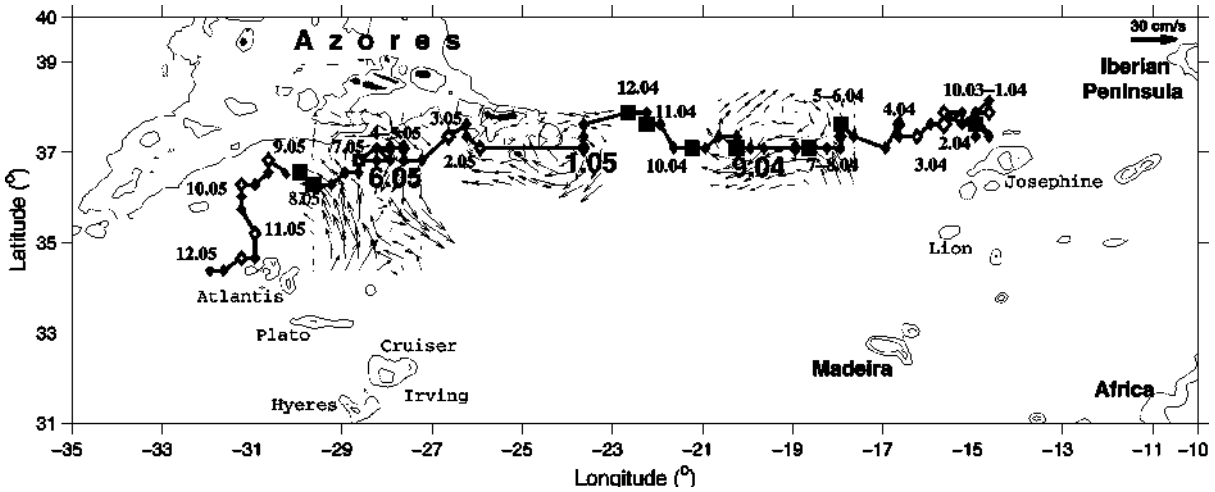

Fig. 6.9. Estimated trajectory of meddy M131, back and forth in time from its position recorded in August 2005 (Fig. 6.1-6.2). Black squares mark meddy locations where there was a marked decrease in water temperature with distance from the inferred meddy center (according to in situ vertical casts at 600-900 m). Surface geostrophic currents (AVISO data) are shown for 3 meddy locations, with dates in bold. 1000 and 2000 m isobaths are shown (from Bashmachnikov et al., 2009a).

The derived path of meddy M131 (Fig. 6.9) was verified using *in situ* vertical casts. All available profiles within a radius of 350 km from the average monthly location of the tracked signal and within 15 days from the date of altimetry observations were selected. Most of the profiles had temperature values only down to 800-900 m, so the analysis used the difference in

temperature anomalies at the 600 m and 800 m relative to the climatological values ($\Delta T = T_{800m} - T_{600m}$): in the presence of a meddy $\Delta T > 0$, which value should exceed the climatological one. The integral of the temperature anomalies between these two levels relative to climatological values (T_{1int}) was also used.

According to observations in August 2005 (Fig. 6.10a), it was shown that both parameters, ΔT and T_{1int}, decrease monotonically with distance from the center of M131 and are well approximated by logarithmic curves with coefficients of determination of 0.43 and 0.86, respectively. For 2004, 75 temperature profiles form World Ocean Database were analyzed (Fig. 6.10b). One can see a steady drop in the estimated anomalies with distance from the supposed center of the meddy and the possibility of approximating the dependence by a logarithmic law with a coefficient of determination of the order of 0.3. Particularly high coefficients of determination were noted in January, May, July, September, October and December 2004, when the average values for all months were 0.6 (see the positions of the surface signal marked with black squares in Fig. 6.9). Thus, analysis of *in situ* data confirms that the path, identified using AVISO altimetry, corresponds to the path of meddy M131.

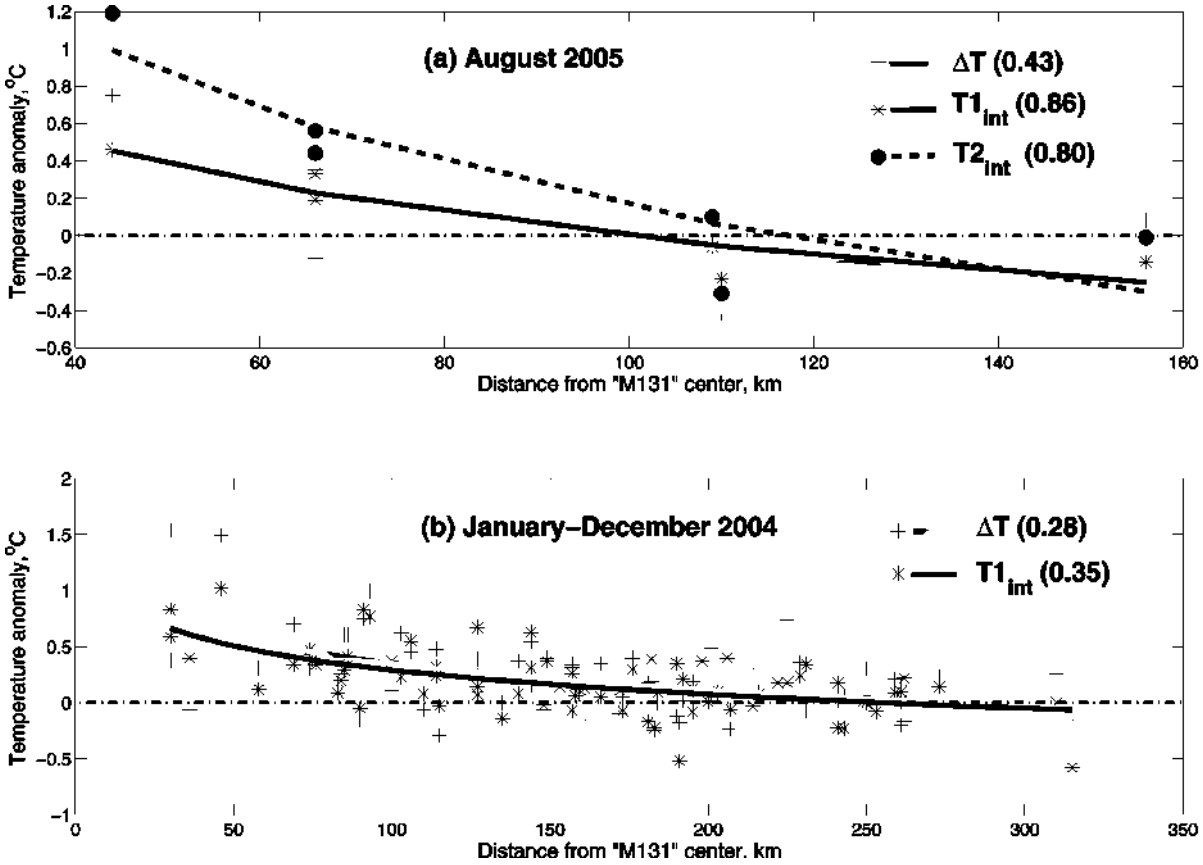

Fig. 6.10. Vertical difference in temperature anomalies at 800 and 600 m relative to climatology (ΔT, gray crosses) and integral temperature anomalies in the 600-800 m layer (T_{1int}, black stars), as a function of the distance to the center of M131: (a) for observations in August 2005 (see Fig. 6.2); (b) from on altimetry tracked trajectory of M131 over January-December 2004 (see Fig. 6.9). In (a) T_{2int} (black dots) is the same as T_{1int}, but determined by temperature anomalies in the 800-1000 m layer. The coefficients of determination of the approximating logarithmic curves are indicated in parentheses (from Bashmachnikov et al., 2009a).

Similar to a successful tracking of M131, the trajectories of other meddies (see Section 6.7), tracked with RAFOS floats, were extended (Figs. 6.5, 6.11).

The surface signal of meddy Zoe (Fig. 6.6) could be tracked forward in time for 9 months (Fig. 6.11, pink trajectory). In June-July 1995, the surface signal of the meddy merged with the anticyclonic meander Azores Current and its further fate is unclear. During the previous period, Zoe could be traced back to January 1994. During this time, the surface track showed that the meddy was moving west (along approximately 36°N) at an average velocity of 4 cm s^{-1}. Before that, in October 1994, a "stagnation" was noted, accompanied by chaotic movements of the meddy around the same point. During the stagnation period, the altimetry signal of the meddy was noticeably weakened. The anticyclonic signal of Zoe can be traced back to the Josephine seamount chain, which the Meddy skirted from the north in June 1993. Meddy Hyperion could also be traced back in time for approximately 10 months prior to its discovery in June 1997. Like Zoe, Hyperion traveled along the Central meddy path (see section 4.3.2). Meddy Ceres can be traced back in time for about two months, from its previous contact with another meander of the Azores Current at 20°W (Fig. 6.11). Meddy Encelade was traced back in time to the Josephine Seamount chain, which it skirted from the south in January–February 1993 (Fig. 6.11). After the breakup of Encelade at Cruiser Seamount, the altimetry signal was only traced over a more intense meddy fragment that traveled west along the Azores Current (can be traced by the series of green circles in Figure 6.11) and that was further stagnated, and, apparently, it disintegrated, in the area between the Cruiser and Plato seamounts. Over another RAFOS float, which was moving south (Fig. 6.11), there was no clear altimetry signal. The float soon stopped rotating, apparently as a result of the collapse of this meddy fragment.

Thus, the study above showed that meddies form sufficiently intense and stable signals on the sea surface: the sea level anomalies from 5 to 20 cm and the relative vorticity anomalies were from -0.05f to -0.15f) to be detected and continuously monitored with AVISO altimetry data for at least several months, and, under favorable conditions, for more than a year. Moreover, the anticyclonic signals over meddies formed the most intense anomaly of relative anticyclonic vorticity in the vicinity of the meddies from 20 to 90% of the total tracking time (Table 6.2), i.e. their intensity can be compared with the most energetic structures of this area – the meanders of the Azores Current

The tracked trajectories of several meddies showed that they spread along the Central path, as most of the southern meddies (see section 4.3.2), which passes north of the Azores Current. All the tracked meddies crossed the Azores Current at different sections of the current. After crossing, the surface signal of some meddies weakened and was soon lost. This confirms the assumption of a partial destruction of meddies during the crossing the current, derived from the previous meddy statistics (see Section 4.4), as well as from the results of model experiments of eddy-current interactions.

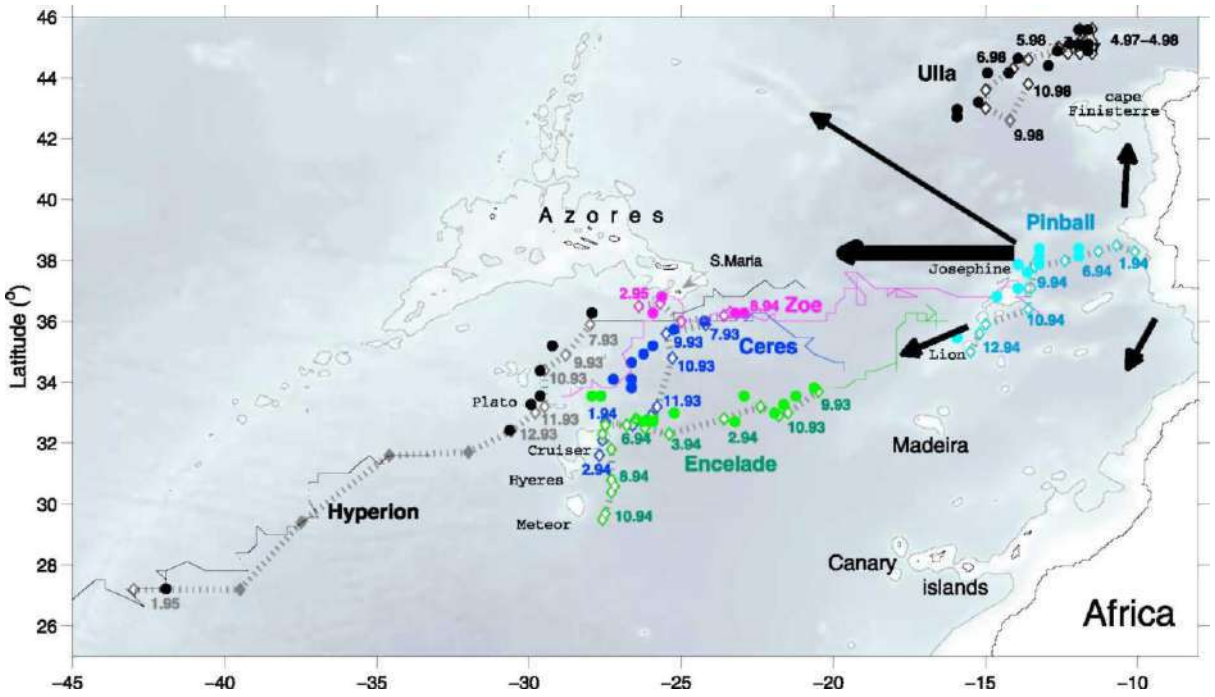

Fig. 6.11. Meddies tracked with RAFOS floats (Richardson et al., 2000) and altimetry. The diamonds connected by dotted lines show the locations and routes of meddy centers tracked with RAFOS (month and year of observation are shown at some of the meddy positions). The nearest points of the same color are the corresponding locations of the centers of the sea surface manifestations of meddies (anticyclonic eddies) tracked in altimetry. Meddies Hyperion and Ulla are shown in black, Zoe in pink, Ceres in blue, Encelade in green, Pinball in light blue. When the two tracks diverge, it means the meddy signal is lost. Solid colored lines show the paths of meddies moving forward and backward in time when there were no in situ observations. The most common paths of propagation of meddies are shown with thick black arrows (from Bashmachnikov et al., 2009a).

6.3 THE THEORY OF SURFACE MANIFESTATIONS OF MEDDIES

6.3.1 THEORETICAL ESTIMATES OF CHARACTERISTICS OF SURFACE MANIFESTATIONS OF MEDDIES IN A THREE-LAYER OCEAN

Meddies almost always move relative to the upper ocean layer above. This is a result of changes in the current velocity with depth, of the difference in the maximum velocity of the background current and the velocity of eddy translation by this current, as well as to the presence for mesoscale eddies of the proper eddy propagation velocity. The latter creates eddy motion relative to the upper ocean even in a motionless background, and also enhances the velocity difference in the subtropical northeast Atlantic, where meddies often move against the mean sea surface current (Hebert, 1988; Paillet et al., 2002; Carton et al., 2002).

The movement of a meddy relative to the upper ocean squeezes the water columns of impinging fluid above the meddy. For a three-layer ocean (layer 1 – above the meddy core, layer 2 – the meddy core layer and layer 3 – below the meddy core), it is easy to estimate the relative

vorticity above the frontal part of the core using the law of conservation of potential vorticity. Written for the upper ocean layer as $q = \dfrac{f + \omega_0}{H_s - H_m}$, we get:

$$\omega_0 = -\frac{\Delta H}{H_s} f \,. \tag{6.1}$$

Here $\Delta H = H_s - H_m$ is the contraction of the upper ocean layer above the meddy, H_s is the average thickness of the upper layer, H_m is the thickness of the upper layer above the center of the meddy (an isopycnal rise above the meddy core).

Expression (6.1) shows that, above the frontal part of the meddy, an anticyclone will be generated, which forms the sea level anomaly associated with the meddy (Fig. 6.12). This mechanism suggests that the meddy surface signal is not a projection of the dynamic signal of the meddy onto the sea surface, but it is an anticyclone in the upper ocean generated by the meddy. This is also indicated by observations (Fig. 6.4). Further interaction of this anticyclone with the meddy below can lead to a merger of their vertical axes, or to a joint rotation of both dynamic structures around a common center (Polvani, 1991).

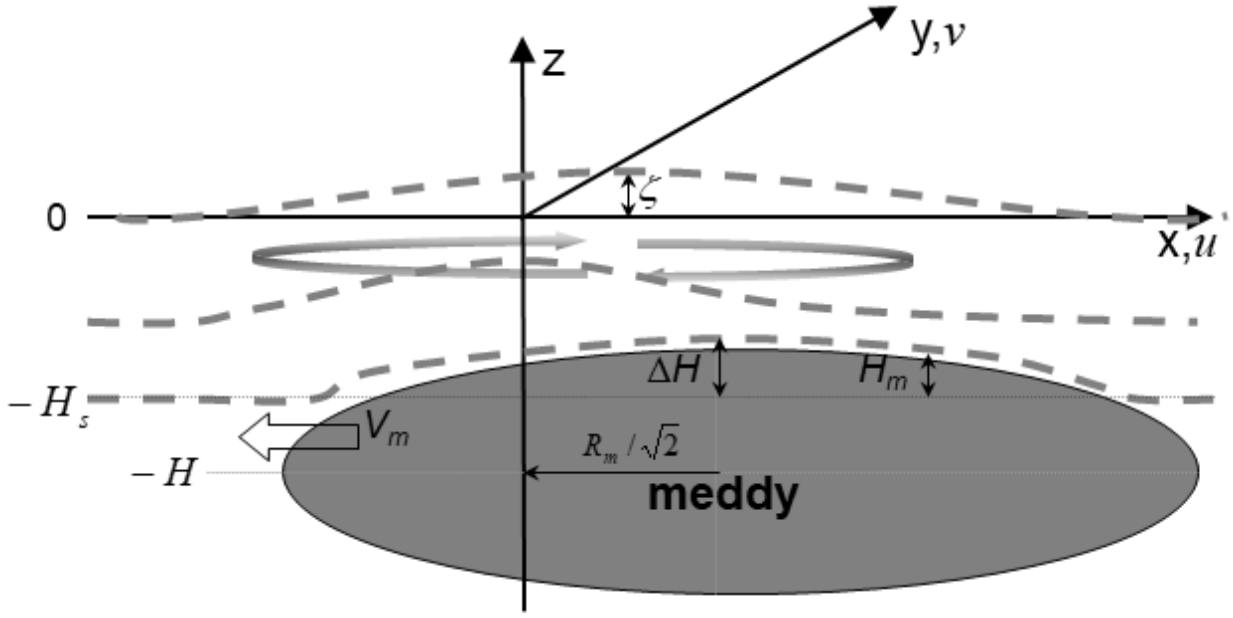

Fig. 6.12 Schematic representation of the mechanism of generation of a sea surface signal over a moving meddy. H is the depth of the center of the meddy core, H_s is the average depth of the isopycnal contouring the meddy from above, H_m and ΔH are the local and maximum vertical displacement of this isopycnal above the moving meddy, ζ is the sea level anomaly formed by the meddy, R_m is the dynamic meddy radius, V_m is the velocity of meddy propagation relative to the upper ocean layer.

The initially generated water divergence above a moving meddy weakens in time under the influence of the Coriolis force, which twists the liquid clockwise. In the three-layer model above, the geostrophic balance of the upper homogeneous layer is achieved due to the rise of the sea level

above the generated anticyclone. The related sea level anomaly can be estimated using expression (6.1) as:

$$\zeta \sim -\frac{f R^2 \omega_0}{4g} \sim \frac{f^2 R^2 \Delta H}{4 g H_s} \ , \qquad (6.2)$$

According to observations described in various literary sources, the maximum value of the isopycnal rise above the meddy ΔH ~ 50-100 m. The characteristic depth of this isopycnal in the surrounding ocean (H_s), as a rule, is 200 m less than the depth of the center of the meddy core (*H)* (Hebert, 1988; Paillet et al., 2002; Carton et al., 2002):

$$H_s = H - 200(m) .$$

With characteristic values *of H* ~ 900 m (Table 6.1), we will take the characteristic value H_s ~ 700 m. Then, according to expression (6.1), the relative vorticity of the previously motionless upper layer ω_0 will form -0.07*f* to -0.14*f*, which is 20 - 40% of the maximum meddy vorticity (ω_m ~ -0.3*f)*. This corresponds well to observations (Tables 6.1 and 6.2). At $f \sim 8 \times 10^{-5}$ s^{-1} and the dynamic radius of the sea surface wake of the meddy of *R* ~ 50 km (Table 6.2, see also Chapter 4), the theoretical average estimate of the maximum azimuthal current velocity on the sea surface $v_{\theta m} \sim \frac{\omega_0 R}{4}$ is ~ 7 – 15 cm s^{-1} has the same order of magnitude as in the observations (Table 6.1). For the same set of parameters, from expression (6.2), ζ= 3-6 cm at *R* ~ 50 km and ζ= 6-12 cm at *R* ~ 70 km, i.e. signals over the meddy will exceed the error of altimetry measurements (2-4 cm, Fu and Cazenave, 2001), as confirmed by observations (Table 6.1, see also Oliveira et al., 2000).

At the initial stage of meddy propagation, following from the same law of conservation of potential vorticity, a cyclonic signal should also begin to form on the “leeward” side of the meddy. At this initial stage, the cyclonic signal can even dominate over the anticyclonic one (perhaps this was the case after the generation of meddy Pinball– Fig. 6.9).

In fact, above a stationary meddy, the potential vorticity of the upper ocean layer is $q = \frac{f}{H_s - \Delta H}$, and after the meddy begins to move, this column moves to the leeward slope and stretches, reaching a value of $\frac{\omega_c + f}{H_s}$. Thus, the vorticity of the resulting cyclone becomes $\omega_c = \frac{f \Delta H}{H_s - \Delta H}$ slightly greater than the initial vorticity of the resulting anticyclone (expression (6.1)). Most likely, the cyclonic signal quickly breaks away from the meddy, while the anticyclonic signal moves toward the central area above the meddy core. This suggests an analogy of the interaction of a seamount with an impinging flow (see, for example, White et al., 2005), where the meddy core plays the role of an underwater obstacle that the flow is forced to bypass. A moving meddy only supports an anticyclonic surface signal, since in this case the isopycnals raised above the meddy return to their original depth after its passage.

6.3.2 THEORETICAL ASSESSMENT OF THE SEA SURFACE MANIFESTATION OF A SUBSURFACE EDDY PATCH IN A CONTINUOUSLY STRATIFIED OCEAN

The above theoretical estimates assume homogeneity of the ocean layer above the meddy, which in the highly stratified upper 1000-m layer of the tropical and subtropical Atlantic (the main thermocline) is a serious simplification. In this section, a theory of surface manifestations of meddies for a stratified upper ocean is considered. In this case, the change in the potential vorticity of the upper ocean is also a function of the buoyancy frequency ($N^2 = -\frac{g}{\bar{\rho}}\frac{\partial \rho}{\partial z}$), and it is convenient to present the potential vorticity in the Ertel's form:

$$q = -\frac{N^2}{g}(f + \omega) \tag{6.3}$$

Reducing the thickness of the upper layer in expression (6.2) is equivalent to increasing N of this layer in expression (6.3). The density gradients, that are formed above the meddy together with the isopycnals rise, create the pressure gradients that support anticyclonic vorticity inside the layer. If the water density gradient becomes sufficiently large, a sea level rise may not be needed to establish the geostrophic balance above the meddy. As a consequence, the signal in the stratified environment gets attenuated towards the sea surface (similar to the attenuation of the anticyclonic signal over seamounts, called the Taylor cone – Owens and Hogg, 1980), and may stay below the noise level of the altimetry data.

As an eddy patch we will call an eddy whose potential vorticity inside a core of radius R_m remains unchanged. To derive a theoretical expression for the magnitude of the meddy signal on the sea surface, consider the case when the surface signal above the meddy has already formed. Under these conditions, there is an area above the meddy where water particles are captured in a closed circulation system (Flierl, 1981). The calculation method used below assumes that the meddy uniformly moves in a given direction relative to the upper ocean layer and that the potential vorticity anomaly in the upper ocean was initially zero. Using the quasi-geostrophic approximation, and also assuming the *f*-plane approximation and a constant value of N in the upper layer, we define the potential vorticity anomaly as:

$$\tilde{q} - \tilde{q}_0 = \left(\frac{\partial^2}{\partial x^2} + \frac{\partial^2}{\partial y^2} + \frac{f^2}{N^2}\frac{\partial^2}{\partial z^2}\right)\psi, \tag{6.4}$$

where $\tilde{q}$ is the potential vorticity in the meddy core, $\tilde{q}_0 = const$ is its background value, ψ is the stream function of the current induced over the meddy core during its movement. The seamount analogy allows a rough estimate (Owens and Hogg, 1980): the disturbance propagates vertically over a distance $\frac{f}{N}L$, where L is the horizontal scale of the anomaly of the layer boundary (meddy). Sea level elevation is calculated by assuming that the pressure disturbance on the sea surface is determined by the rise of the isopycnal representing the ocean surface.

Taking a zero anomaly $\tilde{q} - \tilde{q}_0 = 0$ in the water layer above the meddy and a constant value $\tilde{q}_m = \tilde{q} - \tilde{q}_0$ in the meddy core, and also replacing the vertical coordinate with $\bar{z} = \frac{N}{f} z$, equation (6.4) becomes the Poisson equation:

$$\left(\frac{\partial^2}{\partial x^2} + \frac{\partial^2}{\partial y^2} + \frac{\partial^2}{\partial \bar{z}^2} \right) \psi = \tilde{q}_m \cdot \mathrm{Hv}(R_m - r), \qquad (6.5)$$

Here $r = \sqrt{x^2 + y^2 + \bar{z}^2}$ is the distance from the center of the meddy core, R_m is the dynamic radius of the meddy, and $\mathrm{Hv}(R_m - r) = \begin{cases} 1 & (r \le R_m) \\ 0 & (r > R_m) \end{cases}$ is the Heaviside function.

With the ratio of vertical to horizontal dimensions of the meddy: $\frac{h}{R_m} = \frac{f}{N}$, such a replacement of the vertical coordinate gives a spherical eddy. Replacing rectangular coordinate system with the spherical one $(x,y,\bar{z}) \to \vec{r}(r,\theta,\varphi)$, where θ is the polar angle, measured from the horizontal XY plane upward, and φ is the azimuthal angle, measured clockwise from the X axis, the solution to equation (6.5) can be written as (Weber and Arfken, 2004):

$$\psi(\vec{r}) = -\frac{1}{4\pi} \int_{-\pi/2}^{\pi/2} \cos\theta' d\theta' \int_0^{2\pi} d\phi' \int_0^{\infty} \frac{\tilde{q}_m \, \mathrm{Hv}(R_m - r') r'^2}{|\vec{r} - \vec{r}'|} dr' =$$
$$= -\frac{1}{4\pi} \int_{-\pi/2}^{\pi/2} \cos\theta' d\theta' \int_0^{2\pi} d\phi' \int_0^{R_m} \frac{\tilde{q}_m r'^2}{|\vec{r} - \vec{r}'|} dr' \qquad (6.6)$$

where r is defined as:

$$|\vec{r} - \vec{r}'|^2 = (r'\cos\theta'\cos\varphi' - r\cos\theta\cos\varphi)^2 + (r'\cos\theta'\sin\varphi' - r\cos\theta\sin\varphi)^2 + (r'\sin\theta' - r\sin\theta)^2 =$$
$$= r'^2 + r^2 - 2r'r\sin\theta\sin\theta' - 2r'r\cos\theta\cos\theta'(\cos\varphi\cos\varphi' + \sin\varphi\sin\varphi')$$

Let us assume that the center of the surface signal is located exactly above the meddy center (see section 6.2), i.e. $\theta = \pi/2$. If we assume an isotropic ocean around the meddy, we can arbitrarily choose angle φ. Putting φ=0, we get $|\vec{r} - \vec{r}'| = (r'^2 + r^2 - 2r'r\sin\theta')^{1/2}$. Then expression (6.6) can be simplified as:

$$\psi(\vec{r}) = -\frac{\tilde{q}_m}{2} \int_{-\pi/2}^{\pi/2} \int_0^{R_m} \frac{\cos\theta' r'^2}{(r'^2 + r^2 - 2r'r\sin\theta')^{1/2}} d\theta' dr' =$$
$$= \frac{\tilde{q}_m}{2} \int_0^{R_m} \frac{r'}{r} \left\{ (r'^2 + r^2 - 2r'r\sin\theta')^{1/2} \right\}_{-\pi/2}^{\pi/2} dr'$$

Since $0 \le r' \le R_m \le r$, the expression in curly brackets is equal to: $\left(r'^2 + r^2 - 2r'r\right)^{1/2} - \left(r'^2 + r^2 + 2r'r\right)^{1/2} = |r - r'| - |r + r'| = -2r'$.
Then we get:

$$\psi(\vec{r}) = -\frac{\tilde{q}_m}{r}\int_0^{R_m} r'^2\, dr' = -\frac{\tilde{q}_m R_m^3}{3r} \tag{6.7}$$

We can assume that the sea surface is a horizontal plane at a distance $z = H$ from the meddy center, where, as before, H is the depth of the meddy core. The horizontal distance from the projection of the meddy center onto the sea surface is $s = \sqrt{x^2 + y^2}$. Then in the original coordinate system (x, y, z): $r = \sqrt{s^2 + b^2}$, where the parameter $b = \frac{N H}{f}$. In the quasi-geostrophic approximation, the sea surface stream function is expressed in terms of sea level as $\psi_{z=H} = \frac{g\,\zeta}{f}$, so the sea level rise above the meddy can be expressed as:

$$\zeta(s) = \frac{f|\tilde{q}_m|R_m^3}{3g\sqrt{s^2 + b^2}} \tag{6.8}$$

The azimuthal velocity in the surface meddy signal is then equal to:

$$v_\theta(s) = \frac{g}{f}\frac{\partial\zeta}{\partial s} = -\frac{|\tilde{q}_m|R_m^3}{3}\frac{s}{\left(s^2 + b^2\right)^{3/2}}, \tag{6.9}$$

and its relative vorticity:

$$\omega(s) = \frac{\partial v_\theta}{\partial s} + \frac{v_\theta}{s} = -\frac{|\tilde{q}_m|R_m^3}{3}\frac{2b^2 - s^2}{\left(s^2 + b^2\right)^{5/2}} \tag{6.10}$$

AVISO altimetry data over meddy Hyperion (Fig. 6.7) in May-November 1994, south of the Azores Current, and meddy Zoe (Fig. 6.6) in September 1994 - February 1995, north of the Azores Current, are shown in Figure (6.13). It can be seen that the theory somewhat overestimates the sea level rise above the meddy center, which may equally be a result of the limitations of the observations (the artificial underestimation of the sea level anomalies due to smoothing in AVISO altimetry data). The theory also does not reproduce the transition of the relative vorticity across zero. The latter is a result of the secondary effects of tangential friction stress on the periphery of a rotating surface signal, which is not described by the theory.

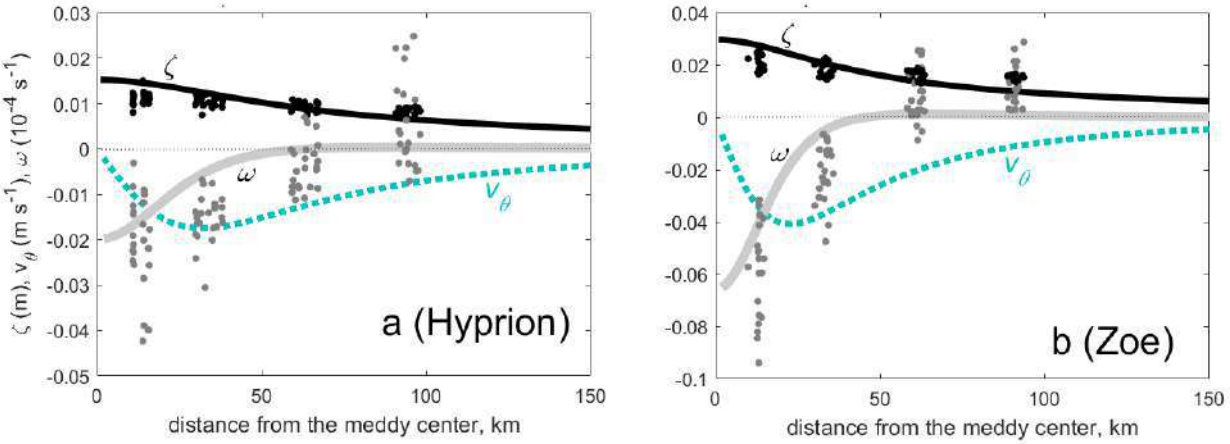

Fig. 6.13. Radial profiles of the dynamic characteristics of the meddy surface signal (solid lines – theory, dots – observations): ζ (m, black line and dots), ω (10^{-4} s^{-1}, gray line and dots). Theoretical calculations were computed with R_m = 35 km, H = 1100 m and $\tilde{q}_m = \tilde{q} - \tilde{q}_0$ = -0.7 f. The theoretical azimuthal velocity v_θ (m s^{-1}, green dotted line) is also plotted. ***(a)*** *For meddy Hyperion (27-30° N, f = 7.3 ×10^{-5} s^{-1}, N = 3 ×10^{-3} s^{-1}),* ***(b)*** *for meddy Zoe (36° N, f = 8.5 ×10^{-5} s^{-1}, N = 2.5 ×10^{-3} s^{-1}), (from Bashmachnikov and Carton, 2012).*

The peak value ζ is reached in the center of the meddy surface signal and, following expression (6.8), is equal to (s =0):

$$\zeta(0) = \frac{|\tilde{q}_m|}{3g}\frac{f^2 R_m^3}{NH} \sim 0.02\frac{f^3 R_m^3}{NH}. \qquad (6.11)$$

Here we use: $\frac{\tilde{q}_m}{\omega_m} = \frac{1}{\omega_m}\left(\omega_m + \frac{f^2}{N_m^2}\frac{\partial^2\psi}{\partial z^2}\right) = 1 + \frac{\frac{f^2}{N_m^2}\frac{\partial^2\psi}{\partial z^2}}{\nabla^2\psi} = 1 + \frac{1}{Bu}$, where N_m is the buoyancy frequency inside the meddy core, in contrast to the buoyancy frequency above the meddy core N ($N > N_m$), and the Burger number $Bu = \frac{\nabla^2\psi}{\frac{f^2}{N^2}\frac{\partial^2\psi}{\partial z^2}} \sim \left(\frac{N\,h}{f\,R}\right)^2$, where h, as before, denotes the vertical power of the meddy core, then $\tilde{q}_m = \left(1 + \frac{1}{Bu}\right)\omega_m$. Setting, according to observations, Bu =0.5 and ω_m = -0.2 f (see Table 6.1 and Section 4.3.3), we obtain the typical multiple on the right-hand side of formula (6.11). Formula (6.11) shows that the intensity of the surface signal is most sensitive to changes in the dynamic radius of the underlying meddy.

The azimuthal velocity of the surface signal reaches its peak values ($v_{\theta 0}$) at $R_{0v} = s = b/\sqrt{2}$, i.e. parameter b characterizes the horizontal scale of the surface signal. Then, according to expression (6.9), the maximum azimuthal velocity in the meddy surface signal is determined as:

$$v_{\theta 0}(R_{0v}) = -\frac{|\tilde{q}_m| R_m^3}{\sqrt{2}\cdot 3\cdot(3/2)^{3/2}}\frac{1}{b^2} = -\frac{|\tilde{q}_m|}{7.8}R_m^3\left(\frac{f}{NH}\right)^2. \qquad (6.12)$$

The relative vorticity reaches its peak above the meddy center (s =0) and, according to expression (6.10), is equal to:

$$\omega_0 = -\frac{|\tilde{q}_m| R_m^3}{3}\frac{2}{b^3} = -\frac{|\tilde{q}_m|}{1.5}\left(\frac{f\,R_m}{N\,H}\right)^3. \qquad (6.13)$$

The dynamic radius of the surface signal over the meddy can be estimated as $R_0 = \sqrt{2}\,b = 2R_{0v}$.

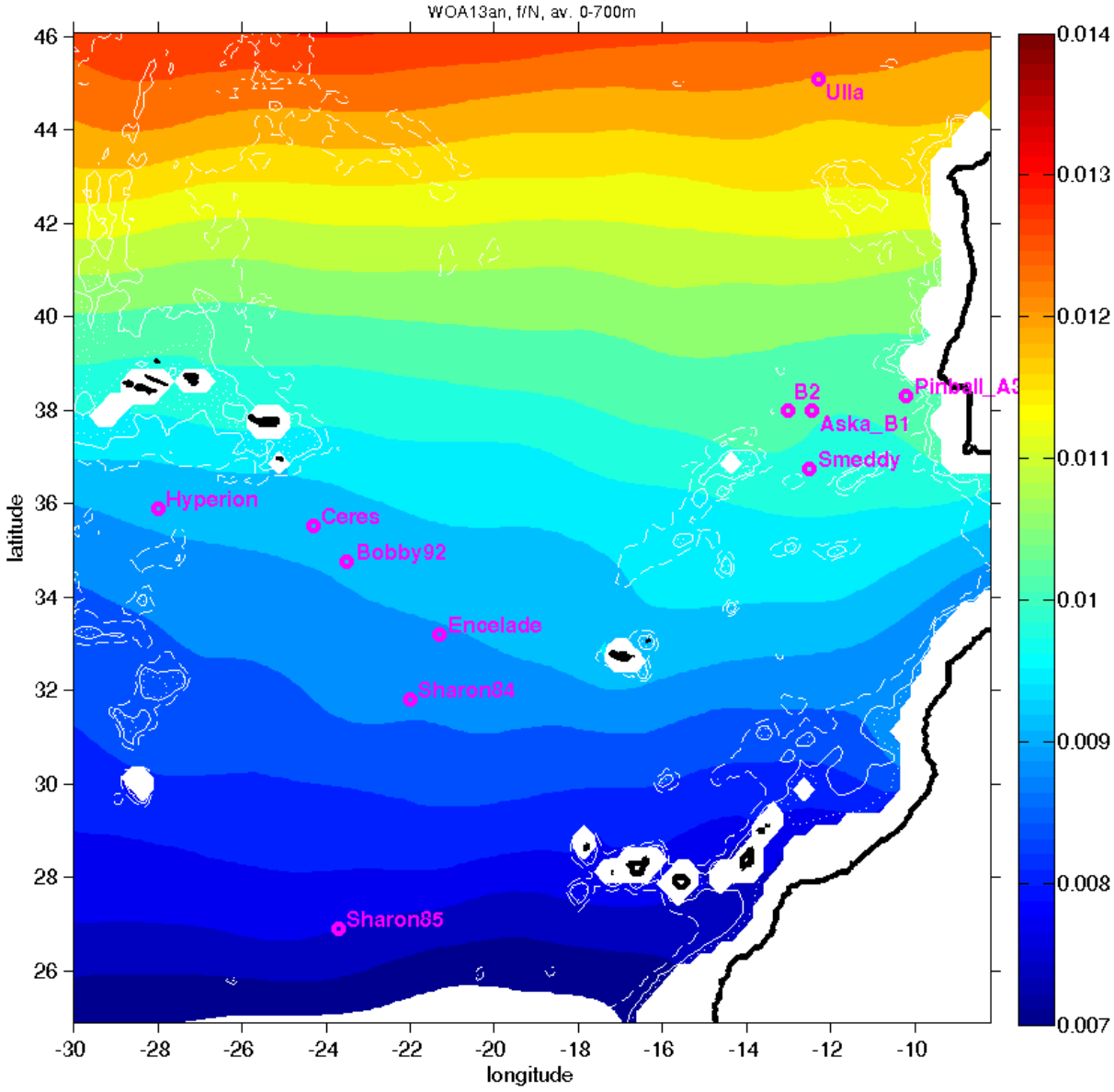

Fig. 6.14. f/N ratio in the upper 700 m layer. Stratification was computed using WOA13 annual mean temperature and salinity profiles. Locations of some meddies from Table 6.1 are shown as purple circles (after Bashmachnikov et al., 2014).

The dynamic characteristics of the meddy surface signal in expressions (6.11)-(6.13) depend on the ocean background conditions via the ratio f/N (Fig. 6.14), and the characteristics of the meddy core. The theoretical results above show that, with other things being equal, the meridional change f/N leads to a more than 6-fold weakening of the relative vorticity of the meddy surface signal from north to south of the MW region (Fig. 6.14). Meddies with a deeper core, as well as meddies observed to the south, have surface signals not only of lower intensity, but also of larger radius (Table 6.3). For northern meddies, the radius of the surface signal is of the same order as the meddy radius, while for generally smaller southern meddies the radius of the surface signal exceeds the meddy radii 2-4 times. This facilitates better capture and tracking of the meddy signal in the satellite altimetry data, where the lack of spatial resolution is often critical for identification of mesoscale structures.

Table 6.3. Characteristics of surface signals over a meddy with a fixed dynamic radius R_m = 30km and with a potential vorticity anomaly of $|\tilde{q}_m| = 0.7f$ for two limiting cases: meddy in mid-latitudes (≥45°N) and *in the southern subtropics (10-35°N). Characteristics of the surface signal of the meddy: ζ(0) – maximum level anomaly above the center of the meddy, R_{0v} – radius of the maximum azimuthal velocity, R_0 – radius of the transition of the relative vorticity across zero.*

Region	H_m, m	ζ(0), cm	radius R_{0v}, km	radius R_0, km
mid-latitudes	600	35	25	35
(≥45°N, f/N =0.03)	1100	19	23	47
southern subtropics	600	8	37	74
(10-35°N, f/N =0.01)	1100	4	68	136

The theory above was further developed by Ciani et al. (2015) for point vortices, which are vertically shielded S-meddies or horizontally shielded R-meddies (Morel and McWilliams, 1997). Screen means the presence around the meddy core of areas with an anomaly of potential vorticity, the sign of which is opposite to that in the eddy core.

In R-meddie, the change in the sign of the potential vorticity horizontally is associated with a change in the sign of the relative vorticity at the periphery of the eddy, like it is in the Rayleigh eddy (Section 1.3). For simulating a meddy with a point anticyclonic eddy, the positive vorticity anomaly of the "screen" was concentrated in a circle of radius R_m at the depth level of the eddy core. The integral vorticity of the "screen" was equal in magnitude and opposite in sign to the potential vorticity of the core. The sea level anomaly over the center of such an R-meddy can be estimated as (Ciani et al., 2015):

$$\zeta_2 \approx 2.4 \frac{f|q_m|}{\pi g} \frac{\left(h/2\right)^2 R_m^2}{H^2}. \qquad (6.14)$$

As before, here H is the depth of the center of the meddy core, and h is the vertical thickness of the meddy core.

The S-meddy is formed in the case of the dominance of the effect of isopycnal stretching in the potential vorticity anomaly of the core of an anticyclonic eddy. At the same time, along with

a decrease in the buoyancy frequency in the core of the subsurface anticyclone, an increase of N is observed above and below the core (see example in Fig. 5.3). For a point anticyclonic meddy, point anomalies of potential vorticity of opposite sign above and below the core were specified, each of which was equal in magnitude to half the potential vorticity anomaly of the meddy core. Then the sea level anomaly above the eddy center can be estimated as (Ciani et al., 2015):

$$\zeta_3 \approx 2.4 \frac{f|q_m|}{\pi g} \frac{\left(h/2\right)^3 R_m^2}{\left(H^2 - \left(h/2\right)^2\right) H} \tag{6.15}$$

The intensity of the surface signal of an eddy with a screen, estimated from expressions (6.14) or (6.15), is less than that of a similar unscreened eddy, estimated from expression (6.11) (Bashmachnikov and Carton, 2012).

6.3.3 DISSIPATION OF THE SURFACE SIGNAL OF A SUBSURFACE EDDY PATCH

Expressions (6.11-6.15) show that the intensity of meddy surface signals depends both, on the magnitude of the external forcing (the meddy) and on external background conditions, primarily on the stratification of the upper ocean. In real ocean, the intensity of the signal is also determined by the intensity of dissipation of its energy (see Chapter 5). In this section, the dissipation of the meddy surface signal through formation of a leeward Rossby wave trains is numerically analyzed (Bashmachnikov et al., 2014). A similar mechanism often plays an important role in during eddy dissipation in the ocean (Flierl, 1984; Early et al., 2011).

A numerical quasi-geostrophic model for a 2.5-layer fluid with weak harmonic or biharmonic dissipation (except in specified cases, harmonic dissipation was not used) was used for the analysis (Carton, 2001; Carton et al., 2014):

$$\frac{\partial q_k}{\partial t} + \vec{V}_k \cdot \nabla q_k = A_k \nabla^4 \psi_k + A_{2k} \nabla^6 \psi_k \tag{6.16}$$

Here ψ_k is the stream function, $\vec{V}_k$ ($v = \frac{\partial \psi}{\partial x}$, $u = -\frac{\partial \psi}{\partial y}$) is the vector of geostrophic current velocity, q_k is the potential vorticity, A_k is the Newtonian viscosity, A_{2k} is the biharmonic viscosity, k =1,2,3 are the indices of the upper, middle and lower layers of the model. The third layer is always at rest. The biharmonic viscosity was taken at a minimum compatible with the numerical stability of the model.

q_k is defined as:

$$\begin{aligned} q_1 &= \nabla^2 \psi_1 + \beta y - F_1(\psi_1 - \psi_2) \\ q_2 &= \nabla^2 \psi_2 + \beta y - F_2(\psi_2 - \psi_1) - F_3(\psi_2 - \psi_3), \\ q_3 &= \nabla^2 \psi_3 + \beta y - F_4(\psi_3 - \psi_2) \end{aligned} \tag{6.17}$$

where $F_1 = \frac{f^2}{g'_1 H_1}$, $F_2 = \frac{f^2}{g'_1 H_2}$, $F_3 = \frac{f^2}{g'_2 H_2}$, $F_4 = \frac{f^2}{g'_2 H_3}$; $g'_1 = g\frac{\rho_2 - \rho_1}{\bar{\rho}}$, $g'_2 = g\frac{\rho_3 - \rho_2}{\bar{\rho}}$ are the reduced accelerations of gravity at the layer interfaces, $\rho_{1,2,3}$ is the density and $H_{1,2,3}$ is the thickness of the model layers.

The modeling area included 512 x 512 points in horizontal; the latitude of the center of the modeling area was taken as 35° N. Meddy was initialized as an anticyclonic eddy in layer 2. It had a radial Rayleigh velocity profile with radius $R_m = Rd/1.4$ (Rd = 30 km is the first baroclinic Rossby deformation radius in the subtropical Atlantic) and a peak relative vorticity $\omega_m = 2\ 10^{-5}\ s^{-1}$. The evolution of potential vorticity in layer 2 (the meddy core) and the stream function in layer 1 (surface wake of the meddy) were monitored during the model experiments.

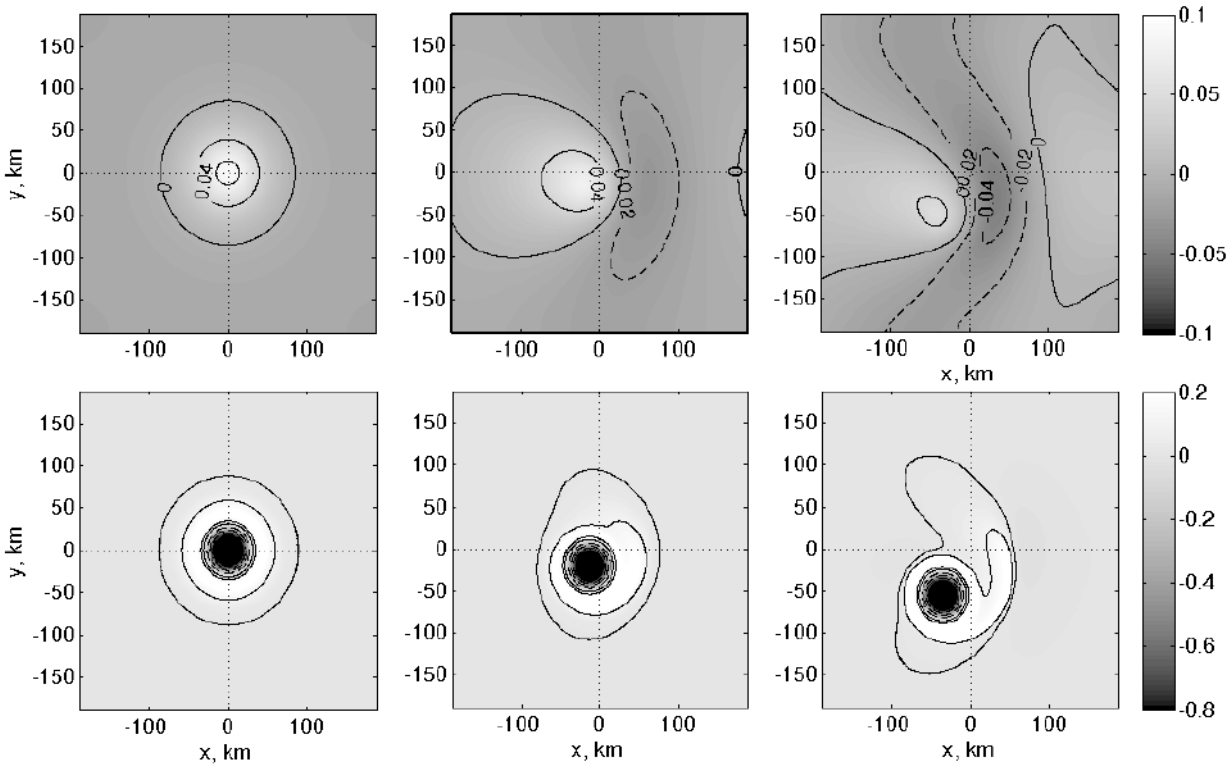

Fig. 6.15. Experiment I at the β-plane: the upper panels show the stream function in layer 1, the lower panels show the potential vorticity in layer 2. The time step is 17.6 days (from Bashmachnikov et al., 2014).

The first experiment (Fig. 6.15) was carried out on the β-plane with no mean flow. The upper layer initially had everywhere zero potential vorticity. This implies that the sea level rise (positive stream function anomalies) forms the anticyclonic relative vorticity in the upper ocean directly above the meddy. As a result of the planetary β-effect, in 35 days the meddy moved approximately 70 km southwestwards with an average propagation velocity of just over 1 cm s^{-1}. During this period, the meddy core in layer 2 underwent minor changes. In layer 1, after half a month, a negative stream function anomaly was formed, which corresponds to a cyclonic relative vorticity anomaly on the lee side of the meddy (Fig. 6.15). It looked like a typical of Rossby wave behind an eddy (Early et al., 2011). Moving westward with more or less uniform beta-drift velocity $V_m \sim \beta\, Rd^2$, equal to the velocity of long baroclinic Rossby waves (Chelton et al., 1998), the surface

signal may generate such waves. Over one month, scattering by Rossby waves led to a twofold decrease in the amplitude of the meddy surface signal.

The second experiment (Fig. 6.16) was carried out on the *f*-plane with a constant background current in layer 2 of a westerly direction and a velocity of U_2 = -5 cm s^{-1}. The mean current caused a baroclinic β-effect equal to $-F_1 U_2$ = -3.2 10^{-11} m^{-1} s^{-1}, approximately 1.6 times higher than the planetary β-effect of the previous experiment and with the opposite sign. The meddy in layer 2 moved northwestwards due to two factors – advection by the background current in layer 2 and the baroclinic beta-drift of the meddy itself. The phase velocity of long baroclinic Rossby waves of the first vertical mode $c_1 \sim U_2 FRd_1^2$ is ~ -1.5 cm s^{-1}, while the velocity of the zonal meddy drift was -3 cm s^{-1} (Fig. 6.16). With a significant difference between these two velocities, the generation of Rossby waves in the lee part of the meddy signal was practically absent (Fig. 6.16).

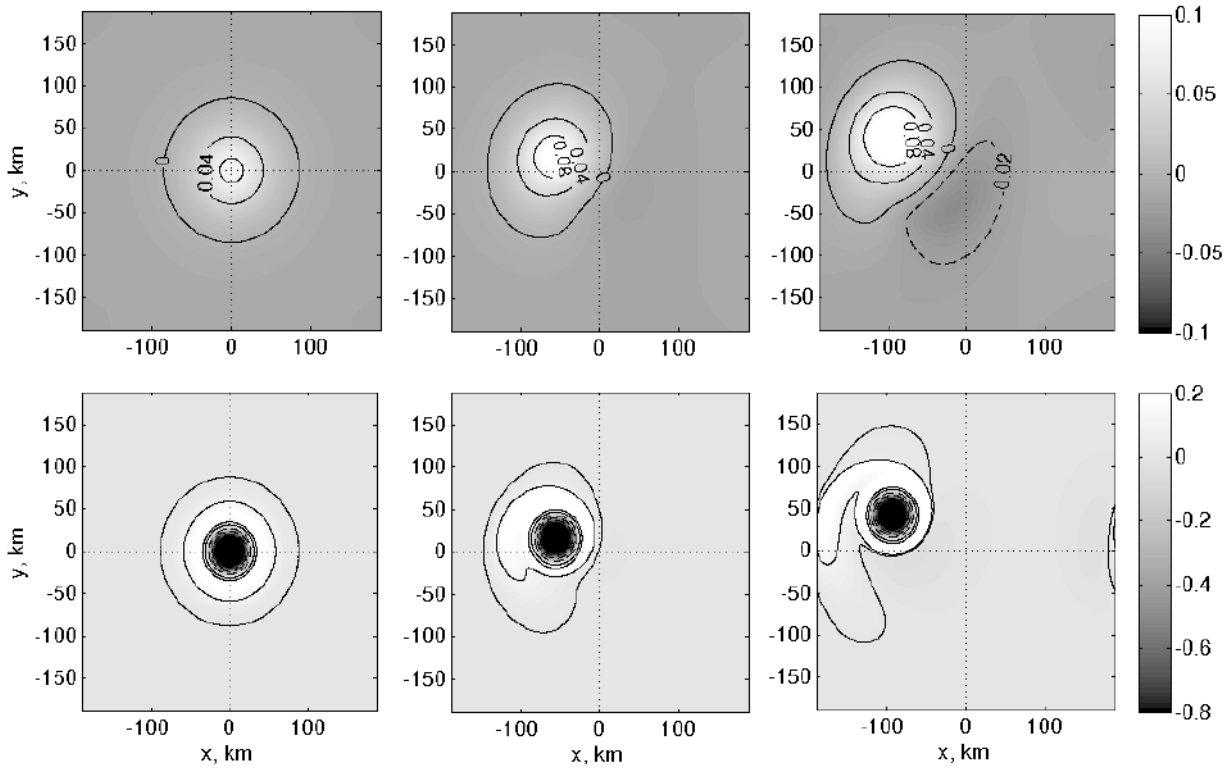

Fig. 6.16. Experiment II for the f-plane: the upper panels show the stream function in layer 1, the lower panels show the potential vorticity in layer 2. The time step is 17.6 days. In layer 2 there is a current in a westerly direction with a constant velocity of 5 cm s^{-1} (from Bashmachnikov et al., 2014).

The third experiment (Fig. 6.17) was also carried out on the *f* -plane with a constant background flow in layer 2in a westerly direction with a velocity of U_2 = -5 cm s^{-1}, the same as in the previous experiment. However, in this experiment there was also a constant background current in the eastern direction in layer 1, with a velocity of U_1 = 5 cm s^{-1}. The propagation of the meddies was similar to the previous case, but with a significantly greater deviation of the trajectory to the north. In the upper layer, a dipole signal was generated, the intensity of which by the end of the simulation period had approximately doubled, opposite to the previous experiment. In this case, the phase velocity of long baroclinic Rossby waves of the first vertical mode is estimated as

-3 cm $s^{-1,}$ while the westerly component of the meddy drift velocity averaged to -1.6 cm s^{-1}. The dissipation of the meddy upper layer signal through generation of Rossby waves was not detected.

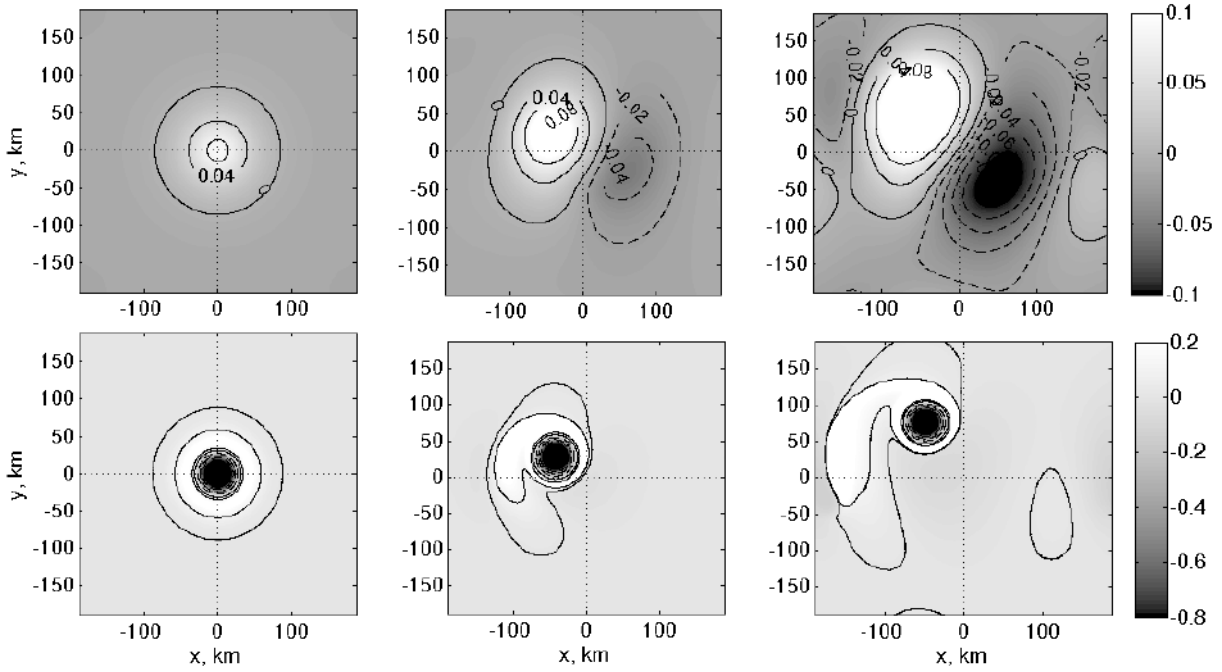

Fig. 6.17. Experiment III for the f-plane: the upper panels show the stream function in layer 1, the lower panels show the potential vorticity in layer 2. The time step is 17.6 days. In layer 2 there is a westwards current, and in layer 1 there is an oppositely directed eastwards current. In both layers the mean current velocity is constant and equal to 5 cm s^{-1} (from Bashmachnikov et al., 2014).

Thus, model experiments show that Rossby wave generation can effectively dissipate the meddy surface signals only if they travel westward at a velocity close to the phase velocity of one of the vertical modes of the baroclinic Rossby waves. One should expect an increased dissipation of surface signals of more intensive and larger eddies, since the velocities of such eddies are usually in better agreement with the phase velocities of long linear Rossby waves (Early et al., 2011). Observations show that the characteristic average velocities of meddies are in the range of Rossby wave velocities (Fig. 4.12, see also Killworth et al., 1997), although at any given time the velocities and directions of meddy motion can differ significantly from these mean values (Richardson et al., 2000). This suggests that the intensity of surface signals of large meddies, theoretically derived in the previous section, may be overestimated.

6.3.4 COMPARISON OF THE THEORETICAL ESTIMATES OF THE SURFACE MANIFESTATION OF AN EDDY PATCH WITH OBSERVATIONS

At the beginning of this section, it is given a comparison of theoretical and observed signals of meddies on the sea surface for the periods of in-situ surveys of the meddy cores (Table 6.1).

Intensity of the sea surface meddy signals was evaluated using AVISO altimetry data (see section 2.3.2). The cell size of the AVISO altimetry grid is 25 km in the meridional direction and varies from 24 km at 30°N. up to 18 km at 50°N, which determines the minimum dynamic radii of meddies for which a surface signal can be identified from these data.

The positions of the meddy centers were determined using to the data of RAFOS floats (Fig. 6.6-6.8 and 6.11). With the 6-hour time step of the original data, RAFOS trajectories were divided into pieces, each of which corresponded to the period of a full rotation of the float around the meddy center (on average, 3 days). *In situ* values of $v_{\theta m}$ and ω_m were determined from the velocity of rotation of the float. R_{vm} was determined from additional in-situ vertical casts (see Section 2.3.1), which were carried out in the meddy immediately before putting the RAFOS floats in the meddy core. Thus, data R_{vm} were available only at the initial point in the meddy trajectory tracked with the float, with the exception of meddy Pinball, which was re-sampled after its merger with another meddy north of Josephine Seamounts. Theoretical values of ω_0 were estimated from expression (6.13) using climatological values of the *N*/*f* ratio at the position of the meddy (Fig. 6.18).

The quality of theoretical estimates was assessed by comparing the observed and theoretical ratio of the vorticity of the surface signal to that of the meddy core (ω_0 / ω_m), which, using expression (6.13), can be written as:

$$\frac{\omega_0}{\omega_m} = \frac{2}{3}\left[\frac{|\tilde{q}_m|}{|\omega_m|}\right]\left(\frac{f\,R_m}{N\,H}\right)^3 . \qquad (6.18)$$

In this expression, the amplitude multiple $\frac{\tilde{q}_m}{\omega_m} = \left(1+\frac{1}{Bu}\right)$ can be set a constant due to the rather small variability of the mean Burger number for meddies (Fig. 4.21). The ratio ω_0 / ω_m for most meddies remained relatively stable and close to 0.25, despite the rather significant (5 times) spread in ω_m values, from 1.2 to 5.5 $\times 10^{-5}$ s^{-1} (Fig. 6.18a). Meddy Ceres only stands out from the overall picture, having ω_0 / ω_m ~1. This is due to an intensification of the surface manifestation of Ceres, at the time of its observations, by an anticyclone generated at the Azores Current and captured by the meddy (Tychensky and Carton, 1998). The episode of signal amplification over Ceres during the capture of a meander is clearly visible when tracking the surface signal of this meddy back in time (Bashmachnikov et al., 2009a). The Ceres surface signal was excluded from further analysis.

The meddies considered below include old ones (Encelade, Hyperion) found south of the Azores, as well as young ones (all others). Young and old meddies differ in the value of ω_m and the ratio R_m/H (Fig. 6.18a), as noted earlier (section 4.3.3). One can also note the presence of a link between the ratios of ω_0/ω_m and R_m/H of meddy cores (Fig. 6.18a), which is consistent with formula (6.18). The analysis below we consider mostly southern meddies, but northern meddy Ulla is also present (Fig. 6.14). Thus, the selection is sufficiently representative.

Comparison of the observed relationship ω_0 / ω_m with the theoretical one shows good agreement both in absolute values and in its variability (Fig. 6.18b). Some overestimation of the theoretical values for old meddies is due to the fact that the amplitude factor of formula (6.18) $\tilde{q}_m/\omega_m = (1+1/Bu)\,Bu$ = 0.5 was used, which rather corresponds to its characteristic value for meddies near the Iberian Peninsula. For older meddies, *Bu* is usually larger (see section 4.3.3.4), which reduces the theoretical ratio of ω_0/ω_m.

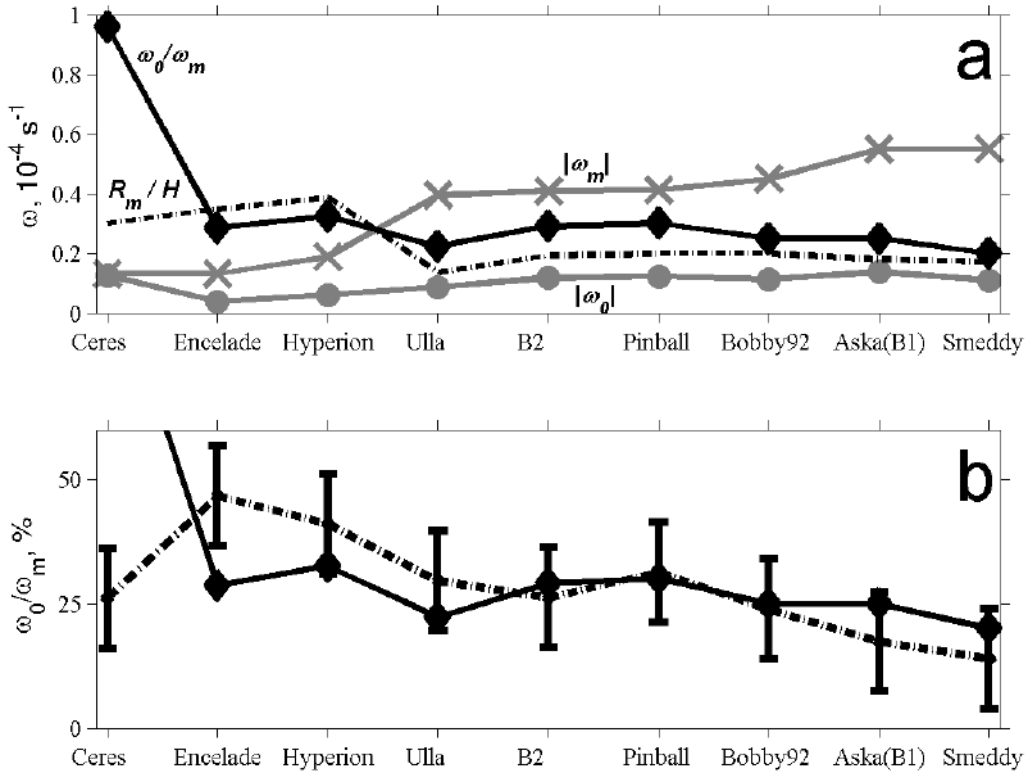

Fig. 6.18. ***(a)*** *Variability of peak relative vorticity in the meddy core (ω_m - gray line with crosses) and peak relative vorticity on the sea surface (ω_0 - gray line with circles), ratio ω_0 / ω_m (black line with diamonds) and ratio R_m / H (dashed black line, not in scale). The X-axis shows the names of the eddies listed in Tables 6.1 and 6.2.* ***(b).*** *The ratio ω_0 / ω_m obtained from observations (solid line) and predicted by formula (6.18) (dash-dotted line). For theoretical calculations, the value ω_m = -0.3 f was used. The vertical bars show the root mean square error of observations, assuming simultaneous errors in the computation of the following parameters: 10% in N, 100 m in H and 3 km in R_m. The buoyancy frequency over the meddy was obtained from MEDTRANS climatology (section 2.2, from Bashmachnikov and Carton, 2012).*

Good correspondence of the theoretical estimates of the meddies surface signals to observations during the periods of the meddy *in situ* vertical casting (when all the characteristics of meddy cores required for the theoretical estimates were known) suggest a possibility of expanding the analysis for the variability of the intensity of surface manifestations of meddies along their trajectories, tracked with RAFOS floats (Fig. 6.11). Computations were carried out under the assumption that all meddy parameters remained constant, as well as when taking into account the expected evolution of depths and radii of meddy cores (see section 4.3). Additional information about the possible evolution of meddy radii can be derived from the results of multiple surveys of meddy Sharon during 1984-1986 (Hebert et al., 1990). The Sharon path along the continental slope of Africa, untypical for the southern meddies, may lead to some deviations relative to the meddies analyzed above. The radius of the thermohaline anomaly of Sharon decreased unevenly, at a rate changing from 2 to 26 km per year, especially rapidly at the final stage of evolution of the meddy. The depth of the center of the core of Sharon slowly decreased as it moved south at a rate of about 100 m/year, while the depth of the upper boundary of the core

did not change. For meddy Hyperion, pressure observations at RAFOS neutral buoyancy floats suggest, conversely, that the meddy core is deepening at a rate of 100 m/year as it moves southwest.

Theoretical estimates with expression (6.11) generally well reproduce the intensity of the surface signal of meddy Hyperion at the initial stage of its tracked trajectory, as well as the general tendency of the sea surface signal intensity to decrease (Fig. 6.19a). This tendency was observed even under the assumption that the characteristics of the core of Hyperion remained unchanged since the beginning of observations (Table 6.1), i.e. the decrease in the intensity of its surface signal is associated with the meddy propagation into more stratified areas to the southwest (an increase in N/f ratio in the upper ocean, Figs. 4.22 b and 6.14). The theory overestimates the surface signal of the meddy by approximately 4 cm after 1.5 years of observations, which is likely due to a decay of the meddy core. Introducing a gradual deepening of the core by 100 m/year (i.e., an increase in the parameter H by 10% per year) and a decrease in the radius of the core by 5 km per year (i.e., a decrease in the parameter R by 10% per year) improves the reproduction of the observed degradation rate of the surface signal by the theory (Fig. 6.19a). At the same time, a change in the radius has a much stronger effect on the magnitude of the surface meddy signal than a change in the depth of the core. Almost perfect reproduction of trends in the dynamics of the surface signal is achieved under the assumption of a sharp decrease in the Hyperion radius by 5-7 km (by 15-20% at the initial value of 35 km) after crossing the Azores Current and contacting with Plato Seamount in October-November 1993 (days 250-270 in Fig. 6.19a). This episode with a sharp change in the behavior of the RAFOS floats was described above (see Fig. 6.7 and its description in the text). During this period, the temperature, measured by the upper RAFOS float at the depth of the upper boundary of the meddy core (870-1000 m), dropped noticeably, although the rotation velocity practically did not change. In the area of the lower boundary of the meddy core (the lower RAFOS float at 1230 m), both the RAFOS temperature and the rotation velocity dropped. Therefore, the destruction proceeded most rapidly in the lower part of the core. This suggests that the decrease in radius was more likely the result of the meddy contacted Plato Seamount.

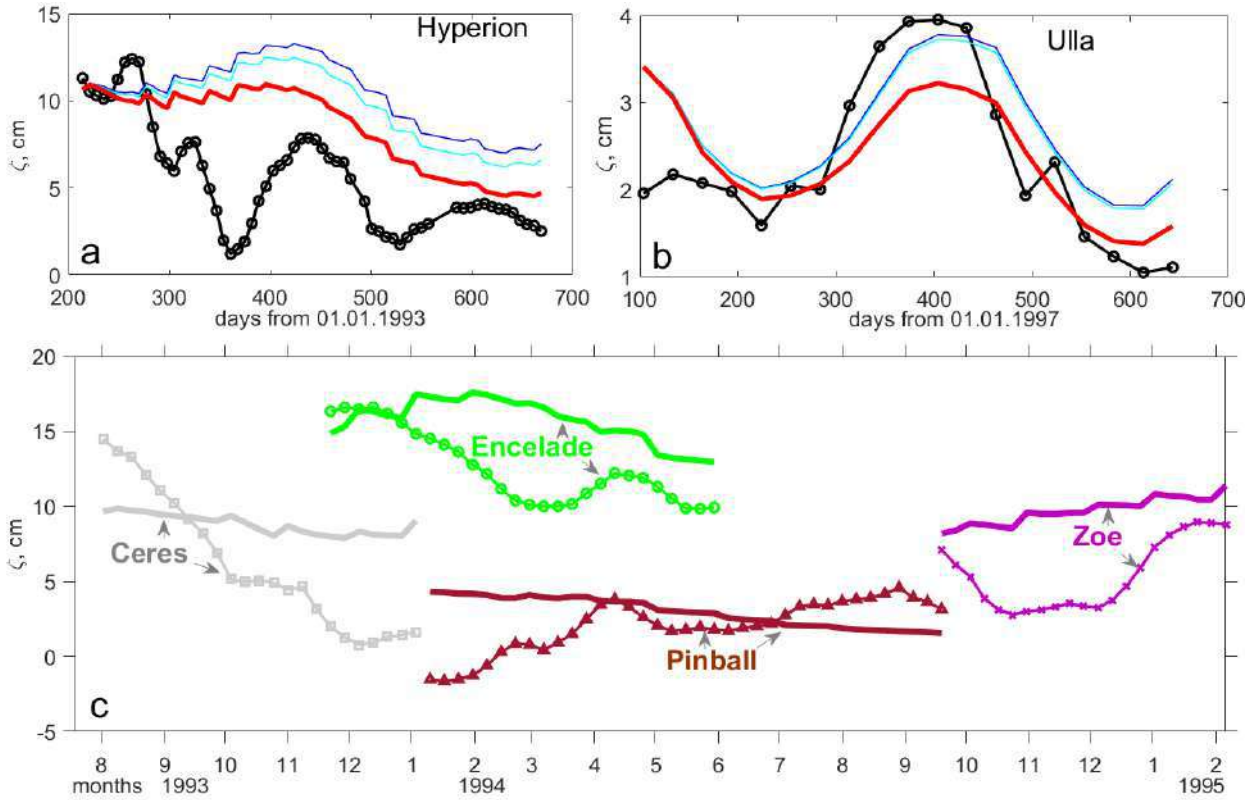

Fig. 6.19. ***(a)*** *Observed sea level anomalies (cm) from AVISO altimetry over the southern meddy Hyperion (black line with markers) and the theoretical assessment using formula (6.11) under various scenarios of degradation of the meddy core: blue line – all characteristics of the core remain unchanged since the beginning of observations, light blue line – the depth of the meddy core increases by 100 m per year, following the depth of RAFOS floats, red line – the depth of the meddy core increases uniformly at a rate of 100 m/year, and the radius of the meddy decreases uniformly at a rate of 3 km/year, red dashed line – the same as the red line, but taking into account the abrupt decrease in the meddy radius by 5-7 km after its interaction with the Azores Current and the Plato Seamount.* ***(b)*** *Observed sea level anomalies (cm) over northern meddy Ulla (black line with markers) and theoretical estimate using formula (6.11).* ***(c)*** *Observed sea level anomalies (cm) over meddies (lines with markers) and their theoretical estimates using formula (6.11) (thick lines) for Encelade (green lines), Pinball (brown lines), Ceres (gray lines) and Zoe (purple lines) assuming that the meddy radii decrease uniformly at a rate of 5 km/year. Trajectories of these meddies are shown in Fig. 6.11. The buoyancy frequency over the meddy is derived from the MEDTRANS climatology (section 2.2).*

The variability of the intensity of the surface signal is clearly connected with the seasonal variability of stratification in the upper 100th layer of the ocean. Thus, with an almost zonal movement of the meddy south of the Azores Current, there is an increase in the sea level anomaly above the meddy by several centimeters in winter (December 1993 - April 1994, days 350-500 in Fig. 6.19a). The theory, of course, cannot describe all peculiarities of variation of its surface signal, as, for example, a significant weakening of the surface signal when the Hyperion was interacting with a pair of cyclones propagating with the meddy (days 340-410, Bashmachnikov et al., 2009a). However, the theory allows assessing the general tendencies in the variability of the surface signal along the meddy trajectory. It gives a possibility to identify the most important features of the evolution of the meddy core, such as, for example, its partial destruction at a seamount.

An illustrative example is the theoretical assessment of the sea surface signal over meddy Ulla (Fig. 6.19b), which, during all 1.5 years of its observations with a RAFOS float, was located in almost the same dynamically quiet area northwest of the Iberian Peninsula (Fig. 6.11). Despite the substantially lower N/f ratio at these more northern latitudes, surface signal of meddy Ulla was significantly weaker than that of Hyperion. This is due to the significantly smaller radius of Ulla (Table 6.1) – formula (6.11) predicts a cubic dependence of the sea level anomaly on the radius of the meddy. Despite the fact that the intensity of the signal of meddy Ulla is at the limit of the accuracy of altimetry observations, observations show sufficient stability of this signal. The pronounced seasonality in the dynamics of the Ulla signal is also in good agreement with theoretical estimates (Fig. 6.19b). A more dynamically quiet environment than along the trajectory of meddy Hyperion resulted in virtually no destruction of the core of Ulla during the first year of observations. This is evidenced by a good agreement with observations of a theoretical signal with a constant radius of the meddy. The decay of the core intensified only at the end of the period of observations, when Ulla began to propagate south with a mean current.

Figure 6.19(c) shows the evolution of the signals of several more meddies. The estimates were carried out under the assumption of a gradual decrease in the dynamic radii of the meddy cores at a rate of 5 km per year, as a consequence of their gradual destruction. The theory well reflects the characteristic values of the surface signals and the general variability of their intensities over the periods of observations including seasonal variability. Thus, the signal of Encelade weakened from winter to summer by 15%, and that of Zoe strengthened from autumn to winter. Deviations from predicted values for meddy Encelade, which extended along the southern boundary of the Azores Current, are associated with an active interaction of the meddy with the current (Fig. 6.11). Meddy Zoe in October-December 1994 interacted with the slope of the Azores plateau and another anticyclone that came from the north (see description to Fig. 6.6). A probable merger resulted in an increased signal on the sea surface in January 1995 (Fig. 6.19c). For meddy Pinball, the theory fairly well reflects the intensity of the signal observed on the sea surface after the meddy had started a unidirectional propagation to the west in April 1994 (see description of Fig. 6.8). In June 1994, Pinball merged with another meddy (Pingree, 2002), as is also evidenced by an increase in the intensity of the meddy signal on the sea surface (Fig. 6.19c). According to the theory (formula 6.11), the observed increase in the intensity of the signal on the sea surface corresponds to an increase in the meddy radius by 10 km. The surface signal of meddy Ceres initially reflected the result of its merger with an anticyclone formed at the Azores Current (see above), and then, after crossing the Azores Current and subsequent interaction with seamounts, the meddy began to rapidly erode. By analogy with Hyperion, the difference between the theory and observation may indicate the loss of part of the core volume during the Ceres crossing of the Azores Current in September 1993.

Thus, a comparison of the theory with observations showed that the theory is able to correctly estimate both the total intensity of the meddy signal on the sea surface (as a function of the meddy characteristics – radius, depth, potential vorticity anomaly of meddy core), and its variations due to variability in background ocean parameters (f / N ratio): its spatial (signal weakening in more southern latitudes), as well as temporal (seasonal variability) variability. Abrupt local changes in signal intensity at intraseasonal time intervals are often consequences of changes in characteristics of the meddy core. It was shown that sharp jumps in the intensity of the surface signal can reveal the evolution of meddy core, in particular, the core mergers or break ups. However, the interpretation of changes in the intensity of the surface meddy signal is complicated

by the fact that this signal can significantly deviate from the estimated values also due to interactions with other dynamic structures (jet streams, surface eddies) or topography, not described by the theory.

6.3.5 THEORETICAL ASSESSMENT OF THE SURFACE MANIFESTATION OF THE SUBSURFACE RAYLEIGH EDDY IN A CONTINUOUSLY STRATIFIED OCEAN

In this section a theory is developed for surface manifestations for a Rayleigh eddy (Section 1.3). The vertical variability of two-dimensional dynamics on the sea surface is considered under the influence of forcing by a subsurface eddy passing below. The origin of the coordinate system is fixed on the undisturbed sea surface above the point of maximum azimuthal velocity $R_m/\sqrt{2}$ of the leading edge of a moving meddy. Here the center of the meddy surface signal is expected to form (Fig. 6.12). Meddy moves relative to the background ocean (or its upper layer) at a constant velocity $\vec{V}_m$. It is assumed that the subsurface meddy itself is not deformed neither by the impinging flow nor by the emerging surface signal (see Section 6.2).

To simplify the system of equations, the standard assumption is used: the vertical gradients of density disturbances $\rho(x,y,z,t)$ are much smaller than the vertical gradients of the average density field $\rho_o(z)$: $\frac{\partial\rho}{\partial z} << \frac{\partial\rho_0}{\partial z}$. In addition, it is assumed that the radial component of the horizontal current velocity over the meddy (v_r) is much less than the azimuthal component (v_θ) and that the radial gradients of all meddy characteristics are much h than the azimuthal ones: $v_r = \varepsilon v_\theta$ and $\frac{1}{r}\frac{\partial..}{\partial\theta} = \varepsilon\frac{\partial..}{\partial r}$, where ε <<1 is a small parameter (Carton, 2001). Thus, we do not consider here the initial stage of geostrophic adjustment, when the radial velocities of the surface signal, generated by a meddy, are comparable to the azimuthal ones. The typical time for geostrophic adjustment is about a day (McWilliams, 1988). For a meddy surface signal, which has an almost axisymmetric structure centered above the leading edge of the meddy, we can then write a system of quasi-geostrophic equations in polar coordinates (r,θ):

$$\begin{cases} fv_\theta = \dfrac{1}{\overline{\rho}}\dfrac{\partial P}{\partial r} \\ \dfrac{\partial v_\theta}{\partial t} + fv_r = -\dfrac{1}{\overline{\rho}\, r}\dfrac{\partial P}{\partial\theta} \\ \dfrac{\partial P}{\partial z} = -g\rho \\ \dfrac{\partial\rho}{\partial t} + w\dfrac{\partial\rho_0}{\partial z} = 0 \\ \nabla_r v_r + \dfrac{1}{r}\dfrac{\partial v_\theta}{\partial\theta} + \dfrac{\partial w}{\partial z} = 0 \end{cases} \qquad (6.19)$$

Here w is the vertical velocity in the upper layer above the meddy, P is the pressure disturbance

associated with the meddy surface signal, $\nabla_r = \frac{1}{r}\frac{\partial(r\ldots)}{\partial r}$. In the system of equations (6.19) we neglected the terms with ε^2, εRo (where *Ro* is the Rossby number) and $\varepsilon\frac{\Delta\rho}{\Delta\rho_0}$. In the first equation, due to the smallness of the Rossby number, we also neglect the centrifugal acceleration.

In the system of equations (6.19), at any moment of formation of the surface signal, quasi-geostrophic and hydrostatic balances are observed, to the first order of accuracy in the parameter ε. In other words, the change in the magnitude of azimuthal velocities, described by the second equation of the system, and, accordingly, the configuration of isobaric surfaces, changes slowly in time compared to the period of revolution of the meddy core (1-3 days).

The meddy itself enters as an external forcing at the lower boundary of the layer described by the system of equations (6.19). Its characteristics and its propagation velocity $\vec{V}_m$ are set as external parameters. Since the independent velocity of movement of the meddy is small, on average 2 cm s^{-1} (Richardson et al., 2000; Bashmachnikov et al., 2015c), the velocity ($\vec{V}_m$) of the upper layer relative to the meddy (Fig. 6.12) will be close to the velocity of the background current in the upper ocean.

With a round shape of the meddy, the spatial distribution of forcing at the lower boundary of the upper layer ($z = -H_s + H_m$) can be written as:

$$w(r,\theta,-H_s+H_m,t) = -\vec{V}_m(t)\cdot\vec{\nabla}H_m(r,\theta) = V_m(t)\cos\left[\theta_m(r,\theta)\right]\frac{\partial H_m(r,\theta)}{\partial r_m}. \qquad (6.20)$$

Here, as before, H_s is the average depth of the undisturbed isopycnal outside the meddy, H_m is the elevation of the isopycnal above the meddy relative to the background (Fig. 6.12), (r_m, θ_m) are polar coordinates in coordinate systems centered at the center of the meddy, $V_m = \left|\vec{V}_m\right|$. In expression (6.20) it is considered only the radial component of the impinging flow averaged along the leading edge of the meddy (Fig. 6.20a).

For the forcing at the lower boundary, the Rayleigh model is used, which for radial profiles of the scalar characteristics of the meddy (Fig. 6.20) allows writing the isopycnal elevation above the meddy as:

$$H_m = \Delta H \, e^{-\frac{r_m^2}{R_m^2}}, \tag{6.21}$$

where ΔH is the maximum isopycnal elevation above the meddy, and R_m, as before, is the meddy dynamic radius, defined as the distance from the center to the line $\omega = 0$.

When generating a signal, the vertical velocity has a maximum at the point of biggest inclination of the isopycnal, i.e., according to formula (6.21), at a distance of $R_{vm} = \frac{R_m}{\sqrt{2}}$ from the meddy center. This point is taken as the center of the signal generated in the upper layer and as the origin of coordinates ($r = 0$).

Since $H_m \le \Delta H << R_m$ and $\Delta H << H_s$, we can assume that, in the layer $\left[-H_s, -H_s + \Delta H\right]$, isopycnic surfaces at different depths rise in a consistent manner, i.e. the vertical velocity throughout the entire thickness of this relatively thin layer will be almost the same as at the lower boundary of the layer (Fig. 6.20). This allows, instead of the condition at the lower boundary of the isopycnal surface $z = -H_s + H_m$, to consider the boundary condition at the surface of constant depth $z = -H_s + \Delta H$. Then, for a circular meddy, the condition on the lower boundary can be approximated with good accuracy by a radially symmetrical form (Fig. 6.20a, b):

$$\frac{\partial H_m}{\partial r_m}\cos\theta_m \approx \sqrt{\frac{2}{e}}\frac{\Delta H}{R_m} e^{-\frac{\pi}{2}\frac{r^2}{R_m^2}}, \tag{6.22}$$

where $\sqrt{\frac{2}{e}}\frac{\Delta H}{R_m} = \frac{\partial H_m}{\partial r_m}(r = 0)$.

With such an approximation, the integral value of the vertical velocity inside a circle with radius R_{vm} will be very close to that for the exact expression on the left side of equation (6.22). This approximation is also justified by model studies and observations of ocean eddies, which indicate that, due to lateral dissipation and separation of filaments, the shape of the generated anticyclone tend to be axisymmetric (Schecter and Montgomery, 2003).

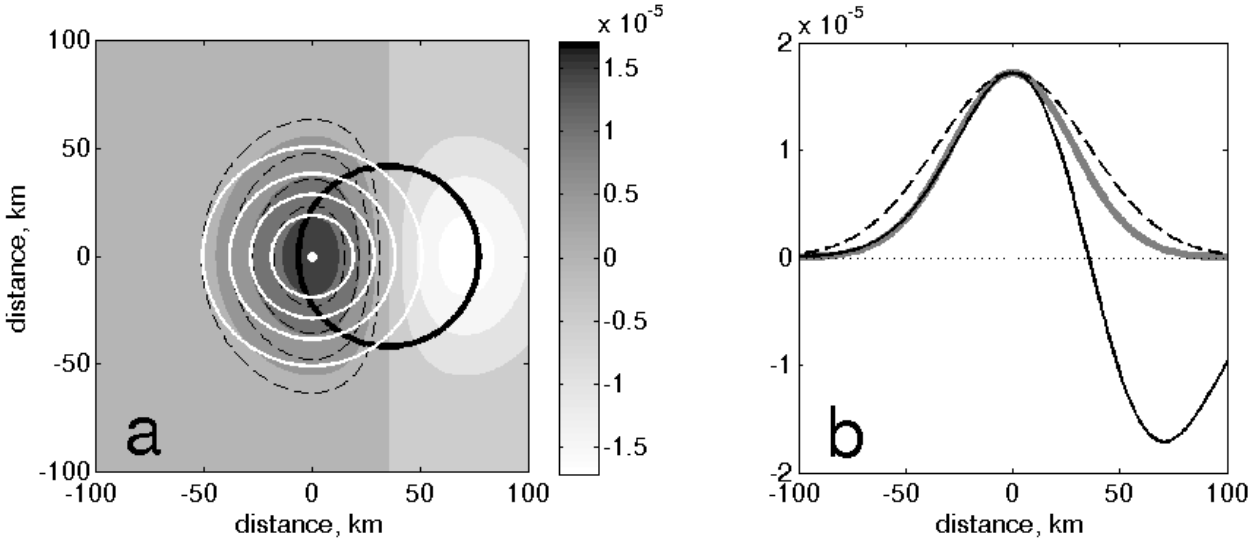

Fig. 6.20 ***a)*** *The exact expression for the vertical velocity* $w \sim \frac{\partial H_m}{\partial r_m}\cos\theta_m$ *(V_m = 1 cm s^{-1} black dashed isolines) and its approximation by a radially symmetrical shape* $\sqrt{\frac{2}{e}}\frac{\Delta H}{R_m}e^{-\frac{\pi}{2}\frac{r^2}{R_m^2}}$ *(white circles), the thick black circle marks the isoline of the maximum azimuthal velocity of the meddy at a distance* $R_m/\sqrt{2}$ *from its center; R_m =30 km.* ***b)*** *Same as* ***a)****, but for section profiles through the meddy center function* $\frac{\partial H_m}{\partial r_m}\cos\theta_m$ *in the zonal direction (solid black line) and in the meridional direction (black dashed line). The radially symmetrical profile* $\sqrt{\frac{2}{e}}\frac{\Delta H}{R_m}e^{-\frac{\pi}{2}\frac{r^2}{R_m^2}}$ *is given in the gray solid line (from Bashmachnikov et al., 2014).*

Expressing v_r and v_θ as functions of P in the first two equations (6.19), substituting the resulting expressions into the continuity equation and differentiating the latter with respect to z, we obtain:

$$\frac{1}{r}\frac{\partial}{\partial r}\left[r\left(\frac{1}{\rho}\frac{\partial^2}{\partial t\partial r}\frac{\partial P}{\partial z}\right)\right] = f^2\frac{\partial^2 w}{\partial z^2}$$

Next, expressing P as a function of the water density using the third equation and finally using the fourth equation, we obtain the equation for the vertical velocity:

$$\frac{1}{r}\frac{\partial}{\partial r}\left[r\left(\frac{\partial}{\partial r}\left(-N^2\right)w\right)\right] = f^2\frac{\partial^2 w}{\partial z^2}.$$

For $N^2 = -\frac{g}{\rho}\frac{\partial \rho_0}{\partial z} = const$, we get Laplace equation:

$$\left(\Delta_r + \frac{f^2}{N^2}\frac{\partial^2}{\partial z^2}\right)w = 0, \tag{6.23}$$

where $\Delta_r = \frac{1}{r}\frac{\partial}{\partial r}\left[r\frac{\partial}{\partial r}\ldots\right]$ is the Laplace operator.

This equation is equivalent to the following equation for the quasi-geostrophic potential vorticity of the upper ocean:

$$\frac{\partial^2 q}{\partial z \partial t} = 0, \tag{6.24}$$

where $q = \left(\Delta_r + \frac{f^2}{N^2}\frac{\partial^2}{\partial z^2}\right)\psi$, since the quasi-geostrophic stream function $\psi = \frac{P}{\bar{\rho} f}$ and from the fourth and third equations of system (6.19) it follows that $w = \frac{f}{N^2}\frac{\partial^2 \psi}{\partial z \partial t}$. Since the characteristics of the surface signal is assumed to vary slowly with time, so that at any given moment the quasi-geostrophic approximation is correct, the resulting equation (6.23) allows a vertical variability of q in the layer above the meddy, which is consistent with observations (Tychensky and Carton, 1998; Paillet et al., 2002). Assuming a constant value of N, this will mean (expression 6.3) that the vertical variability of q is associated with a change in relative vorticity with depth, which is also noted in the cited studies above. This removes some of the contradiction in the study of Bashmachnikov and Carton (2012), where q and N are assumed to be constant in the upper ocean layer, while it is assumed possible changes in the relative vorticity of the surface signal with depth (see Section 6.3.2).

From expressions (6.20) and (6.22) we obtain a condition at the lower boundary, which guarantees a smooth transition from the solution in the upper layer to the upper boundary of the meddy:

$$w(r, -H_s + H_m, t) = V_m(t)\sqrt{\frac{2}{e}}\frac{\Delta H}{R_m}e^{-\frac{\pi}{2}\frac{r^2}{R_m^2}} \tag{6.25}$$

It is logical to also apply the condition for a monotonic decrease $w(r, z)$ upward, to the sea surface.

Now, setting $w(r, z, t) = F(r)\,G(z)\,X(t)$, we obtain a system of equations:

$$\begin{aligned} &\frac{d^2 G}{dz^2} + \frac{N^2}{f^2}\lambda G = 0 \\ &\frac{d^2 F}{dr^2} + \frac{1}{r}\frac{dF}{dr} - \lambda F = 0 \end{aligned}, \tag{6.26}$$

where λ is the unknown separation constant of the variables.

The function *X(t)* cannot be obtained from the original system of equations, because is specified through the forcing function at the lower boundary of the upper layer:

$$X(t) = V_m(t), \tag{6.27}$$

in accordance with the initial assumptions.

The second of equations (6.26) has a solution in the form of Bessel functions. In accordance with the condition on the lower boundary (6.22 or 6.25), from all possible solutions we choose a physically justified one, which has a finite absolute maximum at the point $r = 0$. Then we accept $\lambda = -\lambda^2_i < 0$, and represent *F(r)* as a Fourier-Bessel series expansion:

$$F(r) = \sum_i C_i J_0(\lambda_i r), \tag{6.28}$$

where J_0 is the Bessel function of the first kind.

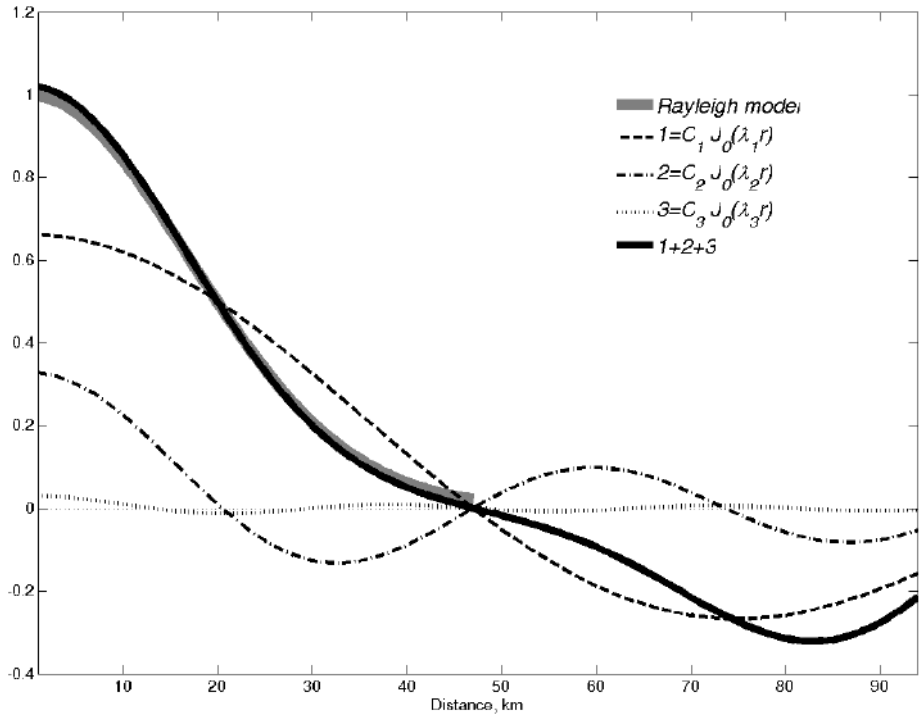

Fig. 6.21. Approximation of the radial profile of the forcing function (6.22) (thick gray line) with the sum of the first three Bessel functions of the expansion (6.28) (thick solid black line) , normalized with $\sqrt{\frac{2}{e}}\frac{\Delta H}{R_m}$*. The Bessel functions 1-3 are shown by dashed, dotted and dotted lines, respectively.* R_m *= 30 km (from Bashmachnikov et al., 2014).*

The coefficients C_i are derived using the Hankel transformation of a function in the form (6.25) in the region for $r \le R_m$ (Guizar-Sicairos and Gutierrez-Vega, 2004). Then $\lambda_i = \frac{2\hat{a}_i}{\pi R_m} = \frac{a_i}{R_m}$, where $\hat{a}_i$ is the first *i*-th zero of the function J_0 and $a_i = \frac{2\hat{a}_i}{\pi}$. Within the selected limits of *r* values,

function (6.22) can be approximated with a fairly high accuracy by the first three Bessel functions, for which $a_{1,2,3} = \frac{2\hat{a}_{1,2,3}}{\pi} = 1.53, 3.51, 5.51$ (Fig. 6.21). At $20 \le R_m \le 100$ km the best approximation is achieved with coefficients $C_1 = 0.67$, $C_2 = 0.33$ and $C_3 = 0.03$, and for R_m of the order of 10 km the coefficients are $C_1 = 0.68$, $C_2 = 0.25$ and $C_3 = -0.03$.

Using the condition $G(-H_s + \Delta H) = 1$, which ensures continuity of w at the lower boundary of the upper layer, and remembering that due to the presence of stratification G must decrease towards the sea surface, the solution to the first equation of system (6.26) becomes:

$$G(z) = e^{-\frac{N\lambda_i}{f}(z+H_s-\Delta H)}, \tag{6.29}$$

We can then introduce a vertical attenuation scale of the signal over a meddy (similar to the Taylor cone attenuation scale over a seamount – see Owens and Hogg, 1980):

$$H_{di} = \frac{f}{\lambda_i N} = \frac{R_m f}{a_i N} \tag{6.30}$$

Since a_i increases rapidly as mode number i increases, H_{di} decreases rapidly with i.

We finally obtain the expression for elevation of the isopycnals over the meddy:

$$w(r,z,t) \approx V_m(t) \sqrt{\frac{2}{e}} \frac{\Delta H}{R_m} \sum_{i=1}^{3} C_i J_0\left(\frac{a_i r}{R_m}\right) e^{-\frac{z+H_s-\Delta H}{H_{di}}} \tag{6.31}$$

Expressing this as the sea surface elevation ($z = 0$), $\frac{\partial \zeta}{\partial t} = w(r,0,t)$:

$$\zeta(r,t) = \sqrt{\frac{2}{e}} \frac{\Delta H}{R_m} \int_{\tau_1}^{\tau_2} V_m(t)dt \sum_{i=1}^{3} C_i J_0\left(\frac{a_i r}{R_m}\right) e^{-\frac{H_s-\Delta H}{H_{di}}} =$$

$$= \int_{\tau_1}^{\tau_2} V_m(t)dt \sum_{i=1}^{3} \bar{C}_i J_0\left(\frac{a_i r}{R_m}\right), \tag{6.32}$$

where

$$\bar{C}_i = \sqrt{\frac{2}{e}} \frac{\Delta H}{R_m} C_i e^{-\frac{H_s-\Delta H}{H_{di}}}. \tag{6.33}$$

Expression (6.33) shows that the vertical attenuation is faster for the higher radial modes, and therefore the approximation with the first three modes (Bessel functions) is even more accurate on the sea surface compared to the isopycnal elevations above the meddy (Fig. 6.21). Values of $\bar{C}_i$ suggest (Table 6.4), that for a wide range of background conditions and meddy characteristics,

only the first or the first two radial modes (i = 1 or 2) are significant on the sea surface. Together, they form approximately 99% of the amplitude of the meddy signal on the sea surface.

Table 6.4. Values of $\overline{C}_i$ on the sea surface according to expression (6.33) for H=800 m, ΔH=50m, f/N = 0.01 (see Fig. 6.14). R_m is the dynamic radius of the meddy, R_0 is the dynamic radius of the meddy surface signal.

R_m, km	$i=1$		$i=2$		$i=3$		R_0, km
	H_{d1}, m	$\overline{C}_1 \cdot 10^4$	H_{d2}, m	$\overline{C}_2 \cdot 10^4$	H_{d3}, m	$\overline{C}_3 \cdot 10^4$	
10	65	0.0003	thirty	0.0000	20	0.0000	22
20	130	0.0460	60	0.0000	35	0.0000	44
thirty	195	0.2060	85	0.0007	55	0.0000	65
40	260	0.4083	115	0.0048	75	0.0000	86
60	390	0.6992	170	0.0294	110	0.0003	100
80	525	0.8487	230	0.0658	145	0.0011	105

Thus, under constant background conditions, expression (6.32) for the maximum sea level elevation of a fully formed surface signal over a meddy can be simplified to:

$$\zeta(0) \approx \int_0^\tau V_m(t)dt \sum_{i=1}^{2} \overline{C}_i = \int_0^\tau V_m(t)dt \sqrt{\frac{2}{e}} \frac{\Delta H}{R_m} \left(0.67\, e^{-1.53 \frac{N(H_s - \Delta H)}{f\, R_m}} + 0.33 e^{-3.51 \frac{N(H_s - \Delta H)}{f\, R_m}} \right), \qquad (6.34)$$

where the time integral is determined by the process of formation of the surface signal, from some initial moment ($\tau_1 = 0$) to the moment, when the signal is fully formed ($\tau_2 = \tau$).

When an anticyclonic eddy is formed over the meddy, the impinging flow is pushed away by the forming eddy and the external forcing weakens. Thus, τ has a limited value. Estimates of τ and $\int_0^\tau V_m(t)dt$ are given at the end of this section. First, expressions for other dynamic characteristics of the meddy surface signal are obtained.

The azimuthal velocity of the meddy surface signal ($v_{\theta 0}$) is:

$$v_{\theta 0}(r) = \frac{g}{f} \frac{\partial \zeta}{\partial r} = \int_0^\tau V_m(t)dt \, \frac{g}{f} \sum_{i=1}^{2} \overline{C}_i \, \frac{\partial}{\partial r} J_0\left(\frac{a_i r}{R_m} \right) = -\int_0^\tau V_m(t)dt \, \frac{g}{f\, R_m} \sum_{i=1}^{2} \overline{C}_i \, a_i \, J_1\left(\frac{a_i r}{R_m} \right). \qquad (6.35)$$

The radius at which the azimuthal velocity on the sea surface reaches its maximum is determined from the equation:

$$\frac{\partial v_{\theta 0}}{\partial r} = -\int_0^\tau V_m(t)dt \, \frac{g}{f\, R_m} \sum_{i=1}^{2} \overline{C}_i \, a_i \, \frac{\partial}{\partial r} J_1\left(\frac{a_i r}{R_m} \right) = 0, \qquad (6.36)$$

in the solution of which we consider only the first non-zero root, the one closest to the center.

We get:

$$\overline{C_1}\ a_1 \frac{d}{dr} J_1\left(\frac{a_1 r}{R_m}\right) + \overline{C_2}\ a_2 \frac{d}{dr} J_1\left(\frac{a_2 r}{R_m}\right) = 0$$

or

$$\frac{\overline{C_1}\ a_1^2}{2R_m}\left[J_0\left(\frac{a_1 r}{R_m}\right) - J_2\left(\frac{a_1 r}{R_m}\right)\right] + \frac{\overline{C_2}\ a_2^2}{2R_m}\left[J_0\left(\frac{a_2 r}{R_m}\right) - J_2\left(\frac{a_2 r}{R_m}\right)\right] = 0$$

Far from the central point (r = 0), the Bessel function can be approximated as:

$$J_0(\lambda_i r) \approx \sqrt{\frac{2}{\pi\lambda_i r}}\cos\left(\lambda_i r - \frac{\pi}{4}\right) \text{And } J_2(\lambda_i r) \approx \sqrt{\frac{2}{\pi\lambda_i r}}\cos\left(\lambda_i r - \frac{5\pi}{4}\right).$$

Then we can write:

$$\overline{C_1}\ a_1^2\sqrt{\frac{2R_m}{\pi a_1 r}}\left[\cos\left(\frac{a_1 r}{R_m} - \frac{\pi}{4}\right) - \cos\left(\frac{a_1 r}{R_m} - \frac{5\pi}{4}\right)\right] + \overline{C_2}\ a_2^2\sqrt{\frac{2R_m}{\pi a_2 r}}\left[\cos\left(\frac{a_2 r}{R_m} - \frac{\pi}{4}\right) - \cos\left(\frac{a_2 r}{R_m} - \frac{5\pi}{4}\right)\right] = 0,$$

which is equivalent

$$\sin\left(\frac{a_1 r}{R_m} - \frac{3\pi}{4}\right) + \frac{\overline{C_2}\ \sqrt{a_2^3}}{\overline{C_1}\ \sqrt{a_1^3}}\sin\left(\frac{a_2 r}{R_m} - \frac{3\pi}{4}\right) = 0\,. \quad (6.37)$$

Equation (6.37) can be solved numerically to estimate the dynamic radius of the meddy surface signal: $r = R_0$. We estimate the background stratification using the average annual climatic vertical profiles of temperature and salinity. Within the range from 25 to 45°N, the *f*/*N* ratio varies from 0.007 to 0.013 (on average 0.01 - Fig. 6.14). For f/N = 0.01, the ratio $\frac{\overline{C_2}\ \sqrt{a_2^3}}{\overline{C_1}\ \sqrt{a_1^3}}$ can be estimated using Table 6.4. For a meddy with a radius $R_m \le 40$ km, the second term in (6.37) can be neglected, i.e. the azimuthal velocity will reach its maximum at $\sin\left(\frac{a_1 R_{0v}}{R_m} - \frac{3\pi}{4}\right) = 0$. The first zero of the function will appear at $R_{0v} = \frac{3\pi}{4a_1} R_m \approx 1.5 R_m$, i.e. $R_0 \approx 2\ R_m$. Thus, when $R_m \le 40$ km, the dynamic radius of the surface signal will be twice the radius of the meddy. This is consistent with observations near the southwestern tip of the Iberian Peninsula (Bashmachnikov et al., 2013): with a meddy radius R_{vm}= 12 km, the radius of the surface signal was twice as large R_{0v}= 25 km (Fig. 6.4).

The radius of the surface signal of small and medium-sized meddies is determined only by the radius of the meddy itself and shows little sensitivity to the depth of the meddy core, as well as to a change in *f/N* ratio. The relationship $R_0 \approx 2\ R_m$ was previously used to estimate surface vorticity from azimuthal velocity in the meddy surface signals from observations (see Table 6.1).

Another limiting case occurs for very large meddies, with radii on the order of 100 km. Then the second term of expression (6.37) becomes the leading one, and the radii of the surface signal becomes close to the meddy radius: $R_0 = \dfrac{3\sqrt{2}\pi}{4a_2} R_m \approx R_m$. With a dynamic meddy radius R_m= 60-80 km and the typical value *f/N* = 0.01, an intermediate result is obtained: $R_0 \sim 1.5\ R_m$ (Table 6.4). Unlike the first limiting case, these results turned out to be sensitive to changes in *f/N* ratio. For the tropics (25°N) R_0 is close to 2 R_m, and for the temperate latitude region (45°N) $R_0 \sim 1.2\ R_m$. The decrease in the size of a meddy surface signal to the north relative to a meddy size is quite logical. To the north, stratification weakens, which leads to less variability in the characteristics of the projection of the eddy with depth. In the limiting barotropic case, there is no vertical variability and the radius of the surface signal is always equal to that of a meddy.

In summary, a northwards increase in meddy radii (Fig. 4.15) is partly compensated by a lower degree of the growth of the radii with depth, which means the meridional differences in the radii of the meddy surface signals will be reduced.

The radial profile of the relative vorticity of the surface meddy signal (ω_0) can be estimated using expression (6.34) as:

$$\omega_0(r) = \frac{g}{f}\Delta_r \zeta = \int_0^\tau V_m(t)dt\ \frac{g}{f}\sum_{i=1}^{2}\overline{C_i}\ \Delta_r J_0\left(\frac{a_i\, r}{R_m}\right) \tag{6.38}$$

The relative vorticity reaches its peak values at the center of the meddy surface signal. For $r \to 0$: $\Delta_r J_0(\lambda_i r) = -\dfrac{2\lambda_i}{r} J_1(\lambda_i r) + \lambda_i^2\ J_2(\lambda_i r) \to -\lambda_i^2$, since for small r the asymptotic dependencies are valid: $J_1(\lambda_i r) \xrightarrow[r\to 0]{} \dfrac{\lambda_i\, r}{2}$ and $J_2(\lambda_i r) \xrightarrow[r\to 0]{} 0$. Thus, the peak vorticity of the surface meddy signal is expressed as:

$$\begin{aligned}\omega_0 &= -\int_0^\tau V_m(t)dt\ \sqrt{\frac{2}{e}}\ \frac{g\Delta H}{f\, R_m}\ \sum_{i=1}^{2} C_i\ \frac{a_i^2}{R_m^2}\ e^{-\frac{H_s-\Delta H}{H_{si}}} = \\ &= -\int_0^\tau V_m(t)dt\ \sqrt{\frac{2}{e}}\ \frac{g\Delta H}{f\, R_m^3}\left(1.57\cdot e^{-1.53\frac{N}{f}\frac{(H_s-\Delta H)}{R_m}} + 4.07\, e^{-3.51\frac{N}{f}\frac{(H_s-\Delta H)}{R_m}}\right)\end{aligned} \tag{6.39}$$

A difficult-to-estimate parameter ΔH can be expressed using other variables. For a quasi-geostrophic eddy $fv_\theta = \dfrac{1}{\rho}\dfrac{\partial P}{\partial r} = -\dfrac{g}{\rho}\int\dfrac{\partial \rho}{\partial r}dz = -\dfrac{g}{\rho}\int\dfrac{\partial \rho}{\partial z}\dfrac{\partial H_m}{\partial r}dz = -\dfrac{g}{\rho}\dfrac{\partial \rho}{\partial z}\int\dfrac{\partial H_m}{\partial r}dz = N^2\int\dfrac{\partial H_m}{\partial r}dz$, where H_m is the depth of the isopycnal surface above the meddy and *N= const.* If the azimuthal velocity has a Rayleigh radial profile, then the maximum isopycnal elevation above the meddy is:

$\frac{\partial H_m}{\partial r}(R_{vm}) \approx -0.86\frac{\Delta H}{R_{vm}}$. Following (6.29), the decrease in the amplitude of variability $\frac{\partial H_m}{\partial r}$ towards the sea surface can be approximated with a quadratic function: $\frac{\partial H_m}{\partial r}(R_{vm}) = -0.86\frac{\Delta H}{H_s{}^2 R_{vm}} z^2$. Then for the peak azimuthal velocity one obtain $fv_{\theta m} \sim -0.86\, N^2 \frac{\Delta H}{3R_{vm}} H_s$ and the parameter ΔH can be computed as:

$$\Delta H \approx \frac{3f\,|v_{\theta m}|R_{vm}}{0.86\,N^2 H_s} = \frac{3f\,|v_{\theta m}|R_m}{0.86\sqrt{2}N^2 H_s} \approx 2.47\frac{f\,|v_{\theta m}|R_m}{N^2 H_s} \qquad (6.40)$$

Next, in order to obtain numerical estimates of the maximum sea level elevation (6.34), peak azimuthal velocity (6.35) and relative vorticity (6.39) of the meddy surface signal, it is necessary to estimate the time integral of the meddy propagation velocity relative to the upper layer $\int_0^\tau V_m(t)dt$, as well as the time interval τ, during which the signal will be fully formed. The integral above actually represents the distance that the background flow travels over the meddy during time τ.

Generation of the meddy surface signal means formation in the upper layer of an anticyclonic eddy which is dynamically associated with the meddy. According to a model study by Cerretelli and Williamson (2003), after its generation, an eddy goes through several stages of its initial adjustment, including the initial "diffusion" stage, which is characterized by a slight increase in its radius, and the following stage of straightening of its vertical axis. Since the initial separation of the meddy center and its surface signal is about half of the meddy radius (Fig. 6.20), the secondary eddy formed above the meddy begin to rotate around the meddy core. For a large meddy (whose radius is greater than the first baroclinic Rossby deformation radius – 20-30 km in the subtropical Atlantic), the vertical alignment of the meddy and its surface signal should eventually occur (Polvani, 1991). After this, in the absence of strong external forcing, the relative position and characteristics of the eddies do not change (Zhmur, 2010).

An increase in the intensity of the surface signal should occur mainly during the first "diffusion" stage. The surface signal, being formed, starts screens the area above the meddy from the impinging flow, reducing the velocity of the motion of the upper layer relative to the meddy: $V_m(t) \to 0$. Ultimately, when the surface signal is fully formed, it covers almost the entire meddy, the process of the meddy surface signal amplification stops. Let us describe this process by the quadratic law of a decrease in the rate of the signal formation in time:

$$V_m(t) = \frac{V_m(0)}{\tau^2}(t-\tau)^2, \quad (0 \le t < \tau),$$

where τ, as before, is the period of formation of the signal above a meddy. Then we get:

$$\int_0^\tau V_m(t)dt = \frac{1}{3}V_m(0)\cdot\tau. \qquad (6.41)$$

If at the initial moment of time $V_m(0)$ = 2-5 cm s^{-1} and τ is 1-3 weeks, then $\int_0^\tau V_m(t)dt$ = 4-30 km. In the next section it will be shown that in-situ data provide the best agreement between theory and observation with $\int_0^\tau V_m(t)dt$ = 3 km for relatively young meddies near the Iberian Peninsula and 2.5 km for old meddies, far from the Peninsula. The distance that a meddy travels to completely form its surface signal, $\int_0^\tau V_m(t)dt$, turns out to be almost constant for different meddies. This should be the result of a faster generation of the surface signal for faster moving meddies (i.e., lower τ corresponds to higher V_m). The small values $\int_0^\tau V_m(t)dt$ obtained from a comparison of the theory with observations indicate that the surface signal of a meddy, moving at a constant average velocity of 2 cm s^{-1} (Fig. 4.12a), should fully develop within a week.

6.3.6 COMPARISON OF THE THEORETICAL ESTIMATES OF THE SURFACE MANIFESTATION OF SUBSURFACE RAYLEIGH EDDIES WITH OBSERVATIONS

In this section, the theoretical results of the previous section are compared with observations of relative vorticity (ω_0) and sea level anomalies (ζ) obtained from AVISO satellite altimetry. Relative vorticity anomalies from AVISO data were assessed as peak values within the meddy radius, and sea level anomalies above the meddy were estimated as the difference between the maximum sea level within 0-20 km from the meddy center and the mean sea level at the meddy periphery (within a ring of 60 -120 km).

The theoretical values *of* ζ and ω_0 in the center of the surface signal above meddies (Fig. 6.22) were estimated using formulas (6.34), (6.39), while the characteristics of the meddies were estimated using in-situ observations (Table 6.1). The average depth of the isopycnal representing the upper boundary of the meddy (H_s), according to observations, was empirically determined relative to the depth of the meddy core (H) as: $H_s = H$ - 200 m. ΔH was determined by formula (6.40), using geostrophic relations and the Rayleigh model of the meddy radial profile. $\int_0^\tau V_m(t)dt$ was determined by formula (6.41). For meddies near the Iberian Peninsula (Smeddy, Ulla, Pinball_A3, Aska_B1 and B2) a value of $\int_0^\tau V_m(t)dt$ = 3 km was used. For older meddies (Sharon 84 and 85, Bobby92, Ceres, Encelade and Hyperion) observed to the west, it was assumed $\int_0^\tau V_m(t)dt$ = 2.5 km. Vertical stratification is determined from the regional MEDTRANS climatology using seasonal climatology, the data of which are interpolated in space and time to the points and periods of meddy observations.

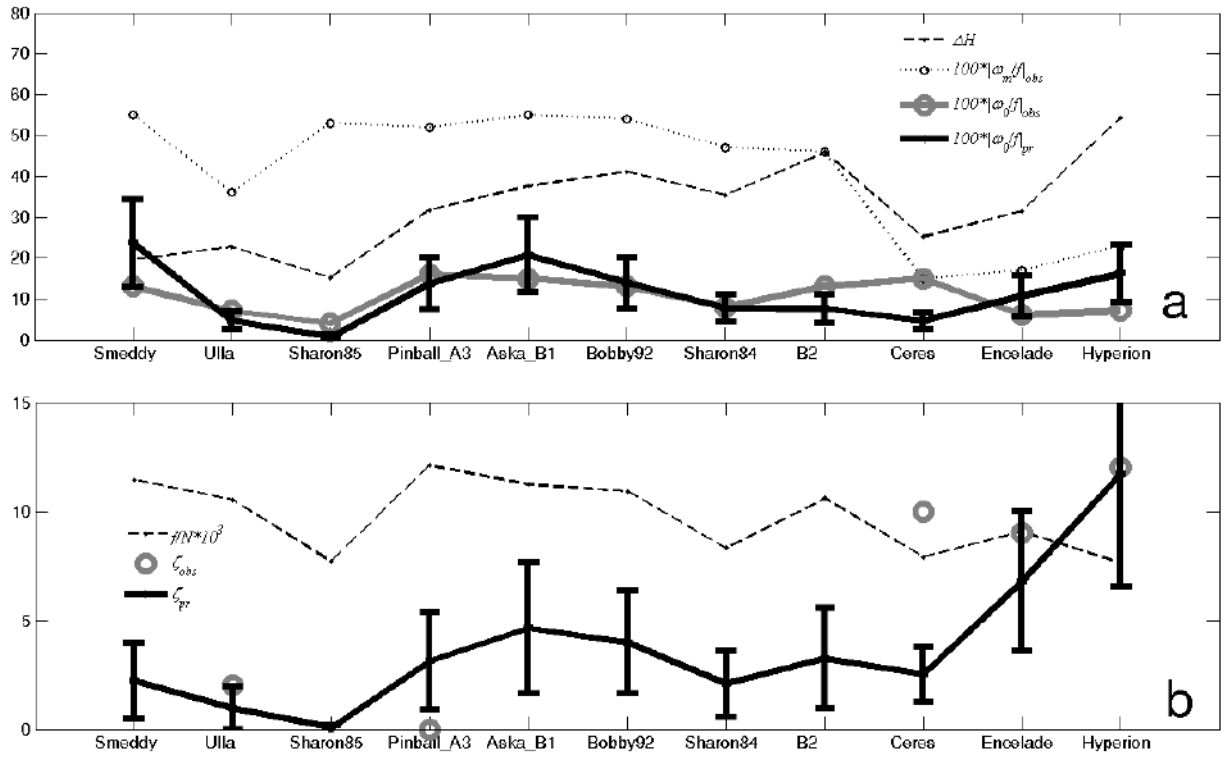

Fig. 6.22. Comparison of theoretical (Section 6.3.5) and observed characteristics of the meddy surface signal. ***a)*** *Normalized relative vorticity of the surface signals of the meddy $|\omega_0|/f$ from observations in AVISO altimetry (solid gray line with circles) and computations using formula* (6.39) *(solid black line with error bars). The maximum relative meddy vorticity $|\omega_m|/f$ is shown by a thin dotted line with circles, the estimated values of ΔH are shown with a dashed black line.* ***b)*** *Sea level anomaly values over meddies: observed in AVISO altimetry (gray circles) and computations using formula* (6.34) *(solid black line with error bars). The dashed thin line shows the $f/N \cdot 10^3$ ratio. Sea level anomalies in AVISO altimetry data are only available for meddies observed after 1993. The maximum errors in the estimates of ζ and ω_0 are given under the assumption that the error in determining ΔH is 50%, and in determining R_m is 20% of the parameter estimate (from Bashmachnikov et al., 2014).*

The observed values of ω_0 in the center of the meddy surface signals correspond to the theoretical ones. As before, the exception is meddy Ceres, the observed anomalously high vorticity over which was the result of its capturing a meander of the Azores Current (Tychensky and Carton, 1998). The zero Pinball anomaly corresponds to the period of meddy formation, when its surface signal had not yet been formed (Fig. 6.8).

Below the analysis along the meddy trajectories, tracked with RAFOS floats, is presented (Fig. 6.23-6.25).

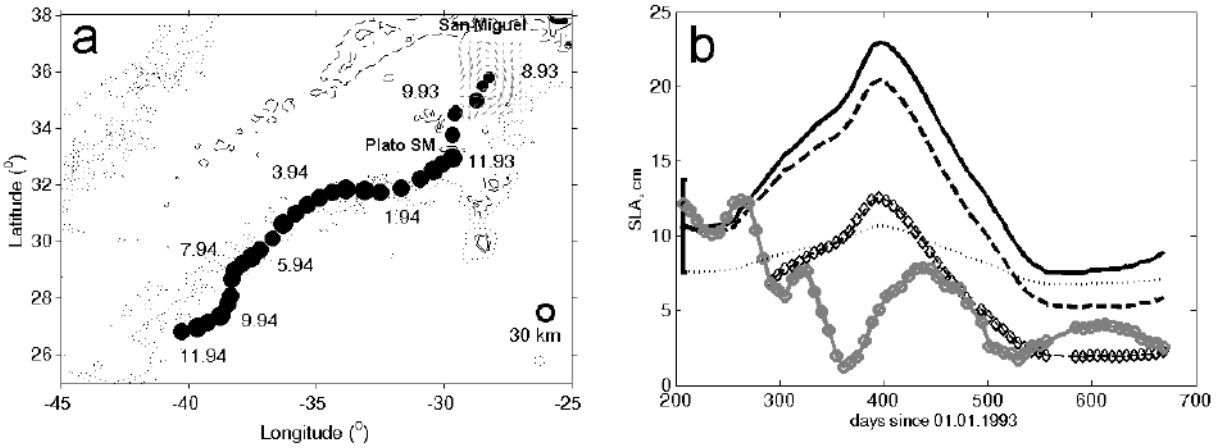

Fig. 6.23. The trajectory and surface manifestation of meddy Hyperion in the sea level. ***(a)*** *Meddy trajectory. The size of the circles reflects the radius of rotation of the RAFOS float. Isobaths of 1000, 2000 and 4000 m are shown.* ***(b)*** *Sea level anomaly over the meddy (cm): observed in AVISO altimetry – gray line with circles; computed using formula (6.34) under the assumption that the meddy parameters are constant over time – black solid line with crosses; under the assumption of an increase in the meddy core depth by 70 m per year (as the observed depth of the RAFOS float) – black dashed line; under the assumption of an abrupt decrease in the meddy radius by 10 km after interaction with the Plato seamount – black dashed line with diamonds. Values of* $N*10^3$*, used in the theoretical estimates – thin dotted line (from Bashmachnikov et al., 2014).*

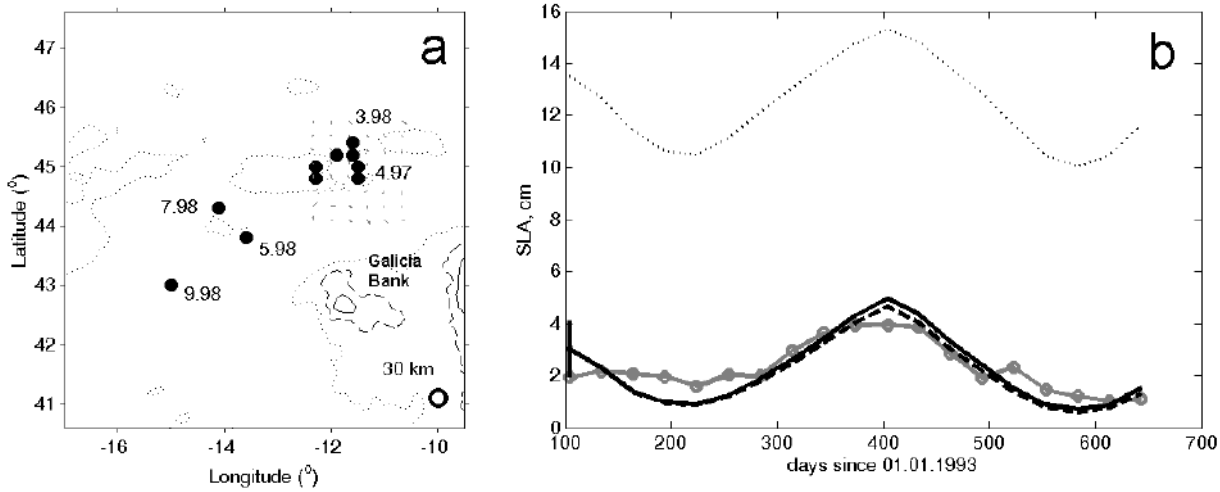

Fig. 6.24. Same as in fig. 6.23, but for meddy Ulla (from Bashmachnikov et al., 2014).

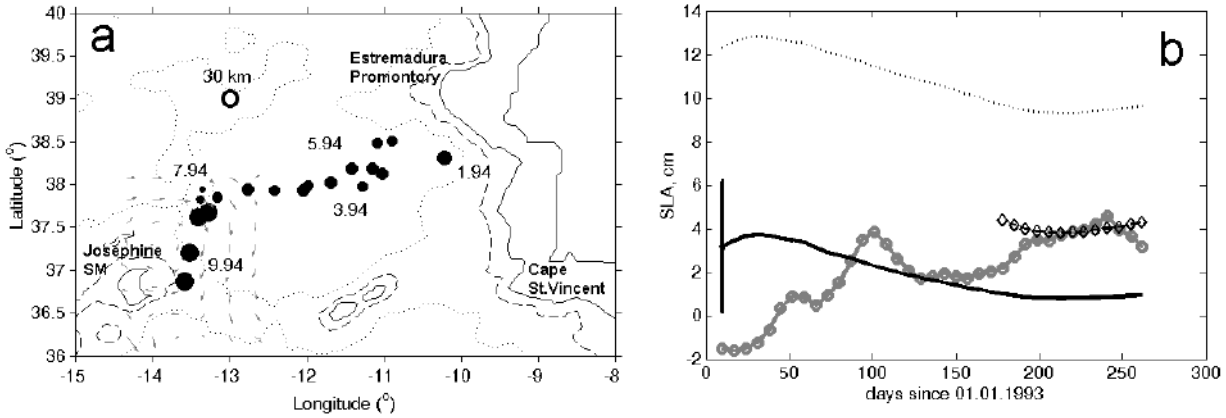

*Fig. 6.25. Same as in fig. 6.23, but for Pinball meddies. In panel (**b**): black line with diamonds shows the sea level anomaly over the meddy (cm) after an assumed increase in the meddy radius by 10 km after its merger with another meddy (from Bashmachnikov et al., 2014).*

The theoretical estimate of variability of the maximum sea level anomaly over meddy Hyperion (Fig. 6.23) confirms the general patterns, theoretically obtained for the eddy patch above (Fig. 6.19). There is a sharp decrease in intensity of the signal after crossing the Azores Current and interacting with the Plato Seamount (approximately on the 300th day). The sea level anomalies over the meddy after this episode are better approximated with observations when the meddy radius is decreased by 10 km. According to formula (4.5), a decrease in R_m from 35 to 25 km is equivalent to the loss of approximately 30% of the salt from the meddy core. A similar result (loss of approximately 25% salt) as a result of the interaction of a meddy with a seamount north of the Azores was obtained in Section 4.3.3.5 (see also Bashmachnikov et al., 2009b). Another period of anomalous weakening of the surface signal of meddy Hyperion corresponds to the period of its close interaction with two cyclones, located one to the west and the other to the east of the meddy (on days 330-400). A similar "diving" of a meddy under a surface cyclone was observed by Carton et al. (2010). On days 390-420, the western cyclone, separated from the triplet and moved to the north, while the meddy, having rotated some distance around the eastern cyclone, moved south. During this period, the meddy regained a surface signal, which became again close to the theoretical one, although significantly weakened by the increased upper ocean stratification.

Similar to the results of Section 6.3.4 for an eddy patch, formula (6.34) for the Ryleigh eddy describes well the seasonal variability of the signal over meddy Ulla (Fig. 6.24) during its period of stagnation.

The evolution of the surface signal of meddy Pinball (Fig. 6.25) begins approximately 70-90 days after the beginning of its observation, when the surface signal of the meddy reached its predicted intensity after the start of its westwards propagation (Fig. 6.25). On the 170th day, the signal increased abnormally, which was the result of the merger of Pinball with another meddy approaching from the north (Richardson et al., 2000). The meddy parameters after the merger are unknown. Model simulation of intrathermocline three-dimensional eddies of the same size show that after the merger, the vertical extent of the resulting eddy remains virtually unchanged, while the eddy radius increases (Reinaud and Dritschel, 2002; Bambrey et al., 2007). Increasing the radius of meddy Pinball by 10 km (from 18 km to 28 km) results in a good agreement between observations and theory at the sea surface. This is also consistent with *in situ* estimates for the meddy by Richardson et al. (2000) based on an analysis of the change in the rotation pattern of the RAFOS float (Fig. 6.25). The volume of the resulting eddy is approximately 80% of the sum of

the volumes of the eddies merged. According to numerical experiments, this phenomenon is not uncommon and is a result of the loss by the merging cores of a part of their volume via generation of secondary submesoscale eddies and filaments (Reinaud and Dritschel, 2002; Zhmur, 2010; Ciani et al., 2016).

6.4 SPATIAL STATISTICS OF SURFACE MANIFESTATIONS OF MEDDIES FROM THEORETICAL ESTIMATES AND OBSERVATIONS

6.4.1 SPATIAL VARIABILITY OF PARAMETERS OF THE SURFACE MANIFESTATIONS OF MEDDIES IN THE SUBTROPICAL ATLANTIC FROM THE THEORETICAL ESTIMATES

Using the theoretical formulae obtained in Sections 6.3.2 and 6.3.5, it is possible to evaluate sea level anomalies formed by a meddy with given characteristics and in a given area of the ocean.

Taking characteristic values $|\tilde{q}_m| = 0.7f$ and H = 800-1100 m (Table 6.1) and using formula (6.11), it is possible to delineate areas where surface meddy signals can, in principle, be registered in AVISO altimetry data. From the range of formal errors of the AVISO altimetry of 2-4 cm (Fu and Cazenave, 2001) the critical value of 2 cm is used, since it has been shown above that even a weak sea level anomaly of 2-4 cm over meddy Ulla can be continuously tracked in AVISO altimetry maps for months (Figs. 6.19 b and 6.24).

The results obtained using the formulae in Section 6.3.2 showed (Fig. 6.26) that in AVISO altimetry it is possible to track meddies with a dynamic radius $R_m \geq 20$ km north of 30-35°N (along the Northern and Central meddy paths – Fig. 4.12), however, to the south (along the Southern meddy paths) the sea surface signal of a meddy with $R_m = 20$ km will be too weak and intermittent for continuous tracking with AVISO data (Fig. 6.26a, b). Meddy with $R_m \geq 30$ km can be tracked throughout the entire study area, with the exception in its southernmost part (south of 25°N, Fig. 6.26c,d). For example, the sea level anomaly of meddy Hyperion in altimetry was 10-15 cm at 34-35°N, but weakened to 5 cm or less became intermittent at the final stage of its trajectory at 27° N (Fig. 6.19 and 6.23). Very high sea level anomalies for $R_m \geq 30$ km in the northern part of the study area seems to be overestimated (Fig. 6.26c,d) and has hardly been observed in practice (see section 6.4.2 below). This is due to the fact that theoretical estimates do not take into account the dissipation of the meddy surface signal, in particular dissipation due to the formation of Rossby waves (see Section 6.3.3). Dissipation will increase with the increasing sea level gradient above the meddy, limiting the magnitude of the meddy signal on the sea surface.

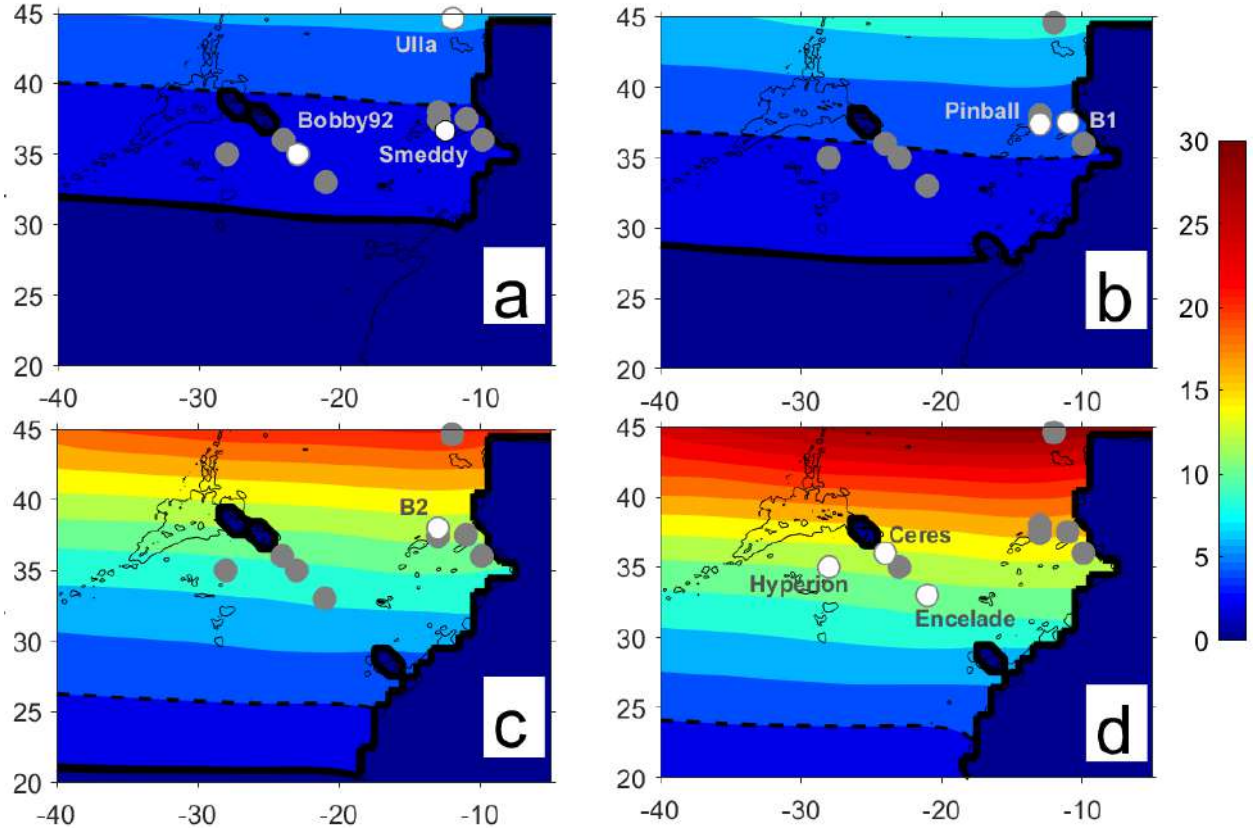

Fig. 6.26. Theoretical estimates of the sea level anomalies of meddy surface signals using formula (6.11) with given characteristics: ***(a)*** *R_m= 20 km and H= 1100 m;* ***(b)*** *R_m= 20 km and H= 800 m,* ***(c)*** *R_m = 30 km m H = 1100 m,* ***(d)*** *R_m = 30 km and H = 800 m. Thick black lines of almost zonal direction mark the values at which the meddy surface signal exceeds the noise level: solid line – ζ_{cr} = 2 cm, dashed line – ζ_{cr} = 4 cm. White circles mark meddies, geometric characteristics (H and R_m) of which correspond to those in the map, and the gray circles indicate other meddies, the surface signals of which are estimated in Fig. 6.22 (see also Table 6.1). Estimates of f/N at each point in the region are given using the annual mean MEDTRANS climatology. 2000 m isobath shown (from Bashmachnikov et al., 2012).*

Isolines of the amplitudes of the sea level anomalies of the surface signals of meddies with given characteristics are extended almost zonally (Fig. 6.26), which is a consequence of the close-to-zonal extent of *f/N* isolines (Fig. 6.14). Thus, the theoretical results can be generalized by identifying a critical latitude (φ_{cr}), south of which meddies with appropriate characteristics cannot be identified in AVISO altimetry (Fig. 6.27). The results show that meddies with $R_m \leq$ 10 km cannot be detected by AVISO altimetry data in the region where the Mediterranean Water is observed (Fig. 6.27a). Minimum theoretically possible dynamic radius for detection of the Northern meddies is $R_m \geq$15 km (Fig. 6.27a), but for reliable signal tracking it is desirable that $R_m \geq$20 km (Fig. 6.27b). For Southern meddies along the Central meddy propagation path (35-40°N, Fig. 4.13), the dynamic meddy radius should be $R_m \geq$20 km (Fig. 6.27a), but to reliably track their surface signal it is desirable that $R_m \geq$20-25 km (Fig. 6.27b). Most of the meddies in Table (6.1) satisfy this criterion, with the exception of some small-radius meddies in the immediate vicinity of the Iberian Peninsula (Fig. 4.15). Thus, meddy Pinball with a radius of 18 km gave a barely perceptible weak signal in AVISO altimetry, which intensified after its merger with another meddy (Figs. 6.19 and 6.25).

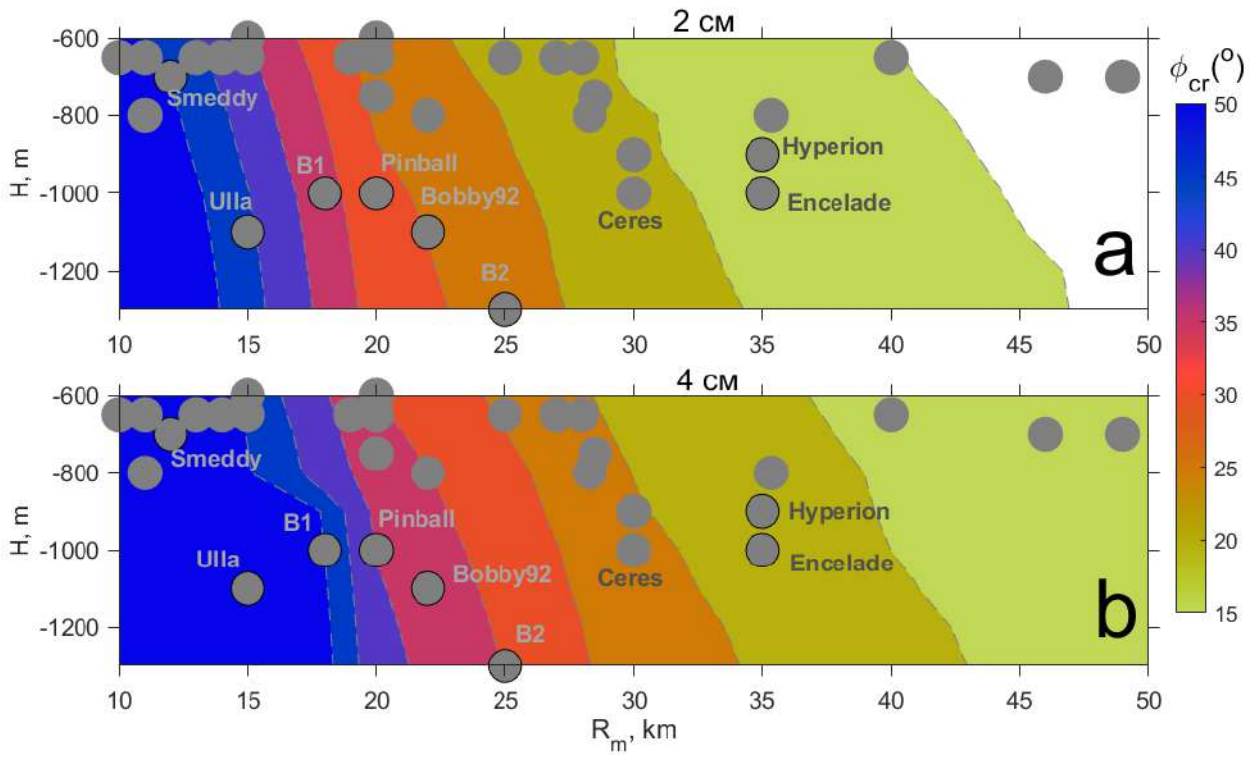

Fig. 6.27. The critical latitude (φ_{cr}), south of which the meddy surface signal cannot be tracked in AVISO altimetry, as a function of the meddy core depth H and its dynamic radius R_m. It is assumed that the minimum value of the anomaly over the meddy should exceed the formal error (noise) in the AVISO altimetry of: ***(a)*** *2 cm and* ***(b)*** *4 cm. The buoyancy frequency is obtained from the annual mean MEDTRANS climatology. The gray circles show the meddies listed in Table 6.1. Names of some meddies, presented in Fig. 6.26, are given in the plot (following Bashmachnikov et al., 2012).*

South of the Azores Current, the minimum meddy radii, that can be tracked using AVISO altimetry, increase rapidly from 20-25 km at 30°N to 30-40 km at 20°N. The observed meddy radii along the Southern meddy path, with rare exceptions, range from 20 to 50 km (Fig. 4.15). This means that many of meddies along the Southern path are not visible in altimetry data, and the surface signals of other meddies is extremely weak. However, 25-30°N is the southern limit of the distribution of the Mediterranean Water (Fig. 4.5) and the probability of meddy penetration into these latitudes is quite low (Fig. 4.9 and 4.12 b). Thus, even the initially big meddy Sharon destroyed at 20°N (Armi et al., 1989).

In the previous estimates, it was not discussed an effect of the anomaly of the potential vorticity of the meddy core, which is an amplitude factor in formula (6.11). The estimate of this parameter is a function of anomaly of the buoyancy frequency in meddy cores (expression 4.9 and Fig. 4.23), as well as of the relative vorticity of the core (Fig. 4.21). The absolute values of the peak relative vorticity of meddy cores vary from 0.05 *f* to 0.30 *f*. The small Burger numbers (on average, *Bu* ~ 0.5, Fig. 4.22) indicate that for most meddies it is the buoyancy anomalies in the cores determine $\tilde{q}_m$. These anomalies are, on average, maximum for meddies along the Southern path (Figure 4.13), which should contribute to slightly more intense signals of such meddies in AVISO altimetry, and, therefore, slightly lower critical latitude values than in Figure (6.27).

For solutions (6.34) and (6.39) of Section 6.3.5, it was carried out a sensitivity analysis to the variability of parameters of the meddy cores, limited by their characteristic ranges derived from *in situ* observations: $R_m \in$[20-80 km], $H \in$[700-1200 m], $\Delta H \in$[20-120 m] (Fig. 6.28). In the computation, as above, 2 cm was taken as the limit of detection meddy signals in the AVISO altimetry sea level data and it was set $f/N = 0.01$, which is characteristic of the subtropical Atlantic (Fig. 6.14). The results show that, within its characteristic values, the surface signal above meddies intensifies as the core depth H decreases and ΔH increases (Fig. 6.28a-c). The change in ΔH is a consequence of the stretching of isopycnals in the meddy core, i.e. an analogue of changes in the potential vorticity anomaly of the core. At the same time, the dependence of the relative vorticity and sea level anomalies of the meddy surface signal on ΔH weakens with decreasing meddy radius. For small meddies with R_m = 10 km, these anomalies are practically independent of ΔH (not shown).

The dependence of the sea level characteristics on meddy radii in Section 6.3.5 (formula 6.34), in general, also agrees well with the results for the meddy patches in Section 6.3.2 (formula 6.11, Fig. 6.19). Thus, analysis of formula (6.34) shows that in the subtropical Atlantic: 1) a large meddy with $R_m \geq 30$ km gives a fairly intense signal on the sea surface, regardless of the depth of the meddy core (Fig. 6.28a), 2) a medium-sized meddy with $R_m \sim 20$ km is visible only if it is shallow and sufficiently intense ($H \leq$ 900-1000 m and $\Delta H \geq 50$ m) (Fig. 6.28b), 3) small meddies with $R_m \sim 10$ km, as a rule, cannot be detected in AVISO altimetry data (the plot is not shown). Theoretically, such small meddies can be detected in sea level anomalies from along-track data if they are shallow ($H \leq$ 800-900 m) and very intense ($\Delta H >$ 70 m), but in AVISO altimetry their signal will be regularly sifted between altimetry tracks.

Using the theoretical results for a meddy with Rayleigh profile of Section 6.3.5 (formula 6.34, Fig. 6.23-6.25), it was found that the radii of the meddy surface signals depend nonlinearly on the radii of the meddy cores. The obtained solutions to equation (6.37) showed that within the subtropics (30-45°N), where most meddies are found, with values of $R_m \leq 40$ km, the radii of surface meddy signals are 2 times larger: $R_0/R_m \sim 2$ (Table 6.4). Thus, even meddies with ~20 km radii produces a surface signal with sufficient radius (~40 km) to be detected in AVISO altimetry data (see Tournadre, 1990). For larger meddies (60 km or more), especially if they are northern meddies, the ratio $R_0/R_m \sim 1.5$, and with a further increase in the radius to 100 km or more, R_0/R_m approaches 1.

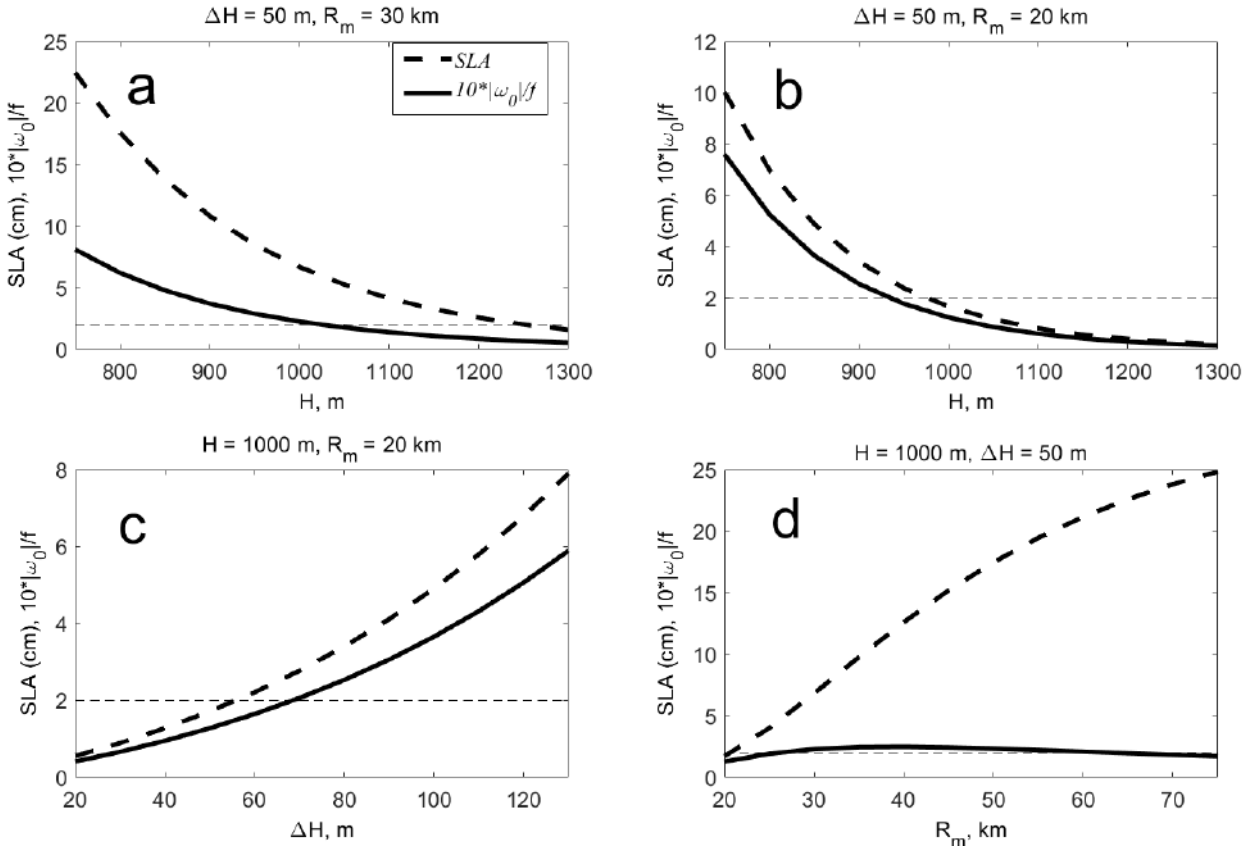

*Fig. 6.28. Analysis of the sensitivity of the theoretical ζ (black dashed line, formula 6.34) and of ω_0/f (*10, black solid line, formula 6.39) to the variability of meddy parameters: **(a)** to changes in the meddy core depth (H) at R_m = 30 km and ΔH = 50 m; **(b)** to the change in H at R_m = 20 km and ΔH = 50 m; **(c)** to the change in ΔH at R_m = 20 km and H = 1000 m; **(d)** to the change in R_m at H = 1000 m and ΔH = 50 m. In all experiments f/N = 0.01 (from Bashmachnikov et al., 2014).*

The results of the theory for a meddy with Rayleigh profile (Section 6.3.5) show some differences from the results of the theory for an eddy patch (Section 6.3.2). Thus, in contrast to the results of Section 6.3.2, the growth of the sea level anomaly (ζ) over a meddy with Rayleigh profile slows down with increasing R_m. In formula (6.34) this is reflected in the fact that, in addition to the exponential dependence of ζ on R_m, there is also an inverse dependence of the amplitude multiplier of ζ on R_m. The latter begins to play an increasingly important role as R_m increases. The point is that the initial assumptions of the theory for the meddy patch in Section 6.3.2 do not imply a dependence of the radius of its surface signal (R_0) on R_m, whereas it was shown above that, for a meddy with Rayleigh profile, R_0 increases with increasing R_m. An increase in R_0 limits the increase in the maximum azimuthal velocity of the surface signal $v_{\theta 0} \sim \zeta / R_0$ with an increase in R_m, that is not observed for an eddy patch. The relative vorticity of the surface meddy signal $\omega_0 \sim 4.7 \frac{v_{\theta 0}}{R_0}$ (formula 1.9) turns out to be practically independent of R_m (Fig. 6.28d). According to formula (6.39), some dependence ω_0 on R_m will still be observed for relatively small meddies (R_m ~ 10 km or less). Thus, the variability in the intensity of the surface signal with changes of the meddy radius add corrections to the simplified theory of a meddy patch.

6.4.2 Spatial variability of characteristics of meddy surface signals in the subtropical Atlantic from observations

The previous sections 6.3.4 and 6.3.6 showed generally good agreement between theory and observations for the magnitudes of the sea surface signals of individual meddies, as well as for the evolution of these signals in time. In this section, a massive comparison for a large population of meddies is performed to reveal the spatial distribution of the meddy surface signals in theory and observations. For the analysis, we used the database of 241 meddies, described in Section 4.3, for which *in situ* observations made it possible to estimate all the meddy parameters necessary for a theoretical assessment of the surface signal: core depth and radius, as well as the buoyancy frequency anomaly of the core, the main component of its potential vorticity anomaly. From the database, 209 meddies were selected, observed since 1993, for which the intensity of their surface signals could be estimated using AVISO satellite altimetry observations. To identify the surface signal, the results of Section 6.2 were used, where it was shown that the centers of surface manifestations of a meddy, in the vast majority of cases, are located within one radius from the meddy center (see, for example, Table 6.2). In this regard, the surface manifestation of a meddy was considered to be the negative relative vorticity anomaly closest to the meddy center and observed within ±10 days from the date of execution of the profiles *in situ*, used to identify meddies. The center of the anomaly should be within two radii from the meddy center, and the average radius of the anomaly should be no more than two radii of the meddy. If such an anomaly was detected, the coordinates of its center and radius (R_0) were determined using the method by Bashmachnikov et al. (2017) (see Section 2.3.2). The maximum sea level anomaly (ζ), as before, was estimated as the difference between the maximum sea level anomaly in the area of the meddy surface signal and the average sea level in the ring 1.5-2.0 R_0.

The results showed that the average distance δ between the centers of meddies (identified with *in situ* data) and the centers of their surface signals (identified from AVISO altimetry data) were less than 10 km (Fig. 6.29a), i.e. the centers of the signals were generally located directly above the centers of the meddies, within the spatial resolution of AVISO altimetry. This indicates the predominant alignment of the meddy and its surface signal into a single vertical structure with a common axis of rotation, often derived for various types of eddies observed *in situ* and in numerical simulations (see, for example, Carton et al., 2013; Bashmachnikov et al., 2013b; Belkin et al., 2020). A relatively small number of surface signals, the centers of which were observed at distances over 100 km from the centers of the corresponding meddies, were within two radial distances from the meddy center. Such eddies can still be considered connected (Carton et al., 2016). Note that in figure (6.29a) there are many points with small δ, which overlap each other. This creates the false impression of a large scatter during visual assessment.

The azimuthal angles between the meddy centers of the eddies and those of their surface signals cover the entire range of possible mutual positions. However, the dominant positions of the centers of the surface signals are to the west and south of the centers of the corresponding meddies, and a slightly smaller number are to the north-west of the meddy centers (see numbers in the sectors in Fig. 6.29a). The same directions are dominant in propagation of meddies (Fig. 4.11). In combination with the opposite directions of the main surface currents in the region, directed east and southeast, it can be stated that the surface signals are generally biased towards the leading edge of moving meddies. This is consistent with the concept of generation of meddy surface signals as a consequence of the conservation of the potential vorticity in the upper ocean

layer during meddy interaction with an impinging flow (Section 6.3.1, Fig. 6.12). However, for connected eddies, including those with cores at different depth levels, their mutual rotation around a common center is often observed (see, for example, Reinaud and Dritschel, 2002; Bersanelli et al., 2016). Therefore, there is a fundamental possibility of finding a surface signal not only over the frontal part of a moving meddy, but also in any azimuth.

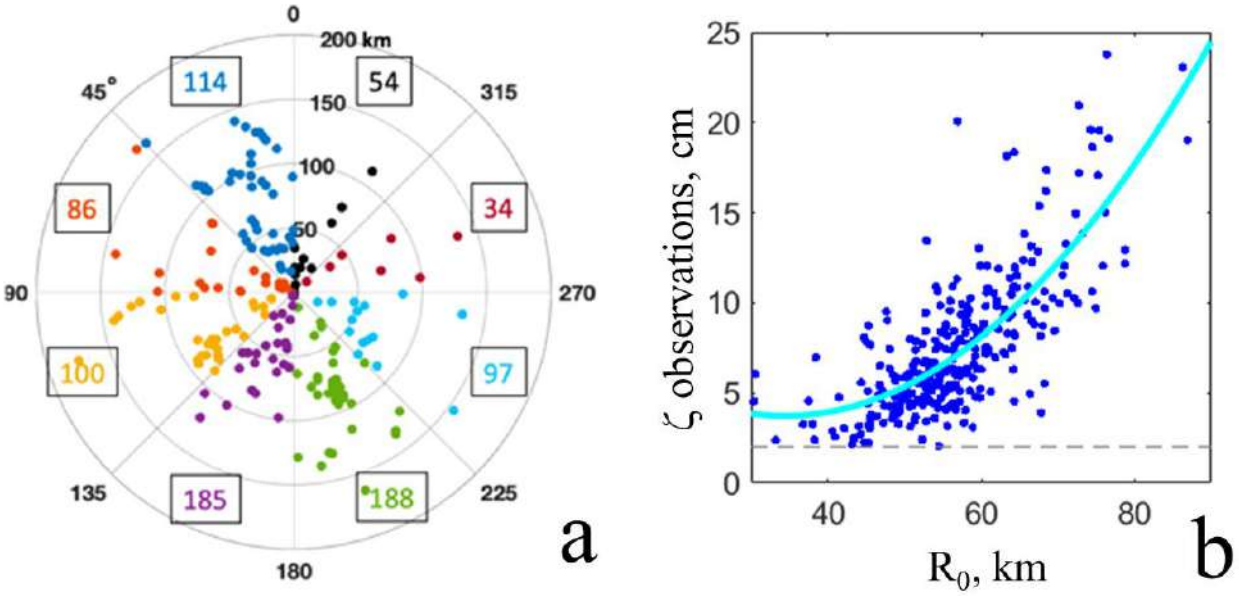

Fig. 6.29 (a) The azimuthal angle α (°) and distance δ (km) between the centers of 209 meddy cores and the centers of their surface signals from observations. The northwards direction is vertically upward. The azimuthal sectors, 45° each, are highlighted in different colors. The numbers in each sector show the total number of observations. (b) The maximum sea level anomalies ζ (cm) of meddy surface signals as a function of the dynamic radius of these anomalies R_0 (km). In the scatterplot, the dependence is approximated by a quadratic function (blue curve); For this approximation, there were used only the surface manifestations of those meddies, for which ζ≥ 2 cm (following Ienna et al., 2022).

The sea level anomaly over the meddies typically exceeded the noise level of 2 cm of AVISO altimetry data and rarely exceeds 20 cm (Figure 6.29b). The properties of the meddy surface signals reveal a quadratic dependence ζ on R_0 (Fig. 6.29b). Such a dependence, with a relative constancy of ω_0 (Fig. 6.18a), suggests a close to geostrophic balance (formula 6.2), as well as a linear increase in the maximum azimuthal velocity in the meddy surface signal with increasing R_0 (see also formula 1.6).

In the geographic distribution of R_0, despite the rather high level of noise associated with both, the variability of the characteristics of meddy cores (section 4.3) and temporal variability of ocean background conditions, certain trends can be observed (Fig. 6.30): 1) R_0, on average, increases from R_0=40-50 km near the Iberian Peninsula to R_0=90 km west of 20°W; 2) the sea level anomaly ζ grows quite quickly from 3-6 cm near the Iberian Peninsula to 7-8 cm between 15-20°W, and then slowly continues to increase to the west, reaching maximum values in the north-west of the study area.

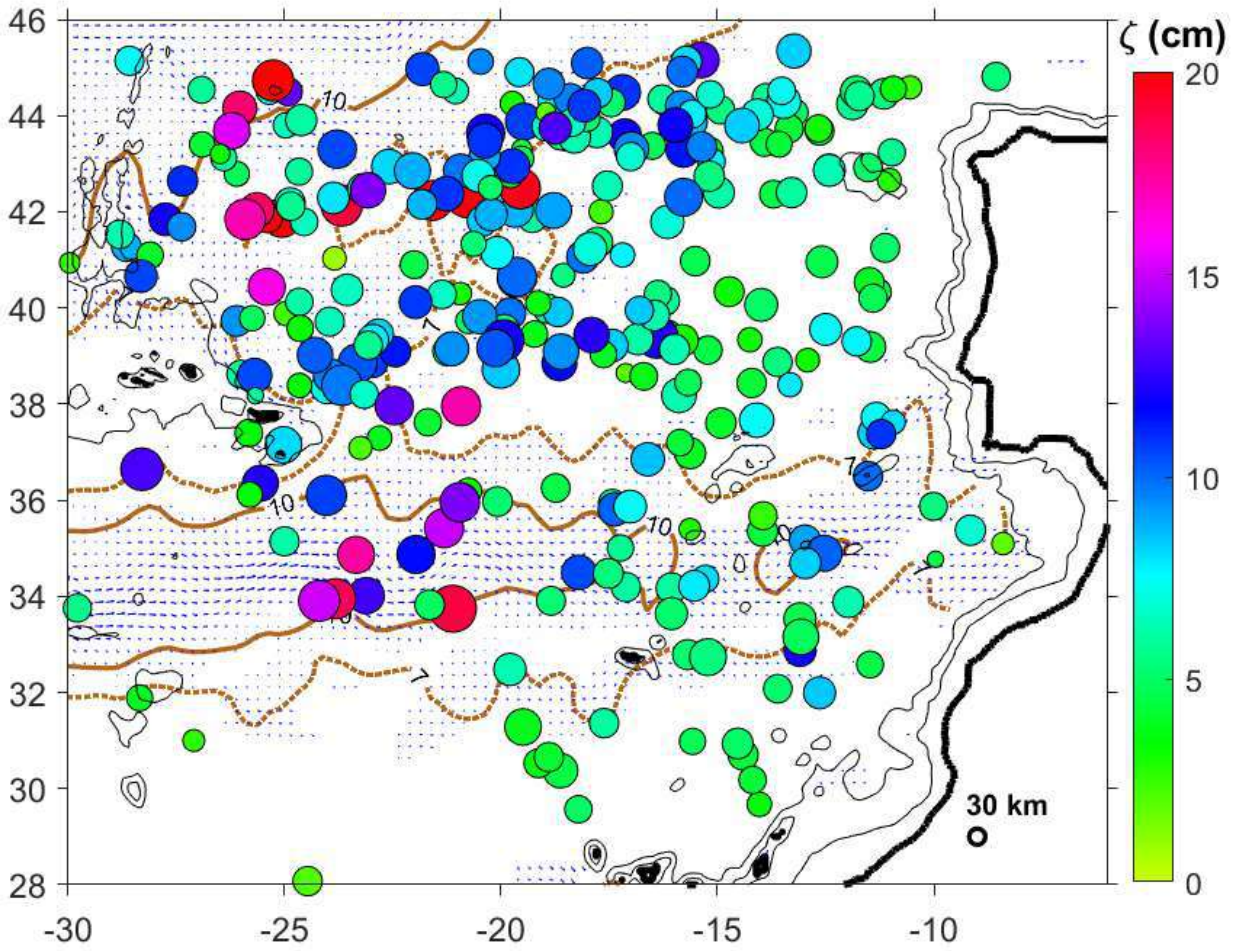

Fig. 6.30. Spatial distribution of the maximum sea level anomalies ζ (cm, color) of the meddy surface signals. The size of the circles corresponds to the dynamic radii of the meddy surface signals (R_0, km); reference value R_0 =30 km is shown in the lower right corner; For better visibility of differences, a nonlinear scale of R_0 was used. The brownish contours show the 75% quartile of the modulus of the sea surface current velocity from AVISO satellite altimetry (solid line – 10 cm s^{-1}, dotted line – 7 cm s^{-1}); the direction of the most intense mean currents is shown in blue arrows.

Theoretical estimates of the intensity of meddy surface signals was carried out using a simpler estimate for the eddy patch of Section 6.3.2 (formula 6.11), as the sea level anomalies were estimated with approximately equal accuracy for the meddy patch model (Sections 6.3.2 and 6.3.4) and for meddy with Rayleigh profile (Sections 6.3.5 and 6.3.6). The anomaly of quasi-geostrophic potential vorticity in the meddy core relative to the background was determined using formula (6.3):

$$\tilde{q}_m = \frac{N_m^2}{g}(\omega_m + f) - \frac{N_0^2}{g} f \approx \frac{f}{g}(0.8N_m^2 - N_0^2)\,. \qquad (6.42)$$

Here, as before, due to the lack of data, it was used $\omega_m = -0.2\,f$ (Fig. 4.20), N_m is the buoyancy frequency of the meddy core and N_0 is the buoyancy frequency of the background in the layer encompassing the meddy core, derived from MEDTRANS climatology. The estimated $\tilde{q}_m$

varied from -6 10^{-5} s^{-1} to 2 10^{-5} s^{-1}, on average being -1.6 10^{-5} s^{-1} (Fig. 6.31a). In anticyclonic meddies, the anomaly $\tilde{q}_m$ should be negative, which is confirmed by observations (see, for example, Tychensky and Carton, 1998; Paillet et al., 2002). Of the 209 meddies, positive values of $\tilde{q}_m$ were obtained only for 15. Apparently the peak relative vorticity of these meddy cores was significantly higher than the average estimate of -0.2 *f*, used in the computations. This can happen for meddy cores (Table 6.1, Fig. 4.20). These 15 meddies were excluded from further statistics.

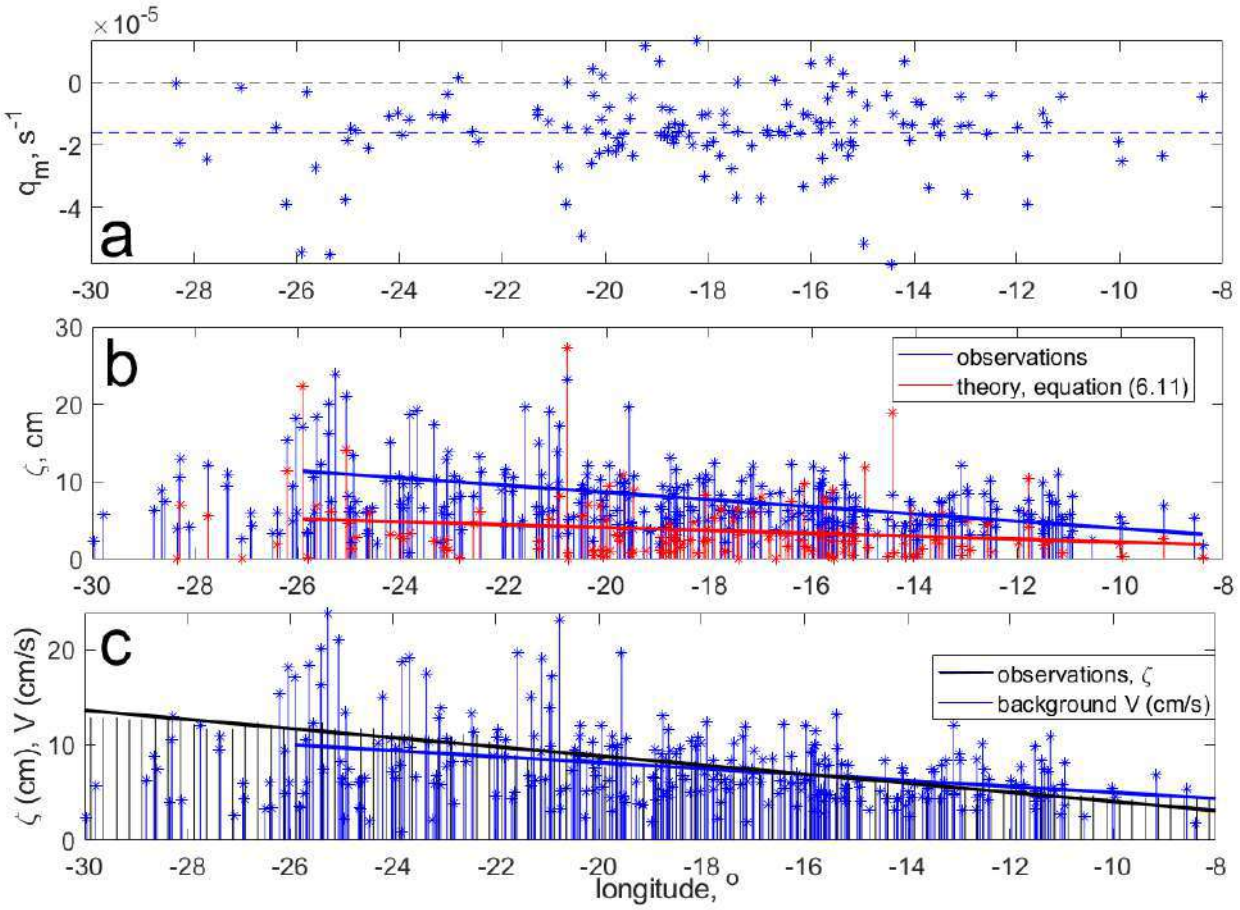

Fig. 6.31 (a) Anomalies of the quasigeostrophic potential vorticity of the meddy core ($\tilde{q}_m$, s^{-1}) according to formula (6.42); mean $\tilde{q}_m$ = -1.6 10^{-5} s^{-1} is marked with a horizontal blue dashed line. (b) The maximum sea level anomaly of the meddy surface signal (ζ) from AVISO satellite altimetry data (blue bars) and its theoretical estimate using formula (6.11) (red bars). The lines show linear trends from 8 °W to 26 °W: the trend in the observations is significant, the theoretical one is slightly above the significance level. (c) The maximum sea level anomaly of the meddy surface signal (ζ, as in panel (b)) from AVISO satellite altimetry data (blue bars) and the velocity of the background current around meddies (V cm s^{-1}, black bars). The results are given as a function of geographic longitude.

The results of the analysis of the relationship between the sea level anomalies and various characteristics of the meddy cores used in formula (6.11) ($\tilde{q}_m$, R_m, H) showed that none of these parameters is dominant in determining the intensity of the meddy signal on the sea surface. Calculated using a high-resolution hydrodynamic model within 900 km of the Iberian Peninsula Ciani et al. (2017) show that the theoretically described above relationship between the intensity of the surface signal and the characteristics of the meddy core is violated when interacting with

surface eddies, the Azores Current, or seamounts. For meddy, which did not enter into such interactions, a direct dependence of the intensity of the surface signal on $\tilde{q}_m$ and an inverse dependence on H was revealed, which is consistent with the theory.

Fig. (6.31b) shows the maximum sea level anomaly obtained from satellite altimetry ($\zeta_{obs,}$ blue bars). Three anomalously high values of $\zeta_{obs} > 20$ cm are identified. To assess their realism, the maximum azimuthal velocities of these meddy surface signals were also estimated using the Rayleigh eddy profiles (formula 1.9). The maximum velocities did not exceed 30 cm s^{-1}, which is a realistic estimate for eddies in the ocean. The moderate speeds are due to these anomalous signals were registered over Northern meddies with big radius (Fig. 4.15d). The latter partially compensates for the high values of ζ in the current velocity estimates. The theory also showed high sea level anomalies in the surface signals of these meddies (Fig. 6.31 b, 6.32), which further confirms their realism.

Theoretical estimates (ζ_{thy}), obtained using formula (6.11), correspond in order of magnitude to ζ_{obs} and generally reproduce the variability ζ_{obs} (Fig. 6.31, 6.32): the correlation coefficient between the series is 0.6. At the same time, the theory underestimates the observed ζ_{obs} value by approximately 50%, on average, as follows from the linear regression equation constructed using the scatterplot (Fig. 6.32):

$$\zeta_{thy} = 0.56\ \zeta_{obs} + 0.47. \qquad (6.43)$$

The low regression coefficient of determination R^2~0.4 is a consequence of the rather large scatter of the theoretical values ζ_{thy} relative to ζ_{obs}. This scatter is associated with a number of reasons: 1) inaccuracy of the estimates of meddy parameters used in the computations of $\zeta_{thy,}$ 2) inaccuracy of the estimates of the observed intensity of meddy surface signals $\zeta_{obs,}$ 3) possible distortion of meddy signals by other dynamic structures, which was noted at some sections of the trajectories of meddies Hyperion, Ceres, Encelade, Zoe and Pinball (V, Fig. 6.19). ζ_{obs} also depends on the intensity of the background current (Fig. 6.31c), which was not taken into account in the theory. The background current has a significant trend, increasing westwards, and the correlation of V with ζ_{obs} is 0.36, while the minimum significant correlation is 0.17.

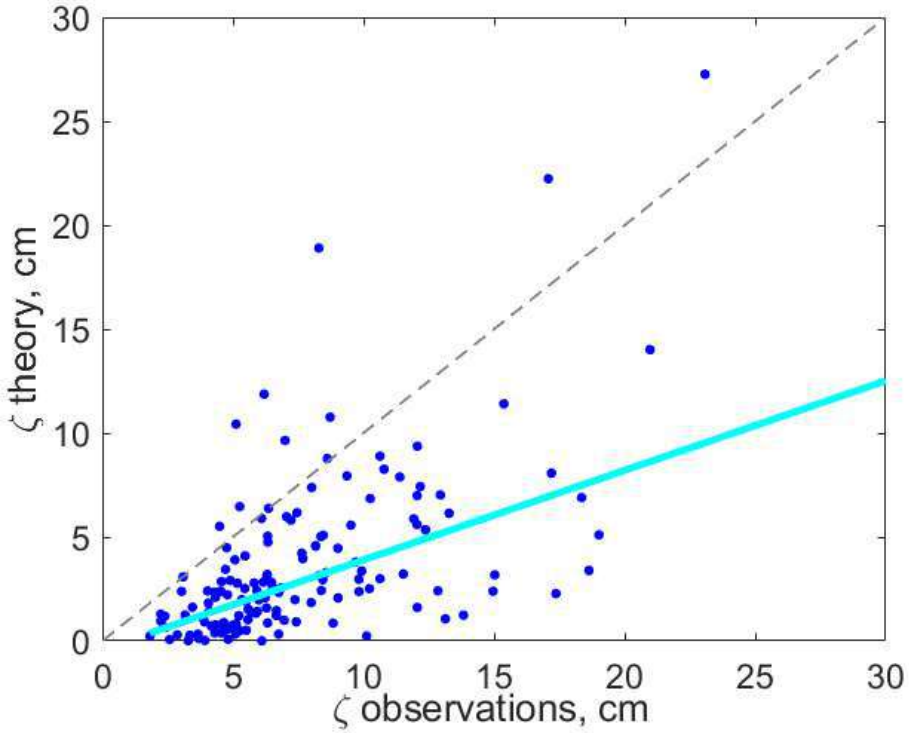

Fig. 6.32. Scatter plot of measured ζ_{obs} and theoretical ζ_{thy} values (cm). The geographical distribution of the meddy surface signals is shown in Fig. (6.30). The linear relationship between the measured and theoretical values of ζ, obtained by the least squares method, is shown with the blue straight line (formula 6.43*) (following Ienna et al., 2022).*

A comparison of all the theoretical relationships obtained above using formulas (6.11), (6.14), (6.15) and (6.34) with observations was carried out for several meddies. Below is an example of such a calculation for meddy ARGO399, tracked using the ARGO float No. 6900399 for more than 1.5 years (from June 2006 to February 2008) and which passed through almost the entire study area from west to east and from north to south (Fig. 6.33). The method for identifying meddies using ARGO floats is described in Section 2.3.1. The meddy radius was determined from several series of vertical casts, when other *in situ* measurements were carried out by ships or other floats in the vicinity of the ARGO float No. 6900399. According to the results obtained, meddy ARGO399 had the following characteristics: R_m = 32 km, H = 1000 m, H_s = 660 m, ΔH = 116 m. The salinity anomaly in meddy ARGO399 reached 0.6, the relative vorticity anomaly of the meddy $\omega_m \sim 1\ 10^{-5}\ s^{-1}$, and the anomaly of the potential vorticity of the meddy core $\tilde{q}_m \sim 6\ 10^{-5}\ s^{-1}$. The *f/N* ratio in the layer above the meddy varied along the meddy trajectory from 0.02 to 0.03.

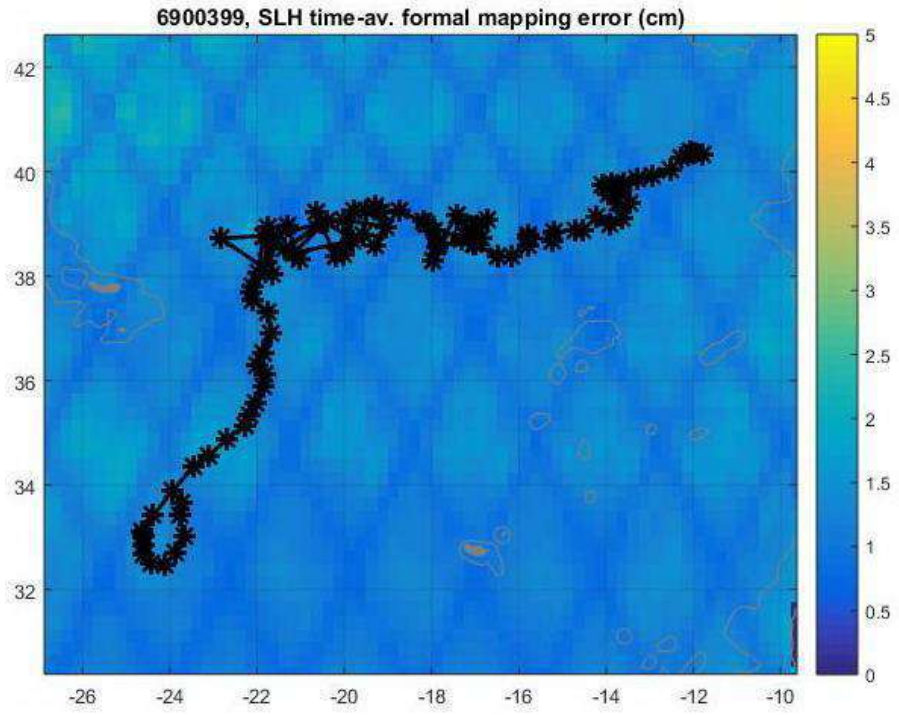

Fig. 6.33. Meddy ARGO399 tracked by an ARGO float (black line with stars). The color indicates the formal error of AVISO altimetry observations (cm).

Analysis of the graphs shows that the theoretical estimates in Section 6.3.2 (Bashmachnikov and Carton, 2012) and Section 6.3.5 (Bashmachnikov et al., 2014), reproduce the average level of the meddy signal relatively well. The estimates using formulae by Ciani et al. (2015) for the R-meddy or S-meddy underestimate the signal intensity. This indicates a weak influence of positive anomalies of the potential vorticity around the meddy core on the signal formed on the sea surface.

Inaccuracies in measuring the meddy parameters lead to a fairly large scatter in estimates of the intensity of its signal on the sea surface (Fig. 6.34a), which, coupled with errors in estimating anomalies of surface signals by AVISO satellite altimetry and the influence on the signal intensity of other dynamic structures, does not allow us to identify the shortcomings of the theory via point-by-point comparison with observations. However, trends in the overall signal intensity statistics for a large number of meddies, as well as the observation of surface signals along fairly long tracks of individual meddies, allow us to draw preliminary conclusions about global factors of signal variability that were not directly reflected in the theoretical estimates.

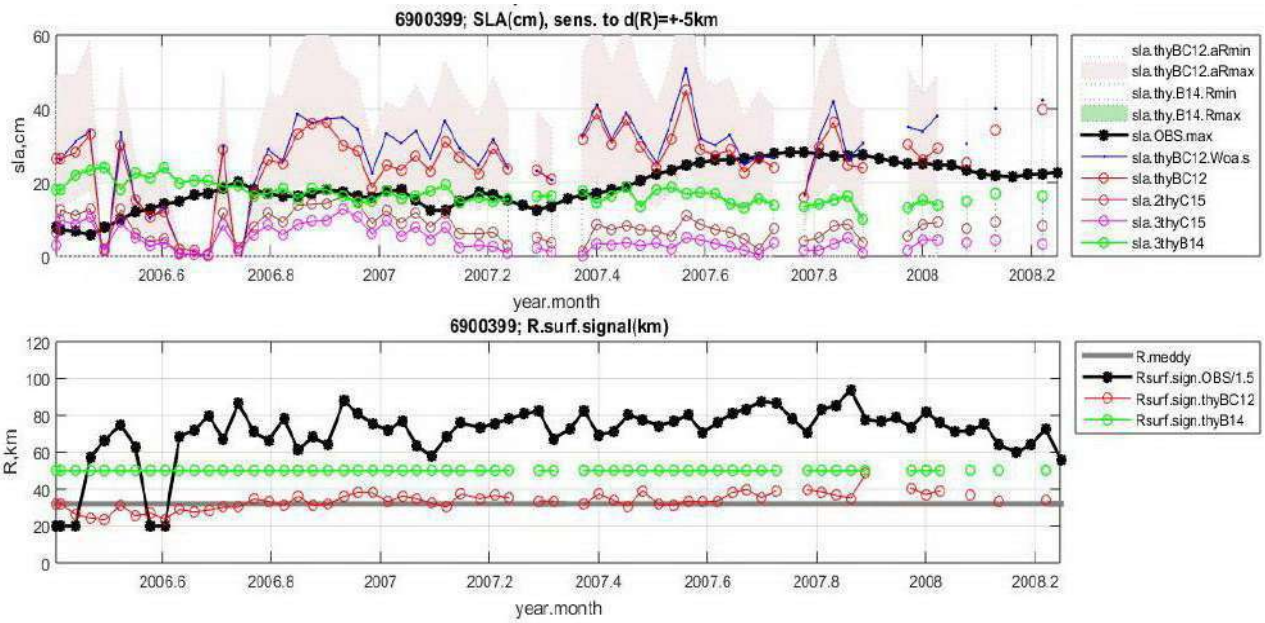

Fig. 6.34. (a) Time variability of the sea level anomaly (cm) over meddy ARGO399. Black line – observations from AVISO; blue and red lines – theoretical estimates of Section 6.3.2 using formula (6.11) (Bashmachnikov and Carton, 2012), where the mean buoyancy frequency of the upper layer above the meddy is estimated using MEDTRANS climatology and using ARGO399 float profiles, respectively; dark red and pink lines – theoretical estimates using formulas (6.14) and (6.15) by Ciani et al. (2015) for S-meddy and R-meddy, respectively; green line – theoretical estimates using formulae (6.34), (6.40) and (6.41) of Section 6.3.5 (Bashmachnikov et al., 2014). The pink background shows the range of variability of the theoretical estimate using formula (6.11) with an error in estimating the meddy radius of 5 km. (b) Time variability of the dynamic radius R_0 (km) of the surface signal over meddy ARGO399: black line – using AVISO altimetry data, red line – using theoretical estimates from Section 6.3.2 (formula (6.10) $R_0 = \sqrt{2}fH / N$): green line – using theoretical estimates of Section 6.3.5 (formula 6.10). The gray line is an estimate of the meddy dynamic radius R_m based on in situ observations.

As for the vast majority of meddies analyzed in Section 6.3, almost the entire trajectory of meddy ARGO399 passed at distances of more than 300-600 km from the Iberian Peninsula, at which a decrease in R_m is typically observed (Fig. 4.14) and with a constant or decreasing with distance from the Iberian Peninsula of the potential anomaly of the meddy core (formula 6.3 and Fig. 4.22) as a result of a gradual dissipation of meddy core. According to formulae (6.11) and (6.34), this should lead to a gradual decrease in the intensity of the surface signal over the meddy westwards. However, observations indicate the opposite (Fig. 6.30, 6.34a). Analysis showed that the increase in time of the sea level anomalies over meddy ARGO399 is associated with the entry of the meddy into the area with stronger background currents. This was also observed over meddies in numerical models (Ciani et al., 2017). The correlation coefficient between the velocity of the incident background flow and the magnitude of the sea level anomaly is 0.5. In the spatial distribution of surface signals of 209 detected meddies (Fig. 6.30), signal amplification also, as a rule, occurred in the areas of the main regional currents, the Azores and North Atlantic Currents.

The link between the intensity of the meddy signal and the intensity of the impinging flow is consistent with the theory on the origin of meddy surface signals, suggested above (Section 6.3.1), but is not taken into account in expression (6.11). Theoretically, this effect can be taken into account in the amplitude multiple of formula (6.34), which includes the integral of the velocity of the upper layer relative to a meddy, derived from formula (6.41) and taken constant in the

computation performed above (Fig. 6.30, 6.34a). However, the assessment of this multiple is complicated by the unknown values of the time period τ, during which the signal intensifies, and the unknown real expression for the variability of the velocity of the background current over a meddy during the generation of such a signal.

6.5 DISCUSSION OF THE RESULTS OF CHAPTER 6

In situ and satellite observations indicate that most of the observed meddies had a well-defined signal in the sea level, the characteristic anomalies of which ranged from 5 to 15-20 cm, as well as the signal in the relative vorticity, the peak values of which on the sea surface can exceed 50% of those in the meddy cores. The weakening of the relative vorticity from the meddy core towards the sea surface (Fig. 6.4, Table 6.1) was expectedly linked to the stratification of the water column. Even attenuated by the stratification, the anomalies formed by meddies on the sea surface were comparable in their intensity and size to those of surface eddies and were persistent enough to be continuously monitored with satellite altimetry data. The periods of the continuous signal tracking ranged from 3-4 months to more than a year. The signals disappeared for only a few days, as a consequence of the crossing of a jet stream (the Azores Current) by a meddy or of its interaction with surface cyclones (Verron, 1986; Vandermeirsch et al., 2003a,b).

The signal on the sea surface, in the overwhelming majority of cases, was located directly above meddies (the average distance between the centers of the signal and of the meddy was less than one meddy radius), forming an eddy structure associated with a meddy. This allows a quite unambiguous interpretation of the anticyclonic structures observed above a meddy as their sea surface signals. The distribution of meddies in a relatively dynamically quiet region of the subtropical North Atlantic, characterized by low velocities of the mean currents and by a low level of eddy activity (Fratantoni, 2001), facilitates the identification of meddy signals on the sea surface.

The meddy signal on the sea surface represents a separate eddy, dynamically associated with the meddy. It is formed due to conservation of the potential vorticity of the water columns of the impinging flow. This is confirmed by observations of the vertical structure of a dynamic signal above a meddy, which demonstrates a clear shift in the eddy axis above the meddy core (Fig. 6.4), the predominant location of the meddy surface signals at the frontal side of meddies (relative to the leading directions of meddy propagation) (Fig. 6.29), and also by successful predictions of signal intensity by the theory based on this assumption (Section 6.3). The process of forming a meddy signal on the sea surface, with permanent background conditions, can take several days. In practice, such constant conditions are often unattainable in the ocean, and the typical signal formation time has been estimated at 1-3 weeks.

The dynamics of coupled eddies assumes their joint propagation and mutual rotation in the horizontal plane around a common center (Reinaud and Dritschel, 2002; Bersanelli et al., 2016). Due to the lower intensity of the surface signal, it is expected that the axis of joint rotation will be located near the meddy center and that it is the surface signal that mainly rotates around it. However, the small distances between the centers of connected eddies and the larger radii of the surface signals covering the entire or almost the entire meddy lead to a relatively small radius of the rotation circle, difficult to detect in altimetry data.

It can be expected that similar dynamic signals with a similar origin is observed under meddies. Thus, anticyclonic coherent rotation was recorded by floats at different levels below

meddy cores. Also, for meddy Ulla, the core of which was observed at 700-1200 m, the LADCP data showed rotation from the sea surface to 2000 m depth (Paillet et al., 2002). A similar propagation of dynamic structure up and down from eddy cores has been also recorded for other subsurface eddies, such as the Lofoten Vortex in the Norwegian Sea (see Chapter 5). The vertical coherence of the rotation above and below meddies creates favorable conditions for their capture of ARGO profiling floats, which, despite periodic vertical casting within the upper 2000-m layer, can drift along with meddies for many months (Fig. 6.33).

Analysis of surface signals along the trajectories of individual meddies, as well as analysis of over 200 meddy surface signals, showed that the theory, both for an eddy patch and for a Rayleigh eddy (Sections 6.3-6.4), allows one to predict the nature of the variability of the signal intensity as a function of meddy parameters (potential vorticity of the core, R_m/H ratio), as well as its spatial and seasonal variability associated with changes in the upper ocean stratification (f/N ratio). The zonal extent of f/N isolines leads to meddies with the similar characteristics giving a stable and easily detectable sea surface signals in the northern part of the subtropical Atlantic, but do not manifest themselves on the sea surface in the southern part of the region.

Errors in estimating the amplitude of the signal in satellite altimetry data, as well as a rather high uncertainty of the theoretical estimates due to inaccuracies in determining the main parameters of meddy cores, do not allow a detailed comparison of the theory with observations. In particular, this partly forms the rather big scatter between the observed and the predicted characteristics of the meddy surface signals (Fig. 6.32). Nevertheless, comparison of the theoretical and observed meddy signals makes it possible to detect on the sea surface the episodes of significant changes in the volume of a meddy core, as a result of its partial disintegration or merger with another meddy.

Further massive comparison of the theory with observations (Bashmachnikov et al., 2014; Ienna et al., 2022), showed that, in addition to the parameters identified in the theory, the intensity of the meddy sea surface signal also depends on the velocity of the impinging current in the upper ocean. An almost twofold increase in the signal above a meddy in the presence of even a fairly weak background current directed against the meddy propagation direction was observed in the modeling results (Fig. 6.17). When studying surface signals above a meddy, it was repeatedly recorded the formation of an anticyclonic meander above the meddy near the Azores Current, which significantly enhanced the surface signal of the meddy (Bashmachnikov et al., 2009a). Moreover, if the meddy did not cross the current, but continued to move west to the north of the current, the meander detached from the current and moved along with the meddy for several weeks, amplifying its sea surface signal. In general, it can be assumed that the unaccounted influence of background currents is the reason why the theory underestimates the signal intensity above the meddy by an average of 2 times.

In the ocean, two processes occur simultaneously: the destruction of the signal above the meddy due to the radiation of Rossby waves and its restoration by the impinging flow. Model experiments have shown that the formation of Rossby waves effectively dissipates sea surface signal over a meddy only if the westerly component of the meddy velocity relative to the surrounding ocean is close to the phase velocity of one of the vertical modes of the baroclinic Rossby waves. A possible weakening of the signal decay in areas of increased velocities of background currents, that disrupt this connection, also can be one of the factors for the observed intensification of the meddy surface signals in these areas.

Further development of the theory should go in the direction of obtaining a dynamically sound relationship between the intensity of the meddy surface signal and the current velocity in the upper ocean, which replaces the parameterization of this dependence with formula (6.41).

6.6 Conclusions of Chapter 6

1. Most of the observed large meddies formed a fairly pronounced and stable signals on the sea surface, which could be tracked using AVISO satellite altimetry data. The periods of the continuous signal tracking ranged from 3-4 months to 1 year, interrupted for several days during close interaction between a meddy and a jet stream or a surface cyclone.
2. The center of the surface signal was typically located directly above the meddy center or within one dynamic radius of the meddy center and was most often located on the leading edge of a moving meddy.
3. The sea level rise in the meddy surface signals reached 15-20 cm. The negative relative vorticity anomaly in the signals reached 0.1 f and was comparable to or exceeded anomalies of the surface anticyclones in the study region. The intensity of the sea level anomalies over meddies increased to the west, in the areas of higher velocity of background currents.
4. A meddy signal on the sea surface represents an independent anticyclone, dynamically linked with the meddy and is formed by virtue of conservation of potential vorticity of the impinging flow above the meddy core. At the initial stage of its evolution, in addition to the upper ocean anticyclone, a surface cyclone could also be formed above a meddy, separated from the meddy.
5. Theoretical estimates showed that the sea level and relative vorticity anomalies on the sea surface depended on both, the characteristics of the meddy core (potential vorticity of the core and R_m/H ratio) and the background conditions (f/N ratio). Given a very gradual temporal variability of characteristics of the majority of meddy cores, the f/N ratio determines the seasonal variability of the meddy signals on the sea surface. The change in the f/N ratio also determines the meridional weakening of the intensity of meddy signals (from north to south), as well as the increase in the radii of the signals, reaching twice the meddy radius in the southern subtropics. These dependencies are nonlinear. In particular, the change in the radius of the sea surface meddy signal with latitude was most pronounced for small meddies.
6. Rapid changes in the intensity of the meddy signals on the sea surface make it possible to detect mergers and break up of meddy cores.
7. Abrupt weakening or complete disappearance of the meddy signals is usually associated with a signal loss when crossing a jet stream or interacting with an intense surface cyclone. Interaction with the jet stream can also lead to an anomalous increase in the signal over the meddy due to the formation of an anticyclonic meander in the mean current. If the meddy does not cross the jet stream, then the anomalous signal enhancement above the meddy can persist even after the meddy has separated from the current.
8. Theoretical estimates describe the impact of a meddy on a horizontally homogeneous upper ocean layer, moving relative to the meddy, for stationary conditions and in the absence of dissipation. The actual magnitude of the meddy signal is a balance between its dissipation and regeneration by the impinging flow. Failure to take into account the peculiarities of the interaction of a meddy with the impinging current leads to the theoretical underestimating

of the intensity of the meddy signals on the sea surface by, on average, about 2 times, as well as to the absence in the theory of the western intensification of these signals. The latter is associated with an increase in the velocity of surface currents to the west.

6.7 APPENDIX OF CHAPTER 6: METHOD FOR TRACKING OF MEDDY SURFACE SIGNALS IN THE SATELLITE ALTIMETRY

Tracking the meddy signal on the sea surface was carried out using the method of the "crawling window" (Bashmachnikov et al., 2009a). The next position of the surface signal above a meddy was determined by the local minimum of the second derivative of the sea level in the zonal and meridional directions (a proxy for the relative vorticity minimum), at a distance of less than one AVISO altimetry grid node from the current position of the center of the meddy signal. This process was repeated iteratively until the nearest local minimum of relative vorticity was reached. To avoid unwanted jumps to an adjacent deeper local minimum, not associated with the meddy, two restrictions were applied. First, the sea level derivatives distributions were formed by averaging the three closest in time successive AVISO maps, summed with decreasing weights depending on the time difference between the timing of the added map and that of the current one. Secondly, a limitation was introduced on the velocity of signal propagation: the next position of the signal center could not be further from the previous position of the meddy than the number of grid nodes corresponding to the distance traveled at a velocity of 4 cm s^{-1} during a period equal to the time step of the dataset used. This typical meddy propagation velocity, allowed meddies to move only one grid-node away in the AVISO satellite altimetry grid per week. However, over short time intervals, meddies can move faster, with a velocity of up to 10 cm s^{-1} (Richardson and Tychensky, 1998). To connect two consecutive meddy positions in such a situation, it was made possible to jump a distance of up to three grid nodes if the extreme (negative) value of the second derivative in all grid nodes adjacent to the identified eddy center fell by more than 50% from their values at the previous step. The latter meant that the algorithm detected the periphery of the eddy, and the center of the eddy had shifted over a larger distance.

The method turned out to be stable and made it possible to get long uninterrupted track propagation of meddy surface signals using satellite altimetry data. With very rare episodes of the signal losses, associated with strong attenuation of the signal by surface dynamic structures, this method ensured that the surface signal anomaly follows very closely the path of the meddies tracked by the RAFOS or ARGO floats. The continuous trajectories of the meddy surface signals, obtained using this method, confirm that it was the dynamic manifestation of the meddies on the sea surface, that were being monitored, and not random local vorticity minima that occasionally happened to be near the meddies.

CHAPTER 7. MANIFESTATION OF SUBSURFACE EDDIES IN THE SEA SURFACE TEMPERATURE AND OCEAN COLOR

7.1 SPECIFIC FEATURES OF THE SEA SURFACE TEMPERATURE ANOMALIES OVER MEDDIES

In the previous Section 6 it was shown that large meddies usually form a pronounced signal on the sea surface. In the satellite altimetry data, this signal practically is no different from the signals of surface anticyclones, which makes identification of subsurface eddies difficult. In this section it is shown that the signals of subsurface anticyclones can be distinguished from those of surface anticyclone using the sea surface temperature (SST). For example, data from the August 2005 showed that meddy, observed with *in situ* data (Fig. 6.1-6.2) and having a strong anticyclonic signal on the sea surface in AVISO altimetry data, was also characterized by a rise in SST along the periphery of its surface signal (Fig. 7.1).

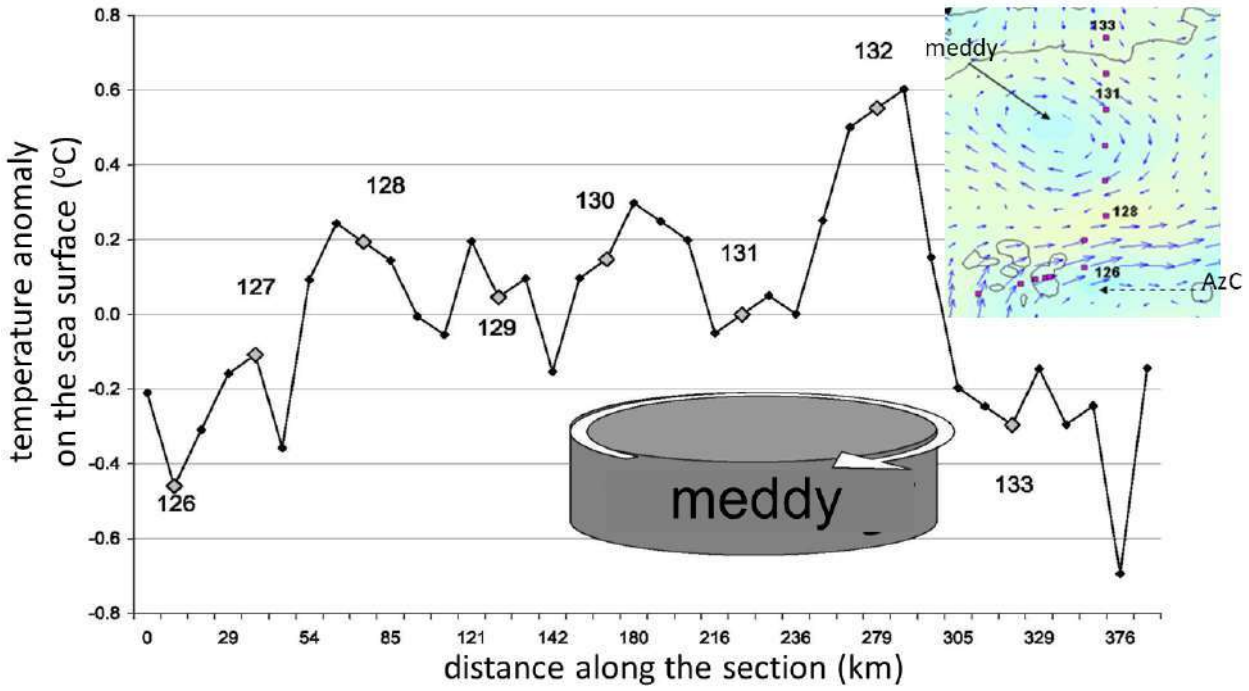

Fig. 7.1. Anomaly of sea surface temperature (°C) observed by a ship-nested temperature sensor (at 3 m depth) on a meridional section across meddy M131 (see inset on the top right), as a function of distance from the beginning of the section (km) on August 17, 2005. The anomaly was formed by removing the mean and linear meridional trend. Large diamonds correspond to the positions of oceanographic stations (the numbers are the station numbers). The inset shows: color - relative vorticity (blue - negative vorticity), vectors - currents on the sea surface according to AVISO altimetry data on the date of the section, red markers - oceanographic stations (followig Bashmachnikov et al., 2009a). AzC is the Azores Current.

The SST anomaly measured with the ship thermometer at the periphery of the meddy surface signal reached 0.6°C relative to the SST in the center of the dynamic signal. Tracking the trajectory of the meddy surface signal back in time (Figs. 6.1 and 6.9) showed that in June 2005, shortly before detection of the meddy with *in situ* data, the meddy interacted with the Azores

Current. During this interaction, the meddy formed and captured a meander of the Azores Current, which results in an intensification of its dynamic signal in the altimetry data.

The SST pattern above demonstrates a temperature decrease in the eddy center, which is not typical for surface anticyclones. Formed primarily from meanders of large-scale currents, the cores of surface anticyclones contain water from the warmer side of the front. The convergence of the warm sea surface water surface anticyclones upholds their warm signals in SST.

For further analysis of stability of the cold signals over subsurface eddies, the Multiscale Ultra-high Resolution database (MUR, 2011) was used. MUR is a combination of nighttime satellite observations in the infrared and microwave ranges. SST data in MUR have a spatial resolution of 1 x 1 km and a daily temporal resolution. The MUR algorithm for merging SST images from various sources is based on the algorithm of the Parameter Matrix Objective Analysis (Mariano and Brown, 1992). The algorithm makes it possible to minimize the effect of artificial smoothing of SST gradients due to a possible displacement of frontal zones when superimposing images taken at different times. In the MUR dataset, the temperature of the upper skin layer measured from satellites is reduced to the temperature of the upper mixed layer, using *in situ* observations from ships and ARGO profiling buoys. Below the manifestation of SST signals along trajectories of several meddies is investigated.

The path of meddy Don Carlos, described in section 6.2 (Figs. 6.3 and 6.4), passed along a satellite altimetry track, which contributed to a good identification of the surface signal of the meddy and of the change in its intensity in time (Fig. 7.2 a, b). The radial structure of the meddy surface signal (Fig. 7.2a) was analyzed by averaging the values of relative vorticity (ω_0) and SST within concentric regions at a distance of 0-25 km (ω_{25}, SST_{25}), 25-50 km (ω_{50}, SST_{50}), 50-75 km (ω_{75}, SST_{75}) and 75-100 km (ω_{100}, SST_{100}) from the center of the meddy surface signal. The latter was defined at the point of peak relative vorticity anomaly (ω_0) above the meddy. The differences SST_{25} -SST_{100} and SST_{50} -SST_{100} between the SST values averaged in one of the central regions of the surface meddy signal and in the ring 75-100 km characterizing the background were used as the study parameters. The results showed that over 5 months of observations, a negative SST anomaly in the central part of the meddy signal was observed 80% of the time and, on average, was -0.11°C with an error of the mean of 0.06°C at the 95% significance level (Fig. 7.2c). Reduction of the SST anomaly in the meddy surface signal in July-August 2010. corresponded to a decrease in the relative vorticity anomaly of the signal associated with its rapid movement to the south. This relationship suggests a dynamic origin of the negative SST anomaly over the meddy.

For comparison, the SST anomaly was studied over the neighboring meander of the Azores Current (Fig. 7.2a), which forms a relative vorticity anomaly of similar intensity and size approximately 100 km west of the trajectory of the meddy Don Carlos. The SST anomaly over this anticyclonic formation, calculated as above, was positive 85% of the time out of 3 months of the observations and, on average, was +0.08°C with an error of the mean of 0.06°C at the 95% significance level (Fig. 7.2d).

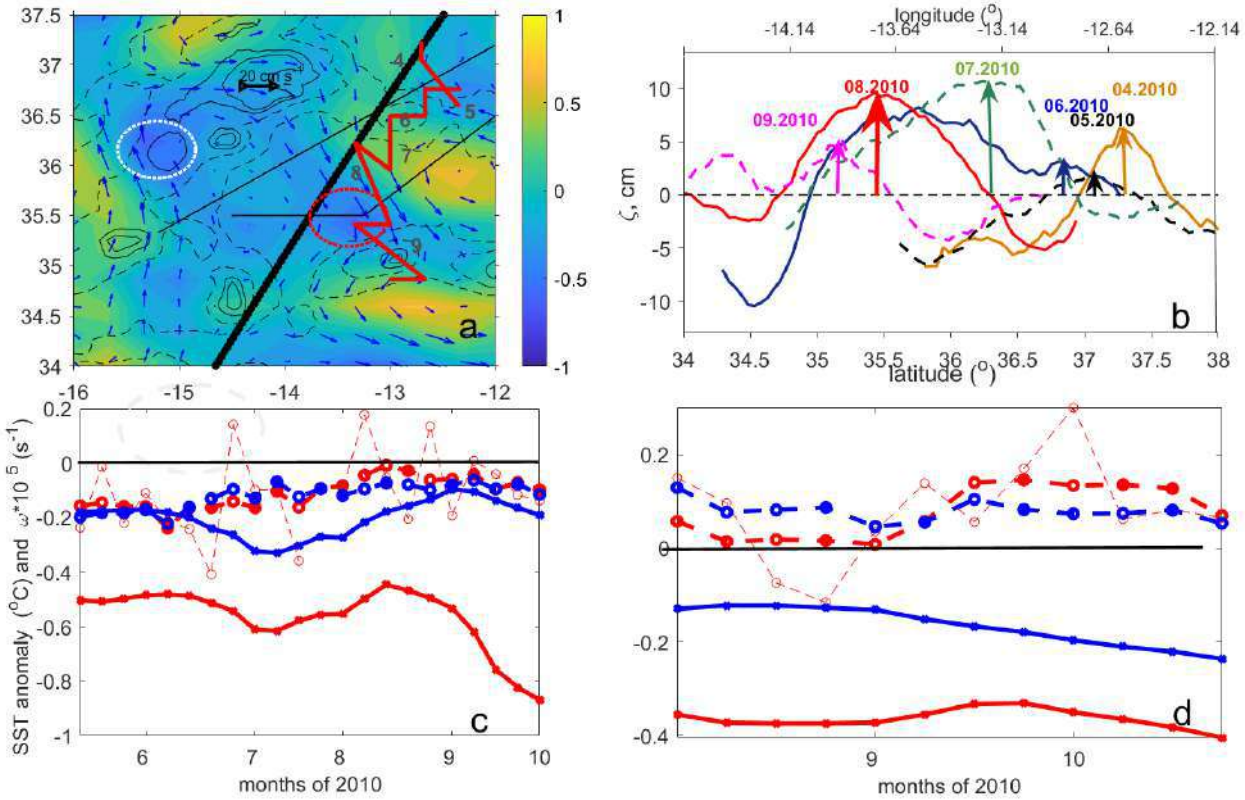

Fig. 7.2. (a) Relative vorticity (10^{-5} s^{-1}, color) and geostrophic currents (cm s^{-1}, blue vectors) on August 24, 2010, calculated using AVISO altimetry. The position of the surface signal of meddy Don Carlos on this date is marked with a red circle, and the position of the anticyclonic meander of the Azores Current is marked with a white circle. Thick black line is the satellite altimetry track (Jaison satellite), thick red line is the meddy track, thin black lines are the sections of in situ ADCP data. The numbers next to the meddy track mark the beginning of the corresponding month. Isobaths of 1000 and 1500 m (solid lines), 3000 and 4000 m (dotted lines) are shown. (b) Local sea level anomalies (cm) from Jaison satellite from April to September 2010, from the RADS data set (only every 3rd profile is shown). The arrows indicate the centers of the detected meddy signal. The red arrow is the meddy center during its detection in situ. (c- d) Anomalies of SST (°C, thick dashed lines) and relative vorticity (10^{-5} s^{-1}, solid lines) for (c) the meddy surface signal and (d) the Azores Current meander. Red thin dotted lines are SST_{25} -SST_{100} at original (weekly) resolution; thick lines are the monthly moving averages: red dotted line with circles are SST_{25} - SST_{100}, red solid line is ω_{25}; blue dotted line with circles is SST_{50} -SST_{100}, blue solid line is ω_{50} (following Bashmachnikov et al., 2013b).

SST anomalies were also assessed along trajectories of the meddy ARGO352 tracked *in situ* using the ARGO profiling float N352 (Fig. 7.3) and meddies tracked with RAFOS neutral buoyancy floats (Fig. 7.4). The meddy ARGO352 (Fig. 7.3a) had the salinity anomaly exceeding 0.3 in the 750-1500 m layer, derived from vertical profiles of the ARGO float. The ARGO float was trapped by the meddy 7 months, since its formation near Lisbon Canyon in October 2005 and until May 2006. At the sea surface, the meddy was accompanied by a pronounced negative relative vorticity anomaly of 0.05-0.08 *f* (Fig. 7.3b). The dynamic radius of the surface manifestation of the meddy was about 50 km the altimetry data. During 75% of the time of observations, the meddy surface signal was characterized by a negative SST anomaly relative to the surrounding ocean: on

average, the anomalies SST_{25} -SST_{100} and SST_{50} -SST_{100} were about -0.15°C, sometimes reaching -0.20°C with an average error of 0.05°C at 95% significance level.

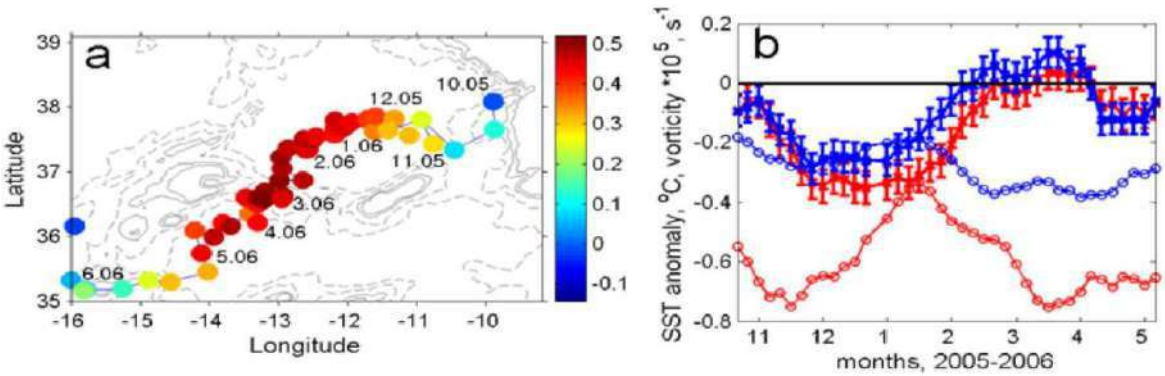

Fig. 7.3. (a) The average salinity anomalies relative to MEDTRANS climatology in the 700-1500m layer for subsequent vertical profiles of ARGO N352 southwest of the Iberian Peninsula. Meddy ARGO352 is detected if the anomalies exceed 0.3. Thin gray lines indicate the bottom topography. (b) Monthly moving averages of SST_{25} -SST_{100} (°C, red lines with error bars) and relative vorticity in the central 25 km circle (10^{-5} s^{-1}, thin red lines with circles). The corresponding blue lines are SST_{50} -SST_{100} and the average relative vorticity in a 25-50 km ring around the center of the meddy surface signal. Error bars characterize the average error in the SST anomaly estimates (from Bashmachnikov et al., 2013b).

Table 7.1 The mean, error of the mean and standard deviation of SST anomalies over the meddy according to NOAA AVHRR data (quality criterion 4), computed as the difference between the average SST within a radius of 75 km from the center of the meddy surface signal and the average SST in the 75-100 km ring around the center of the meddy surface signal. The error of the difference between the means (horizontal dashed lines) was estimated as $E = \frac{2\delta_{\Delta SST}}{\sqrt{N}}$, *where N is the number of points in the internal region and the ring around the center,* $\delta^2_{\Delta SST} = \delta^2_{SST1} + \delta^2_{SST2} - 2cov(SST_1, SST_2)$, δ^2_{SST1}, δ^2_{SST2} *are the standard deviation in the areas, where the average values of* SST_1 *and* SST_2 *were computed.*

meddy	Ceres	Encelade	Hyperion	Iberian
average SST anomaly	-0.10	-0.03	-0.08	-0.04
error of the mean	0.06	0.06	0.03	0.04
standard deviation	0.12	0.14	0.09	0.18

A similar pattern was observed over meddies tracked with RAFOS floats in the mid-1990s and described in detail in Section 6.2 (Fig. 6.11). During this period, there were no satellite microwave SST data yet and all the results were based on infrared data (NOAA AVHRR), which does not allow obtaining continuous series of SST anomalies due to the presence of clouds. Due to the smaller amount of data, SST anomalies were estimated as the difference between the means of the inner circle with a radius of 75 km and the outer ring within 75-100 km from the center of the meddy surface signal. To estimate the SST anomaly, there were used only the days, when SST data could be obtained for at least 50% of the points in both areas. SST anomalies over meddies Ceres (Fig. 7.4b), Encelade (Fig. 7.4c), Hyperion (Fig. 7.4d) and Iberian (Bobby) (Fig. 7.4e) were

predominantly negative. Over meddies Ceres and Hyperion the SST anomalies exceeded the error of the mean (Table 7.1).

Based on the analysis above, the following conclusions can be drawn: 1) meddies form a predominantly negative SST anomaly at the center of their sea surface signals; 2) the SST anomalies are significantly less stable than the dynamic meddy signals in the sea level.

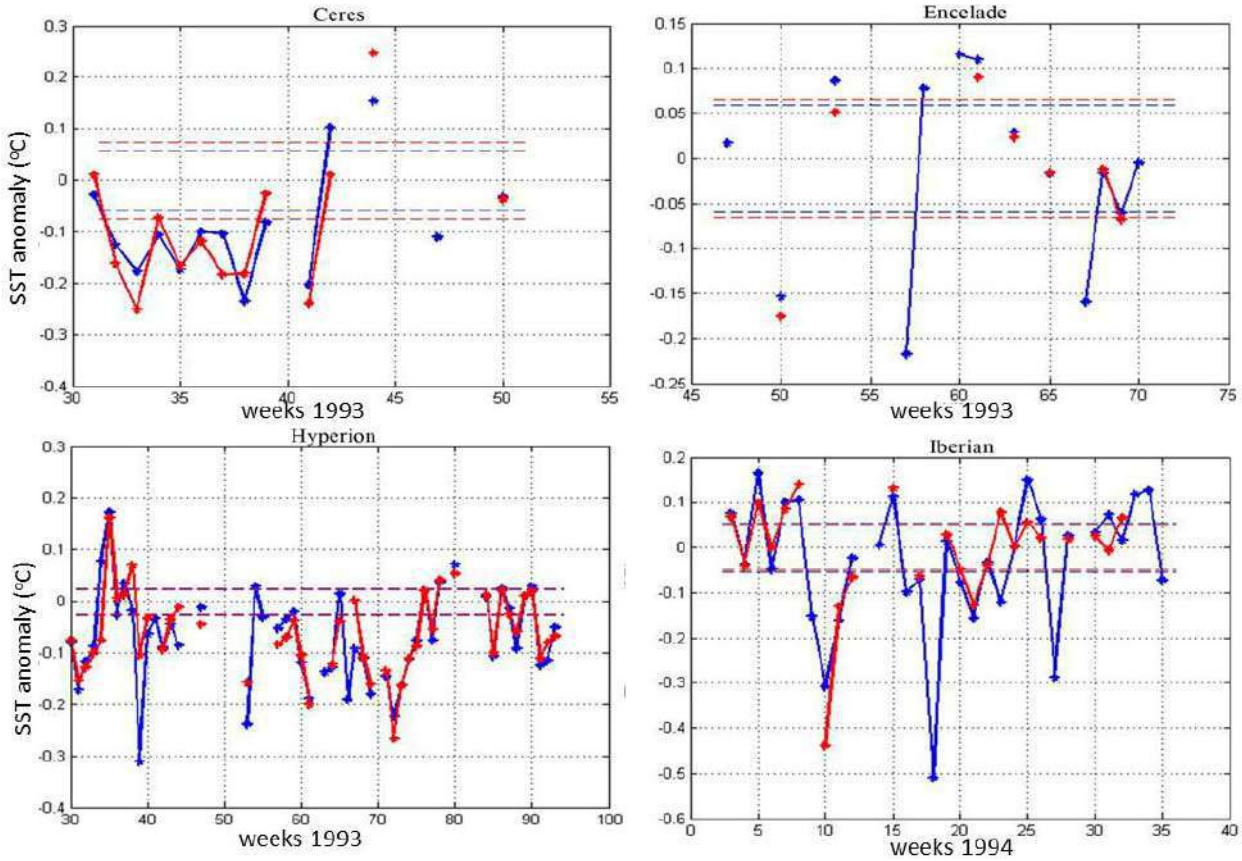

Fig. 7.4. SST anomalies (°C) of meddy surface signals from NOAA AVHRR data (see the meddy trajectories in Fig. 6.11): (b) Ceres, (c) Encelade, (d) Hyperion, (e) Iberian (Bobby). SST anomalies were calculated as the difference between the average SST within a radius of 75 km from the center of the meddy surface signals (SST_1) and the average SST in a 75-100 km ring around the center of the meddy surface signals (SST_2). The blue curves are the estimates from NOAA AVHRR data for quality type 4, the red curves are for type 7. The difference consists in using additional quality criteria for type 7, which potentially better remove the influence of thin clouds in SST data, but also leads to the removal of more valid SST data points. The area between the horizontal dashed lines characterizes insignificant SST anomalies over the Meddy, when the anomaly values are less than the average error in its determination (see Table 7.1).

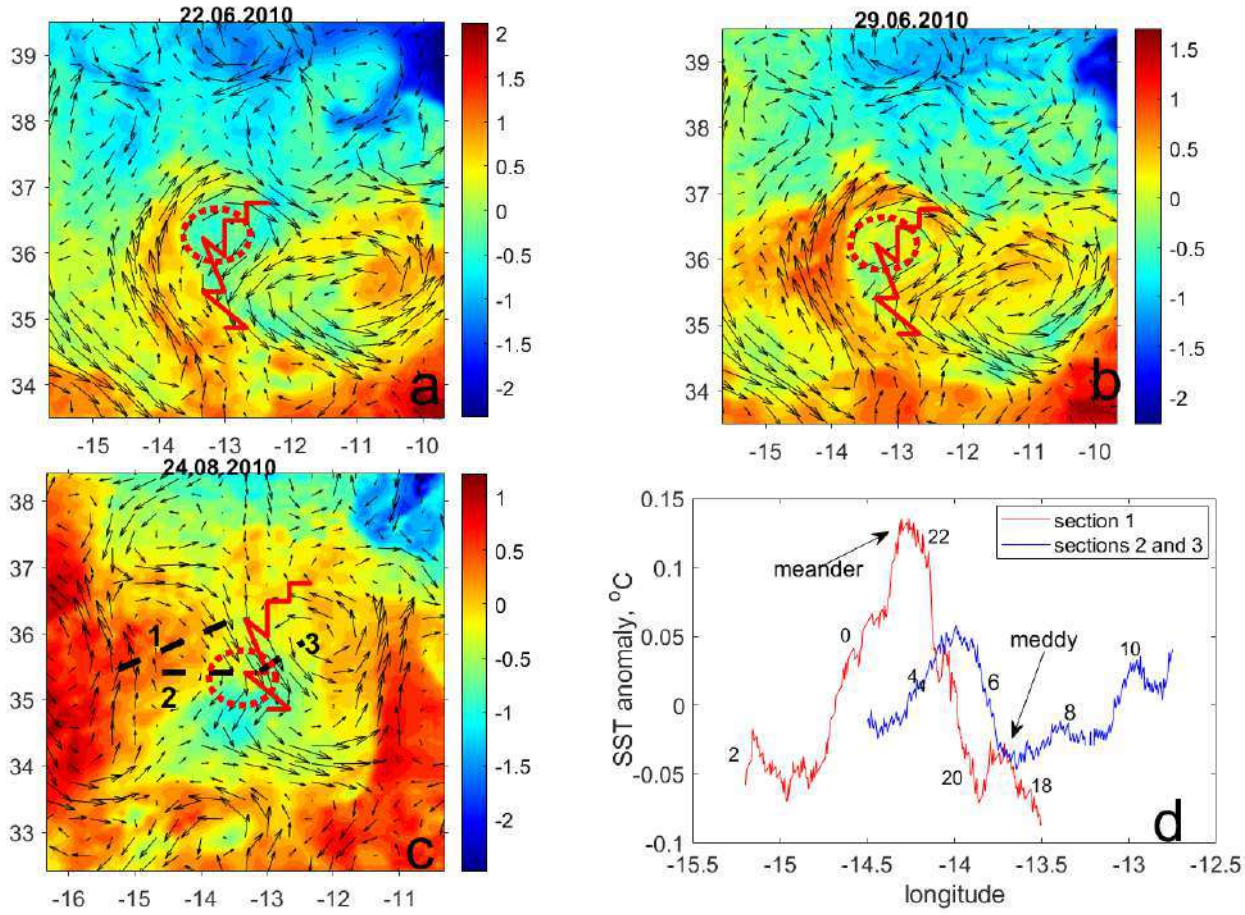

Fig. 7.5. SST anomalies (°C, color) around the surface signal of meddy Don Carlos (outlined with the dotted red circle using the sea surface anomaly of the relative vorticity) for the dates: (a) June 22nd, (b) June 29th, and (c) August 24th of 2010. Anomalies were obtained by subtracting the SST mean for the entire area in the figure. Currents from AVISO altimetry are superimposed. Thick red lines mark the meddy path. The black dotted cross-sections in panel (c) are in situ sections. (d) Temperature anomalies at 4 m depth using the built-in ship thermometer along the transects 1 and 2 shown in (c). The linear trends along sections were removed. The numbers mark the beginning of the hour of the temperature measurement (following Bashmachnikov et al., 2013b).

Below we consider the mechanisms of the formation of negative SST anomalies above anticyclones with a subsurface core.

Figure (7.5) shows an example of the formation of a negative SST anomaly over meddy Don Carlos during its interaction with the Azores Current. First, there was an intrusion of a colder water from the north and northeast into the central part of the meddy surface signal, accompanied by a simultaneous "wrapping" around of warmer waters from the southwest during a northwards excursion of a meander of the Azores Current. By the 3rd week of June, it had been formed a well-defined SST anomaly with a cold core over the meddy compared to the anomalously warm periphery of the meddy surface signal (Fig. 7.5a). By the end of June, the ring of warm water closed (Fig. 7.5b). At the end of August 2010, a cold SST anomaly was still observed over the meddy (Fig. 7.5c), also confirmed by *in situ* observations (Fig. 7.5 d).

For meddy ARGO352 (Fig. 7.3), trapping warmer water in the southwest of the meddy surface signal was observed several times, following by the water "wrapping" around the cold core of the eddy, similar to that shown in figure (7.5) (see for details Bashmachnikov et al., 2013b).

This indicates the importance of the fluid entrainment in the formation of the cold SST anomaly in the meddy surface signal. It can then be expected that the intensification of the anticyclonic circulation over a meddy will lead to an intensification of trapping of the warmer water at its southern side and a subsequent intensification of the meddy-associated negative SST anomaly. To test this hypothesis, cross-correlation coefficients were calculated between the peak vorticity of the meddy surface signal and the SST anomalies in the 0-25 km, 25-50 km and 50-75 km rings relative to 75-100 km ring, all distances are relative to the center of the meddy dynamic signal. With a delay of the SST anomalies by 30 days, the cross-correlations of the negative relative vorticity on the sea surface with the negative SST anomalies in the 25-50 km and 50-75 km rings reached a maximum of 0.7-0.8 for, while with the SST anomaly in the central 0-25 km region the correlation for this lag was 0.5 (all correlations are significant). With a lag of 45 days, the maximum cross-correlations (0.7) were observed already in the 0-25 km and 25-50 km regions, and in the 50-75 km ring the cross-correlation decreased to 0.5. With a lag of 60 days, the cross-correlation remained significant (0.5) only in the central region of 0-25 km. Thus, the negative SST anomaly first intensified at the inner periphery of the meddy surface signal, and then it gradually moved to the center of the surface signal, reaching a maximum approximately 1.5 months after the anticyclonic circulation of the meddy surface signal intensified. Subsequently, the SST anomaly in all three central regions weakened.

In the mesoscale quasi-geostrophic meddy surface signal, the radial velocities are at least an order of magnitude smaller than the azimuthal ones. According to AVISO altimetry data, the azimuthal velocities of the anticyclonic circulation over the meddy were approximately 10 cm s^{-1}. Assuming radial velocities of the order of 1 cm s^{-1}, with a dynamic radius of the surface signal of 50 km, the surrounding water, involved in a circular motion, should reach the center of the meddy surface signal in 2 months. This is close to the time span, at which the SST anomaly at the center of the meddy surface signal passes its peak and begins to weaken.

Thus, the following mechanism can be assumed. The rise of the isopycnals above the meddy (Fig. 6.12) creates conditions for the horizontal transport of colder, denser water from the north into the central part of the surface signal of the meddy, where the water is denser than along its periphery. Warmer and lighter waters, trapped by the eddy from the southwest, cannot penetrate the region of the denser waters above the meddy core and, moving along density gradients, “wrap” around the core of the meddy surface signal.

The isopycnals rise over a subsurface anticyclone, that generates the sea surface signal above meddies, is the precondition for the development of the cold SST core. The high water density in the central part above the subsurface eddy does not allow lighter and warmer waters to penetrate into the core of its surface signal. In this case, the SST signal is significantly amplified due to the capture of cold waters and their penetration into the central part of the surface signal and “wrapping” of warmer waters around the cold center. This explains the delay of several months in the development of the maximum signal in the SST after an acceleration of the anticyclonic circulation over a meddy. Such a process is also possible for the Lofoten Vortex in the Norwegian Sea.

7.2 SECONDARY CIRCULATION OF THE LOFOTEN VORTEX AS A MECHANISM FOR THE DEVELOPMENT OF A NEGATIVE SST ANOMALY ON THE SEA SURFACE

In this section, the secondary ageostrophic circulation in a subsurface eddy is investigated and formulae for estimating the vertical and radial eddy velocities are derived for a Rayleigh-type azimuthal velocity profile. As shown in Kuibin and Akulov (1996), the velocity field in an axisymmetric columnar vortex with helical vortex lines is described with the equations:

$$v_r = 0,\ v_\theta = \frac{1}{r}\Phi(r),\ v_z = v_{z0} - \frac{1}{l}\Phi(r), \tag{7.1}$$

where the function $\Phi(r)$ is a function of the relative vorticity along the *z*- axis of the vortex:

$$\Phi(r) = \int_0^r \omega(r')r'dr' \tag{7.2}$$

Here *r* is the radial distance from the center of the vortex, *l* is the reduced pitch $\hat{h}$ for the spiral vortex lines: $l = \hat{h}/(2\pi)$, v_θ is the azimuthal velocity in the vortex, expressed through its relative vorticity $\omega(r)$, v_r is the radial velocity in the vortex, v_z is the vertical velocity in the vortex, v_{z0} is its value v_z at r =0.

The velocity field of formulae (7.1) satisfies the Euler equations for a density-uniform incompressible inviscid fluid with an arbitrary vorticity distribution. Only the central region of the vortex core is considered, where it is assumed that the water density does not change vertically and horizontally, the radial component of the current velocity is zero, and divergences and convergences are confined exclusively to its upper and lower boundaries outside the region under consideration. Thus, due to the axial symmetry of the vortex and by virtue of the continuity equation, the vertical velocity in the core does not change with *z*.

Taking the Rayleigh radial profile for the azimuthal velocity $v_\theta(r)$, the vertical component of the relative vorticity is written as:

$$\omega(r) = \frac{\Gamma}{\pi R_{vm}^2}\left(1 - \frac{r^2}{2R_{vm}^2}\right)\exp\left(-\frac{r^2}{2R_{vm}^2}\right). \tag{7.3}$$

Here Γ is circulation in the vortex, R_{vm} is the horizontal scale of the vortex, where the azimuthal velocity reaches its maximum (see section 1.3).

Then, according to expression (7.2), the function $\Phi(r)$ has the form:

$$\Phi(r) = \frac{\Gamma}{2\pi R_{vm}^2} r^2 \exp\left(-\frac{r^2}{2R_{vm}^2}\right), \tag{7.4}$$

and expressions for the azimuthal and vertical components of the current velocity in the vortex (Belonenko et al., 2017; Bashmachnikov et al., 2017):

$$v_\theta(r) = \frac{\Gamma}{2\pi}\frac{r}{R_{vm}^2}\exp\left(-\frac{r^2}{2R_{vm}^2}\right), \tag{7.5}$$

$$v_z(r) = v_{z0} - \frac{\Gamma}{2\pi\, l}\frac{r^2}{R_{vm}^2}\exp\left(-\frac{r^2}{2R_{vm}^2}\right). \tag{7.6}$$

When $r = R_{vm}$ the maximum azimuthal velocity is $v_{\theta,\max} = \frac{\Gamma}{2\pi R_{vm}}\exp(-0.5)$. Belonenko et al. (2017) showed that, using the condition of zero integral vertical velocity in the vortex core (vertical transport in the center of the core is balanced by vertical water transport of the opposite sign at its periphery), formula (7.6) becomes:

$$v_z(r) = v_{z0}\left[1 - \frac{n^2}{4 - 2\left(n^2+2\right)\exp\left(-\frac{n^2}{2}\right)}\frac{r^2}{R_{vm}^2}\exp\left(-\frac{r^2}{2R_{vm}^2}\right)\right] \tag{7.7}$$

Here, $r = n\,R_{vm}$ is the radial distance at which the solution is "broken off," that is, it is assumed that beyond this radius the vertical velocities in the vortex is on the background noise level.

Having added an additional condition that the vertical velocity is maximum at the center of the vortex, while it is much less than at the vortex periphery ($v_z(n\,R_{vm})/v_{z0} << 1$), one should look for a value n where the minimum of the function $\left|v_z(n\,R_{vm})/\,v_{z0}\right|$ is achieved. For the Rayleigh vortex, the minimum is achieved at n = 1.9 (Fig. 7.6 a), and $v_z(1.9\,R_{vm})$ =0.

Then we get:

$$v_z(r) = v_{z0}\left[1 - \frac{r^2}{0.6\,R_{vm}}\exp\left(-\frac{r^2}{2R_{vm}}\right)\right], \text{ at } r \le 1.9R_{vm}. \tag{7.8}$$

Though the relative vorticity at a distance of 1.9 R_{vm} of the Rayleigh vortex is small, the azimuthal velocity here decreases only by one half of its peak value (Fig. 7.6 b). Thus, we are forced to terminate the solution on relatively high values of the azimuthal velocity, which is a disadvantage of this solution.

For an anticyclonic vortex with a dynamic radius R_m = 31 km (the distance at which the relative vorticity of the vortex passes through 0, Fig. 7.6 c), the peak azimuthal velocity of the Rayleigh vortex is reached at R_{vm} = 22 km. The vertical velocity component is maximum at the center of the vortex, crosses zero at a distance of r = 20 km and reaches peak negative values at r = 31 km, and then crosses zero again at a distance of 1.9 R_{vm} = 40 km (Fig. 7.6 d).

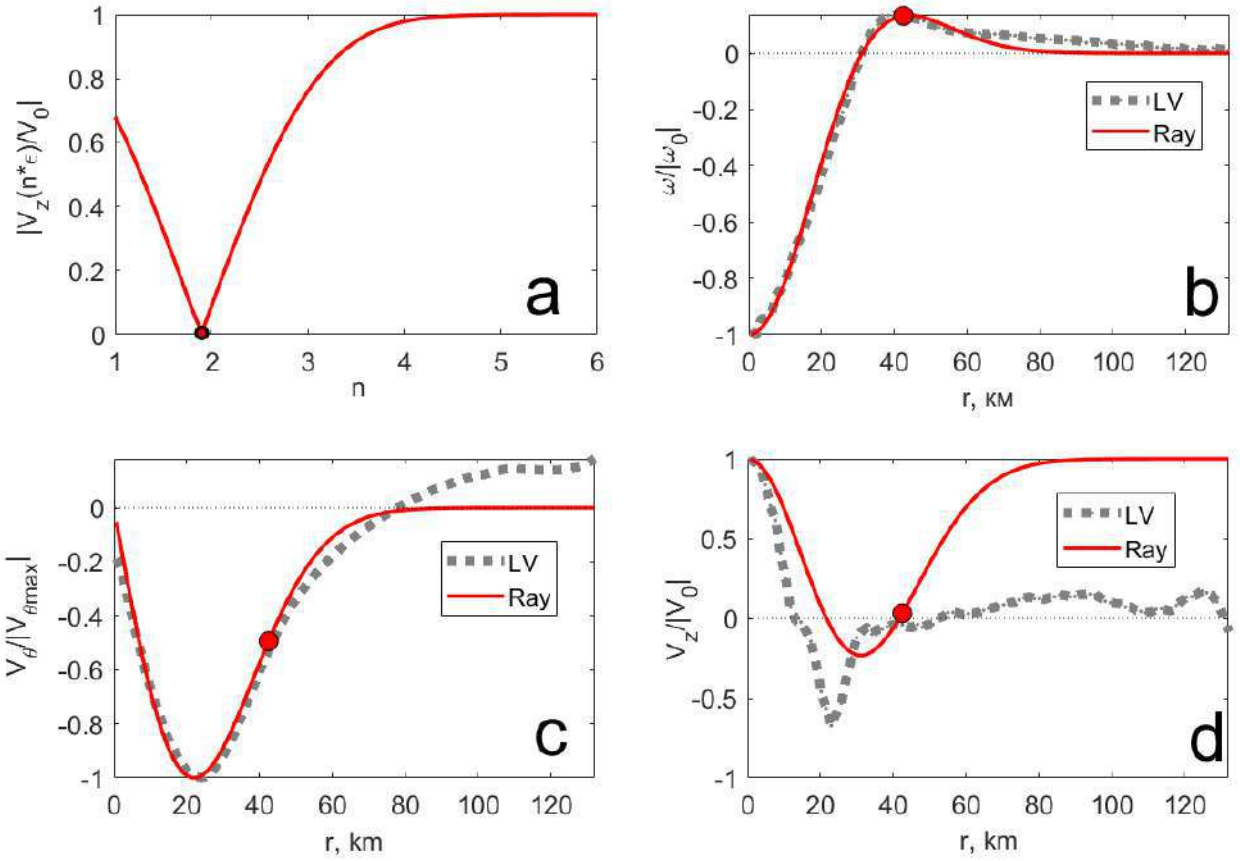

Fig. 7.6. Normalized dynamic characteristics of the vortex core: red solid curves are the theoretical results for the Rayleigh vortex with R_m = 31 km (R_{vm} = 22 km), gray dotted curves are the characteristics of the Lofoten vortex from the MIT GCM model. The time averages for 1993-2015 and the vertical averages in the 0-1000 m layer are plotted: (a) the absolute values of vertical velocity $|v_z(nR_{vm})/v_{z0}(n)|$ as a function of n; (b) radial profiles of the relative vorticity; (c) radial profiles of the azimuthal velocity and (d) radial profiles of the vertical velocity. The artificial cutoff point of the solution is marked with a red circle (n =1.9), i.e. the solution is considered only to the left of the cutoff point (according to Bashmachnikov et al., 2017).

The theory of the vertical velocity field in a vortex, used by Kuibin and Akulov (1996) to derive the original dependencies (7.1) and (7.2), does not take into account the Coriolis force. However, the radial and vertical velocities in the vortex are associated with ageostrophic effects, for which the Coriolis force does not play a leading role.

Comparison with the dynamics of the Lofoten Vortex (LV) in the MIT GCM hydrodynamic model (see section 2.3.7). showed that in the central part of the core the theory gives acceptable results (Fig. 7.6), while at the periphery of the vortex the theory begins to fail. Here the ageostrophic effects of the core weaken and the Coriolis force cannot be neglected.

As was shown in Chapter 5, the hydrodynamic and thermohaline structure of the Lofoten Basin in the MIT GCM model, as well as of the Lofoten Vortex, closely matches observations (see also Nguyen et al 2011, Raj et al 2015, Volkov et al 2015; Bashmachnikov et al 2017; 2018). The azimuthal velocity reaches its peak values in the subsurface core of the Lofoten Vortex (200-1000 m), averaging $v_{\theta,\max,2}$ = 20 cm s^{-1} at a distance of 17-20 km from the center of the vortex; in the layer above the core the values $v_{\theta,\max,1}$ does not exceed 12-15 cm s^{-1}, and below the core and to the

ocean bottom $v_{\theta,\max,3} \sim 5$ cm s^{-1}. The dynamic radius R_m is within 24-35 km, about 30 km, on average, and remains practically unchanged in depth within the vortex core (Fig. 7.6c).

The average vertical velocity characteristics were obtained by averaging the data over time and over the LV azimuth in a coordinate system centered ıın the LV center. The time-averaged distribution of epy vertical velocity in *r*-*z* coordinates has a complex structure (Fig. 7.7a).

The maximum upward vertical velocity is observed in the center of the LV core and reaches $v_{z0} \sim 2\ 10^{-3}$ cm s^{-1}, while the maximum downward vertical velocity is observed at the periphery of the core (at a distance of 12-30 km from the LV center) and is more than 3 times less than $v_{z0} \sim -0.6\ 10^{-3}$ cm s^{-1} (Fig. 7.7a). Taking into account the large area of the outer ring compared to the central region of the vortex, at depths of 0-1000 m, the radially integrated upward transport in the central part of the LV core is approximately compensated by the downward transport at the periphery of the vortex, which is consistent with the assumption used in the derivation of formula (7.8). v_r in the core layer and above is directed to the periphery of the vortex (Fig. 7.6 b), which is consistent with the distribution v_z. In the lower part of the vortex core (1200-1300 m), the downward transport at the periphery of the LV is about 20% stronger than the upward transport along the vortex axis at the same levels, and below, at 1500-2000 m, only a downward transport is detected.

In MIT GCM the Rossby number of the LV is small and amounts to 0.1-0.2 (Bashmachnikov et al., 2017). For such mesoscale eddies, the ratio of radial to azimuthal velocity corresponds to the ratio of ageostrophic to geostrophic forces, which usually differ by about an order of magnitude (Carton, 2001; Barcelo-Llull et al., 2017). Ageostrophic effects in eddies are mainly associated with the centrifugal and frictional forces (Carton 2001), as evidenced by the fact that the radial velocities increase together with the azimuthal velocities (Fig. 7.7b). The ratio of the inertial (centrifugal) force to the geostrophic Coriolis force, $\left[\frac{v_\theta^2}{r}\right] \Big/ \left[f\ v_\theta\right]$, is 0.2-0.3 (Fig. 7.7e). This is close to the ratio of radial and azimuthal velocities in MIT GCM, and also typical for mesoscale eddies of a low Rossby number (Carton, 2001). Consequently, the divergence in the vortex core and the vertical velocity field can be caused by the centrifugal forces of the rotating core.

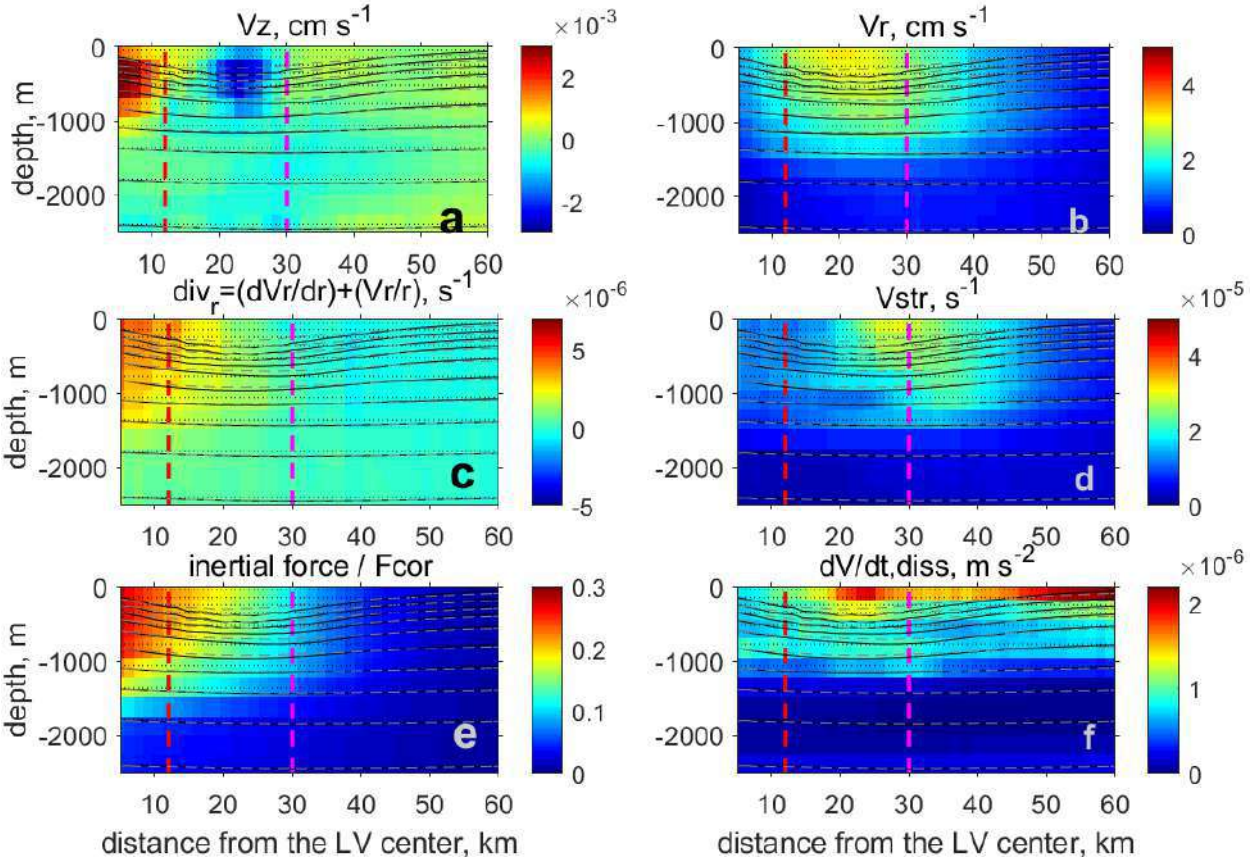

Fig. 7.7. Radial distribution of the LV characteristics averaged over the period of analysis and the LV azimuth in the MIT GCM (0 km marks the LV center): (a) the vertical velocity (positive values are directed upward, cm s^{-1}), (b) the radial velocity (positive values are directed to periphery of the core, cm s^{-1}), (c) the radial divergence (positive is to the periphery of the core, s^{-1}), (d) the horizontal shear (s^{-1}), (e) the Rossby number – the ratio of the centrifugal force to the Coriolis force, (f) the change in horizontal current velocity forced by the turbulent dissipation of kinetic energy (m s^{-2}). Radial distributions (out of scale) of the azimuthal velocity (shown in black solid lines) and of the radial velocity (shown in gray dotted lines) for various vertical levels are measured from reference plains of the corresponding depth (dashed horizontal lines). Red and purple vertical dashed lines indicate radii of 12 km (the vertical velocity in the LV core crosses zero) and 30 km (the relative vorticity in the LV core crosses zero) (from Bashmachnikov et al., 2018).

The maximum radial velocities (Fig. 7.7b) are limited by the inner boundary of the region of the maximum shear (Fig. 7.7d), where the processes of turbulent exchange across the vortex boundary are the most intense. The rate of decrease in horizontal current velocity due to turbulent dissipation, one of the standard MIT GCM variables (Adcroft et al., 2018), reaches its maximum in the inner part of the periphery of the LV core, between the region of the maximum velocity and the maximum shear (Fig. 7.7f). This parameter reaches maximum values at the sea surface and has higher values at the periphery of the core, as well as under the LV core (at a depth of 800-1000 m).

A very similar structure was obtained for the turbulent energy dissipation rate from the results of *in situ* measurements (Fer et al., 2018). Intensifying towards the sea surface, both inertial forces and turbulent velocity dissipation cause an increase in radial divergence towards the sea surface, which leads to the formation of divergence (Fig. 7.7c) and positive values of vertical

velocity in the central part of the LV core. However, the ratio of the force of the turbulent friction to the Coriolis force is about 0.02-0.04, which is an order of magnitude smaller than the ratio of the centrifugal force to the Coriolis force (Fig. 7.7e). Thus, we can assume that the radial ageostrophic component of the current velocity is primarily related to the centrifugal force.

The divergence in the LV core can also be associated with the local divergence of Ekman fluxes of the wind field above the vortex, which can be estimated as (Gaube et al., 2013):

$$v_{z0E} = -\frac{3C_d \rho_a |V_a|}{2\rho f} \bar{\omega}, \tag{7.9}$$

here C_d =10^{-3} is the wind friction coefficient (Bowden, 1988), ρ_a =1.2 kg m^{-3} is the air density, ρ =1030 kg m^{-3} is the water density, f =1.4 10^{-4} s^{-1} is the Coriolis parameter, V_a is the wind velocity above the sea surface, $\bar{\omega}$ is the average relative vorticity of the vortex core.

Taking ρ_a / ρ =10^{-3}, V_a =5 m s^{-1} and $\bar{\omega}$ =3 10^{-5} s^{-1} in the upper part of the LV core, we obtain the vertical velocity: v_{z0E} = 1.5 10^{-4} cm s^{-1}, which is an order of magnitude less than that observed in center of the LV (Fig. 7.7a). Consequently, the effect of local divergence under the influence of the wind above the LV can be neglected compared with the centrifugal force.

Below the LV core, at 1500-2000 m and below, the vertical velocities under the LV core are directed predominantly downward (Fig. 7.7a). This may be associated with the Ekman divergence of the anticyclonic rotational flow in the presence of bottom friction. The related characteristic vertical velocity can be estimated as (Pedlosky, 2013):

$$v_{z0} = C \bar{\omega}_b, \tag{7.10}$$

where $C = \sqrt{\frac{K_z}{2f}}$, K_z is the coefficient of the vertical turbulent viscosity, and $\bar{\omega}_b$ is the mean relative vorticity in the bottom layer. For $v_{\theta,\max}$ ~ 10 cm s^{-1}, $K_z \sim 2.5 \cdot 10^{-3} v_\theta \sim$ 2.5 10^{-4} m^2 s^{-1} (Bowden, 1983; Ozmidov, 1986; Siedler et al., 2001; Bashmachnikov et al., 2013b).

Setting, according to MIT GCM, the average relative vorticity in the lower part of the LV as $\bar{\omega}_b \approx$ -3 10^{-6} s^{-1}, we obtain $v_{z0} \approx$ -0.5 10^{-3} cm s^{-1}. These values are close to the vertical velocity recorded at the lower levels of the model (Fig. 7.7a). Thus, friction at the ocean bottom may cause the observed downward velocities at below the vortex.

Ascending vertical velocity in the core and above the vortex, combined with the descending fluxes at the periphery of the vortex, are reflected in the configuration of isopycnals (Fig. 7.8 a, b). In this case, the structure of vertical velocity field increases the radial gradients of water density above the vortex core, thereby maintaining the anticyclonic circulation in the vortex against dissipation.

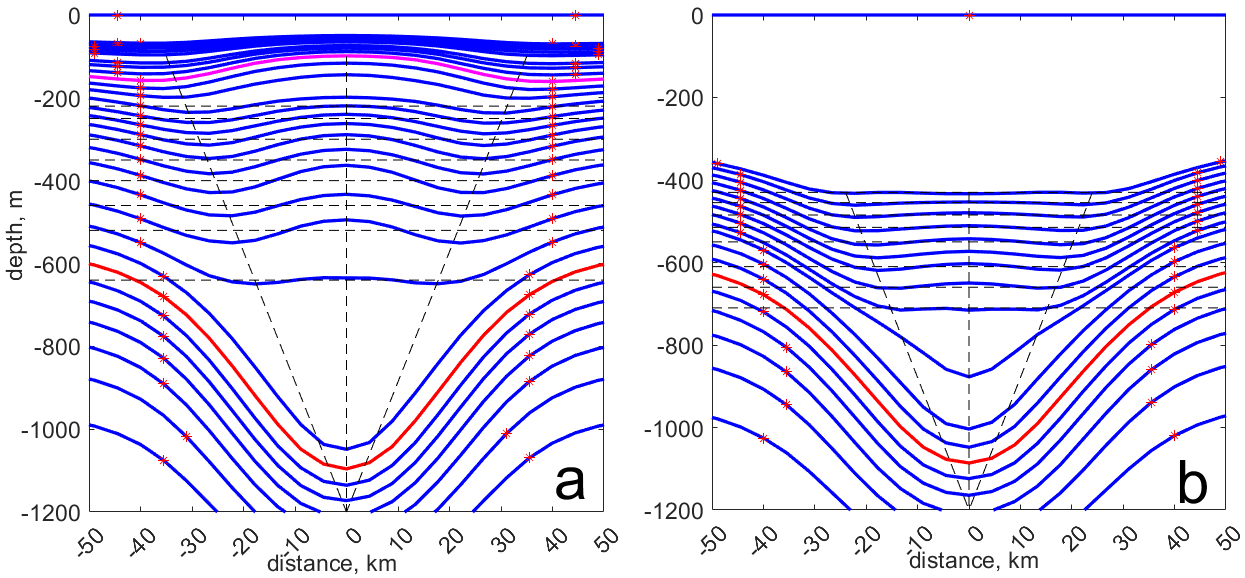

Fig. 7.8. (a) The mean configuration of isopycnals (blue lines) in the LV as a function of distance from the eddy center during the warm season. (b) Same as (a), but for the cold season. Red stars indicate the dynamic radius (R_m, where the relative vorticity changes sign) at a given level. The purple and red isopycnals indicate the upper and lower boundaries of the LV core, respectively. Vertical dotted lines indicate the local maxima and minima of isopycnal depths in the LV core (from Bashmachnikov et al., 2018).

The ascending vertical velocity in the central part of the core leads to a rise of the isotherms in the center of the LV (Fig. 7.8 b). This contributes to the formation of a negative SST (salinity) anomaly over the core, which is confirmed by satellite and in-situ observations (Fig. 7.9a,b).

Such ageostrophic circulation creates the conditions for the emergence of a mechanism of horizontal differential entrainment of colder and warmer water by a rotating eddy, described in the previous section as the main reason for the formation of the negative SST anomalies over meddies (see also Bashmachnikov et al., 2013b, Ciani et al., 2015; Gupta et al., 2020). Indeed, modeling data indicate that the mechanism of capturing the warmer liquid (the Norwegian Current) and "wrapping" it around the core of the subsurface anticyclone is also involved in formation of the SST anomaly over the LV (Fig. 7.9a). Analysis of the SST in the surface anticyclones in the Lofoten Basin, based on *in situ* data, showed that they are characterized by a predominantly positive SST anomaly of their cores (Sandalyuk et al., 2020).

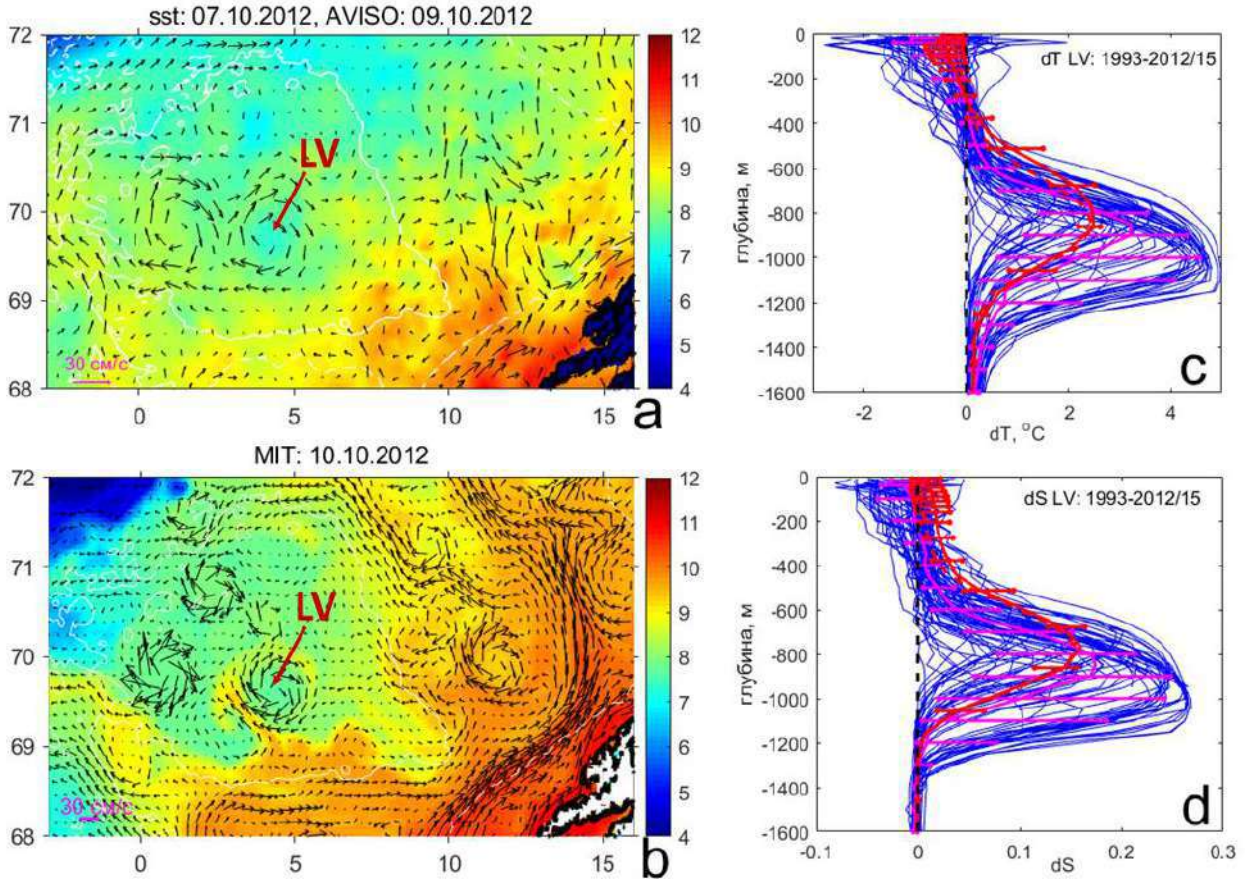

Fig. 7.9. (a) SST from the combined infrared and microwave satellite images of MUR dataset (color, ℃) and the ocean surface currents (vectors) from AVISO satellite altimetry in the Lofoten Basin on 10.10.2012. (b) SST (color, ℃) and current velocity (vectors, only every 3rd vector is represented) from the MIT GCM on 10.10.2012. Vertical profiles of anomalies: (c) water temperature (°C) and (d) water salinity relative to the mean at the corresponding water level from in situ vertical profiles of the EN4 dataset (blue lines). The data, averaged over 1993-2015, in situ (pink lines) and MIT GCM (red lines) are also shown. Horizontal segments show the standard deviation of parameters for selected levels. LV is the Lofoten Vortex (following Bashmachnikov et al., 2018).

To conclude this section, we note that the LV characteristics used here, determined from the model MIT GCM, underestimate the peak azimuthal velocities. Thus, the Rossby number of the LV in the model is 0.2-0.3, while in *in situ* observations it was 0.6-0.8 (Soyland et al., 2016; Fer et al., 2018; Bashamchnikov et al., 2018). This means that the model underestimates the relative contribution of the centrifugal inertial force. Therefore, in the real LV, the divergent fluxes in the upper part of its core should be even more intense. On the other hand, in contrast to the real LV, the LV characteristics in MIT GCM are closer to those of typical large mesoscale anticyclones in the ocean, which makes it possible to directly extend the results obtained to other subsurface anticyclones. We also note that at each individual moment in time the structure of the vertical velocities can be very noisy due to more intense vertical movements of dynamic disturbances of the vortex (Fig. 5.13). Therefore, the above mean pattern of the vertical velocities in the LV (Fig. 7.7a) appears only after averaging both in time and azimuth.

7.3 WHAT DO OCEAN COLOR ANOMALIES ABOVE SUBSURFACE EDDIES INDICATE?

The presence of divergences and convergences in the surface manifestations of subsurface eddies can be identified in chlorophyll-a (Fig. 7.10). An increased chlorophyll concentration in the center of the LV in summer (Fig. 7.10a) may indicate an upwelling of water, while a reduced chlorophyll content at the periphery of the LV may indicate a downwelling. As shown above, both fluxes are connected (Fig. 7.7a).

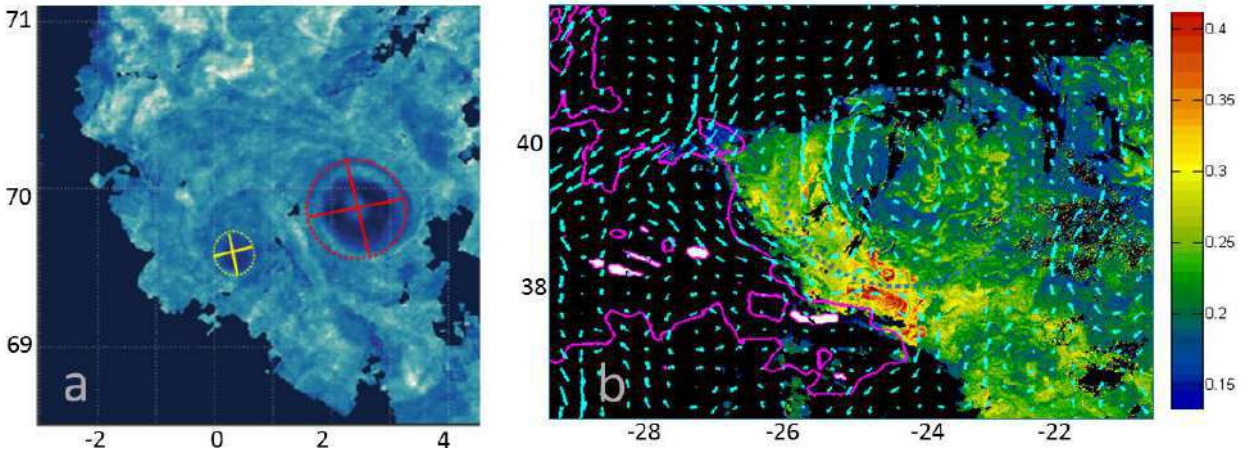

Fig. 7.10. (a) Lofoten Vortex (red circle) and cyclonic vortex (yellow circle) in the chlorophyll-a (color) 07.22.2016 (by Yu. Novikova). (b) Surface manifestation of a meddy (red circle) in MODIS chlorophyll (color) in the subtropical Atlantic north of the Azores on 03.01.2003. AVISO altimetry surface currents are superimposed.

Above the meddy, a convergence of waters entering the central area of the meddy surface signal from the north is clearly seen in chlorophyll-a (Fig. 7.10b). This is consistent with the results obtained from the analysis of the SST distribution (Fig. 7.5). If we assume that filaments of a higher chlorophyll concentration travel a distance of 0.5 eddy radius per half revolution of the meddy surface signal around its axis, then the radial velocity of the convergence is approximately 6 times less than the azimuthal velocity in the meddy surface signal. Estimating the azimuthal velocity from AVISO altimetry as 10 cm s^{-1} and a radius of the surface meddy signal of 100 km, then the azimuthal path traveled with as π*100 km. Then the time, during which the filament (Fig. 7.10b) performs a half-turn around the center, is 35 days. With a radial advance to the center of the meddy surface signal over this period of 50-80 km, a radial velocity directed towards the center of the signal is 1-3 cm s^{-1}. However, the ageostrophic convergence of waters in the meddy surface signal is opposite to the water divergence above the LV core (Fig. 7.7a-c). This indicates a difference in the vertical circulation systems in the meddy surface signal and in the LV. This is not surprising given that the LV core directly impacts the sea surface, while the meddy surface signal is an independent surface anticyclone generated by the movement of the meddy at bigger depth.

7.4 DISCUSSION OF THE RESULTS OF CHAPTER 7

In this section, it was shown that subsurface eddies, both with a deep core (like meddies) and with a core, the upper boundary of which is located in the close proximity to the sea surface

(like the Lofoten Vortex), create a statistically significant negative anomaly in SST, which opposes to a positive SST anomaly, characteristic of surface anticyclones.

While the dynamic (anticyclonic) surface signal of a subsurface anticyclone detected in satellite altimetry is not fundamentally different from that of the signal of a surface anticyclone generated by instability of sea surface currents, the sign of the related SST anomalies provides a potential to separate surface and subsurface eddies. This method was successfully applied in practice to detect a meddy (Fig. 7.5), which was identified in the satellite images before a cruise due to a negative SST anomaly in the central area of an anticyclone. The study above showed that the stability of the meddy signal in SST is significantly lower than the stability of its dynamic signal in the sea level. First, this is due to a small SST anomaly formed. It is often at the limit of accuracy of SST assessment from modern satellite observations, while an overall noise level of the SST field is high. There are many reasons for the relatively high level of noise in the SST distribution: change in the intensity of the vertical mixing across the seasonal thermocline due to changes in the wind velocity, the incomplete removal of the effects of thin clouds, of aerosols, etc. However, the mean negative SST anomalies over meddy centers, averaged over several months, were statistically significant. This makes it possible to reliably distinguish between surface and subsurface anticyclones, combining altimetry and SST data, for eddies that could be tracked for a sufficiently long time. When analyzing tracks, it should be taken into account that surface anticyclones, moving along inclined isopycnals, can become subsurface ones (Barcelo-Llull et al., 2017), and the accompanying SST anomaly may, at some point, change its sign.

Positive SST anomalies at a surface anticyclone are not only formed during their generation by trapping water on the warm side of the front, but are also further supported by the convergence of surface water in the upper part of its core. The mechanism of this convergence is usually associated with Ekman divergence at the lower boundary of an anticyclone due to friction against the undelaying layer or the bottom layer (Pedlosky, 2013), and the associated downwelling of water in the central part of the core of an anticyclone (Fig. 7.11a).

Analysis of the results of the MIT GCM hydrodynamic model showed that the vertical secondary circulation in subsurface anticyclones differs significantly from that in surface anticyclones (Fig. 7.11b). In the upper part of the core of subsurface anticyclones a water divergence is observed, which leads to the upwelling along the axis of the anticyclone, compensated by a downwelling along its periphery. This pattern also differs from the secondary circulation over seamounts in the subsurface Taylor cones, which is similar to that in the surface anticyclones (Mullineaux and Mills, 1997, White et al., 2007). A gradual convergence of the maxima of the downward vertical velocity towards the vortex axis with depth was additionally revealed. The reason for the divergence at the upper boundary of the core presumably are the inertial (centrifugal) accelerations. Previous studies have emphasized the importance of the inertial forces in dynamics of ocean mesoscale eddies (see, e.g., Carton, 2001, Chelton et al., 2011). The accelerated dissipation of the kinetic energy of anticyclones near the sea surface also plays a role, both being due to an increase in the dynamic instability generated by the inertial components of the rapidly rotating core, and by a higher dissipation due to an increase of the turbulent friction coefficients near the dynamically active sea surface. The dominant downwelling under the core, as in surface anticyclones, is a consequence of Ekman divergence in the bottom layer (Fig. 7.11b).

It is shown above that reduced SST values over subsurface anticyclones can be associated with several different processes. The most obvious is the rise of isopycnals (and isotherms) above the core of a subsurface eddy due to the secondary circulation of the core (see Section 7.2), which

further supports anticyclonic rotation and adds in increasing stability of the subsurface anticyclone. In subtropical latitudes, as well as in subpolar latitudes in summer, such SST anomalies can be masked with the seasonal thermocline, occasionally appearing during the periods of increased wind mixing. During the cold season, convection Lofoten Vortex reaches the warm core of the anticyclone and can, on the contrary, form positive SST anomalies.

In addition to the isopycnal rise, an equally important reason for the formation of a negative SST anomaly above a subsurface anticyclone is the differential involvement of the surrounding liquid in the anticyclonic rotation in the surface layer. In this case, relatively cold and dense water (usually entrained from the north) is transported to the center of the surface signal of the subsurface eddy, and warmer water (usually entrained from the south) swirls along the periphery of the emerging cold core. This mechanism is ensured by the dome-shaped rise of isopycnals above the core of a subsurface anticyclone, which does not allow less dense warm water to penetrate into the central region above the eddy. For anticyclones with deep cores, such as meddies, the latter mechanism seems to be the main one, although this mechanism was also observed in the Lofoten Vortex. For the effective functioning of the mechanism of capturing and "wrapping" of warm waters around the surface dynamic signal of a meddy, the presence of sufficiently intense background SST gradients is required. In the subtropical Atlantic, the meridional SST gradient increases in winter and spring, and it is during these seasons that the most pronounced negative SST anomalies over meddies should be expected.

The difference between the mechanisms of generation of the negative SST anomaly over a meddy and over the LV is also associated with the much lower *f/N* ratio in the subtropics than in the subpolar regions. The LV core is located close to the sea surface (200-1000 m), and therefore, with weak stratification of the upper ocean, processes in the upper part of the LV core are directly manifested on the sea surface (Fig. 7.11 b).

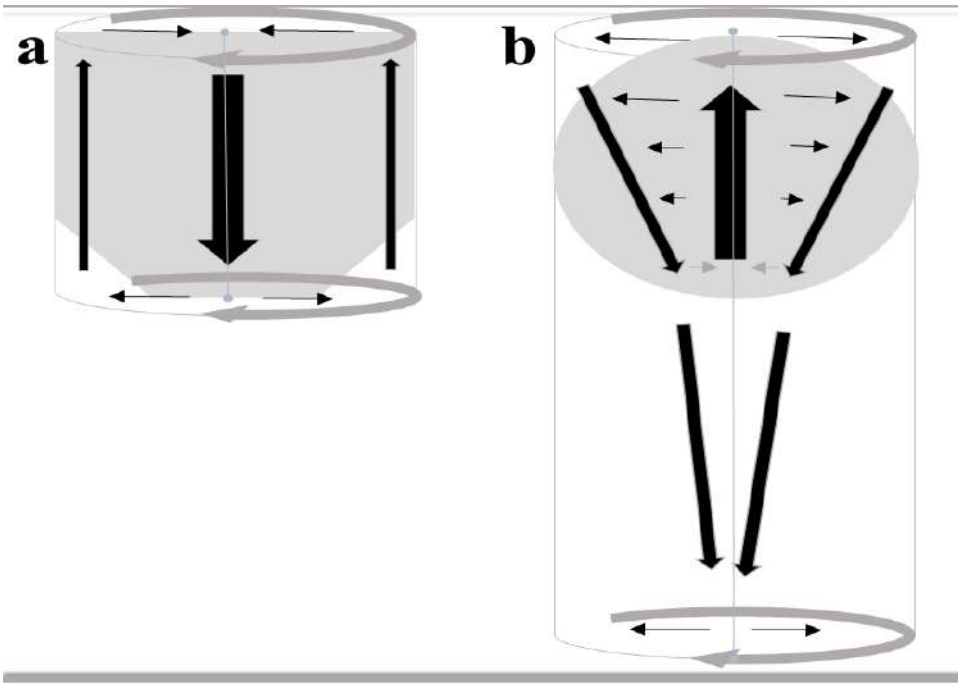

Fig. 7.11. Schematic representation of the secondary circulation for: (a) a surface anticyclone, (b) a subsurface anticyclone with a shallow core. The blue and yellow horizontal lines represent the sea surface and the ocean bottom, respectively.

7.5 CONCLUSIONS OF CHAPTER 7

1. Unlike surface anticyclones, surface signals of subsurface anticyclonic eddies appear in the SST as cold anomalies, often surrounded with a ring of warmer water.
2. Two mechanisms for the formation of negative SST anomalies over subsurface anticyclones have been proposed: for anticyclones with a shallow core – the rise of isopycnals above the core, for anticyclones with a deep core – the transport of colder waters to the central part of the surface signal of the subsurface anticyclone and "wrapping" of warmer waters around the cold core.
3. A new scheme of the secondary ageostrophic circulation in a subsurface anticyclone is proposed. Vertical velocities in such a subsurface anticyclone are directed upward along the vortex axis and downward along its periphery. The water density anomalies formed by these ageostrophic current velocities contribute to maintaining the anticyclonic rotation of the eddy. Under the eddy core, vertical velocities are directed downward everywhere. Theoretical estimates of the pattern of vertical ageostrophic velocities in the Rayleigh vortex are obtained.
4. It is shown that inertial terms, together with the intensified water dynamics in the upper ocean, form the most probable mechanism for an enhanced dissipation of the kinetic energy of a subsurface anticyclone in the upper part of its shallow core, which generates divergence in the upper part of the core and forces the secondary ageostrophic circulation.

8. FINAL REMARKS

The dissertation presents the results of the research on dynamics of surface and subsurface mesoscale eddies in the North Atlantic and the Nordic Seas. The main results of the work are linked to the dynamics of intrathermocline Mediterranean water eddies (meddies) with deep cores (600-1500 m) and of the quasi-permanent Lofoten Vortex (LV) with a near-surface core (200-1000 m). Particular attention is paid to life cycles of subsurface eddies, the characteristic features of their dynamics at different stages of their life cycles, as well as of their manifestations on the sea surface. The work uses *in situ* observations, including those performed by the author, satellite observations (satellite altimetry, sea surface temperature, ocean color and SAR images), as well as data from high-resolution numerical models (quasi-geostrophic and primitive equation models).

Quite significant differences in the characteristics (primarily, in the core depth) and life cycles of the studied eddies contributed to the identification of general characteristics of subsurface vortices, as well as of dynamics of eddies with deep and near-surface cores. This makes the results of the analysis of meddies and LV dynamics complementary. Meddies, the cores of which does not directly affect the ocean surface, are generated at the eastern boundary of the ocean and move westward across the areas with a gradually increasing level of background intensity of ocean dynamics. This makes it possible to investigate interactions of eddies with the mean currents and seamounts for gradually changing background conditions and for different age of the eddy core. The LV, on the contrary, directly affects the ocean surface. The vortex is permanently located in the central part of the Lofoten Basin, and does not directly interact with the steep slopes of the basin or with the topographically trapped branches of the Norwegian Current. This creates "idealized" conditions for identifying the basic dynamic processes in an eddy and its interaction with other eddies. The long existence of the LV makes it possible obtaining statistics on such interactions under the similar background ocean conditions. Despite the differences in the characteristics of eddies and of the background ocean conditions, many of the results obtained for meddies and for the LV are the same. This suggests that basic features of the dynamics of subsurface vortices were describer, that can be extended to the dynamics of mesoscale eddies in any other area of the open ocean.

For the first time, the regularity of the meddy merger has been shown using *in situ* observations (Chapter 4). Mergers increase the lifespan of meddies and provide the opportunity for them to spread over distances comparable to the size of the ocean. The mechanisms of eddy merger and dissipation were studied using the Lofoten Vortex, as an example (Chapter 5), which can be treated as a “natural laboratory” for such studies. Accumulated statistics have revealed how mergers, one of the main mechanisms of regeneration of the LV, affect the kinetic and available potential energy of the vortex. The conditions for merging were refined, one of which is the presence of a background velocity pushing one of the anticyclones towards the other. Such a velocity pattern could be formed by a cyclone located in the immediate vicinity of two interacting anticyclones and often formed as a result of interaction of these anticyclones. The results suggest that the limitations in the freedom of movement of the interacting eddies may facilitate their merger. Besides the field of an external velocity, such conditions may be also linked to topography. The curved shape of the “Horseshoe” seamount chain, limiting the western and southern Iberian Basin and forming a barrier across one of the main meddy propagation paths (the Central path), is suggested to contribute to the observed active meddy merger in this particular area.

The mechanisms of vortex energy dissipation were also examined in detail using the LV as an example (Chapter 5). The results of various idealized experiments with a quasi-geostrophic model were compared with a more realistic results of the primitive equations hydrodynamic model MIT GCM, which had previously undergone multiple validations against observations of the characteristics of the LV and the Lofoten Basin. It was shown that the presence of small topographic features (bottom depression by less than 10% of the sea depth) leads to a significant stabilization of the LV if, together with the background currents, these features minimize the

gradients of the background potential vorticity distribution in the vicinity of the vortex. Under such conditions, the lifetime of the LV increased by more than two times compared to the flat bottom version of the model. A significant increase of the eddy stability in the MIT GCM was also a result of the presence of a strong nonlinearity of development of disturbances. The latter is not a part of a simplified approximation of the vortex in the quasi-geostrophic model used in the study. In the MIT GCM, disturbances concentrated in the vortex skirt, where a strong velocity shear is observed. Here the filaments are generated. Through the separation of filaments, the vortex “gets rid” of the disturbances, preventing instability from penetrating deeply into the core and adding to its disintegration. The presence of such filaments was previously identified from *in situ* observations of meddies. This indicates the universality of this mechanism, which increases the long lifespan of meddies, among other reasons.

The quasi-permanent existence of the LV made it possible to identify and theoretically describe a new scheme of ageostrophic (secondary) circulation in the subsurface anticyclone (Chapter 7). Such a system of ageostrophic circulation should be characteristic of all subsurface anticyclones, but was not previously identified due to the presence of the strong noise from instabilities of the cores of anticyclones, where the vertical velocities are much higher than the vertical velocities of the mean ageostrophic circulation in the core. To isolate the mean ageostrophic circulation, multi-month time series of high-resolution observations are required, preferably with space-time homogeneous conditions in the surrounding ocean, which case is very rare in the ocean.

Based on the analysis of the mid-depth currents, of the mechanism of spreading of the tongue of Mediterranean Water and of the spatial distribution of meddies, the hypothesis on the critically important role of meddies in the spreading of the Mediterranean Water was confirmed. The quantitative of these estimates are complicated due to the lack of information on the average number of meddies generated per year. Similar studies for surface eddies in the Norwegian Sea showed that the Norwegian Current loses a total of about 30% of its heat through the generation of mesoscale eddies along the Scandinavian Peninsula (Chapter 3). Heat transport with mesoscale eddies makes a significant contribution to the formation of an anomalously large reservoir of warm water in the Lofoten Basinю Therefore, transport with mesoscale eddies and can be comparable to water advection in spreading of water masses in the ocean.

A significant part of the present research is devoted to the analysis of the manifestations of subsurface eddies on the sea surface (Chapters 6 and 7). In particular, for the first time, a detailed statistical and theoretical analysis of the appearance of meddies in the altimetry and SST was carried out. A link has been established between the intensity of the surface signal of subsurface eddies and the main characteristics of the eddies and of the background ocean. It has been found that a subsurface anticyclone, in contrast to a surface one, forms a predominantly negative SST anomaly, which makes it possible identifying subsurface anticyclones in satellite data. Unfortunately, the small values and not very high stability of such anomalies reduce the representativeness of the observed signal of subsurface eddies, preventing an unambiguous interpretation of an individual observation of the SST anomaly. An accumulation of their statistics over a certain period of time is required. Two mechanisms for the formation of negative SST anomalies over subsurface anticyclones were identified, the relative role of which depends on the depth of the eddy core. For deep-core anticyclones (meddies), the dominant mechanism is the "wrapping" of the warm water being entrained in a circulation around the cold core of the surface eddy signal. For anticyclones with a near-surface core (the LV), a formation of the cold SST anomaly due to the secondary circulation of the core, which leads to a rise in isotherms in the center of the vortex, forms another important mechanism.

The results of this research lay the foundation for creating algorithms for identifying subsurface eddies on the ocean surface using satellite data. However, to create stable algorithms, a number of issues still need to be resolved. In particular, the relative role of different mechanisms for possible intensification of the surface eddy signals by the mean current and near topography needs to be investigated. Further statistics on the characteristics of the signals of subsurface eddies

on the sea surface depending on the characteristics of these eddies and the background ocean conditions is required. Due to our present the limited abilities in observing subsurface eddies with *in situ* data and a number of known shortcomings of numerical models, identification and tracking of subsurface eddies on the sea surface can become one of the promising directions for resolving the issue of the relative contribution of subsurface eddies in the spreading of the mid-depth water masses in the ocean.

LIST OF THE BASIC NOTATIONS AND ABBREVIATIONS

AC – anticyclone
ACC – the Antarctic Circumpolar Current
IR - infrared range
LV – the Lofoten Vortex
meddy –Mediterranean water eddy
MOC – the Meridional Overturning Circulation
SAR – synthetic aperture radar image
MW – the Mediterranean Water
SST – sea surface temperature
OC – ocean color (chlorophyll-a)
JEBAR – Joint Effect of Baroclinicity and Bottom Relief
MIT GCM - MIT hydrodynamic climate model
MUC – the Mediterranean Undercurrent
NwAC – the Norwegian Atlantic Current
NwAFC – the Norwegian Atlantic Front Current (the western branch)
NwASC – the Norwegian Atlantic Slope Current (the eastern branch)
QG – quasigeostrophic model
WSC – the West Spitsbergen Current

Bu – Burger number
E_k – kinetic energy of an eddy
E_p – available potential energy of an eddy
f – the Coriolis parameter
g – the acceleration of gravity
H_L – water depth
H – depth of eddy core
H_s – average depth of an undisturbed isopycnal outside a meddy
H_m – elevation of an isopycnal above a meddy relative to the background
ΔH – the maximum elevation of an isopycnal above tahe meddy
h – vertical extent of the eddy
N – buoyancy frequency
P – water pressure
q – quasi-geostrophic potential vorticity
$\tilde{q}$ – potential vorticity in the meddy core,
$\tilde{q}_0$ – background potential vorticity
r – distance from the center of an eddy in the polar coordinates
R – vortex radius
R_m – radius of transition of the eddy relative vortex across zero
R_{vm} – radius at which the azimuthal velocity v_θ reaches its maximum ($v_{\theta\max}$)
$Rd = \frac{N H}{f}$ – 1st baroclinic Rossby deformation radius

$Re = \frac{v_\theta R}{\upsilon}$ – eddy Reynolds number

$Ri = N^2 \Big/ \left(\partial v_\theta / \partial z\right)^2$ – Richardson number

$Ro = \frac{V_\theta}{f R}$ – eddy Rossby number

S – water salinity

T - water temperature

u – meridional component of the current velocity

v – zonal component of the current velocity

v_θ ($v_{\theta m}$) – (maximum) azimuthal velocity in the eddy core

v_0 – maximum azimuthal velocity of the signal of a subsurface eddy on the sea surface

v_r – radial velocity in an eddy

v_m – the maximum azimuthal velocity in the core of a subsurface vortex

w – vertical velocity

β – rate of a linear change of the Coriolis parameter with latitude ($f = f_0 + \beta y$)

δ – distance between the centers of eddies or the centers of their surface signals

ε – turbulent energy dissipation rate

P – potential vorticity

θ – azimuth in the polar coordinates

ρ – water density

ρ_0 – average value of water density (a constant)

τ – the period of time during which a sea surface signal is formed above a subsurface eddy

$\ddot{\upsilon}$ – molecular viscosity

ω – relative vorticity

ω_m – maximum value of relative vorticity in the center of a subsurface eddy

ω_0 – maximum value of relative vorticity at the center of the sea surface signal of a subsurface eddy

ψ – stream function

ζ - sea level

REFERENCES

1. Alekseev G.V., Bagryantsev M.V., Bogorodsky P.V. et al. Structure and circulation of water in the northeast of the Norwegian Sea // Problems of the Arctic and Antarctic. – 1991. – No. 65. – pp. 14-23. (in Russian)
2. Atajanova O. A., Zimin A. V., Romanenkov D. A., Kozlov I. E. Observation of small eddies in the White, Barents and Kara seas according to satellite radar measurements // Marine Hydrophysical Journal. – 2017. – No. 2 (194). – P. 80-90. (in Russian)
3. Afanasyev Ya. D., Voropaev S. I. On the spiral structure of mushroom-shaped currents in the ocean // Izvestia of the USSR Academy of Sciences. – 1989. – T. 308. – No. 1. – pp. 179-183. (in Russian)
4. Afanasyev Ya. D., Voropaev S. I., Filippov I. A. Model of mushroom-shaped flows in a stratified fluid under continuous action of a pulse source // Izvestia RAS. Physics of the atmosphere and ocean. – 1989. – T. 25. – No. 7. – pp. 741-749. (in Russian)
5. Bashmachnikov I. L., Yurova A. Yu., Bobylev L. P., Vesman A. V. Seasonal and interannual variability of heat fluxes in the Barents Sea region // Izvestia of RAS. Physics of the atmosphere and ocean. – 2018. – T. 54. – No. 2. – pp. 239-250. (in Russian)
6. Bashmachnikov I. L., Belonenko T. V., Kuibin P. A. Application of the theory of columnar Q-vortices with a helical structure to the description of the dynamic characteristics of the Lofoten eddy of the Norwegian Sea // Bulletin of St. Petersburg University. Geosciences. – 2017. – No. 3. – pp. 221-236. (in Russian)
7. Belkin I.M., Kostyanoy A.G. Intrathermocline vortices in the World Ocean and their regional features // Coherent structures and self-organization of oceanic movements. – 1992. – P. 112. (in Russian)
8. Belkin I.M., Emelyanov M.V., Kostyanoy A.G., Fedorov K.N. Thermohaline structure of intermediate ocean waters and intrathermoclinic vortices // Intrathermoclinic vortices in the ocean / Ed. KN Fedorov. M.: IOAN USSR. – 1986. – P. 8-34. (in Russian)
9. Belonenko T.V., Bashmachnikov I.L., Koldunov A.V., Kuibin P.A. On the vertical component of velocity in the Lofoten mesoscale eddy of the Norwegian Sea // Izvestia of RAS. Physics of the atmosphere and ocean. – 2017. – T. 53. – No. 6. – pp. 728-737. (in Russian)
10. Belonenko T.V., Volkov D.L., Norden Yu.E., Ozhigin V.K. Water circulation in the Lofoten Basin of the Norwegian Sea // Bulletin of St. Petersburg University. Geosciences. – 2014. – No. 2. – pp. 108-121. (in Russian)
11. Belonenko T.V., Koldunov A.V., Sentyabov E.V., Karsakov A.L. Thermohaline structure of the Lofoten eddy of the Norwegian Sea based on expeditionary research and hydrodynamic modeling data // Bulletin of St. Petersburg University. Geosciences. – 2018. – T. 63. – No. 4. – pp. 502-519. (in Russian)
12. Belonenko T.V., Sandaluk N.V. Comparison of the contribution of linear and nonlinear effects to sea level variability using satellite data //Modern problems of remote sensing of the Earth from space. – 2018. – T. 15. – No. 1. – pp. 29-41. (in Russian)
13. Belonenko T.V., Zakharchuk E.A., Fuks V.R. Gradient-eddy waves in the ocean. St. Petersburg University Publishing House, 2004. 212 p. (in Russian)
14. Belonenko T.V. et al. Thermohaline structure of the Lofoten eddy of the Norwegian Sea based on expeditionary research and hydrodynamic modeling data // Bulletin of St. Petersburg University. Geosciences. – 2018. – T. 63. – No. 4. – pp. 502-519. (in Russian)
15. Belyakov L.N., Volkov V.A. Spatial distribution of mesoscale subsurface currents in the Amerasian sub-basin of the Arctic Ocean // Dokladi of the Academy of Sciences. – 1980. – T. 254. – No. 3. (in Russian)
16. Benilov A. Yu., Safray A. S., Filyushkin B. N., Kozhelupova N. G. On the nonlinear dynamics of lenses of Mediterranean water “meddie” // Fundamental and Applied Hydrophysics. – 2021. – T. 13. – No. 3. – pp. 20-42. (in Russian)

17. Bowden K. Physical oceanography of coastal waters. M.: Mir, 1988. 324 p. (in Russian)
18. Ginzburg A.I., Fedorov K.N. Mushroom-shaped currents in the ocean according to satellite image data // Investigation of the Earth from Space. – 1984. – No. 3. – pp. 19-26. (in Russian)
19. Ginzburg A. I., Krek E. V., Kostyanoy A. G., Solovyov D. M. Evolution of a mesoscale anticyclonic vortex and vortex dipoles/multipoles based on it in the South-Eastern Baltic (satellite information: May–July 2015) //Oceanological research. – 2017. – T. 45. – No. 1. – pp. 10-22. (in Russian)
20. Grachev Yu. M., Enikeev V. Kh., Koshlyakov M. N. Structure and evolution of the field of synoptic vortices at the POLIMODE test site in March-May 1978 // Izv. POLYMODE. M.: IOAN USSR. – 1982. – No. 8. – pp. 13-31. (in Russian)
21. Demidov A. N., Filyushkin B. N., Kozhelupova N. G. Detection of Mediterranean lenses in the Atlantic Ocean according to measurements of profilers of the ARGO project // Oceanology. – 2012. – T. 52. – No. 2. – pp. 190-190. (in Russian)
22. Dykhno L. A., Morozov E. G., Nikitin S. V. et al. About one mechanism of destruction of lenses of Mediterranean waters in the ocean // Oceanology. – 1991. – T. 31. – No. 1. – P. 55. (in Russian)
23. Egorikhin V.D., Ivanov Yu.A., Kort V.G. et al. Intra-thermocline lens of Mediterranean water in the tropical part of the North Atlantic // Oceanology. – 1987. – T. 27. – No. 2. – pp. 165-175. (in Russian)
24. Elkin D.N., Zatsepin A.G. Laboratory study of the mechanism of periodic vortex formation behind capes in the coastal zone of the sea // Oceanology. – 2013. – T. 53. – No. 1. – pp. 29-41. (in Russian)
25. Zhmur V.V. Mesoscale eddies of the ocean. M: GEOS, 2010. 290 p. (in Russian)
26. Zhmur V.V., Novoselova E.V., Belonenko T.V. Potential vorticity in the ocean: Ertel and Rossby approaches with estimates for the Lofoten eddy // Izvestia RAS. Physics of the atmosphere and ocean. – 2021. – T. 57. – No. 6. – pp. 721-732. (in Russian)
27. Zhmur V.V., Sviridov S.A., Tarakanov R.Yu. A path of 90 years. On the occasion of the 90th anniversary of the participant in the experiment, Test Site 70, Professor M.N. Koshlyakova //Oceanological research. – 2020. – T. 48. – No. 3. – pp. 226-244. (in Russian)
28. Zhmur V.V., Belonenko T.V., Novoselova E.V., Suetin B.P. Direct and reverse energy cascade when pulling vortices in the ocean // Dokladi of the Russian Academy of Sciences. – 2023. – T. 508. – No. 2. – pp. 270-274. (in Russian)
29. Zhurbas V. M., Lozovatsky I. D., Ozmidov V. S. The influence of seamounts on the distribution of lenses of Mediterranean water in the Atlantic Ocean // Dokladi of the USSR Academy of Sciences. – 1991. – T. 313. – No. 5. – pp. 1224-1229. (in Russian)
30. Zatsepin A. G., Kostyanoy A. G. Laboratory studies of the instability of baroclinic vortices and fronts // Coherent structures and self-organization of ocean movements. – 1992. – P. 163–176. (in Russian)
31. Zatsepin A. G., Didkovsky V. L., Semenov A. V. Self-oscillating mechanism of formation of a periodic vortex structure from a stationary local source on an inclined bottom in a rotating fluid // Oceanology. – 1998. – T. 38. – No. 1. – P. 47–55. (in Russian)
32. Zatsepin A.G., Baranov V.I., Kondrashov A.A. et al. Submesoscale eddies on the Caucasian shelf of the Black Sea and the mechanisms generating them // Oceanology. – 2011. – T. 51. – No. 4. – pp. 592-605. (in Russian)
33. Zimin A.V. Regularities of submesoscale processes and phenomena in the White Sea // Scientific notes of the Russian State Humanitarian University. – 2016. – No. 44. – pp. 104-120. (in Russian)
34. Zimin A.V., Atajanova O.A., Romanenkov D.A. et al. Submesoscale eddies in the White Sea according to satellite radar measurements // Investigation of the Earth from Space. – 2016. – No. 1-2. – pp. 129-135. (in Russian)
35. Zimin A.V., Romanenkov D.A., Atatdzhanova O.A. et al. Submesoscale processes and phenomena in the tidal Arctic seas (White, Barents and Kara) // Collection of proceedings of

the International Symposium “Mesoscale and submesoscale processes in the hydrosphere and atmosphere” " – 2018. – pp. 147-150. (in Russian)
36. Zyryanov V. N. Topographic eddies in the dynamics of sea currents // Institute of Water Problems of the Russian Academy of Sciences. M.: IVP, 1995. 238 p. (in Russian)
37. Zyryanov V.N., Egorova V.M. Vortexes in a stratified rotating fluid with a complex bottom topography // Scientific problems of improving the health of Russian rivers and ways to solve them. – 2019. – pp. 144-149. (in Russian)
38. Ivanov Yu. A., Mikhailechenko Yu. G., Nikitin S. V. et al. Formation and evolution of intrathermocline lenses of Mediterranean origin // Dokladi of the Academy of Sciences. – 1990. – T. 310. – No. 4. – P. 980-983. (in Russian)
39. Ivanov V.V., Korablev A.A. Formation and regeneration of an intrapycnocline lens in the Norwegian Sea // Meteorology and Hydrology. – 1995 a . – No. 9. – pp. 102-110. (in Russian)
40. Ivanov V.V., Korablev, A.A. Dynamics of the intrapycnocline lens in the Norwegian Sea // Meteorology and Hydrology. – 1995b . – T. 10. – P. 55-62. (in Russian)
41. Kalavichchi K. A., Bashmachnikov I. L. To the mechanism of positive feedback of long-term variability of the convergence of oceanic and atmospheric heat fluxes and ice cover area in the Barents Sea // Izvestia of RAS. Physics of the atmosphere and ocean. – 2019. – T. 55. – No. 6. – pp. 171-181. (in Russian)
42. Kamenkovich V.M., Koshlyakov M.N., Monin A.S. Synoptic eddies in the ocean. Leningrad: Gidrometeoizdat , 1987. 509 p. (in Russian)
43. Karimova S.S. Study of submesoscale eddies of the Black and Baltic Seas using radar and radiometric satellite data // Collection of reports of the Russian scientific conference “Sensing of Earth Covers with Synthetic Aperture Radars”. – 2010. – P. 148-159. (in Russian)
44. Kozlov V.F. Method of contour dynamics in model problems on topographic cyclogenesis in the ocean // Izvestia of the USSR Academy of Sciences. Physics of the atmosphere and ocean. – 1983. – T. 19. – No. 8. – pp. 845-854. (in Russian)
45. Kozlov V.F., Makarov V.G., Sokolovsky M.A. Numerical model of baroclinic instability of axisymmetric vortices in a two-layer ocean // Izvestia of the USSR Academy of Sciences. Physics of the atmosphere and ocean. – 1986. – T. 22. – No. 8. – pp. 868-874. (in Russian)
46. Kondrik D.V., Popov A.V., Rubchenya A.V. The role of mesoscale formations in the distribution of desalinated waters in the surface layer of the Arctic Ocean // Bulletin of St. Petersburg University. Geosciences. – 2016. – No. 3. – pp. 106-117. (in Russian)
47. Kort V. G., Neiman V. G. Atlantic hydrophysical test site 1970. Atlantic hydrophysical test site-70 // M.: Nauka, 1974. 317 p. (in Russian)
48. Kort, W. G. (ed.). Hydrophysical research under the Mesopolygon program // Collection of scientific papers. Science , 1988. 263 p. (in Russian)
49. Kostyanoy A. G., Shapiro G. I. Evolution and structure of an intrathermoclinic vortex // Izvestia of the USSR Academy of Sciences. Physics of the atmosphere and ocean. – 1986. – T. 22. – No. 10. – pp. 1098-1105. (in Russian)
50. Kostyanoy A. G., Shapiro G. I. On the forecast of trajectories of vortex lenses in the ocean. //Dokladi of the Academy of Sciences. – 1989. – T. 309. – No. 5. – pp. 1219-1222 . (in Russian)
51. Kostyanoy A. G., Ginzburg A. I., Lavrova O. Yu., Mityagina M. I. Remote sensing of submesoscale eddies in the seas of Russia // Collection of proceedings of the International Symposium “Mesoscale and submesoscale processes in the hydrosphere and atmosphere” (MSP-2018). – 2018. – pp. 184-187. (in Russian)
52. Koshlyakov M.N., Panteleev G.G. Thermohaline characteristics of the lens of Mediterranean water in the tropical zone of the North Atlantic //Hydrophysical research under the Mesopolygon program: Collection of scientific papers. – 1988. – P. 46-57. (in Russian)
53. Koshlyakov M. N., Yaremchuk M. I. Synoptic and mesoscale ocean eddies according to the data of the main buoy system of the Mesopolygon // Hydrophysical research under the Mesopolygon program. – 1988. – P. 17-27. (in Russian)

54. Koshlyakov M.N., Tarakanov R.Yu. Water transfer across the Subantarctic Front and the Global Ocean Conveyor // Oceanology. – 2011. – T. 51. – No. 5. – pp. 773-787. (in Russian)
55. Koshlyakov M.N. EXPERIMENT POLYGON-70 //Oceanological Research. – 2020. – T. 48. – No. 3. – pp. 5-9. (in Russian)
56. Kuibin P. A., Okulov V. L. One-dimensional solutions for flows with helical symmetry // Thermophysics and Aeromechanics. – 1996. – T. 3. – No. 4. – pp. 311–315. (in Russian)
57. Lavrova, O. Yu., Kostyanoy, A. G., Lebedev, S. A., et al. Integrated satellite monitoring of Russian seas. – 2011. – Moscow, IKI RAS. ISBN 978-5-9903101-1-7. – 480p. (in Russian)
58. Maksimenko N. A., Orlov O. I. Integral characteristics of the core of a quasi-stationary "Gaussian" vortex in a homogeneous or shear flow // Oceanology. – 1991. – T. 31. – No. 1. – pp. 34-41. (in Russian)
59. Malysheva A. A., Kubryakov A. A., Koldunov A. V., Belonenko T. V. Estimation of Agulyasov transport based on satellite altimetry and Argo floats // Investigation of the Earth from Space. – 2020. – No. 2. – pp. 24-34. (in Russian)
60. Monin A.S., Ozmidov R.V. Ocean turbulence //L.: Gidrometeoizdat, 1981. 320 p. (in Russian)
61. Monin A. S., Zhikharev G. M. Ocean eddies // Advances in physical sciences. – 1990. – T. 160. – No. 5. – P. 1-47. (in Russian)
62. Nezlin M.V. Rossby solitons (experimental studies and laboratory model of natural vortices such as Jupiter's Great Red Spot) // Advances in Physical Sciences. – 1986. – T. 150. – No. 9. – P. 3-60. (in Russian)
63. Nezlin M.V., Snezhkin E.N. Rossby vortices and spiral structures: Astrophysics and plasma physics in experiments on shallow water // M.: Nauka, 1990. 237 p. (in Russian)
64. Neiman V.G., Morozov E.G. Experiment POLYGON-70—the beginning of a new stage of hydrophysical research of the World Ocean (to the 50th anniversary of the discovery of ocean synoptic eddies) //Oceanological Research. – 2020. – T. 48. – No. 3. – pp. 10-30. (in Russian)
65. Novikova Yu. S., Bashmachnikov I. L. Eddies of the Lofoten Basin according to satellite altimetry data, images in the radar and visible ranges // Seas of Russia: Year of Science and Technology in the Russian Federation - UN Decade of Ocean Sciences. – 2021. – P. 291-292. (in Russian)
66. Ozmidov R.V. Diffusion of contaminants in the ocean. L.: Gidrometeoizdat, 1986. 280 p. (in Russian)
67. Pereskokov A.I. On the physical nature of the large-scale anticyclonic circulation in the water column of the Norwegian Sea // Dokladi of the Academy of Sciences. – 1999. – T. 364. – No. 4. – pp. 549-552. (in Russian)
68. Rodionov A. A., Romanenkov D. A., Zimin A. B. and others. Submesoscale structures of the White Sea waters and their dynamics. State of the art and directions of research // Fundamental and Applied Hydrophysics. – 2022. – T. 7. – No. 3. – pp. 29-41. (in Russian)
69. Romanenkov D. A., Zimin A. V., Rodionov A. A. et al. Variability of frontal sections and features of mesoscale dynamics of the White Sea waters // Fundamental and Applied Hydrophysics. – 2022. – T. 9. – No. 1. – pp. 59-72. (in Russian)
70. Romantsev V. A. Large-scale structure and features of the average water circulation // Problems of the Arctic and Antarctic. – 1991. – T. 65. – P. 75–97. (in Russian)
71. Santieva E.K., Bashmachnikov I.L., Sokolovsky M.A. On the stability of the Lofoten eddy of the Norwegian Sea //Oceanology. – 2021. – T. 61. – No. 3. – pp. 353-365. (in Russian)
72. Sokolovsky M.A. Numerical modeling of nonlinear instability of axisymmetric two-layer vortices // Izvestia of the USSR Academy of Sciences. Physics of the atmosphere and ocean. – 1988. – T. 24. – No. 7. – pp. 735-743. (in Russian)
73. Sokolovsky M.A. Modeling of three-layer vortex movements in the ocean by the method of contour dynamics // Izvestia of the USSR Academy of Sciences. Physics of the Atmosphere and Ocean . – 1991. – T. 27. – No. 5. – pp. 550-562. (in Russian)

74. Sokolovsky M. A., Filyushkin B. N. Behavior of intrathermoclinic lenses near synoptic eddies // Mesoscale and submesoscale processes in the hydrosphere and atmosphere MSP-2018. – 2018. – P. 325-328. (in Russian)
75. Fedorov A. M., Bashmachnikov I. L., Belonenko T. V. Winter convection in the Lofoten Basin according to Argo floats and hydrodynamic modeling // Bulletin of St. Petersburg University. Geosciences. – 2019. – T. 64. – No. 3. – pp. 491-511. (in Russian)
76. Fedorov K.N., Ginzburg A.I., Kostyanoy A.G. Generation and evolution of vortex dipoles in laboratory conditions //Coherent structures and self-organization of oceanic movements. – 1992. – P. 21–26. (in Russian)
77. Filyushkin B.N., Aleynik D.L., Gruzinov V.M., Kozhelupova N.G. Dynamic destruction of Mediterranean lenses in the Atlantic Ocean // Dokladi of the Academy of Sciences. – 2002. – T. 387. – No. 4. – pp. 545-548. (in Russian)
78. Filyushkin B.N., Aleynik D.L., Kozhelupova N.G., Moshonkin S.N. Features of the horizontal transport of Mediterranean waters in the Atlantic Ocean // Proceedings of the State Oceanographic Institute. – 2009. – No. 212. – pp. 76-88. (in Russian)
79. Filyushkin B. N., Sokolovsky M. A., Kozhelupova N. G., Vagina I. M. On the dynamics of intrathermocline lenses // Dokladi of the Academy of Sciences. – 2010. – T. 434. – No. 5. – pp. 688-691. (in Russian)
80. Filyushkin B.N. Sokolovsky M.A., Kozhelupova N.G., Vagina I.M. Evolution of intrathermoclinic vortices when passing over an underwater hill // Dokladi of the Academy of Sciences. – 2011. – T. 441. – No. 6. – pp. 825-825. (in Russian)
81. Filyushkin B.N., Sokolovsky M.A., Kozhelupova N.G., Vagina I.M. Dynamics of Mediterranean lenses on the current over seamounts // Proceedings of the State Oceanographic Institute. – 2014. – No. 215. – pp. 53-74. (in Russian)
82. Filyushkin B.N., Lebedev K.V., Kozhelupova N.G. Detection of intermediate Mediterranean waters in the Atlantic Ocean from observations of Argo floats // Oceanology. – 2017 a . – T. 57. – No. 6. – pp. 847-857. (in Russian)
83. Filyushkin B.N., Sokolovsky M.A., Lebedev K.V. On the movement of an intrathermoclinic lens over the Lofoten Basin // Modern problems of thermohydromechanics of the ocean. – 2017b . – pp. 177-179. (in Russian)
84. Filyushkin B.N., Kozhelupova N.G. Review of studies of Mediterranean intrathermocline eddies in the Atlantic Ocean //Oceanological Research. – 2020. – T. 48. – No. 3. – pp. 123-147
85. Fuks V.R. Planetary waves in the ocean // Leningrad: Leningrad State University Publishing House, 1977. 176 p. (in Russian)
86. Shapiro G.I., Meshchanov S.L., Emelyanov M.V. Lens of Mediterranean waters after a collision with seamounts // Oceanology. – 1992. – T. 32. – No. 3. – pp. 420-427. (in Russian)

87. Abernathey R., Haller G. Transport by Lagrangian vortices in the eastern Pacific //Journal of Physical Oceanography. – 2018. – V. 48. – №. 3. – P. 667-685.
88. Acheson D. J. Elementary fluid dynamics. – . – 1990. – P. 1-397.
89. Adcroft A, Campin JM, Dutkiewicz S, Evangelinos C, Ferreira D, Follows M, ..., Hill E (2018) MITgcm Documentation, 306 c.
90. Adduce C., Cenedese C. An experimental study of a mesoscale vortex colliding with topography of varying geometry in a rotating fluid //Journal of Marine Research. – 2004. – V. 62. – №. 5. – P. 611-638.
91. Aiki H., Yamagata T. A numerical study on the successive formation of Meddy-like lenses //Journal of Geophysical Research: Oceans. – 2004. – V. 109. – №. C6, doi: 10.1029/2003JC001952.

92. Alvarez M. et al. Physical and biogeochemical transports structure in the North Atlantic subpolar gyre //Journal of Geophysical Research: Oceans. – 2004. – V. 109. – №. C3, doi: 10.1029/2003JC002015.
93. Alves M. L. G. R., Colin de Verdière A. Instability dynamics of a subtropical jet and applications to the Azores Front Current System: eddy-driven mean flow //Journal of Physical Oceanography. – 1999. – V. 29. – №. 5. – P. 837-864.
94. Alves M. et al. Circulation patterns and transport of the Azores Front-Current system //Deep Sea Research Part II: Topical Studies in Oceanography. – 2002. – V. 49. – №. 19. – P. 3983-4002.
95. Ambar I., Howe M. R., Abdullah M. I. A physical and chemical description of the Mediterranean outflow in the Gulf of Cadiz //Deutsche Hydrographische Zeitschrift. – 1976. – V. 29. – №. 2. – P. 58-68.
96. Ambar I., Howe M. R. Observations of the Mediterranean outflow—I mixing in the Mediterranean outflow //Deep Sea Research Part A. Oceanographic Research Papers. – 1979. – V. 26. – №. 5. – P. 535-554.
97. Ambar I., Howe M. R. Observations of the Mediterranean outflow—II The deep circulation in the vicinity of the Gulf of Cadiz //Deep Sea Research Part A. Oceanographic Research Papers. – 1979. – V. 26. – №. 5. – P. 555-568.
98. Ambar I. A shallow core of Mediterranean water off western Portugal //Deep Sea Research Part A. Oceanographic Research Papers. – 1983. – V. 30. – №. 6. – P. 677-680.
99. Ambar I. et al. Observations of the Mediterranean Undercurrent and eddies in the Gulf of Cadiz during 2001 //Journal of Marine Systems. – 2008. – V. 71. – №. 1-2. – P. 195-220.
100. Anderson L. A., Sarmiento J. L. Redfield ratios of remineralization determined by nutrient data analysis //Global biogeochemical cycles. – 1994. – V. 8. – №. 1. – P. 65-80.
101. Arbic B. K. et al. Effects of stencil width on surface ocean geostrophic velocity and vorticity estimation from gridded satellite altimeter data //Journal of Geophysical Research: Oceans. – 2012. – V. 117. – №. C3.
102. Arhan M., De Verdiére A. C. Dynamics of eddy motions in the eastern North Atlantic //Journal of physical oceanography. – 1985. – V. 15. – №. 2. – P. 153-170.
103. Arhan M. The North Atlantic current and subarctic intermediate water //Journal of Marine Research. – 1990. – V. 48. – №. 1. – P. 109-144.
104. Arhan M., Colin De Verdiére A., Mémery L. The eastern boundary of the subtropical North Atlantic //Journal of Physical Oceanography. – 1994. – V. 24. – №. 6. – P. 1295-1316.
105. Armi L., Stommel H. Four views of a portion of the North Atlantic subtropical gyre //Journal of Physical Oceanography. – 1983. – V. 13. – №. 5. – P. 828-857.
106. Armi L., Zenk W. Large lenses of highly saline Mediterranean water //Journal of Physical Oceanography. – 1984. – V. 14. – №. 10. – P. 1560-1576.
107. Armi L. et al. Two years in the life of a Mediterranean salt lens //Journal of Physical Oceanography. – 1989. – V. 19. – №. 3. – P. 354-370.
108. Atadzhanova O. A. et al. Satellite radar observations of small eddies in the White, Barents and Kara Seas //Physical Oceanography. – 2017. – №. 2. – P. 75-83.
109. Bacon S. et al. Arctic mass, freshwater and heat fluxes: Methods and modelled seasonal variability //Philosophical Transactions of the Royal Society A: Mathematical, Physical and Engineering Sciences. – 2015. – V. 373. – №. 2052. – P. 20140169.

110. Baey J. M., Carton X. Vortex multipoles in two-layer rotating shallow-water flows //Journal of Fluid Mechanics. – 2002. – V. 460. – P. 151-175.
111. Bambrey R. R., Reinaud J. N., Dritschel D. G. Strong interactions between two corotating quasi-geostrophic vortices //Journal of Fluid Mechanics. – 2007. – V. 592. – P. 117-133.
112. Barbero L. et al. Variability of the water mass transports and fluxes in the eastern North Atlantic during 2001 //Journal of Geophysical Research: Oceans. – 2010. – V. 115. – №. C3, doi: 10.1029/2008JC005212.
113. Barbosa Aguiar A. C. et al. Zonal structure of the mean flow and eddies in the Azores Current system //Journal of Geophysical Research: Oceans. – 2011. – V. 116. – №. C2, doi:10.1016/j.pocean.2014.11.008
114. Barbosa Aguiar A. C. B., Peliz A., Carton X. A census of Meddies in a long-term high-resolution simulation //Progress in Oceanography. – 2013. – V. 116. – P. 80-94.
115. Barbosa Aguiar, A.C., A. Peliz, F. Neves, I. Bashmachnikov, X. Carton. Mediterranean outflow transports and entrainment estimates from observations and high resolution modelling //Progress in Oceanography. – 2015. – Т. 131. – С. 33-45
116. Barcelo-Llull B. et al. Anatomy of a subtropical intrathermocline eddy //Deep Sea Research Part I: Oceanographic Research Papers. – 2017. – V. 124. – P. 126-139.
117. Baringer M. O. N., Price J. F. Mixing and spreading of the Mediterranean outflow //Journal of Physical Oceanography. – 1997. – V. 27. – №. 8. – P. 1654-1677.
118. Barnes S. L. A technique for maximizing details in numerical weather map analysis //Journal of Applied Meteorology and Climatology. – 1964. – V. 3. – №. 4. – P. 396-409.
119. Bashmachnikov I. et al. *In situ* and remote sensing signature of meddies east of the mid-Atlantic ridge //Journal of Geophysical Research: Oceans. – 2009a. – V. 114. – №. C5.
120. Bashmachnikov I. et al. Interaction of Mediterranean water eddies with Sedlo and Seine seamounts, subtropical Northeast Atlantic //Deep Sea Research Part II: Topical Studies in Oceanography. – 2009b. – V. 56. – №. 25. – P. 2593-2605.
121. Bashmachnikov I., Carton X. Surface signature of Mediterranean water eddies in the Northeastern Atlantic: effect of the upper ocean stratification //Ocean Science. – 2012. – V. 8. – №. 6. – P. 931-943.
122. Bashmachnikov, I., C. Loureiro, A. Martins. Topographically induced circulation patterns and mixing over Condor seamount //Deep Sea Research Part II: Topical Studies in Oceanography. – 2013a. – Т. 98. – С. 38-51.
123. Bashmachnikov I., Boutov D., Dias J. Manifestation of two meddies in altimetry and sea-surface temperature //Ocean Science. – 2013b. – V. 9. – №. 2. – P. 249-259.
124. Bashmachnikov I., Carton X., Belonenko T. V. Characteristics of surface signatures of Mediterranean water eddies //Journal of Geophysical Research: Oceans. – 2014. – V. 119. – №. 10. – P. 7245-7266.
125. Bashmachnikov I. et al. Temperature–salinity distribution in the northeastern Atlantic from ship and Argo vertical casts //Ocean Science. – 2015a. – V. 11. – №. 2. – P. 215-236.
126. Bashmachnikov I. et al. Distribution of intermediate water masses in the subtropical northeast Atlantic //Ocean Science. – 2015b. – V. 11. – №. 5. – P. 803-827.
127. Bashmachnikov I. et al. Properties and pathways of Mediterranean water eddies in the Atlantic //Progress in Oceanography. – 2015c. – V. 137. – P. 149-172.

128. Bashmachnikov I. L. et al. On the vertical structure and stability of the Lofoten vortex in the Norwegian Sea //Deep Sea Research Part I: Oceanographic Research Papers. – 2017. – V. 128. – P. 1-27.
129. Bashmachnikov I. et al. Pattern of vertical velocity in the Lofoten vortex (the Norwegian Sea) //Ocean Dynamics. – 2018. – V. 68. – P. 1711-1725.
130. Bashmachnikov I. L. et al. Eddies in the North Greenland Sea and Fram Strait from satellite altimetry, SAR and high-resolution model data //Journal of Geophysical Research: Oceans. – 2020. – V. 125. – №. 7. – P. e2019JC015832.
131. Bashmachnikov I. L. et al. Heat transport by mesoscale eddies in the Norwegian and Greenland seas //Journal of Geophysical Research: Oceans. – 2023. – V. 128. – №. 2. – P. e2022JC018987, 1-19, doi: 10.1029/2022JC018987
132. Batchelor G. K. Axial flow in trailing line vortices //Journal of Fluid Mechanics. – 1964. – V. 20. – №. 4. – P. 645-658
133. Belkin I. et al. A double-thermostad warm-core ring of the Gulf Stream //Journal of Physical Oceanography. – 2020. – V. 50. – №. 2. – P. 489-507.
134. Bell G. I. Interaction between vortices and waves in a simple model of geophysical flow //Physics of Fluids A: Fluid Dynamics. – 1990. – V. 2. – №. 4. – P. 575-586.
135. Belonenko T. et al. Evaluation of heat and salt transports by mesoscale eddies in the Lofoten Basin //Russian Journal of Earth Sciences. – 2020. – V. 20. – №. 6. – P. 1-14, doi:10.2205/2020ES000720.
136. Belonenko T. V. et al. Topographic experiments over dynamical processes in the Norwegian Sea //Russian Journal of Earth Sciences. – 2021. – Т. 21. – №. 1 (ES1006). – С. 1-15.
137. Benilov E. S., Broutman D., Kuznetsova E. P. On the stability of large-amplitude vortices in a continuously stratified fluid on the f-plane //Journal of Fluid Mechanics. – 1998. – V. 355. – P. 139-162.
138. Benilov E. S. The dynamics of a near-surface vortex in a two-layer ocean on the beta-plane //Journal of Fluid Mechanics. – 2000. – V. 420. – P. 277-299.
139. Benilov E. S. Instability of quasi-geostrophic vortices in a two-layer ocean with a thin upper layer //Journal of Fluid Mechanics. – 2003. – V. 475. – P. 303-331.
140. Benilov E. S. Stability of vortices in a two-layer ocean with uniform potential vorticity in the lower layer //Journal of Fluid Mechanics. – 2004. – V. 502. – P. 207-232.
141. Benilov E. S. Stability of a two-layer quasigeostrophic vortex over axisymmetric localized topography //Journal of physical oceanography. – 2005a. – V. 35. – №. 1. – P. 123-130.
142. Benilov E. S. On the stability of oceanic vortices: A solution to the problem? //Dynamics of atmospheres and oceans. – 2005b. – V. 40. – №. 3. – P. 133-149.
143. Bersanelli M. et al. Models of interacting pairs of thin, quasi-geostrophic vortices: steady-state solutions and nonlinear stability //Geophysical & Astrophysical Fluid Dynamics. – 2016. – V. 110. – №. 6. – P. 491-517.
144. Beszczynska-Moller A. et al. Variability in Atlantic water temperature and transport at the entrance to the Arctic Ocean, 1997–2010 //ICES Journal of Marine Science. – 2012. – V. 69. – №. 5. – P. 852-863.
145. Biescas B. et al. Imaging meddy finestructure using multichannel seismic reflection data //Geophysical Research Letters. – 2008. – V. 35. – №. 11. – P. 1-5.

146. Bjork G., Gustafsson B. G., Stigebrandt A. Upper layer circulation of the Nordic seas as inferred from the spatial distribution of heat and freshwater content and potential energy //Polar Research. – 2001. – V. 20. – №. 2. – P. 161-168.
147. Blindhein J. Cascading of Barents Sea bottom water into the Norwegian Sea //Rapp. P. Reun. Cons. Int. Explor. Mer. – 1989. – V. 188. – P. 161-189.
148. Bondevik E. Studies of eddies in the marginal ice zone along the east Greenland current using spaceborne synthetic aperture radar (SAR): дис. – The University of Bergen, 2011.
149. Boss E., Paldor N., Thompson L. Stability of a potential vorticity front: from quasi-geostrophy to shallow water //Journal of Fluid Mechanics. – 1996. – V. 315. – P. 65-84.
150. Bosse A., Fer I. Mean structure and seasonality of the Norwegian Atlantic Front Current along the Mohn Ridge from repeated glider transects //Geophysical Research Letters. – 2019. – V. 46. – №. 22. – P. 13170-13179.
151. Bosse A. et al. Dynamical controls on the longevity of a non-linear vortex: The case of the Lofoten Basin Eddy //Scientific reports. – 2019. – V. 9. – №. 1. –13448, C. 1-13.
152. Bower A. et al. Lagrangian views of the pathways of the Atlantic Meridional Overturning Circulation //Journal of Geophysical Research: Oceans. – 2019. – V. 124. – №. 8. – P. 5313-5335.
153. Bower A. S., Armi L., Ambar I. Lagrangian observations of meddy formation during a Mediterranean undercurrent seeding experiment //Journal of Physical Oceanography. – 1997. – V. 27. – №. 12. – P. 2545-2575.
154. Bower A. S. et al. Directly measured mid-depth circulation in the northeastern North Atlantic Ocean //Nature. – 2002. – V. 419. – №. 6907. – P. 603-607.
155. Bower A. S., Serra N., Ambar I. Structure of the Mediterranean Undercurrent and Mediterranean Water spreading around the southwestern Iberian Peninsula //Journal of Geophysical Research: Oceans. – 2002. – V. 107. – №. C10. – P. 3161, doi: 10.1029/2001JC001007.
156. Boyd T. J., D'Asaro E. A. Cooling of the West Spitsbergen Current: wintertime observations west of Svalbard //Journal of Geophysical Research: Oceans. – 1994. – V. 99. – №. C11. – P. 22597-22618.
157. Boyer T. P. et al. Linear trends in salinity for the World Ocean, 1955–1998 //Geophysical Research Letters. – 2005. – V. 32. – №. 1, L01604.
158. Brix H., Gerdes R. North Atlantic Deep Water and Antarctic Bottom Water: Their interaction and influence on the variability of the global ocean circulation //Journal of Geophysical Research: Oceans. – 2003. – V. 108. – №. C2, C. 3022, doi:10.1029/2002JC001335.
159. Buckley M. W., Marshall J. Observations, inferences, and mechanisms of the Atlantic Meridional Overturning Circulation: A review //Reviews of Geophysics. – 2016. – V. 54. – №. 1. – P. 5-63.
160. Cabecadas G., Brogueira M. J., Gonçalves C. The chemistry of Mediterranean outflow and its interactions with surrounding waters //Deep Sea Research Part II: Topical Studies in Oceanography. – 2002. – V. 49. – №. 19. – P. 4263-4270.
161. Capet A. et al. Implications of refined altimetry on estimates of mesoscale activity and eddy-driven offshore transport in the eastern boundary upwelling systems //Geophysical Research Letters. – 2014. – V. 41. – №. 21. – P. 7602-7610.

162. Carracedo L. I. et al. Seasonal dynamics in the Azores–Gibraltar Strait region: A climatologically-based study //Progress in oceanography. – 2014. – V. 122. – P. 116-130.
163. Carton X. J., McWilliams J. C. Barotropic and baroclinic instabilities of axisymmetric vortices in a quasigeostrophic model //Elsevier oceanography series. – Elsevier, 1989. – V. 50. – P. 225-244.
164. Carton X. J., Flierl G. R., Polvani L. M. The generation of tripoles from unstable axisymmetric isolated vortex structures //Europhysics letters. – 1989. – V. 9. – №. 4. – P. 339-344.
165. Carton X. J. On the merger of shielded vortices //Europhysics letters. – 1992. – V. 18. – №. 8. – P. 697-703.
166. Carton X. Hydrodynamical modeling of oceanic vortices //Surveys in Geophysics. – 2001. – V. 22. – №. 3. – P. 179-263.
167. Carton X. et al. Meddy coupling with a deep cyclone in the Gulf of Cadiz //Journal of Marine Systems. – 2002. – V. 32. – №. 1-3. – P. 13-42.
168. Carton X. et al. Meddy dynamics and interaction with neighboring eddies southwest of Portugal: Observations and modeling //Journal of Geophysical Research: Oceans. – 2010. – V. 115. – №. C6, C06017, doi: 10.1029/2009JC005646.
169. Carton X. et al. Interactions of surface and deep anticyclonic eddies in the Bay of Biscay //Journal of Marine Systems. – 2013. – V. 109. – P. S45-S59.
170. Carton X. et al. Vortex stability in a multi-layer quasi-geostrophic model: application to Mediterranean Water eddies //Fluid Dynamics Research. – 2014. – V. 46. – №. 6. – P. 061401.
171. Carton X. et al. Vortex merger in surface quasi-geostrophy //Geophysical & Astrophysical Fluid Dynamics. – 2016. – V. 110. – №. 1. – P. 1-22.
172. Carton X. et al. Vortex merger near a topographic slope in a homogeneous rotating fluid //Regular and Chaotic Dynamics. – 2017. – V. 22. – P. 455-478.
173. Cenedese C. Laboratory experiments on mesoscale vortices colliding with a seamount //Journal of Geophysical Research: Oceans. – 2002. – V. 107. – №. C6. – P. 3053, doi: 10.1029/2000JC000599
174. Cerretelli C., Williamson C. H. K. The physical mechanism for vortex merging //Journal of Fluid Mechanics. – 2003. – V. 475. – P. 41-77.
175. Chafik L. et al. On the flow of Atlantic water and temperature anomalies in the Nordic Seas toward the Arctic Ocean //Journal of Geophysical Research: Oceans. – 2015. – V. 120. – №. 12. – P. 7897-7918.
176. Chaigneau A., Gizolme A., Grados C. Mesoscale eddies off Peru in altimeter records: Identification algorithms and eddy spatio-temporal patterns //Progress in Oceanography. – 2008. – V. 79. – №. 2-4. – P. 106-119.
177. Chatterjee S. et al. Role of Greenland Sea gyre circulation on Atlantic water temperature variability in the Fram Strait //Geophysical Research Letters. – 2018. – V. 45. – №. 16. – P. 8399-8406.
178. Chavanne C. P., Klein P. Can oceanic submesoscale processes be observed with satellite altimetry? //Geophysical Research Letters. – 2010. – V. 37. – №. 22, – L22602, doi:10.1029/2010GL045057
179. Chelton D. B. et al. Geographical variability of the first baroclinic Rossby radius of deformation //Journal of Physical Oceanography. – 1998. – V. 28. – №. 3. – P. 433-460

180. Chelton D. B. et al. Global observations of large oceanic eddies //Geophysical Research Letters. – 2007. – V. 34. – №. 15 – P. 1-5.
181. Chelton D. B., Schlax M. G., Samelson R. M. Global observations of nonlinear mesoscale eddies //Progress in oceanography. – 2011. – V. 91. – №. 2. – P. 167-216.
182. Cherubin L. et al. Instability of the Mediterranean Water undercurrents southwest of Portugal: effects of baroclinicity and of topography //Oceanologica Acta. – 2000. – V. 23. – №. 5. – P. 551-573.
183. Cherubin L., Carton X., Dritschel D. G. Vortex dipole formation by baroclinic instability of boundary currents //Journal of physical oceanography. – 2007. – V. 37. – №. 6. – P. 1661-1677
184. Chouksey A., Gula J., Carton X. J. Long-lived Deep Coherent Vortices in the Northeast Atlantic Ocean //Journal of Geophysical Research: Oceans. – 2023. – P. 1-33
185. Cianca A. et al. Modal composition of the central water in the North Atlantic subtropical gyre //Ocean Science Discussions. – 2009. – V. 6. – №. 3. – P. 2487-2506.
186. Ciani D. et al. Influence of deep vortices on the ocean surface //Discontinuity Nonlinearity Complexity – 2015. – V. 4. – №. 3. – P. 281–311.
187. Ciani D. Subsurface-intensified oceanic vortices: impact on the sea-surface and mutual interactions: дис. – Université de Bretagne occidentale-Brest, 2016.
188. Ciani D., Carton X., Verron J. On the merger of subsurface isolated vortices //Geophysical & Astrophysical Fluid Dynamics. – 2016. – V. 110. – №. 1. – P. 23-49.
189. Ciani D. et al. Surface signature of Mediterranean water eddies in a long-term high-resolution simulation //Deep Sea Research Part I: Oceanographic Research Papers. – 2017. – V. 130. – P. 12-29.
190. Cohen Y., Dvorkin Y., Paldor N. Linear instability of constant PV cold-core eddies in a two-layer ocean //Quarterly Journal of the Royal Meteorological Society. – 2015. – V. 141. – №. 692. – P. 2886-2897.
191. Colin de Verdiere A. On the southward motion of Mediterranean salt lenses //Journal of physical oceanography. – 1992. – V. 22. – №. 4. – P. 413-420.
192. Comas-Rodríguez I. et al. The Azores Current System from a meridional section at 24.5 W //Journal of Geophysical Research: Oceans. – 2011. – V. 116. – №. C9, C09021, doi: 10.1029/2011JC007129
193. Comiso J. C. et al. Seasonal and interannual variability of the Odden ice tongue and a study of environmental effects //Journal of Geophysical Research: Oceans. – 2001. – V. 106. – №. C5. – P. 9093-9116.
194. Cushman-Roisin B., Tang B., Chassignet E. P. Westward motion of mesoscale eddies //Journal of Physical Oceanography. – 1990. – V. 20. – №. 5. – P. 758-768.
195. Cushman-Roisin B., Beckers J. M. Introduction to geophysical fluid dynamics: physical and numerical aspects. – Academic press, 2011. 828 pp.
196. Cushman-Roisin B., Beckers J. M. Geostrophic flows and vorticity dynamics //International Geophysics. – Academic Press, 2011. – V. 101. – P. 205-238.
197. Dafner E. V., Boscolo R., Bryden H. L. The N: Si: P molar ratio in the Strait of Gibraltar //Geophysical Research Letters. – 2003. – V. 30. – №. 10. - P. 1506, doi: 10.1029/2002GL016274.
198. Danabasoglu G., McWilliams J. C., Gent P. R. The role of mesoscale tracer transports in the global ocean circulation //Science. – 1994. – V. 264. – №. 5162. – P. 1123-1126.

199. Daniault N., Mazé J. P., Arhan M. Circulation and mixing of Mediterranean Water west of the Iberian Peninsula //Deep Sea Research Part I: Oceanographic Research Papers. – 1994. – V. 41. – №. 11-12. – P. 1685-1714.
200. Danilov S., Gurarie D. Rhines scale and spectra of the β-plane turbulence with bottom drag //Physical Review E. – 2002. – V. 65. – №. 6. – P. 067301.
201. D'Asaro E. A. Generation of submesoscale vortices: A new mechanism //Journal of Geophysical Research: Oceans. – 1988. – V. 93. – №. C6. – P. 6685-6693.
202. Davey M. K. Baroclinic instability in a fluid with three layers //Journal of Atmospheric Sciences. – 1977. – V. 34. – №. 8. – P. 1224-1234.
203. Demidov A. N., Filyushkin B. N., Kozhelupova N. G. Detection of Mediterranean lenses in the Atlantic ocean by profilers of the Argo project //Oceanology. – 2012. – V. 52. – P. 171-180.
204. Dewar W. K., Killworth P. D. On the stability of oceanic rings //Journal of Physical Oceanography. – 1995. – V. 25. – №. 6. – P. 1467-1487.
205. Dewar W. K., Meng H. The propagation of submesoscale coherent vortices //Journal of physical oceanography. – 1995. – V. 25. – №. 8. – P. 1745-1770.
206. Dickson, R.R., Meincke, J., Rhines, P. (Eds.). Arctic, Sub-arctic Ocean Fluxes: Defining the Role of the Northern Seas in Climate. – 2008. – Springer . – P. 1-736.
207. Dokken S. T., Wahl T. Observations of spiral eddies along the Norwegian Coast in ERS SAR images //Norwegian Defence Research Establishment (NDRE), Rep. 96/01463. – 1996. – P. 1-29. https://doi.org/10.1029/2005JC003384
208. Dong C. et al. An automated approach to detect oceanic eddies from satellite remotely sensed sea surface temperature data //IEEE Geoscience and Remote Sensing Letters. – 2011. – V. 8. – №. 6. – P. 1055-1059
209. Dong C. et al. Global heat and salt transports by eddy movement //Nature communications. – 2014. – V. 5. – №. 1. – P. 3294.
210. Dritschel D. G., JuáRez M. D. L. T. The instability and breakdown of tall columnar vortices in a quasi-geostrophic fluid //Journal of Fluid Mechanics. – 1996. – V. 328. – P. 129-160.
211. Dritschel D. G., Zabusky N. J. On the nature of vortex interactions and models in unforced nearly-inviscid two-dimensional turbulence //Physics of Fluids. – 1996. – V. 8. – №. 5. – P. 1252-1256.
212. Dritschel D. G. Vortex merger in rotating stratified flows //Journal of Fluid Mechanics. – 2002. – V. 455. – P. 83-101.
213. Ducet N., Le Traon P. Y., Reverdin G. Global high-resolution mapping of ocean circulation from TOPEX/Poseidon and ERS-1 and-2 //Journal of Geophysical Research: Oceans. – 2000. – V. 105. – №. C8. – P. 19477-19498.
214. Dutkiewicz S., Rothstein L., Rossby T. Pathways of cross-frontal exchange in the North Atlantic Current //Journal of Geophysical Research: Oceans. – 2001. – V. 106. – №. C11. – P. 26917-26928.
215. Early J. J., Samelson R. M., Chelton D. B. The evolution and propagation of quasigeostrophic ocean eddies //Journal of Physical Oceanography. – 2011. – V. 41. – №. 8. – P. 1535-1555.
216. Eldevik T., Dysthe K. B. Spiral eddies //Journal of Physical Oceanography. – 2002. – V. 32. – №. 3. – P. 851-869.

217. Emery W. J., Lee W. G., Magaard L. Geographic and seasonal distributions of Brunt-Väisälä frequency and Rossby radii in the North Pacific and North Atlantic // Journal of Physical Oceanography. – 1984. – V. 14. – №. 2. – P. 294-317.
218. Thomson R. E., Emery W. J. Data analysis methods in physical oceanography. – 1997. Pergamon, UK. – P. 1-634.
219. Espedal H. A. et al. COASTWATCH'95: ERS 1/2 SAR detection of natural film on the ocean surface //Journal of Geophysical Research: Oceans. – 1998. – V. 103. – №. C11. – P. 24969-24982.
220. Fahrbach E. ASOF-N: Arctic-Subarctic Ocean Flux Array for European Climate: North; Contract No: EVK2-CT-2002-00139; final report //Arctic-Subarctic Ocean Flux Array for European Climate: North. – 2006.
221. Fedorov A. M., Bashmachnikov I. L. Accuracy of the deep convection intensity from a limited number of casts //Dynamics of Atmospheres and Oceans. – 2020. – V. 92. – P. 101164.
222. Fedorov A. M. et al. Lagrangian modeling of water circulation in the Lofoten Basin //Dynamics of Atmospheres and Oceans. – 2021. – V. 96. – P. 101258.
223. Fer I. et al. The dissipation of kinetic energy in the Lofoten Basin Eddy //Journal of Physical Oceanography. – 2018. – V. 48. – №. 6. – P. 1299-1316.
224. Fernandes A. M. Study on the automatic recognition of oceanic eddies in satellite images by ellipse center detection—the Iberian coast case //IEEE Transactions on Geoscience and Remote Sensing. – 2009. – V. 47. – №. 8. – P. 2478-2491.
225. Fiuza A. F. G. et al. Water masses and their circulation off western Iberia during May 1993 //Deep Sea Research Part I: Oceanographic Research Papers. – 1998. – V. 45. – №. 7. – P. 1127-1160.
226. Flierl G. R. Particle motions in large-amplitude wave fields //Geophysical & Astrophysical Fluid Dynamics. – 1981. – V. 18. – №. 1-2. – P. 39-74.
227. Flierl G. R. Rossby wave radiation from a strongly nonlinear warm eddy //Journal of Physical Oceanography. – 1984. – V. 14. – №. 1. – P. 47-58.
228. Flierl G. R. On the instability of geostrophic vortices //Journal of fluid mechanics. – 1988. – V. 197. – P. 349-388.
229. Fraile-Nuez E. et al. Nine years of mass transport data in the eastern boundary of the North Atlantic Subtropical Gyre //Journal of Geophysical Research: Oceans. – 2010. – V. 115. – №. C9.
230. Fratantoni D. M. North Atlantic surface circulation during the 1990's observed with satellite-tracked drifters //Journal of Geophysical Research: Oceans. – 2001. – V. 106. – №. C10. – P. 22067-22093.
231. Fu L. L. Pattern and velocity of propagation of the global ocean eddy variability //Journal of Geophysical Research: Oceans. – 2009. – V. 114. – №. C11. – C11017.
232. Fu L. L., Cazenave A. (ed.). Satellite altimetry and earth sciences: a handbook of techniques and applications. – Elsevier, International Geophysics Series 69, Academic Press, London . – 2000. – 463 pp.
233. Garcia D. A fast all-in-one method for automated post-processing of PIV data //Experiments in fluids. – 2011. – V. 50. – №. 5. – P. 1247-1259.
234. Gascard J. C., Mork K. A. Climatic importance of large-scale and mesoscale circulation in the Lofoten Basin deduced from Lagrangian observations //Arctic–Subarctic Ocean Fluxes:

Defining the Role of the Northern Seas in Climate. – Dordrecht : Springer Netherlands, 2008. – P. 131-143.

235. Gasparin F. et al. Water mass analysis of the Coral Sea through an Optimum Multiparameter method //Journal of Geophysical Research: Oceans. – 2014. – V. 119. – №. 10. – P. 7229-7244.

236. Gaube P. et al. Satellite observations of chlorophyll, phytoplankton biomass, and Ekman pumping in nonlinear mesoscale eddies //Journal of Geophysical Research: Oceans. – 2013. – V. 118. – №. 12. – P. 6349-6370.

237. Gentemann C. L. et al. Diurnal signals in satellite sea surface temperature measurements //Geophysical Research Letters. – 2003. – V. 30. – №. 3.

238. Germe A. et al. Greenland Sea sea ice variability over 1979–2007 and its link to the surface atmosphere //Journal of Geophysical Research: Oceans. – 2011. – V. 116. – №. C10.

239. Ghaffari P. et al. The influence of topography on the stability of the Norwegian Atlantic Current off northern Norway //Journal of Physical Oceanography. – 2018. – V. 48. – №. 11. – P. 2761-2777.

240. Good S. A., Martin M. J., Rayner N. A. EN4: Quality controlled ocean temperature and salinity profiles and monthly objective analyses with uncertainty estimates //Journal of Geophysical Research: Oceans. – 2013. – V. 118. – №. 12. – P. 6704-6716.

241. Gould W. J. Physical oceanography of the Azores Front //Progress in Oceanography. – 1985. – V. 14. – P. 167-190.

242. Gouretski V., Koltermann K. P. WOCE global hydrographic climatology //Berichte des BSH. – 2004. – V. 35. – P. 1-52.

243. Groeskamp S. et al. Full-depth global estimates of ocean mesoscale eddy mixing from observations and theory //Geophysical Research Letters. – 2020. – V. 47. – №. 18. – P. e2020GL089425.

244. Guizar-Sicairos M., Gutiérrez-Vega J. C. Computation of quasi-discrete Hankel transforms of integer order for propagating optical wave fields //JOSA A. – 2004. – V. 21. – №. 1. – P. 53-58.

245. Gula J., Molemaker M. J., McWilliams J. C. Topographic vorticity generation, submesoscale instability and vortex street formation in the Gulf Stream //Geophysical Research Letters. – 2015. – V. 42. – №. 10. – P. 4054-4062.

246. Gupta M. et al. Sea-ice melt driven by ice-ocean stresses on the mesoscale //Journal of Geophysical Research: Oceans. – 2020. – V. 125. – №. 11. – P. e2020JC016404.

247. Hakkinen S. Coupled ice-ocean dynamics in the marginal ice zones: Upwelling/downwelling and eddy generation //Journal of Geophysical Research: Oceans. – 1986. – V. 91. – №. C1. – P. 819-832.

248. Halo I. F. M. The Mozambique Channel eddies: Characteristics and mechanisms of formation. дис. University of Cape Town. – 2012,

249. Hansen B., Osterhus S. North atlantic–nordic seas exchanges //Progress in oceanography. – 2000. – V. 45. – №. 2. – P. 109-208.

250. Hansen B. et al. The inflow of Atlantic water, heat, and salt to the nordic seas across the Greenland–Scotland ridge //Arctic–subarctic ocean fluxes: Defining the role of the northern seas in climate. – 2008. – P. 15-43.

251. Harvey J. θ-S relationships and water masses in the eastern North Atlantic //Deep Sea Research Part A. Oceanographic Research Papers. – 1982. – V. 29. – №. 8. – P. 1021-1033.

252. Harvey J., Arhan M. The water masses of the central North Atlantic in 1983-84 //Journal of Physical Oceanography. – 1988. – V. 18. – №. 12. – P. 1855-1875.
253. Hassanzadeh P., Marcus P. S., Le Gal P. The universal aspect ratio of vortices in rotating stratified flows: theory and simulation //Journal of Fluid Mechanics. – 2012. – V. 706. – P. 46-57.
254. Hattermann T. et al. Eddy-driven recirculation of Atlantic water in Fram Strait //Geophysical Research Letters. – 2016. – V. 43. – №. 7. – P. 3406-3414.
255. Havik L. et al. Evolution of the E ast G reenland C urrent from F ram S trait to D enmark S trait: Synoptic measurements from summer 2012 //Journal of Geophysical Research: Oceans. – 2017. – V. 122. – №. 3. – P. 1974-1994.
256. Hebert D. L. A Mediterranean salt lens // дис. – Dalhousie University, UK. – 1988. – P. 1-187.
257. Hebert D., Oakey N., Ruddick B. Evolution of a Mediterranean salt lens: Scalar properties //Journal of Physical Oceanography. – 1990. – V. 20. – №. 9. – P. 1468-1483.
258. Helfrich K. R., Send U. Finite-amplitude evolution of two-layer geostrophic vortices //Journal of Fluid Mechanics. – 1988. – V. 197. – P. 331-348.
259. Herbette S., Morel Y., Arhan M. Erosion of a surface vortex by a seamount //Journal of Physical Oceanography. – 2003. – V. 33. – №. 8. – P. 1664-1679.
260. Hinrichsen H. H., Tomczak M. Optimum multiparameter analysis of the water mass structure in the western North Atlantic Ocean //Journal of Geophysical Research: Oceans. – 1993. – V. 98. – №. C6. – P. 10155-10169.
261. Hinrichsen H. H. et al. The Mediterranean Water tongue and its chlorofluoromethane signal in the Iberian Basin in early summer 1989 //Journal of Geophysical Research: Oceans. – 1993. – V. 98. – №. C5. – P. 8405-8412.
262. Hofmann Z., von Appen W. J., Wekerle C. Seasonal and mesoscale variability of the two Atlantic water recirculation pathways in Fram Strait //Journal of Geophysical Research: Oceans. – 2021. – V. 126. – №. 7. – P. e2020JC017057.
263. Holmboe J. Instability of baroclinic three-layer models of the atmosphere. – Univ.-Forl., Oslo. – 1968. – P. 1-27.
264. Hua B. L. et al. Layering and turbulence surrounding an anticyclonic oceanic vortex: *In situ* observations and quasi-geostrophic numerical simulations //Journal of Fluid Mechanics. – 2013. – V. 731. – P. 418-442.
265. Huang N. E., Shen Z., Long S. R. A new view of nonlinear water waves: the Hilbert spectrum //Annual review of fluid mechanics. – 1999. – V. 31. – №. 1. – P. 417-457.
266. Huppert H. E. Some remarks on the initiation of inertial Taylor columns //Journal of Fluid Mechanics. – 1975. – V. 67. – №. 2. – P. 397-412.
267. Ienna F., Bashmachnikov I., Dias J. Meddies and their sea surface expressions: Observations and theory //Journal of Physical Oceanography. – 2022. – V. 52. – №. 11. – P. 2643-2656.
268. Ikeda M. Instability and splitting of mesoscale rings using a two-layer quasi-geostrophic model on an f-plane //Journal of Physical Oceanography. – 1981. – V. 11. – №. 7. – P. 987-998.
269. Ikeda M. Linear instability of a current flowing along a bottom slope using a three-layer model //Journal of Physical Oceanography. – 1983. – V. 13. – №. 2. – P. 208-223.

270. Iorga M. C., Lozier M. S. Signatures of the Mediterranean outflow from a North Atlantic climatology: 1. Salinity and density fields //Journal of Geophysical Research: Oceans. – 1999a. – V. 104. – №. C11. – P. 25985-26009.
271. Iorga M. C., Lozier M. S. Signatures of the Mediterranean outflow from a North Atlantic climatology: 2. Diagnostic velocity fields //Journal of Geophysical Research: Oceans. – 1999b. – V. 104. – №. C11. – P. 26011-26029.
272. Isachsen P. E. Baroclinic instability and the mesoscale eddy field around the Lofoten Basin //Journal of Geophysical Research: Oceans. – 2015. – V. 120. – №. 4. – P. 2884-2903.
273. Isern-Fontanet J., García-Ladona E., Font J. Vortices of the Mediterranean Sea: An altimetric perspective //Journal of physical oceanography. – 2006. – V. 36. – №. 1. – P. 87-103.
274. Jackett D. R., McDougall T. J. A neutral density variable for the world's oceans //Journal of Physical Oceanography. – 1997. – V. 27. – №. 2. – P. 237-263.
275. Jacobs G. A., Barron C. N., Rhodes R. C. Mesoscale characteristics //Journal of Geophysical Research: Oceans. – 2001. – V. 106. – №. C9. – P. 19581-19595.
276. Jakobsen P. K. et al. Near-surface circulation in the northern North Atlantic as inferred from Lagrangian drifters: Variability from the mesoscale to interannual //Journal of Geophysical Research: Oceans. – 2003. – V. 108. – №. C8. – P. 3251-3264.
277. Jia Y. Formation of an Azores Current due to Mediterranean overflow in a modeling study of the North Atlantic //Journal of Physical Oceanography. – 2000. – V. 30. – №. 9. – P. 2342-2358.
278. Johannessen J. A. et al. Mesoscale eddies in the Fram Strait marginal ice zone during the 1983 and 1984 Marginal Ice Zone Experiments //Journal of Geophysical Research: Oceans. – 1987. – V. 92. – №. C7. – P. 6754-6772.
279. Johannessen J. A. et al. Coastal ocean fronts and eddies imaged with ERS 1 synthetic aperture radar //Journal of Geophysical Research: Oceans. – 1996. – V. 101. – №. C3. – P. 6651-6667
280. Johannessen J. A. et al. On radar imaging of current features: 2. Mesoscale eddy and current front detection //Journal of Geophysical Research: Oceans. – 2005. – V. 110. – №. C7. – P. 1–14. https://doi.org/10.1029/2004JC002802
281. Johannessen O. M. et al. Oceanographic conditions in the marginal ice zone north of Svalbard in early fall 1979 with an emphasis on mesoscale processes //Journal of Geophysical Research: Oceans. – 1983. – V. 88. – №. C5. – P. 2755-2769.
282. Kantha, L. H., Clayson, C. A. Numerical models of oceans and oceanic processes. – Elsevier. International Geophysics series v.66, Acad. Press, San Diego. – 2000. – 887 pp.
283. Karimova S. Spiral eddies in the Baltic, Black and Caspian seas as seen by satellite radar data //Advances in Space Research. – 2012. – V. 50. – №. 8. – P. 1107-1124
284. Karimova S., Gade M. Improved statistics of sub-mesoscale eddies in the Baltic Sea retrieved from SAR imagery //International Journal of Remote Sensing. – 2016. – V. 37. – №. 10. – P. 2394-2414.
285. Karstensen J., Tomczak M. Ventilation processes and water mass ages in the thermocline of the southeast Indian Ocean //Geophysical Research Letters. – 1997. – V. 24. – №. 22. – P. 2777-2780.
286. Kase R. H., Beckmann A., Hinrichsen H. H. Observational evidence of salt lens formation in the Iberian Basin //Journal of Geophysical Research: Oceans. – 1989. – V. 94. – №. C4. – P. 4905-4912.

287. Kase R. H., Siedler G. Meandering of the subtropical front south-east of the Azores //Nature. – 1982. – V. 300. – №. 5889. – P. 245-246.
288. Kase R. H., Zenk W. Reconstructed Mediterranean salt lens trajectories //Journal of Physical Oceanography. – 1987. – V. 17. – №. 1. – P. 158-163.
289. Kase R. H., Zenk W. Structure of the Mediterranean Water and meddy characteristics in the northeastern Atlantic. In: Kraus (Ed.), Warmwatersphere of the North Atlantic Ocean. – Gebruder Borntraeger, Berlin. – 1996. – P. 365-395.
290. Katsman C. A. et al. Stability of multilayer ocean vortices: A parameter study including realistic Gulf Stream and Agulhas rings //Journal of physical oceanography. – 2003. – V. 33. – №. 6. – P. 1197-1218.
291. Killworth P. D., Blundell J. R., Dewar W. K. Primitive equation instability of wide oceanic rings. Part I: Linear theory //Journal of Physical Oceanography. – 1997. – V. 27. – №. 6. – P. 941-962.
292. Klein B., Siedler G. On the origin of the Azores Current //Journal of Geophysical Research: Oceans. – 1989. – V. 94. – №. C5. – P. 6159-6168.
293. Klein B., Tomczak M. Identification of diapycnal mixing through optimum multiparameter analysis: 2. Evidence for unidirectional diapycnal mixing in the front between North and South Atlantic Central Water //Journal of Geophysical Research: Oceans. – 1994. – V. 99. – №. C12. – P. 25275-25280.
294. Kohl A. Generation and stability of a quasi-permanent vortex in the Lofoten Basin //Journal of Physical Oceanography. – 2007. – V. 37. – №. 11. – P. 2637-2651.
295. Kolas E., Fer I. Hydrography, transport and mixing of the West Spitsbergen Current: the Svalbard Branch in summer 2015 //Ocean Science. – 2018. – V. 14. – №. 6. – P. 1603-1618.
296. Koldunov A. et al. Steric sea-level fluctuations from remote sensing, oceanic reanalyses and objective analyses in the North Atlantic //Russian Journal of Earth Sciences. – 2020. – V. 20. – №. 3. – P. 1-14. doi:10.2205/2020ES000702
297. Kostianoy A. G., Belkin I. M. A survey of observations on intrathermocline eddies in the world ocean //Elsevier oceanography series. – Elsevier, 1989. – V. 50. – P. 821-841
298. Kostianoy A. G. et al. Satellite remote sensing of submesoscale eddies in the Russian seas //The Ocean in Motion: Circulation, Waves, Polar Oceanography. – 2018. – P. 397-413.
299. Koszalka I. et al. Surface circulation in the Nordic Seas from clustered drifters //Deep Sea Research Part I: Oceanographic Research Papers. – 2011. – V. 58. – №. 4. – P. 468-485.
300. Kovalevsky D. V., Bashmachnikov I. L., Alekseev G. V. Formation and decay of a deep convective chimney //Ocean Modelling. – 2020. – V. 148. – P. 101583.
301. Kozlov I. E. et al. ASAR imaging for coastal upwelling in the Baltic Sea //Advances in Space Research. – 2012. – V. 50. – №. 8. – P. 1125-1137.
302. Kozlov I. E. et al. Characteristics of short-period internal waves in the Kara Sea inferred from satellite SAR data //Izvestiya, Atmospheric and Oceanic Physics. – 2015. – V. 51. – P. 1073-1087.
303. Kozlov I. E. et al. Eddies in the Western Arctic Ocean from spaceborne SAR observations over open ocean and marginal ice zones //Journal of Geophysical Research: Oceans. – 2019. – V. 124. – №. 9. – P. 6601-6616.
304. Kozlov I. E., Plotnikov E. V., Manucharyan G. E. Brief Communication: Mesoscale and submesoscale dynamics in the marginal ice zone from sequential synthetic aperture radar observations //The Cryosphere. – 2020. – V. 14. – №. 9. – P. 2941-2947.

305. Kozlov I. E., Atadzhanova O. A. Eddies in the marginal ice zone of Fram Strait and Svalbard from spaceborne SAR observations in winter //Remote Sensing. – 2022. – V. 14. – №. 134. – P. 1-19. https://doi.org/10.3390/rs14010134
306. Kremeur A. S. et al. Impact of the subtropical mode water biogeochemical properties on primary production in the North Atlantic: New insights from an idealized model study //Journal of Geophysical Research: Oceans. – 2009. – V. 114. – №. C7. doi: 10.1029/2008JC005161.
307. Kubryakov A. A., Kozlov I. E., Manucharyan G. E. Large mesoscale eddies in the Western Arctic Ocean from satellite altimetry measurements //Journal of Geophysical Research: Oceans. – 2021. – V. 126. – №. 5. – P. e2020JC016670.
308. Kubryakov, A., Aleskerova, A., Plotnikov, E., Mizyuk, A., Medvedeva, A., & Stanichny, S. Accumulation and Cross-Shelf Transport of Coastal Waters by Submesoscale Cyclones in the Black Sea //Remote Sensing. – 2023. – V. 15. – №. 18 (4386). – P. 1-24.
309. Kudryavtsev V. et al. Quad-polarization SAR features of ocean currents //Journal of Geophysical Research: Oceans. – 2014. – V. 119. – №. 9. – P. 6046-6065.
310. Lai D. Y., Richardson P. L. Distribution and movement of Gulf Stream rings //Journal of Physical Oceanography. – 1977. – V. 7. – №. 5. – P. 670-683.
311. Lamb H. Hydrodynamics. – Cambridge University Press. – 1885. – 604 pp.
312. Lapeyre G., Klein P. Dynamics of the upper oceanic layers in terms of surface quasigeostrophy theory //Journal of physical oceanography. – 2006. – V. 36. – №. 2. – P. 165-176.
313. Large W. G., McWilliams J. C., Doney S. C. Oceanic vertical mixing: A review and a model with a nonlocal boundary layer parameterization //Reviews of geophysics. – 1994. – V. 32. – №. 4. – P. 363-403.
314. Large W. G., Yeager S. G. The global climatology of an interannually varying air–sea flux data set //Climate dynamics. – 2009. – V. 33. – P. 341-364.
315. Lavender K. L., Owens W. B., Davis R. E. The mid-depth circulation of the subpolar North Atlantic Ocean as measured by subsurface floats //Deep Sea Research Part I: Oceanographic Research Papers. – 2005. – V. 52. – №. 5. – P. 767-785.
316. Lazaro C. (2008). The NE Atlantic Ocean from 11 Years of Multi-mission Satellite Altimetry: the Azores Current Case Study: – дис. – University of Porto. Portugal. – 2008.
317. Le Cann B. et al. Observed mean and mesoscale upper ocean circulation in the midlatitude northeast Atlantic //Journal of Geophysical Research: Oceans. – 2005. – V. 110. – №. C7.
318. Le Traon P. Y., Rouquet M. C., Boissier C. Spatial scales of mesoscale variability in the North Atlantic as deduced from Geosat data //Journal of Geophysical Research: Oceans. – 1990. – V. 95. – №. C11. – P. 20267-20285.
319. Le Traon P. Y., Nadal F., Ducet N. An improved mapping method of multisatellite altimeter data //Journal of atmospheric and oceanic technology. – 1998. – V. 15. – №. 2. – P. 522-534.
320. Le Traon P. Y., Ogor F. ERS-1/2 orbit improvement using TOPEX/POSEIDON: The 2 cm challenge //Journal of Geophysical Research: Oceans. – 1998. – V. 103. – №. C4. – P. 8045-8057.
321. Levitus S. et al. Global ocean heat content 1955–2008 in light of recently revealed instrumentation problems //Geophysical Research Letters. – 2009. – V. 36. – №. 7. – P. 1-5
322. L'Hegaret P. et al. Evidence of Mediterranean water dipole collision in the Gulf of Cadiz //Journal of Geophysical Research: Oceans. – 2014. – V. 119. – №. 8. – P. 5337-5359.

323. Losch M. et al. On the formulation of sea-ice models. Part 1: Effects of different solver implementations and parameterizations //Ocean Modelling. – 2010. – V. 33. – №. 1-2. – P. 129-144.
324. Louarn E., Morin P. Antarctic intermediate water influence on Mediterranean Sea water outflow //Deep Sea Research Part I: Oceanographic Research Papers. – 2011. – V. 58. – №. 9. – P. 932-942.
325. Lozier M. S., McCartney M. S., Owens W. B. Anomalous anomalies in averaged hydrographic data //Journal of Physical Oceanography. – 1994. – V. 24. – №. 12. – P. 2624-2638.
326. Lozier M. S., Stewart N. M. On the temporally varying northward penetration of Mediterranean Overflow Water and eastward penetration of Labrador Sea Water //Journal of Physical Oceanography. – 2008. – V. 38. – №. 9. – P. 2097-2103.
327. Lozier M. S. Deconstructing the conveyor belt //Science. – 2010. – V. 328. – №. 5985. – P. 1507-1511.
328. Lumpkin R., Speer K. Global ocean meridional overturning //Journal of Physical Oceanography. – 2007. – V. 37. – №. 10. – P. 2550-2562.
329. Lumpkin R., Johnson G. C. Global ocean surface velocities from drifters: Mean, variance, El Niño–Southern Oscillation response, and seasonal cycle //Journal of Geophysical Research: Oceans. – 2013. – V. 118. – №. 6. – P. 2992-3006.
330. Luo D., Lu Y. The influence of negative viscosity on wind-driven, barotropic ocean circulation in a subtropical basin //Journal of physical oceanography. – 2000. – V. 30. – №. 5. – P. 916-932.
331. Machin F., Hernández-Guerra A., Pelegrí J. L. Mass fluxes in the Canary Basin //Progress in Oceanography. – 2006. – V. 70. – №. 2-4. – P. 416-447.
332. Machin F., Pelegri J. L. Northward penetration of Antarctic intermediate water off Northwest Africa //Journal of Physical Oceanography. – 2009. – V. 39. – №. 3. – P. 512-535.
333. Maddison J. R., Marshall D. P., Shipton J. On the dynamical influence of ocean eddy potential vorticity fluxes //Ocean Modelling. – 2015. – V. 92. – P. 169-182.
334. Makarov V. G., Sokolovskiy M. A., Kizner Z. Doubly symmetric finite-core heton equilibria //Journal of fluid mechanics. – 2012. – V. 708. – P. 397-417.
335. Manucharyan G. E., Thompson A. F. Submesoscale sea ice-ocean interactions in marginal ice zones //Journal of Geophysical Research: Oceans. – 2017. – V. 122. – №. 12. – P. 9455-9475.
336. Mariano A. J., Brown O. B. Efficient objective analysis of dynamically heterogeneous and nonstationary fields via the parameter matrix //Deep Sea Research Part A. Oceanographic Research Papers. – 1992. – V. 39. – №. 7-8. – P. 1255-1271.
337. Mariotti A., Legras B., Dritschel D. G. Vortex stripping and the erosion of coherent structures in two-dimensional flows //Physics of Fluids. – 1994. – V. 6. – №. 12. – P. 3954-3962.
338. Marshall J. Submarine salt lenses //Nature. – 1988. – V. 333. – P. 594-595.
339. Marshall J. et al. A finite-volume, incompressible Navier Stokes model for studies of the ocean on parallel computers //Journal of Geophysical Research: Oceans. – 1997. – V. 102. – №. C3. – P. 5753-5766.
340. Marshall J., Speer K. Closure of the meridional overturning circulation through Southern Ocean upwelling //Nature geoscience. – 2012. – V. 5. – №. 3. – P. 171-180.

341. Martin A. P. et al. Horizontal dispersion within an anticyclonic mesoscale eddy //Deep Sea Research Part II: Topical Studies in Oceanography. – 2001. – V. 48. – №. 4-5. – P. 739-755.
342. Martins C. S., Hamann M., Fiúza A. F. G. Surface circulation in the eastern North Atlantic, from drifters and altimetry //Journal of Geophysical Research: Oceans. – 2002. – V. 107. – №. C12. – P. 1-15.
343. Mauritzen C., Morel Y., Paillet J. On the influence of Mediterranean water on the central waters of the North Atlantic Ocean //Deep Sea Research Part I: Oceanographic Research Papers. – 2001. – V. 48. – №. 2. – P. 347-381.
344. Maximenko N. A. et al. Hydrophysical experiment "Megapolygon-87" in the northwestern Pacific subarctic frontal zone //Journal of Geophysical Research: Oceans. – 2001. – V. 106. – №. C7. – P. 14143-14163.
345. Maze J. P., Arhan M., Mercier H. Volume budget of the eastern boundary layer off the Iberian Peninsula //Deep Sea Research Part I: Oceanographic Research Papers. – 1997. – V. 44. – №. 9-10. – P. 1543-1574.
346. Maze G., Carton X., Lapeyre G. Dynamics of a 2D vortex doublet under external deformation //Regular and Chaotic Dynamics. – 2004. – V. 9. – №. 4. – P. 477-497.
347. Maze G., Marshall J. Diagnosing the observed seasonal cycle of Atlantic subtropical mode water using potential vorticity and its attendant theorems //Journal of physical oceanography. – 2011. – V. 41. – №. 10. – P. 1986-1999.
348. McCartney M. S. The subtropical recirculation of mode waters //Journal of Marine Research . –1982. – 40. Supplement. – P. 427-464.
349. McCartney M. S., Talley L. D. The subpolar mode water of the North Atlantic Ocean //Journal of Physical Oceanography. – 1982. – V. 12. – №. 11. – P. 1169-1188.
350. McDougall T. J. Neutral surfaces //Journal of Physical Oceanography. – 1987. – V. 17. – №. 11. – P. 1950-1964.
351. McDowell S. E., Rossby H. T. Mediterranean water: An intense mesoscale eddy off the Bahamas //Science. – 1978. – V. 202. – №. 4372. – P. 1085-1087. https://doi.org/10.1126/science.202.4372.1085
352. McWilliams J. C. Submesoscale, coherent vortices in the ocean //Reviews of Geophysics. – 1985. – V. 23. – №. 2. – P. 165-182.
353. McWilliams J. C. Vortex generation through balanced adjustment //Journal of Physical Oceanography. – 1988. – V. 18. – №. 8. – P. 1178-1192.
354. McWilliams J. C. Submesoscale currents in the ocean //Proceedings of the Royal Society A: Mathematical, Physical and Engineering Sciences. – 2016. – V. 472. – №. 20160117. – P. 1-32.
355. Meneghello G. et al. Observational inferences of lateral eddy diffusivity in the halocline of the Beaufort Gyre //Geophysical Research Letters. – 2017. – V. 44. – №. 24. – P. 12331-12338.
356. Meneghello G. et al. The ice-ocean governor: Ice-ocean stress feedback limits Beaufort Gyre spin-up //Geophysical Research Letters. – 2018. – V. 45. – №. 20. – P. 11293-11299.
357. Meneghello G. et al. Genesis and decay of mesoscale baroclinic eddies in the seasonally ice-covered interior Arctic Ocean //Journal of Physical Oceanography. – 2021. – V. 51. – №. 1. – P. 115-129.
358. Menemenlis D., Fukumori I., Lee T. Using Green's functions to calibrate an ocean general circulation model //Monthly weather review. – 2005. – V. 133. – №. 5. – P. 1224-1240.

359. Menesguen C. et al. Arms winding around a meddy seen in seismic reflection data close to the Morocco coastline //Geophysical Research Letters. – 2012. – V. 39. – №. 5. – P. 1-6
360. Mensa J. A. et al. Surface drifter observations from the Arctic Ocean's Beaufort Sea: Evidence for submesoscale dynamics //Journal of Geophysical Research: Oceans. – 2018. – V. 123. – №. 4. – P. 2635-2645.
361. Mercier H., De Verdiére A. C. Space and time scales of mesoscale motions in the eastern North Atlantic //Journal of physical oceanography. – 1985. – V. 15. – №. 2. – P. 171-183.
362. Mesqutta S. B., Prahalad Y. S. Statistical stationary states for a two-layer quasi-geostrophic system //Proceedings of the Indian Academy of Sciences-Mathematical Sciences. – Springer India. – 1999. – V. 109. – P. 107-115.
363. Meunier P., Le Dizes S., Leweke T. Physics of vortex merging //Comptes Rendus Physique. – 2005. – V. 6. – №. 4-5. – P. 431-450.
364. Meunier T. et al. Tracer stirring around a meddy: The formation of layering //Journal of Physical Oceanography. – 2015. – V. 45. – №. 2. – P. 407-423.
365. Mohn, C., White, M., Bashmachnikov, I., Jose, F., Pelegri J.L. Dynamics at an elongated, intermediate depth seamount in the North Atlantic (Sedlo Seamount, 40°20'N, 26°40'W) //Deep Sea Research Part II: Topical Studies in Oceanography. – 2009. – Т. 56. – №. 25. – С. 2582-2592
366. Morel Y. The effect of an upper-thermocline current on intra-thermocline eddies //Journal of physical oceanography. – 1995. – V. 25. – P. 3247-3252.
367. Morel Y., McWilliams J. Evolution of isolated interior vortices in the ocean //Journal of physical oceanography. – 1997. – V. 27. – №. 5. – P. 727-748.
368. Mork K. A., Skagseth Ø. A quantitative description of the Norwegian Atlantic Current by combining altimetry and hydrography //Ocean Science. – 2010. – V. 6. – №. 4. – P. 901-911.
369. Mork K. A., Skagseth Ø., Søiland H. Recent warming and freshening of the Norwegian Sea observed by Argo data //Journal of Climate. – 2019. – V. 32. – №. 12. – P. 3695-3705.
370. Morozov E. A., Kozlov I. E. Eddies in the Arctic Ocean Revealed from MODIS Optical Imagery //Remote Sensing. – 2023. – V. 15. – №. 6. – P. 1608.
371. Morrow R. et al. Divergent pathways of cyclonic and anti-cyclonic ocean eddies //Geophysical Research Letters. – 2004. – V. 31. – №. 24. – P. L24311.
372. Mourino B. et al. Significance of cyclonic SubTropical Oceanic Rings of Magnitude (STORM) eddies for the carbon budget of the euphotic layer in the subtropical northeast Atlantic //Journal of Geophysical Research: Oceans. – 2003. – V. 108. – №. C12.
373. Muller F. L. et al. Monitoring the Arctic seas: How satellite altimetry can be used to detect open water in sea-ice regions //Remote Sensing. – 2017. – V. 9. – №. 6. – P. 551.
374. Muller F. L. et al. Dynamic ocean topography of the northern Nordic seas: a comparison between satellite altimetry and ocean modeling //The Cryosphere. – 2019. – V. 13. – №. 2. – P. 611-626.
375. Mullineau L. S., Mills S. W. A test of the larval retention hypothesis in seamount-generated flows //Deep Sea Research Part I: Oceanographic Research Papers. – 1997. – V. 44. – №. 5. – P. 745-770.
376. Munk W. et al. Spirals on the sea //Proceedings of the Royal Society of London. Series A: Mathematical, Physical and Engineering Sciences. – 2000. – V. 456. – №. 1997. – P. 1217-1280.

377. MUR, Multi-scale Ultra-high Resolution Sea Surface Temperature, provided by Jet Propulsion Laboratory at California Institute of Technology, http://mur.jpl.nasa.gov/InformationText.php.
378. Navarro-Perez E., Barton E. D. Seasonal and interannual variability of the Canary Current //Scientia Marina. – 2001. – V. 65. – №. S1. – P. 205-213.
379. Nencioli F. et al. A vector geometry–based eddy detection algorithm and its application to a high-resolution numerical model product and high-frequency radar surface velocities in the Southern California Bight //Journal of atmospheric and oceanic technology. – 2010. – V. 27. – №. 3. – P. 564-579.
380. New A. L. et al. On the role of the Azores Current in the ventilation of the North Atlantic Ocean //Progress in oceanography. – 2001. – V. 48. – №. 2-3. – P. 163-194.
381. Nguyen A. T., Menemenlis D., Kwok R. Arctic ice-ocean simulation with optimized model parameters: Approach and assessment //Journal of Geophysical Research: Oceans. – 2011. – V. 116. – №. C4.
382. Nilsen F., Gjevik B., Schauer U. Cooling of the West Spitsbergen Current: Isopycnal diffusion by topographic vorticity waves //Journal of Geophysical Research: Oceans. – 2006. – V. 111. – №. C8.
383. Nilsen J. E. Ø., Falck E. Variations of mixed layer properties in the Norwegian Sea for the period 1948–1999 //Progress in Oceanography. – 2006. – V. 70. – №. 1. – P. 58-90.
384. Nof D. On the β-induced movement of isolated baroclinic eddies //Journal of Physical Oceanography. – 1981. – V. 11. – №. 12. – P. 1662-1672.
385. Nof D. Generation of ringlets //Tellus A. – 1993. – V. 45. – №. 4. – P. 299-310.
386. Nolasco R. et al. A high-resolution modeling study of the Western Iberian Margin mean and seasonal upper ocean circulation //Ocean Dynamics. – 2013. – V. 63. – P. 1041-1062.
387. Nost O. A., Isachsen P. E. The large-scale time-mean ocean circulation in the Nordic Seas and Arctic Ocean estimated from simplified dynamics //Journal of Marine Research. – 2003. – V. 61. – №. 2. – P. 175-210.
388. Nurser A. J. G., Bacon S. The Rossby radius in the Arctic Ocean //Ocean Science. – 2014. – V. 10. – №. 6. – P. 967-975.
389. Oliveira P. B. et al. A study of meddies using simultaneous in-situ and satellite observations // Satellites, Oceanograpy and Society (Ed. D. Halpern). – Elsevier, 2000. – V. 63. – P. 125-148.
390. Oliveira P. B. et al. Winter geostrophic currents and eddies in the western Iberia coastal transition zone //Deep Sea Research Part I: Oceanographic Research Papers. – 2004. – V. 51. – №. 3. – P. 367-381.
391. Olson D. B. Rings in the ocean //Annual Review of Earth and Planetary Sciences. – 1991. – V. 19. – №. 1. – P. 283-311.
392. Oort A. H. et al. New estimates of the available potential energy in the world ocean //Journal of Geophysical Research: Oceans. – 1989. – V. 94. – №. C3. – P. 3187-3200.
393. Orsi A. H. et al. Cooling and ventilating the abyssal ocean //Geophysical Research Letters. – 2001. – V. 28. – №. 15. – P. 2923-2926.
394. Orvik K. A. The deepening of the Atlantic water in the Lofoten Basin of the Norwegian Sea, demonstrated by using an active reduced gravity model //Geophysical Research Letters. – 2004. – V. 31. – №. 1. – P. L01306.

395. Oulhen E., Reinaud J. N., Carton X. Formation of small-scale vortices in the core of a large merged vortex //Geophysical & Astrophysical Fluid Dynamics. – 2022. – T. 116. – №. 5-6. – C. 411-432.
396. Owens W. B., Hogg N. G. Oceanic observations of stratified Taylor columns near a bump //Deep Sea Research Part A. Oceanographic Research Papers. – 1980. – V. 27. – №. 12. – P. 1029-1045.
397. Paillet J., Arhan M. Shallow pycnoclines and mode water subduction in the eastern North Atlantic //Journal of Physical Oceanography. – 1996a. – V. 26. – №. 1. – P. 96-114.
398. Paillet J., Arhan M. Oceanic ventilation in the eastern North Atlantic //Journal of physical oceanography. – 1996b. – V. 26. – №. 10. – P. 2036-2052.
399. Paillet J., Mercier H. An inverse model of the eastern North Atlantic general circulation and thermocline ventilation //Deep Sea Research Part I: Oceanographic Research Papers. – 1997. – V. 44. – №. 8. – P. 1293-1328.
400. Paillet J., Arhan M., McCartney M. S. Spreading of Labrador sea water in the eastern North Atlantic //Journal of Geophysical Research: Oceans. – 1998. – V. 103. – №. C5. – P. 10223-10239.
401. Paillet J. et al. Real-time tracking of a Galician Meddy //Geophysical Research Letters. – 1999. – V. 26. – №. 13. – P. 1877-1880.
402. Paillet J. et al. Dynamics and evolution of a northern meddy //Journal of Physical Oceanography. – 2002. – V. 32. – №. 1. – P. 55-79.
403. Pastor M. V. et al. Meridional changes in water mass distributions off NW Africa during November 2007/2008 //Ciencias Marinas. – 2012. – V. 38. – №. 1B. – P. 223-244.
404. Pedlosky J. Ocean circulation theory. – Springer Science & Business Media. – 1998. – 453 pp.
405. Pedlosky J. Geophysical fluid dynamics. – Springer Science & Business Media. – 2013. – 710 pp.
406. Pelegri J. L. et al. Coupling between the open ocean and the coastal upwelling region off northwest Africa: water recirculation and offshore pumping of organic matter //Journal of Marine Systems. – 2005. – V. 54. – №. 1-4. – P. 3-37.
407. Perez F. F. et al. Displacement of water masses and remineralization rates off the Iberian Peninsula by nutrient anomalies //Journal of Marine Research. – 1993. – V. 51. – № 4. – P. 869-892.
408. Perez F. F. et al. Mixing analysis of nutrients, oxygen and dissolved inorganic carbon in the upper and middle North Atlantic Ocean east of the Azores //Journal of Marine Systems. – 1998. – V. 16. – №. 3-4. – P. 219-233.
409. Perez F. F. et al. Mixing analysis of nutrients, oxygen and inorganic carbon in the Canary Islands region //Journal of Marine Systems. – 2001. – V. 28. – №. 3-4. – P. 183-201.
410. Pichevin T., Nof D. The momentum imbalance paradox //Tellus A. – 1997. – V. 49. – №. 2. – P. 298-319.
411. Piedeleu M. et al. An observational study of oceanic eddy generation mechanisms by tall deep-water islands (Gran Canaria) //Geophysical Research Letters. – 2009. – V. 36. – №. 14. – P. 1-5.
412. Piip A. T. Large cells of Mediterranean Water in the Madeira-Canaries region //EOS Transactions-American Geophysical Union . – 1969. – V. 50. – P. 193.

413. Pingree R. D., Le Cann B. Anticyclonic eddy X91 in the southern Bay of Biscay, May 1991 to February 1992 //Journal of Geophysical Research: Oceans. – 1992a. – V. 97. – №. C9. – P. 14353-14367.
414. Pingree R. D., Le Cann B. Three anticyclonic Slope Water Oceanic eDDIES (SWODDIES) in the southern Bay of Biscay in 1990 //Deep Sea Research Part A. Oceanographic Research Papers. – 1992b. – V. 39. – №. 7-8. – P. 1147-1175.
415. Pingree R. D., Le Cann B. A shallow meddy (a smeddy) from the secondary Mediterranean salinity maximum //Journal of Geophysical Research: Oceans. – 1993a. – V. 98. – №. C11. – P. 20169-20185.
416. Pingree R. D., Le Cann B. Structure of a meddy (Bobby 92) southeast of the Azores //Deep Sea Research Part I: Oceanographic Research Papers. – 1993b. – V. 40. – №. 10. – P. 2077-2103.
417. Pingree R. D. The droguing of Meddy Pinball and seeding with ALACE floats //Journal of the Marine Biological Association of the United Kingdom. – 1995. – V. 75. – №. 1. – P. 235-252.
418. Pingree R. D., Sinha B. Dynamic topography (ERS-1/2 and Seatruth) of subtropical ring (STORM 0) in the STORM corridor (32–34 N, eastern basin, North Atlantic Ocean) //Journal of the Marine Biological Association of the United Kingdom. – 1998. – V. 78. – №. 2. – P. 351-376.
419. Pingree R. D., Garcia-Soto C., Sinha B. Position and structure of the Subtropical/Azores Front region from combined Lagrangian and remote sensing (IR/altimeter/SeaWiFS) measurements //Journal of the Marine Biological Association of the United Kingdom. – 1999. – V. 79. – №. 5. – P. 769-792.
420. Pingree R. Ocean structure and climate (Eastern North Atlantic): *in situ* measurement and remote sensing (altimeter) //Journal of the Marine Biological Association of the United Kingdom. – 2002. – V. 82. – №. 5. – P. 681-707.
421. Pollard R. T., Pu S. Structure and circulation of the upper Atlantic Ocean northeast of the Azores //Progress in Oceanography. – 1985. – V. 14. – P. 443-462.
422. Pollard R. T. et al. Vivaldi 1991-A study of the formation, circulation and ventilation of Eastern North Atlantic Central Water //Progress in Oceanography. – 1996. – V. 37. – №. 2. – P. 167-192.
423. Polvani L. M., Zabusky N. J., Flierl G. R. Two-layer geostrophic vortex dynamics. Part 1. Upper-layer V-states and merger //Journal of Fluid Mechanics. – 1989. – V. 205. – P. 215-242.
424. Polvani L. M. Two-layer geostrophic vortex dynamics. Part 2. Alignment and two-layer V-states //Journal of fluid mechanics. – 1991. – V. 225. – P. 241-270.
425. Poole R., Tomczak M. Optimum multiparameter analysis of the water mass structure in the Atlantic Ocean thermocline //Deep Sea Research Part I: Oceanographic Research Papers. – 1999. – V. 46. – №. 11. – P. 1895-1921.
426. Poulain P. M., Warn-Varnas A., Niiler P. P. Near-surface circulation of the Nordic seas as measured by Lagrangian drifters //Journal of Geophysical Research: Oceans. – 1996. – V. 101. – №. C8. – P. 18237-18258.
427. Prater M. D. Observations and hypothesized generation of a meddy in the Gulf of Cadiz. – Technical Report APL-UW TR9210. University of Washington. – 1992. – 132 pp.
428. Prater M. D., Sanford T. B. A meddy off cape St. Vincent. Part I: description //Journal of Physical Oceanography. – 1994. – V. 24. – №. 7. – P. 1572-1586.

429. Price J. F. et al. Mediterranean outflow mixing and dynamics //Science. – 1993. – V. 259. – №. 5099. – P. 1277-1282.
430. Proudman J. On the motion of solids in a liquid possessing vorticity //Proceedings of the Royal Society of London. Series A, Containing Papers of a Mathematical and Physical Character. – 1916. – V. 92. – №. 642. – P. 408-424.
431. Raj R. P. et al. The Lofoten vortex of the Nordic seas //Deep Sea Research Part I: Oceanographic Research Papers. – 2015. – V. 96. – P. 1-14.
432. Raj R. P., Halo I. Monitoring the mesoscale eddies of the Lofoten Basin: i mportance, progress, and challenges //International Journal of Remote Sensing. – 2016. – V. 37. – №. 16. – P. 3712-3728.
433. Raj R. P. et al. Quantifying mesoscale eddies in the Lofoten Basin //Journal of Geophysical Research: Oceans. – 2016. – V. 121. – №. 7. – P. 4503-4521.
434. Raj R. P. et al. Quantifying Atlantic Water transport to the Nordic Seas by remote sensing //Remote sensing of environment. – 2018. – V. 216. – P. 758-769.
435. Raj R. P. et al. Interaction between mesoscale eddies and the gyre circulation in the Lofoten Basin //Journal of Geophysical Research: Oceans. – 2020. – V. 125. – №. 7. – P. e2020JC016102.
436. Redfield A. C. et al. The influence of organisms on the composition of seawater //The sea: Ideas and Observations on Progress in the Study of the Seas (Ed. M.N. Hill). – 1963. – V. 2. – №. 2. – P. 26-77.
437. Reid J. L. On the middepth circulation and salinity field in the North Atlantic Ocean //Journal of Geophysical Research: Oceans. – 1978. – V. 83. – №. C10. – P. 5063-5067.
438. Reinaud J. N., Dritschel D. G. The merger of vertically offset quasi-geostrophic vortices //Journal of Fluid Mechanics. – 2002. – V. 469. – P. 287-315.
439. Reinaud J. N., Carton X. The stability and the nonlinear evolution of quasi-geostrophic hetons //Journal of fluid mechanics. – 2009. – V. 636. – P. 109-135.
440. Reinaud J. N., Carton X. Quasi-geostrophic vortex vertical alignment in near collapse interactions //Geophysical & Astrophysical Fluid Dynamics. – 2023. – V. 117. – №. 5. – P. 292-314.
441. Rhein M., Hinrichsen H. H. Modification of Mediterranean Water in the Gulf of Cadiz, studied with hydrographic, nutrient and chlorofluoromethane data //Deep Sea Research Part I: Oceanographic Research Papers. – 1993. – V. 40. – №. 2. – P. 267-291.
442. Rhines P. B. Waves and turbulence on a beta-plane //Journal of Fluid Mechanics. – 1975. – V. 69. – №. 3. – P. 417-443.
443. Richards C. G., Straneo F. Observations of water mass transformation and eddies in the Lofoten Basin of the Nordic Seas //Journal of Physical Oceanography. – 2015. – V. 45. – №. 6. – P. 1735-1756.
444. Richardson P. L. et al. Tracking three meddies with SOFAR floats //Journal of Physical Oceanography. – 1989. – V. 19. – №. 3. – P. 371-383.
445. Richardson P. L., McCartney M. S., Maillard C. A search for meddies in historical data //Dynamics of Atmospheres and Oceans. – 1991. – V. 15. – №. 3-5. – P. 241-265.
446. Richardson P. L., Tychensky A. Meddy trajectories in the Canary Basin measured during the SEMAPHORE experiment, 1993–1995 //Journal of Geophysical Research: Oceans. – 1998. – V. 103. – №. C11. – P. 25029-25045.

447. Richardson P. L., Wooding C. M. RAFOS float trajectories in Meddies during the Semaphore Experiment, 1993-1995. –Technical Report, 10.1575/1912/81. Woods Hole Oceanographic Institution. – 1999. – P. 0094.
448. Richardson P. L., Bower A. S., Zenk W. A census of Meddies tracked by floats //Progress in Oceanography. – 2000. – V. 45. – №. 2. – P. 209-250.
449. Ripa P. Instability of a solid-body rotating vortex in a two-layer model //Journal of Fluid Mechanics. – 1992. – V. 242. – P. 395-417.
450. Robinson A. R. Overview and Summary of Eddy Science BT–Eddies in Marine Science. Springer. Berlin. – 1983. – P. 3-15.
451. Rodriguez-Marroyo R., Viudez A., Ruiz S. Vortex merger in oceanic tripoles //Journal of Physical Oceanography. – 2011. – V. 41. – №. 6. – P. 1239-1251.
452. Roemmich D., Gilson J. The 2004–2008 mean and annual cycle of temperature, salinity, and steric height in the global ocean from the Argo Program //Progress in Oceanography. – 2009. – V. 82. – №. 2. – P. 81-100.
453. Rosell-Fieschi M., Pelegri J. L., Gourrion J. Zonal jets in the equatorial Atlantic Ocean //Progress in Oceanography. – 2015. – V. 130. – P. 1-18.
454. Rosmorduc V., Hernandez F. Two altimetric satellites minimum are needed for ocean observation and forecasting //AVISO Newsletter. – 2003. – V. 9. – P. 12-14.
455. Rossby T. et al. An isopycnal view of the Nordic Seas hydrography with focus on properties of the Lofoten Basin //Deep Sea Research Part I: Oceanographic Research Papers. – 2009. – V. 56. – №. 11. – P. 1955-1971.
456. Rossby T., Prater M. D., Søiland H. Pathways of inflow and dispersion of warm waters in the Nordic seas //Journal of Geophysical Research: Oceans. – 2009. – V. 114. – №. C4. – P. C04011.
457. Rudels B. et al. Circulation and transformation of Atlantic water in the Eurasian Basin and the contribution of the Fram Strait inflow branch to the Arctic Ocean heat budget //Progress in Oceanography. – 2015. – V. 132. – P. 128-152.
458. Sandalyuk N. V., Bosse A., Belonenko T. V. The 3-D structure of mesoscale eddies in the Lofoten Basin of the Norwegian Sea: A composite analysis from altimetry and *in situ* data //Journal of Geophysical Research: Oceans. – 2020. – V. 125. – №. 10. – P. e2020JC016331.
459. Sandven S., Johannessen O. M., Johannessen J. A. Mesoscale eddies and chimneys in the marginal ice zone //Journal of Marine Systems. – 1991. – V. 2. – №. 1-2. – P. 195-208.
460. Sangra . et al. The Canary Eddy Corridor: A major pathway for long-lived eddies in the subtropical North Atlantic //Deep Sea Research Part I: Oceanographic Research Papers. – 2009. – V. 56. – №. 12. – P. 2100-2114.
461. Sathyendranath S. et al. An ocean-colour time series for use in climate studies: the experience of the ocean-colour climate change initiative (OC-CCI) //Sensors. – 2019. – V. 19. – №. 19. – P. 4285.
462. Schaffer J. et al. A global, high-resolution data set of ice sheet topography, cavity geometry, and ocean bathymetry //Earth System Science Data. – 2016. – V. 8. – №. 2. – P. 543-557
463. Schauer U. et al. Arctic warming through the Fram Strait: Oceanic heat transport from 3 years of measurements //Journal of Geophysical Research: Oceans. – 2004. – V. 109. – №. C6. – P. C06026.

464. Schauer U. et al. Variation of measured heat flow through the Fram Strait between 1997 and 2006 //Arctic–Subarctic Ocean Fluxes: Defining the Role of the Northern Seas in Climate (Eds.Dickson, R.R., Meincke, J., Rhines, P.). – 2008. – P. 65-85.
465. Schauer U., Beszczynska-Möller A. Problems with estimation and interpretation of oceanic heat transport-conceptual remarks for the case of Fram Strait in the Arctic Ocean //Ocean Science. – 2009. – V. 5. – №. 4. – P. 487–494.
466. Schecter D. A., Montgomery M. T. On the symmetrization rate of an intense geophysical vortex //Dynamics of atmospheres and oceans. – 2003. – V. 37. – №. 1. – P. 55-88.
467. Schmidtko S., Johnson G. C., Lyman J. M. MIMOC: A global monthly isopycnal upper-ocean climatology with mixed layers //Journal of Geophysical Research: Oceans. – 2013. – V. 118. – №. 4. – P. 1658-1672.
468. Schmitz W. J. On the World Ocean Circulation. Volume 1. Some Global Features. – Thecnical report No. WHOI-96-03-VOL-1. Woods Hole Oceanographic Institution. – 1996.
469. Schultz Tokos K. S., Rossby T. Kinematics and dynamics of a Mediterranean salt lens //Journal of Physical Oceanography. – 1991. – V. 21. – №. 6. – P. 879-892.
470. Schultz Tokos K. L., Hinrichsen H. H., Zenk W. Merging and migration of two meddies //Journal of Physical Oceanography. – 1994. – V. 24. – №. 10. – P. 2129-2141.
471. Scully M. Computation of helicopter rotor wake geometry and its influence on rotor harmonic airloads : дис. – Massachusetts Institute of Technology. – 1975.
472. Selyuzhenok V. et al. Sea ice volume variability and water temperature in the Greenland Sea //The Cryosphere. – 2020. – V. 14. – №. 2. – P. 477-495.
473. Serra N., Ambar I. Eddy generation in the Mediterranean undercurrent //Deep Sea Research Part II: Topical Studies in Oceanography. – 2002. – V. 49. – №. 19. – P. 4225-4243.
474. Serra N. et al. Observations and laboratory modeling of meddy generation at Cape St. Vincent //Journal of Physical Oceanography. – 2002. – V. 32. – №. 1. – P. 3-25.
475. Serra N., Ambar I., Käse R. H. Observations and numerical modelling of the Mediterranean outflow splitting and eddy generation //Deep Sea Research Part II: Topical Studies in Oceanography. – 2005. – V. 52. – №. 3-4. – P. 383-408.
476. Shapiro G. I., Meschanov S. L., Emelianov M. V. Mediterranean lens Irving after its collision with seamounts //Oceanographic Literature Review. – 1996a. – V. 6. – №. 43. – P. 536
477. Shapiro G. I. et al. Self-similarity of the meddy family in the eastern North Atlantic //Oceanographic Literature Review. – 1996b. – V. 4. – №. 43. – P. 335.
478. Shapiro G. I., Meschanov S. L. Spreading pattern and mesoscale structure of Mediterranean outflow in the Iberian Basin estimated from historical data //Journal of Marine Systems. – 1996. – V. 7. – №. 2-4. – P. 337-348.
479. Shchepetkin A. F. Interaction of turbulent barotropic shallow-water flow with topography //Topographic Effects in the Ocean: Proceedings, ‘Aha Huliko’a Hawaiian Winter Workshop, Honolulu, HI, University of Hawaii at M. – 1995. – P. 225-237.
480. Shoosmith D. R. et al. Discrete eddies in the northern North Atlantic as observed by looping RAFOS floats //Deep Sea Research Part II: Topical Studies in Oceanography. – 2005. – V. 52. – №. 3-4. – P. 627-650.
481. Siedler G., Gould J., Church J. A. Ocean circulation and climate: observing and modelling the global ocean. – International Geophysics Series. Elsevier. – 2001. – P. 1-715.

482. Siedler G., Armi L., Müller T. J. Meddies and decadal changes at the Azores Front from 1980 to 2000 //Deep Sea Research Part II: Topical Studies in Oceanography. – 2005. – V. 52. – №. 3-4. – P. 583-604.
483. Siedler G., Kuhl A., Zenk W. The Madeira mode water //Journal of Physical Oceanography. – 1987. – V. 17. – №. 10. – P. 1561-1570.
484. Skagseth O., Drinkwater K. F., Terrile E. Wind-and buoyancy-induced transport of the Norwegian Coastal Current in the Barents Sea //Journal of Geophysical Research: Oceans. – 2011. – V. 116. – №. C8. – P. C08007.
485. Skagseth O. et al. Volume and heat transports to the Arctic Ocean via the Norwegian and Barents Seas //Arctic–Subarctic Ocean Fluxes: Defining the Role of the Northern Seas in Climate. – 2008. – P. 45-64.
486. Smedsrud L. H. et al. The role of the Barents Sea in the Arctic climate system //Reviews of Geophysics. – 2013. – V. 51. – №. 3. – P. 415-449.
487. Smedsrud L. H. et al. Heat in the Barents Sea: Transport, storage, and surface fluxes //Ocean Science. – 2010. – V. 6. – №. 1. – P. 219-234.
488. Smedsrud L. H. et al. Nordic Seas heat loss, Atlantic inflow, and Arctic sea ice cover over the last century //Reviews of Geophysics. – 2022. – V. 60. – №. 1. – P. e2020RG000725.
489. Smeed D. A. Baroclinic instability of three-layer flows Part 1. Linear stability //Journal of Fluid Mechanics. – 1988a. – V. 194. – P. 217-231.
490. Smeed D. A. Baroclinic instability of three-layer flows Part 2. Experiments with eddies //Journal of Fluid Mechanics. – 1988b. – V. 194. – P. 233-259.
491. Smith W. H. F., Sandwell D. T. Global sea floor topography from satellite altimetry and ship depth soundings //Science. – 1997. – V. 277. – №. 5334. – P. 1956-1962.
492. Soiland H., Prater M. D., Rossby T. Rigid topographic control of currents in the Nordic Seas //Geophysical Research Letters. – 2008. – V. 35. – №. 18. – P. L18607.
493. Soiland H., Rossby T. On the structure of the Lofoten Basin Eddy //Journal of Geophysical Research: Oceans. – 2013. – V. 118. – №. 9. – P. 4201-4212.
494. Sokolovskiy M. A. Stability analysis of the axisymmetric three-layered vortex using contour dynamics method //Computational Fluid Dynamics Journal. – 1997a. – V. 6. – №. S2. – P. 133-156.
495. Sokolovskiy M. A. Stability of an axisymmetric three-layer vortex //Izvestiya Atmospheric and Oceanic Physics. – 1997b. – V. 33. – №. 1. – P. 16-26.
496. Sokolovskiy M. A., Verron J. Finite-core hetons: stability and interactions //Journal of Fluid Mechanics. – 2000. – V. 423. – P. 127-154.
497. Sokolovskiy M. et al. On instability of elliptical hetons //150 Years of Vortex Dynamics. – Springer, Dordrecht. – 2009. – P. 133-139.
498. Sokolovskiy M. A., Filyushkin B. N., Carton X. J. Dynamics of intrathermocline vortices in a gyre flow over a seamount chain //Ocean Dynamics. – 2013. – V. 63. – P. 741-760.
499. Sokolovskiy M. A., Verron J. Dynamics of vortex structures in a stratified rotating fluid. – Springer International Publishing. – 2014. – 382 pp.
500. Spall M. A., Chapman D. C. On the efficiency of baroclinic eddy heat transport across narrow fronts //Journal of physical oceanography. – 1998. – V. 28. – №. 11. – P. 2275-2287.
501. Sparnocchia S., Manzella G. M. R., La Violette P. E. The interannual and seasonal variability of the MAW and LIW core properties in the Western Mediterranean Sea //Seasonal and interannual variability of the Western Mediterranean Sea. – 1994. – V. 46. – P. 177-194.

502. Sparrow M. et al. Two circulation regimes of the Mediterranean outflow revealed by Lagrangian measurements //Journal of Physical Oceanography. – 2002. – V. 32. – №. 5. – P. 1322-1330.
503. Spreen G., Kaleschke L., Heygster G. Sea ice remote sensing using AMSR-E 89-GHz channels //Journal of Geophysical Research: Oceans. – 2008. – V. 113. – №. C2. – P. 1–14. https://doi.org/10.1029/2005JC003384
504. Stammer D., Hinrichsen H. H., Käse R. H. Can meddies be detected by satellite altimetry? //Journal of Geophysical Research: Oceans. – 1991. – V. 96. – №. C4. – P. 7005-7014.
505. Stammer D. Global characteristics of ocean variability estimated from regional TOPEX/POSEIDON altimeter measurements //Journal of Physical Oceanography. – 1997. – V. 27. – №. 8. – P. 1743-1769.
506. Stammer D., Cazenave A. (ed.). Satellite altimetry over oceans and land surfaces. – CRC press. – 2017. – 617 pp.
507. Straneo F., Pickart R. S., Lavender K. Spreading of Labrador sea water: an advective-diffusive study based on Lagrangian data //Deep Sea Research Part I: Oceanographic Research Papers. – 2003. – V. 50. – №. 6. – P. 701-719.
508. Sukoriansky S., Dikovskaya N., Galperin B. On the arrest of inverse energy cascade and the Rhines scale //Journal of the Atmospheric Sciences. – 2007. – V. 64. – №. 9. – P. 3312-3327.
509. Sutyrin G. Why compensated cold-core rings look stable //Geophysical Research Letters. – 2015. – V. 42. – №. 13. – P. 5395-5402.
510. Sutyrin G. G. How baroclinic vortices intensify resulting from erosion of their cores and/or changing environment //Ocean Modelling. – 2020. – Т. 156 (101711). – С. 1-6.
511. Swallow J. C. A deep eddy off Cape St Vincent //Deep-Sea Research. – 1969. – P. 285.
512. Taburet G. et al. DUACS DT2018: 25 years of reprocessed sea level altimetry products //Ocean Science. – 2019. – V. 15. – №. 5. – P. 1207-1224.
513. Talley L. D., McCartney M. S. Distribution and circulation of Labrador Sea water //Journal of Physical Oceanography. – 1982. – V. 12. – №. 11. – P. 1189-1205.
514. Taylor G. I. Motion of solids in fluids when the flow is not irrotational //Proceedings of the Royal Society of London. Series A, Containing Papers of a Mathematical and Physical Character. – 1917. – V. 93. – №. 648. – P. 99-113.
515. Thomas L. N. Formation of intrathermocline eddies at ocean fronts by wind-driven destruction of potential vorticity //Dynamics of Atmospheres and Oceans. – 2008. – V. 45. – №. 3-4. – P. 252-273.
516. Thomas L. N. et al. Symmetric instability, inertial oscillations, and turbulence at the Gulf Stream front //Journal of Physical Oceanography. – 2016. – V. 46. – №. 1. – P. 197-217.
517. Timmermans M. L. et al. Eddies in the Canada Basin, Arctic Ocean, observed from ice-tethered profilers //Journal of Physical Oceanography. – 2008. – V. 38. – №. 1. – P. 133-145.
518. Tomczak M., Godfrey J. S. Regional oceanography: an introduction. – Daya books. – 2003. http://gaea.es.flinders.edu.au/~mattom/regoc/pdfversion.html
519. Tomczak M., Large D. G. B. Optimum multiparameter analysis of mixing in the thermocline of the eastern Indian Ocean //Journal of Geophysical Research: Oceans. – 1989. – V. 94. – №. C11. – P. 16141-16149.
520. Torrence C., Compo G. P. A practical guide to wavelet analysis //Bulletin of the American Meteorological society. – 1998. – V. 79. – №. 1. – P. 61-78.

521. Tournadre J. Sampling of oceanic rings by satellite radar altimeter //Journal of Geophysical Research: Oceans. – 1990. – V. 95. – №. C1. – P. 693-697.
522. Travkin V. S., Belonenko T. V. Seasonal variability of mesoscale eddies of the Lofoten Basin using satellite and model data //Russian Journal of Earth Sciences. – 2019. – V. 19. – №. 5. – P. 3.
523. Trodahl M., Isachsen P. E. Topographic influence on baroclinic instability and the mesoscale eddy field in the northern North Atlantic Ocean and the Nordic Seas //Journal of Physical Oceanography. – 2018. – V. 48. – №. 11. – P. 2593-2607.
524. Trodahl M. et al. The regeneration of the Lofoten Vortex through vertical alignment //Journal of Physical Oceanography. – 2020. – V. 50. – №. 9. – P. 2689-2711.
525. Troupin C. et al. High-resolution climatology of the northeast Atlantic using Data-Interpolating Variational Analysis (DIVA) //Journal of Geophysical Research: Oceans. – 2010. – V. 115. – №. C8.
526. Tsuchiya M. Circulation of the Antarctic intermediate water in the North Atlantic Ocean //Journal of Marine Research. – 1989. – V. 47. – №. 4. – P. 747-755.
527. Tsuchiya M., Talley L. D., McCartney M. S. An eastern Atlantic section from Iceland southward across the equator //Deep Sea Research Part A. Oceanographic Research Papers. – 1992. – V. 39. – №. 11-12. – P. 1885-1917.
528. Tychensky A., Carton X. Hydrological and dynamical characterization of meddies in the Azores region: a paradigm for baroclinic vortex dynamics //Journal of Geophysical Research: Oceans. – 1998. – V. 103. – №. C11. – P. 25061-25079.
529. Van Aken H. M. The hydrography of the mid-latitude northeast Atlantic Ocean: I: The deep water masses //Deep Sea Research Part I: Oceanographic Research Papers. – 2000a. – V. 47. – №. 5. – P. 757-788.
530. Van Aken H. M. The hydrography of the mid-latitude northeast Atlantic Ocean II: The intermediate water masses //Deep-Sea Research I. – 2000b. – V. 47. – P. 789-824.
531. Van Aken H. M. The hydrography of the mid-latitude northeast Atlantic Ocean—Part III: The subducted thermocline water mass //Deep Sea Research Part I: Oceanographic Research Papers. – 2001. – V. 48. – №. 1. – P. 237-267.
532. Van Geffen J., Davies P. A. A monopolar vortex encounters an isolated topographic feature on a β-plane //Dynamics of atmospheres and oceans. – 2000. – V. 32. – №. 1. – P. 1-26.
533. van Leeuwen P. J. The propagation mechanism of a vortex on the β plane //Journal of Physical Oceanography. – 2007. – V. 37. – №. 9. – P. 2316-2330.
534. Vandermeirsch F. O., Carton X. J., Morel Y. G. Interaction between an eddy and a zonal jet: Part II. Two-and-a-half-layer model //Dynamics of Atmospheres and Oceans. – 2003a. – V. 36. – №. 4. – P. 271-296.
535. Vandermeirsch F. O., Carton X. J., Morel Y. G. Interaction between an eddy and a zonal jet: Part II. Two-and-a-half-layer model //Dynamics of Atmospheres and Oceans. – 2003b. – V. 36. – №. 4. – P. 271-296.
536. Velasco Fuentes O. U., Van Heijst G. J. F. Collision of dipolar vortices on a β plane //Physics of Fluids. – 1995. – V. 7. – №. 11. – P. 2735-2750.
537. Verron J. Topographic eddies in temporally varying oceanic flows //Geophysical & Astrophysical Fluid Dynamics. – 1986. – V. 35. – №. 1-4. – P. 257-276.
538. Vesman A. V., Bashmachnikov I. L., Golubkin P. A., Raj R. The coherence of the oceanic heat transport through the Nordic seas: Oceanic heat budget and interannual variability //Russian Journal of Earth Sciences. – 2023. – V. 23. – №. 3. – P. 1-26.
539. Visbeck M., Marshall J., Jones H. Dynamics of isolated convective regions in the ocean //Journal of Physical Oceanography. – 1996. – V. 26. – №. 9. – P. 1721-1734.

540. Volkov D. L., Lee T., Fu L. L. Eddy-induced meridional heat transport in the ocean //Geophysical Research Letters. – 2008. – V. 35. – №. 20.
541. Volkov D. L., Fu L. L. On the reasons for the formation and variability of the Azores Current //Journal of Physical Oceanography. – 2010. – V. 40. – №. 10. – P. 2197-2220.
542. Volkov D. L., Pujol M. I. Quality assessment of a satellite altimetry data product in the Nordic, Barents, and Kara seas //Journal of Geophysical Research: Oceans. – 2012. – V. 117. – №. C3.
543. Volkov D. L., Belonenko T. V., Foux V. R. Puzzling over the dynamics of the Lofoten Basin-a sub-Arctic hot spot of ocean variability //Geophysical Research Letters. – 2013. – V. 40. – №. 4. – P. 738-743.
544. Volkov D. L., Kubryakov A. A., Lumpkin R. Formation and variability of the Lofoten basin vortex in a high-resolution ocean model //Deep Sea Research Part I: Oceanographic Research Papers. – 2015. – V. 105. – P. 142-157.
545. von Appen W. J., Schauer U., Somavilla R. et al. Exchange of warming deep waters across Fram Strait //Deep Sea Research Part I: Oceanographic Research Papers. – 2015. – V. 103. – P. 86-100.
546. von Appen W. J. V., Schauer U., Hattermann T., Beszczynska-Möller A. Seasonal cycle of mesoscale instability of the West Spitsbergen Current //Journal of Physical Oceanography. – 2016. – V. 46. – №. 4. – P. 1231-1254.
547. Walczowski W. Atlantic water in the nordic seas //Properties, Variability, Climatic Importance, GeoPlanet: Earth and Planetary Sciences (Berlin: Springer International Publishing). – 2014. – V. 174.
548. Wang G., Dewar W. K. Meddy–seamount interactions: implications for the Mediterranean salt tongue //Journal of physical oceanography. – 2003. – V. 33. – №. 11. – P. 2446-2461.
549. Wang Q., Danilov S., Sidorenko D. et al. The Finite Element Sea Ice-Ocean Model (FESOM) v. 1.4: formulation of an ocean general circulation model //Geoscientific Model Development. – 2014. – V. 7. – №. 2. – P. 663-693.
550. Wang Q., Koldunov N. V., Danilov S. et al. Eddy kinetic energy in the Arctic Ocean from a global simulation with a 1-km Arctic //Geophysical Research Letters. – 2020. – V. 47. – №. 14. – P. e2020GL088550.
551. Wang Z. F., Sun L., Li Q. Y., Cheng H. Two typical merging events of oceanic mesoscale anticyclonic eddies //Ocean Science. – 2019. – V. 15. – №. 6. – P. 1545-1559.
552. Weber H. J., Arfken G. B. Essential mathematical methods for physicists, ISE. – Elsevier, 2003.
553. Wekerle C., Wang Q., von Appen W. J. et al. Eddy-resolving simulation of the Atlantic water circulation in the Fram Strait with focus on the seasonal cycle //Journal of Geophysical Research: Oceans. – 2017. – V. 122. – №. 11. – P. 8385-8405.
554. Wekerle C., Hattermann T., Wang Q. et al. Properties and dynamics of mesoscale eddies in Fram Strait from a comparison between two high-resolution ocean–sea ice models. Ocean Science. – 2020. – V. 16. – №. 5. – P. 1225-1246.
555. White M., Bashmachnikov I., Aristegui J., Martins A. Chapter 4. Physical Processes and Seamount Productivity. In: "Seamounts: Ecology, Conservation and Management" (eds. Pitcher, T.J., Morato, T., Hart, P.J.B., Clark, M.R., Haggan, N. and Santos, R.S.). Fish and Aquatic Resources Series, Blackwell, Oxford, UK, ISBN: 9781405133432, 2007. 65-84 pp.
556. Wright D. G. On the stability of a fluid with specialized density stratification. Part I: Baroclinic instability and constant bottom slope //Journal of Physical Oceanography. – 1980. – V. 10. – №. 5. – P. 639-666.
557. Wu J. Z., Ma H. Y., Zhou M. D. Vorticity and vortex dynamics. Springer, Berlin, 2007. 776 p.
558. Wunsch, C. The ocean circulation inverse problem //Cambridge Univ. Press, New York, 1996. 442 pp.

559. Wunsch C. Where do ocean eddy heat fluxes matter? //Journal of Geophysical Research: Oceans. – 1999. – V. 104. – №. C6. – P. 13235-13249.
560. Wunsch C. Ocean observations and the climate forecast problem //International Geophysics. – Academic Press, 2002. – V. 83. – P. 233-245.
561. Wunsch C., Ferrari R. Vertical mixing, energy, and the general circulation of the oceans //Annu. Rev. Fluid Mech. – 2004. – V. 36. – P. 281-314.
562. Wyrtki K., Magaard L., Hager J. Eddy energy in the oceans //Journal of Geophysical Research. – 1976. – V. 81. – №. 15. – P. 2641-2646.
563. Yashayaev I., Seidov D. The role of the Atlantic Water in multidecadal ocean variability in the Nordic and Barents Seas //Progress in Oceanography. – 2015. – V. 132. – P. 68-127.
564. Yu L. S., Bosse A., Fer I. et al. The Lofoten Basin eddy: Three years of evolution as observed by Seagliders //Journal of Geophysical Research: Oceans. – 2017. – V. 122. – №. 8. – P. 6814-6834.
565. Zabusky N. J., Hughes M. H., Roberts K. V. Contour dynamics for the Euler equations in two dimensions //Journal of computational physics. – 1979. – V. 30. – №. 1. – P. 96-106.
566. Zatsepin A., Kubryakov A., Aleskerova A. et al. Physical mechanisms of submesoscale eddies generation: evidences from laboratory modeling and satellite data in the Black Sea //Ocean dynamics. – 2019. – V. 69. – P. 253-266.
567. Zenk W., Schultz Tokos K., Boebel O. New observations of meddy movement south of the Tejo Plateau //Geophysical Research Letters. – 1992. – V. 19. – №. 24. – P. 2389-2392.
568. Zhurbas V., Väli G., Kuzmina N. Rotation of floating particles in submesoscale cyclonic and anticyclonic eddies: a model study for the southeastern Baltic Sea //Ocean Science. – 2019. – V. 15. – №. 6. – P. 1691-1705.
569. Zou S., Bower A. S., Lozier M. S., Furey H. H. Deep ocean circulation in the subpolar North Atlantic observed by acoustically-tracked floats //Progress in Oceanography. – 2023. – V. 211. – P. 102975.